Band Edge Spectroscopy of CdSe Quantum Dots

by

Masaru Kenneth Kuno

B.A. Chemistry
Washington University in St. Louis (1993)

Submitted to the Department of Chemistry
in partial fulfillment of the requirements for the degree of

Doctor of Philosophy

at the

MASSACHUSETTS INSTITUTE OF TECHNOLOGY

September 1998

Author .....
Department of Chemistry
July 7, 1998

Certified by .....
Moungi G. Bawendi
Professor of Chemistry
Thesis Supervisor

Accepted by .....
Dietmar Seyferth
Chairman, Department Committee on Graduate Students

Band Edge Spectroscopy of CdSe Quantum Dots

by

Masaru Kenneth Kuno

Submitted to the Department of Chemistry
on July 7, 1998, in partial fulfillment of the
requirements for the degree of
Doctor of Philosophy

Abstract

In this thesis, I describe work done to understand the band edge exciton fine structure of CdSe quantum dots (QDs). These QDs or nanocrystallites are the result of recent synthetic efforts in the Bawendi group to produce nearly monodisperse nanocrystalline materials. The QDs are roughly spherical in shape and range in size from 10 to 50 Å in radius. A number of optical experiments have been conducted on the material to understand its optical properties, particularly, the absorption and luminescence. However, several longstanding questions remain. Among them is the origin of the material's band edge luminescence. The emission is unusual because it displays long (μs) lifetimes and exhibits a characteristic, size dependent, Stokes shift. As a consequence, many past studies have implicated the surface as the origin of the emission. In this respect, the surface localization of photogenerated carriers qualitatively explains both the long lifetimes and redshift of the luminescence.

Recent theoretical and experimental studies, however, have suggested that the emission arises from an intrinsic core state analogous to a triplet state in small molecules. We describe the theoretical modeling of the QD electronic structure including the effects of shape, crystal field and the electron-hole exchange interaction. When all symmetry breaking effects are considered, we predict the presence of five fine structure states underlying the band edge exciton rather than an eightfold degenerate exciton ground state. Following this, we intentionally modify the surface of the nanocrystallites to see the effect this has on the luminescence. Our results suggest that, to a large extent, the surface plays little role in the energetics of the emission. For QDs passivated with different organic and inorganic ligands we find little or no change in values of the "resonant" and "non-resonant" Stokes shift. This strongly supports the above mentioned fine structure model. Subsequent chapters take the proposed theory a step further, using it to explain the unusual behavior of the nanocrystallites subjected to an external magnetic field. The last two chapters pose the question of what happens when the QDs are intentionally doped with a paramagnetic impurity such as manganese. We expected that spin interactions between

host and dopant will result in interesting optical phenomena such as the activation of dark excitons as well as shifts in fine structure energies due to an exchange induced mixing of states.

Thesis Supervisor: Moungi G. Bawendi
Title: Professor of Chemistry

This doctoral thesis has been examined by a committee of the Department of Chemistry as follows:

Robert W. Field .....
Chairman

Moungi G. Bawendi .....
Thesis Supervisor

Robert G. Griffin .....

To my parents

Goro and Yoshiko Kuno

Acknowledgments

This thesis would not be complete if it were void of my "outside lab" experiences at MIT. I first want to thank my advisor, Moungi, for his constant support and help during my time here. I've learned much from you and, yes, I'll take you up on that ride back to lab.[1] Sasha has always been a pillar of knowledge and always receptive to us experimentalists. I truly enjoyed working with you. Theory never looked so good.

I also want to thank the citizens of 2-081, 2-077 both past and present. David and Chris were always willing to answer my questions. They also showed me the MIT way of doing work. Manoj taught me (although not too successfully) how to be politically savy. He also showed me the great date spots in Boston/Cambridge. Lol, imagine that, the blind leading the blind. We should run the magnet again for old times sake. Bashir showed me that it takes all kinds to make the world go around. See you at Friendly's fellow third worldly. How long is a Dabbous? Ann, I think we rode the same boat together doing perturbation spectroscopy. You've shown me that there is life after Stark horrors and Peter Zeeman. Cherie, my blood pressure will never be the same :) let's try this again. Dean, you're an excellent person. I'm amazed that you had the patience to find all the "secrets" in our two man Doom adventures. Jin-Kyu, showed me the virtues of special side dishes, although in my case, that was 90 cents extra at Walker. Hedi, I think we went through a lot together, from our Corning "let's kick @ss" presentation to our frequent "intellectual" discussions. I admire your positive outlook on things. Thanks for all the support both past and present. I'll network your PC anyday.

Fred, we probably should be called the survivors of experiments gone awry. I will long remember our endless PLE/FLN scans, superfluid runs, EPR crashes and magnet popsicles. Thanks for being there each and every time. Steve, you are probably the most organized fellow I've ever met. I'm going to have to start coming in at 7 every morning and get a basketball. Then will I know the meaning of success. Catherine, we should have done the Miracle of Science thing more often. I wish you the best of luck. Dima, no thesis would be complete without some reference to "the man" or the material of the future. Lab would have been too uneventful without your frequent witty comments or "insightful" interpretations. Wing, I will always wonder what you are doing up all night, every night. I should make it a point to come in at 4 AM one day and find out. Ken and Vic, we just met but I trust that I will soon come to hear of your good deeds. Robert, lol, I think that you are the living embodiment of the uncertainty principle. Maybe we will play baseball together one day.

MMOAS has always been an important insitution while here. The Friday night showings in the Andrew St. cineplex were always fun, albeit, no HPS4000 sound system (80% more power, 90% less distortion). David, Kevin, Doug, Brett, Kerry, MIT Monopoly was terribly decadent. I'll always remember that the key to success is to stay liquid! We should have more April blizzards. Oh, and profit sharing should be legalized. Thanks for the good times.

I've been priviledged to have wonderful classmates while here. Dora, Kerstin, Kevin, David, Rose, James, Henry, and Chad made working on problem sets more enjoyable. Learning to complete the square is so important! How we survived the Nelson computer project is still a mystery to this day. Outside lab, seeing the leaves change color, ice hockey and the trips to the beach were great opportunities to get out and see sunlight.

Finally, I want to thank all the inhabitants of the basement/first floor who have made being here an interesting and memorable experience. The Nelson group past and present. (Lisa and John, Yang [my ride one cold and rainy Christmas day], Dutch [my 5.33 partner in crime :)], Marc, Greg, Tim, Richard [Hey, I finally got you to say hi :)], Rebecca and all those Japanese postdocs, here one day gone the next. The Field group past and present. (Jon O'Brien, Ilia, Leah, Michelle, Selen, Richard, Sergey, and Jason [Only tornado or earthquake left!]) The Ceyer group past and present. (David and Ted, Matt, Judson, Stacy) Last but not least, are the cryogenic guys, especially Don,

[1] In reference to "The Rock"

who kept those dewars coming. None of the experiments could have been done without you.

Contents

List of Figures

List of Tables

Call me Ishmael. Some years ago—never mind how long precisely—having little or no money in my purse, and nothing particular to interest me on shore, I thought I would sail about a little and see the watery half of the world.

Herman Melville, *Moby Dick*

Chapter 1

Introduction

1.1 Quantum Dots

Semiconductor quantum dots (QDs) are novel materials that span the gap between molecules and bulk compounds. They have sizes ranging from 10 to 100 Å in radius and exhibit interesting optical/electrical properties (quantum confinement effects). This is a result of the spatial confinement of excitations when the physical size of the QD is comparable to or smaller than the bulk exciton Bohr radius. One of the better known confinement effects is the blueshift of the absorption with decreasing size. This effect as well as other features due to quantum confinement are described in excellent review articles by Brus and Alivisatos.[1, 2, 3, 4]

Quantum dots may play a role in future generations of optical and electrical devices. Among proposed uses for nanocrystallites are light emitting diodes [5, 6, 7], optical switches, lasing materials [8], and single electron transistors [9, 10]. One property that can be readily exploited is the size dependent luminescence of the

nanocrystallites. The band edge luminescence of CdSe QDs can be tuned continuously through the visible with quantum efficiencies exceeding 50% in some cases. The luminescence is also spectrally narrow (typically 30-40 nm) so that a host of colors can be realized simply by varying the size of the nanocrystallite.

Fundamentally, QDs promise to let us study the evolution of bulk semiconductor properties from that of atoms simply by varying the size of the nanocrystallite. Properties such as the formation of bulk bands and their angular momentum/spin description can be investigated. To this end, a number of studies have been conducted on the size dependent absorption and emission of CdSe QDs.[11, 12, 13, 14, 15]

However, the investigation of size dependent effects in semiconductors has long been an active area of research. Beginning in the late 70's a number of studies focused on the size dependent properties of quasi two dimensional materials.[16, 17] These systems later became known as quantum wells (QWs) and are composed of a thin layer of semiconducting material sandwiched between two insulating layers.

When the physical dimensions of the QW are comparable to the natural length scale of the electron-hole pair, confinement of photo-excited carriers occurs along the direction perpendicular to the plane of the semiconducting material. This is analogous to the problem of a particle in a one dimensional box where the length of the box is the z axis. There are two (electronic) degrees of "freedom" within the plane of the semiconductor, giving the name, "two dimensional material".

Quantum wires were developed later and are examples of "one" dimensional materials. In these systems, confinement of excited carriers occurs along two dimensions, leaving one degree of freedom, the length of the wire. Typical systems

include GaAs/AlGaAs wire structures made by MBE and other epitaxial growth techniques.[18, 19]

Quantum dots are the latest manifestation in this trend towards reduced dimensionality. They exhibit confinement in all three dimensions leaving zero degrees of freedom for the "trapped" electron and hole. These systems are called "zero dimensional" materials and are also referred to as "artificial" atoms.[20]

Figure 1-1 is a schematic showing the loss in dimensionality as we progress from quantum wells to quantum wires to quantum dots.

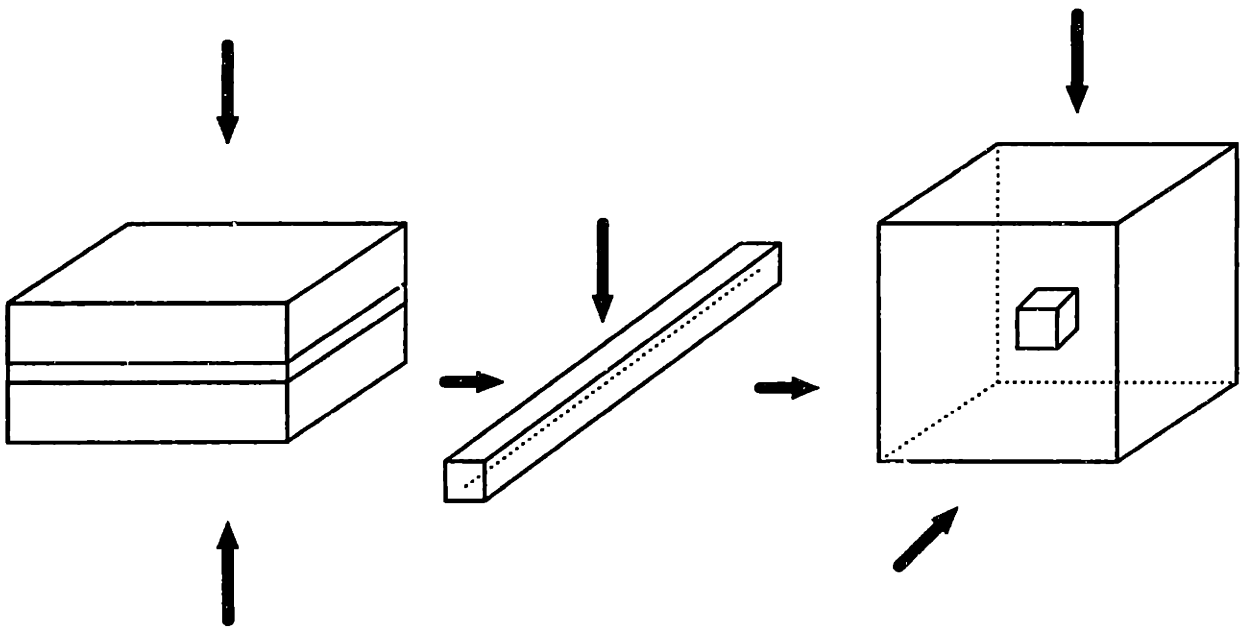

Figure 1-1: From left to right: quantum well, quantum wire, and quantum dot. The arrows show the degree of confinement within each structure. The well is the thin semiconductor slab sandwiched between two thicker insulating layers. The wire is the dotted structure confined in two dimensions. The QD is a small box surrounded in all three dimensions by a higher band gap material or insulator.

1.2 Preparation of QDs

Historically, QDs were first discovered in doped silicate glasses by Ekimov and Onushchenko.[21, 22, 23, 24] A supersaturated (solid) solution of copper and chlorine compounds in glass was heated at high temperatures resulting in the precipitation of CuCl. The initial size of the nuclei was found to depend on the concentration of precursors and the temperature of the melt. Growth of the nanocrystallites was carried out at temperatures ranging from 550 to 700°C. By carefully monitoring the heat treatment, Ekimov and Onushchenko were able to systematically create CuCl QDs with radii ranging from tens to hundreds of Angstroms.

Today, a wide variety of methods are available for making QDs. New techniques based on photo-lithography, x-ray lithography, ion implantation, sonication, reduction of metal precursors and growth in restricted environments are being developed. Some of the more common ones are listed below.[1]

1.2.1 Glasses

Growth of QDs in glasses is still used by many in the field. Samples are created by melting silicate glasses at high temperatures. Once molten, the glass is doped with metal salts of the desired semiconducting material. The melt is then rapidly quenched resulting in a discrete temporal nucleation of the semiconductor nanocrystallites. The glass then undergoes a secondary heat treatment with temperatures ranging

[1] An interesting observation is the biosynthesis of CdS QDs. It has been found that certain yeasts produce CdS nanocrystallites in the presence of large amounts of Cd salts as a means of protecting themselves from excess amounts of the heavy metal. These particles are observed to have very narrow size distributions and exhibit a rock-salt structure unlike bulk CdS. Apparently, nature too, has realized the potential boon for nanotechnology! [25]

anywhere from 400 to 1000°C. As with Ekimov and Onushchenko, the average size of the nanocrystallites is determined by the temperature and duration of the secondary heat treatment. Producing QDs in a glass matrix has the advantage that very large nanocrystallites can be supported, up to 100's of Angstroms in radii. In addition, because of the high temperatures used, the material is often very crystalline. A disadvantage, though, is that the particles are trapped within the glass matrix and cannot easily be manipulated after their synthesis. Nanocrystallites made this way include the copper halides, CuCl, CuBr, and the II-VI semiconductors CdS and CdSe.

1.2.2 Inverse Micelles

Wet colloidal synthesis of nanocrystallites is another common way of making QDs.[26, 27] In this preparation, surfactants are used to create small inverse micelles with hydrophillic interiors and hydrophobic exteriors. Metal salts are then introduced into these water pools creating semiconductor nanocrystallites. The material is extracted by adding a passivating agent to the surface of the QDs forcing them to fall out of solution. The powder is collected and redissolved in a suitable solvent. To a first approximation, the average size of the nanocrystallites is determined by the ratio of water to surfactant or "W" value. This preparation is done at room temperature and suffers from problems of poor crystallinity. However, unlike the case of QDs produced in glasses, numerous surface chemistries are possible allowing the post synthesis manipulation of the nanocrystallites into polymers and other hosts. Examples of systems made this way are CdS, CdSe, ZnS, and ZnSe QDs.

1.2.3 Strain-Induced Growth

With the advent of molecular beam epitaxy (MBE) and other epitaxial growth techniques such as metal-organic vapor phase epitaxy (MOVPE), and chemical beam epitaxy (CBE) the strain-induced growth of semiconductor QDs has been achieved.[28, 29, 30, 31] Typical systems include GaAs/AlGaAs and InP/GaInP heterostructures. Growth of the nanocrystallites is based on the lattice mismatch between the semiconductor and its substrate. In the process, a thin film of the semiconductor is grown epitaxially onto another (slightly mismatched) semiconductor. After several monolayers have been deposited, the strain on the thin film changes the mode of growth from within the plane to out of the plane. Small islands are formed generating QDs. This is known as the Stranski-Krastanow growth mechanism.

1.2.4 Pyrolysis, Our Preparation

More recently, high quality CdSe QDs have been created through the pyrolysis of organometallic precursors in a hot coordinating solvent.[32] This synthesis is based on classic colloidal chemistry developed by La Mer. A temporally discrete nucleation is followed by slow controlled growth of the material through Ostwald ripening. In the preparation developed by Murray, the precursors dimethylcadmium ($CdMe_2$) and trioctylphosphine selenide (TOPSe) [dispersed in trioctylphosphine (TOP)] are injected at high temperatures ($\sim 350^{\circ}C$) into trioctylphosphine oxide (TOPO). Decomposition of the precursors leads to the immediate formation of CdSe nuclei. At the same time the temperature of the solution falls because of the amount of TOP introduced ($\sim 50\%$ by volume). Growth of the material is achieved through Ostwald ripening by

raising the temperature back up to $\sim 300^{\circ}C$. In this process, larger nanocrystallites grow at the expense of smaller ones due to a difference in surface free energies which favors larger QDs.

When a desired size is reached (as monitored by the UV/Visible absorption maxima of the first optical feature) the temperature is dropped stopping the growth. The QDs are recovered from the growth solution by adding butanol and methanol to the mixture. The butanol prevents TOPO from solidifying and methanol (a non-solvent) destabilizes the QDs. When sufficient methanol has been added, the nanocrystallites begin to flocculate and fall out of solution. The precipitate can be recovered and redispersed in a "good" solvent such as hexane.

The QDs produced in this manner have a wurtzite crystal structure. They are slightly prolate and have sizes ranging from 10 to 50 Å in radius. The surface of the nanocrystallites are passivated with the organic ligands, TOPO and TOPSe.[32, 33, 34] These ligands can be replaced with other organic and inorganic moieties.[2] The size distribution of the QDs typically ranges from 10-20% in the growth medium and can be reduced to values less than 5% by performing "size selective precipitation".

Size Selective Precipitation

This method is very similar to the way in which the QDs were first extracted from the growth solution. A small amount of butanol is added to the nanocrystallites dispersed in hexane.[3] Methanol is then added dropwise to the mixture to destabilize the QDs. When the Van der Waals attraction between nanocrystallites overcomes

[2]This is the subject of Chapter 3.

[3]The presence of butanol prevents phase separation between hexane and any methanol added to the solution.

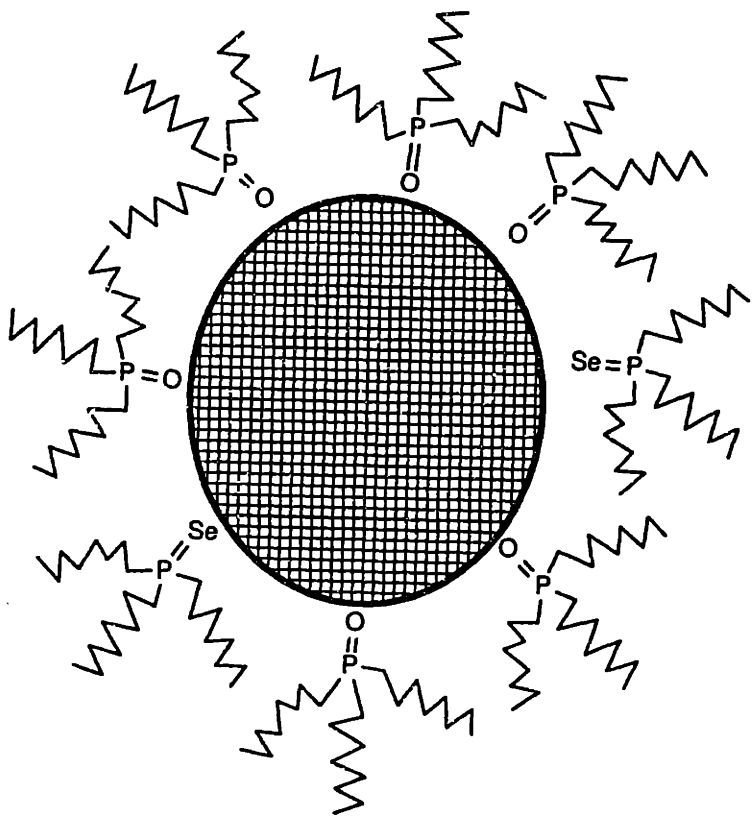

Figure 1-2: A depiction of CdSe QDs produced through the pyrolysis of organometallic precursors. The nanocrystallites have a crystalline (wurtzite) core, are slightly prolate and have sizes ranging from 10 to 50 Å in radii. The surface of the QDs are passivated with the organic ligands, trioctylphosphine oxide (TOPO) and trioctylphosphine selenide (TOPSe).

all repulsive interactions, the particles begin to flocculate. Care is taken not to add too much methanol as this worsens the size distribution. The recovered precipitate is enriched in larger QD sizes and in this manner the distribution is effectively narrowed. Repeated size selective precipitation reduces the size distribution to $\sigma \leq 5\%$.

1.3 Characterization

A number of structural studies have been conducted on QDs to determine their physical properties. Early studies focused on determining the size, shape and size distribution of the nanocrystallites.[22] The crystallinity was also of interest because of its direct influence on optical properties. Work by Avery and Alivisatos have shown melting point depressions in semiconductor QDs, with values up to 50% of their bulk melting temperature.[35] In addition, the phase transition of CdSe QDs from wurtzite to rock salt has been investigated by Tolbert.[36] This study showed that CdSe QDs in the wurtzite phase are direct band gap semiconductors, whereas in the rock salt phase they are indirect band gap materials. More recent work by Carter has focused on characterizing the surface of CdSe nanocrystallites using EXAFS.[37]

A list of common characterization methods and a brief description of each is provided in Appendix A. Several size dependent properties of CdSe QDs are also summarized in Appendix B.

1.4 Optical Studies

Initial optical studies were aimed at correlating the blueshift of the absorption with quantum confinement effects. Simple models were created to explain size dependent shifts in the linear absorption. The non-linear optical properties of the nanocrystallites were also of interest, primarily because of large non-linearities ($\chi^{(3)}$) observed in commercial color glass filters sold by Corning and Schott.[38][4] These filters were found to contain CdS_xSe_{1-x} nanocrystallites with large size distributions and sizes ranging from 100 to 1000 Å in radius.[39] Another major area of interest was the emission of the nanocrystallites with much work devoted towards enhancing the luminescence quantum yield and identifying the origin of the band edge emission. The early investigations of Brus, Henglein and McLendon are particularly informative about the state of the field in the late 80's.[40, 41, 42, 43, 44, 45, 46, 47]

In this section we present several theoretical treatments which reflect the evolution of our understanding about QD optical properties, in particular, those of CdSe nanocrystallites. The particle in a sphere model is described.[48] Further refinements form the basis of the effective mass approximation (EMA) which is the foundation of all electronic structure calculations described in this thesis. Additional refinements, such as the explicit consideration of symmetry breaking effects due to crystal field splitting, QD geometry and the electron-hole exchange interaction complicate EMA results leading to optical fine structure in the linear absorption of the nanocrystallites.

[4]The impetus here being the use of QDs as optical switching and frequency conversion elements in the telecommunications industry. Some of the glasses investigated include: Schott OG530, OG550, OG570, RG645, Corning 2-59, 2-61, 2-64, 3-68, Toshiba R62, R63.

1.4.1 Particle in a Sphere Model

A simple model which qualitatively explains size dependent trends in the QD linear absorption is the particle in a sphere model. In this picture, a particle of mass, m, is confined to a spherical potential with conditions

$$U(r) = \begin{cases} 0 & \text{if } r < a \\ \infty & \text{if } r > a \end{cases} \tag{1.1}$$

where a is the radius of the QD. We solve Schrödinger's equation, $H\Psi = E\Psi$, under these boundary conditions to determine the energies and wavefunctions of the particle. Using the Hamiltonian, $H = \mathbf{p}^2/2m$ ($\mathbf{p} = \hbar/i\ \nabla$), we obtain solutions of the form

$$\Psi_{n,l,m}(r,\theta,\phi) = j_l(k_{n,l}, r)Y_{l,m}(\theta,\phi) \tag{1.2}$$

where $j_l(k_{n,l}, r)$ is the lth order spherical Bessel function and $Y_{l,m}(\theta,\phi)$ are spherical harmonics.[5] The energies are

$$E = \frac{\hbar^2 k_{n,l}^2}{2m} \tag{1.3}$$

where $k_{n,l} = \alpha_{n,l}/a$ and $\alpha_{n,l}$ is the nth zero of j_l.

Since there are two particles in the QD, the electron and the hole which are separate entities in the "strong confinement regime", the calculation is repeated for the other carrier. The strong confinement regime is a term coined by Efros and Efros and represents a range of sizes where the Coulomb interaction between the electron and hole is dominated by the confinement energy of each carrier.[49] This arises

[5]Appendix A lists the spherical Bessel functions and spherical harmonics.

because the Coulomb and confinement interactions have different size dependences, $1/a$ vs $1/a^2$. Each carrier behaves as an individual entity rather than the strongly coupled electron-hole pair or exciton.[6]

Since the problem is separable, the total energy is the sum of the electron and hole contributions. Likewise, the total wavefunction is the product of their wavefunctions. Adding the bulk band gap, E_g, gives QD energies of the form

$$E = E_g + \frac{\hbar^2 k^2_{n_e,l_e}}{2m_e} + \frac{\hbar^2 k^2_{n_h,l_h}}{2m_h} \tag{1.4}$$

where E_g is 1.74 (1.84) eV for CdSe at 300 (10) K, $n_{e(h)}$, $l_{e(h)}$ are labels for the electron (hole) and $m_{e(h)}$ are their respective free masses. The total wavefunction is given by the product

$$\Psi_{tot}(r,\theta,\phi) = \left[j_l(k_{n_e,l_e},r)Y_{l_e,m_e}(\theta,\phi)\right]_e \left[j_l(k_{n_h,l_h},r)Y_{l_h,m_h}(\theta,\phi)\right]_h \tag{1.5}$$

where $j_l(k,r)$ are spherical Bessel functions, $Y_{l,m}(\theta,\phi)$ are spherical harmonics and the subscripts $e(h)$ refer to the electron (hole). In this respect, QD wavefunctions are atomic-like because they exhibit s, p, d... symmetry.

The particle in a sphere model predicts discrete optical transitions and shows that as the size of the box decreases the first excited state moves to higher energies (blueshifts). Since the energies scale as $1/a^2$ the separation between excited states increases with decreasing particle size. These predictions explain observed trends in

[6]In general, the range of sizes defining the strong confinement regime is material dependent and is expressed by the condition $a < a_{ex}$ where a_{ex} is the bulk exciton Bohr radius. There are also other confinement regimes such as the intermediate and weak confinement regimes. They are described by the conditions $a \sim a_{ex}$ and $a \gg a_{ex}$ respectively. In CdSe, $a_{ex} = 56$ Å .

the size dependent linear absorption of the nanocrystallites.

1.4.2 Effective Mass Approximation

How does the particle in a sphere model compare to reality? Not as poorly as one might think. However, one problem with our approximation is that both carriers are treated as free particles when, in reality, both the electron and hole experience a non-zero potential from constituent atoms of the semiconductor.

To overcome this deficiency, we turn to bulk descriptions. In bulk CdSe the electron and hole wavefunctions are written in the form (Bloch's Theorem)

$$\Psi(r) = u(r) \exp\,(i\vec{k} \cdot \vec{r}) \tag{1.6}$$

where $u(r)$ is a unit cell term that reflects the periodic potential felt by the carrier in the crystal. Recall that in the case of real semiconductors, the carriers do not reside in empty space but rather amidst a sea of atoms composing the material. The Bloch function is a way to explicitly consider the influence of the external potential on the wavefunction. The exponential term is the "envelope" part of the wavefunction which is simply a plane wave and would be the wavefunction of a free particle.

The energies are written in the form

$$E_e = \frac{\hbar^2 k^2}{2m^e_{eff}} \quad ; \qquad E_h = -\frac{\hbar^2 k^2}{2m^h_{eff}} \tag{1.7}$$

which is similar to the energies derived for the particle in a sphere. However, one difference is that "effective" masses are used, $m^{e,h}_{eff}$. This is because the kinetic ener-

gies of the electron and hole are influenced by the periodic potential which surrounds them. The effective mass is a way to incorporate the effects of the potential and still retain a simple free particle picture. This is the "effective mass approximation" (EMA).

In terms of the band structure of the material, the above approximation is a simple two band picture. The real band structure of semiconductors is often very complicated but in direct gap semiconductors, where there exists a potential minimum (maximum) near $k = 0$ for both the conduction band and valence band, this is a reasonable approximation. The curvature of the two bands is directly related to the effective mass through equation 1.7.[7] Figure 1-3 is a schematic of the two band effective mass picture.

Now if we go from bulk to QDs, the same picture can be kept *provided* that the nanocrystallite is not too small.[8] Numerically, this means that our approximation will hold only if the size of the QD is much larger than the lattice constant, a_0, of the material. In practice the condition $a \gg 2a_0$ is used. This is one criterion for validity of the EMA approximation when applied to QDs.

Although the periodic potential experienced by the electron and hole remains unaffected, the wavefunctions do change. Since the QD introduces spherical boundary conditions, the carriers cannot exist as plane waves. Rather, the boundary condition forces the electron (hole) wavefunction to vanish at the QD/matrix interface. Since we assume that the QD is large enough on an atomic scale that the periodic potential remains unaffected, the unit cell part of the carrier wavefunction stays the same (see

[7]Take the second derivative of the energies.
[8]Not too big, not too small, but just right.

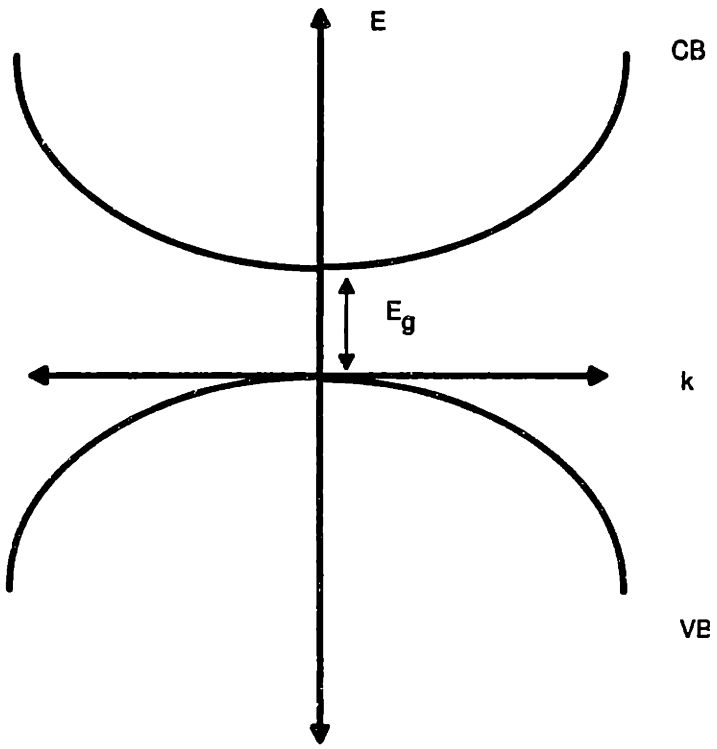

Figure 1-3: Simple two band picture of a direct gap semiconductor. The top parabola, CB, is the conduction band. The bottom parabola, VB, is the valence band. The two are separated by the bulk band gap, E_g. There are a continuum of states in both the valence band and conduction band. The electron energy increases going "up". Similarly, the hole energy increases going "down".

Equation 1.6). The only thing that changes is the envelope part of the wavefunction. It simply becomes the solution to the problem of a particle in a sphere, something we solved earlier.[50]

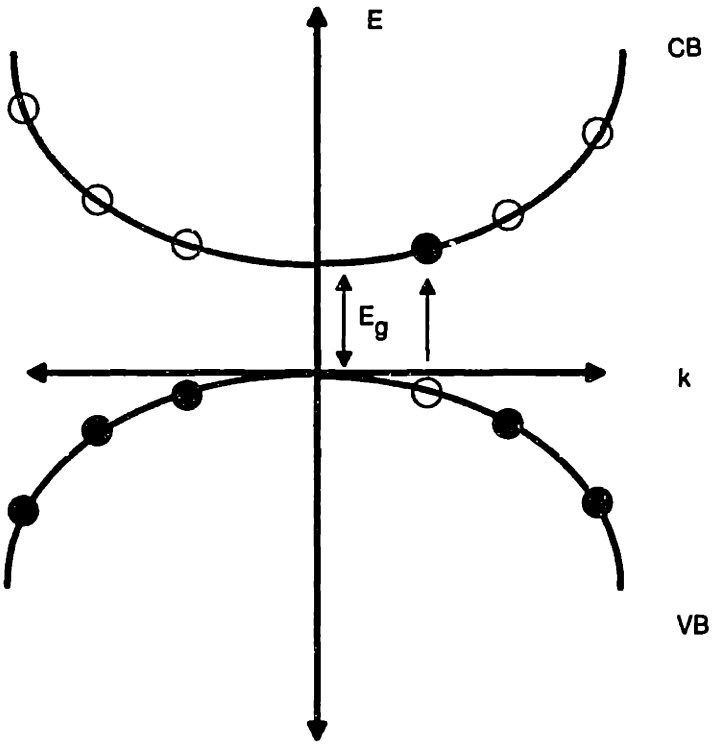

Figure 1-4: Simple two band picture of a direct gap semiconductor under the influence of quantum confinement. Rather than a continuum of states, we obtain discrete states, shown by the open (vacant) and closed (filled) circles. Transitions between the valence and conduction band occurs between these discrete states, shown by the upward pointing arrow. This reflects the conservation of k.

The energies we obtain are of the form:

$$E = E_g + \frac{\hbar^2 k^2_{n_e,l_e}}{2m^e_{eff}} + \frac{\hbar^2 k^2_{n_h,l_h}}{2m^h_{eff}} \tag{1.8}$$

where $n_{e(h)}$ and $l_{e(h)}$ are electron (hole) labels, and $m^{e(h)}_{eff}$ are *effective* electron (hole)

masses. The wavefunctions are:

$$\Psi_{tot}(r,\theta,\phi) = \Big[j_l(k_{n_e,l_e},r)Y_{l_e,m_e}(\theta,\phi)u_c(r)\Big]_e\Big[j_l(k_{n_h,l_h},r)Y_{l_h,m_h}(\theta,\phi)u_v(r)\Big]_h \quad (1.9)$$

where $u_c(r)$ and $u_v(r)$ are the conduction band and valence band unit cell functions.[9] $Y_{l,m}(\theta,\phi)$ are spherical harmonics, $j_l(k_{n,l},r)$ are spherical Bessel functions and, as before, the subscripts e and h refer to the electron and hole respectively.

Transition Probabilities

Transition probabilities can be calculated from the above wavefunctions. The form of the probability is

$$P = |<\Psi_{exc}|e\cdot\hat{p}|0>|^2 \quad (1.10)$$

where $|\Psi_{exc}>$ is the exciton wavefunction, $|0>$ is the vacuum state, e is the polarization vector of the light, and $\hat{p}$ is the momentum operator. Since we assume uncoupled carriers in the strong confinement regime, the probability can be expressed as a transition between a hole state and an electron state. We obtain the equivalent expression,

$$P = |<\Psi_e|e\cdot\hat{p}|\Psi_h>|^2 \quad (1.11)$$

where $\Psi_{e(h)}$ is the uncoupled electron (hole) wavefunction.

Using expressions derived earlier and the fact that $\hat{p}$ acts only on unit cell func-

[9]Chapter 2 provides explicit expressions for these functions.

tions, this simplifies to

$$P = | < u_c|e \cdot \hat{p}|u_v > |^2 \delta_{n_e,n_h} \delta_{l_e,l_h} \tag{1.12}$$

The orthonormality of the spherical Bessel functions and spherical harmonics leads to the conditions $\Delta n = 0$ and $\Delta l = 0$. In effect, transitions only occur between states having the same envelope function.

1.4.3 Additional Refinements

The EMA approximation is probably the simplest model describing the optical properties of QDs (in particular, CdSe nanocrystallites). However, several simplifications made during the course of the calculation are actually important and we will see later on, that they should not be neglected. At this point we focus on CdSe QDs and note that complications arise from the fact that CdSe has more than one valence band.

There are three valence bands in CdSe known as the heavy hole, light hole and split off bands. These three bands are also called the A, B and C bands and are labeled by their angular momentum projection along the c axis of the nanocrystallite ($J_m = \pm 3/2$, $\pm 1/2$ and $\pm 1/2$).[10]

The existence of three bands can be understood as follows. The valence band of CdSe is composed of Se 4p orbitals. In terms of their angular momentum, the orbital contribution is $l = 1$ for a p orbital and the spin contribution is $s = 1/2$. Adding

[10]The "c" or unique axis of the nanocrystallite arises because CdSe has a hexagonal lattice structure. It is elongated along one direction.

the two gives a total momentum (J = l+s) of 3/2 and 1/2 each with projections $J_m = \pm 3/2,\ \pm 1/2$ and $J_m = \pm 1/2$ respectively. Including the spin-orbit interaction raises the energy of the $J = 1/2$ split off band moving it away from the $J = 3/2$ band. Figure 1-5 shows the band structure in this level of complexity. We have a four-fold degenerate band and a two-fold degenerate split off band separated by the spin-orbit splitting, $\Delta_{so} = 0.42$ eV.

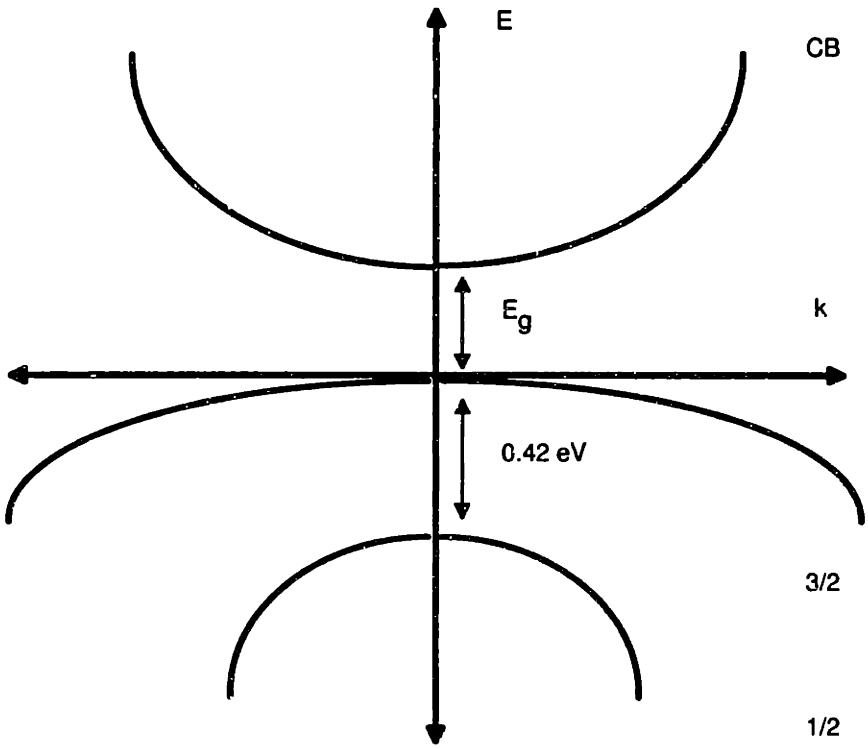

Figure 1-5: Band structure of CdSe when spin orbit coupling is considered. The conduction band is unaffected. The valence band, however, splits into a four-fold degenerate $J = 3/2$ band and a two-fold degenerate $J = 1/2$ band (referred to as the split off band). The separation of the two bands is $\Delta_{so} = 0.42$ eV.

Adding the crystal field further lifts the degeneracy of the $J = 3/2$ band splitting it into its respective projections $J_m = |3/2|$ and $|1/2|$. This is the origin of the heavy hole (A) and light hole (B) bands. However, the magnitude of the crystal field splitting is on the order of 25 meV and is ignored in most theoretical calculations.

(i.e. the material is modeled as cubic) Figure 1-6 is a picture of the three bands when both spin orbit and crystal field interactions are considered.

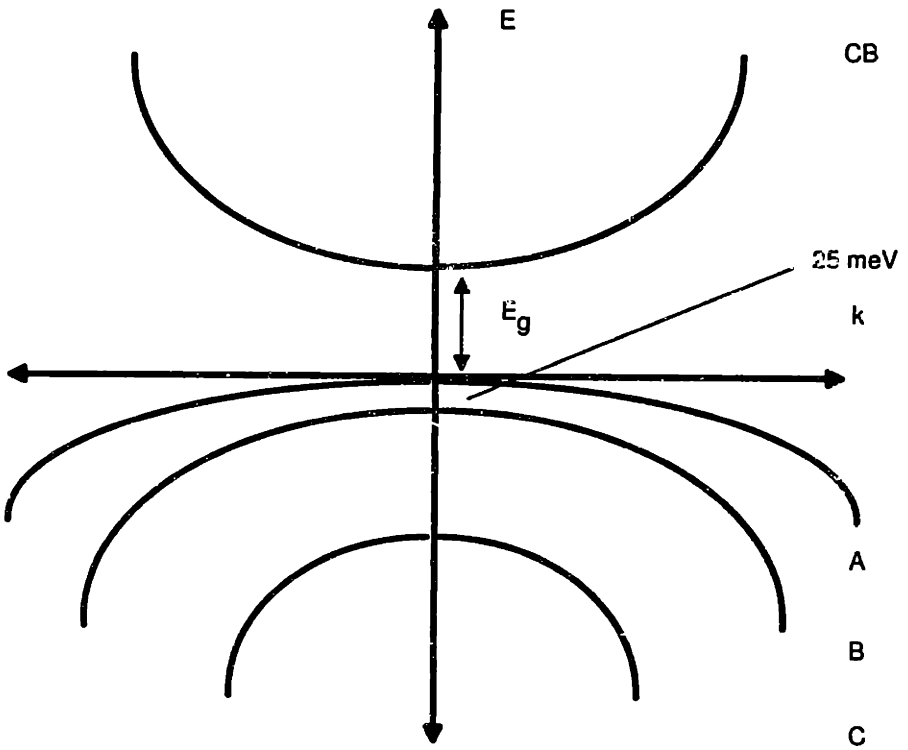

Figure 1-6: Band structure of CdSe when spin orbit coupling and crystal field splitting are considered. Again, the conduction band is relatively unaffected. The valence band splits into three separate bands known as the heavy hole (A), light hole (B) and split off (C) bands. The crystal field splitting between the heavy hole and light hole bands is 25 meV. The splitting of the split off band is 0.42 eV from the top of the valence band. The spin projections of the three bands are $\pm 3/2$, $\pm 1/2$ and $\pm 1/2$ respectively.

To model the energies and wavefunctions in this level of valence band complexity, a number of methods have been developed. An explicit consideration of the valence band complexity strongly affects the final form of the carrier energies and wavefunctions. The $k \cdot p$ method is one approach that has been adopted by Efros and Grigoryan to calculate the energies and wavefunctions of CdSe (CdS) QDs.[51, 15, 52] Solving for the hole wavefunctions involves diagonalizing the 6×6 Luttinger Hamiltonian

under spherical symmetry.

$$\hat{H} = \frac{\hbar^2}{2m_0}(\gamma_1 + \frac{5}{2}\gamma)k^2 - \frac{\hbar^2}{m_0}\gamma(k \cdot J)^2 \tag{1.13}$$

where $\gamma = (2\gamma_2 + 3\gamma_3)/5$, m_0 is the free electron mass, γ_1, γ_2, γ_3 are Luttinger's parameters and J_x, J_y, J_z are 4×4 angular momentum matrices.[53] The electron energies and wavefunctions are approximated using the Kane model which accounts for the non-parabolicity of the conduction band.[54][11] These calculations are described in refs.[15, 51] and more details can be found in Appendix C. An example of a hole wavefunction derived in this approximation is given by

$$\begin{aligned} |\frac{3}{2}, +\frac{3}{2}>^{+} \;=\; & \left(R_{h2en}(r)Y_{0,0} + \frac{1}{\sqrt{5}}R_{h1en}(r)Y_{2,0}\right)|\frac{3}{2}, \frac{3}{2}> \\ & + \left(\frac{2}{\sqrt{10}}R_{h1en}(r)Y_{2,2}\right)|\frac{3}{2}, -\frac{1}{2}> \\ & + \left(-\frac{2}{\sqrt{10}}R_{h1en}(r)Y_{2,1}\right)|\frac{3}{2}, \frac{1}{2}> \\ & + \left(-\frac{1}{\sqrt{5}}R_{sen}(r)Y_{2,1}\right)|\frac{1}{2}, \frac{1}{2}> \\ & + \left(\frac{2}{\sqrt{5}}R_{sen}(r)Y_{2,2}\right)|\frac{1}{2}, -\frac{1}{2}> \end{aligned} \tag{1.14}$$

This is the wavefunction of the "lowest" hole state with total angular momentum projection $F_m = +3/2$. Contributions to the total come from the spherical harmonics and the unit cell terms in kets. The radial contributions R_{h2en}, R_{h1en}, and R_{sen} are spherical Bessel functions.[51, 15]

Historically speaking, this is the so called "spherical approximation" of QD elec-

[11] The non-parabolicity of the conduction band arises from interactions with the valence band.

tronic states. It is the starting point for all electronic structure calculations discussed in this thesis. The QDs are modeled as cubic (no crystal field splitting) and the complicated valence band structure of CdSe is accounted for (e.g. we consider hole wavefunctions of the form shown in Eq. 1.13). In addition, the nonparabolicity of the conduction band is considered. Further refinements to the model are discussed in Chapter 2 and comprise the fine structure model used to explain results described in subsequent chapters.

1.5 The Surface

The spherical model of QD electronic states has been very successful in describing the linear absorption of CdSe nanocrystallites. Up to ten excited states have been assigned in the absorption and theoretical avoided crossings have been confirmed experimentally. However, one unfortunate aspect of the model is that it does not account for the luminescence of the nanocrystallites.

An intriguing observation in QDs is the nearly universal redshift of the emission maxima relative to the first absorption feature. This redshift has been seen not only in CdSe QDs but also in other nanocrystalline systems such as Si, InP, CdS and InGaAs QDs.[55, 56, 57, 58, 59, 60, 61, 12, 62, 13, 63, 64, 44, 65, 66, 67, 68, 69, 30, 70] In general, two types of emission are observed. The first is a very broad (100's nm FWHM), strongly redshifted emission (0.5-1 eV), referred to as "deep" trap luminescence. The second type of emission occurs closer to the band edge. It is much narrower and is called the "band edge" luminescence. In both cases, the redshift indicates that the emitting state (whether band edge or deep trap) differs

from the absorbing state.

However, the presence of a residual size distribution causes a natural redshift of the emission. This happens when samples are excited far from the band edge absorption because, here, the excitation probability is proportional to the number of participating states and therefore to the volume of the nanocrystallite ($\sim a^3$).[64] Since the band edge of larger QDs occurs at lower energies than in smaller nanocrystallites, the effective emission is skewed towards larger sizes.

Despite a natural explanation for a redshifted emission, size selective experiments such as fluorescence line narrowing (FLN), which probe a much smaller subset of QDs, still show an intrinsic *size dependent* redshift of the band edge luminescence. Since theoretical models describing QD excited states do not predict separate absorbing and emitting states, both band edge and deep trap emission have often been attributed to the radiative recombination of surface localized carriers.

In QDs a large fraction of atoms reside on the surface, up to 40% in small nanocrystallites. The presence of impurities, dangling bonds, defects and even the QD analog of bulk surface bands all potentially localize photogenerated carriers. The surface "trapping" of electrons and holes qualitatively explains observed redshifts in the emission. There is some experimental evidence for these surface states as EPR results by Koch [71, 72] have shown the existence of certain dangling bond states which are the likely source of the near-IR emission in porous Si. Recent XPS and NMR investigations on CdSe QDs have also shown that the nanocrystallites are not fully passivated.[73, 74, 34] Theoretical work suggests that these unpassivated cation or anion dangling bond sites create states well within the band gap of the material

leading to a strongly redshifted emission. Luminescence from these surface states is consistent with highly localized carriers and with the "deep" trap emission seen in many QD samples.[75]

The origin of the band edge luminescence is a more challenging problem. In the case of CdSe QDs simple spherical EMA models such as those described above do not explain unusual experimental features of the emission, mainly its size dependent redshift and long radiative lifetimes at low temperatures ($\tau_r \sim 1\mu$s, 10 K). These results are puzzling because many models which properly describe the linear absorption also predict emission behavior similar to the bulk. (The radiative lifetime of bulk CdSe is on the order of several nanoseconds, not microseconds. Shifts in the emission are also not observed.)[12]

Phenomenologically, the band edge luminescence can be explained in terms of a three level system. Figure 1-7 depicts this where a transition from the ground state to the first optically active state is followed by non-radiative relaxation into the final emitting state. The nature of the emitting state is unknown although, traditionally, it has been assigned to the radiative recombination of "shallow"[13] surface-localized carriers. Several other possibilities exist and are described below.

On a brief aside, one experimental result not accounted for by many of the proposed models is the differing magnitudes of the "resonant" and "non-resonant" Stokes shifts seen in photoluminescence (PL) and fluorescence line narrowing (FLN) experiments. This unusual feature of the band edge emission is discussed in more detail in

[12]Here we refer to the intrinsic exciton luminescence and not impurity luminescence or donor-acceptor emission.

[13]By "shallow" we refer to states with similar energies to the absorbing state. "Deep" refers to states well within the band gap and have much larger energy differences.

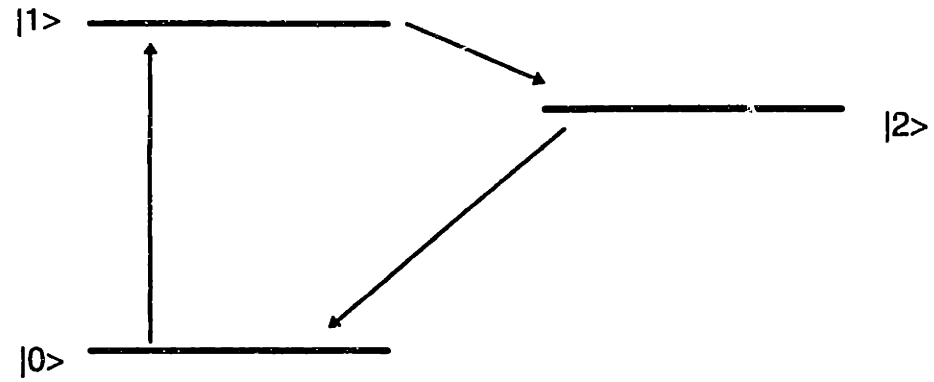

Figure 1-7: General schematic of a three level system that qualitatively reproduces the emission behavior of the nanocrystallites. Absorption of light results in a transition from the ground state, $|0>$, to the first excited state, $|1>$. This is followed by non-radiative relaxation to the emitting state, $|2>$, which may or may not be surface related. Emission then follows to the ground state with a characteristic redshift given by the energy difference between the absorbing and emitting states ($E_{|1>} - E_{|2>}$).

Chapters 2 and 3. The discrepancy arises because, in principle, it should be possible to reproduce the full luminescence (i.e. the non-resonant Stokes shift) by convoluting the line narrowed emission with the intrinsic size distribution of the sample (σ ~5%). However, this is not the case and predicted non-resonant shifts are much smaller than those actually measured.[34] We will see later on that this discrepancy is resolved by the presence of optical fine structure underlying the band edge exciton.[64, 34]

Surface States

The first and most common suggestion is that the band edge emission arises from shallow surface states of the QD. The presence of defects, vacancies, dangling bonds, and the QD analog of bulk surface bands makes this a distinct possibility. Theoretical work on bulk surfaces have shown that shallow surface bands can appear through the surface reconstruction of cadmium and selenium atoms. This surface band is expected

to occur within 0.2 eV of the valence band maximum. Another band arising from hybridized Cd 5s orbitals is predicted to appear within 0.5 eV of the conduction band.[76]

In light of recent results on InP and CdSe QDs, this explanation appears unlikely. Surface modification of these nanocrystallites through HF etching and ligand exchange/overcoating do not show dramatic changes in the energetics of the band edge luminescence.[66, 67, 34] This strongly suggests that the emitting state is unrelated to the surface. In addition, a surface model is inconsistent with results from photoluminescence and fluorescence line narrowing experiments on CdSe QDs where the "non-resonant" and "resonant" Stokes shifts are measured. Chapters 2 and 3 describe this in more detail.

Spatially Forbidden States

Another possibility is that the emitting state is an internal core state but that transitions to and from this state are forbidden due to lack of orbital symmetry. In this regard, the envelope function of the electron and hole wavefunctions have different spatial symmetries (for example, s and p symmetry) Recall that in the simple EMA approximation, our transition probabilities required both initial and final states to have the same envelope function (Equation 1.12). In the case of CdSe, the spherical approximation has shown that the highest hole state has s symmetry. However, using the same approach, Grigoryan showed that the highest hole state in CdS has p symmetry.[51] More recently, Richard has shown that the highest hole state in CdSe QDs can have either s or p symmetry depending on size.[77] For sufficiently

small nanocrystallites, the highest hole state has p symmetry. In effect, transitions between the hole state and the electron state with s symmetry are formally forbidden in small QDs. Since the $k \cdot p$ wavefunctions and energies are sensitive to the actual values of the Luttinger parameters used it is difficult to completely eliminate this possibility. The band edge emission of CdSe QDs may originate from a orbitally forbidden state not observed in the linear absorption.

Dark Exciton Models

The basis for many of these "dark exciton" models is the enhancement of the electron-hole exchange interaction in small nanocrystallites.[75, 78, 79, 55, 80, 81, 82, 83, 84, 85, 86, 87] This is due to the increased overlap of the electron and hole wavefunctions. In bulk CdSe the exchange splitting is on the order of 0.13 meV. However, in QDs it is predicted to become sufficiently enhanced to cause a noticeable splitting in the optical spectra. We consider one of these dark exciton models, in particular, one developed by Efros and Rosen to explain our results.[64] The basis of the model and its key considerations are discussed in the next section.[14]

1.6 Optical Fine Structure

Our work, in collaboration with Al. L. Efros, describes the effects of three symmetry breaking perturbations to the electronic states of the nominally eight-fold degenerate exciton ground state. In particular, we consider crystal field splitting, the

[14]There are currently several dark exciton models being debated. Prominent among them are those by: Calcott/Nash (porous Si), Normura (CdSe), Chamarro/Lavallard (CdSe), Fu/Zunger (InP), and Leung/Whaley (CdSe).

QD shape asymmetry and the electron-hole exchange interaction. The crystal field interaction is important because CdSe has a hexagonal lattice structure. Most theoretical models describe CdSe with a cubic lattice because of the small magnitude of the bulk crystal field splitting, 25 meV. The shape asymmetry is also important because careful TEM and SAXS measurements indicate that the nanocrystallites are not perfectly spherical.[32] In fact, they are slightly prolate with a size dependent ellipticity varying from 0 to 0.3. Finally, the electron-hole exchange interaction is considered because of predicted enhancements in nanometer-sized structures due to the increased overlap of the electron and hole wavefunctions.

When all three effects are considered together, the model predicts that underlying the band edge exciton of CdSe nanocrystallites are five fine structure states. These fine structure states are labeled by their total angular momentum projection (N) along the c axis of the nanocrystallites. There are two doubly degenerate states with projection $N = \pm 1$, two states with projection $N = 0$ and one doubly degenerate state with projection $N = \pm 2$. Figure 1-8 shows the order of the fine structure states where optically active (bright) and optically passive (dark) states are denoted by solid and dashed lines respectively.

An important consequence of the fine structure model is that it predicts that the lowest excited state in CdSe QDs is an optically passive "dark" exciton. Transitions to and from this state are formally forbidden in the electric dipole approximation because changes in angular momentum of two are required. This accounts for the long radiative lifetimes at low temperatures; the emission originates from a state having a good amount of triplet character. The model also explains the size dependent redshift

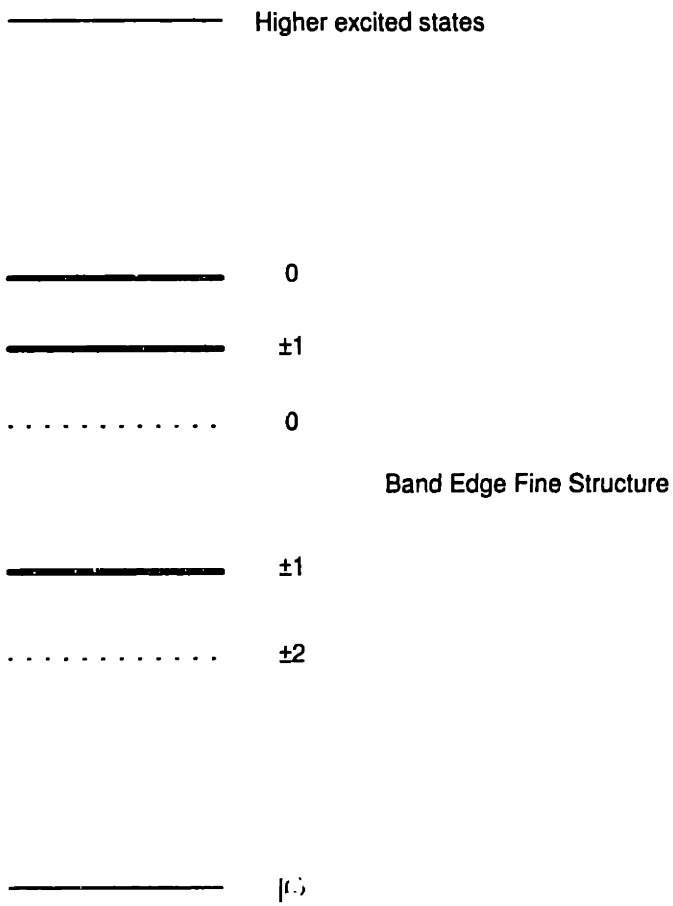

Figure 1-8: Predicted band edge fine structure of CdSe QDs. The shape asymmetry, crystal field and electron-hole exchange interaction split the eight-fold degenerate exciton state (in spherical symmetry) into five fine structure states. Each state is labeled by its angular momentum projection along the c axis of the nanocrystallite. Three of the states are optically active (solid line) and two are optically passive (dashed line).

seen in resonant and non-resonant excitation experiments through the optical fine structure. In addition, it accounts for the unusual behavior of the nanocrystallites in the presence of a magnetic field (i.e. decreased radiative lifetimes with increasing magnetic field and changes in the Huang-Rhys parameter) as well as size dependent changes in the sign of the second excited state's g factor. We describe the good agreement between experiment and theory in subsequent chapters.

1.7 The Future

QDs have been studied for close to 20 years now. There is still much work being done in terms of the synthesis of high quality semiconductor and metal nanocrystallites. The best systems, to date, in terms of size distribution, are CdSe [32], CdS [88, 22], InP [67], Ag [89], Au [90], and more recently Co nanoparticles [91, 92]. What will become of these mesoscopic systems remains to be seen. However, the trend in cluster science seems to be headed toward the study of collective interactions between nanocrystallites. QDs have been linked together as dimers and trimers. Superlattices (colloidal crystals) [93] have also been created from these materials and the hope is that "artificial" solids can be created whose properties (optical, electrical, and magnetic) are all tunable by changing the composition of constituent "artificial" atoms.

1.8 Thesis Summary

This thesis is structured as follows. Chapter 2 describes the optical spectroscopy of CdSe QDs and describes a fine structure model which explains some of the unusual

and controversial results surrounding the nanocrystallites, mainly the behavior of the band edge luminescence. The model also explains the presence of fine structure in the linear absorption of the nanocrystallites. Chapter 3 addresses the origin of the band edge luminescence by intentionally modifying the surface of CdSe QDs with different organic and inorganic ligands. The purpose being to see if changing the surface has an effect on the energetics of the band edge emission. Chapter 4 considers the fine structure model to explain the unusual absorption behavior of nanocrystallites subjected to an external magnetic field. Chapter 5 is an extension of this study. It presents all theoretical considerations used in the first Zeeman study and also investigates predicted (field induced) size dependent behavior of excited states. Chapter 6 deals with the fine structure model from a slightly different perspective. QDs are intentionally doped with paramagnetic impurities to see the effect this has on the optical fine structure. Chapter 7 describes, in more detail, the effects of paramagnetic impurities on the optical properties of CdSe QDs. The Appendix is an attempt to preserve relevant work used to determine the equations and concepts described in Chapters 1 through 7.

Chapter 2

Band Edge Fine Structure

This chapter presents a theoretical analysis of the band-edge exciton fine structure in nanocrystallites of direct band gap semiconductors with a cubic or hexagonal lattice structure within the framework of a quasicubic model. The lowest energy exciton, eightfold degenerate in spherically symmetric QDs, is split into five levels by the crystal shape asymmetry, the intrinsic crystal field (in hexagonal lattice structures), and the electron-hole exchange interaction. Transition oscillator strengths and the size dependence of the splittings are calculated. Two of the five states, including the ground state, are optically passive (dark excitons). The oscillator strengths of the other three levels (bright excitons) depend strongly on the crystal size, shape and energy band parameters. The relative ordering of the energy levels is also heavily influenced by these parameters. The distance between the first optically active state and the optically forbidden exciton ground state increases with decreasing size, leading to an increase of the Stokes shift in the luminescence. Our results are in good agreement with size dependent resonant and non-resonant Stokes shifts obtained in

fluorescence line narrowing and photoluminescence experiments in CdSe nanocrystallites. Mixing of dark and bright excitons in an external magnetic field allows the direct optical recombination of the dark exciton ground state. The observed shortening of the luminescence lifetime in CdSe QDs subjected to an external magnetic field is in excellent agreement with theory, giving further support to the validity of our model.

2.1 Introduction

Size dependent optical spectroscopy of semiconductor quantum dots (QDs) has now reached the state held by magnetooptical spectroscopy during the mid-sixties, when the availability of high quality semiconductor materials on one hand, and the development of multiband Landau level theory by Pidgeon and Brown [94] on the other, enabled the description of the magnetic field dependent absorption spectra of zincblende semiconductors (see, for example, the review by Aggarwal [95]). The high quality of recently available nanometer-sized CdSe QDs has allowed us to resolve and study the size dependence of up to ten excited states in their absorption spectra [15, 12, 96]. These excitation spectra, obtained in the strong confinement regime where the nanocrystallites are small compared to the bulk exciton Bohr radius, are the result of transitions between discrete quantum size levels of electrons and holes [49, 1]. The small value of the crystal field splitting in CdSe (25 meV) allows us to consider this semiconductor as a zincblende material to a first approximation [52]. As a result, multiband effective mass theory which takes the degenerate valence band structure into account [51] has successfully described the excitation spectra obtained

in absorption [15], hole burning [12] and photoluminescence excitation experiments [96, 97, 98].

The data on CdSe quantum dots, however, has also provided us with a number of puzzles. While the large scale structure of the absorption spectrum is now well understood [15, 12, 96, 97, 98] the nature of the emitting state remains controversial. The photoluminescence of high quality samples with large quantum yields is red shifted with respect to the excitation frequency and has an unusually long radiative lifetime at low temperatures ($\tau_R \sim 1\mu$s at 10 K) [60] compared to the bulk exciton lifetime ($\tau_R \sim$1 ns). Simple parabolic band theory cannot explain these results in terms of recombination through internal core states. Rather, the band edge emission in II-VI QDs has been explained as a surface effect and is attributed to the recombination of weakly overlapping, surface-localized carriers [60, 44, 65]. However, these two effects can be explained if the exciton ground state is an optically forbidden state split from the first optically active exciton by the electron-hole exchange interaction [86, 84, 63, 82, 96].

Another puzzling observation is the very large Stokes shift of the band edge luminescence relative to the first absorption maximum for excitation far to the blue of the band edge. Its magnitude reaches $\sim$ 100 meV in 16 Å radius CdSe QDs [60] whereas the Stokes shift of the resonant photoluminescence is only $\sim$ 9 meV.[1]

In this chapter we present a realistic multiband calculation of the band edge exciton fine structure in semiconductor QDs with a degenerate valence band. The model takes into account the effects of the electron-hole exchange interaction, non-

[1]The terms "resonant" and "non-resonant" will be described in more detail in the following sections.

sphericity of the crystal shape and the intrinsic hexagonal lattice structure. We predict and describe a size dependent Stokes shift for both the resonant and non-resonant photoluminescence, fine structure in the absorption and hole burning spectra and predict the formation of a long-lived Dark Exciton [99]. We show below that fluorescence line narrowing (FLN) and photoluminescence (PL) spectra of CdSe QDs support the picture of Dark Exciton formation via excitation of higher energy fine structure states followed by rapid thermalization to the exciton ground state. Strong confirmation of our model is found in the magnetic field dependence of the Dark Exciton luminescence lifetime [63].

In Section 2-2 we calculate the energy structure of the band edge exciton and obtain transition oscillator strengths. We also calculate the lifetime of the optically passive exciton ground state in an external magnetic field. In Section 2-3 we present new data on the size dependence of the resonant and non-resonant photoluminescence Stokes shift as well as the magnetic field dependence of the Dark Exciton lifetime in CdSe QDs. These experimental results are compared with theory in Section 2-4 and conclusions are drawn from this comparison.

2.2 Theory

In semiconductor QDs smaller than the bulk exciton Bohr radius the energy spectrum and wavefunctions of electron-hole pairs can be approximated through the independent quantization of the electron and hole motion (the so-called strong confinement regime). The electron and hole quantum confinement energies and their wavefunctions are found in the framework of the multiband effective mass approxima-

tion [100]. The formal procedure for applying this method requires that the external potential be smooth. In the case of nanometer-sized semiconductor QDs this leads to the condition $2a \gg a_0$, where a is the radius of the crystal and a_0 is the lattice constant. In addition, the effective mass approximation holds only if the typical energies of the electron and hole are sufficiently close to the bottom of the conduction band and to the top of the valence band (i.e. near $k = 0$.). In practice this means that the quantization energy must be much smaller than the energy separation to the next higher (lower) energy extremum in the conduction (valence) band.

In the framework of the effective mass approximation, for spherically symmetric crystals (i.e. finite size spherical crystals having a cubic lattice structure), the first quantum size level of electrons is a $1S_e$ state doubly degenerate with respect to its spin projection, and the first quantum size level of holes is a $1S_{3/2}$ state, 4-fold degenerate with respect to its total angular momentum projection, $\mathcal{K}$, ($M = 3/2,\ 1/2,\ -1/2,$ and $-3/2$) [51, 15]. The energies and wavefunctions of these quantum size levels are easily found in the parabolic band approximation. For electrons they are:

$$E_{1S} = \frac{\hbar^2\pi^2}{2m_e a^2} ;$$

$$\psi_\alpha(\mathbf{r}) = \xi(\mathbf{r})|S\alpha> = \sqrt{\frac{2}{a}}\frac{\sin(\pi r/a)}{r}Y_{00}(\Omega)|S\alpha> , \qquad (2.1)$$

where m_e is the electron effective mass, a is the radius of the crystal, $Y_{lm}(\Omega)$ are spherical harmonics, $|S\alpha>$ are the Bloch functions of the conduction band, and $\alpha = \uparrow\ (\downarrow)$ is the projection of the electron spin, $s_z = +(-)1/2$. For holes in the

four-fold degenerate valence band the energies and wavefunctions can be written as:

$$E_{3/2}(\beta) = \frac{\hbar^2 \varphi^2(\beta)}{2 m_{hh} a^2} \ , \tag{2.2}$$

$$\psi_M(\mathbf{r}) = 2 \sum_{l=0,2} R_l(r) (-1)^{M-3/2} \sum_{m+\mu=M} \begin{pmatrix} 3/2 & l & 3/2 \\ \mu & m & -M \end{pmatrix} Y_{lm}(\Omega) u_\mu \ , \tag{2.3}$$

where $\beta = m_{lh}/m_{hh}$ is the ratio of the light to heavy hole effective masses, $\varphi(\beta)$ is the first root of the equation [101, 102, 103, 104, 105, 52]:

$$j_0(\varphi) j_2(\sqrt{\beta}\varphi) + j_2(\varphi) j_0(\sqrt{\beta}\varphi) = 0 \ , \tag{2.4}$$

where $j_n(x)$ are spherical Bessel functions, $\begin{pmatrix} i & k & l \\ m & n & p \end{pmatrix}$ are Wigner 3j-symbols, and $u_\mu (\mu = \pm 1/2, \pm 3/2)$ are Bloch functions of the four-fold degenerate valence band Γ_8 [106]:

$$\begin{aligned} u_{3/2} &= \frac{1}{\sqrt{2}}(X + iY) \uparrow \\ u_{-3/2} &= \frac{i}{\sqrt{2}}(X - iY) \downarrow \\ u_{1/2} &= \frac{i}{\sqrt{6}}[(X + iY) \downarrow -2Z \uparrow] \\ u_{-1/2} &= \frac{1}{\sqrt{6}}[(X - iY) \uparrow +2Z \downarrow] \end{aligned} \tag{2.5}$$

The radial functions $R_l(r)$ are [101, 103, 104, 52]:

$$\begin{aligned} R_2(r) &= \frac{A}{a^{3/2}} \left[j_2(\varphi r/a) + \frac{j_0(\varphi)}{j_0(\varphi\sqrt{\beta})} j_2(\varphi\sqrt{\beta} r/a) \right] \ , \\ R_0(r) &= \frac{A}{a^{3/2}} \left[j_0(\varphi r/a) - \frac{j_0(\varphi)}{j_0(\varphi\sqrt{\beta})} j_0(\varphi\sqrt{\beta} r/a) \right] \ , \end{aligned} \tag{2.6}$$

where the constant A is determined by the normalization condition:

$$\int dr r^2 [R_0^2(r) + R_2^2(r)] = 1. \tag{2.7}$$

The dependence of φ on β [52] is shown in Fig. 2-1 a.

For spherical QDs, the exciton ground state ($1S_{3/2}1S_e$) is eight-fold degenerate. However, shape and internal crystal structure anisotropy together with the electron-hole exchange interaction lifts this degeneracy. The splitting and the transition oscillator strengths of the states, as well as their order, are sensitive to the crystal size and shape, as shown below. We calculate this splitting neglecting the warping of the valence band and the non-parabolicity of the electron and light hole energy spectra.

2.2.1 Energy spectrum and wavefunctions

Nanocrystal asymmetry lifts the hole state degeneracy. This asymmetry has two sources: the intrinsic asymmetry due to the hexagonal lattice of the crystal [52] and the non-spherical shape of the QD [107]. Both split the four-fold degenerate hole state into two two-fold degenerate states - Kramers doublets- having $|M| = 1/2$ and $3/2$, respectively.

The splitting due to the intrinsic hexagonal lattice structure, Δ_{int}, can be written [52]:

$$\Delta_{int} = \Delta_{cr} v(\beta) \quad , \tag{2.8}$$

where Δ_{cr} is the crystal field splitting and equals the distance between the A and B valence subbands in bulk semiconductors having a hexagonal lattice structure (25

meV in CdSe). Eq. 2-8 is obtained within the framework of a quasicubic model where the crystal field splitting is considered a perturbation [52]. The Kramers doublet splitting does not depend on the crystal size but only on the ratio of the light to heavy hole effective masses. The dimensionless function $v(\beta)$ [52] describing this dependence is shown in Fig. 2-1 b and varies rapidly in the region $0 < \beta < 0.3$. The $|M| = 3/2$ state is the ground state.

We model the non-sphericity of the nanocrystal by taking it to be an ellipsoid whose deviation from sphericity is characterized by the ratio $c/b = 1 + \mu$ of its major to minor axes. Here μ is the ellipticity of the crystal and is positive (negative) for prolate (oblate) crystals. The splitting arising from this deviation is calculated in first order perturbation theory [107]:

$$\Delta_{sh} = 2\mu u(\beta) E_{3/2}(\beta) \quad , \tag{2.9}$$

where $E_{3/2}$ is the $1S_{3/2}$ hole ground state energy for spherical crystals of radius $a = (b^2 c)^{1/3}$. $E_{3/2}$ is inversely proportional to a^2 (see Eq. 2-2). The shape splitting is therefore a sensitive function of the crystal size. The function $u(\beta)$ [107] decreases from a value of 4/15 at $\beta = 0$, changes sign at $\beta = 0.14$ and goes to zero at $\beta = 1$ (see Fig. 2-1 c).

The net splitting of the hole state, $\Delta(a, \beta, \mu)$, is the sum of the crystal field and shape splitting,

$$\Delta(a, \beta, \mu) = \Delta_{sh} + \Delta_{int} \quad . \tag{2.10}$$

In nanocrystals where the function $u(\beta)$ is negative, e.g. in CdSe QDs where $\beta = 0.28$

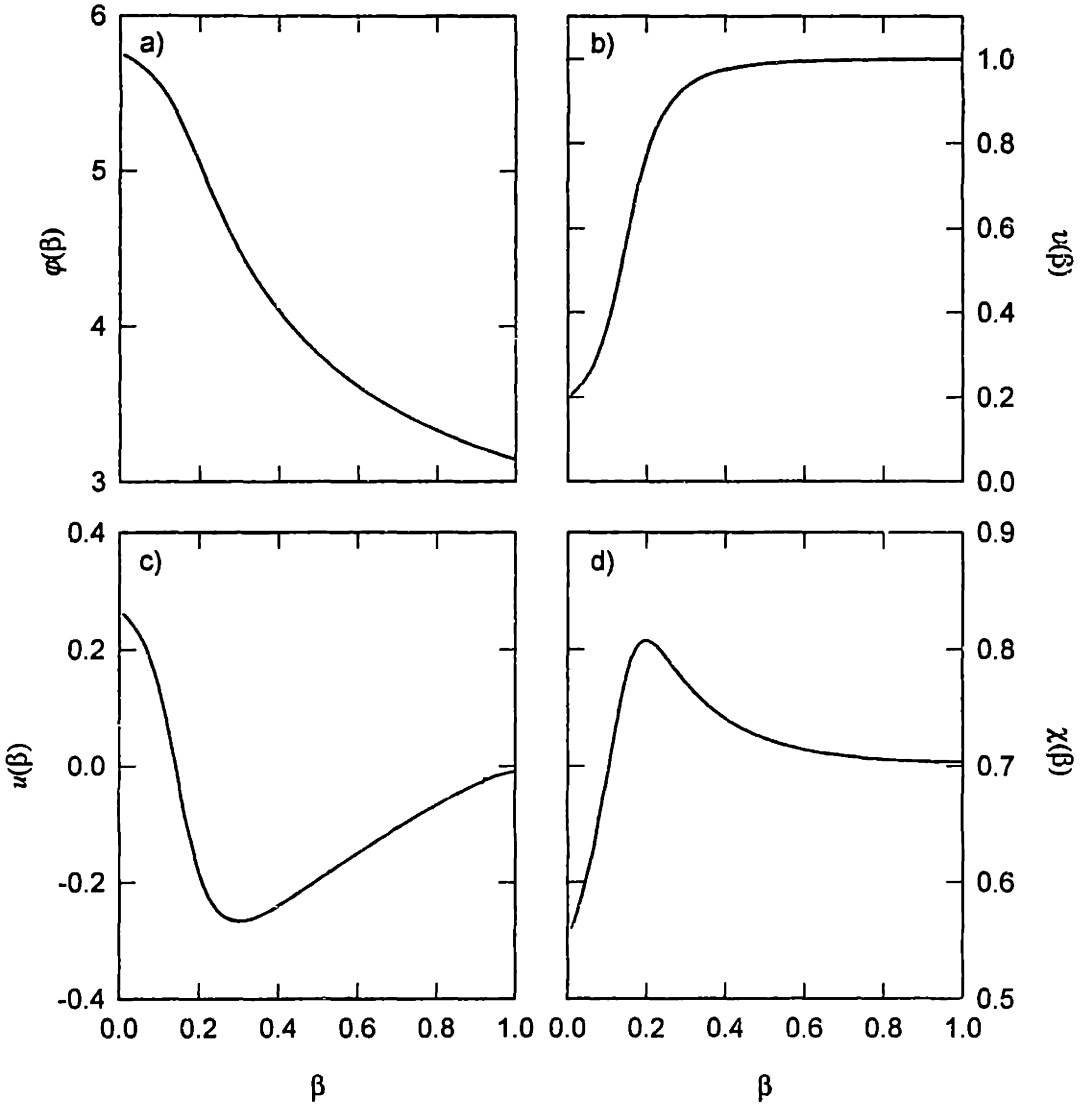

Figure 2-1: (a) The dependence of the hole ground state function $\phi(\beta)$ on the light to heavy hole effective mass ratio β; (b) the dimensionless function $\nu(\beta)$ associated with hole level splitting due to hexagonal lattice structure; (c) the dimensionless function $u(\beta)$ associated with hole level splitting due to crystal shape asymmetry; (d) the dimensionless function $\chi(\beta)$ associated with exciton splitting due to the electron-hole exchange interaction.

[96], the net splitting decreases with size in prolate ($\mu > 0$) crystals. Even the order of the hole levels can change, with the $|M| = 1/2$ state becoming the hole ground state for sufficiently small nanocrystallites [108]. This can be qualitatively understood within a model of uncoupled A and B valence subbands. In prolate crystals the energy of the lowest hole quantum size level is determined by its motion within the plane perpendicular to the hexagonal axis. In this plane the hole effective mass in the lowest A subband is smaller than in the higher B subband [52]. Decreasing the size of the crystal causes a shift of the quantum size levels inversely proportional to both the effective mass and the square of the nanocrystal radius. The shift is therefore larger for the A subband than for the B subband and, as a result, can change the order of the levels in small crystals. In oblate ($\mu < 0$) QDs where the states are determined by motion along the hexagonal axis, the B subband has a smaller mass. Hence the net splitting increases with decreasing size and the levels maintain their original order.

The 8-fold degeneracy of the spherical band edge exciton is also broken by the electron-hole exchange interaction which mixes different electron and hole spin states. It has the form [109, 106]:

$$\hat{H}_{exch} = -(2/3)\varepsilon_{exch}(a_0)^3\delta(\mathbf{r}_e - \mathbf{r}_h)\boldsymbol{\sigma}\boldsymbol{J} \quad , \tag{2.11}$$

where $\boldsymbol{\sigma}$ is the electron Pauli spin-1/2 matrix, $\boldsymbol{J}$ is the hole spin 3/2 matrix, a_0 is the lattice constant, and ε_{exch} is the exchange strength constant. In bulk crystals with a cubic lattice structure this term splits the 8-fold degenerate exciton ground state into a 5-fold degenerate (optically passive) state with total angular momentum 2 and a 3-fold degenerate (optically active) state with total angular momentum 1.

The splitting can be expressed in terms of the bulk exciton Bohr radius, a_{ex}:

$$\hbar\omega_{ST} = (8/3\pi)(a_0/a_{ex})^3\varepsilon_{exch} \quad . \tag{2.12}$$

In bulk crystals with a hexagonal lattice structure this term splits the 4-fold degenerate exciton ground state into a singlet and a triplet state, separated by

$$\hbar\omega_{ST} = (2/\pi)(a_0/a_{ex})^3\varepsilon_{exch} \quad . \tag{2.13}$$

Equations 2-12 and 2-13 allow us to evaluate the exchange strength constant. In CdSe where $\hbar\omega_{ST} = 0.13$ meV [110], a value of $\varepsilon_{exch} = 450$ meV is obtained using a_{ex}=56 Å.

Taken together, the hexagonal lattice structure, crystal shape asymmetry, and the electron-hole exchange interaction split the original "spherical " 8-fold degenerate exciton into five levels. These states are labeled by the magnitude of the exciton total angular momentum projection, $F = M + s_z$. We obtain one level with $F = \pm 2$, two with $F = \pm 1$, and two with $F = 0$. The level energies, $\varepsilon_{|F|}$, are determined by solving the secular equation $\det(\hat{E} - \varepsilon_{|F|}) = 0$, where the matrix $\hat{E}$ consists of matrix elements of the asymmetry perturbations and the exchange interaction, $\hat{H}_{exch}$, taken

between the exciton wavefunctions $\Psi_{\alpha,M}(\mathbf{r}_e,\mathbf{r}_h)=\psi_\alpha(\mathbf{r}_e)\psi_M(\mathbf{r}_h)$:

	⇑,3/2	⇑,1/2	⇑,-1/2	⇑,-3/2	⇓,3/2	⇓,1/2	⇓,-1/2	⇓,-3/2
⇑,3/2	$\frac{-3\eta}{2}-\frac{\Delta}{2}$	0	0	0	0	0	0	0
⇑,1/2	0	$\frac{-\eta}{2}+\frac{\Delta}{2}$	0	0	$-i\sqrt{3}\eta$	0	0	0
⇑,-1/2	0	0	$\frac{\eta}{2}+\frac{\Delta}{2}$	0	0	$-i2\eta$	0	0
⇑,-3/2	0	0	0	$\frac{3\eta}{2}-\frac{\Delta}{2}$	0	0	$-i\sqrt{3}\eta$	0
⇓,3/2	0	$i\sqrt{3}\eta$	0	0	$\frac{3\eta}{2}-\frac{\Delta}{2}$	0	0	0
⇓,1/2	0	0	$i2\eta$	0	0	$\frac{\eta}{2}+\frac{\Delta}{2}$	0	0
⇓,-1/2	0	0	0	$i\sqrt{3}\eta$	0	0	$\frac{-\eta}{2}+\frac{\Delta}{2}$	0
⇓,-3/2	0	0	0	0	0	0	0	$\frac{-3\eta}{2}-\frac{\Delta}{2}$

(2.14)

where $\eta=(a_{ex}/a)^3\hbar\omega_{ST}\chi(\beta)$, and the dimensionless function $\chi(\beta)$ is written in terms of the electron and hole radial wavefunctions,

$$\chi(\beta)=(1/6)a^2\int_0^a dr\sin^2(\pi r/a)[R_0^2(r)+0.2R_2^2(r)]\ . \tag{2.15}$$

The dependence of χ on the parameter β is shown in Fig. 2-1 d.

The solution of the secular equation yields five exciton states. The energy of the level with total angular momentum projection $|F|=2$ and its dependence on crystal size is given by:

$$\varepsilon_2=-3\eta/2-\Delta/2\ . \tag{2.16}$$

Its respective wavefunctions are:

$$\begin{aligned}\Psi_{-2}(\mathbf{r}_e,\mathbf{r}_h) &= \Psi_{\downarrow,-3/2}(\mathbf{r}_e,\mathbf{r}_h)\ ,\\ \Psi_{2}(\mathbf{r}_e,\mathbf{r}_h) &= \Psi_{\uparrow,3/2}(\mathbf{r}_e,\mathbf{r}_h)\ .\end{aligned} \tag{2.17}$$

The energies and size dependence of the two levels, with total momentum projection $|F| = 1$, are given by

$$\varepsilon_1^{U,L} = \eta/2 \pm \sqrt{(2\eta - \Delta)^2/4 + 3\eta^2} \quad . \tag{2.18}$$

where U and L correspond to the upper ("+") or lower ("-") sign respectively. We denote these states by $\pm 1^U$ and $\pm 1^L$, i.e. the upper and lower state with projection $F = \pm 1$. The corresponding wavefunctions for the states with $F = +1$ are

$$\Psi_1^{U,L}(\mathbf{r}_e, \mathbf{r}_h) = \mp i C^{\pm} \Psi_{\uparrow,1/2}(\mathbf{r}_e, \mathbf{r}_h) + C^{\mp} \Psi_{\downarrow,3/2}(\mathbf{r}_e, \mathbf{r}_h) \tag{2.19}$$

Likewise, for the states with $F = -1$

$$\Psi_{-1}^{U,L}(\mathbf{r}_e, \mathbf{r}_h) = \mp i C^{\mp} \Psi_{\uparrow,-3/2}(\mathbf{r}_e, \mathbf{r}_h) + C^{\pm} \Psi_{\downarrow,-1/2}(\mathbf{r}_e, \mathbf{r}_h) \tag{2.20}$$

where

$$C^{\pm} = \sqrt{\frac{\sqrt{f^2 + d} \pm f}{2\sqrt{f^2 + d}}} \quad , \tag{2.21}$$

$f = (-2\eta + \Delta)/2$ and $d = 3\eta^2$. The energies and size dependence of the two $F = 0$ exciton levels are given by:

$$\varepsilon_0^{U,L} = \eta/2 + \Delta/2 \pm 2\eta \tag{2.22}$$

we denote the two $F = 0$ states by 0^U and 0^L, with corresponding wavefunctions:

$$\Psi_0^{U,L}(\mathbf{r}_e, \mathbf{r}_h) = \frac{1}{\sqrt{2}} \left[\mp i \Psi_{\uparrow,-1/2}(\mathbf{r}_e, \mathbf{r}_h) + \Psi_{\downarrow,1/2}(\mathbf{r}_e, \mathbf{r}_h) \right] \quad , \tag{2.23}$$

The size dependence of the band edge exciton splitting for hexagonal CdSe QDs with different shapes is shown in Fig. 2-2. The calculation is done using $\beta = 0.28$ [96]. In spherical crystals (Fig. 2-2 a) the $F = \pm 2$ state is the exciton ground state for all sizes, and is optically passive [52]. The separation between the ground state and the lower optically active $F = \pm 1$ state increases with decreasing size as $1/a^3$ but tends to $3\Delta/4$ for very small crystals. In oblate QDs (Fig. 2-2 b) the order of the exciton levels is the same as in spherical ones. However, the splitting does not saturate, because in these crystals Δ increases with decreasing size. In prolate crystals Δ becomes negative with decreasing size and changes the order of the exciton levels at some value of the radius (Fig. 2-2 c); in small crystals the optically passive[2] $F = 0$ state becomes the exciton ground state. The crossing occurs when Δ goes through 0. In nanocrystallites of this size the shape asymmetry exactly compensates for the asymmetry connected with the hexagonal lattice structure [108] and the exciton levels have "spherical" symmetry. As a result, there is one 5-fold degenerate exciton with total angular momentum 2 (reflected in the crossing of the 0^L, $\pm 1^L$ and ± 2 levels) and one 3-fold degenerate exciton with total angular momentum 1 (seen in the crossing of the 0^U and $\pm 1^U$ levels). In Fig. 2-2 d the band edge exciton fine structure is shown for the case where the ellipticity varies with size[3] corresponding to SAXS and TEM

[2]This is shown in the next section.

[3]In accordance with SAXS and TEM measurements the ellipticity is approximated by the polynomial $\mu(a) = 0.101 - 0.034a + 3.507 \times 10^{-3}a^2 - 1.177 \times 10^{-4}a^3 + 1.863 \times 10^{-6}a^4 - 1.418 \times 10^{-8}a^5 +$

measurements of our CdSe nanocrystallites [32]. The level structure closely resembles that of spherical crystals.

The size dependence of the band edge exciton splitting in cubic CdTe crystals with different shapes is shown in Fig. 2-3. The calculation is done using the parameters $\beta = 0.086$ and $\hbar\omega_{ST} = 0.04\,\mathrm{meV}$. One can see that in spherical nanocrystals the electron-hole exchange interaction splits the eight-fold degenerate band edge exciton into a 5-fold degenerate state with total angular momentum 2 and a 3-fold degenerate exciton with total angular momentum 1 (Fig. 3-3 a). Crystal shape asymmetry lifts the degeneracy of these states and determines the relative order of the exciton levels (see Fig. 3-3 b and Fig. 3-3 c for comparison).

2.2.2 Selection rules and transition oscillator strengths

To describe the fine structure responsible for the absorption spectra and photoluminescence we calculate transition oscillator strengths for these five states. The mixing of electron and hole spin states by the electron-hole exchange interaction strongly affects the optical transition probabilities. The wavefunctions of the $|F| = 2$ exciton state are unaffected by this interaction (see Eq. 2-17); they are optically passive in the electric dipole approximation because absorbed or emitted photons cannot have an angular momentum projection of ± 2. The probability of optically exciting or recombining from an exciton with total angular momentum projection F is proportional to the square of the matrix element determined by the momentum operator

---

$4.196 \times 10^{-11} a^6$

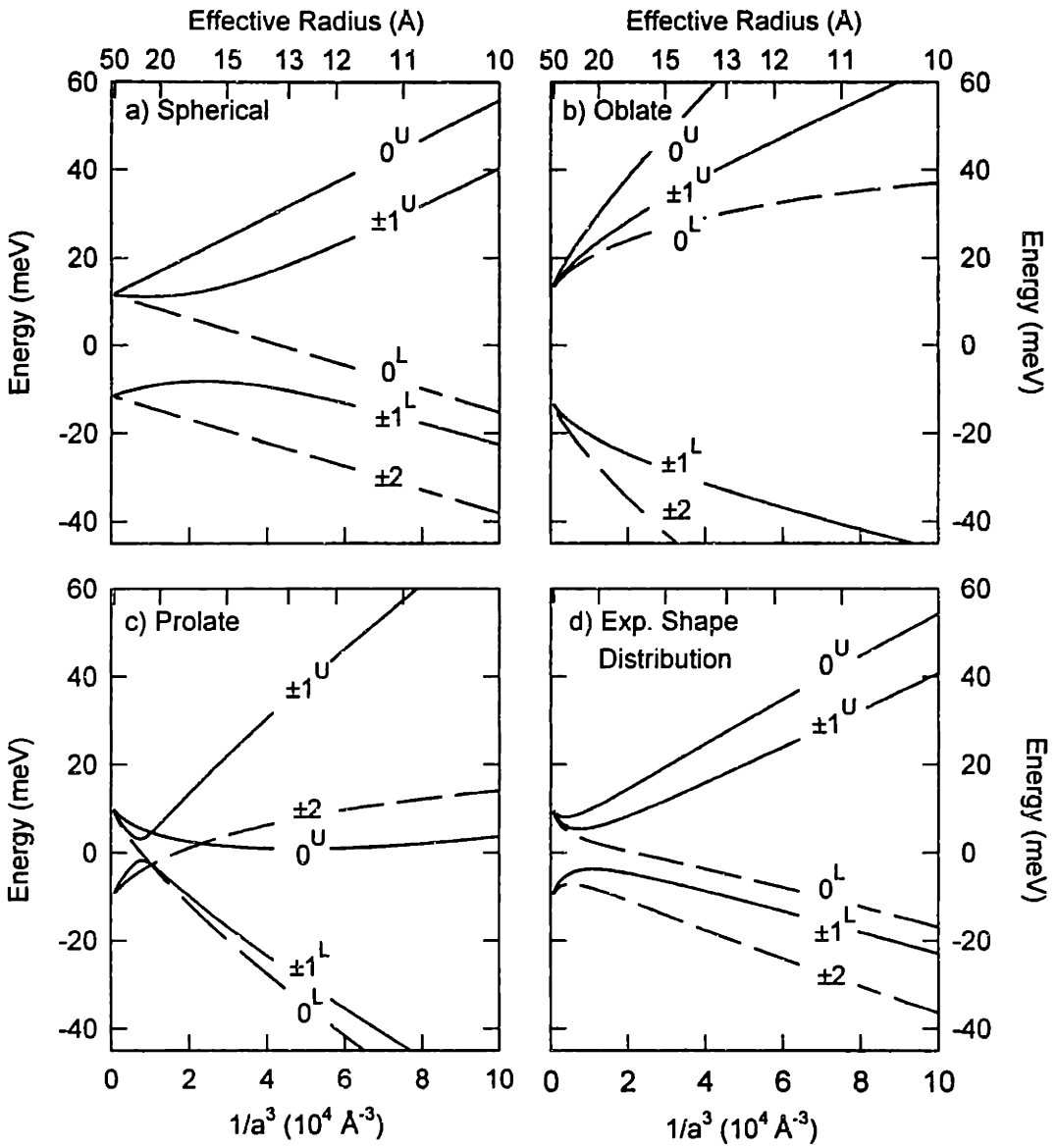

Figure 2-2: The size dependence of the exciton band- edge structure in ellipsoidal hexagonal CdSe quantum dots with ellipticity μ: (a) spherical dots (μ = 0); (b) oblate dots (μ=-0.28); (c) prolate dots (μ = 0.28); (d) dots having a size dependent ellipticity as determined from SAXS and TEM measurements. Solid (dashed) lines indicate optically active (passive) levels.

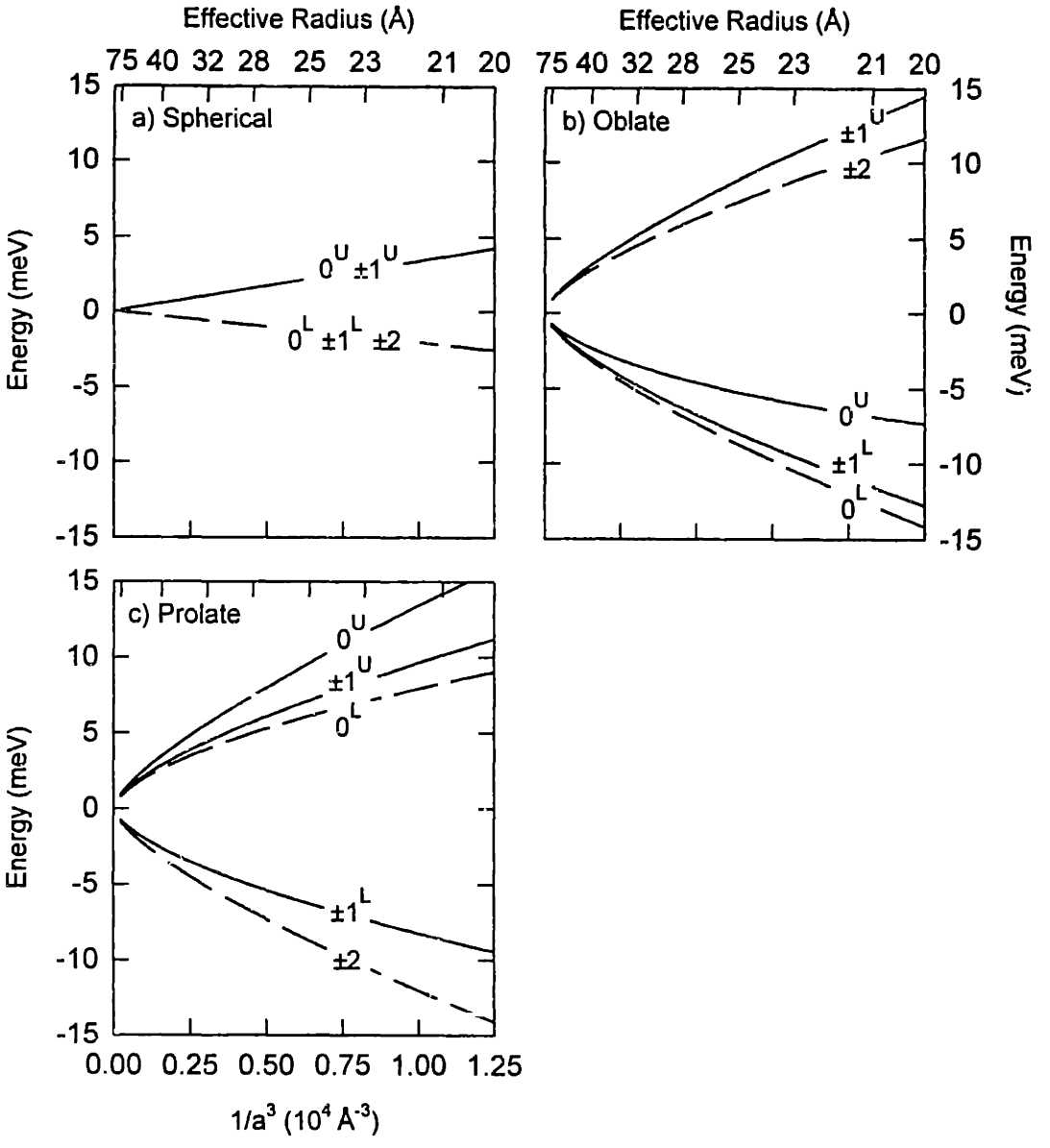

Figure 2-3: The size dependence of the exciton band-edge structure in ellipsoidal cubic CdTe quantum dots with ellipticity μ: (a) spherical dots ($\mu = 0$); (b) oblate dots ($\mu = -0.28$); (c) prolate dots ($\mu = 0.28$); Solid (dashed) lines indicate optically active (passive) levels.

$\mathbf{e}\hat{\mathbf{p}}$ sandwiched between that state and the vacuum state

$$P_F = | < 0|\mathbf{e}\hat{\mathbf{p}}|\tilde{\Psi}_F > |^2. \tag{2.24}$$

Here $|0>= \delta(\mathbf{r}_e - \mathbf{r}_h)$, $\mathbf{e}$ is the polarization vector of the absorbed or emitted light, $\hat{\mathbf{p}}$ (the momentum operator) acts only on the valence band Bloch functions (see Eq. 2-5) and the exciton wavefunction, $\tilde{\Psi}_F$, is written in the electron-electron representation. Exciton wavefunctions in the electron-hole representation are transformed to the electron-electron representation by taking the complex conjugate of Eqs. 2-17, 2-19, 2-20, 2-23 and flipping the spin projections in the hole Bloch functions ($\uparrow$ and $\downarrow$ to $\downarrow$ and $\uparrow$).

For the exciton state with $F = 0$ we obtain

$$P_0^{U,L} = | < 0|\mathbf{e}\hat{\mathbf{p}}|\tilde{\Psi}_0^{U,L} > |^2 = \frac{(1 \pm 1)^2}{3} K P^2 \cos^2(\theta) \quad , \tag{2.25}$$

where $P =< S|\hat{p}_z|Z >$ is the Kane interband matrix element, θ is the angle between the polarization vector of the emitted or absorbed light and the hexagonal axis of the crystal. K is the square of the overlap integral [52]:

$$K = \frac{2}{a} \left| \int dr r \sin(\pi r/a) R_0(r) \right|^2 \quad . \tag{2.26}$$

Its value is independent of crystal size and depends only on β; hence the excitation probability of the $F = 0$ state does not depend on crystal size. For the lower exciton state, 0^L, it is identically zero. At the same time the exchange interaction increases

the excitation probability of the 0^U exciton state by a factor of two. This arises from the constructive and destructive interference of the wavefunctions for the two indistinguishable excitons $|\uparrow, -1/2>$ and $|\downarrow, 1/2>$ (see Eq. 2-23).

For the exciton state with $F = 1$ we obtain:

$$P_1^{U,L} = \frac{1}{3}\left(\frac{2\sqrt{f^2+d} \mp f \pm \sqrt{3d}}{2\sqrt{f^2+d}}\right) KP^2 \sin^2(\theta) \quad . \tag{2.27}$$

The excitation probability of the $F = -1$ state is equal to that of the $F = 1$ state. As a result, the total transition probability to the doubly degenerate $|F| = 1$ exciton is equal to $2P_1^{U,L}$.

Equations 2-25 and 2-27 show that the $F = 0$ and $|F| = 1$ excitation probabilities differ in their dependence on the angle between the light polarization vector and the hexagonal axis of the nanocrystallites. If the crystal hexagonal axes are aligned perpendicular to the light direction, only the active $F = 0$ state is excited. Alternatively, when the crystals are aligned along the light propagation direction, only the upper and lower $|F| = 1$ states absorb light. For the case of randomly oriented QDs, polarized excitation resonant with one of these exciton states selectively excites suitably oriented nanocrystallites, leading to polarized luminescence [52]. Observation of this effect has been reported in several papers [60, 61, 84]. Furthermore, a large energy splitting between the $F = 0$ and $|F| = 1$ states leads to different Stokes shifts in the polarized luminescence.

To find the probability of optically exciting a system of randomly oriented nanocrystallites we average Eqs. 2-25 and 2-27 over all possible solid angles. The respective

transition probabilities are proportional to:

$$\begin{aligned} \overline{P_0^{U,L}} &= \frac{(1\pm 1)^2 K P^2}{9}, \\ \overline{P_1^{U,L}} &= \overline{P_{-1}^{U,L}} = \frac{2KP^2}{9}\left(\frac{2\sqrt{f^2+d}\mp f\pm\sqrt{3d}}{2\sqrt{f^2+d}}\right). \end{aligned} \tag{2.28}$$

There are three optically active states with relative oscillator strengths $\overline{P_0^U}$, $2\overline{P_1^U}$, and $2\overline{P_1^L}$. The dependence of these probabilities with size and shape is shown in Fig. 2-4 for QDs with a hexagonal lattice structure. We see that the shape of the crystal strongly influences this dependence. For example, in prolate crystals (Fig. 2-4 c) the $\pm 1^L$ oscillator strength goes to zero for those QDs where $\Delta = 0$; i.e., the crystal shape asymmetry exactly compensates for the internal asymmetry connected with the hexagonal lattice structure. In these nanocrystallites the oscillator strengths of all upper states (0^U, 1^U, and -1^U) are equal. Nevertheless, one can see that for all shapes the excitation probability of the lower $|F| = 1$ exciton state, $2\overline{P_1^L}$, decreases with size and that the upper $|F| = 1$ exciton gains its oscillator strength.

This behavior can be understood by examining the spherically symmetric limit. In spherical nanocrystals the exchange interaction leads to the formation of two exciton states - with total angular momentum 2 and 1. The ground state is the optically passive exciton with total angular momentum 2. This state is 5-fold degenerate with respect to its total angular momentum projection. For small QDs the splitting of the exciton levels due to the nanocrystal asymmetry can be considered a perturbation relative to the exchange interaction, which grows as $1/a^3$. In this situation the wavefunctions of the $\pm 1^L$, 0^L, and ± 2 excitons turn into the wavefunctions of the optically

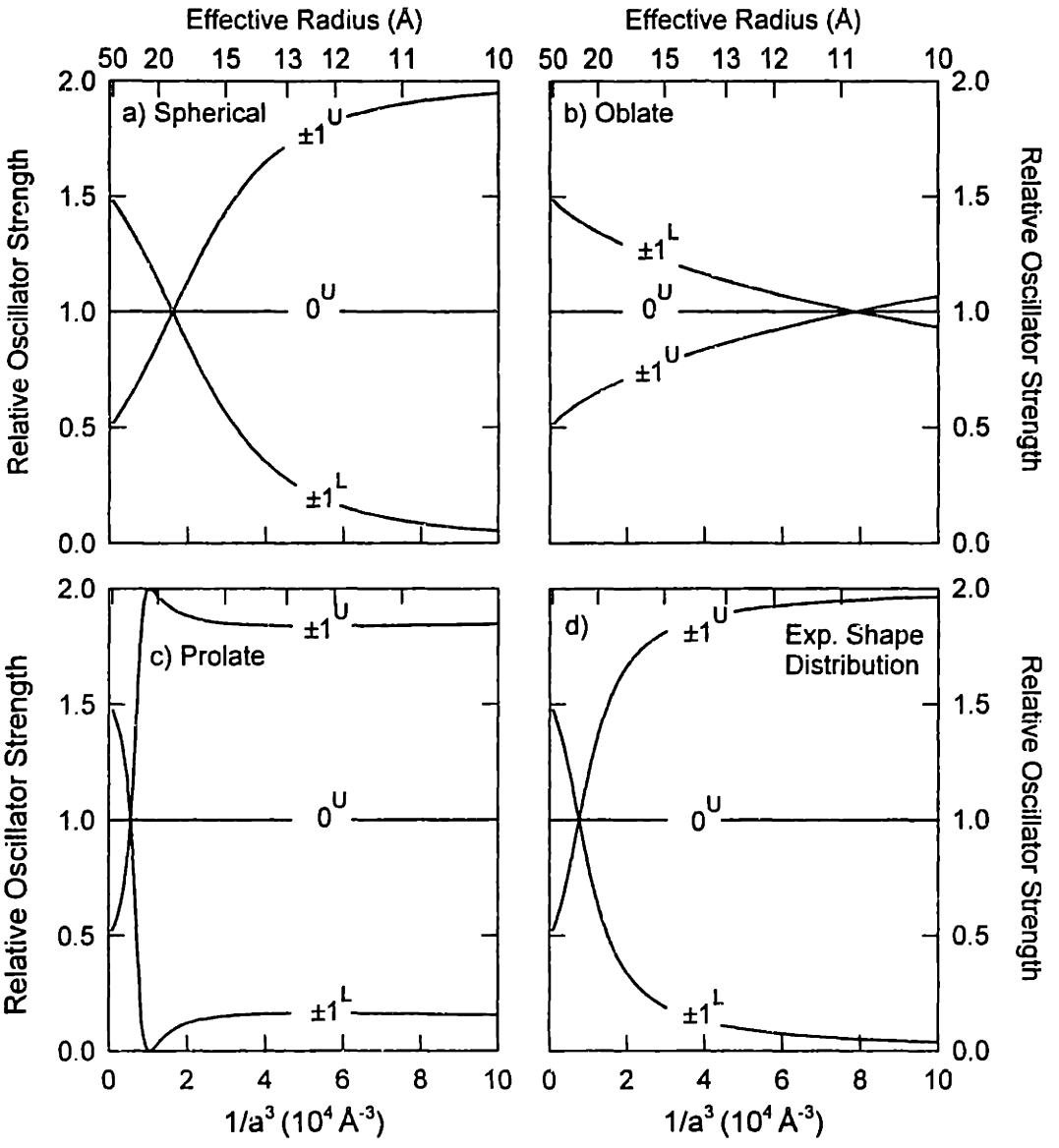

Figure 2-4: The size dependence of the oscillator strengths, relative to that of the 0^U state, for the optically active states in hexagonal CdSe quantum dots with ellipticity μ: (a) spherical dots ($\mu = 0$); (b) oblate dots ($\mu = -0.28$); (c) prolate dots ($\mu = 0.28$); (d) dots having a size dependent ellipticity as determined from SAXS and TEM measurements.

passive state with total angular momentum 2. The wavefunctions of the $\pm 1^U$ and 0^U excitons become those of the optically active state with total angular momentum 1. These three states therefore carry nearly all of the oscillator strength.

In large nanocrystallites, for all possible shapes, we neglect the exchange interaction (which decreases as $1/a^3$), and there are only two four-fold degenerate exciton states (see Fig. 2-3). The splitting here is determined by the shape asymmetry and the intrinsic crystal field. In a system of randomly oriented crystals, the excitation probability for both these states is the same: $\overline{P_0^U} + 2\overline{P_1^U} = 2\overline{P_1^L} = \frac{2KP^2}{3}$ [52].

In Fig. 2-5 we show these dependences for cubic CdTe nanocrystallites having different shapes.

It is necessary to note here that despite the fact that the exchange interaction dramatically changes the structure and the oscillator strengths of the band edge exciton, the polarization properties of the nanocrystallites are determined by the internal and crystal shape asymmetries. All polarization effects are proportional to the net splitting parameter Δ and go to zero when $\Delta = 0$.

2.2.3 Recombination of the Dark Exciton in Magnetic Fields

Lifetime measurements of the Dark Exciton in CdSe QDs in the presence of an external magnetic field strongly supports our model [63]. Recombination of the Dark Exciton is allowed if the magnetic field is not directed along the hexagonal axis of the nanocrystallite. In this case F is no longer a good quantum number and the ± 2 Dark Exciton state is admixed with optically active ± 1 Bright Exciton states. This now allows the direct optical recombination of the ± 2 exciton ground state.

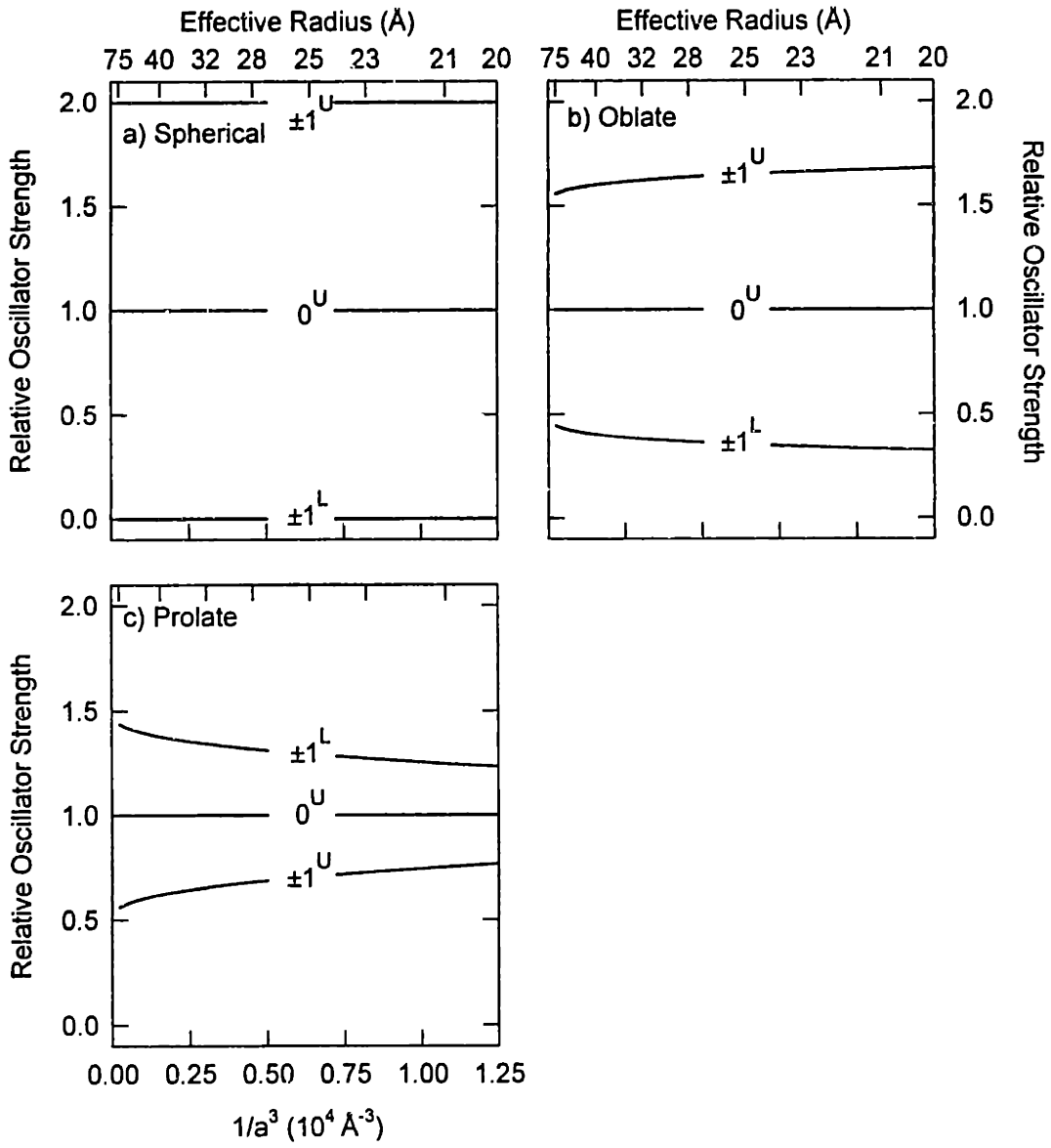

Figure 2-5: The size dependence of the oscillator strengths, relative to that of the 0^U state, for the optically active states in cubic CdTe quantum dots with ellipticity μ: (a) spherical dots ($\mu = 0$); (b) oblate dots ($\mu = -0.28$); (c) prolate dots ($\mu = 0.28$).

For nanometer sized semiconductor quantum dots the effect of an external magnetic field, **H**, is well described as a molecular Zeeman effect:

$$\hat{H}_H = \frac{1}{2} g_e \mu_B \boldsymbol{\sigma} \mathbf{H} - g_h \mu_B \mathcal{K} \mathbf{H} \quad , \tag{2.29}$$

Here g_e and g_h are the electron and hole g factors respectively and μ_B is the Bohr magneton. For electrons in CdSe $g_e = 0.68$ [111]. The value of the hole g factor is calculated in the appendix using the results of [112], and is $g_h = -1.09$. In Eq. 2-29 we neglect the diamagnetic, H^2, terms because the dots are significantly smaller than the characteristic magnetic length [$\sim$ 115 Å at 10 T].

Treating the magnetic interaction as a perturbation, we determine the influence of the magnetic field on the unperturbed exciton using the perturbation matrix $\hat{E'}_H = < \Psi_{\alpha,M} | \mu_B^{-1} \hat{H}_H | \Psi_{\alpha',M'} >$:

	⇑,3/2	⇑,1/2	⇑,-1/2	⇑,-3/2	⇓,3/2	⇓,1/2	⇓,-1/2	⇓,-3/2
⇑,3/2	$\frac{H_z D}{2}$	$\frac{-i\sqrt{3} g_h H_-}{2}$	0	0	$\frac{g_e H_-}{2}$	0	0	0
⇑,1/2	$\frac{i\sqrt{3} g_h H_+}{2}$	$\frac{H_z C}{2}$	$-i g_h H_-$	0	0	$\frac{g_e H_-}{2}$	0	0
⇑,-1/2	0	$i g_h H_+$	$\frac{H_z A}{2}$	$\frac{-i\sqrt{3} g_h H_-}{2}$	0	0	$\frac{g_e H_-}{2}$	0
⇑,-3/2	0	0	$\frac{i\sqrt{3} g_h H_+}{2}$	$\frac{H_z B}{2}$	0	0	0	$\frac{g_e H_-}{2}$
⇓,3/2	$\frac{g_e H_+}{2}$	0	0	0	$\frac{-H_z B}{2}$	$\frac{-i\sqrt{3} g_h H_-}{2}$	0	0
⇓,1/2	0	$\frac{g_e H_+}{2}$	0	0	$\frac{i\sqrt{3} g_h H_+}{2}$	$\frac{-H_z A}{2}$	$-i g_h H_-$	0
⇓,-1/2	0	0	$\frac{g_e H_+}{2}$	0	0	$i g_h H_+$	$\frac{-H_z C}{2}$	$\frac{-i\sqrt{3} g_h H_-}{2}$
⇓,-3/2	0	0	0	$\frac{g_e H_+}{2}$	0	0	$\frac{i\sqrt{3} g_h H_+}{2}$	$\frac{-H_z D}{2}$

(2.30)

where $A = (g_e + g_h)$, $B = (g_e + 3g_h)$, $C = (g_e - g_h)$, $D = (g_e - 3g_h)$, H_z is the magnetic field projection along the crystal hexagonal axis and $H_\pm = H_x \pm i H_y$. One can see from Eq. 2-30 that components of the magnetic field perpendicular to the hexagonal

axis mix the $F = \pm 2$ dark exciton with respective optically active $F = \pm 1$ Bright excitons. In small nanocrystallites, where η is on the order of 10 meV, the influence of even the strongest magnetic field can be considered a perturbation. The case of large crystals where η is of the same order as $\mu_B g_e H$ will be considered later. The admixture in the $F = 2$ state is given by:

$$\Delta\Psi_2 = \frac{\mu_B H_-}{2} \times \left[\frac{g_e C^- - \sqrt{3} g_h C^+}{\varepsilon_2 - \varepsilon_1^+} \Psi_1^+ + \frac{\sqrt{3} g_h C^- + g_e C^+}{\varepsilon_2 - \varepsilon_1^-} \Psi_1^- \right] , \tag{2.31}$$

where the constants $C^{\pm}$ are given in Eq. 2-21. The admixture in the $F = -2$ exciton by the $F = -1$ state is described similarly.

This admixture of optically active Bright excitons allows the optical recombination of the Dark Exciton. In general, the radiative recombination rate of an exciton state, F, can be obtained by summing Eq. 2-24 over all light polarizations.[113] We obtain the expression:

$$\frac{1}{\tau_{|F|}} = \frac{4e^2 \omega n_r}{3 m_0^2 c^3 \hbar} | < 0 | \hat{p}_\mu | \tilde{\Psi}_F > |^2 , \tag{2.32}$$

where ω and c are the light frequency and velocity, n_r is the refractive index, and m_0 is the free electron mass. Using Eqs. 2-25 through 2-27 we obtain the radiative decay time for the upper exciton state with $F = 0$,

$$\frac{1}{\tau_0} = \frac{8 \omega n_r P^2 K}{9 \times 137 m_0^2 c^2} ; \tag{2.33}$$

likewise, for the upper and lower exciton states with $|F| = 1$

$$\frac{1}{\tau_1^{U,L}} = \left(\frac{2\sqrt{f^2+d} \mp f \pm \sqrt{3d}}{2\sqrt{f^2+d}} \right) \frac{1}{\tau_0} \quad . \tag{2.34}$$

Using the admixture of the $|F| = 1$ states in the $|F| = 2$ exciton given by Eq. 2-31, we calculate the recombination rate of the $|F| = 2$ exciton in a magnetic field,

$$\frac{1}{\tau_2(H)} = \frac{3\mu_B^2 H^2 \sin^2(\theta)}{8\Delta^2} \left(2g_h - g_e \frac{2\eta + \Delta}{3\eta} \right)^2 \frac{1}{\tau_0} \quad . \tag{2.35}$$

The characteristic time τ_0 does not depend on the nanocrystal radius. For CdSe, calculations using $2P^2/m_0 = 17.5\,\mathrm{eV}$ [15] give $\tau_0 = 1.6\,\mathrm{ns}$.

In large crystals the magnetic field splitting, $\mu_B g_e H$, is on the same order as the exchange interaction, η, and cannot be considered a perturbation. At the same time, both these energies are much smaller than the splitting due to the crystal asymmetry. We consider here the admixture of the $|F| = 2$ Dark Exciton with the lowest $|F| = 1$ state. This can be calculated exactly. The magnetic field also lifts the degeneracy of the exciton states with respect to the sign of the total angular momentum projection F. The energies of the former $F = -2$ and $F = -1$ states are:

$$\varepsilon_{1,2}^{\pm} = \frac{\Delta + 3\mu_B g_h H_z}{2} \pm \frac{\sqrt{(3\eta + \mu_B g_e H_z)^2 + (\mu_B g_e)^2 H_\perp^2}}{2} \, , \tag{2.36}$$

where +(-) refers to the $F = -1$ state with an $F = -2$ admixture ($F = -2$ state with

an $F = -1$ admixture) and $H_\perp = \sqrt{H_x^2 + H_y^2}$. The corresponding wavefunctions are:

$$\Psi^{\pm}_{-1,-2} = \sqrt{\frac{\sqrt{p^2+|n|^2} \pm p}{2\sqrt{p^2+|n|^2}}}\Psi_{\uparrow,-3/2} \mp \frac{n}{\sqrt{2\sqrt{p^2+|n|^2}(\sqrt{p^2+|n|^2} \pm p)}}\Psi_{\downarrow,-3/2} \quad , \quad (2.37)$$

where $n = \mu_B g_e H_+$ and $p = 3\eta + \mu_B g_e H_z$. The energies and wavefunctions of the former $F = 2, 1$ states are (using notation similar to that used above):

$$\varepsilon^{\pm}_{1,2} = \frac{-\Delta - 3\mu_B g_h H_z}{2} \pm \frac{\sqrt{(3\eta - \mu_B g_e H_z)^2 + (\mu_B g_e)^2 H_\perp^2}}{2} \quad , \quad (2.38)$$

$$\Psi^{\pm}_{1,2} = \sqrt{\frac{\sqrt{p'^2+|n'|^2} \pm p'}{2\sqrt{p'^2+|n'|^2}}}\Psi_{\downarrow,3/2} \mp \frac{n'}{\sqrt{2\sqrt{p'^2+|n'|^2}(\sqrt{p'^2+|n'|^2} \pm p')}}\Psi_{\uparrow,3/2} \quad , \quad (2.39)$$

where $n' = \mu_B g_e H_-$ and $p' = 3\eta - \mu_B g_e H_z$. As a result, the lifetime of the Dark Exciton in an external magnetic field can be written as:

$$\frac{1}{\tau(H)} = \frac{\sqrt{1+\zeta^2+2\zeta\cos\theta} - 1 - \zeta\cos\theta}{2\sqrt{1+\zeta^2+2\zeta\cos\theta}} \frac{3}{2\tau_0} \quad (2.40)$$

where $\zeta = \mu_B g_e H/3\eta$. The probability of exciton recombination increases in weak magnetic fields ($\zeta << 1$) as $\frac{(0.5\mu_B g_e H)^2}{(3\eta)^2}\frac{3\sin^2(\theta)}{2\tau_0}$, and saturates in strong magnetic fields ($\zeta >> 1$), reaching $\frac{3(1-\cos\theta)}{4\tau_0}[1 - \frac{3\eta}{\mu_B g_e H}(1+\cos\theta)]$.

One can see from Eqs. 2-35 and 2-40 that the lifetime depends on the angle between the crystal hexagonal axis and the magnetic field. The recombination time is different for different crystal orientations, leading to a nonexponential lifetime for a system of randomly oriented nanocrystallites.

2.3 Experiment

The samples in our Stokes shift study were prepared using the synthetic technique described in [32]. This method produces nearly monodisperse wurtzite crystallites of CdSe ($\sigma < 5\%$) which are slightly prolate and have surfaces passivated by an organic layer of tri-n-octylphosphine/tri-n-octylphosphine oxide ligands. In total 18 samples were prepared for this study. Their effective radii, as determined by small angle x-ray scattering and TEM measurements, range from 12 Å to 56 Å. The samples were isolated as a powder and redispersed into a mixture of o-terphenyl in tri-n-butylphosphine (200 mg/ml) to form an optically clear glass at liquid helium temperatures. Each sample was loaded between sapphire flats separated by a 0.5 mm Teflon spacer and mounted in a helium cold finger cryostat for low temperature optical work. The 12 Å sample used in the magnetic field and luminescence lifetime experiments was left in its original growth solution without being redispersed in tri-n-butylphosphine and o-terphenyl. With the exception of the 12 Å sample just described, all samples in our Stokes shift study were prepared specifically for this study.

Absorption, luminescence and fluorescence line narrowed spectra were taken on the same optical setup. In the absorption experiment, light from a 300 W Xe arc lamp is passed through the sample and the transmitted light detected with an optical multichannel analyzer (OMA) coupled to a 0.33 m single spectrometer. The full luminescence spectra of each sample is obtained by passing light from a 300 W Hg-Xe arc lamp through a 0.25 m spectrometer and exciting the sample far above its band edge. Typically, the excitation light is kept spectrally broad ($\sim$ 50 nm FWHM)

to prevent any possible optical size selection of the QDs. The emitted light is then dispersed and detected with the spectrometer/OMA combination described in the absorption experiment.

Fluorescence line narrowed spectra are acquired by exciting the samples with the output of a Q-switched Nd:YAG/dye laser system ($\sim$ 7 ns pulses). The laser power is attenuated to ensure that the luminescence varies linearly with the excitation intensity. The measured emission is dispersed and detected with a 0.33 m spectrometer coupled to a 5 ns gated OMA.

Magnetic field studies are conducted by placing the sample within the bore of a variable field superconducting magnet. The excitation source is the Nd:YAG/dye laser system described above. The resulting luminescence is dispersed with a 0.66 m single spectrometer and detected with a 5 ns time gated OMA. Luminescence decays are recorded with the following: a 500 MHz digitizing oscilloscope, a photomultiplier tube with 2 ns resolution and a 0.75 m subtractive double spectrometer to eliminate scattered laser light.

2.3.1 Stokes shift of the resonant photoluminescence

We observe strong evidence for the predicted band edge fine structure in our fluorescence line narrowing (FLN) experiments. By exciting our samples on the red edge of the absorption we selectively excite the largest dots present in the residual size distribution of each sample. This reduces the inhomogeneous broadening of the luminescence and the resulting emission is spectrally narrow, displaying a well resolved longitudinal optical (LO) phonon progression. In practice, we excite our samples on

the red edge of their band edge absorption at roughly 1/3 the peak height. Figure 2-6 shows the FLN spectra for the size series considered. The peak of the zero LO phonon line (ZPL) is observed to be shifted with respect to the excitation frequency. This Stokes shift is size dependent and ranges from $\sim$ 20 meV in small crystals to $\sim$ 2 meV at large sizes. Moving the excitation position does not noticeably affect the Stokes shift of the larger samples; however, it does make a difference for the smaller sizes. We attribute this difference to exciting different sized QDs within the size distribution of the sample, causing the observed Stokes shift to change. The effect is largest in the case of small nanocrystallites because of the size dependence of the Stokes shift (see Fig. 2-7).

In terms of the proposed model, exciting the red edge of the absorption probes the lowest $|F| = 1$ Bright Exciton (see Fig. 2-2 d). The transition to this state is followed by thermal relaxation to the Dark $|F| = 2$ state, from where recombination occurs through a phonon assisted [63, 52] or nuclear/paramagnetic spin-flip assisted transition [63]. The observed Stokes shift is the difference in energy between the $\pm 1^L$ state and the Dark ± 2 state and increases with decreasing size.

We find good agreement between experimental values of the size dependent Stokes shift and values derived from theory. Fig. 2-7 compares the two results. The only parameters used in the theoretical calculation are taken from the literature: $a_{ex} =$ 56 Å [15], $\hbar\omega_{ST} = 0.13$ meV [110] and $\beta = 0.28$ [12, 96]. The comparison shows that there is good quantitative agreement between experiment and theory at large sizes. For small crystals, however, the theoretical splitting based largely on the size dependent exchange interaction begins to underestimate the observed Stokes shift.

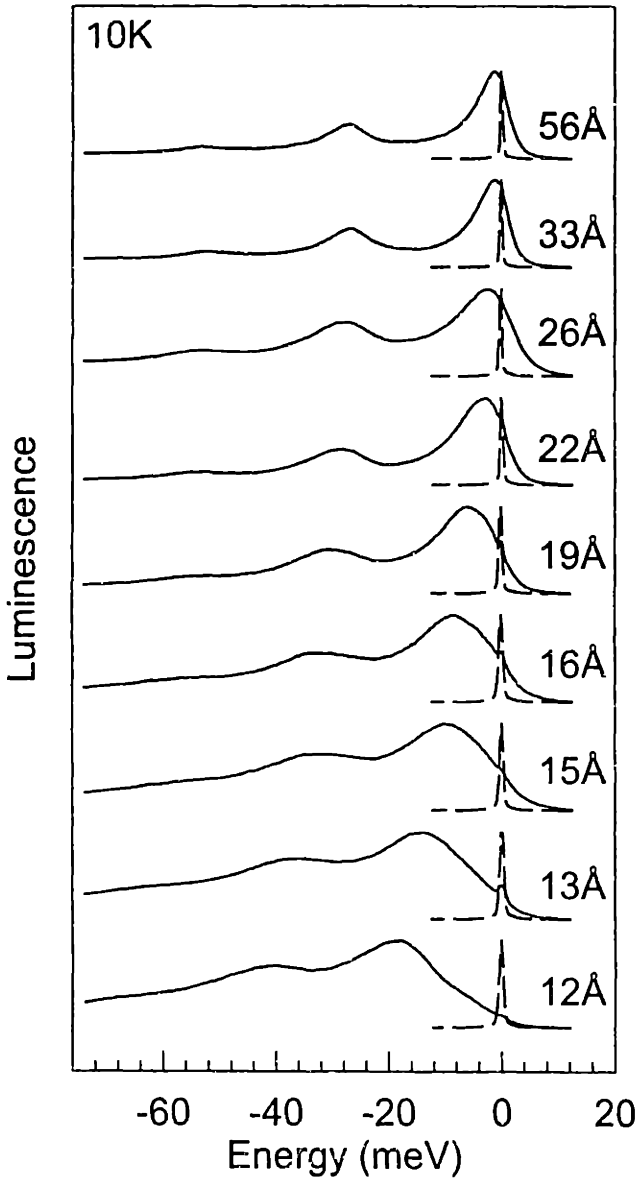

Figure 2-6: Normalized FLN spectra for CdSe QDs between 12 and 56 Å in radius. The mean radii of the dots are determined from SAXS and TEM measurements. A 10 Hz Q-switched Nd:YAG/dye laser system ($\sim$ 7 ns pulses) serves as the excitation source. Detection of the FLN signal is accomplished using a time gated OMA. The laser line is included in the figure (dotted line) for reference purposes. All FLN spectra are taken at 10 K.

This discrepancy may be due to the added contribution of acoustic phonons to the Stokes shift or by a breakdown in the effective mass approximation.[114, 115]

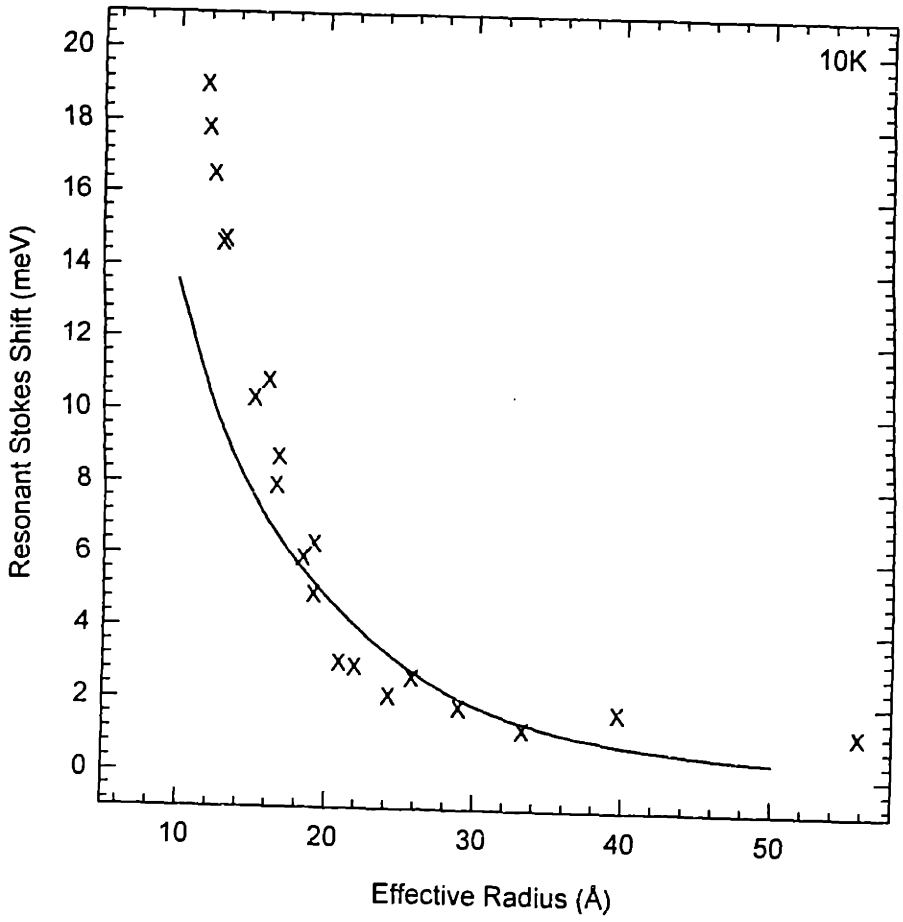

Figure 2-7: The size dependence of the resonant Stokes shift. This Stokes shift is the difference in energy between the pump energy and the peak of the ZPL in the FLN experiment. The points labeled by × are the experimental values. The solid line is the theoretical size dependent splitting between the $\pm 1^L$ state and the ± 2 exciton ground state [see Fig. 2-2 d].

2.3.2 Stokes shift of the non-resonant photoluminescence

We have also studied the Stokes shift of the non-resonant photoluminescence. In this experiment we excite our samples far to the blue of their band edge absorption. The resulting "full" luminescence contains contributions from all nanocrystallites in

the sample's residual size distribution and is inhomogeneously broadened. It shows no distinct phonon structure. This is unlike the FLN experiment where we suppress the inhomogeneous broadening of the luminescence by selectively exciting a narrow subset of nanocrystallites. Fig. 2-8 presents the full luminescence spectrum measured for 9 sizes in the series considered. As with the FLN data, the full luminescence shows a strong size dependent Stokes shift, ranging from $\sim$ 100 meV at small sizes to $\sim$ 25 meV at large sizes. Note that the full luminescence Stokes shift is taken as the difference in energy between the peak of the band edge absorption and the peak of the full luminescence. We denote the full luminescence shift as the "non-resonant" Stokes shift. This shift requires too large a Huang-Rhys S parameter to be readily explained by exciton-phonon coupling [116]. Two explanations, however, account for the large value of the non-resonant Stokes shift.

The first one is directly related to the nanocrystal size distribution. In the strong confinement regime the total oscillator strength of transitions between the electron and hole quantum size levels does not depend on size. However, the excitation probability is proportional to the number of participating states and is therefore proportional to the crystal volume ($\propto a^3$) for excitations far from the band edge [49]. Thus while the first absorption peak generally follows the nanocrystal size distribution, the position of the luminescence for non-resonant excitation is determined by the largest QDs within the distribution. This causes an intrinsic Stokes shift because the band edge transition of larger nanocrystallites occurs at lower energies than in smaller ones.

This, however, is not the main source of the non-resonant shift in our samples, which have narrow size distributions ($\sigma \leq 5\%$). The non-resonant Stokes shift in this

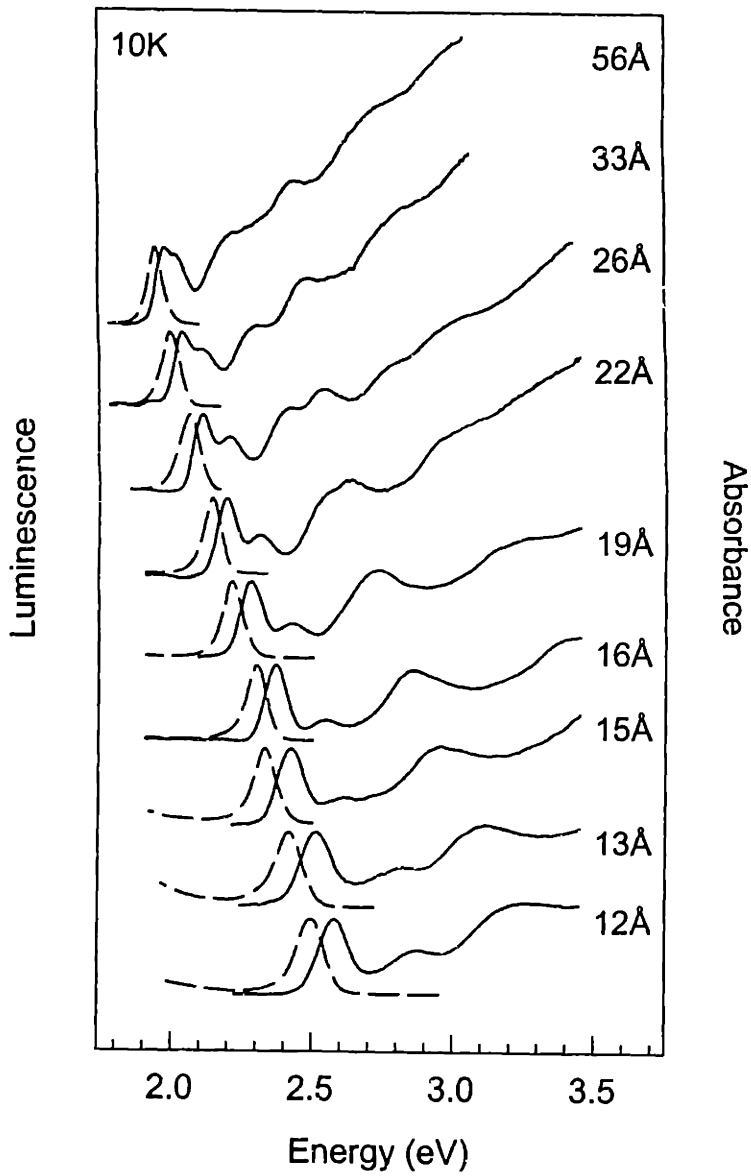

Figure 2-8: Normalized absorption and full luminescence spectra for CdSe QDs between 12 and 56 Å in radius. A 300 W Xe arc lamp serves as the excitation source for both absorption and luminescence experiments. The excitation light is intentionally broad (50 nm FWHM) to prevent possible size selection of the dots. Detection of the transmission/luminescence signal is carried out with an OMA coupled to a 0.33 m spectrometer. The absorption spectra are indicated by solid lines; the corresponding luminescence spectra by dotted lines.

case is primarily related to the band edge exciton fine structure. In small nanocrystallites the two upper states of the fine structure ($\pm 1^U$, 0^U) possess nearly all of the oscillator strength of the band edge transition (see Fig. 2-4 d), and the first absorption maximum is therefore determined by the positions of these two states. The non-resonant Stokes shift is then the difference in energy between these upper states and the ± 2 exciton ground state. This accounts for the sizable magnitude of the non-resonant Stokes shift.

To describe the band edge absorption we convolute the three optically active states with the intrinsic size distribution of the sample and weight each state with its respective oscillator strength. The peak of the band edge absorption occurs at the weighted energetic mean of these three states. We obtain the position of the full luminescence by convoluting the position of the ± 2 Dark exciton with the size distribution weighted by the nanocrystal excitation probability ($\sim a^3$).

Figure 2-9 compares the shifts predicted by theory for a sample with a 5% size distribution to experimental values of the non-resonant Stokes shift. The theory is shown as a dashed line in the figure. We find reasonable agreement between the two, but the theory underestimates the Stokes shift for all sizes considered. However, we have not taken into account the presence of phonons, seen experimentally as LO phonon progressions in FLN and PLE spectra [117, 13, 63, 118]. We include the contribution of the phonons to the theoretical Stokes shift by phenomenologically including in the convolution the phonon dependent absorption $[A(\nu, \nu')]$ and emission

$[E(\nu,\nu')]$ lineshape for single CdSe quantum dots. We assume the following forms,

$$A(\nu,\nu') = \sum_{l=1}^{3}\sum_{m=0}^{4} \frac{(S_a)^m}{\sqrt{2\pi}\gamma_{l,m}m!} \exp\left(\frac{-[\nu-(\nu'+\Delta_l+m\omega_{LO})]^2}{2\gamma_{l,m}^2}\right) \tag{2.41}$$

$$E(\nu,\nu') = \sum_{n=0}^{4} \frac{(S_e)^n}{\sqrt{2\pi}\gamma_n n!} \exp\left(\frac{-[\nu-(\nu'-m\omega_{LO})]^2}{2\gamma_n^2}\right) \quad . \tag{2.42}$$

where we consider the first five LO phonon replicas associated with each of the three bright states (denoted by l) in the absorption as well as the first five LO phonon replicas in the emission. In Eqs. 2-42 and 2-43, ν' denotes the position of the zero phonon line, ω_{LO} is the LO phonon frequency separating the phonon replicas, Δ_l is the offset of the lth Bright Exciton from the $|F| = 2$ Dark Exciton ground state, γ_n is the linewidth of the nth phonon replica in absorption and emission, and $\gamma_{l,m}$ is the width of the mth phonon replica for absorption into the lth Bright Exciton state. The value $S_{a(e)}$ is the absorption (emission) exciton-LO phonon coupling constant. It is equivalent to the Huang-Rhys S parameter assuming a displaced harmonic oscillator model [119]. The values we use for $S_{a(e)}$ are derived from experimental results.[4] Including the phonon contribution moves the predicted band edge absorption maxima to the blue and the emission to the red. This results in the solid curve shown in Fig. 2-9. The modified curve still underestimates the non-resonant Stokes shift, but is in reasonable agreement with the experimental data.

We note that the non-resonant Stokes shift depends on the size distribution. This is illustrated in Fig. 2-9, where we show the increase of the calculated Stokes shift for a sample with a 10% size distribution. The good fit to the experimental data does

[4]The values of $S_e = 0.45$ and $S_a = 0.14$ are consistent with experimental measurements [118]

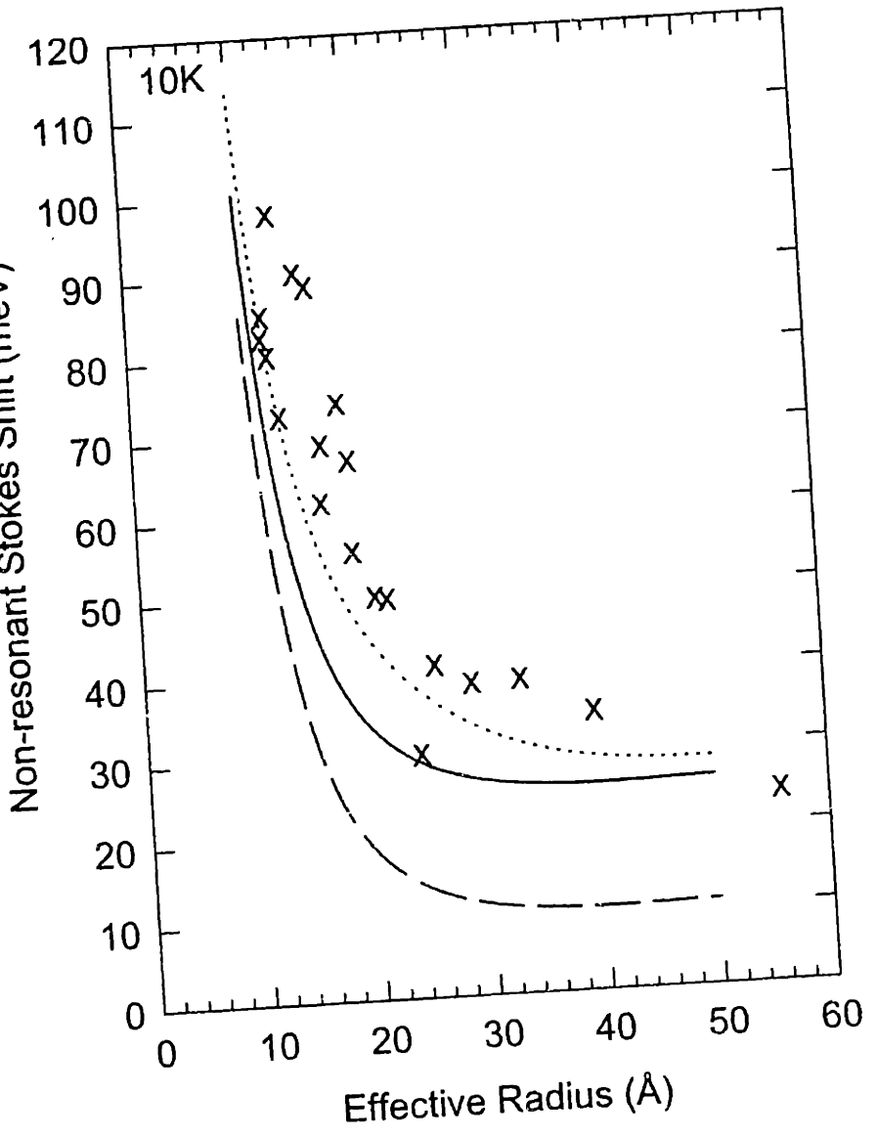

Figure 2-9: The size dependence of the non-resonant Stokes shift. This Stokes shift is considered as the difference in energy between the peak of the band-edge absorption and the peak of the full luminescence. Experimental values are represented by ×. The dashed line is the theoretical Stokes shift calculated for a sample with a $\sigma = 5\%$ size distribution. It is the difference between the mean energy of the three light exciton states and the mean position of the ± 2 exciton ground states of the participating crystals. The solid line includes the contribution of phonons to the theoretical splitting. The dotted line shows the theoretical results for a sample with a 10% size distribution.

not necessarily imply though that we have a 10% size distribution. Any other form of inhomogeneous broadening leads to an additional Stokes shift under non-resonant excitation conditions. The non-resonant Stokes shift may contain contributions from shape distributions, structural inhomogeneities, and differences in chemical environment experienced by the QDs dispersed in the glassy matrix.

2.3.3 Dark exciton lifetime in a magnetic field

Strong evidence for the Dark exciton is found in the FLN spectra and luminescence decays taken in the presence of an external magnetic field. In Fig. 2-10 a we show the magnetic field dependence of the FLN between 0 and 10 T for 12 Å radius QDs. Each spectrum is normalized to the (zero field) one phonon line for clarity. In isolation the ± 2 state would have an infinite lifetime within the electric dipole approximation because the emitted photon cannot carry off an angular momentum of ± 2. However, the Dark Exciton can recombine via an LO-phonon-assisted momentum-conserving transition. [55] Spherical LO phonons with orbital angular momenta of 1 or 2 are expected to participate in these transitions; the selection rules are determined by coupling mechanisms described in refs. [52, 116]. Consequently, for zero field conditions the LO phonon line is strongly enhanced relative to the ZPL. With increasing magnetic field, however, the ± 2 level gains allowed character from the ± 1 exciton (Eq. 2-30). This diminishes the need for an LO phonon assisted transition in QDs whose hexagonal axis is not parallel to the magnetic field. The dramatic rise of the ZPL intensity relative to higher LO phonon replicas with increasing magnetic field can be explained in this manner.

The field induced admixture of optically active states shortens the exciton radiative lifetime. Luminescence decays for 12 Å radius QDs between 0 and 10 T at 1.7 K are shown in Fig. 2-10 b. The sample was excited far to the blue of the first absorption maximum to avoid orientational selection in the excitation process because the transition dipole of the $|F| = 1$ states is predicted to lie perpendicular to the "c" axis (Eq. 2-27). Excitons rapidly thermalize to the ground state through acoustic and optical phonon emission. The long μs luminescence at zero field is consistent with an LO phonon assisted recombination from this state. Although the light emission occurs primarily from the ± 2 state, its long radiative lifetime allows the partially populated (thermally) $\pm 1^L$ state to contribute to the luminescence. With increasing magnetic field the luminescence lifetime decreases. Since the quantum yield remains essentially the same, we interpret this as an enhancement of the radiative rate.

The magnetic field dependence of the luminescence decays can be reproduced using 3-level kinetics with $\pm 1^L$ and ± 2 emitting states [63]. The respective radiative rates from these states, $\Gamma_1(\theta, H)$ and $\Gamma_2(\theta, H)$, in a particular QD, depend on the angle θ between the magnetic field and the crystal hexagonal axis. The thermalization rate, Γ_{th}, of the $\pm 1^L$ state to the ± 2 level is determined independently from picosecond time resolved measurements. The population of the $\pm 1^L$ level is determined by microscopic reversibility. We assume that the magnetic field does not affect the zero field recombination but rather opens up an additional channel for ground state recombination via admixture in the ± 2 state of ± 1 states: $\Gamma_2(\theta, H) = \Gamma_2(0, 0) + 1/\tau_2(\theta, H)$. This also causes a slight decrease in the recombination rate of the $\pm 1^L$ state.

The decay at zero field is multiexponential, presumably due to sample inhomo-

geneities (e.g. shape and symmetry breaking impurity contaminations). We describe the decay using three 3-level systems, each having a different value of $\Gamma_2(0,0)$ and each representing a class of QDs within the inhomogeneous distribution. These three level systems are then weighted to reproduce the zero field decay (Fig. 2-8 c). We obtain average values of $1/\Gamma_2(0,0) = 1.42$ μs and $1/\Gamma_1(0,0) = 10.0$ ns in good agreement with the theoretical value of the radiative lifetime for the $\pm 1^L$ state, $\tau_1^L = 13.3$ ns, calculated for a 12 Å nanocrystal using Eq. 2-33.

In a magnetic field the angle dependent decay rates $[\Gamma_1(\theta, H), \Gamma_2(\theta, H)]$ are determined from Eq. 2-35. The field dependent decay is then calculated, averaging over all angles to account for the random orientation of the QD "c" axes. The simulated decay at 10 T (Fig. 2-8 c), using the bulk value of $g_e = 0.68$ [111] and the calculated values for Δ (19.4 meV) and η (10.3 meV) for 12 Å radius QDs, is in excellent agreement with experiment. The hole g factor is treated as a fitting parameter since reliable values are not available. We used $g_h = -1.00$ consistent with theoretical estimates for this parameter, $g_h = -1.09$ (see Appendix).

2.4 Discussion

The size dependence of the Stokes shift obtained for resonant excitation of the band edge absorption is in excellent agreement with the size dependent splitting between the lowest optically active Bright Exciton state and the optically passive exciton ground state. The discrepancy at small sizes may be related to problems with the effective mass approximation or to the increased role played by phonons in the luminescence. The phonon interaction through the deformation potential was

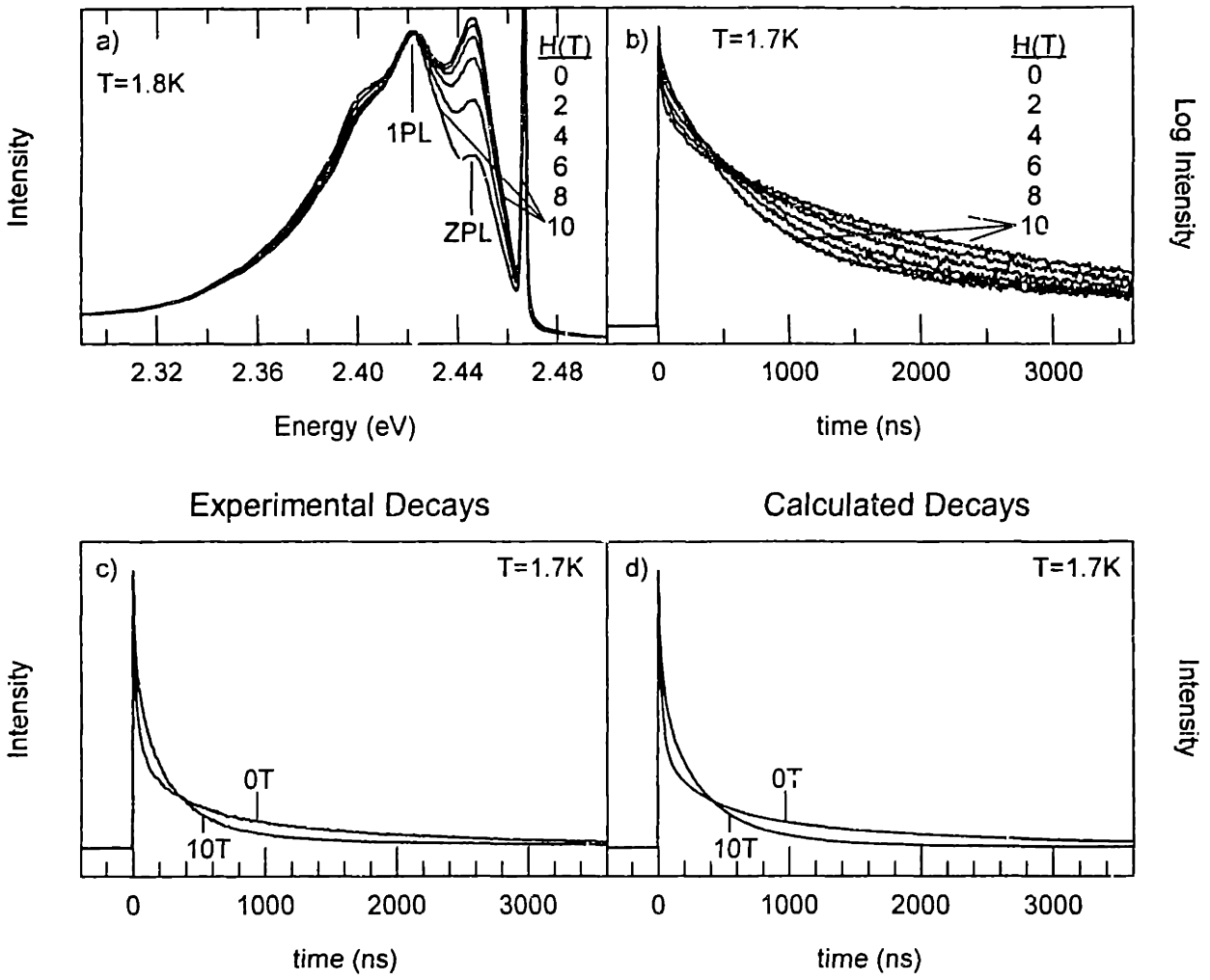

Figure 2-10: (a) FLN spectra of 12 Å radius QDs as a function of external magnetic field. The spectra are normalized to their one phonon lines (1PL). A small fraction of the excitation laser, included for reference purposes, appears as a sharp feature at 2.467 eV to the blue of the zero phonon line (ZPL). (b) Luminescence decays for 12 Å radius QDs for magnetic fields between 0 and 10 T measured at the peak of the "full" luminescence (2.436 eV). The pump energy is 2.736 eV. All experiments were done in the Faraday configuration ($H||K$). (c) Observed luminescence decays for 12 Å radius QDs at 0 and 10 T. (d) Calculated decays based on the three-level model described in the text. Three weighted three-level systems were used to simulate the decay at zero field with different values of γ_2 (0.033, 0.0033, and 0.00056 ns^{-1}) Weighting factors were 1, 3.8 and 15.3 respectively. γ_1 (0.1 ns^{-1}) and γ_{th} (0.026 ps^{-1}) were held fixed in all three systems.

shown both theoretically [120] and experimentally [121, 122, 123] to increase with decreasing size. This can lead to the formation of an exciton-polaron and be the source of an additional Stokes shift in the luminescence [114].

The large difference in magnitude between resonant and non-resonant Stokes shifts is related to the difference in oscillator strengths of the upper and lower optically active Bright Exciton states. In the smallest crystals, the upper Bright Excitons ($\pm 1^U$, 0^U) gain the oscillator strength of the lower Bright state ($\pm 1^L$) and give the main contribution to the absorption. The non-resonant Stokes shift in this case is the energy difference between the upper Bright Excitons and the optically passive Dark Exciton ground state. The experimental size dependence of the non-resonant Stokes shift is in reasonable agreement with theory. What discrepancy remains may be attributed to phonon participation in the luminescence, which is theoretically not well understood for CdSe QDs [124].

While surface effects, previously invoked to explain the photophysical behavior of CdSe quantum dots, may still play a role, especially via non-radiative processes, the energetics and dynamics of the band edge emission can be quantitatively understood in terms of the intrinsic band edge exciton fine structure. Exciton thermalization to a dipole forbidden ± 2 Dark Exciton resolves the issue of long lifetimes at low temperatures. An external magnetic field mixes the Dark Exciton with optically active Bright excitons allowing its recombination. The magnetic field dependence of the emission decays and the observed LO phonon structure confirm the presence of this "dark" exciton.

In zero external magnetic field, recombination of the ± 2 Dark Exciton can take

place via an LO phonon assisted transition. Phonons can contribute to the total angular momentum projection, ± 2, which cannot be accounted for by a photon alone. However, even in the absence of an external magnetic field the zero LO phonon line is weakly allowed, suggesting an alternate recombination pathway, for example through coupling to acoustic phonons. Interaction with paramagnetic defects in the lattice can also provide an important additional mechanism for radiative recombination. The spins of these defects potentially generate strong effective internal magnetic fields, which, depending on the strength of the spin-spin exchange interaction with the carriers and on the crystal radius, can reach several tens of Tesla inducing spin-flip assisted transitions from the ± 2 state. This enables zero phonon recombination to occur. Preliminary EPR spectra do, in fact, indicate a small concentration of paramagnetic centers in our samples and efforts under way to introduce an electrically neutral magnetic impurity such as Mn^{+2} into the lattice may confirm this mechanism.[5]

Despite the success of our model in describing the electronic structure of the band edge excitation in CdSe nanocrystallites, several questions remain unanswered. They include the increase of the homogeneous linewidth with decreasing size [125] and the underestimation of the resonant Stokes shift at small sizes. Both issues may be related to our lack of knowledge about the main mechanism of exciton interaction with polar optical phonons [124].

[5]See Chapter 6 for more details.

2.5 Conclusion

In conclusion, we have described the origin of the band edge fine structure underlying the nominally 8-fold degenerate $1S_{3/2}1S_e$ transition and have explained in a self-consistent way most of the complex and controversial results in nanometer-sized CdSe QDs, e.g. the small Stokes shift of the resonant photoluminescence, the large Stokes shift of the non-resonant PL, the long radiative lifetime, its decrease in magnetic fields, and the fine structure seen in fluorescence line narrowing and photoluminescence excitation experiments [118].

2.6 Appendix: Calculation of the hole g factor

The expression for the g factor of a hole localized in a spherically symmetric potential was obtained by Gel'mont and D'yakonov and is:[112]

$$g_h = \frac{4}{5}\gamma_1 I_2 + \frac{8}{5}\gamma(I_1 - I_2) + 3\kappa(1 - \frac{4}{5}I_2) \ , \tag{2.43}$$

where γ_1, γ, and κ are the Luttinger parameters [126] and $I_{1,2}$ are integrals of the hole radial wavefunctions [see Eq. (6)]:

$$I_1 = \int_0^a dr r^3 R_2 \frac{dR_0}{dr} \ , \qquad I_2 = \int_0^a dr r^2 R_2^2 \ . \tag{2.44}$$

These integrals depend only on the parameter β, and their dependence is shown in Fig. 2-11. Using $\gamma_1 = 2.04$ and $\gamma = 0.58$[96], and the relationship $\kappa = -2/3 + 5\gamma/3 - \gamma_1/3$[127], we obtain $g_h = -1.09$.

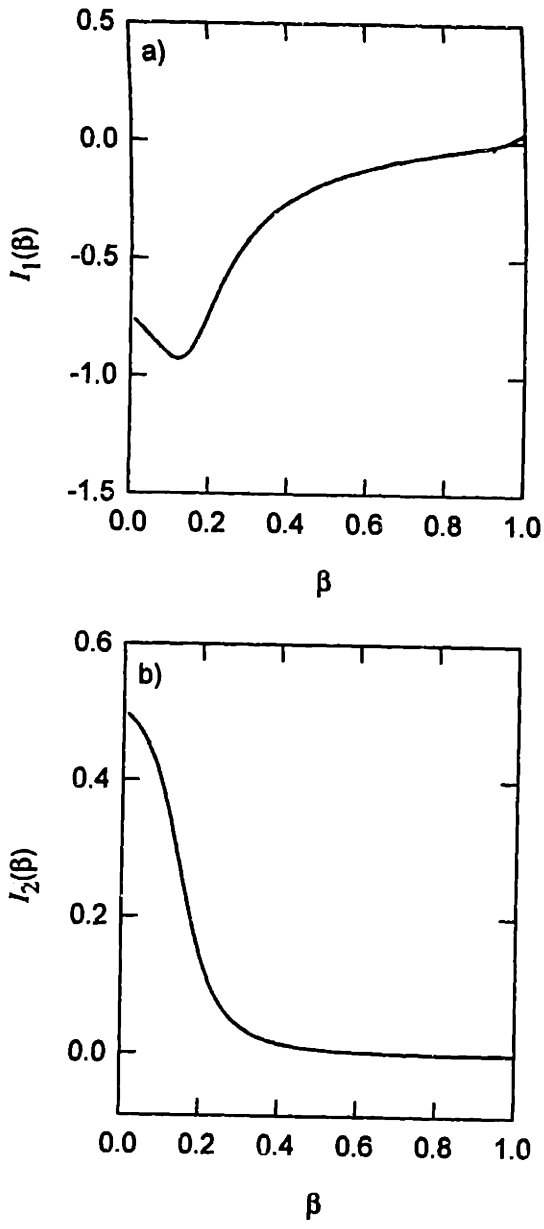

Figure 2-11: Dependence of the hole radial function integrals I_1 and I_2, which enter in the expression for the hole g factor, on the hole effective mass ratio, β.

Chapter 3

The Surface

In this chapter, we study the luminescence of surface modified CdSe nanocrystallites. There has been much speculation as to the origin of the band edge emission in these quantum confined structures. Because of their large surface to volume ratios it has been suggested that the emission originates from surface-related states. However, recent theory suggests that the band edge luminescence arises from an optically inactive fine structure state or "dark" exciton. To address this issue we modify the surface of CdSe nanocrystallites with a variety of organic and inorganic ligands. We then monitor the effect changing the surface has on the energetics of the band edge luminescence through photoluminescence and fluorescence line narrowing experiments. Our results are compared with theoretical predictions for the non-resonant and resonant luminescence. We find good agreement between experiment and theory for CdSe nanocrystallites passivated with trioctylphosphine oxide, ZnS, 4-picoline, 4-(trifluoromethyl)thicphenol and tris(2-ethylhexyl)phosphate. The lack of dependence of our data on surface modification is consistent with a dark exciton description of

the band edge luminescence.

3.1 Introduction

Over the course of the last decade there has been considerable interest in the optical properties of small semiconductor quantum dots. These quantum dots (QDs) or nanocrystallites represent a general class of materials (mesoscopic materials) that span the physical domain between bulk materials and molecular compounds. Interesting optical properties occur when the size of the QD becomes comparable to or smaller than the bulk exciton Bohr radius. These effects arise from the spatial confinement of electronic excitations to the physical dimensions of the nanocrystallite and are referred to as quantum confinement effects.[49, 1] One such effect is the quantization of the bulk valence and conduction bands which results in discrete atomic-like transitions that shift to higher energies as the size of the nanocrystallite decreases.

To date much work has focused on describing the size dependent absorption spectrum of these QDs.[49, 1, 119, 128, 129, 130, 131, 51, 107, 60, 132, 12, 133, 134, 96, 118, 62, 15] Various models have been proposed which qualitatively, if not quantitatively, explain the observed trends and for the most part the linear absorption is thought to be well understood. The emission of these dots, however, remains harder to characterize. This is due to the fact that the luminescence of many QD samples is dominated by a broad featureless emission (known as "deep trap" emission) strongly redshifted from the band edge. Recent results obtained from high quality CdSe QDs have shown strong luminescence near the band edge and in doing so have raised a number of questions regarding the nature of the emitting state.[15, 13, 61] For in-

stance, the emission has an unusually long recombination time ($\sim 1\mu s$ at 10 K). This is in contrast to the nanosecond lifetimes seen in the bulk. In addition, the band edge luminescence displays a prominent, size dependent, redshift from the peak of the band edge absorption.

To account for these observations the band edge luminescence has often been attributed to the recombination of surface localized carriers.[60, 13, 41, 61] The role of surface related states is a likely possibility since a large number of atoms composing the nanocrystallite reside on its surface. Uneven passivation, defects, and the QD analog of bulk surface bands all could potentially create "trap" states with energies within the band gap of the material. These trap states could subsequently act to localize one or both charge carriers upon photo-excitation of the nanocrystallite. The recombination of weakly overlapping surface localized carriers would then explain the long lifetimes as well as the redshift in the band edge luminescence.

While these luminescence results are consistent with proposed surface models they can also be explained with models which do not invoke the role of surface states but instead explain the luminescence in terms of recombination through internal core states.[87, 84, 82, 86, 75] We consider one such model which takes into account various contributions lifting the degeneracy of the band edge exciton in CdSe nanocrystallites.[63, 64] When these effects are accounted for the model predicts that the lowest excited state in CdSe QDs is an optically inactive fine structure state or "Dark" exciton with angular momentum projection ± 2. The presence of the Dark exciton explains both the long lifetimes and the redshift of the luminescence as linear optical transitions into and out of this state are formally spin forbidden.

To address the issue of whether the luminescence from CdSe QDs is surface related or arises from the radiative recombination of core states we systematically alter the surface of CdSe nanocrystallites with a variety of organic and inorganic ligands.[135, 136, 66, 67, 137, 138] We then monitor the effect this has on the luminescence through two experiments; a photoluminescence (PL) and a fluorescence line narrowing (FLN) experiment. In these experiments we measure the non-resonant and resonant Stokes shift for a series of surface modified CdSe QDs. The luminescence results we obtain for QDs passivated by trioctylphosphine oxide, ZnS, 4-picoline, 4-(trifluoromethyl)thiophenol and tris(2-ethylhexyl)phosphate are in good agreement with each other and with the predictions of the intrinsic exciton model.

3.2 Experiment

As much of the work relies upon the synthesis and subsequent manipulation of high quality CdSe nanocrystallites, we describe in some detail our preparation procedures. We synthesize CdSe QDs according to the method described in ref. [32]. Briefly, 40 grams of trioctylphosphine oxide (TOPO, 90% Strem) is dried and degassed under vacuum at 160°C for approximately 4 hours. In a glovebox, 32 mls of trioctylphosphine (TOP, 95% Fluka) is mixed with 8 mls of a 1M solution of TOPSe. Once the TOPO has been dried and degassed the reaction flask is backfilled with N_2 and the temperature is increased to $330 - 350^{\circ}$C. 400 ml of dimethylcadmium ($CdMe_2$, Fluka) is then added to the TOP/TOPSe solution in the glovebox and the mixture is brought out in a 50 ml syringe. When the temperature has stabilized this solution is injected into the hot, stirring TOPO resulting in nucleation and growth of

the QDs. The growth is typically carried out at $\geq 300^{\circ}$C and is monitored through the UV/Visible absorption spectra of the dots. When the desired size is reached the growth is terminated by removing the heat.

The QDs produced in this manner have a wurtzite crystal structure, are slightly prolate and have surfaces passivated by TOPO and TOPSe.[32, 33] They differ from CdSe QDs prepared by many other synthetic methods in that they luminesce strongly at the band edge (quantum yields ~10-20% at 300 K and 10-90% at 10 K) [96] and show little deep trap emission.

To obtain nearly monodisperse samples we follow the growth of the QDs with size selective precipitation. This procedure, described in ref. [32], involves precipitating out of solution the largest QDs present in the initial growth mixture. By repeatedly performing this procedure it is possible to obtain distributions with standard deviations (σ) $\leq$ 5%. In our experiments we used material which had been size selected at most twice. As a consequence our distributions may be somewhat larger than 5%. This was done to ensure that we had sufficient material to divide the preparation into four parts. One fraction was kept in its native state (i.e. passivated with TOPO/TOPSe) and the other three were subjected to surface modification through ligand exchange with various organic capping groups. Another size series was also created, one fraction of which was left in its native state and the other overcoated with ZnS.

3.2.1 Surface Exchanged QDs

To modify the surface of size selected CdSe QDs with different organic ligands we employed the following procedure. 4-Picoline, 4-(trifluoromethyl) thiophenol and tris (2-ethylhexyl) phosphate were purchased from Aldrich, Trans World Chemicals and Fluka respectively. The chemicals were used as received without any further purification. For surface modification with 4-picoline, size selected QDs were recovered as a powder and redispersed in a small volume (typically 5-10 mls) of neat 4-picoline. After overnight stirring the QDs were precipitated from solution by adding an excess of n-hexane. The resulting suspension was then centrifuged and the recovered precipitate dispersed in neat 4-picoline (5-10 mls). This solution was left to stir for ~5 hours whereupon the dots were precipitated, redispersed in 4-picoline as above and left to stir for an additional 5 hours. The QDs were again precipitated from solution and stored in neat 4-picoline.

To passivate the surface of the QD with 4-(trifluoromethyl)thiophenol, size selected dots were recovered as a powder by drying the QD precipitate under a continuous flow of N_2. The isolated QDs were brought into a glovebox where they were dissolved in 3 mls of $CHCl_3$. An estimated 20 fold molar excess[1] of 4-(trifluoromethyl)thiophenol was added to the chloroform solution and the mixture was left to stir for 4 days in a glovebox. At the end of the exchange reaction, the QDs were recovered as a precipitate by adding an excess of n-hexane to the solution. The dots were then redispersed in neat 4-(trifluoromethyl)thiophenol for storage.

Passivating the QDs with tris(2-ethylhexyl)phosphate required first exchanging

[1]The estimate was determined by assuming that all the Cd added to the reaction was consumed to form a particular sized QD. In fact this value is an upper bound.

the surface with pyridine. The procedure we used is identical to the method described for ligand exchange with 4-picoline. Once modified with pyridine, the QDs were precipitated from solution with hexane. To the moist precipitate we typically added 10 mls of neat tris(2-ethylhexyl)phosphate. The precipitate was redispersed in the neat phosphate by heating the mixture under N_2 at 160°C for several hours. The QDs were then isolated as a precipitate by adding excess methanol and redispersed in neat phosphate for storage.

3.2.2 ZnS Overcoated QDs

To passivate the surface of size selected QDs with a ZnS overcoat we followed a procedure similar to those described in refs. [139, 140, 141]. Size selected QDs dispersed in hexane were added to 5-10 grams of warm TOPO (70°C). The TOPO had been previously dried and degassed under vacuum at 200°C. Inside a glove-box equimolar amounts of diethylzinc (DEZn, Fluka) and hexamethyldisilathiane [$(TMS)_2S$, Aldrich] were mixed together with 5 mls of TOP. The amount of zinc and sulfur precursors added varied from preparation to preparation and was adjusted to achieve an estimated 2-3 monolayer coverage on the QD surface. Once the solution had been prepared the temperature of the TOPO solution was increased to 180°C. The ZnS mixture was then added to the QD solution at a rate of approximately 0.5 ml/min through an addition funnel. Afterwards the temperature of the mixture was lowered to 100°C and the solution left to stir for several hours. The overcoated QDs were later recovered by precipitation with methanol. These overcoated QDs were characterized using a variety of techniques, including TEM, XPS, small angle x-ray

scattering (SAXS), wide angle x-ray scattering (wide angle x-ray scattering, WAXS) and the WDS attachment on a SEM.[141]

3.2.3 Control Experiments

Various control experiments were conducted to monitor the extent of ligand exchange. QDs were prepared in several different ways from the standard preparation described above. This was done to evaluate the extent of surface passivation by TOPO and TOPSe. Clusters were prepared with an excess of TOPO over TOP. This involved excluding TOP in our injection solution. (100 mls of $CdMe_2$ and 2 mls of TOPSe were injected into 10 grams of TOPO in a fashion similar to the standard preparation). QDs were also prepared exclusively in TOPO by replacing our TOPSe precursor with bis(trimethylsilyl)selenium, $(TMS)_2Se$, and excluding TOP in the injection solution [400 mls of $CdMe_2$, 400 mls of $(TMS)_2Se$ (prepared according to literature methods) [142] and 20 mls of Squalane were injected into 40 grams of TOPO at 80°C]. The low injection temperature was necessary to prevent chaotic growth of the QDs. The temperature was slowly increased to 300°C and growth of the nanocrystallites was carried out normally.

In addition to these control experiments, QDs synthesized through the standard preparation were subjected to ligand exchange with pyridine and thiophenol for use in NMR experiments. Ligand exchange with pyridine was conducted in the same manner as described for the exchange with 4-picoline. Surface modification with thiophenol involved recovering the QDs as a powder, redispersing them in 5 mls of neat thiophenol and stirring the solution in a glovebox for a day. Both pyridine and

thiophenol capped nanocrystallites could be recovered as powders by adding an excess of n-hexane.

3.2.4 Optical Measurements

To make optical samples from the ZnS overcoated nanocrystallites and their respective TOPO counterparts we isolated the QDs as powders and redispersed them in a mixture of o-terphenyl in tri-n-butylphosphine (200 mg/ml). The o-terphenyl/tri-n-butylphosphine mixture makes an optically clear glass at liquid helium temperatures. Similarly, for the ligand exchanged material, concentrated solutions consisting of the QDs dispersed in their new capping ligand were added to a known volume of 1-butanol. Each sample was then loaded between sapphire flats separated by a 0.5 mm Teflon spacer. The absorbance of all samples was kept below 0.3 at the first absorption feature to minimize re-absorption of the luminescence. The prepared samples were attached to the cold finger of a helium vapor flow cryostat for low temperature optical work.

Our absorption, luminescence and FLN experiments were conducted on the same optical setup. Light from a 300 W Hg-Xe lamp was passed through each sample and the transmitted light dispersed through a 0.33 m spectrometer. An optical multichannel analyzer (OMA) was used to detect the light. The photoluminescence spectra of each sample was obtained by passing light from a 300 W Hg-Xe lamp through a 0.25 m monochromator and using the output to excite the samples far above the band edge. Typically the excitation light was kept spectrally broad (~50 nm FWHM) to prevent any optical size selection of the dots. The resulting luminescence was dispersed and

detected with the spectrometer/OMA combination.

Fluorescence line narrowed spectra were acquired by exciting the samples on the red edge of their absorption with the output of a Q-switched Nd:YAG/dye laser system. In practice, each sample was excited where its low temperature absorbance was approximately 1/3 the peak value of the first absorption feature. By exciting the samples on their red edge we selectively excite only the largest QDs present in the residual size distribution of each sample. This reduces the inhomogeneous broadening of the luminescence and the resulting emission is spectrally narrow, displaying a well resolved longitudinal optical (LO) phonon progression. In our experiments the laser intensity was attenuated to ensure a linear correspondence with the luminescence intensity. The emission was then collected and dispersed using the spectrometer/OMA combination, with the OMA gated to reduce scattered laser light (See Figure 3-1).

3.3 Observations

3.3.1 Characterizing the Surface

During the course of our investigation we made an unexpected observation. In our ligand exchange experiments we found ourselves unable to completely change the surface of the QDs. This was confirmed by solution state proton NMR experiments. The NMR spectra of QDs passivated with thiophenol, 4-(trifluoromethyl)thiophenol, pyridine and 4-picoline all show residual alkyl protons upfield from the aromatic resonances characteristic of these ligands. Based on the relative integrated intensities of the proton peaks we find that 85-90% of the ligands passivating the surface of the

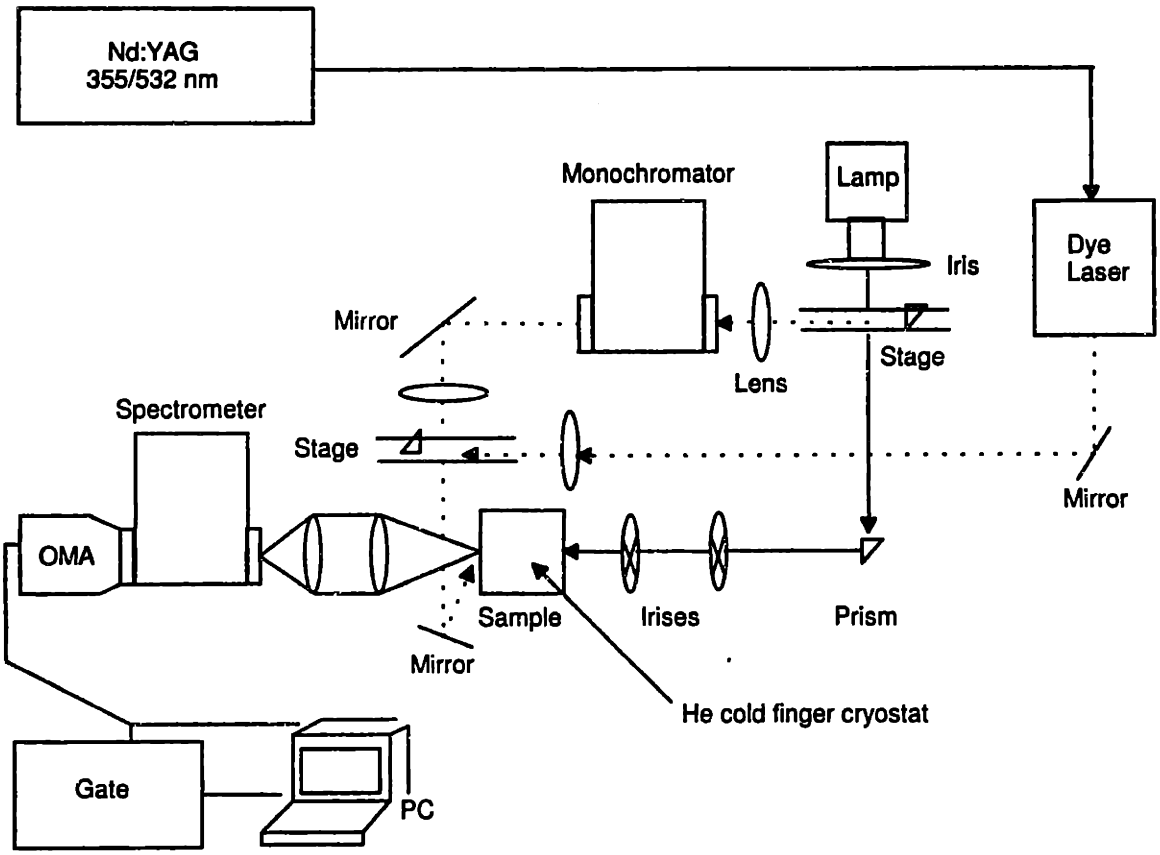

Figure 3-1: Abbreviated schematic of the experimental apparatus used in optical experiments. White light from a 300 W Hg-Xe arc lamp is used in both absorption and photoluminescence (PL) experiments. For absorption measurements the light is brought through a series of irises and passed through the sample into a spectrometer/OMA. For PL experiments, the light is passed through a 0.25 m monochromator. The output light ($\approx$ 50 nm FWHM) is used to excite the sample far above the band edge. The luminescence is detected with the spectrometer/OMA. Light from a 10/50 Hz Nd:YAG is used to pump a dye laser to get tunable frequencies in the FLN experiment. This light is used to excite the sample on the red edge of the absorption. A gate is used to remove scattered laser light from the FLN spectrum.

QDs are the newly introduced capping species. The remaining 10-15% are native capping ligands reflecting the incomplete exchange of the QD surface. Similar results have been seen by Katari et al. in CdSe nanocrystallites exchanged with pyridine.[74]

To overcome this problem we varied the length and number of times the QDs were exposed to the new capping species. Samples were heated during the exchange reactions and in some instances refluxed. In all cases, we found that neither length nor time had a significant effect on the ligand exchange reactions as 10 to 15% of the total surface species remained unaltered.

Several control experiments were carried out to determine the reason for the incomplete exchange reactions. Of interest was the identity of the tightly bound surface species; whether it was TOPO, TOP, TOPSe or some impurity in our TOPO source such as phosphinic acid. The first control experiment involved preparing the QDs using an excess of TOPO. As described in the experimental section this involved excluding TOP in the injection solution. The nanocrystallites prepared in this manner were subjected to ligand exchange with thiophenol. The exchange reaction showed that 91% of the surface species consisted of the newly introduced cap, in agreement with previous results. A second control experiment involved preparing the QDs exclusively in TOPO. This meant excluding TOP in our injection solution and replacing our TOPSe precursor with $(TMS)_2Se$. The exchange reaction of this material with thiophenol was also incomplete and showed a 95% exchange.

Both experiments suggested that TOPO was specially coordinated to the surface of the QD but did not exclude the possibility that TOPSe or TOP was also tightly bound. To eliminate the possibility that the special surface species was an impurity

from our technical grade TOPO we prepared QDs according to the method described in ref. [74]. This procedure uses higher purity TOPO (99% Aldrich) and minimizes the potential contribution from a host of impurities such as phosphinic acid. (See ref. [143] for a careful investigation of common impurities found in TOPO) The exchange reaction in this case was also incomplete (86%) and suggested that TOPO, possibly TOPSe/TOP, remains strongly bound to the surface even in the presence of a large excess of coordinating ligands.

Several ^{31}P NMR experiments were conducted to give us more insight into the nature of the tightly bound surface species. The proton decoupled ^{31}P NMR of normally prepared QDs in deuterated chloroform is shown in Figure 3-2 a. Most prominent in the spectrum is a broad feature centered between 20 to 30 ppm. It appears to be composed of three peaks and is neighbored by two smaller peaks on either side of its center. The frequency difference between the center peak and each of the two neighboring peaks (~3600 Hz) makes it unlikely that they are spinning sidebands. Another possibility is that the peaks are the result of couplings between phosphorous and cadmium (or selenium). However, known coupling constants for cadmium or selenium are much smaller than the values we observe.[2][144, 145] T_1 measurements confirm that the two neighboring peaks are not coupling/spinning sidebands of the central feature. (Measured T_1 values are listed in Table 3-1.) As a consequence, these three peaks along with a small feature centered at -20 ppm indicate the existence of at least four distinct chemical environments for the ^{31}P nuclei on the surface of the QD. Several of these peaks have been seen before in the solid state ^{31}P NMR of CdSe

[2] $J_{P-Se} = 500 - 700$ Hz, $J_{P-Cd} = 40 - 60$ Hz

QDs.[33]

We attribute the broadness of the NMR features to the inhomogeneous distribution of magnetic environments found on the QD surface, not to the equilibrium between free and bound ligands. Measuring the proton coupled ^{31}P NMR had little effect on the observed peak widths. This result in conjunction with structural studies indicating a disordered or reconstructed surface supports the notion that the spectral broadness is due to the multiple environments found on the QD surface. [32, 33, 146, 73]

To help assign the features in the QD ^{31}P spectra we measured the ^{31}P NMR of TOPO, TOP and TOPSe in several deuterated solvents. TOPO has a peak around 50 ppm in chloroform; TOPSe has a peak at 30 ppm in benzene and TOP has a resonance at -30 ppm in chloroform. A list of observed peak positions for TOPO, TOPSe, TOP and normally prepared QDs can be found in Table 3-1. One puzzling feature of the QD ^{31}P NMR which becomes apparent after comparing the various peak positions is that a number of phosphorous resonances appear to have shifted upfield rather than downfield. This is inconsistent with deshielding effects normally observed when a phosphine oxide is bound to an electrophile. For example, triphenylphosphine oxide has a resonance at -25 ppm. When placed in the presence of an electrophile such as formic acid, sulfuric acid or Cd^{+2} the phosphorous resonance moves further downfield to 37 ppm, 60 ppm and 37-39 ppm respectively.[144, 147] If we assume that the broad feature between 20 and 30 ppm arises from TOPO/TOPSe bound to the QD surface, this implies that the surface shields rather than deshields the phosphorous nuclei moving its resonance to higher energies. Possible explanations

for this effect may lie in the presence of Se lone pairs on the surface of the QD or in the high electron density of the nanocrystallite which can screen the ^{31}P nuclei from external magnetic fields.

The ^{31}P NMR of TOPO/TOPSe passivated QDs dispersed in deuterated pyridine (Figure 3-2 b) shows that the broad peak centered at 25 ppm splits into at least two components revealing a sharp peak at 22 ppm superimposed on top of a broader peak centered at 20-25 ppm bordered by two neighboring peaks. The spectrum also shows that the small feature at -20 ppm diminishes in intensity and is replaced by a sharp peak at -32 ppm which we interpret as free TOP in solution. If we monitor the ^{31}P NMR with time we observe that the narrow peak at 22 ppm diminishes in intensity and is followed by the appearance of a sharp peak at 47 ppm. Based on a comparison to known peak positions we interpret this feature as free TOPO in solution. These results suggest that an excess of pyridine can successfully displace both TOP and TOPO from the surface of the QD. We tentatively assign the small feature at -20 ppm in the QD chloroform spectra as TOP loosely bound to surface selenium atoms and also assign the narrow feature at 22 ppm in the QD pyridine spectra as TOPO bound to surface cadmium atoms. The identity of the broad central feature accompanied by its two neighboring peaks is still unknown at this point.

To further clarify the identity of the various phosphorous resonances, we measured the ^{31}P NMR of QDs made exclusively in TOPO. The spectrum is shown in Figure 3-2 c. As with the first chloroform spectra, we observe a broad feature centered at 20-30 ppm bordered by two neighboring peaks. There are differences between spectrum 3-2 c and 3-2 a. The broad central feature in this case appears to be composed of two

peaks, not three. In addition, the small peak at -20 ppm is absent. Since no TOP or TOPSe was introduced at any point in the sample preparation, the appearance of the exclusive TOPO spectra supports our initial assignment that the peak at -20 ppm in the chloroform spectra is due to TOP bound to surface selenium atoms. The presence of the broad central feature with symmetric neighbors also suggests that these peaks are TOPO related and the absence of a third component to the central feature implies that this contribution arises from TOPSe bound to surface cadmium atoms.

The ^{31}P NMR of normally prepared QDs which have been repeatedly washed with pyridine is shown in Figure 3-2 d. It indicates that even after extensive exposure to a new coordinating solvent there are still native ligands which remain tightly bound to the QD surface. Although the signal to noise is poor we identify the dominant central peak at 20-30 ppm. If our assignments are correct, the presence of this peak suggests that there are sites on the QD surface which coordinate strongly to TOPO and possibly TOPSe.

To give a measure of the amount of TOPO/TOPSe on the surface of the QD before and after ligand exchange we performed thermal gravimetric analysis (TGA) measurements in conjunction with quantitative proton NMR measurements. Table 3-2 summarizes our results and indicates that in normally prepared QDs only 30% of surface cadmium atoms are passivated by TOPO/TOPSe. Exposing the QDs to an excess of pyridine replaces approximately 2/3 of the initial TOPO/TOPSe ligands leaving 1/3 of the sites unchanged. At the same time the absolute coverage of surface cadmium sites appears to increase dramatically, from roughly 30% to 90%. These

Table 3.1: ^{31}P NMR data on capping ligands and passivating QDs.

	Solvent	Chemical shift (ppm)[3]	T_1 (s)	
TOP	$CDCl_3$	-30	···	
TOPO	$CDCl_3$	50	···	
TOPSe	C_6D_6	30	···	
Normally prepared QDs	$CDCl_3$	54	1.9	Broad
		25	4.4	Broad, three peaks
		-3	8.7	Broad
		-20	6.2	Broad
	pyr-d_5	47	···	Broad
		20	···	Broad w. one narrow peak at 22 ppm
		-2	···	Broad
		-32	···	Sharp, free TOP
Exclusive TOPO QDs[4]	$CDCl_3$	55	···	Broad
		34,35	···	Broad, two peaks
		-4	···	Broad

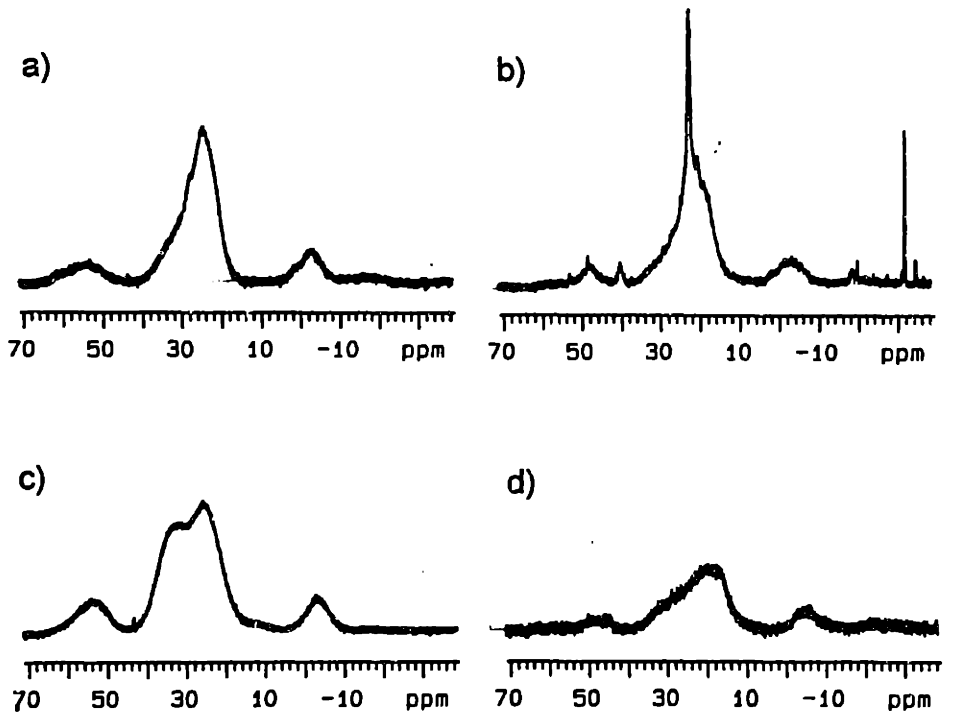

Figure 3-2: ^{31}P NMR of (a) normally prepared QDs dispersed in $CDCl_3$, (b) normally prepared QDs dispersed in pyr-d_5, (c) QDs made exclusively in TOPO using $(TMS)_2Se$ instead of TOPSe (in $CdCl_3$), (d) pyridine capped QDs (in pyr-d_5).

results are consistent with NMR measurements indicating that 85 to 90% of the ligands on the surface are the new capping species and that roughly 10 to 15% are the original TOPO/TOPSe molecules. The amount of unchanged Cd sites can also be expressed in terms of the amount of residual TOPO left on the surface of the QD after ligand exchange, 38% (from TGA) compared to 40% from NMR measurements (see Table 3-2. Note that our analysis assumes TOPO rather than TOPO/TOPSe passivation for simplicity).

At this point we can only speculate that the unremoved TOPO/TOPSe occupy special sites related to selenium vacancies on the surface which leave behind empty voids of exposed cadmium atoms. Bonding by TOPO (TOPSe) could then take the form of bridging positions over several cadmium atoms which would account for the stronger bonding strengths observed. Further work is needed to clarify the true surface morphology of the QDs.

3.3.2 Results from Optical Measurements

Figure 3-3 presents the room temperature absorption and luminescence spectra for QDs passivated with (a) TOPO/TOPSe, (b) ZnS, (c) 4-picoline and (d) 4-(trifluoromethyl) thiophenol. Each graph shows the evolution of QD optical properties as the size of a particular surface modified nanocrystallite increases from roughly 12 Å to 43 Å in radius. The solid line represents the absorption spectrum of the QD and the dotted line is its accompanying band edge emission. Although there do not appear to be significant differences between the absorption spectra of the surface modified QDs and their TOPO/TOPSe counterparts there are slight changes which

occur when the surface is modified. In particular, we observe that the absorption spectra of the surface modified QDs shifts on occasions to either lower or higher energies. We interpret this shift as a slight increase or decrease in the effective size of the QD.[9] (The samples in Figures 3-3 c and 3-3 d were prepared using the QDs shown in Figure 3-3 a. Changes in their size can be seen as differences in the effective radii presented on the right of each curve.) Another effect of modifying the surface is a slight broadening of the absorption spectra which we account for as a small increase of the effective size distribution of the sample.

While the absorption properties of the QDs are only slightly perturbed when the surface is modified there are significant changes which occur in the luminescence. For instance, the emission from ligand exchanged samples shows much more deep trap emission than QDs passivated with TOPO/TOPSe.[10] This is seen in Figures 3-3 c and 3-3 d as a rising tail in the band edge luminescence of several samples at low energies. The band edge quantum yield (QY) of the ligand exchanged nanocrystallites is also strongly affected by the exchange procedure. It decreases from 10%-15% to less than 1% at room temperature. We attribute both changes to a loss of passivation on the surface of the QD which creates new defects and opens up pathways for non-radiative relaxation. The luminescence of ZnS overcoated QDs, however, shows a dramatic improvement over QDs passivated with TOPO/TOPSe. There is very little deep trap emission and the band edge QY of the material increases to 30-45% at room temperature. This improvement in luminescence efficiency has been previously

[9]Sizing of the QDs is determined from extensive TEM and SAXS measurements.

[10]By deep trap emission we refer to the near IR emission. Its exact origin is unknown but may be related to vacancies or to incomplete passivation of the surface.

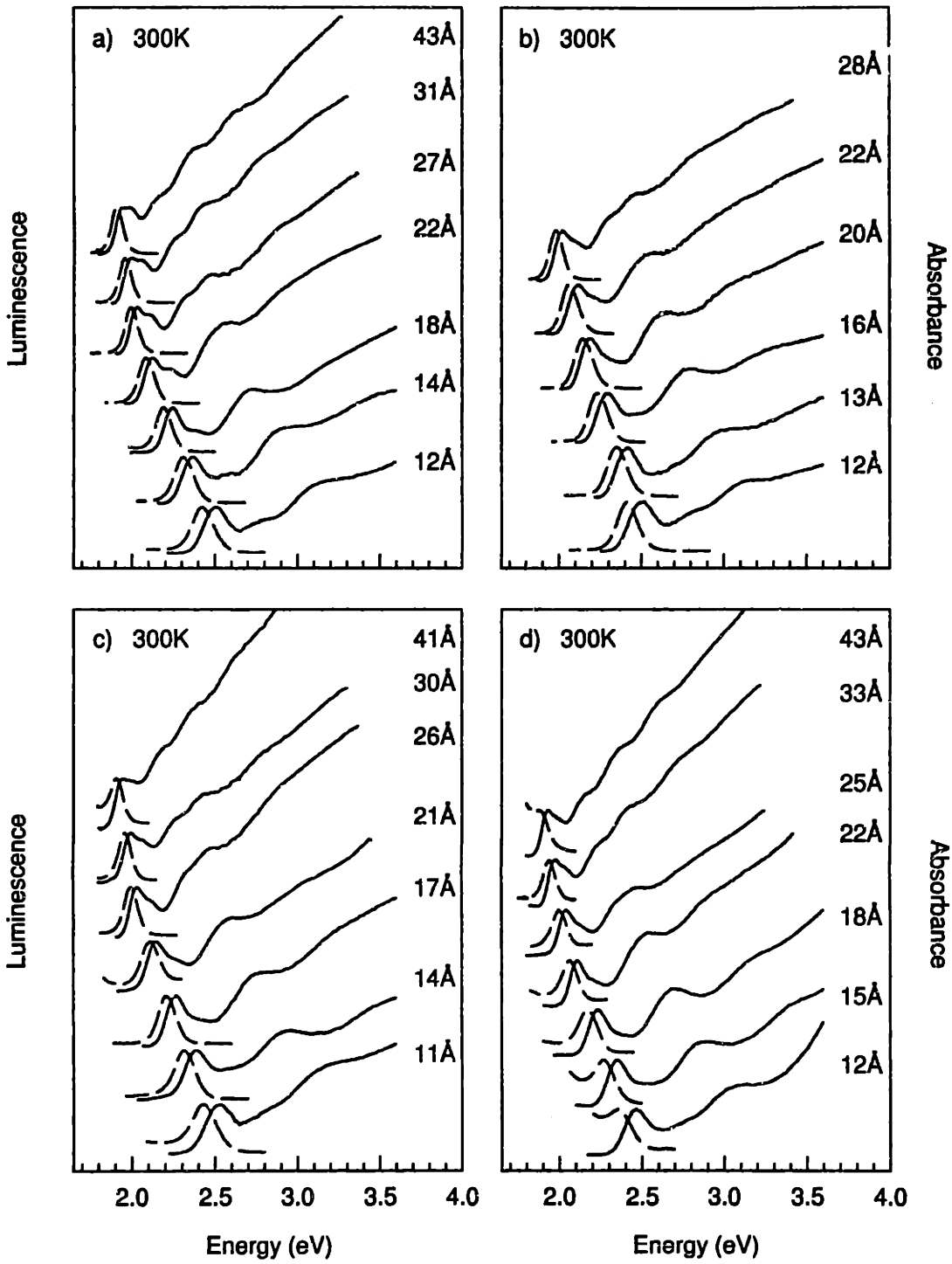

Figure 3-3: Room temperature absorption and luminescence spectra of CdSe QDs passivated with (a) TOPO/TOPSe, (b) ZnS, (c) 4-Picoline, and (d) 4- (trifluoromethyl)thiophenol. The effective radius of each sample is at the right of its spectrum. Samples in (a), (c), and (d) were created from the same preparation to minimize differences in size, shape and internal structure.

observed and is attributed to the effective passivation of surface states by the newly deposited semiconductor layer. [139, 140, 141, 148, 149, 150, 151, 152, 153]

Figure 3-4 shows the low temperature (10 K) absorption and luminescence spectra for QDs passivated with (a) TOPO/TOPSe, (b) ZnS, (c) 4-picoline and (d) 4-(trifluoromethyl)thiophenol. There are differences between the room temperature (RT) and low temperature (LT) data. At 10 K the absorption and emission linewidths are narrower due to a decrease in their homogeneous linewidths. This results in a noticeable enhancement of features particularly in the absorption spectra of the nanocrystallites. The peak positions in both absorption and emission also shift to higher energies because of the larger band gap at low temperatures (E_g = 1.839 eV, 10 K). In the luminescence the QY improves and is accompanied by a reduction in the amount of deep trap emission.

The FLN spectra of all samples is shown in Figures 3-5 (a-d). The solid line denotes the line narrowed spectra and the dashed line is the laser excitation included for reference purposes. As described in the experimental section these spectra were obtained by exciting the samples on the red edge of their absorption at 10 K. The resulting luminescence shows a well resolved longitudinal optical (LO) phonon progression and is characteristic of the emission from a narrow subset of QDs present in the residual size distribution of each sample. At large sizes the peaks are sharp and well defined. As the size of the sample decreases the linewidths begin to increase. This trend is paralleled by a similar change in the LO phonon frequency with decreasing size. Figure 3-6 shows data extracted from our FLN spectra. At large sizes the frequency approaches the bulk value of $\sim$210 cm^{-1} and as the size of the QD decreases

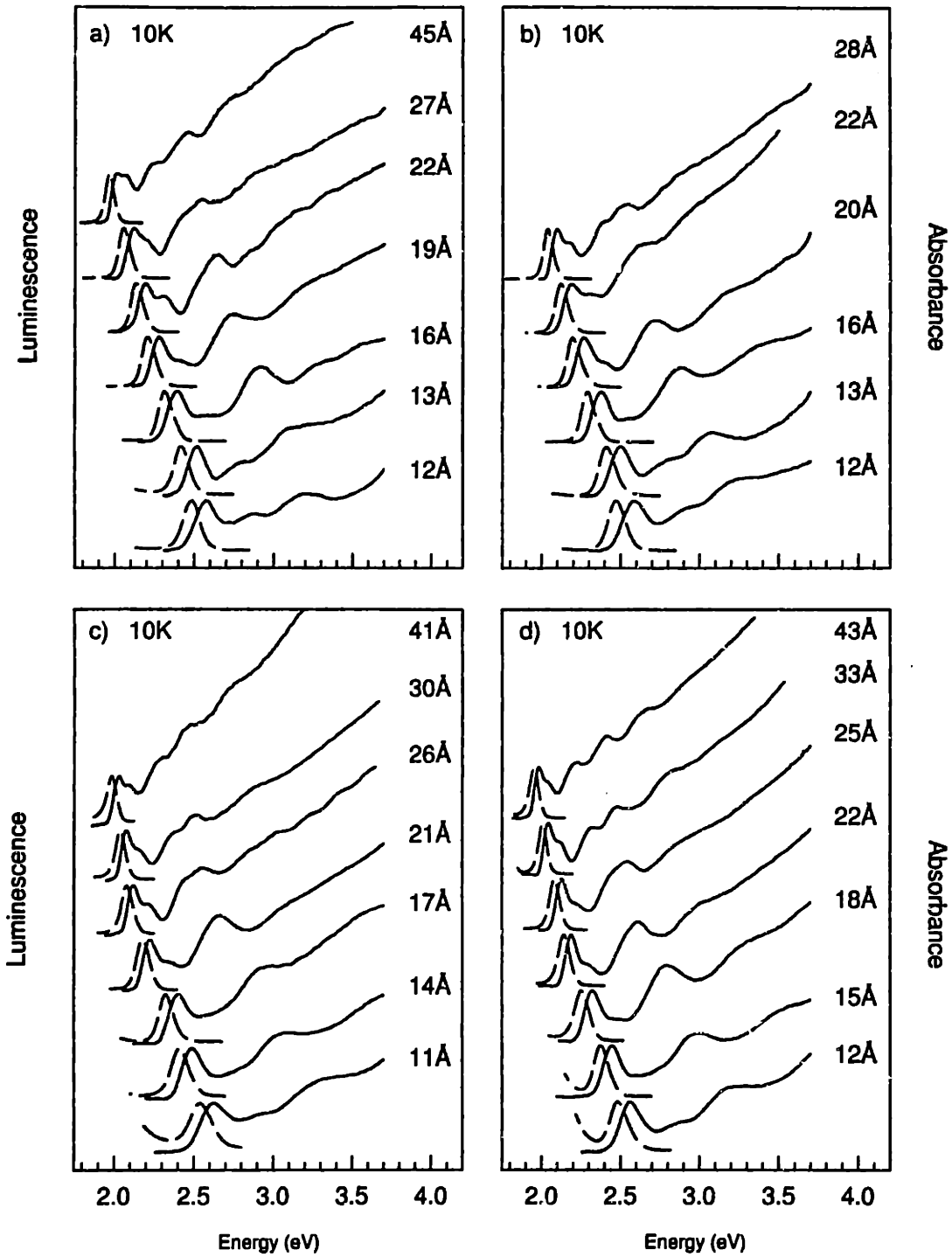

Figure 3-4: Low temperature (10 K) absorption and luminescence spectra of CdSe QDs passivated with (a) TOPO/TOPSe, (b) ZnS, (c) 4-Picoline, and (d) 4-(trifluoromethyl)thiophenol. The effective radius of each sample is presented on the right of its respective spectrum. Samples in (a) and (b) as well as samples in (c) and (d) originate from the same preparation in order to minimize differences in size, shape, and internal structure.

the LO phonon frequency exhibits a negative dispersion progressing towards a value close to 177 cm^{-1}. Attempts to fit the experimental dispersion relation with a simple model for the LO phonon confinement [154, 155, 156, 157, 158, 159] suggest that the observed mode may not be purely LO in nature but rather a linear combination of LO and transverse optical (TO) modes. Additional work is needed to clarify these observed changes in frequency and linewidth.

3.4 Discussion

Previous theoretical work modeling the excited state absorption in CdSe QDs has successfully described the evolution of the band edge exciton as well as the evolution of higher excited states with size.[51, 107, 15] The theory, based on the effective mass approximation takes into account the non-parabolicity, of the conduction band and the degeneracy of the valence band. It also models the QDs with a cubic or zinc blende crystal structure in light of the small crystal field splitting in CdSe (25 meV). The electron-hole Coulomb interaction is corrected for in first order perturbation theory by adding $-1.8e^2/\varepsilon a$ to the energy of S-like electron states and $-1.7e^2/\varepsilon a$ to the energy of P-like electron states.[11][160, 161] Figure 3-7 compares theoretical predictions of the size dependent band edge exciton energy to experimental values obtained at two different temperatures (300 K and 10 K). We model the theory following the example of Refs. [51, 96, 15]. Figure 3-7 shows good quantitative agreement at moderate sizes but discrepancies occur on either large or small size extremes.

[11] Here e is the charge of the carrier, ϵ is the static dielectric constant, and a is the effective radii of the QD.

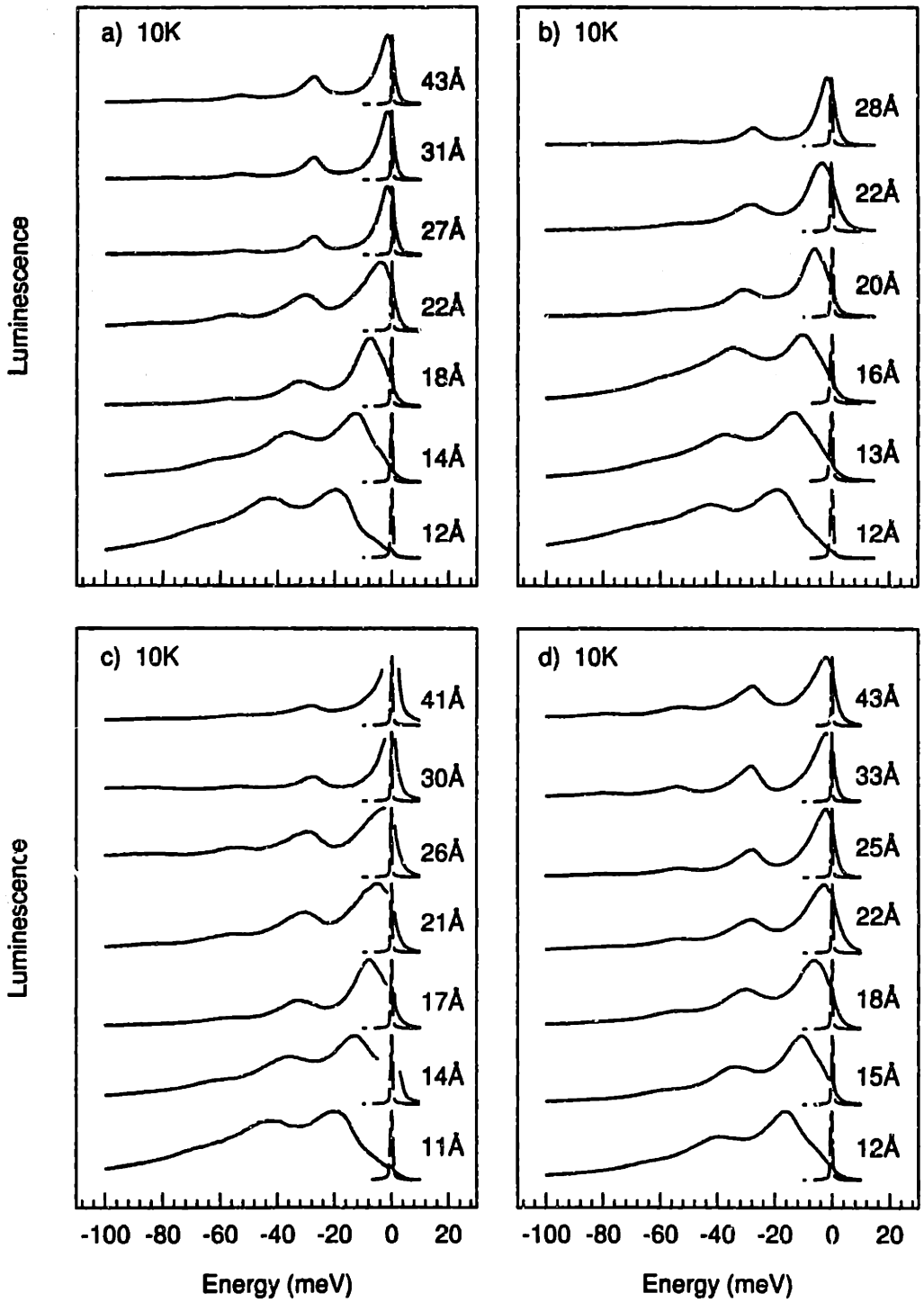

Figure 3-5: Low temperature (10 K) FLN spectra of CdSe QDs passivated with (a) TOPO/TOPSe, (b) ZnS, (c) 4-Picoline, and (d) 4-(trifluoromethyl)thiophenol. The dashed line is the laser excitation included for reference purposes. The effective radius of each sample is presented on the right of its respective spectrum. Samples in (a), (c), and (d) originate from the same preparation to minimize differences in size, shape, and internal structure.

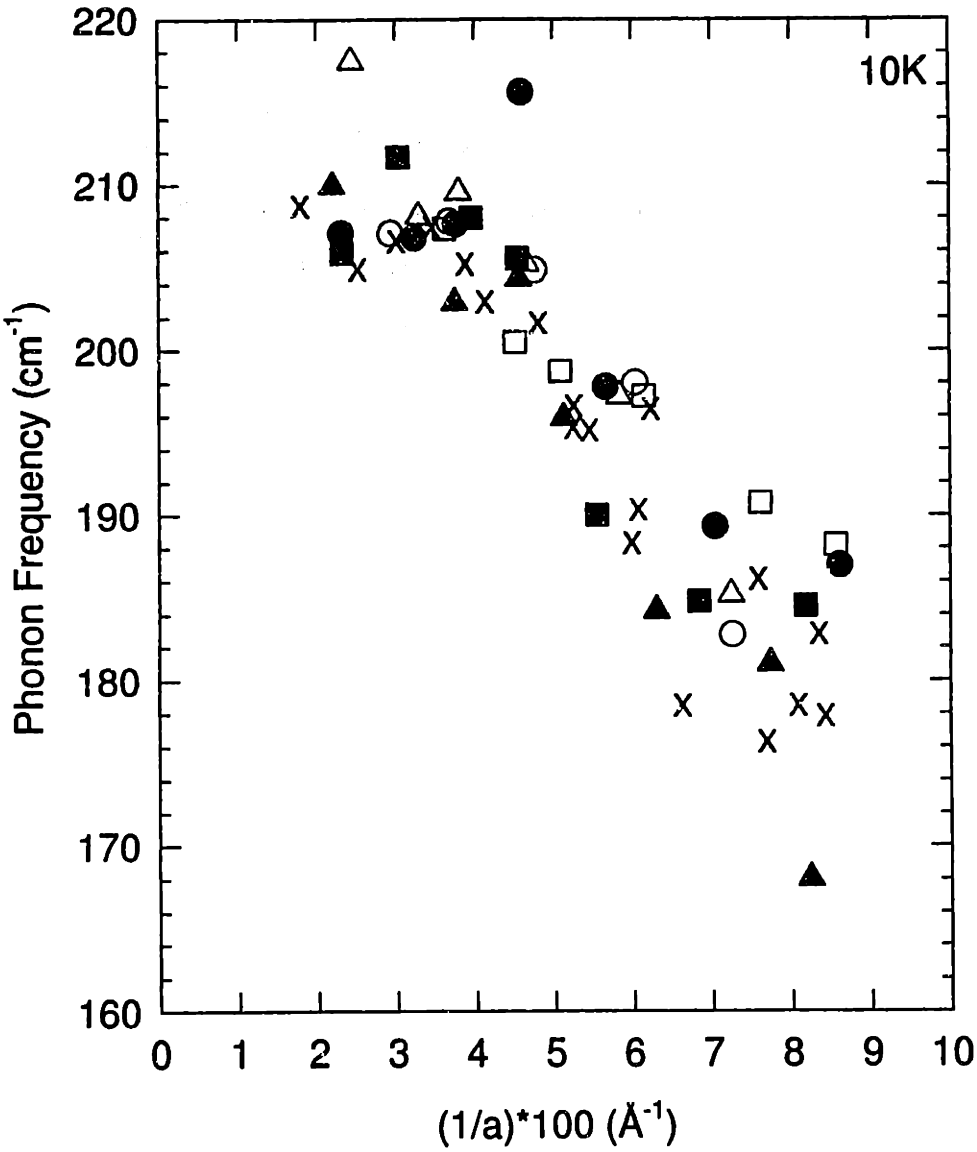

Figure 3-6: Size dependent LO phonon frequency extracted from the FLN spectra of surface modified CdSe QDs. Values were determined by taking the difference in energy between the zero and one phonon lines. (solid triangles) QDs passivated with TOPO/TOPSe in o-terphenyl/tri-n-butylphosphine, (open squares) QDs passivated with ZnS in o-terphenyl/tri-n-butylphosphine, (solid circles) QDs passivated with TOPO/TOPSe in 1-butanol, (open triangles) QDs passivated with 4-picoline, (open circles) QDs passivated with tris(2-ethylhexyl)phosphate, (solid squares) QDs passivated with 4-(trifluoromethyl)thiophenol.

Table 3.2: Quantitative analysis for the ligand coverage in CdSe QDs.

	TOPO capped QD ($a = 18.4$)	Pyr capped QD ($a = 18.4$)	
Sample wt.	11.772 mg	10.248 mg	
Wt. loss[5]	2.75 mg (23% loss due to TOPO)	1.015 mg (10% due to pyr)	0.676 mg (6.6% due to TOPO)
Mole loss	5.4 μmol of TOPO	12.8 μmol of pyr	1.8 μmole of TOPO
CdSe core weight	9.647 mg (50.4 μmol)	8.557 mg (44.7 μmol)	
Estimated moles of surface Cd[6]	18.6 μmol	16.5 μmol	
Surface Cd coverage by TGA[7]	5.37/18.6 = 0.29 (29% due to TOPO)	12.8/16.5 = 0.78 (78% due to pyr)	1.8/16.5 = 0.11 (11% due to TOPO)
NMR integrated area of TOPO aliphatic protons[8]	10.0	3.99	
TGA Summary	11/29 = 38% TOPO passivation of initially occupied Cd sites		
NMR Summary	3.99/10.0 = 40% TOPO passivation of initially occupied Cd sites		

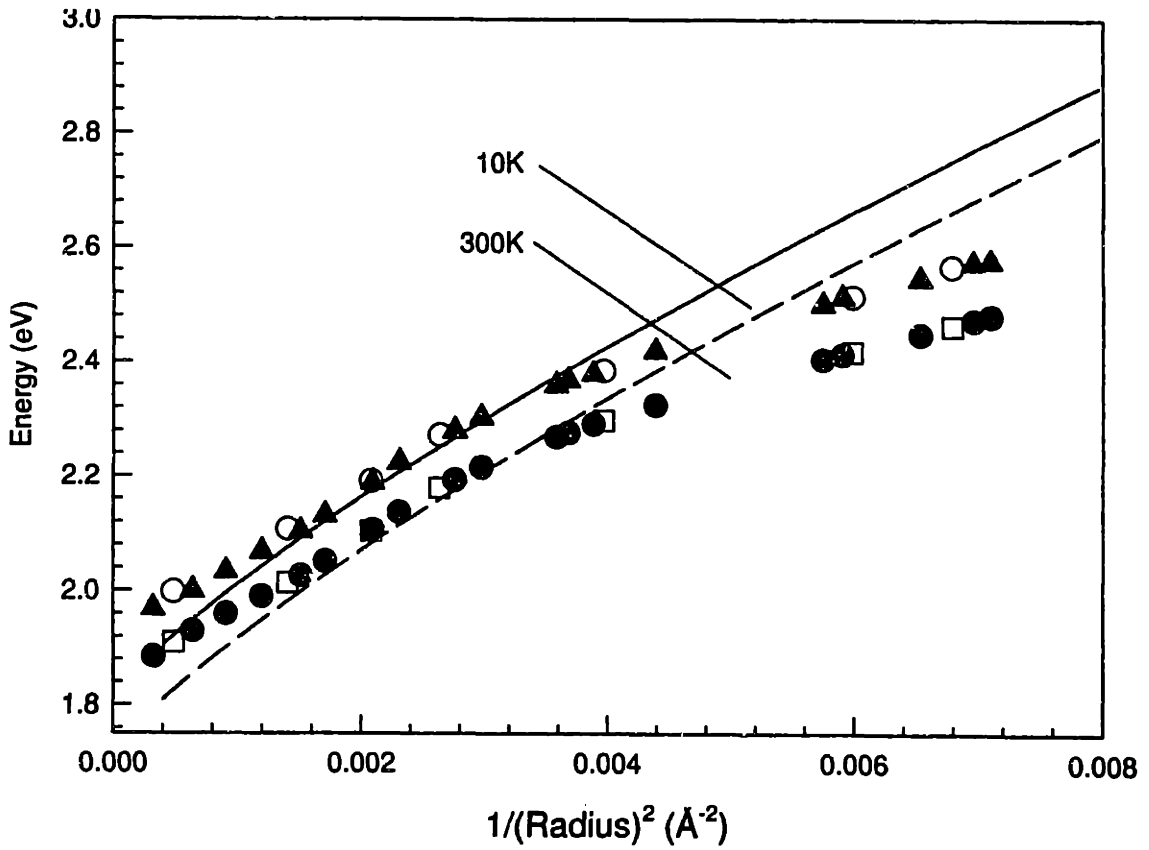

Figure 3-7: Comparison between the energy of the band edge absorption at room temperature/10 K and theory. The solid symbols are points taken from ref. [25] and the open symbols are values measured in this work. Both sets of experimental results are taken from QDs passivated with TOPO/TOPSe dispersed in o-terphenyl/tri- n-butylphosphine. The solid/dashed lines are the theoretical predictions at 10 K and 300 K respectively.

Although the theory does well in describing the absorption properties of the QDs it does not, at this stage, explain the redshift of the band edge luminescence and the long radiative lifetimes observed at low temperatures. Because the theory considers a spherically symmetric and cubic QD the band edge exciton (or $1S_{3/2}1S_e$ transition) is 8-fold degenerate. In this highly degenerate situation there is no predicted shift in the band edge luminescence nor is there an appreciable difference in lifetimes from bulk values. This has led to speculation that the luminescence from CdSe QDs is surface related.

However, a careful consideration of symmetry breaking terms in the Hamiltonian reveals that it is not necessary to explain the luminescence through the use of surface states. Rather, the unusual properties of the band edge luminescence can be accounted for by the presence of fine structure within the band edge exciton. In a recent study we have considered effects such as the non-spherical geometry of the nanocrystallites, the intrinsic hexagonal lattice structure and the electron-hole exchange interaction which lift the degeneracy of the band edge exciton.[63, 64]

The hexagonal lattice is important because of its associated crystal field splitting (25 meV in the bulk) of the 4-fold degenerate hole state ($F_h = 3/2$) into two 2-fold degenerate states ($F_{hm} = \pm 3/2$ and $F_{hm} = \pm 1/2$). The non-sphericity of the QD also breaks the symmetry of the electronic potential, similarly lifting the degeneracy of the same hole states. Note that the 2-fold degenerate electron state ($F_{em} = \pm 1/2$) is not split by the shape. We model the non-sphericity by considering the QD to be an ellipsoid whose ellipticity, μ, is size dependent.[12] The splitting of the hole states

[12]The ellipticity is approximated with the polynomial: $\mu(a) = 0.101 - 0.034a + 3.507 \times 10^{-3}a^2 - 1.177 \times 10^{-4}a^3 + 1.863 \times 10^{-6}a^4 - 1.418 \times 10^{-8}a^5 + 4.197 \times 10^{-11}a^6$ in accordance with extensive

from the shape asymmetry is calculated in first order perturbation theory. More details including exact expressions can be found in reference [64]. In nanometer sized structures the electron-hole exchange interaction is predicted to be strongly enhanced with respect to the bulk.[86, 162, 120, 163] This occurs because of the increased spatial overlap of the electron and hole wavefunctions. As the size of the nanocrystallite decreases the exchange interaction becomes important and along with the crystal field/shape asymmetry acts to split the 8-fold degenerate band edge exciton.

Figure 3-8 a describes the splitting of the hole states due to the shape asymmetry and the crystal field. The size dependence is only due to the shape asymmetry as the crystal field splitting is independent of size. All transitions are optically active under these circumstances. Figure 3-8 b ignores the crystal field/shape asymmetry and describes the band edge exciton splitting due to the electron-hole exchange interaction. This is the spherical limit and portrays the case of a spherical QD with a cubic lattice. In the absence of the intrinsic crystal field and non-sphericity the exchange interaction splits the band edge exciton into two states, an optically active 3-fold degenerate exciton with total angular momentum $N = 1$ (solid line) and an optically passive 5-fold degenerate exciton with angular momentum $N = 2$ (dashed line).

When all three symmetry breaking effects are considered jointly the theory predicts that the band edge exciton consists of five fine structure states. These fine structure states are labeled by their total angular momentum projection ($N_m = F_{hm} + F_{em}$) along the "c" or unique axis of the nanocrystallite. F_{em} and F_{hm} are the angular

TEM and SAXS measurements.

momentum contributions of the electron and hole respectively and are the sum of momentum contributions from the envelope and Bloch components of each carriers wavefunction.

There are two states with projection $|N_m| = 1$, two states with projection $|N_m| = 0$ and one state with projection $|N_m| = 2$. States with projection $|N_m| = 1$ or 2 are doubly degenerate. Of the five states three are optically active (bright) and two are optically passive (dark). The energy of the $|N_m| = 2$ state is described by [64]

$$\epsilon_2 = -\frac{3\eta}{2} - \frac{\Delta}{2} \tag{3.1}$$

where η is the exchange contribution and Δ is the splitting from the intrinsic hexagonal lattice and nanocrystal asymmetry. States with projection $|N_m| = 1$ have energies [64]

$$\epsilon_1^{U,L} = \frac{\eta}{2} \pm \sqrt{(2\eta - \Delta)^2/4 + 3\eta^2} \tag{3.2}$$

The superscripts "U" and "L" refer to upper and lower to distinguish states with the same angular momentum projection. Similarly, for states with projection $|N_m| = 0$ the energies are [64]

$$\epsilon_0^{U,L} = \frac{\eta}{2} + \frac{\Delta}{2} \pm 2\eta \tag{3.3}$$

Figure 3-8 c shows the evolution of these fine structure states as the size of the QD progresses from bulk-like sizes to molecular-like species. Optically active states are denoted in the figure by a solid line and optically inactive states are drawn with

a dashed line.

At large sizes there are two 4-fold degenerate states. These states are analogous to the bulk A and B excitons and are split by the intrinsic crystal field of the hexagonal lattice (Δ_{int}) and the non-spherical geometry of the QDs (Δ_{sh}). The net splitting is described by the sum

$$\Delta(a, \beta, \mu) = \Delta_{int} + \Delta_{sh} \tag{3.4}$$

where β is the ratio of light to heavy hole effective masses along the c axis,[126] μ is the ellipticity of the QD [$\mu = c/b - 1$; $c(b)$ is the major (minor) axis of the QD][107, 52] and a is the effective radius of the nanocrystallite [$a = 1/2(b^2c)^{1/3}$].

As the size of the QD decreases the electron-hole exchange interaction, which scales as $1/a^3$, becomes important in defining the order of the fine structure states. Figure 3-8 c shows a plot of fine structure energies against $1/a^3$. At small sizes the five states move apart in energy and the lowest excited state is predicted to be optically inactive.

In Figure 3-8 d the oscillator strengths of the three optically active fine structure states are shown relative to the oscillator strength of the 0^U state. At large sizes the combined oscillator strength of the $\pm 1^U$ and 0^U states equals the oscillator strength of the $\pm 1^L$ state. The net transition probability is divided equally among the two 4-fold degenerate states near the origin of Figure 3-8 c which resemble the bulk A and B excitons.

As the size of the QD decreases the oscillator strength of the $\pm 1^L$ state drops off rapidly and is matched by a concomitant increase in the oscillator strength of the $\pm 1^U$

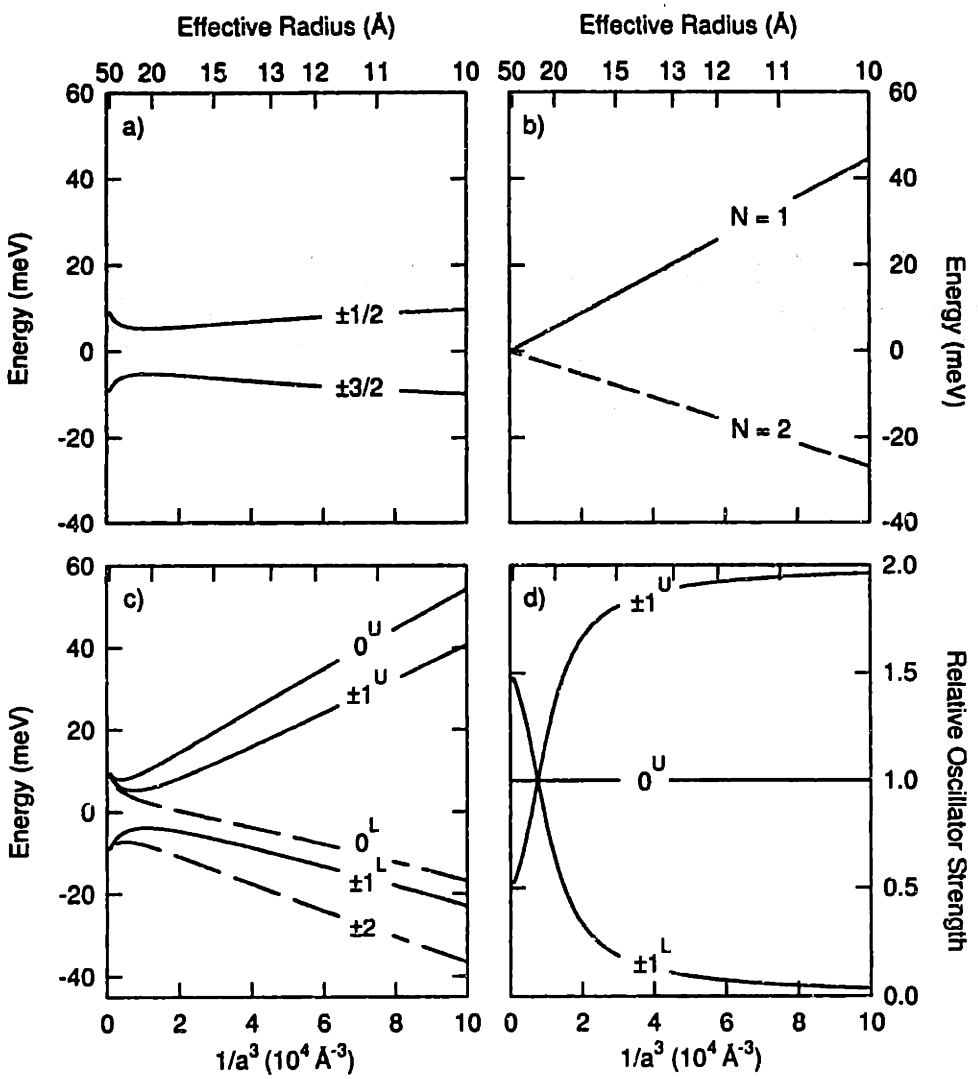

Figure 3-8: (a) Size dependent splitting of the hole states from the nanocrystal shape asymmetry and the crystal field splitting. Values are determined using expressions in ref. [27]. There are two fourfold degenerate states which resemble the bulk A and B excitons. Both states are optically active and are labeled by the hole angular momentum projection along the unique axis of the nanocrystallite. (b) Size dependent splitting of the exciton states from the electron-hole exchange interaction. Exact values are determined from expressions in ref. [27]. The exchange interaction creates an optically active 3-fold degenerate exciton with total angular momentum $N = 1$ (solid line) and a 5-fold degenerate exciton with total angular momentum projection $N = 2$ (dashed line). (c) Theoretical prediction of the size dependent band edge exciton fine structure. States are labeled by their angular momentum projection along the unique axis of the nanocrystallite. Optically active states are denoted by solid lines and optically inactive states are drawn with dashed lines. The exciton ground state is predicted to be a state with angular momentum projection $|N_m| = 2$. The superscripts "U" and "L" refer to upper and lower to distinguish states with the same angular momentum projection. (d) Oscillator strengths of the three optically active fine structure states relative to the oscillator strength of the 0^U state. At large sizes the oscillator strength is divided equally among states with the superscripts U and L. As the size of the QD decreases the $\pm 1^L$ state gives up its oscillator strength to the $\pm 1^U$ state.

state. This behavior is understood by examining the role of the exchange interaction at small sizes. In small QDs most of the fine structure splitting originates from the exchange interaction (Fig. 3-8 c). The contributions of the intrinsic crystal field and non-sphericity are small compared to the role of the exchange splitting. In their absence (the spherical limit) the exchange interaction creates two states, an optically active 3-fold degenerate state with total angular momentum $N = 1$ and an optically passive 5-fold degenerate state with total angular momentum $N = 2$ (Fig. 3-8 b). The $\pm 1^L$ state which arises from the $N = 2$ exciton when the crystal field splitting and non-sphericity are introduced is therefore relatively dark or passive at small sizes. States which arise from the $N = 1$ exciton make up for this lost oscillator strength and explains why the oscillator strength of the $\pm 1^U$ state increases with decreasing size.

An important consequence of the theory is that it predicts that the lowest excited state in CdSe QDs is a dark exciton with angular momentum projection $|N_m| = 2$. This explains the long radiative lifetimes as transitions into and out of this state are formally forbidden in the electric dipole approximation. Transitions involving the exciton ground state or "Dark Exciton" require the assistance of phonons which can carry the excess unit of angular momentum.[118, 63, 64]

The band edge exciton fine structure also accounts for the resonant and non-resonant Stokes shifts seen in the luminescence. Previous surface models have been unable to describe the difference between these two shifts and the ability of the intrinsic exciton model to explain their origin is consequently important. The resonant Stokes shift for all samples is highly size dependent and ranges from 2 meV at large

sizes to roughly 20 meV at small sizes. The non-resonant Stokes shift is also size dependent and ranges from 20 meV at large sizes to over 100 meV at small sizes. A puzzling feature of these two shifts is the large discrepancy in their magnitudes. The non-resonant Stokes shift is abnormally large based on a comparison to values of the resonant Stokes shift. This is because, in principle, it should be possible to reproduce the non-resonant Stokes shift by convoluting the FLN or "single" particle spectrum [116] with the intrinsic size distribution of the sample. However, repeated attempts to do so have yielded values of the non-resonant Stokes shift which are consistently smaller than measured experimental values.

We highlight the discrepancy between the magnitude of the resonant and non-resonant Stokes shifts with the following graph. Figure 3-9 a shows the low temperature absorption and FLN spectra of 18 Å radius QDs. The arrow at the bottom denotes the laser excitation position in the FLN experiment. The resonant Stokes shift in this case is 6 meV. If we assume the existence of a single absorbing and single emitting state, convoluting the FLN spectrum with the intrinsic size distribution of the sample reproduces the non-resonant luminescence. In Figure 3-9 b we show the same absorption spectrum and include the non-resonant luminescence (solid line) obtained when we excite far from the band edge. The excitation position is denoted by the arrow at the bottom of the figure near 2.8 eV. The non-resonant Stokes shift is 74 meV. An attempt to reproduce the non-resonant luminescence by convoluting the line narrowed spectrum with the intrinsic size distribution of the sample yields the peak drawn with the dashed line. Although the shape and width of the luminescence are well represented there is poor agreement between the observed and predicted values of

the non-resonant Stokes shift (74 meV versus 12 meV). The band edge luminescence is therefore anomalous because it requires too large a Huang-Rhys S parameter to be explained by simple electron-phonon coupling.[110]

To describe the resonant Stokes shift in terms of the intrinsic exciton model we consider the implications of the predicted band edge fine structure. Since the lowest excited state is optically passive exciting the red edge of the absorption probes the lowest optically active $\pm 1^L$ exciton of the largest nanocrystallites present in the residual size distribution of the sample. The transition into this state is followed by rapid thermal relaxation to the $\pm 2^L$ Dark Exciton. Radiative recombination to the ground state is then achieved by a phonon assisted [63, 52] or a nuclear/paramagnetic spin flip assisted [63] transition. The resonant Stokes shift is described as the difference in energy between the $\pm 1^L$ and $\pm 2^L$ fine structure states.

Figure 3-10 plots the resonant Stokes shift versus mean size for all samples used in our ligand exchange experiments. A remarkable achievement of the theory is its ability to reproduce the size dependent trend of the resonant Stokes shift without the use of any adjustable parameters. We model the theory using only the following literature values, $a_{ex} = 56$ Å [15], $\hbar\omega_{ST} = 0.13$ meV [13][164] and $\beta = 0.28$ [12, 96] where is the bulk exciton Bohr radius, is the bulk singlet-triplet splitting and β is the ratio of light to heavy hole effective masses. The theory is shown as the solid line in the figure. There is good quantitative agreement at large sizes but as the size of the QD decreases the theory begins to increasingly underestimate the resonant Stokes shift. This discrepancy may be due to the added contribution of acoustic phonons to the

[13]The luminescence from single CdSe QDs has recently been reported. Our FLN spectra are only approximations as the true linewidths are much narrower

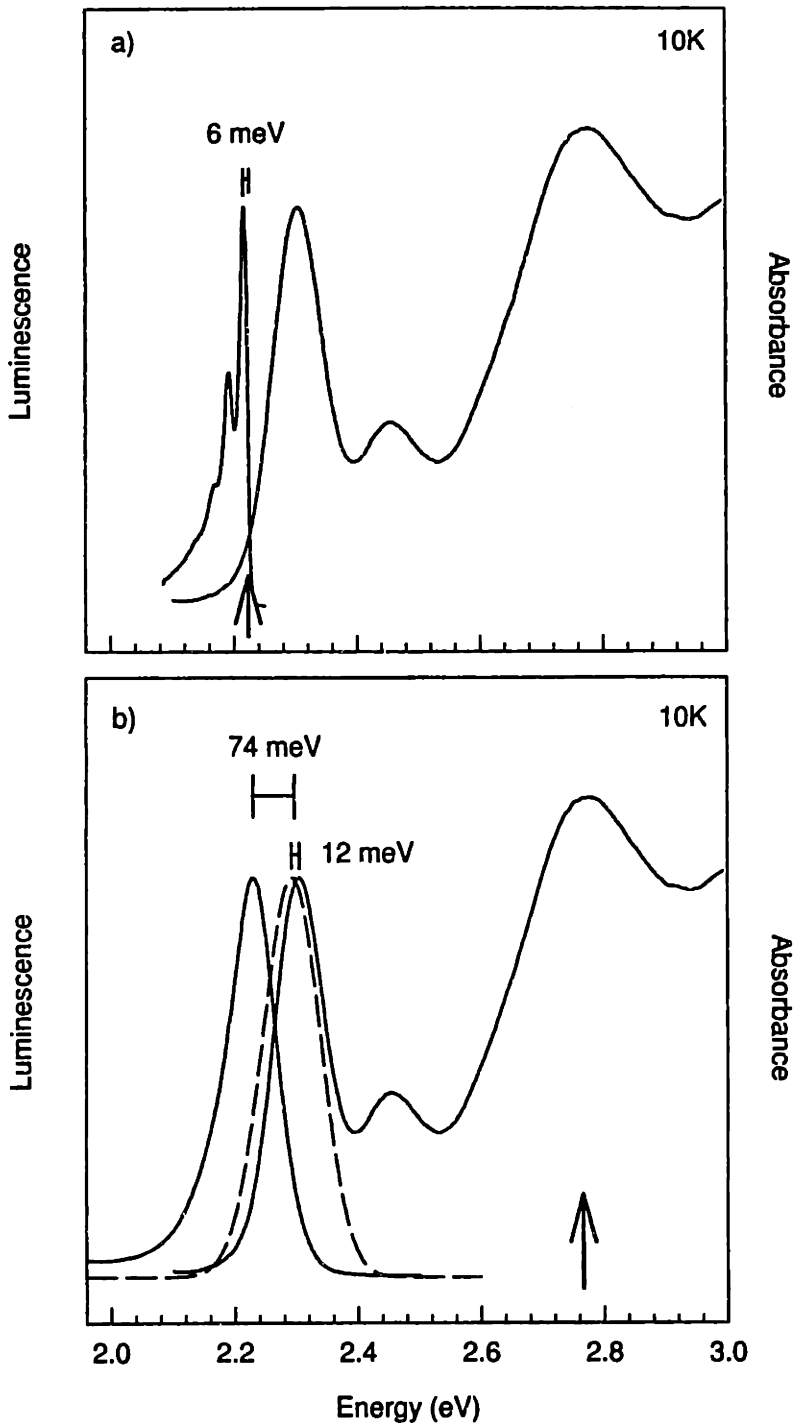

Figure 3-9: (a) Low temperature absorption and FLN spectra of 18 Å radius QDs. The resonant Stokes shift is 6 meV. The arrow denotes the laser excitation position. (b) Low temperature absorption and full luminescence spectra of 18 Å radius QDs. (solid lines) The non-resonant Stokes shift is 74 meV. The arrow near 2.8 eV denotes the excitation position. The dashed line is the result of convoluting the line narrowed spectrum with the intrinsic size distribution of the sample. The predicted non-resonant Stokes shift is 12 meV and is much smaller than the measured value.

resonant Stokes shift or a breakdown in the effective mass approximation.[114, 115]

Figure 3-10 also shows that modifying the surface of the QD has little effect on the energetics of the band edge luminescence. Samples passivated with TOPO/TOPSe, 4-picoline, 4-(trifluoromethyl)thiophenol, tris(2-ethylhexyl)phosphate and ZnS show the same resonant Stokes shift for all sizes considered. This can be seen in Figure 3-11 where the resonant Stokes shift is plotted against the laser excitation energy. We plot the resonant Stokes shift in this manner (i.e. with excitation energy as the x axis) because of difficulties in determining the exact size that we probe when we excite on the red edge of the absorption. A slight shift of the laser excitation to the red or to the blue produces a change in the value of the resonant Stokes shift. This is consistent with exciting a larger or smaller sized nanocrystallite present in the residual size distribution of the sample.

Figure 3-11 shows data taken from the entire size series and includes data from samples excited at different points on the red edge of their first absorption feature. The consistency of the resonant Stokes shift for all sizes and for all instances of surface modification strongly suggests that the band edge luminescence is unrelated to the surface.

To explain the non-resonant Stokes shift we recall that the model predicts the existence of three optically active fine structure states ($\pm 1^L$, $\pm 1^U$ and 0^U). When these three states are weighted with their respective oscillator strengths and are convoluted with the intrinsic size distribution of the sample the peak of the band edge absorption occurs at the energetic mean of these three states. Similarly, the energy of the band edge emission is determined by convoluting the position of the $\pm 2^L$ Dark Exciton

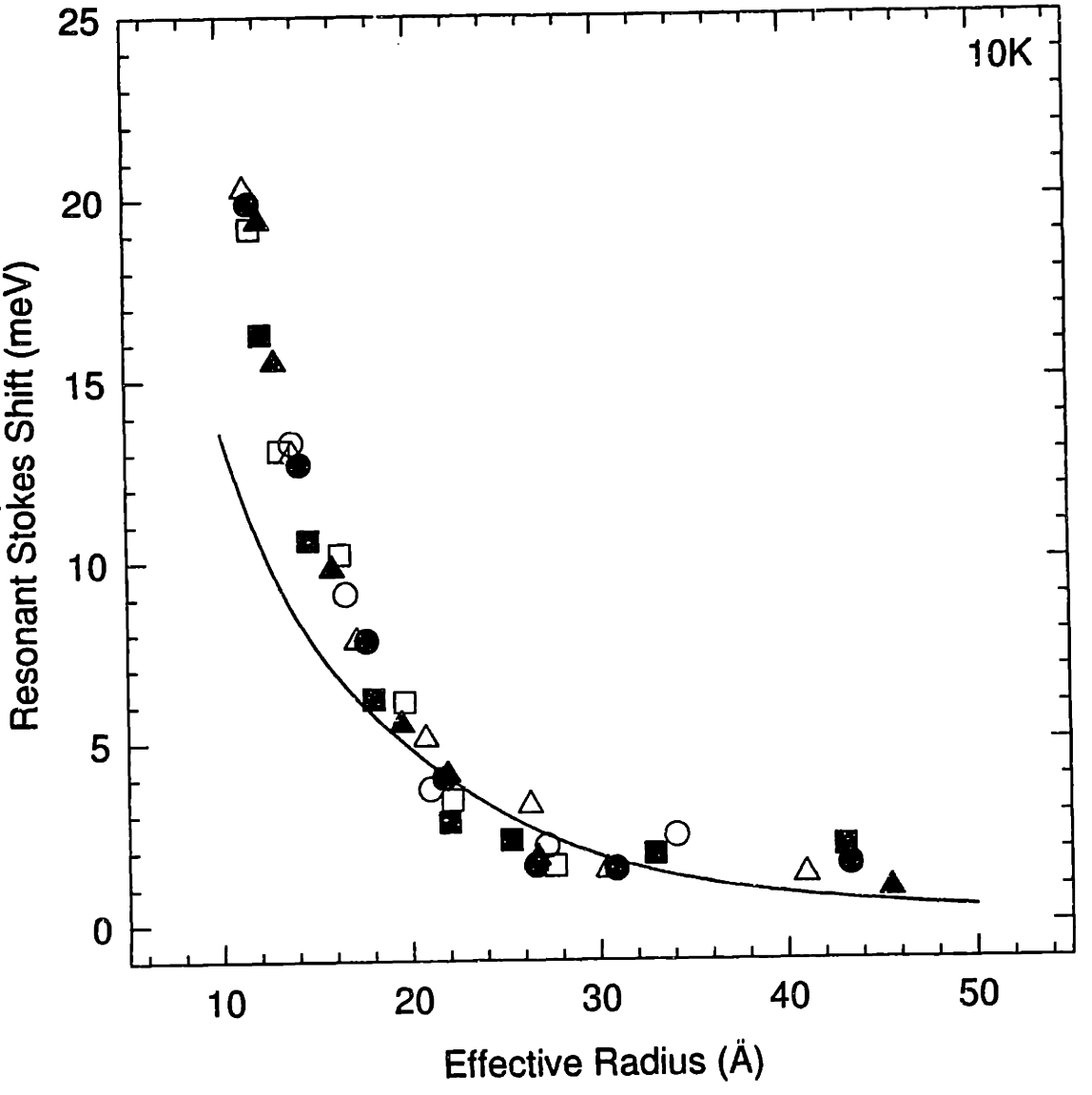

Figure 3-10: Resonant Stokes shift plotted against the mean effective radius of each sample. The solid line is the prediction of the band edge exciton model which describes the resonant shift as the difference in energy between the $\pm 1^L$ and the $\pm 2^L$ fine structure states. (solid triangles) QDs passivated with TOPO/TOPSe in o-terphenyl/tri-n-butylphosphine, (open squares) QDs passivated with ZnS in o-terphenyl/tri-n-butylphosphine, (solid circles) QDs passivated with TOPO/TOPSe in 1-butanol, (open triangles) QDs passivated with 4-picoline, (open circles) QDs passivated with tris(2-ethylhexyl)phosphate, (solid squares) QDs passivated with 4-(trifluoromethyl)thiophenol.

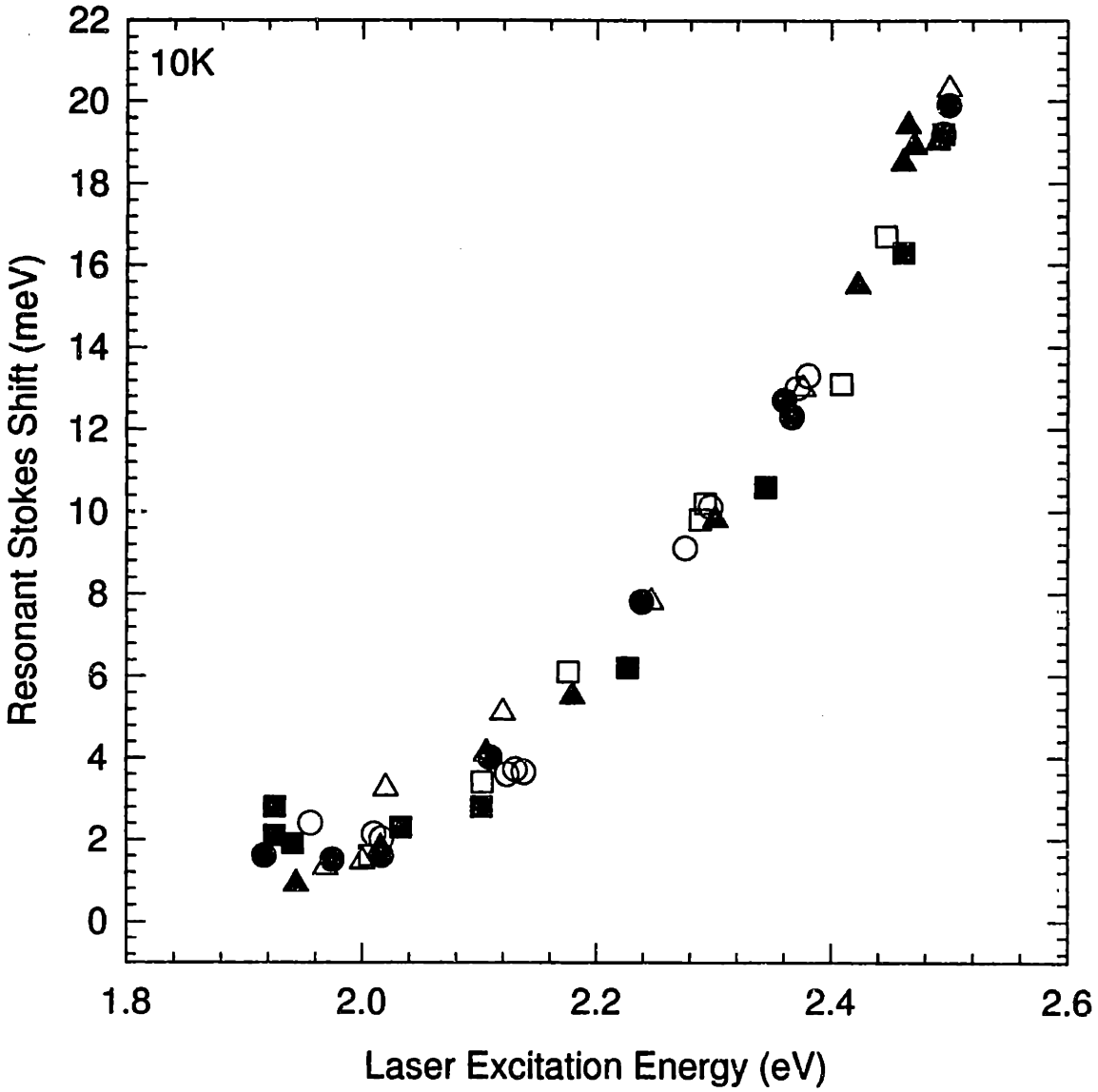

Figure 3-11: Size dependent resonant Stokes shift plotted against laser excitation energy. Included are values taken where we have excited the same sample at different points on the red edge of its first absorption feature. The data suggests that a change in the value of the resonant Stokes shift which occurs when we move the excitation to the red or blue arises from exciting larger or smaller sized QDs present in the residual size distribution of each sample. (solid triangles) QDs passivated with TOPO/TOPSe in o-terphenyl/tri-n- butylphosphine, (open squares) QDs passivated with ZnS in o-terphenyl/tri-n- butylphosphine, (solid circles) QDs passivated with TOPO/TOPSe in 1-butanol, (open triangles) QDs passivated with 4-picoline, (open circles) QDs passivated with tris(2- ethylhexyl)phosphate, (solid squares) QDs passivated with 4-(trifluoromethyl)thiophenol.

with the intrinsic size distribution of the sample. In terms of the model, then, the non-resonant Stokes shift is described as the difference in energy between the mean position of these three optically active fine structure states and the net energy of the $\pm 2^L$ Dark Exciton. This explains the large magnitude of the non-resonant Stokes shift.

Two other effects add to the size of the non-resonant Stokes shift. The first involves the experimentally observed LO phonons [64] and the second stems from the size distribution of the sample. To account for the role of phonons in the non-resonant Stokes shift we phenomenologically model the absorption and emission lineshapes with the following equations

$$A(\nu,\nu') = \sum_{l=1}^{3}\sum_{m=0}^{4} \frac{(S_a)^m}{\sqrt{2\pi}\gamma_{l,m}m!} \exp\left(-\frac{[\nu-(\nu'+\Delta_l+m\omega_{LO})]^2}{2\gamma_{l,m}^2}\right) \tag{3.5}$$

$$E(\nu,\nu') = \sum_{n=0}^{4} \frac{(S_e)^n}{\sqrt{2\pi}\gamma_n n!} \exp\left(-\frac{[\nu-(\nu'-m\omega_{LO})]^2}{2\gamma_n^2}\right) \tag{3.6}$$

We consider the first five LO phonon replicas associated with each of the three optically active fine structure states and the first five LO phonon replicas in the emission. In the above equations ν' represents the position of the zero phonon line, ω_{LO} is the bulk LO phonon frequency ($\sim$26 meV), Δ_l is the energy offset of the lth optically active exciton from the $\pm 2^L$ Dark Exciton, $\gamma_{l,m}$ is the width of the mth phonon replica in the lth state of the absorption and γ_n is the linewidth of the nth phonon replica in the emission. $S_{a(e)}$ is the absorption (emission) electron-phonon

coupling constant and is derived from experimental results.[14] Including the effect of phonons moves the predicted energy of the band edge absorption to the blue and causes a similar shift in the emission to the red. The net result is a larger value for the modeled non-resonant Stokes shift.

The second contribution to the non-resonant Stokes shift arises from the intrinsic size distribution of the sample. Because the excitation probability far from the band edge is proportional to the density of states, larger nanocrystallites participate more strongly in the absorption.[64] This implies an increase in the non-resonant Stokes shift because of preferential absorption into large nanocrystallites. Since the number of participating states is proportional to the volume of the QD we convolute the size distribution with a^3 to obtain the mean energy of the $\pm 2^L$ Dark exciton luminescence. This results in a slight redshift in the modeled emission and increases the predicted value of the non-resonant Stokes shift.

In Figure 3-12 a we compare the theoretical predictions of the non-resonant Stokes shift to experimental values obtained at 10 K. The theory is reproduced as the dashed line which includes the contribution of phonons, a 10% size distribution and assumes that all emission originates from the $\pm 2^L$ state. The $\pm 1^L$ state should not be thermally repopulated at this temperature. Although the theory underestimates the non-resonant Stokes shift for all sizes, it is in reasonable agreement with the data. The observed discrepancy may stem from a tendency of the model to underestimate the splitting as well as the oscillator strengths of the various fine structure states. (See ref. [118] for a recent PLE investigation addressing this issue.)

[14]The values $S_e = 0.45$ and $S_a = 0.14$ are in good agreement with experimental measurements in Ref. [118]

In Figure 3-12 b we compare the theoretical predictions of the non-resonant Stokes shift to experimental values obtained at room temperature. The theory is shown as a dashed line and a solid line. The dashed line includes the role of phonons, a 10% size distribution and assumes that all emission originates from the $\pm 2^L$ exciton ground state (as in Figure 3-12 a). However, since the difference in energy between the $\pm 2^L$ state and higher optically active states ($\pm 1^L$, $\pm 1^U$, 0^U) never exceeds kT at room temperature it is possible to thermally repopulate these three states. To model this we consider a Boltzman population for each available state and weight their contributions with the relative difference in radiative lifetimes between optically active states and the exciton ground state. (We assume that radiative recombination from optically active states is 100 times faster than recombination from the Dark Exciton.) The solid line represents the simulated emission with the added contributions from the $\pm 1^L$, $\pm 1^U$ and 0^U exciton states. In the figure most of the experimental points fall near the solid curve, showing good agreement between experiment and theory.

Both figures also demonstrate the insensitivity of the non-resonant Stokes shift to the nature of the QD surface. At room temperature all surface modified samples show essentially the same luminescence behavior. At 10 K the same holds but more scatter is seen in the measurement of the non-resonant Stokes shift. This may be related to experimental difficulties in determining the peak of the first absorption feature at low temperatures as well as to differences in size, shape, structure and local environment of the QDs.

Although we have been unable to fully exchange the surface of the QDs in our ligand exchange experiments our results are consistent with emission from states

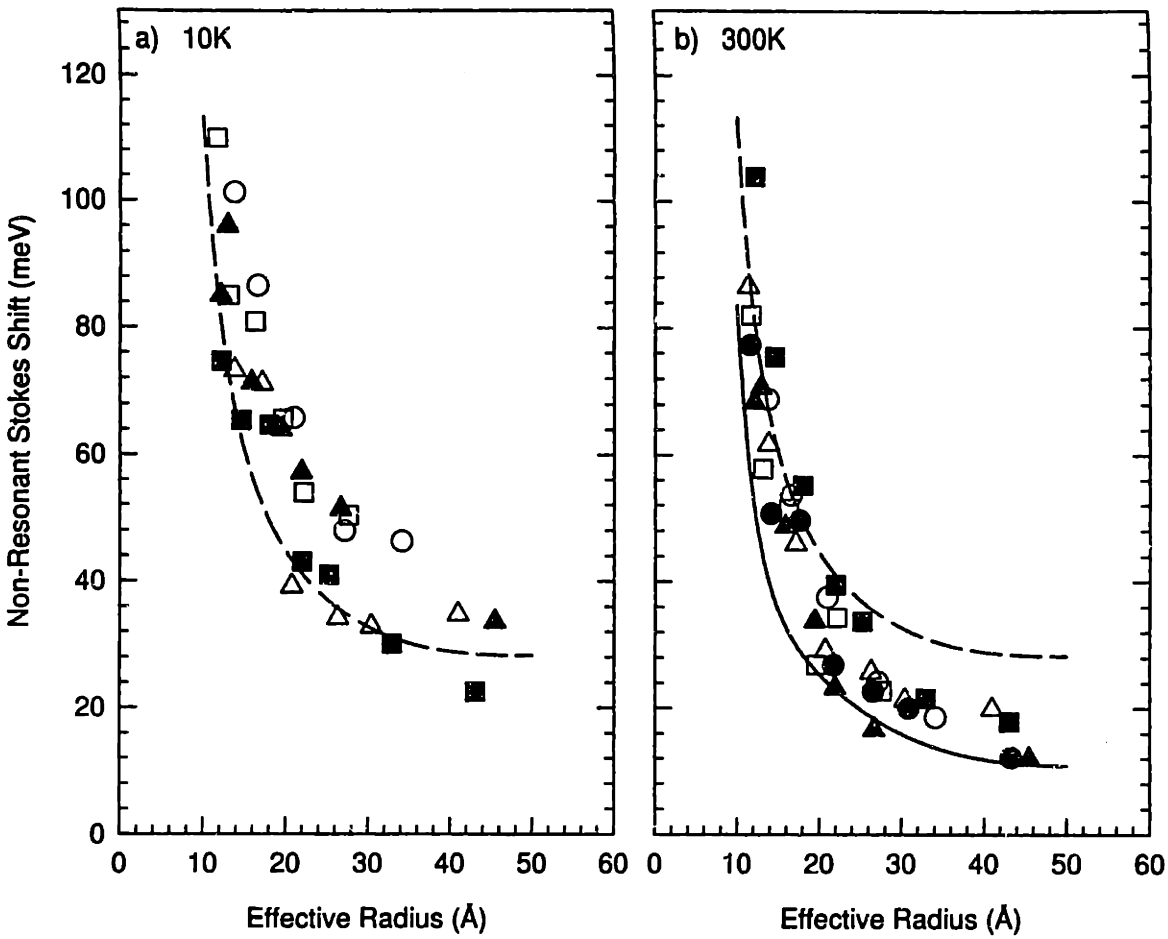

Figure 3-12: (a) Values of the non-resonant Stokes shift at 10 K. The dashed line is the theory. It considers the role of phonons, a 10% size distribution and assumes that all emission originates from the $\pm 2^L$ Dark Exciton. We consider only emission from the exciton ground state because at low temperatures the difference in energy between the $\pm 1^L$ and $\pm 2^L$ excitons exceeds kT. (b) Values of the non-resonant Stokes shift measured at room temperature. The dashed/solid lines represent the theory. The dashed line considers the role of phonons, a 10% size distribution and assumes that all emission originates from the $\pm 2^L$ Dark Exciton [as in (a)]. The solid line considers the role of phonons, a 10% size distribution and assumes thermal population of higher excited states. We consider a weighted Boltzman population for the $\pm 2^L$, $\pm 1^L$, $\pm 1^U$, and 0^U states. An estimate for the relative difference in radiative lifetimes (1/100) between the Dark Exciton and optically active states is included in the weighting scheme. In figures (a) and (b) (solid triangles) QDs passivated with TOPO/TOPSe in o-terphenyl/tri-n-butylphosphine, (open squares) QDs passivated with ZnS in o-terphenyl/tri-n-butylphosphine, (solid circles) QDs passivated with TOPO/TOPSe in 1-butanol, (open triangles) QDs passivated with 4-picoline, (open circles) QDs passivated with tris(2-ethylhexyl)phosphate, (solid squares) QDs passivated with 4-(trifluoromethyl)thiophenol.

unrelated to the surface. Both resonant and non-resonant Stokes shifts show no correlation to the type of ligand passivating the surface of the QD. Results obtained from ZnS overcoated QDs showing a much higher QY than dots passivated with TOPO/TOPSe also demonstrate the invariance of the luminescence to the nature of the passivated surface. In addition, the intrinsic exciton model can quantitatively account for the luminescence both at room temperature and 10 K. While the optical properties of the nanocrystallites may still be influenced by the surface primarily through non-radiative means the unusual properties of the band edge luminescence appear to be explained by the presence of fine structure within the band edge exciton and the optically passive exciton ground state.

3.5 Conclusion

We have studied the band edge luminescence of surface modified CdSe QDs. To address the issue of whether the luminescence is surface related or arises from internal core states we have modified the surface of CdSe QDs with a variety of organic and inorganic ligands. Our results demonstrate that changing the surface has little effect on the energetics of the radiative recombination in these nanocrystallites. For a particular sized QD we observe little or no change in the values of the resonant and non-resonant Stokes shift upon altering the surface. The good agreement between experiment and theory suggests that the band edge luminescence of CdSe QDs can be quantitatively understood using an intrinsic exciton model and that the role of the surface in the optical properties of the QDs lies in its defects which create deep red radiative and non-radiative pathways for recombination of the electron and hole

upon photo-excitation of the nanocrystallite.

Chapter 4

Magnetic Circular Dichroism Study of CdSe QDs

In this chapter we study the magnetic circular dichroism (MCD) of exciton states near the band edge of CdSe nanocrystallites (quantum dots). The experiment probes the difference between left and right circularly polarized transitions in the presence of an external magnetic field. Analysis of the MCD signal determines the sign and magnitude of the exciton g-factor which is shown to be highly sensitive to the energy band parameters used in the effective mass approximation. The observation of theoretically predicted changes in the sign of the exciton g-factor between the first two transitions is in agreement with recent theory describing the presence of fine structure underlying the optical transitions of CdSe nanocrystallites.

4.1 Introduction

The recent development of high quality semiconductor nanocrystallites or quantum dots (QDs) has led to a number of studies dealing with the optical properties of these novel materials. Of interest are unique features which stem from the three dimensional confinement of the electron and hole within the QD. This occurs when the size of the nanocrystallite is comparable to or smaller than the exciton Bohr radius of the semiconductor. Prominent among these features is the formation of discrete excitation spectra which blue shifts as the size of the nanocrystallite decreases [1, 2].

The theoretical understanding of the QD optical response is still much debated, providing ample motivation for direct comparisons between experiment and theory. Magneto-optical experiments give new information about the electronic properties of semiconductors and may prove useful in determining the validity of a particular model. Direct magneto-optical measurements of excited state Zeeman splittings have been difficult because of the large inhomogeneous broadening which arises from the residual size distribution that currently occurs in all nanocrystalline systems. To overcome this limitation, magnetic circular dichroism (MCD) experiments have been conducted on several QD materials, most notably CuCl and CdS_xSe_{1-x} [165, 166, 167, 168, 115]. This differential technique probes the linear absorption of the nanocrystallites and provides the difference spectrum for left and right circularly polarized Zeeman transitions. The magnitude and direction of the splitting depends on the exciton g-factor which, in turn, is determined by the g-factors of its constituent electron and hole. Knowledge of these values is important for the proper theoretical description of the band structure and motivates our investigation.

4.2 Experiment

We study CdSe QDs prepared by the method described in Ref. [32]. The preparation yields nearly monodisperse ($\sigma \leq 5\%$) wurtzite nanocrystallites which are slightly prolate and have surfaces passivated by organic ligands. The effective radii of the QDs, as determined by extensive TEM/small angle x-ray scattering (SAXS) measurements, range from 10 to 50 Å. Figure 4-1 shows the low temperature (10 K) absorbance and the corresponding 10 Tesla MCD signal for two QD sizes (19 Å and 25 Å). The MCD spectrum ($\Delta OD = OD_L - OD_R$ [1]) exhibits a characteristic first derivative line shape. The absorption and MCD spectrum are superimposed to compare the energy at which the MCD signal crosses zero with the peak of the first transition. In both cases there is good agreement between the two, suggesting that diamagnetic shifts are negligible for QDs of this size.

Experiments were conducted at five field strengths: 2, 4, 6, 8, and 10 Tesla. In all cases the magnitude of the signal scales linearly with magnetic field while the position of the MCD maximum (minimum) remains constant. A study of the temperature dependence of the MCD signal was also conducted on both samples. At 10 Tesla no significant thermal effect was found; a slight redshift of the zero crossing with increasing temperature is attributed to the temperature dependent bandgap of CdSe. No changes in intensity or splittings are observed.

Figure 4-2 shows an abbreviated schematic of the experimental setup. The experiment essentially entails bringing white light from a 300 W Xe arc lamp through a

[1] OD is optical density and the subscripts L and R refer to left and right circularly polarized excitation.

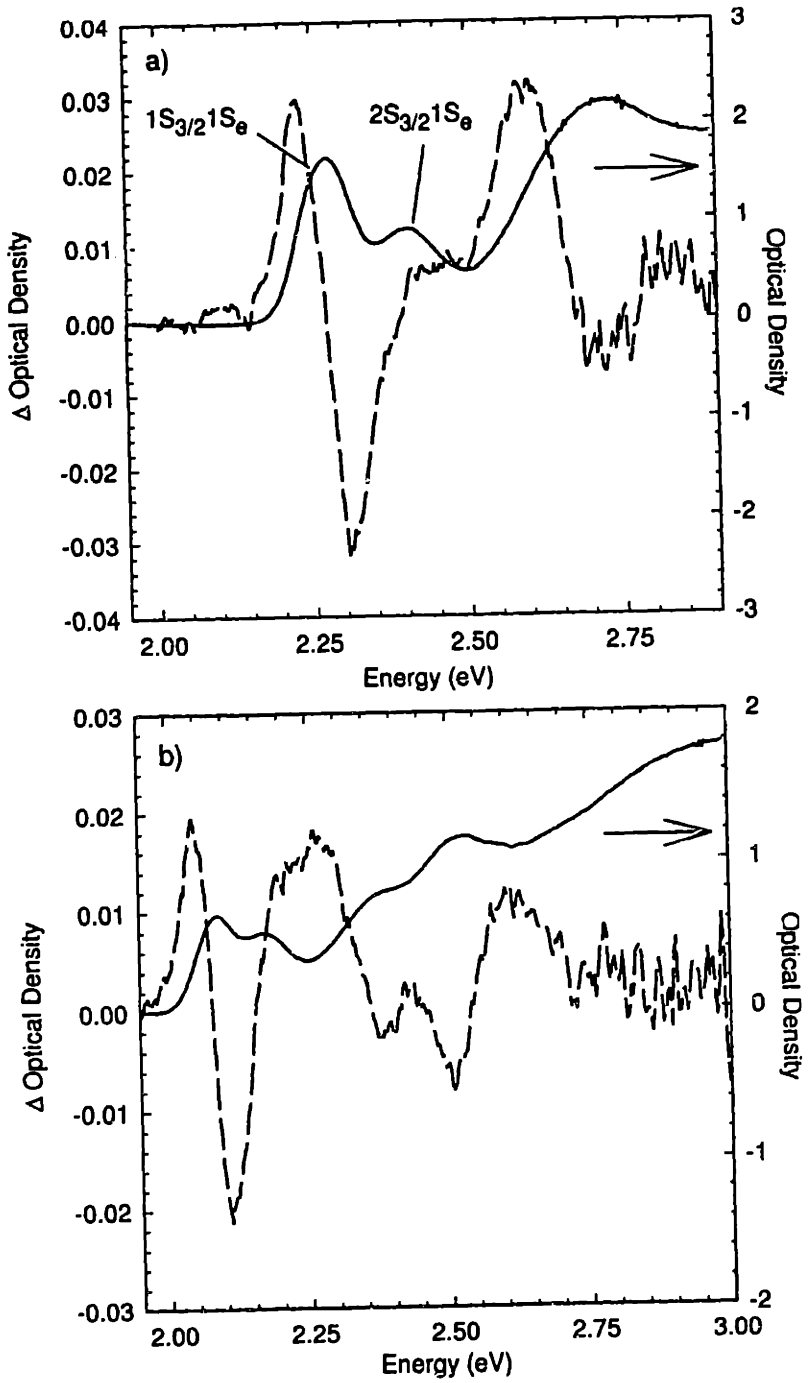

Figure 4-1: (a) Comparison of the (10 Tesla) MCD signal to the low temperature absorption of nominally 19 Å radius CdSe nanocrystallites. The first optical transition is labeled $1S_{3/2}1S_e$ and the second $2S_{3/2}1S_e$ [9]. In the MCD experiment, white light from a 300 W Xe arc lamp is passed through a depolarizer, a Glan Taylor polarizer and a Fresnel rhomb to produce circularly polarized light. The light is then brought into the bore of a superconducting magnet. Experiments are conducted in the Faraday geometry and the signal is generated by altering the input circular polarization of the excitation light. (b) Comparison of the (10 Tesla) MCD signal to the low temperature absorption of nominally 25 Å radius QDs. In both cases there is good agreement between the zero crossing of the MCD signal and the peak of the first absorption feature. Further comparisons at higher energies are difficult due to overlapping transitions.

series of optics including a broadband depolarizer, linear polarizer and Fresnel rhomb into the bore of a superconducting magnet. The sample sits at the center of a variable magnetic field which ranges from 0-10 Tesla.[2] Transmitted light is brought out of the magnet through a fiber and passed through a spectrometer/OMA. The difference spectrum is taken on a PC.

MCD results are fit using a non-linear least squares fitting program. The signal is modeled as the difference spectrum between left and right circularly polarized absorption coefficients. The fitting procedure varies the value of the Zeeman splitting, keeping all other experimental parameters (amplitude, linewidth and zero field energy of the absorption bands) fixed as determined in an independent absorption measurement. The MCD signal can be approximated by the expression:

$$\alpha_{MCD}(\varepsilon) = 2C\frac{\Delta\varepsilon(\varepsilon-\varepsilon_0)}{\sigma^2}\frac{1}{\sqrt{2\pi}\sigma}\exp\left(-\frac{(\varepsilon-\varepsilon_0)^2}{2\sigma^2}\right) \tag{4.1}$$

where C is a constant proportional to the oscillator strength of the state, $\Delta\varepsilon$ is the Zeeman splitting of the levels (proportional to the exciton g-factor and the magnetic field), ε_0 is the position of the exciton level in zero magnetic field, and σ is the exciton linewidth for a particular size distribution. Figures 4-4 (a) and (b) show best fits to the experimental data.

[2]Up to 11 Tesla if quenches don't frighten you.

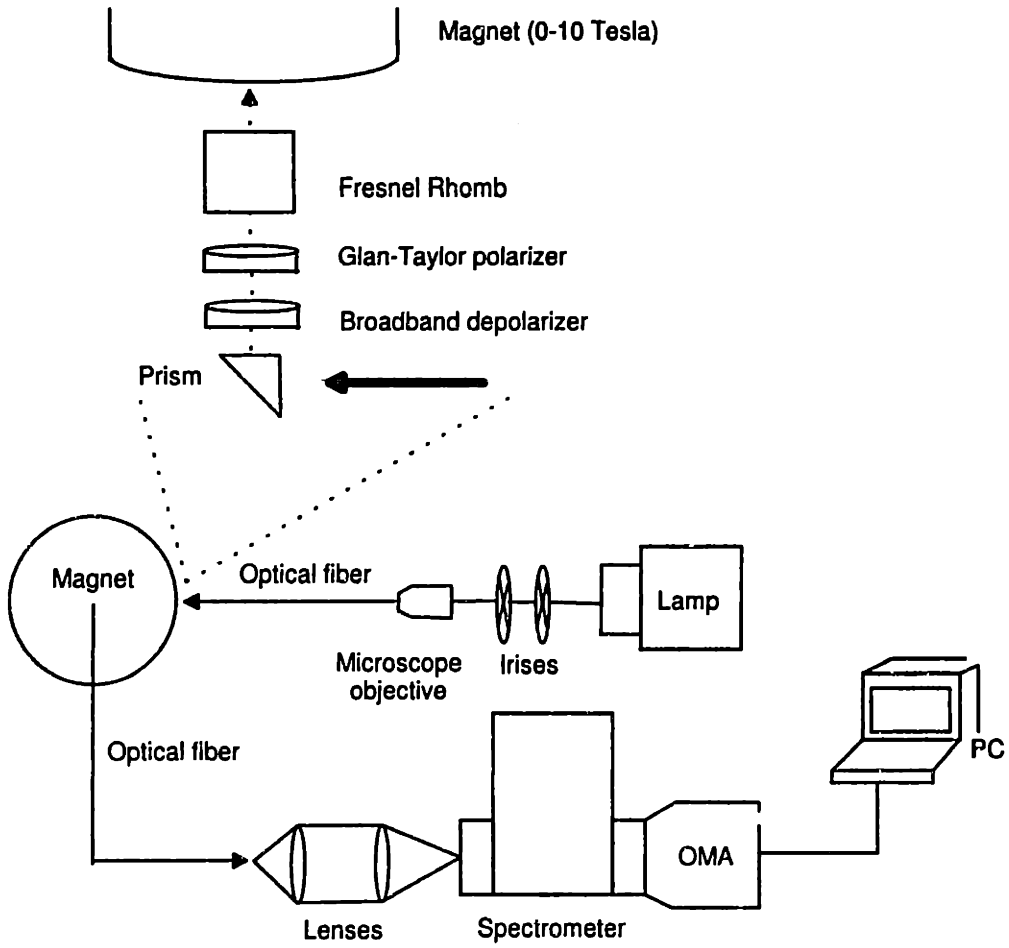

Figure 4-2: Abbreviated schematic of the experimental setup. White light from a 300 W Xe arc lamp is brought through a microscope objective into a fiber optic cable. The light is then passed through a depolarizer, linear polarizer and Fresnel rhomb to produce circularly polarized light. The light passes through a sample at the center of a variable magnetic field (0-10 Tesla). Transmitted light is brought out of the fiber and is dispersed using a spectrometer/OMA. The difference spectrum is taken on a PC.

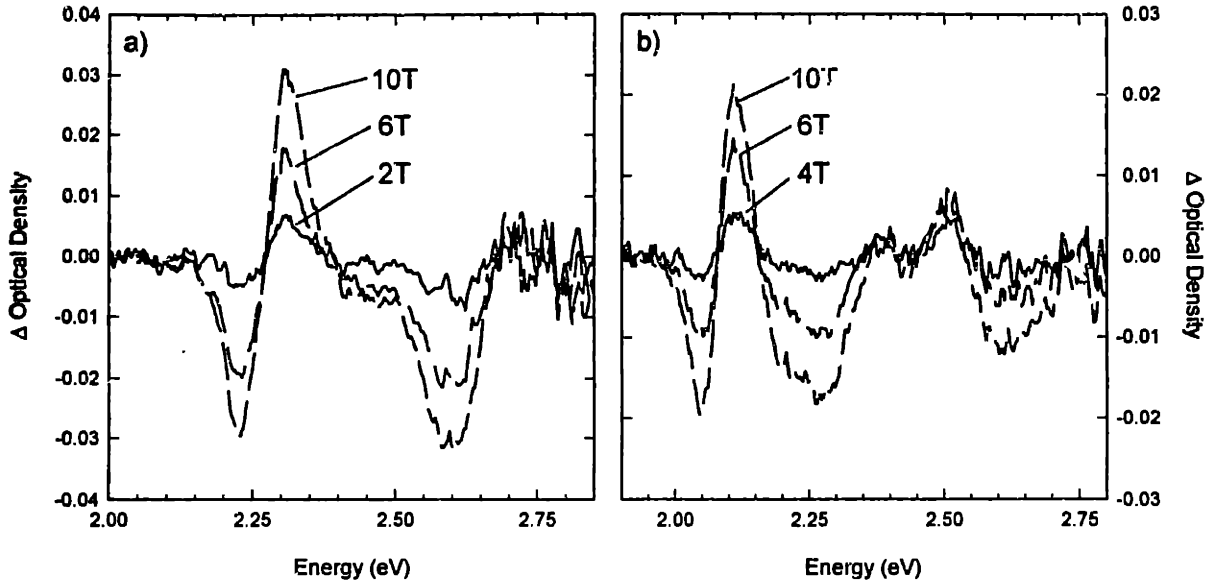

Figure 4-3: Magnetic field dependence of the MCD signal. Shown are results for the two samples (a) 19 Å and (b) 25 ÅThree fields are plotted to show the linear dependence of the effect. In both cases the sample temperature is 10K.

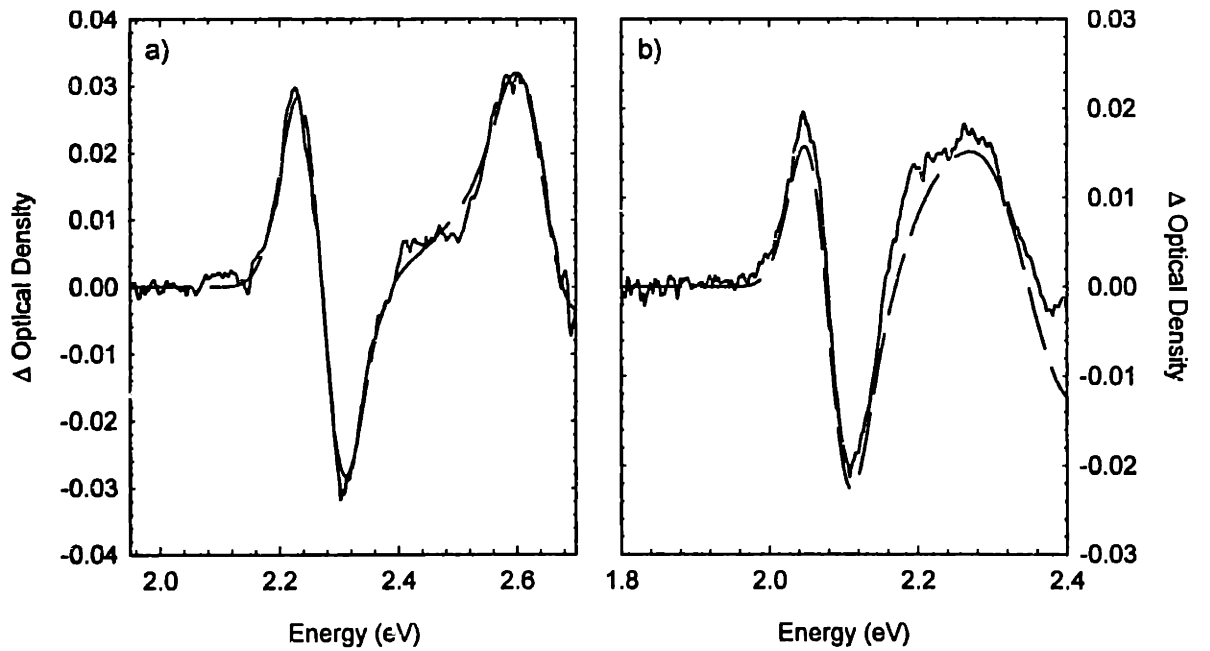

Figure 4-4: (a) Best fit to the 19 Å MCD spectrum at 10 Tesla. The fitting routine varies only the value of the Zeeman splitting keeping all other variables (determined through an independent absorption measurement) fixed. (b) Best fit to the 25 Å MCD spectrum at 10 Tesla. In all cases the sample temperature is 10 K.

4.3 Results

Results from the fitting procedure are shown in Figure 4-5. Figures 4-5 (a) and (b) show the Zeeman splitting of the $1S_{3/2}1S_e$ and $2S_{3/2}1S_e$ states for the 19 Å sample. The $1S_{3/2}1S_e$ state Zeeman splitting has a positive slope while that of the $2S_{3/2}1S_e$ state is negative. Similarly, Figs. 4-5 (c) and (d) show the same behavior for the 25 Å sample. The graphs clearly indicate the sign and relative magnitude of the (effective) exciton g-factors. The $1S_{3/2}1S_e$ exciton has a positive g-factor while the $2S_{3/2}1S_e$ g-factor is negative and smaller in magnitude.

4.4 Discussion

For CdSe QDs in the strong confinement regime the influence of an external magnetic field can be treated as a molecular Zeeman effect. The Hamiltonian describing the Zeeman splitting has the form [64]

$$\hat{H}_H = \frac{1}{2} g_e \mu_B \boldsymbol{\sigma} \mathbf{H} - g_h \mu_B \mathcal{K} \mathbf{H} \ , \tag{4.2}$$

where g_e and g_h are the electron and hole g-factors respectively, μ_B is the Bohr magneton, and $\mathcal{K}$ is the hole angular momentum operator ($\mathcal{K} = 3/2$ for the $1S_{3/2}$ and $2S_{3/2}$ states). In Eq. 4-2 we neglect diamagnetic, H^2, terms because the dots are significantly smaller than the characteristic magnetic length [$\sim 115\mathring{A}$ at 10T]. For electrons in CdSe $g_e = 0.68$ [111]. The value of the hole g-factor is calculated using expressions by Gel'mont and D'yakonov for a hole localized in a spherically symmetric potential [112]. Equation A1 from [64] gives $g_h = -1.09$ and $g_h = -0.053$

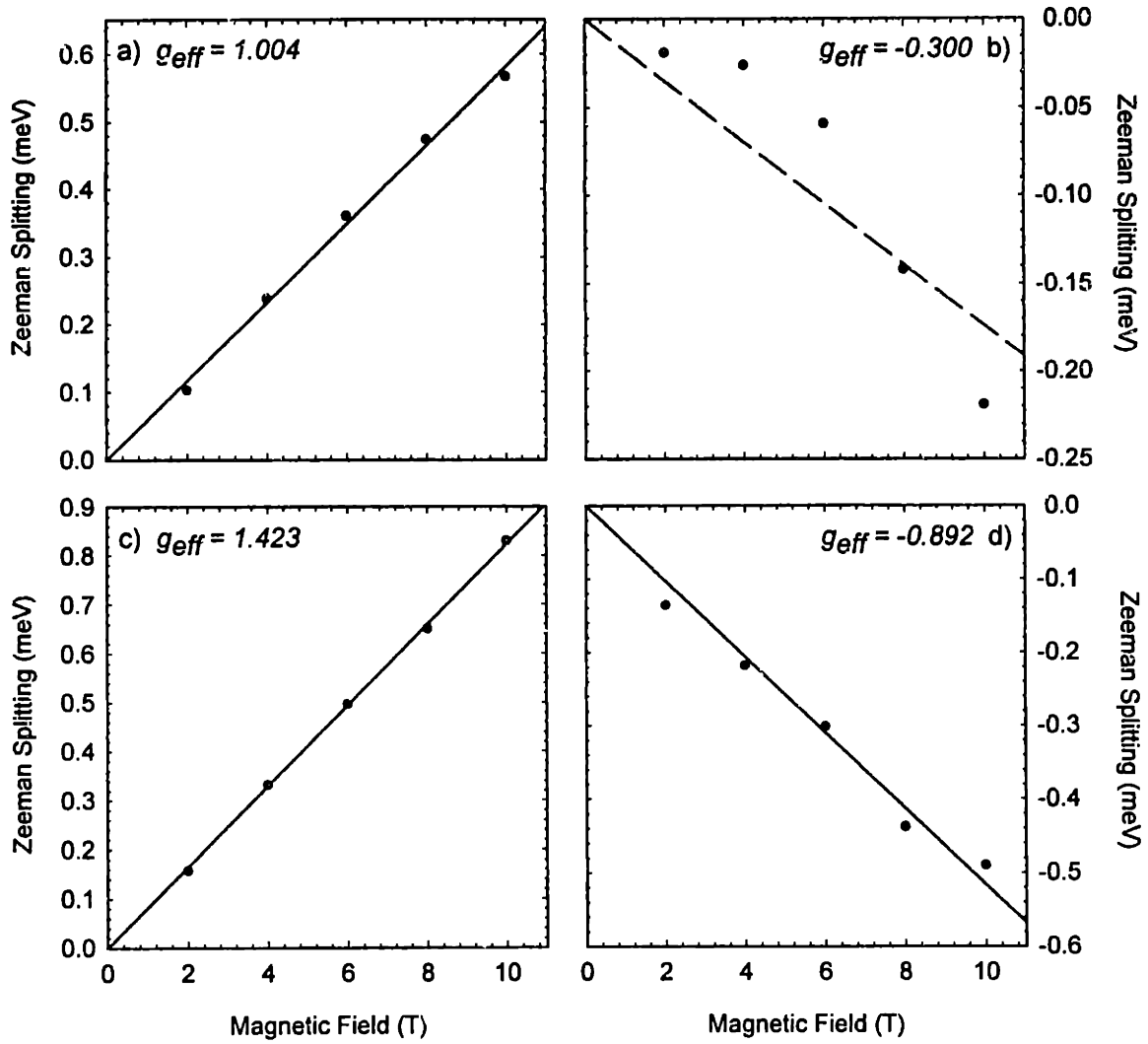

Figure 4-5: (a) Resulting Zeeman splittings extracted from the fitting procedure for the $1S_{3/2}1S_e$ state (a = 19 Å). The splittings are linear with magnetic field and exhibit a positive slope. Lines are a linear fit to the data. (b) Extracted Zeeman splittings for the $2S_{3/2}1S_e$ state (a = 19 Å). The splittings exhibit a negative slope indicating a negative sign for the exciton g-factor. See Ref.[17]. (c) Extracted Zeeman splittings for the $1S_{3/2}1S_e$ state (a = 25 Å). The splittings are linear with field and indicate a positive exciton g-factor. (d) Extracted splittings for the $2S_{3/2}1S_e$ state (a = 25 Å). As with the 19 Å sample, the splittings indicate a negative sign for the exciton g-factor.

for the $1S_{3/2}$ and $2S_{3/2}$ hole states respectively.

Although the spherical approximation has been successful in modeling the linear absorption of CdSe QDs [15, 12, 96], it is not consistent with recent experimental results suggesting the presence of fine structure underlying these optical transitions. The success of the approximation stems from the much larger spacing of electron and hole quantum size levels relative to the fine structure splittings resulting from internal (hexagonal lattice structure) and external (non-sphericity of the crystal shape) asymmetries as well as the electron hole exchange interaction. Since the Zeeman splittings are on the same order as the splittings due to fine structure effects, a proper theoretical treatment requires that the Hamiltonian (2) be used as a perturbation within the non-spherical theory [64] which describes this fine structure.

In the spherical approximation any $nS_{3/2}$ hole state is 4-fold degenerate with respect to its angular momentum projection ($M = 3/2, 1/2, -1/2, -3/2$). All $nS_{3/2}1S_e$ exciton states are therefore eight fold degenerate since the $1S_e$ electron state is doubly degenerate with respect to its spin projection $s_z = \pm 1/2$. Recent theory has shown that the non-spherical shape of the nanocrystals, the intrinsic hexagonal lattice asymmetry and the electron-hole exchange interaction lift the degeneracy of the $nS_{3/2}1S_e$ states splitting them into five states which underly each spherical optical transition [64, 63]. These fine structure states are labeled by their total angular momentum projection along the hexagonal axis of the nanocrystallites, $N = F_{hm} + F_{em}$. There are two states with angular momentum projection $|N| = 1$, two states with projection $|N| = 0$ and one state with projection $|N| = 2$. The $|N| = 1, 2$ states are each doubly degenerate. Three of the five states are optically active (bright) and two (including

the exciton ground state) are optically passive (dark). This exciton fine structure is consistent with recent photoluminescence excitation and fluorescence line narrowing experiments done on the ($1S_{3/2}1S_e$) band edge exciton of CdSe nanocrystallites [118, 82, 83, 81]. The $2S_{3/2}1S_e$ exciton fine structure is similar to that of the band edge transition $1S_{3/2}1S_e$ [64].

The Zeeman splittings ($\Delta\varepsilon$) of optically active $|N| = 1$ states are determined by considering Eq. 4-2 as a first order perturbation to the full Hamiltonian in Ref. [64] (Eq.14) giving:

$$\Delta\varepsilon_{|1|}^{U,L} = \varepsilon_1^{U,L} - \varepsilon_{-1}^{U,L} = 2\mu_B H_z g_1^{U,L} \quad , \tag{4.3}$$

where

$$g_1^{U,L} = g_e\left(\frac{\pm f}{\sqrt{f^2+d}}\right) - g_h\left(\frac{2\sqrt{f^2+d} \mp f}{\sqrt{f^2+d}}\right) \tag{4.4}$$

and f, d are functions related to the electron-hole exchange interaction and to the hole level splitting arising from the asymmetry of the nanocrystals (see Eq. 21 in Ref. [64]). The superscripts U (upper) and L (lower) distinguish different states with the same angular momentum projection. While the optically active $N = 0$ exciton state is not split by an external magnetic field, Eq. 4-3 shows that the splittings of the $|N| = 1$ states are proportional to the projection of the magnetic field onto the crystal hexagonal axis, H_z.

Figures 4-6 (a), (b) show the size dependence of $g_1^{U,L}$ for the first two exciton states. For the $1S_{3/2}1S_e$ transition (Fig. 4-6 a) both fine structure g-factors, $g_1^{U,L}$, are positive. Figure 4-6 b shows the size dependence of $g_1^{U,L}$ for the $2S_{3/2}1S_e$ fine structure. Here g_1^L becomes negative while g_1^U remains positive. Figures 4-6 (c) and (d) show the relative

oscillator strengths of the $1S_{3/2}1S_e$ ($2S_{3/2}1S_e$) fine structure states respectively. In both cases the relative oscillator strength of the $\pm 1^L$ state is larger than that of the $\pm 1^U$ state at large sizes. As the size of the nanocrystallite decreases the $\pm 1^L$ oscillator strength falls because the electron-hole exchange interaction increases [64]. A difference, however, is that the $(2S_{3/2}1S_e)$ $\pm 1^L$ oscillator strength decreases more slowly than in the case of the $1S_{3/2}1S_e$ state.

The magnitude of the Zeeman splitting in Eq. 4-3 depends on the angle θ between the magnetic field and the crystal hexagonal axis. The probability of optically exciting each state also depends on this angle (in the Faraday geometry the direction of the light is parallel to the magnetic field). For $\sigma^{\pm}$ excitation of the 0^U state the probability is $P_0^U(\sigma^{\pm}) = N_0^U \sin^2(\theta)$, where $N_0^U = 4/3$. Similarly, expressions for the $\pm 1^{U,L}$ states are:

$$P_{N=1}^{U,L}(\sigma^{\pm}) = N_1^{U,L}(1 \pm \cos\theta)^2 , \tag{4.5}$$

$$P_{N=-1}^{U,L}(\sigma^{\pm}) = N_1^{U,L}(1 \mp \cos\theta)^2 , \tag{4.6}$$

where

$$N_1^{U,L} = \frac{1}{3}\left(\frac{2\sqrt{f^2+d} \mp f \pm \sqrt{3d}}{2\sqrt{f^2+d}}\right) \tag{4.7}$$

The size dependence of the relative excitation probabilities, $N_1^{U,L}$, are shown in Figs. 4-6 (c), (d). The effective Zeeman splittings for these states are obtained by averaging their values, weighted by each state's excitation probability, over all angles θ.

Because of the inhomogeneous broadening of $nS_{3/2}1S_e$ excitons due to the size distribution we cannot distinguish individual fine structure contributions to the ex-

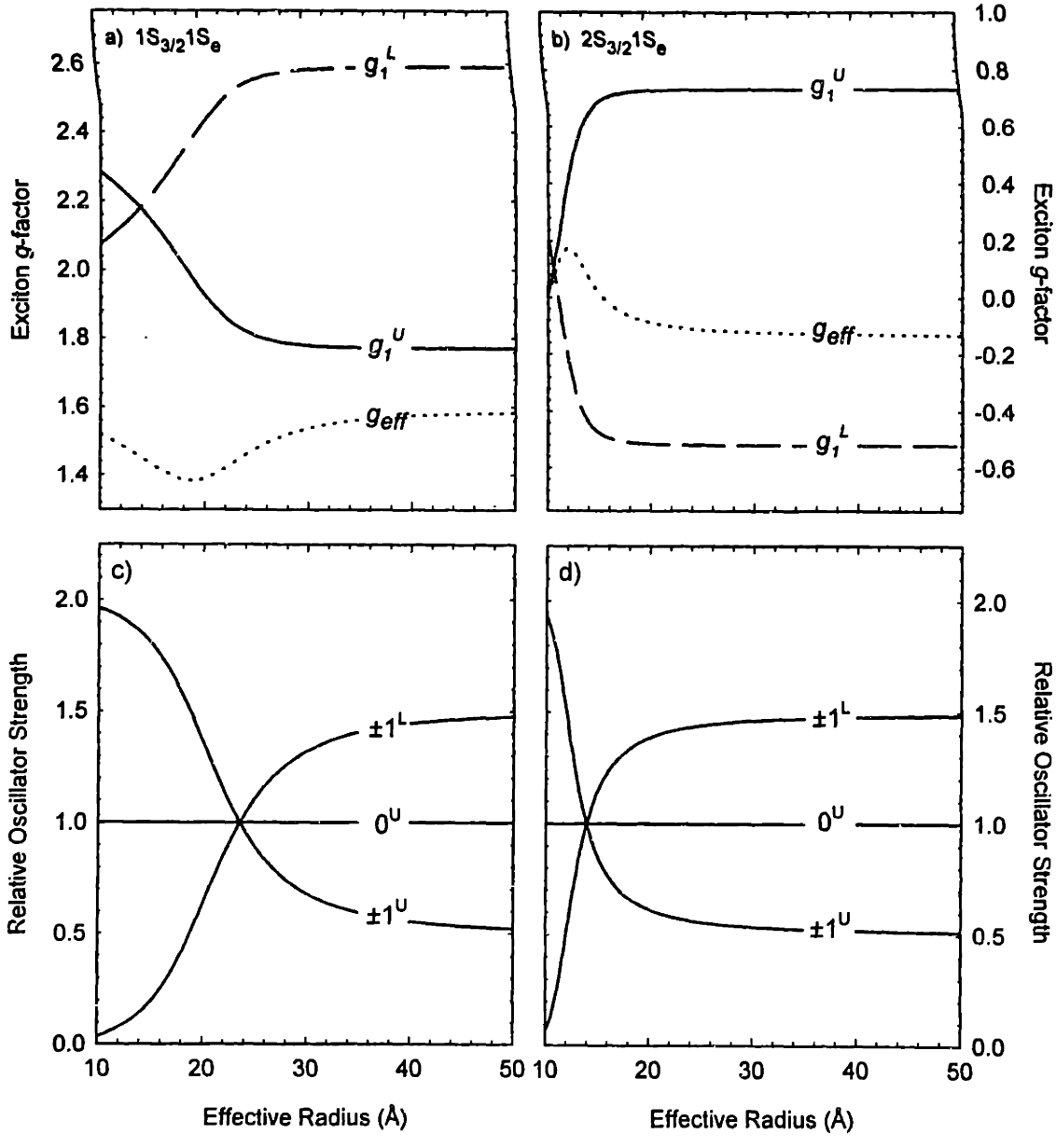

Figure 4-6: (a) Predicted ($1S_{3/2}1S_e$) exciton g-factors for the $\pm1^L$ (dashed) and $\pm1^U$ (solid) fine structure states as a function of nanocrystal size. Both g-factors remain positive over the sizes of interest and predict a net positive g-factor for the first optical transition (dotted line determined from Eq.7). (b) Theoretical ($2S_{3/2}1S_e$) exciton g-factors for the $\pm1^L$ (dashed) and $\pm1^U$ (solid) fine structure states as a function of size. The g-factor of the $\pm1^L$ state rapidly becomes negative while the g-factor of the $\pm1^U$ state remains positive. The effective $2S_{3/2}1S_e$ g-factor, determined from Eq.7, is shown as the dotted line. (c) Oscillator strengths of the optically active ($1S_{3/2}1S_e$) fine structure states relative to the $F = 0$ state. (d) Relative oscillator strengths of the ($2S_{3/2}1S_e$) fine structure. The $\pm1^L$ state has a larger oscillator strength relative to the $\pm1^U$ state over a greater range of sizes than in the $1S_{3/2}1S_e$ case. This accounts for the negative g- factor of the $2S_{3/2}1S_e$ state. (See Eq. 4-7)

perimental Zeeman splittings. We compare experiment and theory by summing the normalized contributions of each $N = \pm 1$ state and angle averaging to account for the random orientation of c axis in the sample. The $N = 0$ state must also be considered because it contributes to the absorption of circularly polarized light even though it doesn't split in the magnetic field. We obtain an effective Zeeman splitting:

$$\Delta\varepsilon = \mu_B H \frac{N_1^U g_1^U + N_1^L g_1^L}{N_1^U + N_1^L + N_0^U/4} = \mu_B H g_{\text{eff}} \tag{4.8}$$

where the denominator is the sum of the oscillator strengths of the three optically active fine structure states. Equation 4-7 allows us to directly compare theoretical Zeeman splittings to the experimental values shown in Fig. 4-5. Theoretical exciton g-factors are plotted as dotted lines in Figs. 4-6 (a),(b).

The observation of an inverted splitting for the second state [Figs. 4-5 (b), (d)] is significant, as such a change is not expected in spherical symmetry. Equation 2 shows that changing the hole g-factor from g_h $(1S_{3/2})$ = -1.09 to g_h $(2S_{3/2})$ = -0.053 does not alter the sign of the Zeeman splitting within a spherical approximation. The $2S_{3/2}1S_e$ g-factor is still predicted to be positive. We should expect both $1S_{3/2}1S_e$ and $2S_{3/2}1S_e$ states to behave similarly. However, breaking the spherical symmetry with the introduction of fine structure does allow such an inversion to occur. Equations 4-4, 4-5 and Fig. 4-6 show the subtle interplay between g-factors and transition probabilities for the various fine structure states which when taken together (Eq. 4-7) leads to an experimentally observed negative g-factor for the second state. This stresses the need for a proper theoretical description of excited states.

A comparison of theoretical exciton g-factors to experimental values gives rea-

sonable agreement between the two. For the 25 Å (19 Å) $1S_{3/2}1S_e$ exciton, theory predicts $g_{\text{eff}} = 1.479$ (1.385) compared to the values $g_{\text{eff}} = 1.423$ (1.004) determined experimentally. A further comparison for the $2S_{3/2}1S_e$ state gives $g_{\text{eff}} = -0.114$ (-0.08) versus the experimental values $g_{\text{eff}} = -0.892$ (-0.3). The larger discrepancy in g-factors for the $2S_{3/2}1S_e$ exciton may be due to experimental inaccuracies in the measured half width, σ, or oscillator strengths of the $2S_{3/2}1S_e$ transition. It may also arise from a tendency by the theory to overestimate/underestimate the oscillator strengths of the various fine structure states. See Ref. [118] for a recent PLE investigation addressing this issue.

Using Eqs. 4-4 and 4-7 we also extract values for the hole g-factor. Assuming $g_e = 0.68$, we extract $g_h = -1.04$ (-0.76) for the 25 Å (19 Å) $1S_{3/2}1S_e$ hole g-factor in good agreement with theory ($g_h = -1.09$). Similarly, the $2S_{3/2}1S_e$ transition gives a value of $g_h = 0.09$ for the 19 Å sample.[3] There is a discrepancy, though, in the extracted g-factor for the (25 Å) $2S_{3/2}1S_e$ state. Its value ($g_h = 0.42$) is much larger than predicted ($g_h = -0.053$). This discrepancy may stem from the experimental and theoretical inaccuracies described above.

4.5 Conclusion

In summary, we have conducted MCD experiments on high quality CdSe QDs. Values for the effective g-factors of the $1S_{3/2}1S_e$ and $2S_{3/2}1S_e$ excitons have been

[3]Analysis of the 19 Å $2S_{3/2}1S_e$ Zeeman splitting is less certain due to difficulties in the fitting procedure. A state not resolved in the absorption spectrum of the sample is seen in the MCD spectrum. Lack of knowledge about the relative oscillator strength and linewidth of this state prevents a unique fit for the $2S_{3/2}1S_e$ state. This accounts for the odd shape of the $2S_{3/2}1S_e$ field dependent splitting. Figure 4-5(b)

experimentally determined. More importantly, an inverted splitting of the second exciton has been observed. This qualitative observation is in good agreement with recent theory which explains the presence of fine structure in the absorption and the long lived emitting state of CdSe nanocrystallites.

Chapter 5

Size Dependent MCD

In this chapter, detailed magnetic circular dichroism (MCD) studies are conducted on the band edge exciton of nanometer-sized CdSe quantum dots (QDs). The experiment probes the absorption of left and right circularly polarized light in the presence of an external magnetic field. Analysis of the MCD signal determines the sign and magnitude of the exciton g factor. We observe a change in the sign of the g factor between the first two transitions in the linear absorption of the nanocrystallites, consistent with recent theory describing the presence of fine structure in CdSe QDs. More importantly, the sign of the second transition's g factor exhibits a characteristic size dependence. The inverted splitting of the second state and its subsequent reversal at small sizes is important as it is not predicted by spherical models of the electronic structure. The fine structure model we use to describe our results has previously explained the origin of the band edge luminescence in CdSe nanocrystallites.

5.1 Introduction

The use of magnetic fields to probe the electronic structure of materials is an established and powerful technique. From early on, it was recognized that magneto-optical experiments were particularly useful in the study of atomic and molecular systems because of their sensitivity to internal angular momentum and spin states. The introduction of Zeeman splittings and the lifting of spin degeneracies have been instrumental in determining excited state symmetries, angular momenta and excited state g factors in atoms and molecules [169, 170, 171]. In the bulk, magneto-optical experiments have studied both intraband and interband transitions allowing the determination of effective g factors for free carriers and excitons [95, 172, 173, 174, 175, 176, 177].

Recently a number of efforts have aimed at studying the magneto-optical properties of low dimensional systems [178, 179, 180, 181, 182, 183, 184]. Of particular interest are semiconductor quantum dots (QDs) which are unique systems bridging the gap between molecular and bulk compounds. These QDs or "artificial atoms" have sizes ranging from 10 to 100 Å in radius and as a consequence exhibit interesting optical/electrical properties (quantum confinement effects). This is a result of the spatial confinement of excitations when the physical size of the QD is comparable to or smaller than the bulk exciton Bohr radius. One of the better known quantum confinement effects is the blueshift of the absorption with decreasing size. This effect as well as other features due to quantum confinement are described in excellent review articles by Brus and Alivisatos[1, 2, 3].

Among the various magneto-optical techniques, magnetic circular dichroism (MCD) experiments have been conducted on several QD systems, most notably CuCl, CdS_xSe_{1-x}

and CdSe [165, 166, 168, 115, 87, 167, 178, 185]. This experiment probes the linear absorption of the nanocrystallites and provides the difference spectrum for left and right circularly polarized Zeeman transitions. The magnitude and direction of the Zeeman splitting depends on the exciton g factor which, in turn, is determined by the g factors of its constituent electron and hole. The MCD or difference technique is most useful when the individual circularly polarized transitions are obscured by overlapping states or sample inhomogeneities. This is the case for many QD systems where current synthetic methods yield samples with residual size distributions necessitating the use of size selective optical techniques to probe underlying excited states.

We perform MCD experiments on high quality CdSe QDs with narrow size distributions. The study is interesting because the QD can be thought of as an artificial atom having discrete, quantized transitions. At the same time it retains characteristic features of the bulk having enough atoms to describe each carrier through bulk Bloch wavefunctions. The first three transitions in the linear absorption of the nanocrystallites are labeled $1S_{3/2}1S_e$, $2S_{3/2}1S_e$, and $1P_{3/2}1P_e$. These symmetry notations for the electron and hole arise from theoretical descriptions of the QD band structure which assume spherical boundary conditions within an effective mass model [51, 15, 12]. However, recent experimental and theoretical work have shown the possibility for the existence of fine structure underlying these transitions [63, 64, 118, 62, 84, 82, 81]. These fine structure states are thought to originate from symmetry breaking perturbations such as those caused by structural asymmetries in the QD and the electron hole exchange interaction.

As the theoretical understanding of the QD electronic structure is still debated, direct magneto-optical measurements on excited state Zeeman splittings may prove useful in determining the validity of a particular model by providing new information about the band structure of nanocrystalline materials.

The presence of fine structure has been instrumental in resolving many of the unusual properties of the nanocrystallites. In this respect, while spherical effective mass models [15, 12] have successfully explained the linear absorption of the nanocrystallites, the luminescence of CdSe QDs remains controversial and difficult to interpret because it exhibits unusually long lifetimes ($\tau_r \sim 1\mu s$ at 10 K) and a size dependent redshift.[61, 34] These observations are not explained by such electronic structure models which predict highly degenerate excited states. The band edge luminescence has therefore been attributed to the radiative recombination of surface localized carriers.[61, 47, 13] With the introduction of fine structure, a single model consistently explains many features in both the absorption and luminescence of CdSe QDs. [64]

Sec. II describes details of the MCD experiment. Sec. III summarizes our results and Sec.IV outlines the theory which enables us to extract predicted Zeeman splittings and exciton g factors. Discussion and summary are given in Secs. V and VI.

5.2 Experiment

We study a size series of CdSe QDs prepared by the method described in Ref.[32]. The preparation yields wurtzite nanocrystallites which are slightly prolate and have surfaces passivated by organic ligands, trioctylphosphine oxide (TOPO) and tri-

octylphosphine selenide (TOPSe). The effective radii of the QDs as determined by extensive TEM/SAXS measurements range from 10 to 50 Å. Narrow size distributions ($\sigma < 5\%$) are obtained through size selective precipitation. More details about the material and its characterization are found in references [33, 74, 73, 34, 137, 138, 37, 186].

Optical samples are created by recovering the QDs as a powder and redispersing the material into a 10% (by volume) solution of octane in hexane. The sample is then drop cast onto a fused silica flat and left to dry overnight. Once the solvent has evaporated, an optically clear (close packed) thin film of QDs is obtained. Another quartz flat is added to cover the sample. Typical optical densities range from 1.0 to 1.5 at the peak of the first absorption feature.

In the MCD experiment white light from a 300 W Xe arc lamp is passed through a depolarizer, Glan Taylor polarizer and a Fresnel rhomb to produce circularly polarized light. The light is then brought into the bore of a superconducting magnet where the sample sits at the center of a variable (0-10 Tesla) magnetic field. Experiments are conducted in the Faraday geometry. Transmitted light is brought out of the magnet through a fiber optic cable and acquisition of the signal accomplished with a 0.25 m spectrometer coupled to an optical multichannel analyzer (OMA). The MCD signal is generated by altering the input circular polarization of the excitation light and the difference spectrum is obtained through use of a computerized data acquisition program. The sample temperature is 10 K.

An independent absorption experiment is conducted using the white light from a 300 W Xe arc lamp. The transmitted light is passed through a 0.33 m spectrometer

coupled to an OMA. As in the MCD experiment, the sample temperature is 10 K in all cases.

5.3 Results

Figure 5-1 shows the low temperature (10 K) absorption and corresponding 10 Tesla MCD signal for four different QD sizes [radius (a) $\approx$ 10, 12, 21 and 32 Å]. The absorption and MCD spectra are superimposed to compare the zero crossing of the MCD signal. In all cases, there is good agreement between the two, suggesting that diamagnetic shifts are negligible for QDs of this size.

The MCD experiment is conducted at eight field strengths; 2, 4, 5, 6, 7, 8, 9, and 10 Tesla. Figure 5-2 shows the field dependence of the signal for four sizes in the series considered. Only results for five fields are shown. In all cases the signal scales linearly with magnetic field. Higher fields induce larger splittings which in turn create larger MCD signals. The position of the MCD maximum and minimum also remains relatively constant.

In a previous study, the temperature dependence of the MCD signal was conducted on several samples at two different temperatures (10 K and 100 K). No significant temperature dependence of the signal was observed. We attribute a slight redshift of the zero crossings to the temperature dependent bandgap of CdSe. Neither intensity nor splittings change dramatically with temperature.

MCD results are fit using a non-linear least squares fitting program. The signal is modeled as the difference spectrum between left and right circularly polarized

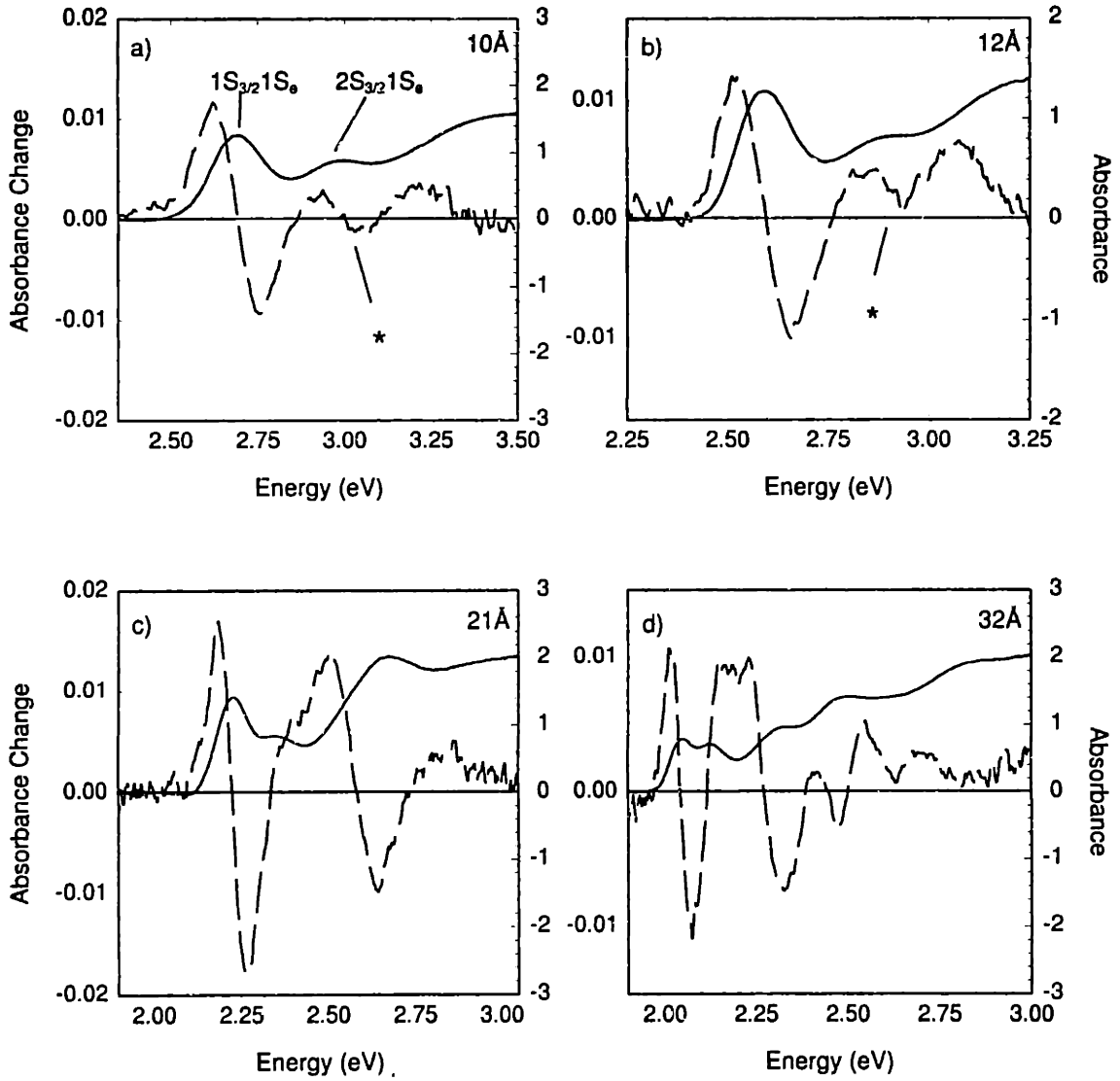

Figure 5-1: Absorption and corresponding 10 Tesla MCD signal from (a) 10 Å QDs (b) 12 Å QDs (c) 21 Å QDs and (d) 32 Å QDs. The sample temperature is 10 K in all cases.

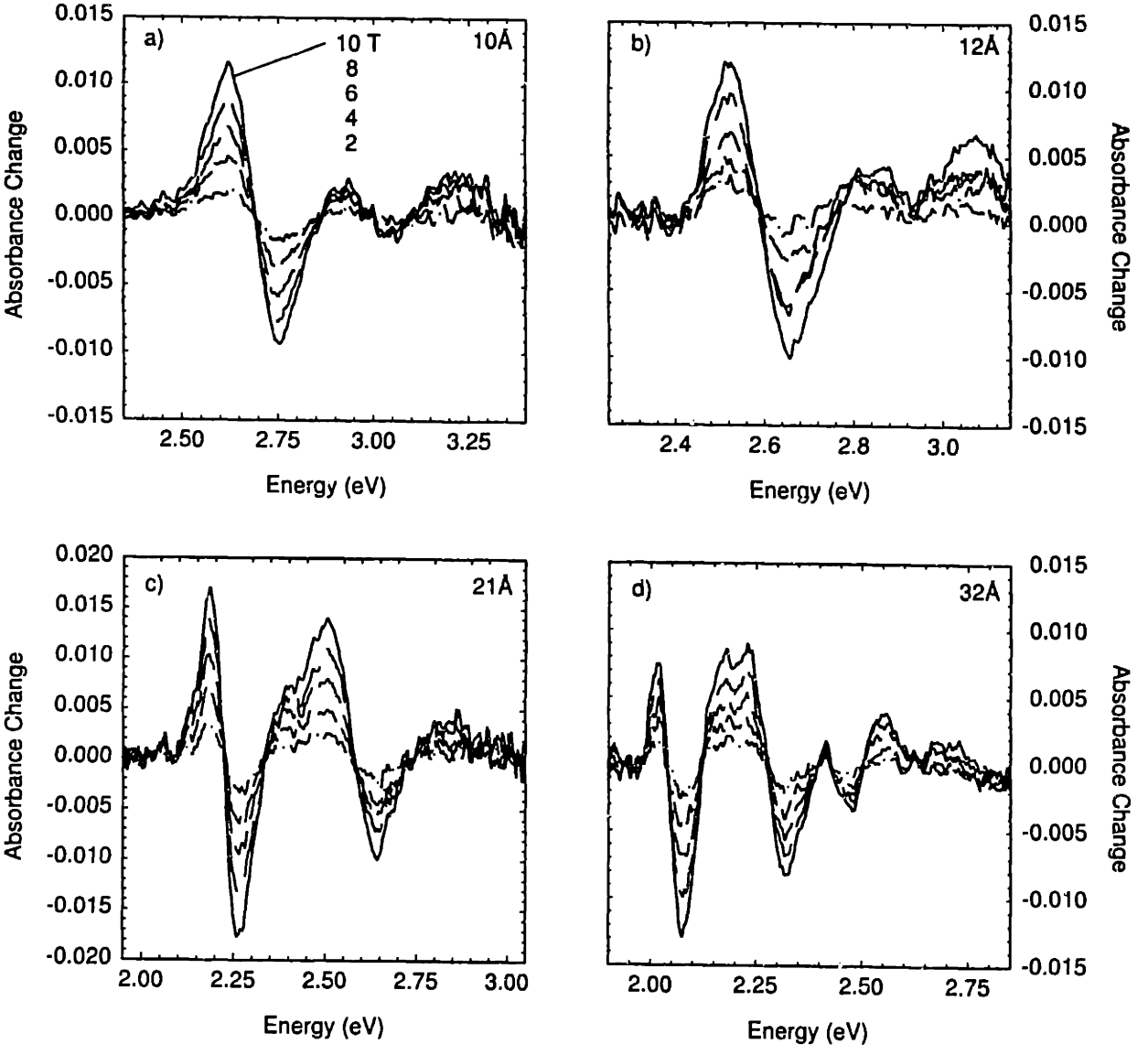

Figure 5-2: Magnetic field dependence of the MCD signal for (a) 10 Å QDs (b) 12 Å QDs (c) 21 Å QDs and (d) 32 Å QDs. The magnetic fields used are 2, 4, 6, 8, and 10 Tesla. The temperature is 10 K in all cases.

absorption coefficients ($\alpha_{MCD} = \alpha^- - \alpha^+$).[1] The fitting procedure varies the value of the Zeeman splitting, keeping all other experimental parameters (optical density, linewidth, and the zero field energy) fixed as determined in an independent absorption measurement. Figure 4-3 shows results of the (10 Tesla) fitting procedure for the four sizes considered. There is very good agreement between the fit and the data strongly suggesting that the MCD signal originates from the Zeeman splitting of states observed in the linear absorption.

Figure 5-4 shows the field dependent results of the fitting procedure for two of the four sizes. We consider the largest and smallest sizes to illustrate several interesting observations in the MCD data. For both sizes we show fitting results for the first two transitions ($1S_{3/2}1S_e$ and $2S_{3/2}1S_e$). The fits show that both transitions in the smallest size have positive g factors (characterized by positive slopes in the graph). The largest size also exhibits a positive $1S_{3/2}1S_e$ g factor. However, surprisingly, the $2S_{3/2}1S_e$ transition has a negative g factor (negative slope).

For all sizes considered, we find that the $1S_{3/2}1S_e$ g factor is positive valued and fairly constant in magnitude. We also follow the sign of the $2S_{3/2}1S_e$ g factor through the size series and observe that for most sizes, the $2S_{3/2}1S_e$ g factor is negative. At small sizes, in the vicinity of 14 Å radius, it suddenly becomes positive. These results are exciting (and altogether unexpected) because the inverted splitting of the second state and its subsequent reversal at small sizes are not predicted by existing models of the QD electronic structure based on spherical effective mass approximations.

[1] "left" is defined by counterclockwise rotation of the electric vector when facing the oncoming light. Likewise, "right" refers to clockwise rotation of the electric vector. Other conventions exist and in one scheme, left (right) refers to counterclockwise (clockwise) rotation of the electric vector seen when traveling in the same direction as the light.

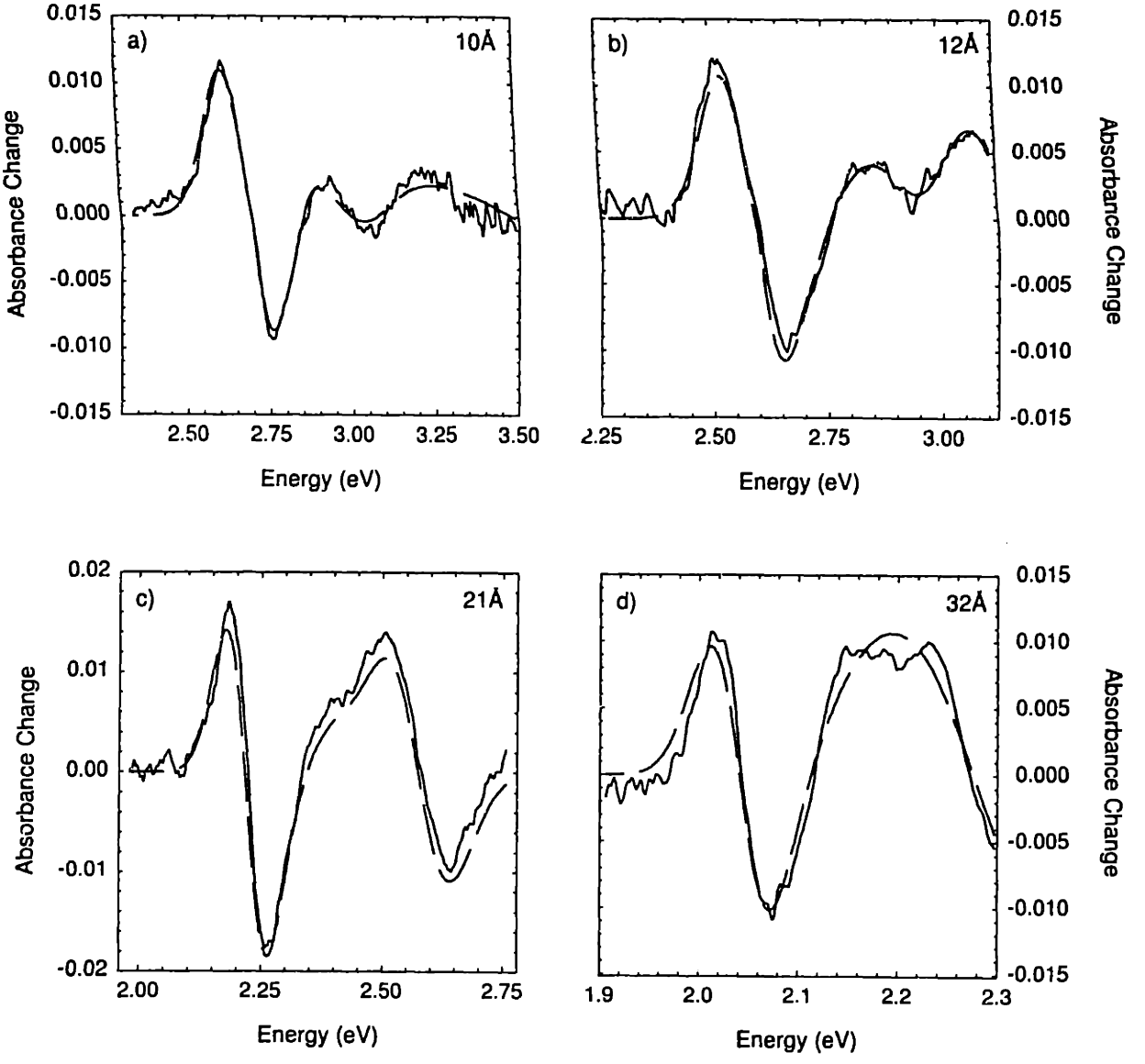

Figure 5-3: Best fits to the 10 Tesla MCD signal for (a) 10 Å QDs (b) 12 Å QDs (c) 21 Å QDs and (d) 32 Å QDs. The fitting procedure models the MCD signal as a derivative lineshape resulting from two Gaussians undergoing a rigid shift. Only the Zeeman splitting is varied. All other parameters such as the amplitude, linewidth and center position are determined in an independent absorption measurement.

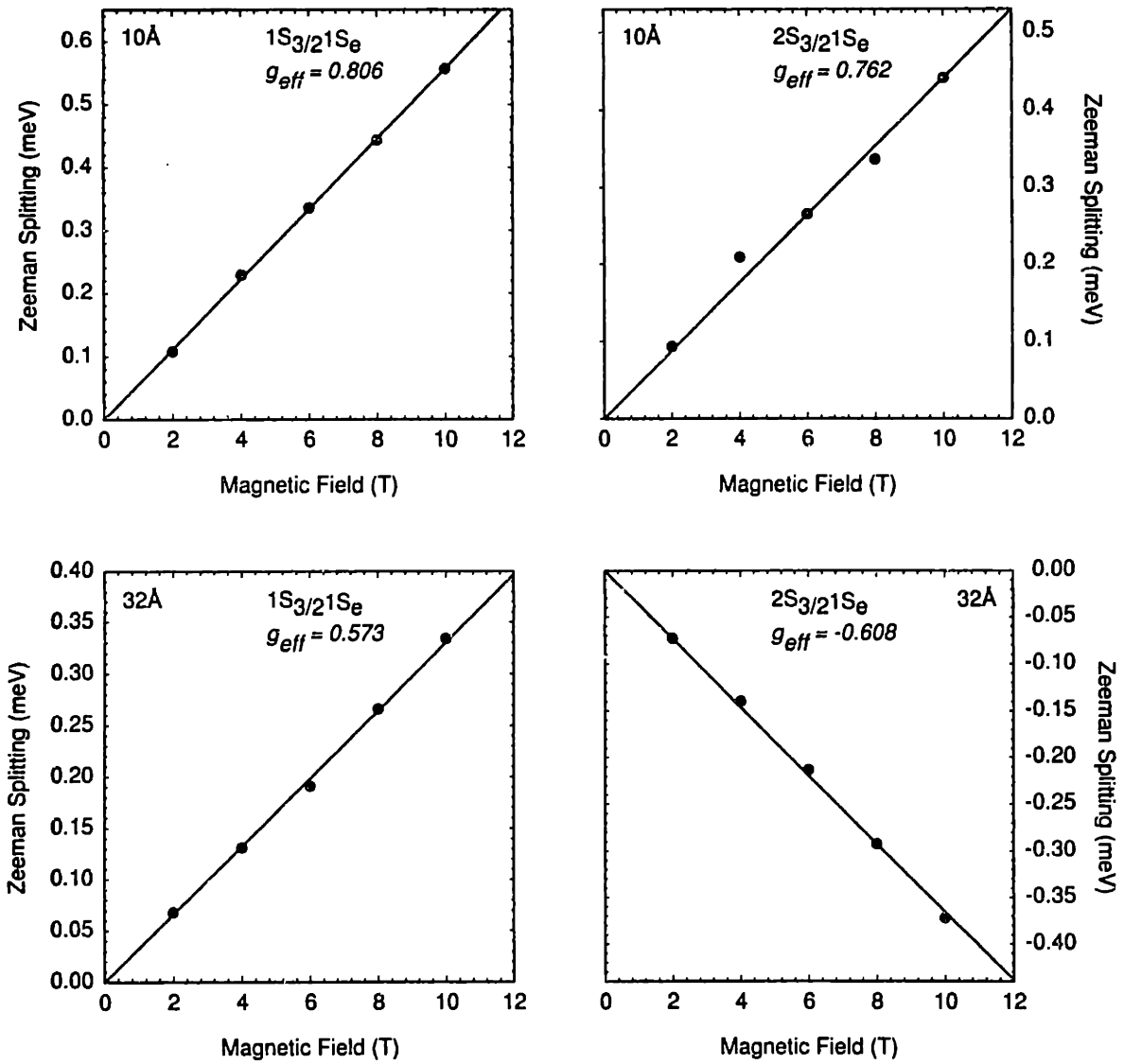

Figure 5-4: Fitting results of the MCD experiment at different magnetic fields for the largest and smallest sizes considered. (a) 10 Å QDs (b) 32 Å QDs. As before, only the value of the Zeeman splitting is varied in the fit. All other parameters are determined in an independent absorption measurement and are kept fixed.

To explain these results we turn to a recently developed theory which predicts the presence of fine structure underlying the optical transitions in CdSe QDs. This model has been used successfully to explain the band edge emission of the nanocrystallites. It accounts for both the long lifetimes and the resonant/non-resonant Stokes shift seen in recent emission experiments. The model considers several symmetry breaking perturbations to the electronic structure such as those arising from structural asymmetries (CFSE and QD geometry) and the electron-hole exchange interaction. When these effects are accounted for, the model predicts that underlying the $1S_{3/2}1S_e$ and $2S_{3/2}1S_e$ transitions are a number of fine structure states. Details of the theory are described in the next section.

5.4 Theory

5.4.1 The Fine Structure of $nS_{3/2}1S_e$ Exciton States in CdSe Quantum Dots

The fine structure of the $1S_{3/2}1S_e$ optically active exciton has been considered in detail in Refs. [63, 64]. Here we briefly summarize the theoretical considerations necessary for any $nS_{3/2}1S_e$ exciton in order to find the fine structure of the $2S_{3/2}1S_e$ transition.

For spherically symmetric CdSe QDs, i.e. finite size spherical crystals having a cubic lattice structure, the $1S_e$ electron ground state is doubly degenerate with respect to its spin projection. All $nS_{3/2}$ hole states are also 4-fold degenerate with respect to their total angular momentum projection, $\mathcal{K}$, (M = 3/2, 1/2, $-1/2$, and $-3/2$)

[51, 15]. The energies and wavefunctions of these quantum size levels are found in the parabolic approximation. For electrons they are:

$$E_{1S} = \frac{\hbar^2\pi^2}{2m_e a^2} ,$$

$$\psi_\alpha(\mathbf{r}) = \sqrt{\frac{2}{a}}\frac{\sin(\pi r/a)}{r}Y_{00}(\Omega)|S\alpha\rangle , \tag{5.1}$$

where m_e is the electron effective mass, a is the radius of the nanocrystal, $Y_{lm}(\Omega)$ are spherical harmonics, and $|S\alpha\rangle$ are Bloch functions of the conduction band; $\alpha = \uparrow (\downarrow)$ is the projection of the electron spin, $s_z = \pm 1/2$. For holes in the four-fold degenerate valence band they can be written:

$$E_{3/2,n}(\beta) = \frac{\hbar^2\varphi_n^2(\beta)}{2m_{hh}a^2} , \tag{5.2}$$

$$\psi_{M,n}(\mathbf{r}) = 2\sum_{l=0,2} R_{l,n}(r)(-1)^{M-3/2}\sum_{m+\mu=M}\begin{pmatrix} 3/2 & l & 3/2 \\ \mu & m & -M \end{pmatrix} Y_{lm}u_\mu , \tag{5.3}$$

where $\beta = m_{lh}/m_{hh}$ is the ratio of the light to heavy hole effective masses, $\varphi_n(\beta)$ is the nth root of the equation:

$$j_0(\varphi_n)j_2(\sqrt{\beta}\varphi_n) + j_2(\varphi_n)j_0(\sqrt{\beta}\varphi_n) = 0 , \tag{5.4}$$

$j_{0,2}(x)$ are spherical Bessel functions (the dependence of φ_n on β [52] for n=1 and 2 is shown in Fig. 5-5 a), $\begin{pmatrix} i & k & l \\ m & n & p \end{pmatrix}$ are Wigner 3j-symbols, and u_μ ($\mu = \pm 1/2, \pm 3/2$) are

Bloch functions of the four-fold degenerate valence band Γ_8 given in [106]:

$$\begin{aligned} u_{3/2} &= \frac{1}{\sqrt{2}}(X+iY)\uparrow \ , \\ u_{-3/2} &= \frac{i}{\sqrt{2}}(X-iY)\downarrow \ , \\ u_{1/2} &= \frac{i}{\sqrt{6}}[(X+iY)\downarrow -2Z\uparrow] \ , \\ u_{-1/2} &= \frac{1}{\sqrt{6}}[(X-iY)\uparrow +2Z\downarrow] \ . \end{aligned} \tag{5.5}$$

The radial functions $R_{l,n}(r)$ are [101, 52]:

$$\begin{aligned} R_{2,n}(r) &= \frac{A}{a^{3/2}}\left[j_2(\frac{\varphi_n r}{a}) + \frac{j_0(\varphi_n)}{j_0(\varphi_n\sqrt{\beta})}j_2(\frac{\varphi_n\sqrt{\beta}r}{a})\right] \ , \\ R_{0,n}(r) &= \frac{A}{a^{3/2}}\left[j_0(\frac{\varphi_n r}{a}) - \frac{j_0(\varphi_n)}{j_0(\varphi_n\sqrt{\beta})}j_0(\frac{\varphi_n\sqrt{\beta}r}{a})\right] \ , \end{aligned} \tag{5.6}$$

where the constant A is determined by the normalization condition:

$$\int dr r^2[R^2_{0,n}(r) + R^2_{2,n}(r)] = 1 \ . \tag{5.7}$$

In this level of approximation (a spherical approximation), all $nS_{3/2}1S_e$ exciton states are eight-fold degenerate. However this degeneracy can be lifted by structural asymmetries and the electron-hole exchange interaction. The nanocrystal asymmetry lifts the hole state degeneracy and splits it into two two-fold degenerate states - a Kramer's doublet having momentum projections $|M| = 1/2$ and $3/2$. We consider two sources for this asymmetry: the intrinsic asymmetry from the hexagonal lattice structure of CdSe [52] and the nonspherical shape of a prolate nanocrystallite [107].

The splitting due to the intrinsic hexagonal lattice structure, $\Delta_{int,n}$, can be written

[52]:

$$\Delta_{int,n} = \Delta_{cr} v_n(\beta) \quad , \tag{5.8}$$

where Δ_{cr} is the crystal field splitting in bulk CdSe (25 meV). The functions $v_n(\beta)$, expressed in terms of the radial functions $R_{0,2}$ in Ref. [52], are shown in Fig. 5-5 b for n=1 and 2.

The deviation from sphericity of an elliptically shaped nanocrystal is characterized by the ratio $c/b = 1 + \mu$ of its major to minor axis; μ is the ellipticity of the crystal and is positive (negative) for prolate (oblate) nanocrystals. The splitting arising from this deviation is given by [107]:

$$\Delta_{sh,n} = 2\mu u_n(\beta) E_{3/2,n}(\beta) \quad , \tag{5.9}$$

where $E_{3/2,n}$ is the $nS_{3/2}$ hole energy for spherical nanocrystals of radius $a = (b^2 c)^{1/3}$ and varies as the inverse square of a. The functions $u_n(\beta)$, expressed in terms of the radial functions $R_{0,2}$ in Ref. [107], are shown in Fig. 5-5 c for n=1 and 2.

The net splitting of the hole state from structural asymmetries, $\Delta_n(a, \beta, \mu)$, is then the sum of Eq. 5-8 and Eq. 5-9,

$$\Delta_n(a, \beta, \mu) = \Delta_{sh,n} + \Delta_{int,n} \; . \tag{5.10}$$

Fig. 5-6 a portrays the ground hole state splitting from the shape asymmetry and the crystal field in the absence of other symmetry breaking effects. We obtain two fourfold degenerate states with angular momentum projections $|M| = 3/2$ and $1/2$.

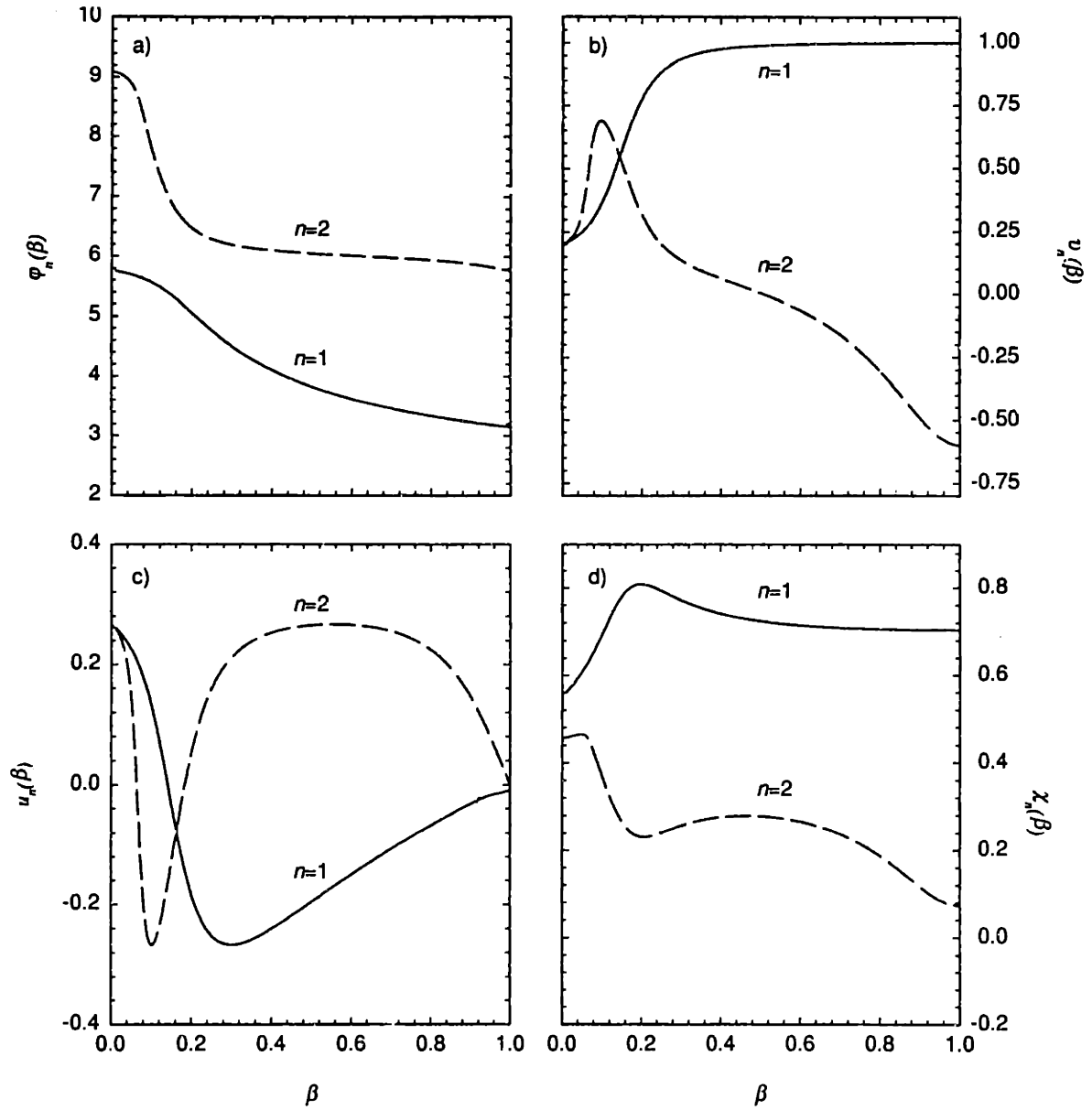

Figure 5-5: (a) The dependence of the hole ground state function $\phi_n(\beta)$ on the light to heavy hole effective mass ratio, β, for $n = 1$ (solid) and $n = 2$ (dashed). (b) the dimensionless function $\nu_n(\beta)$ associated with the hole level splitting due to the hexagonal lattice structure; plotted for $n = 1$ (solid) and $n = 2$ (dashed). (c) the dimensionless function $u_n(\beta)$ associated with the hole level splitting due to the crystal shape asymmetry; plotted for $n = 1$ (solid) and $n = 2$ (dashed). (d) the dimensionless function $\chi_n(\beta)$ associated with the exciton splitting due to the electron hole exchange interaction; plotted for $n = 1$ (solid) and $n = 2$ (dashed).

Both states are optically active and resemble the bulk A and B excitons.

In addition to structural asymmetries, we also consider the electron-hole exchange interaction which mixes different electron and hole spin states. The exchange interaction can be expressed in the following form [64]:

$$\hat{H}_{exch} = -(\pi/3)\hbar\omega_{ST}(a_{ex})^3\delta(\mathbf{r}_e - \mathbf{r}_h)\boldsymbol{\sigma}\cdot\boldsymbol{J}\ , \tag{5.11}$$

where $\boldsymbol{\sigma}$ is the electron Pauli spin 1/2 matrix, $\boldsymbol{J}$ is the hole spin 3/2 matrix, and $a_{ex} = 56$ Å is the bulk exciton Bohr radius. In bulk CdSe, this term splits the 4-fold degenerate exciton ground state into a singlet and a triplet state, separated by $\hbar\omega_{ST} = 0.13$ meV [110]. Fig. 5-6 b describes the ground hole state splitting from the electron-hole exchange interaction acting alone. We obtain two states, an optically active threefold degenerate exciton with total angular momentum $N = 1$ and an optically passive fivefold degenerate exciton with angular momentum $N = 2$.

The hexagonal lattice structure, crystal shape asymmetry, and the electron-hole exchange interaction all act concertedly to split the original "spherical " 8-fold degenerate exciton into five levels. Each level is labeled by its total angular momentum projection along the "c" axis of the nanocrystallite, $F = M + s_z$. We obtain one level with $F = \pm 2$, two with $F = \pm 1$, and two with $F = 0$. The wavefunctions of these states are linear combinations of the independent wavefunctions $\Psi_{\alpha,M,n}(\mathbf{r}_e, \mathbf{r}_h) = \psi_\alpha(\mathbf{r}_e)\psi_{M,n}(\mathbf{r}_h)$.

The energy of the exciton with total angular momentum projection $|F| = 2$ and

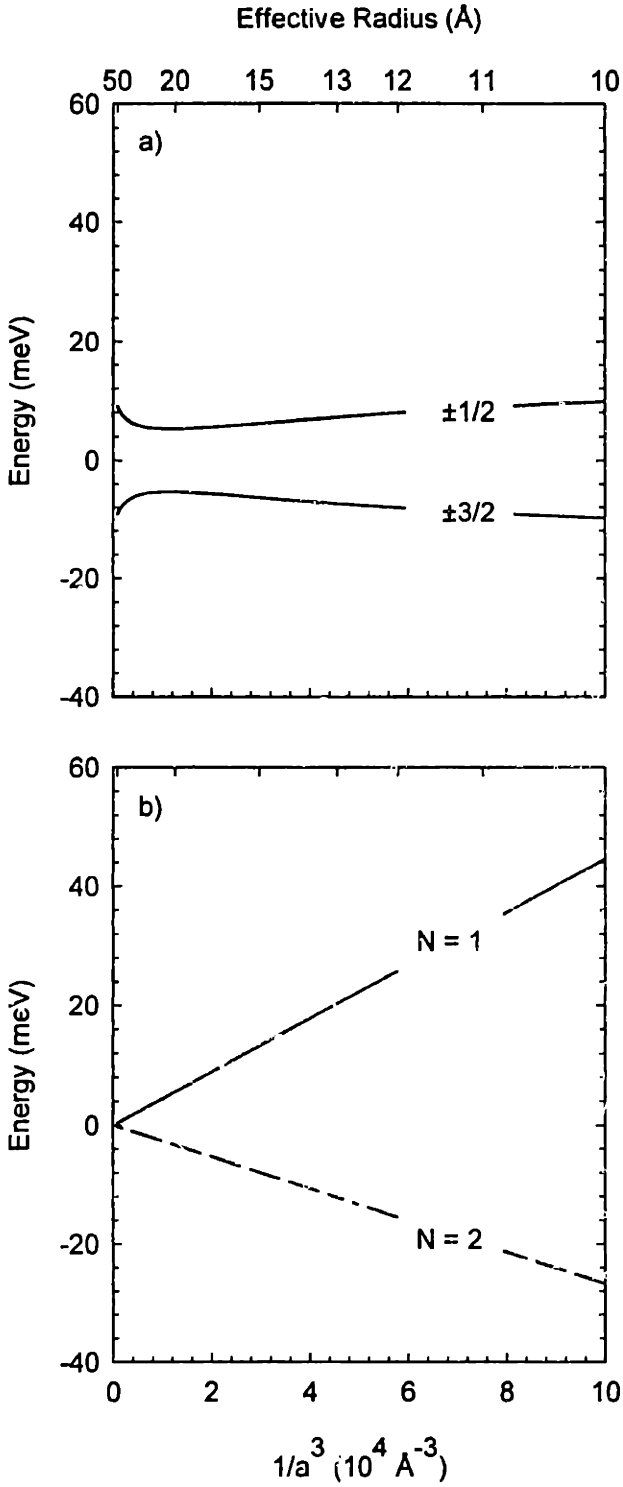

Figure 5-6: (a) Effect of crystal field splitting and the shape asymmetry on the band edge fine structure. Both split the lowest excited state into two fourfold degenerate states with angular momentum projections $|M| = 3/2$ and $1/2$ Both states are optically active. (b) Effect of the electron-hole exchange interaction acting alone on the band edge state. The exchange interaction splits the exciton ground state into an optically active, threefold degenerate, state with angular momentum projection $N = 1$ (solid line). It also creates an optically passive, fivefold degenerate, state with angular momentum projection $N = 2$ (dashed line).

its dependence on nanocrystal size is given by:

$$\varepsilon_{2,n} = -3\eta_n/2 - \Delta_n/2 \quad . \tag{5.12}$$

Its respective wavefunctions are:

$$\begin{aligned} \Psi_{-2,n}(\mathbf{r}_e, \mathbf{r}_h) &= \Psi_{\downarrow,-3/2,n}(\mathbf{r}_e, \mathbf{r}_h) \ , \\ \Psi_{2,n}(\mathbf{r}_e, \mathbf{r}_h) &= \Psi_{\uparrow,3/2,n}(\mathbf{r}_e, \mathbf{r}_h) \ , \end{aligned} \tag{5.13}$$

where $\eta_n = (a_{ex}/a)^3 \hbar\omega_{ST}\chi_n(\beta)$, and the dimensionless function $\chi_n(\beta)$ is written in terms of the electron and hole radial wavefunctions,

$$\chi_n(\beta) = \frac{a^2}{6}\int_0^a dr \sin^2(\frac{\pi r}{a})[R_{0,n}^2(r) + \frac{1}{5}R_{2,n}^2(r)] \quad . \tag{5.14}$$

The dependence of χ_n on the parameter β for n=1 and 2 is shown in Fig. 5-5 d.

The energies of the two levels with total momentum projection $|F| = 1$ are given by

$$\varepsilon_{1,n}^{U,L} = \eta_n/2 \pm \sqrt{(2\eta_n - \Delta_n)^2/4 + 3\eta_n^2} \ , \tag{5.15}$$

where the superscripts "U" and "L" refer to upper and lower to distinguish states with the same angular momentum projection. The exciton wavefunction for the $F = 1$ state is

$$\Psi_{1,n}^{U,L}(\mathbf{r}_e, \mathbf{r}_h) = \mp iC_n^{\pm}\Psi_{\uparrow,1/2,n}(\mathbf{r}_e, \mathbf{r}_h) + C_n^{\mp}\Psi_{\downarrow,3/2,n}(\mathbf{r}_e, \mathbf{r}_h) \ ; \tag{5.16}$$

and likewise the exciton wavefunction for the $F = -1$ state is:

$$\Psi^{U,L}_{-1,n}(\mathbf{r}_e, \mathbf{r}_h) = \mp i C^{\mp}_n \Psi_{\uparrow,-3/2,n}(\mathbf{r}_e, \mathbf{r}_h) + C^{\pm}_n \Psi_{\downarrow,-1/2,n}(\mathbf{r}_e, \mathbf{r}_h) \ . \tag{5.17}$$

In both cases

$$C^{\pm}_n = \sqrt{\frac{\sqrt{f_n^2 + d_n} \pm f_n}{2\sqrt{f_n^2 + d_n}}} \ , \tag{5.18}$$

$f_n = (-2\eta_n + \Delta_n)/2$, and $d_n = 3\eta_n^2$. The energies of the two F=0 exciton levels have a size dependence described by:

$$\varepsilon^{U,L}_{0,n} = \eta_n/2 + \Delta_n/2 \pm 2\eta_n \ , \tag{5.19}$$

where the corresponding wavefunctions are:

$$\Psi^{U,L}_{0,n}(\mathbf{r}_e, \mathbf{r}_h) = \frac{1}{\sqrt{2}}(\mp i \Psi_{\uparrow,-1/2,n}(\mathbf{r}_e, \mathbf{r}_h) + \Psi_{\downarrow,1/2,n}(\mathbf{r}_e, \mathbf{r}_h)) \ . \tag{5.20}$$

Figures 5-7 a and 5-7 c show the size dependence of the exciton fine structure for the first two transitions in the linear absorption of CdSe nanocrystallites ($1S_{3/2}1S_e$ and $2S_{3/2}1S_e$).

5.4.2 Selection rules and transition oscillator strengths

Optical transition probabilities to different exciton states have previously been determined for linearly polarized light, assuming independent electron-hole states. [52, 107] These were later modified to take into account the electron hole exchange interaction, which mixes electron spin and hole momentum projection states [64]. To

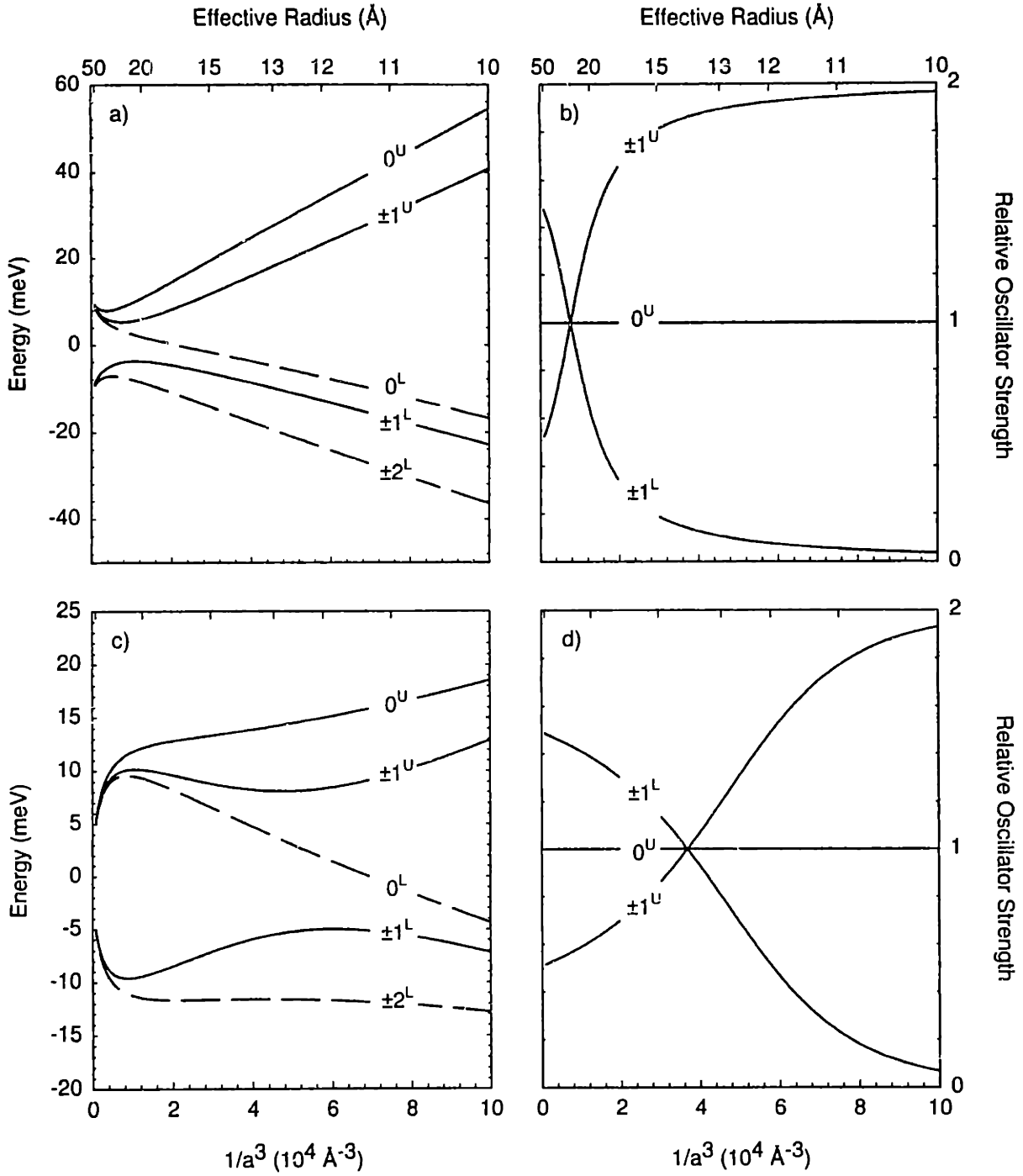

Figure 5-7: The size dependence of the exciton fine structure for (a) the first excited state, $n = 1$, and (b) the second excited state, $n = 2$. Size dependence of the transition probabilities into optically active fine structure states for (c) the first excited state, $n = 1$ and (d) the second excited state, $n = 2$. The behavior for both states is qualitatively similar, with the $\pm 1^U$ and 0^U states having most of the oscillator strength in small QDs.

describe the MCD experiment we determine, in a similar fashion, the selection rules for circularly polarized light. These selection rules are determined by the matrix element operator: $e_{\pm}\hat{p}_{\mp}$. The polarization vector, $e_{\pm} = e_x \pm ie_y$, and the momentum operator, $\hat{p}_{\pm} = \hat{p}_x \pm i\hat{p}_y$, are taken in the axis perpendicular to the light propagation direction. In a vector representation this operator can be expressed as:

$$e_{\pm}\hat{p}_{\mp} = \mathbf{e}\hat{\mathbf{p}} \pm i\mathbf{e}'\hat{\mathbf{p}} \ , \tag{5.21}$$

where $\mathbf{e} \perp \mathbf{c}$, $\mathbf{c}$ is a unit vector parallel to the light propagation direction, $\mathbf{e}' = (\mathbf{e} \times \mathbf{c})$, and the scalar product: $(\mathbf{e}\mathbf{e}') = 0$ follows from the definition of $\mathbf{e}'$. To calculate individual matrix elements we project the operator onto the hexagonal axis of the nanocrystallites (z direction) and obtain:

$$e_{\pm}\hat{p}_{\mp} = \boldsymbol{\epsilon}^{\pm}\hat{\mathbf{p}} = \epsilon_z^{\pm}\hat{p}_z + \frac{1}{2}[\epsilon_+^{\pm}\hat{p}_- + \epsilon_-^{\pm}\hat{p}_+] \ , \tag{5.22}$$

where $\boldsymbol{\epsilon}^{\pm} = \mathbf{e} \pm i\mathbf{e}'$ and $\epsilon_{\pm}^{\pm} = \epsilon_x^{\pm} \pm i\epsilon_y^{\pm}$. The probability of optically exciting each nth exciton state with total angular momentum projection F using $\sigma^{\pm}$ polarized light is proportional to the square of the matrix element operator $e_{\pm}\hat{p}_{\mp}$ sandwiched between that state and the vacuum state $|0> = \delta(\mathbf{r}_e - \mathbf{r}_h)$.

$$P_{F,n} = |\langle 0|e_{\pm}\hat{p}_{\mp}|\tilde{\Psi}_{F,n}\rangle|^2. \tag{5.23}$$

The momentum operator $\hat{p}_{\pm}$ acts only on the valence band Bloch functions (see Eq. 5-5) and the exciton wavefunctions, $\tilde{\Psi}_{F,n}$, are written in the electron-electron

representation. The electron-hole representation can be transformed to the electron-electron representation by taking the complex conjugate of the exciton wavefunction (Eqs. 5-13, 5-16, 5-17 and 5-18) and flipping the spin projections of the hole Bloch functions ($\uparrow$ and $\downarrow$ to $\downarrow$ and $\uparrow$).

For the exciton state with angular momentum projection $F = 0$ we obtain

$$\begin{aligned} P_{0,n}^{U,L}(\sigma^{\pm}) &= |\langle 0|e_{\pm}\hat{p}_{\mp}|\tilde{\Psi}_{0,n}^{U,L}\rangle|^2 = |\epsilon_z^{\pm}\langle 0|\hat{p}_z|\tilde{\Psi}_{0,n}^{U,L}\rangle|^2 \\ &= (\mathbf{e}_z^2 + \mathbf{e}_z'^2)N_{0,n}^{U,L} = N_{0,n}^{U,L}\sin^2(\theta)\ , \end{aligned} \tag{5.24}$$

where $N_{0,n}^{L} = 0$, $N_{0,n}^{U} = 4K_nP^2/3$, $P =< S|\hat{p}_z|Z >$ is the Kane interband matrix element, and θ is the angle between the direction of the exciting light and the hexagonal axis of the crystal. K is the square of the overlap integral and can be expressed as [52]:

$$K_n = \frac{2}{a}\left|\int dr r\sin(\pi r/a)R_{0,n}(r)\right|^2 \ . \tag{5.25}$$

Its value is independent of the crystal size, a, and depends only on β. To derive Eq. 5-23 we use the identity for three orthogonal vectors ($\mathbf{e}$, $\mathbf{e}'$, and $\mathbf{c}$): $\cos^2(\theta_e) + \cos^2(\theta_e') + \cos^2(\theta) = 1$, where θ_e and θ_e' are angles between the crystal hexagonal axis and the vectors $\mathbf{e}$ and $\mathbf{e}'$ respectively. Eq. 5-24 shows that the transition probability to the upper (+) $F = 0$ state is independent of crystal size, and that for the lower state (-) it equals zero. The lower $F = 0$ exciton state is therefore predicted to be optically passive.

For nth exciton states with $F = +1$ we obtain:

$$\begin{aligned} P^{U,L}_{F=1,n}(\sigma^{\pm}) &= |\langle 0|e_{\mp}\hat{p}_{\pm}|\tilde{\Psi}^{U,L}_{1,n}\rangle|^2 = \frac{1}{4}|\epsilon^{\mp}_{-}\langle 0|\hat{p}_{+}|\tilde{\Psi}^{U,L}_{1,n}\rangle|^2 \\ &= \frac{1}{4}|e_{-} \mp ie'_{-}|^2 N^{U,L}_n = N^{U,L}_n(1 \pm \cos\theta)^2 \ , \end{aligned} \tag{5.26}$$

where $N^{U,L}_n$

$$N^{U,L}_n = \frac{1}{3}\left(\frac{2\sqrt{f_n^2 + d_n} \mp f_n \pm \sqrt{3d_n}}{2\sqrt{f_n^2 + d_n}}\right) K_n P^2 \ . \tag{5.27}$$

A similar calculation gives the transition probability of the $F = -1$ state:

$$P^{U,L}_{F=-1,n}(\sigma^{\pm}) = N^{U,L}_n(1 \mp \cos\theta)^2 \ . \tag{5.28}$$

Equations 5-26 and 5-28 were derived using the orthogonality condition: $(\mathbf{e} \cdot \mathbf{c}) = 0$. Figures 5-7 b and 5-7 d show the size dependence of the fine structure transition probabilities for the $1S_{3/2}1S_e$ and $2S_{3/2}1S_e$ states.

The behavior of the transition probabilities can be understood by considering the role of the exchange interaction. At large sizes, the exchange interaction is small relative to perturbations from the crystal field and shape asymmetry. At small sizes, however, the exchange interaction dominates, causing the large scale splitting in Figures 5-7 a and 5-7 b. In the absence of crystal field and shape effects we have the limit of a fivefold degenerate (optically passive) $N = 2$ exciton ground state and a threefold degenerate (optically active) $N = 1$ state (Figure 5-6 b). Both crystal field splitting and shape effects act to lift this degeneracy causing the $\pm 1^L$ state to emerge from the $N = 2$ exciton. Since it originates from a dark state, it also has relatively little oscil-

lator strength. This explains why the $\pm 1^L$ state has little oscillator strength at small sizes (with the $\pm 1^U$ state dominating) and gains oscillator strength with increasing size.

5.4.3 Splitting of the levels in a magnetic field

In the fine structure model there are three optically active exciton states near the band edge of CdSe and two optically passive ones. An external magnetic field splits all two fold degenerate states with total angular momentum projection ± 1 and ± 2. Figure 5-8 a gives a qualitative picture for the $1S_{3/2}1S_e$ fine structure and shows states that are accessed by left and right circularly polarized light.

The magnitude of each state's Zeeman splitting depends on the projection of the magnetic field onto the crystal hexagonal axis and is different for different nanocrystals in an ensemble of randomly oriented QDs. The probability of exciting these states also depends on the nanocrystal orientation with respect to the direction of the exciting light (Eqs. 5-24, 5-26, 5-28) and distinguishes MCD experiments in quantum wells [181], from measurements in QDs. An analysis of the MCD signal from an ensemble of QDs must take into account the orientational distribution of the nanocrystallites.

For nanometer-sized quantum dots the effect of an external magnetic field, $\mathbf{H}$, can be described as a molecular Zeeman effect:

$$\hat{H}_H = \frac{1}{2} g_e \mu_B \boldsymbol{\sigma} \mathbf{H} - g_{h,n} \mu_B \boldsymbol{\mathcal{K}} \mathbf{H} \quad , \tag{5.29}$$

where g_e and $g_{h,n}$ are the electron and hole g factors respectively, and μ_B is the Bohr

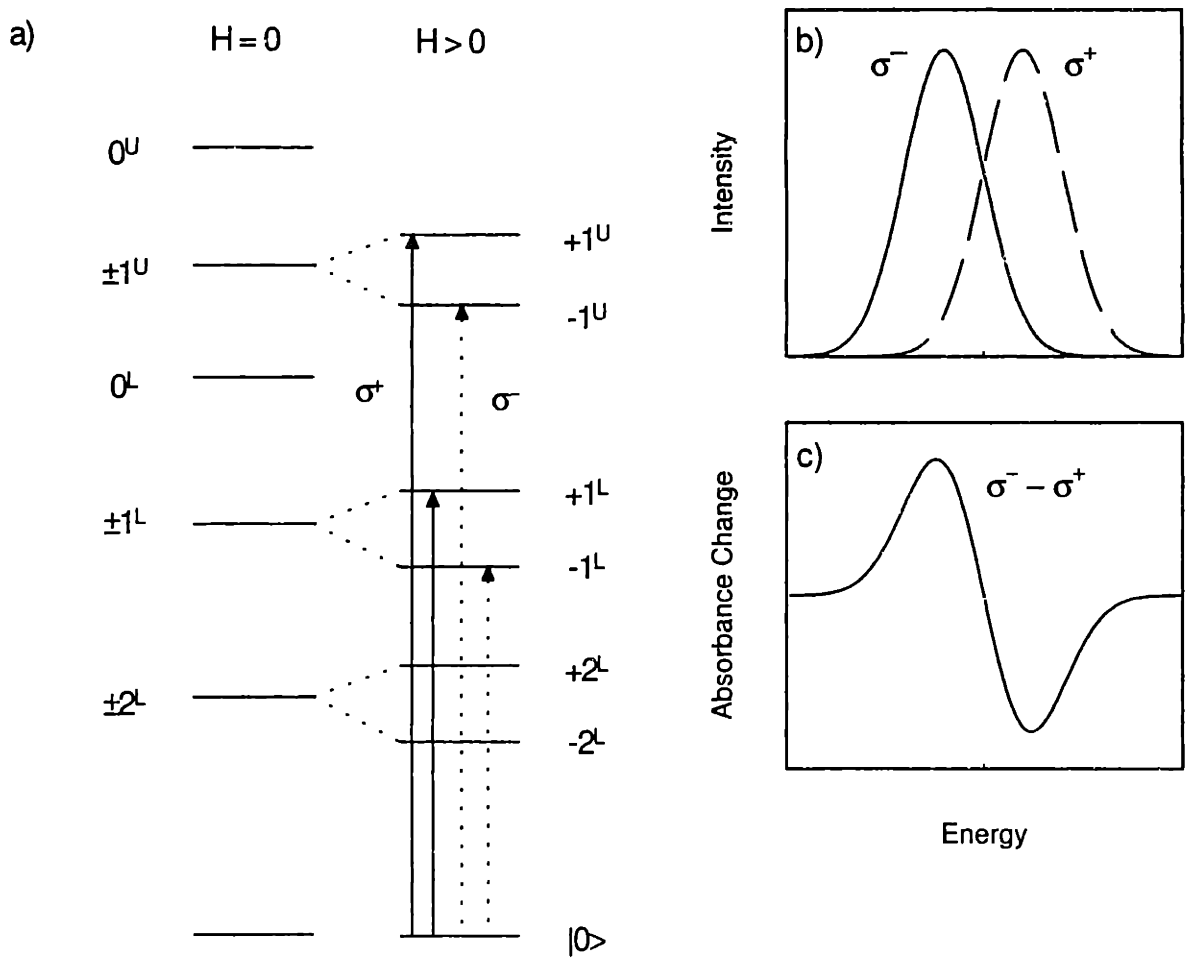

Figure 5-8: (a) Qualitative depiction of the MCD experiment on the band edge exciton fine structure, $n = 1$. All twofold degenerate states are split into their respective projections. Transitions involving right circularly polarized light (σ^+) are denoted by solid lines. Transitions involving left circularly polarized light (σ^-) are denoted by dashed lines. (b) Qualitative representation of the absorption of left and right circularly polarized light. (c) The MCD signal can be modeled by the difference spectrum of left and right circularly polarized absorptions.

magneton. For electrons in CdSe $g_e = 0.68$ [111]. Hole g factors for the $1S_{3/2}$ and $2S_{3/2}$ states are calculated using the results of [112, 64], and are $g_{h,1} = -1.09$ and $g_{h,2} = -0.053$, respectively. In Eq. 5-29 we neglect diamagnetic, H^2, terms because the dots are significantly smaller than the magnetic length [$\sim$ 115 Å at 10 T].

By considering the magnetic field in Eq. 5-29 as a perturbation, we determine the Zeeman splitting of the optically active $F = \pm 1$ nth state:

$$\Delta\varepsilon^{U,L}_{|1|,n} = \varepsilon^{U,L}_{1,n} - \varepsilon^{U,L}_{-1,n} = 2\mu_B H_z\{[(C^{\pm}_n)^2 - (C^{\mp}_n)^2]g_e - [(C^{\pm}_n)^2 + 3(C^{\mp}_n)^2]g_{h,n}\} \ . \quad (5.30)$$

This splitting, linear with magnetic field, is proportional to the magnetic field projection H_z on the crystal hexagonal axis. Substituting Eq. 5-18 for $C^{\pm}$ in Eq. 5-30 we obtain the dependence of the splitting on the nanocrystal radius:

$$\Delta\varepsilon^{U,L}_{|1|,n} = 2g^{U,L}_{|1|,n}\mu_B H\cos\theta \ , \quad (5.31)$$

where the individual exciton g factors are expressed as

$$g^{U,L}_{|1|,n} = g_e\frac{\pm f_n}{\sqrt{f_n^2 + d_n}} - g_{h,n}\frac{2\sqrt{f_n^2 + d_n} \mp f_n}{\sqrt{f_n^2 + d_n}} \ . \quad (5.32)$$

The average Zeeman splitting for a system of randomly oriented nanocrystals can then be obtained by angle averaging

$$\Delta\varepsilon = \overline{\Delta\varepsilon^{U,L}_{|1|,n}} = g^{U,L}_{|1|,n}\mu_B H \ . \quad (5.33)$$

There is no splitting of the $F = 0$ optically active exciton state.

Figures 5-9 a,b show the size dependence of $g^{U,L}_{|1|,n}$ for the n=1 and 2 ($nS_{3/2}1S_e$) fine structure states. In Figure 5-9 a both optically active fine structure states underlying the $1S_{3/2}1S_e$ transition have positive g factors. When combined with the respective oscillator strength of each fine structure state, the effective $1S_{3/2}1S_e$ g factor (g_{eff}) is shown by the dashed line. Its value is positive and fairly constant over a large range of sizes. Figure 5-9 b shows the fine structure g factors of the second state. Here the $\pm 1^U$ state has a positive g factor while the $\pm 1^L$ g factor is negative valued. Again, the effective $2S_{3/2}1S_e$ g factor (g_{eff}) is shown by the dashed line. At large sizes, g_{eff} is negative and fairly constant in magnitude. At small sizes, between 10 and 20 Å, it suddenly becomes positive with the crossing occuring somewhere in the vicinity of 15 Å radius (15.35 Å).

5.4.4 Magnetic Circular Dichroism Signal

Since the field induced splitting of the various exciton levels is much smaller than the inhomogeneous width of the absorption line it cannot be directly seen in absorption experiments. However this splitting can be observed in MCD experiments, where the difference between the absorption coefficients, $\alpha^{\pm}$, for right and left circular polarized light ($\sigma^{\pm}$) can be measured with a high degree of accuracy. Assuming a Gaussian form for the inhomogeneous exciton lineshape, we find that for exciton states with identical Zeeman shifts the MCD signal takes the form [181]:

$$\alpha_{\mathrm{MCD}}(\varepsilon, \varepsilon_0) = \alpha^{-}(\varepsilon, H)\alpha^{+}(\varepsilon, H)$$

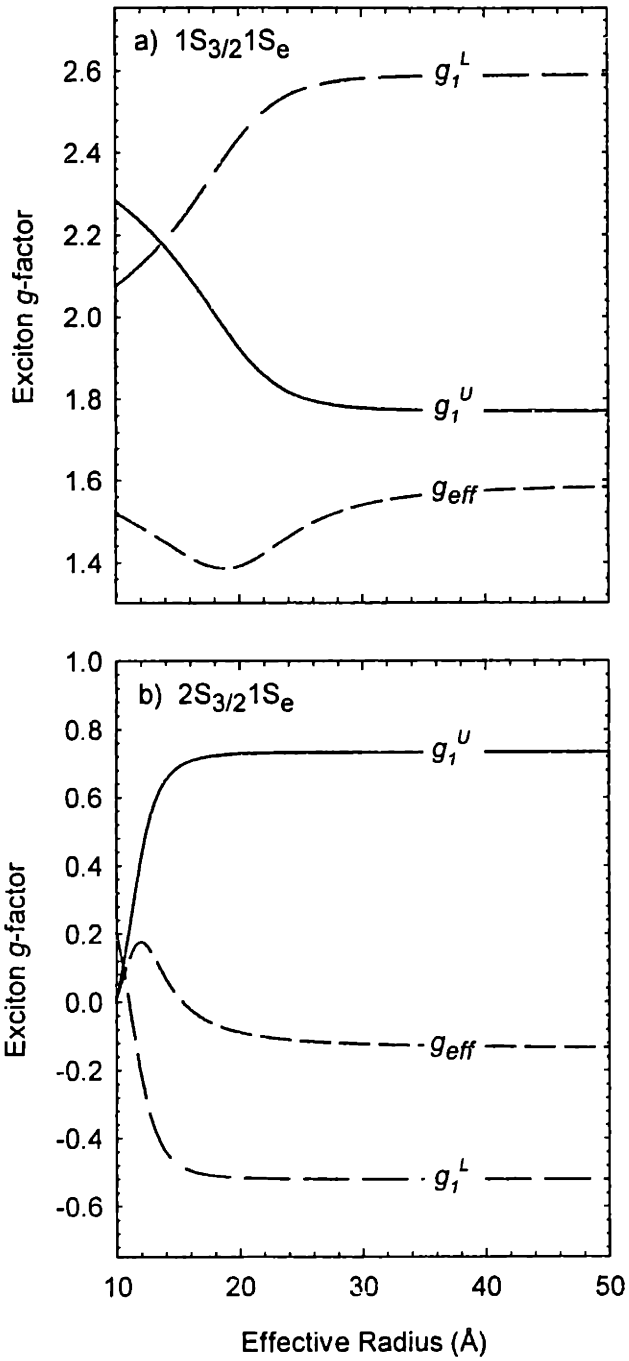

Figure 5-9: (a) Predicted ($1S_{3/2}1S_e$) exciton g-factors for the $\pm 1^L$ (dashed) and $\pm 1^U$ (solid) fine structure states as a function of size. For the band edge state, both g-factors are positive over the full range of sizes. The effective g-factor (dotted line) observed in the experiment is therefore positive for all sizes. (b) Predicted ($2S_{3/2}1S_e$) g-factors for the $\pm 1^L$ and $\pm 1^U$ fine structure states. In this case, the $\pm 1^L$ g-factor is negative valued for most sizes but becomes positive at small size. The $\pm 1^U$ g-factor is positive valued for all sizes. The effective g-factor seen in the experiment is therefore negative valued for most sizes but becomes positive valued at small sizes.

$$= 2C\Delta\varepsilon\frac{\varepsilon-\varepsilon_0}{\sigma^2}\frac{1}{\sqrt{2\pi}\sigma}\exp\left[-\frac{(\varepsilon-\varepsilon_0)^2}{2\sigma^2}\right] , \qquad (5.34)$$

where C is a constant related to the oscillator strength of the state, $\Delta\varepsilon$ is the field dependent Zeeman splitting, σ is the inhomogeneous linewidth, and ε_0 is the peak position of the transition in the absence of a magnetic field. Figures 5-5 b and 5-5 c provide a qualitative description of the MCD signal which can be modeled by this difference of two Gaussian lineshapes.

The MCD signal for a single transition has a characteristic derivative shape with extrema separated by 2σ. Its intensity is proportional to the Zeeman splitting of the levels, $\Delta\varepsilon$, and grows linearly with magnetic field. To formally extract absolute values of the splitting we must normalize the MCD signal which is proportional to the unknown constant C, to the sum $\alpha_{\mathrm{SUM}} = \alpha^+ + \alpha^-$. Once normalized, the value of the Zeeman splitting is directly related to the amplitude of the MCD signal.

Eq. 5-34 can also be used to describe the MCD signal from an ensemble of randomly oriented quantum dots. In this case, $\Delta\varepsilon$ represents the average effective splitting of the exciton states in a magnetic field. The following reasons apply. The Zeeman splitting of each fine structure state was shown to depend on the angle between the magnetic field and the nanocrystal axis (θ) (Eq. 5-31). The two polarizations of the incoming light ($\sigma^{\pm}$) also excite both fine structure projections, $F = \pm 1$, because of the random orientation of the nanocrystallites. Finally, excitation probabilities for both fine structure projections depend on the angle between the light direction and the nanocrystal axis (θ in our experiments, see Eqs. 5-26, 5-28).

The absorption coefficient for $\sigma^{\pm}$ polarized excitation of $|F| = 1$ exciton states

has the form:

$$\alpha^{\pm}_{F,n}(\varepsilon-\varepsilon^{U,L}_{F,n}) \sim \frac{N^{U,L}_{1,n}}{\sqrt{2\pi}\sigma_1}(1 \pm F\cos\theta)^2 \exp\left(-\frac{(\varepsilon-\varepsilon^{U,L}_{F,n})^2}{2\sigma_1^2}\right) , \qquad (5.35)$$

where θ is the angle between the hexagonal axis and the light direction, $N^{U,L}_{1,n}$ is a constant related to the oscillator strength of the state (Eqs. 5-26, 5-28), σ_1 and $\varepsilon_{F,n}$ are the linewidth and average energy of $|F| = 1$ exciton states for a given nanocrystal distribution. The field induced Zeeman splitting leads to the MCD signal, α_{MCD}:

$$\alpha^{U,L,n}_{MCD} \sim \frac{1}{2}\sum_{F=\pm1} \times \int [\alpha^{+}_{F}(\varepsilon-\varepsilon^{U,L}_{F,n}(H)) - \alpha^{-}_{F}(\varepsilon-\varepsilon^{U,L}_{F,n}(H))] d\cos\theta \, . \qquad (5.36)$$

This expression can be simplified if the intrinsic transition linewidth of the state is much larger than the magnitude of the Zeeman splitting. Substituting Eq. 5-35 into Eq. 5-36, we find after angle averaging

$$\alpha^{U,L,n}_{MCD} \sim 2N^{U,L}_{1,n}\Delta\varepsilon\frac{(\varepsilon-\overline{\varepsilon_{1,n}})}{\sigma_1^2}\frac{1}{\sqrt{2\pi}\sigma_1}\exp\left(-\frac{(\varepsilon-\overline{\varepsilon_{1,n}})^2}{2\sigma_1^2}\right), \qquad (5.37)$$

where $\Delta\varepsilon = \mu_B H g^{U,L}_{|1|,n}$ (see Eq. 5-31, 5-33) and $\overline{\varepsilon_{1,n}} = \overline{\varepsilon^{U,L}_{1,n}}$ is the average position of the exciton level in the absence of a magnetic field.

The magnitude of the MCD signal is proportional to the magnetic field and the direction of the splitting depends on the sign of the effective exciton g-factor, g_{exc}. This explains the difference between the MCD signal for the 10 Å $1S_{3/2}1S_e$ and $2S_{3/2}1S_e$ excitons: g_{exc} for the first is positive and for the second is negative.

To formally extract absolute values of g_{exc} from the experiment we normalize

the MCD signal. Two cases are considered, depending on whether the exciton line broadening is smaller or larger than the spacing between the $F = 0$ and $|F| = 1$ fine structure states [63, 64]. In the first case, the sum of the absorption coefficients for σ^+ and σ^- polarized light can be obtained from Eq. 5-35 after angle averaging:

$$\begin{aligned} \alpha_{\mathrm{SUM}}^{U,L,n} &\sim \frac{1}{2}\sum_{F=\pm} \times \int [\alpha_{F,n}^{+}(\varepsilon - \varepsilon_{F,n}^{U,L}(H)) + \alpha_{F,n}^{-}(\varepsilon - \varepsilon_{F,n}^{U,L}(H))] d\cos\theta \\ &= \frac{2N_{1,n}^{U,L}}{\sqrt{2\pi}\sigma_1} \exp\left(-\frac{(\varepsilon - \overline{\varepsilon_{1,n}})^2}{2\sigma_1^2}\right) . \end{aligned} \tag{5.38}$$

Normalizing α_{MCD} using α_{SUM} allows us to extract the absolute value of the exciton g factor through Eq. 5-33.

In the second case, where the inhomogeneous broadening is larger than the fine structure spacings, both upper and lower states with $|F| = 1$ as well as the $F = 0$ state contribute to the MCD signal and must be considered when normalizing the MCD signal. The absorption coefficient for $\sigma^{\pm}$ excitation of $F = 0$ exciton states has the form:

$$\alpha_{0,n}^{\pm}(\varepsilon - \overline{\varepsilon_{0,n}}) \sim \frac{N_{0,n}^{U}}{\sqrt{2\pi}\sigma_0} \sin^2\theta \exp\left(-\frac{(\varepsilon - \overline{\varepsilon_{0,n}})^2}{2\sigma_0^2}\right), \tag{5.39}$$

where again, θ is the angle between the hexagonal axis and the light direction. $N_{0,n}^{U}$ is a constant related to the transition oscillator strength (Eq. 5-24), σ_0 and $\overline{\varepsilon_{0,n}} = \overline{\varepsilon_{0,n}^{U}}$ are the linewidth and the average energy of the optically active $F = 0$ exciton for a given nanocrystal distribution.

By assuming the following, that the inhomogeneous broadening of all exciton states is the same and is much larger than the spacing between fine structure states, that $\sigma_1^U = \sigma_1^L = \sigma_0 = \sigma$, and by averaging over all solid angles we obtain the effective

Zeeman splitting for the $nS_{3/2}1S_e$ transition:

$$\Delta\varepsilon = \mu_B H \frac{N^U_{1,n} g^U_{1,n} + N^L_{1,n} g^L_{1,n}}{N^U_{1,n} + N^L_{1,n} + N^U_{0,n}/4} = \mu_B H g_{\mathrm{eff},n} \ . \tag{5.40}$$

The MCD analysis becomes increasingly difficult for higher excited states ($1P_{3/2}1P_e$) both in experiment and in theory because of overlapping transitions. This being the case, we exclude the $1P_{3/2}1P_e$ state in the formal analysis.

5.5 Discussion

Previous theoretical considerations have successfully modeled the excited state absorption of CdSe QDs. Based on the effective mass approximation, the theory considers the non-parabolicity of the conduction band and the degeneracy of the valence band. A cubic crystal structure is also assumed because of the small crystal field splitting in the bulk (25 meV). Following conventions developed in the theory, optical transitions in the linear absorption are labeled by "particle in a sphere" symmetry notations ($n_h L_F n_e L_e$) where n_e and n_h are numbers ordering the progression of electron and hole eigenstates and L_e, L_h are angular momentum quantum numbers.

Although the spherical approximation has been successful in modeling the linear absorption of CdSe QDs, it is not consistent with recent experimental results suggesting the presence of fine structure underlying these optical transitions. Much of the success of the spherical approximation stems from the much larger spacing of electron and hole quantum size levels relative to fine structure splittings resulting from internal (hexagonal lattice structure) and external (prolateness of the QD) asymmetries.

These spacings are also much larger than splitting due to the electron-hole exchange interaction.

Since the Zeeman splittings are on the same order as splittings due to fine structure effects, a proper theoretical description of magneto-optical experiments requires us to consider the presence of fine structure. The importance of this is particularly evident when explaining the seemingly unusual behavior of the $2S_{3/2}1S_e$ exciton g factor. The spherical approximation predicts that both $1S_{3/2}1S_e$ and $2S_{3/2}1S_e$ states have positive g factors for all sizes. Equation 5-29 shows that changing the hole g factor from $g_h(1S_{3/2}) = -1.09$ to $g_h(2S_{3/2}) = -0.053$ predicts a positive $2S_{3/2}1S_e$ g factor. Remarkably, the fine structure model predicts that for most sizes the effective exciton g factor of the second state is negative. At small sizes, due to the interplay between fine structure g factors and fine structure oscillator strengths, the effective $2S_{3/2}1S_e$ g factor changes sign. Equations 5-26, 5-28 and 5-32 illustrate the important interplay of fine structure g factors and transition oscillator strengths.

The predicted values of the Zeeman splitting are also in reasonable agreement with experiment. There are, however, discrepancies in the absolute values obtained. This may have to do with problems associated with loss of polarization due to scattering from the close packed QD films. It may also have to do with experimental inaccuracies in the measured half width, σ, and oscillator strengths of the various transitions. In this sense, complications arise from overlapping higher excited states. Since the simple absorption experiment does not resolve the multiple (MCD active) states that lie beneath the third peak ($1P_{3/2}1P_e$) in the linear absorption, the fitting procedure is often difficult for the second ($2S_{3/2}1S_e$) state. This has to do with uncertainties

in the center energies, linewidths and amplitudes of the different neighboring transitions at higher energies. Finally, there are problems inherent to the fine structure model having to do with overestimating/underestimating the oscillator strengths of the fine structure states. Ref. [118] is a recent photoluminescence excitation (PLE) investigation that addresses this issue.

Figure 5-10 compares experimental values of the $1S_{3/2}1S_e$ and $2S_{3/2}1S_e$ g factors to theoretical values for the entire size series. Experimental points are shown by closed circles and the theory is given by the solid line. Although there are discrepancies in the absolute values of the g factors obtained, remarkably, the experiment confirms most qualitative predictions of the fine structure model. All sizes have positive $1S_{3/2}1S_e$ g factors. These values are also fairly constant with size. Most sizes show negative $2S_{3/2}1S_e$ g factors and a crossing from negative to positive occurs in the vicinity of 14 Å radius. One discrepancy, though, is that a turnover in the splitting magnitude of the second state is not seen in the experimental data down to 10 Å radius. This may simply have to do with not looking at small enough sizes or it may stem from theoretical problems due to a breakdown of the effective mass approximation. The results, nevertheless, suggest that fine structure effects are important considerations that must be included in explicit calculations of the QD electronic structure. Table I summarizes our results for the effective g factors of the first and second excited states.

5.6 Conclusions

We have performed MCD experiments on high quality CdSe QDs. The Zeeman splittings of the $1S_{3/2}1S_e$ and $2S_{3/2}1S_e$ excitons yield effective g factors for these

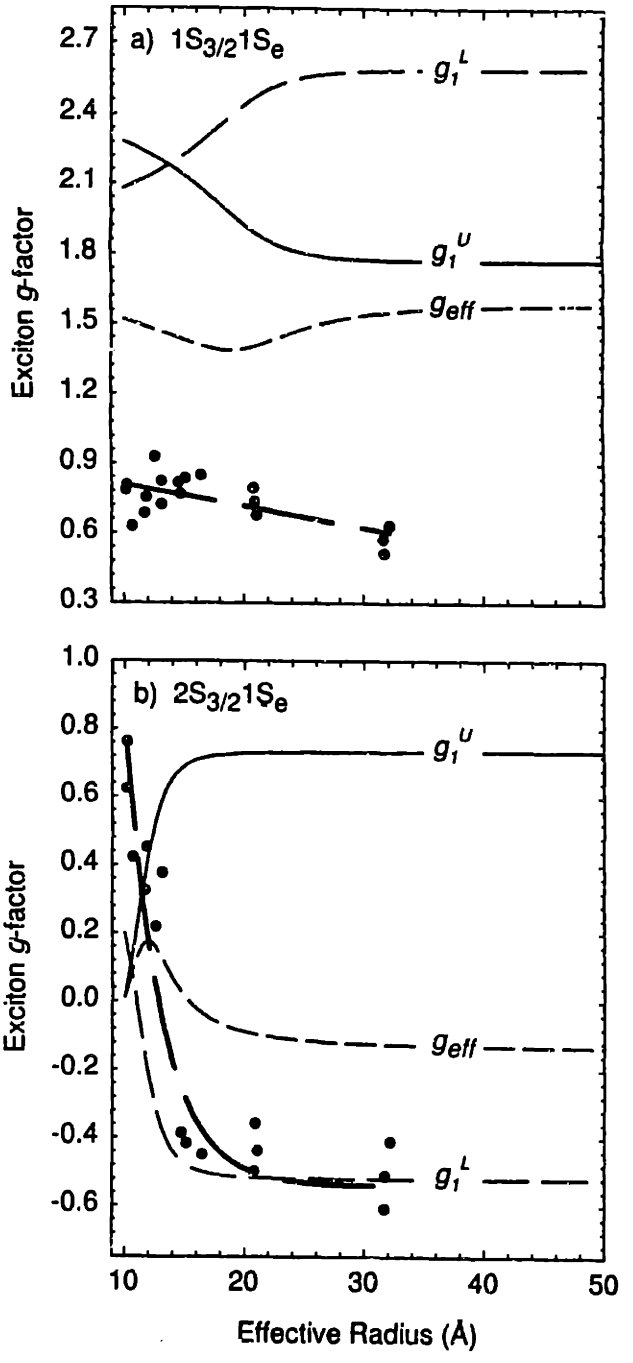

Figure 5-10: (a) Comparison between experimental values of the $1S_{3/2}1S_e$ effective g factor (closed circles) to theoretical predictions (solid line). For all sizes g_{eff} is positive. The heavy dashed line is a guide to the eye. (b) Comparison between experimental values of the $2S_{3/2}1S_e$ g factor (closed circles) to theoretical predictions (solid line). Most sizes exhibit negative g factors. A crossing from negative to positive occurs in the vicinity of 14 Å radius in reasonable agreement with theory. However, at small sizes, no turnover of the splitting magnitude is seen. This may simply be a problem with the theory stemming from a breakdown of the effective mass approximation or with experimental difficulties in obtaining small enough sizes to see the effect. The heavy dashed line is a guide to the eye.

transitions. The $1S_{3/2}1S_e$ g factor exhibits a positive g factor and is fairly constant over most sizes. The $2S_{3/2}1S_e$ g factor, however, shows unusual behavior not explained by spherical models of the electronic structure. This behavior is explained by the presence of fine structure and by an interplay of fine structure g factors and corresponding oscillator strengths. We predict that the $2S_{3/2}1S_e$ g factor is negative valued over most sizes but that at small sizes (somewhere near 15 Å) it changes sign becoming positive valued. This strongly supports a fine structure picture of the QD electronic structure and points to the usefulness of magneto-optical experiments in probing the electronic structure of nanocrystalline materials.

The observation of a sizable MCD signal also suggests the feasibility of magneto-luminescence experiments on CdSe QDs. Given the presence of fine structure, it may prove instructive to conduct circularly polarized PLE experiments to directly measure fine structure splittings and exciton g factors. In the case of the $2S_{3/2}1S_e$ fine structure, this is particularly useful as little is known about the actual ordering and spacing of states.

Table 5.1: Table summarizing effective g factors for $1S_{3/2}1S_e$ and $2S_{3/2}1S_e$ excitons

Name	Effective Radius (Å)	$1S_{3/2}1S_e$ g_{eff}	$2S_{3/2}1S_e$ g_{eff}
478#1	10.3	0.806	0.762
478#2	10.2	0.785	0.623
484-d	10.8	0.628	0.422
500#1	11.9	0.754	0.452
500#2	11.7	0.684	0.326
510#1	12.6	0.929	0.219
510#2	13.1	0.722	—
510-redo	13.2	0.824	0.377
528-redo	15.2	0.838	-0.416
530#1	14.6	0.818	-0.905
530#2	14.7	0.768	-0.387
550#2	16.5	0.850	-0.449
570#1	20.9	0.734	-0.358
570#2	21.1	0.675	-0.437
570#3	20.8	0.793	-0.498
632#1	32.2	0.631	-0.410
632#2	31.7	0.573	-0.608
632#3	31.7	0.514	-0.510

Chapter 6

Doped Nanocrystallites

This chapter describes the synthesis and optical characterization of high quality nanometer-sized $Cd_{1-x}Mn_xSe$ nanocrystallites. Single source manganese and selenium precursors such as $Mn_2(\mu-SeMe)_2(CO)_8$ are found to be effective dopants for CdSe QDs. Exhaustive surface ligand exchange is performed on all samples to ensure that elemental analysis detects only those impurities incorporated into the nanocrystallite core. Manganese concentrations determined by electron paramagnetic resonance (EPR) and wavelength dispersive x-ray spectroscopy (WDS) are consistent with each other and indicate doping levels of one manganese atom per QD in nearly monodisperse samples ($\sigma \sim 5\%$).

The influence of the manganese impurity on the nuclear/electronic properties of CdSe QDs can be seen in the ^{113}Cd solid state nuclear magnetic resonance (NMR) of doped nanocrystallites. We observe a decreases in the lifetime (T_1) and shifts in the peak position of the cadmium resonance. New features in the ^{113}Cd NMR spectrum also indicate different chemical environments for cadmium atoms close to the

manganese impurity from those further away. The effects of the magnetic impurity are also observed in the fluorescence line narrowing (FLN) and photoluminescence excitation (PLE) spectra of doped and undoped nanocrystallites. An effective single QD lineshape extracted from experimental PLE/FLN data shows that the low temperature emission of doped nanocrystallites behaves as though under the influence of a large (effective) magnetic field. Results from these optical experiments are consistent with a fine structure model of the band edge exciton described in previous chapters. However, there are still many unanswered questions about the optical properties of nanometer-sized $Cd_{1-x}Mn_xSe$ QDs making this a potentially fruitful area of investigation.

6.1 Introduction

There are few reports concerning nanometer-sized transition metal doped semiconductor particles.[38, 187, 188, 189, 190, 191, 192, 193, 194, 195, 196, 197] Difficulties preparing such ternary systems in a small size regime have prevented extensive investigations in this area, a natural extension of the younger field of semiconductor quantum dots (QDs)[4] and the more mature field of diluted magnetic semiconductors (DMS).[198]

Recent advances in the organometallic synthesis of nanometer sized semiconductor QDs have made possible the production of nearly monodisperse samples.[32, 88, 67] Such high quality nanocrystallites have enabled the fabrication of ordered superstructures and, in special cases, true single crystals. These samples have also led to detailed investigations of QD electronic states and the development of theoretical

models describing their size dependence.

A current fine structure model which describes the band edge luminescence of CdSe QDs in terms of emission from an optically forbidden "dark" exciton has successfully explained much of its unusual behavior (the relatively long photoluminescence lifetimes, $\tau_r \sim 1\mu s$ at 10 K, and the accompanying size dependent Stokes shift). However, low temperature FLN spectra of small CdSe nanocrystallites shows emission from this formally dark state. At such temperatures and sizes, (T~1.7-10 K, 10-12 Å radius), the nearest optically active state is too far removed for there to be any significant repopulation of nearby bright states. The phonon contribution to an assisted transition is also expected to be minimal at these temperatures. An alternate mechanism must therefore be present to explain radiative recombination from the Dark exciton. Efros et al., has considered these results in conjunction with optical experiments performed on CdSe QDs in high magnetic fields and has postulated the existence of a paramagnetic impurity whose unpaired spin(s) assist in the radiative recombination of the dark exciton through a nuclear/paramagnetic spin flip assisted transition.

The synthesis of nanocrystallites intentionally doped with a transition metal is a way to test the validity of this postulate and to gauge its relative importance. If reasonable control over the doping level is achieved, such systems also provide the opportunity to study magnetic field effects on QD optical properties without having to resort to large external fields (> 10 Tesla). Both reasons motivate our current investigation.

In addition to being of theoretical interest, transition metal doped semiconductor

nanocrystallites are examples of zero dimensional diluted magnetic semiconductors (DMS). Analogous bulk DMS compounds, in which some fraction of the cations in a II-VI semiconductor are replaced with a paramagnetic ion, have been studied since the 60's. The dopant is usually manganese, due to its large spin (S = 5/2), and because substitution of Mn^{+2} in a II-VI host leaves the lattice electrically neutral. Their best known properties, such as the giant Faraday rotation of polarized light, originate from a strong sp-d exchange interaction between the carriers of the semiconductor and the unpaired electrons of the dopant.

These materials are interesting examples of dilute magnetic systems where phenomena such as short range magnetic order, spin glasses, small ion clusters, and isolated spins have been observed. Nanocrystalline DMS gives us the opportunity to study the competition between quantum size effects and novel spin interactions. Changes in the magnetic behavior of thin $Cd_{1-x}Mn_xTe$ films as a function of layer thickness suggests that quantum confinement affects Mn-Mn spin interactions.[199]

Whereas bulk DMS materials are well-characterized, only a handful of papers exist about the optical properties of zero dimensional DMS compounds. There have been some reports of enhanced optical properties, the first by Bhargava [200] claiming increased photoluminescence quantum yields and decreased lifetimes for quantum-sized $Zn_{1-x}Mn_xS$ relative to bulk samples.[1] Bhattacharjee [201] has also predicted exciton localization near Mn impurities in $Cd_{1-x}Mn_xTe$ QDs, forming a zero dimensional exciton magnetic polaron. This is expected to lead to a sizable redshift in the emission of the nanocrystallites.

[1]This result is controversial because others have not been able to reproduce these dramatically shortened lifetimes.

Reported preparations of quantum-sized DMS compounds include sol-gel synthesis, low temperature reaction of metal polychalcogenides, inverse micelle methods, rf sputtering, and various solution phase methods. To date, however, the overall quality of quantum-sized DMS materials has been low, with samples displaying poor crystallinity and/or large polydispersities. The method developed in this laboratory for synthesizing II-VI semiconductor nanocrystallites produces highly crystalline, nearly monodisperse ($\sigma < 5\%$) samples. Based on the high temperature pyrolysis of organometallic precursors in a coordinating solvent, the procedure is general and will tolerate a variety of starting materials. By judicious choice of precursors, nanocrystallites can be produced which are not only doped with manganese but also retain the high quality associated with similar undoped samples (size distribution, crystallinity).

We describe the use of manganese and chalcogen containing organometallic complexes such as $Mn_2(\mu - SeMe)_2(CO)_8$ to prepare $Cd_{1-x}Mn_xSe$ QDs of various sizes. Simpler precursors containing only manganese are found to be ineffective dopants when incorporated into the present method for making QDs. Extensive purification and surface ligand exchange is performed to ensure that our quantitative measurements detect only manganese ions incorporated into the QD lattice, rather than species loosely bound to the nanocrystallite surface. Wavelength dispersive X-ray spectroscopy (WDS) and electron paramagnetic resonance (EPR) are used to quantify dopant concentrations. Additional EPR experiments confirm the presence sizable amounts of paramagnetic impurities in "undoped" nanocrystallites as well as other signals whose intensities are dependent upon sample handling and the extent of purification.

For $Cd_{1-x}Mn_xSe$ QDs, good agreement is found between manganese concentrations determined by WDS and results from EPR measurements. Solid-state ^{113}Cd nuclear magnetic resonance (NMR) spectra of both nanocrystalline CdSe and $Cd_{1-x}Mn_xSe$ are compared to bulk spectra. Experimental fluorescence line narrowing (FLN) and photoluminescence excitation (PLE) spectra of both CdSe and $Cd_{1-x}Mn_xSe$ quantum dots are fit using a dark exciton model. The differences between doped and undoped samples are discussed in later sections

6.2 Experimental

6.2.1 Materials

Unless otherwise noted, all reactions are carried out in a dry, oxygen-free, nitrogen atmosphere. Solvents used in the precursor synthesis are either anhydrous grade or are dried via distillation over a suitable drying agent. OmniSolv grade solvents used in QD purification were purchased from EM Science. Methyl lithium (1.4M in ether) was purchased from Aldrich. Trioctylphosphine (TOP, 95%) was purchased from Fluka. Selenium shot, tellurium powder, tricarbonyl methylcyclopentadienylmanganese (TCPMn) and manganese (II) cyclohexanebutyrate (an atomic absorption spectroscopy standard) were purchased from Alfa. Trioctylphosphine oxide (TOPO, 90%), $CdMe_2$, $Mn_2(CO)_{10}$, $Mn(CO)_5Br$, $Co_2(CO)_8$, and $Fe(CO)_5$ were obtained from Strem. All chemicals were used as received, except TOPO, which was dried under vacuum ($\sim$ 0.5 Torr) at 180°C for 1 hour, and $CdMe_2$, which was passed through a 0.2 μm PTFE syringe filter.

6.2.2 Precursors

The precursors, $MnMe_2$, $Mn(CO)_5Me$, $Mn(CO)_5(CH)_2C_6H_5$), $[MnTe(CO)_3(PEt_3)_2]_2$, and $Co_6Se_8(PEt_3)_6$ were synthesized according to literature methods.[202, 203, 204, 205] These compounds were used in early attempts to dope the nanocrystallites before settling on the following single source precursor which we found effective in doping the QDs.

$Mn_2(\mu-SeMe)_2(CO)_8$ was synthesized by adapting Coleman's procedure for making the analogous tellurium compound.[206] In the preparation, 13 mL (18 mmol) of a 1.4M solution of methyl lithium in ether is added dropwise to a stirring suspension of 1.46 g (18.5 mmol) of selenium powder in 100 mL THF. The resulting clear (slightly black) mixture is stirred at room temperature for 15 minutes. A solution consisting of 5.01 g (18.2 mmol) of $Mn(CO)_5Br$ in 50 mL THF is then added dropwise to the mixture. A dark red solution is obtained and allowed to stir for 15 minutes. The solvent is removed under vacuum leaving an oil. A solid can be recovered by exposing the oil to boiling hexane and removing the solvent under vacuum. This gives an orange-brown solid (ca. 75% yield) whose IR spectrum (carbonyl region) and ^1H NMR spectrum match literature values for the desired product, $Mn_2(\mu - SeMe)_2(CO)_8$.[207]

Undoped CdSe quantum dots are synthesized according to previously described literature methods.[32, 34] Doped nanocrystallites are prepared in a similar fashion by introducing a small amount of impurity precursor (2-200 mg) to the cadmium/selenium injection solution. This involves adding $Mn_2(\mu - SeMe)_2(CO)_8$ to 16 mL of TOP. The manganese precursor is dissolved by sonicating the suspension

for 10-30 minutes to give a clear, red-brown solution.[2] $CdMe_2$ [200μL (2.78 mmol)] and 1M TOPSe (3 mL in TOP) are then added to the mixture to create the injection solution. This solution is mixed and loaded into a disposable syringe. Rapid injection into 30 g of dry TOPO follows at 350°C.

Upon injecting, the reaction temperature falls to $\sim$ 260°C and the solution immediately turns yellow/orange. The initial UV/Visible absorption has a λ max in the range of 480 to 510 nm, indicating the presence of small 10-15 Å radius QDs.[3] Heating is restored to the reaction flask and the temperature raised to $\sim$ 300°C in $5-10$°C increments to promote steady growth of the nanocrystallites. The growth is monitored by the UV/Visible absorbance of the first excited state and doping levels can be increased by adding (dropwise) more injection solution to the hot reaction mixture.

Once the sample has reached a desired size, the temperature is lowered to 60°C and 15 mLs of butanol is added to the growth solution, to prevent TOPO from solidifying. The nanocrystallites are precipitated from solution by adding methanol. The (sometimes oily) flocculate is isolated using a centrifuge and the recovered material is dispersed in hexane. The QDs are subsequently purified by size selective precipitation.[32, 208]

[2]Using more of the impurity precursor results in a larger initial QD size, as well as a broader size distribution. Apparently the dopant alters the kinetics of the cluster growth.

[3]This is based on the sizing curves determined by SAXS and TEM. See Appendix B.

6.2.3 Electron Paramagnetic Resonance (EPR) Spectroscopy

Room temperature (300 K, 9.77 GHz) and low temperature (4.2 K, 9.44 GHz) EPR spectra are obtained using a Bruker ESP 300 instrument. Quantitative standards are prepared by adding known amounts of a manganese (II) cyclohexanebutyrate stock solution to undoped CdSe QDs in toluene. The concentration of nanocrystallites in the standard and the unknown are approximately equal. Areas related to the abundance of each compound are determined by double integration of the experimental first derivative spectra.

Light enhanced experiments are conducted using the white light output of a 300 W Xe arc lamp. The output is passed through a microscope objective into a fiber optic cable. The end of the fiber is positioned just outside the microwave cavity and the light directed onto the sample. A doubled diode laser is also used in these experiments to provide light on resonance with the nanocrystal absorption (appx. 527 nm). The TFR (tightly folded resonator, Spectra Physics) laser is Q-switched and operates at 1kHz providing 100 μJs of energy per pulse.

6.2.4 Wavelength Dispersive X-ray Spectroscopy (WDS)

A JEOL SEM 733 electron microprobe operating at 15 kV is used to determine manganese concentrations. The takeoff angle to the detector is 40° and the magnification is 1000×. Samples are prepared by precipitating TOPO/TOPSe capped nanocrystallites from solution and washing the material three times with methanol. Following the third wash, the QDs are dissolved in a small amount of pyridine. One drop of the concentrated pyridine solution is placed on a silicon (100) wafer, and dried

under vacuum at 80°C for 24 hours. The films are later coated with a thin layer of amorphous carbon to prevent charging effects under the electron beam.

6.2.5 Solid-state NMR

NMR experiments are performed using a homebuilt 211 MHz NMR spectrometer (47 MHz for ^{113}Cd) and a homebuilt, two channel transmission line probe. The $\pi/2$ pulse width is 5 μs. Hahn echo pulse sequences are used in acquiring all spectra, with the interpulse delay, τ, equal to the rotor period. A 5 mm Chemagnetics spinning system (Otsuka Electronics, USA) is used for magic angle spinning (MAS) with sample spinning speeds varying from 6.5 to 9 kHz (stability of $\simeq$ 20 Hz).

6.2.6 Optical Spectroscopy

Variable temperature fluorescence line narrowing (FLN) and photoluminescence excitation (PLE) experiments are conducted on doped and undoped QDs using a SPEX Fluorolog-2 spectrofluorometer. The entrance and exit slits of both excitation and emission spectrometers are set to 125 μm to give an optical resolution of $\sim$ 0.15 – 0.2 nm. Samples are prepared by loading hexane solutions of TOPO/TOPSe capped nanocrystallites between two sapphire flats separated by a 0.5 mm Teflon spacer. The absorbance of all samples is kept below 1.0 to minimize reabsorption of the luminescence.[4]

The FLN experiment is conducted by choosing five energies over the full luminescence profile of the nanocrystallites. The sample is then excited sequentially at

[4]Occasionally, high optical densities were required because of the very low quantum yield of "purified" $Cd_{1-x}Mn_xSe$ QDs.

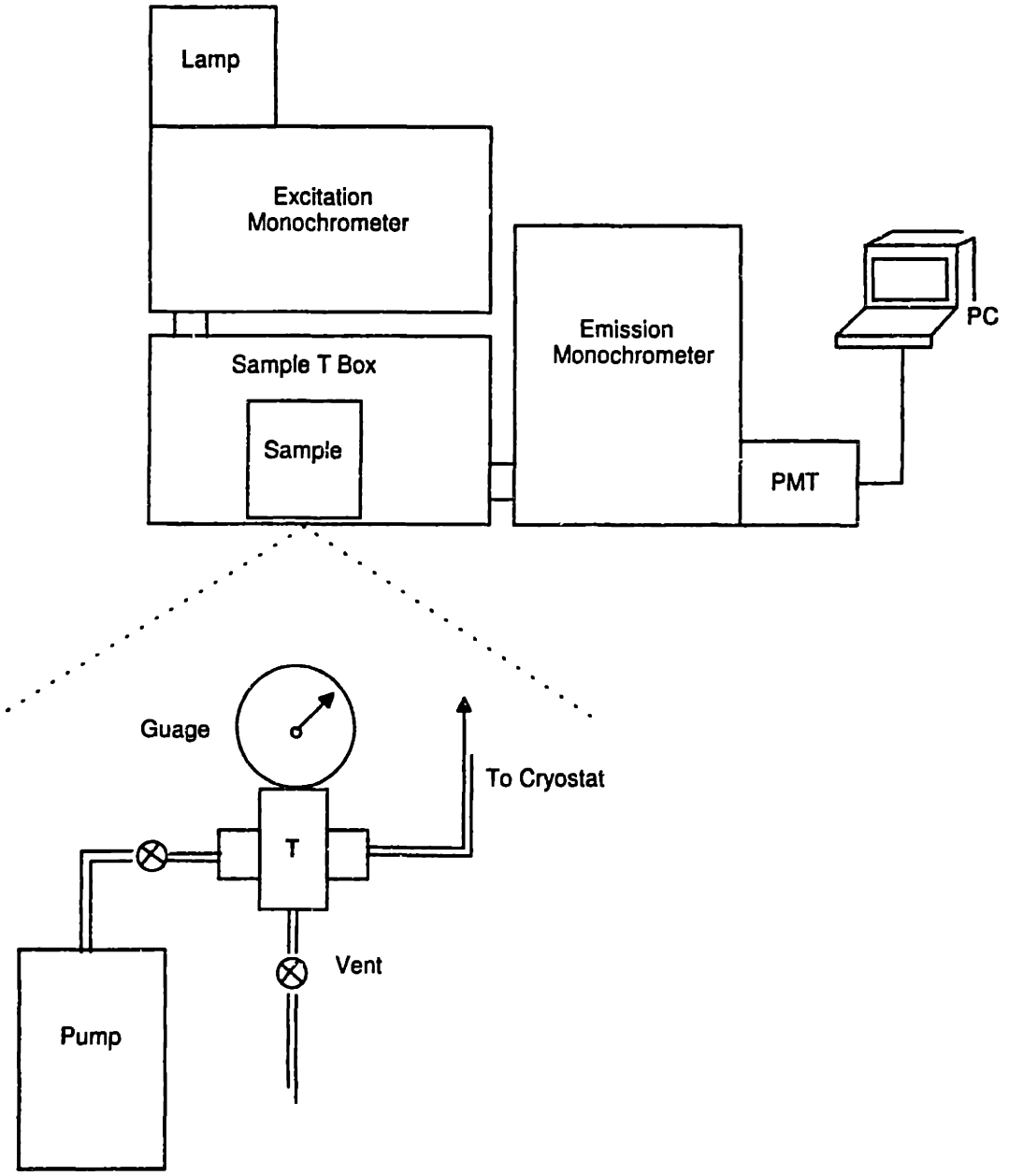

Figure 6-1: FLN/PLE setup consisting of a 450 W Xe arc lamp, excitation and emission monochromators and a PMT detector. The apparatus used to achieve temperatures lower than 4 K is shown in the enlarged inset.

each of these energies and the resulting luminescence detected through the emission spectrometer/PMT. The PLE experiment follows in a similar fashion. In this case, the detector is fixed at a particular wavelength (energy) and the excitation spectrometer is scanned to the blue of this position to reproduce the absorption profile of the nanocrystallites. The detector energy is determined by choosing the peak of the zero phonon line (ZPL) in each of the five emission scans. In this manner the absorption and emission of five "effective" QD sizes is determined using one sample.

Figure 6-1 is a schematic of the fluorimeter (Spex Fluorolog 2) used in the experiment. Light from a 450 W Xe arc lamp is passed through a 0.22 m double monochromator to produce the excitation light. Emission from the sample is passed through another 0.22 m double monochromator and detected with a thermoelectrically cooled PMT (Hammamatsu R928). The enlarged inset shows the apparatus used to achieve temperatures below 4 K. A mechanical pump is attached to the He vapor flow cryostat to produce a vacuum. Temperatures as low as 2 K are achieved in this manner. To create superfluid helium, the cryostat is flooded with liquid helium (typically 12 min fill time) and once the sample is immersed in helium, vacuum is applied. Hold times as long a 2 hrs have been achieved.

6.3 Discussion

The use of organometallic manganese complexes as precursors in the chemical vapor deposition (CVD) of DMS films is well documented.[209, 210] Such compounds are attractive candidates for nanocrystalline DMS synthesis because they are compatible with solvents used in the present method and they decompose cleanly at low

temperatures. For example, TCPMn decomposes at 300-500°C and $Mn(CO)_5Me$ at 100°C. These precursors are slightly soluble in TOP and are easily dispersed in the standard injection solution at concentrations up to $\sim$ 10 mg/1 mL. The low concentration of precursors does not greatly disrupt growth of the host CdSe lattice allowing us to keep the good size distribution and crystallinity characteristic of CdSe nanocrystallites.

Samples made using each of the four reagents above are purified three times by size selective precipitation and are analyzed for Mn. Initial, EPR and WDS data gave evidence for manganese incorporation (Figure 6-2 a). However, after ligand exchange with pyridine, all samples were void of Mn signals (Figure 6-2 b). We now believe that most of the signal we observe originates from loosely bound surface species or manganese containing decomposition products not removed by size selective precipitation.

Regardless of the origin, two important results are obtained from these experiments. The first is that any sample destined for elemental analysis must be thoroughly purified by multiple ligand exchange. This procedure is known to replace appx. 80% of the original TOPO/TOPSe ligands on the surface of the nanocrystallite.[34] In fact, for samples cap exchanged three times with pyridine and three times with TOPO/TOP, the peak of the first absorption feature often shifts 2-6 nm to shorter wavelengths, indicating a shrinkage of the average QD size. This purification sequence slightly etches the nanocrystallites "cleaning" the surface of any stray manganese species. A second notable result is that precursors containing only manganese are ineffective dopants in this particular synthesis.

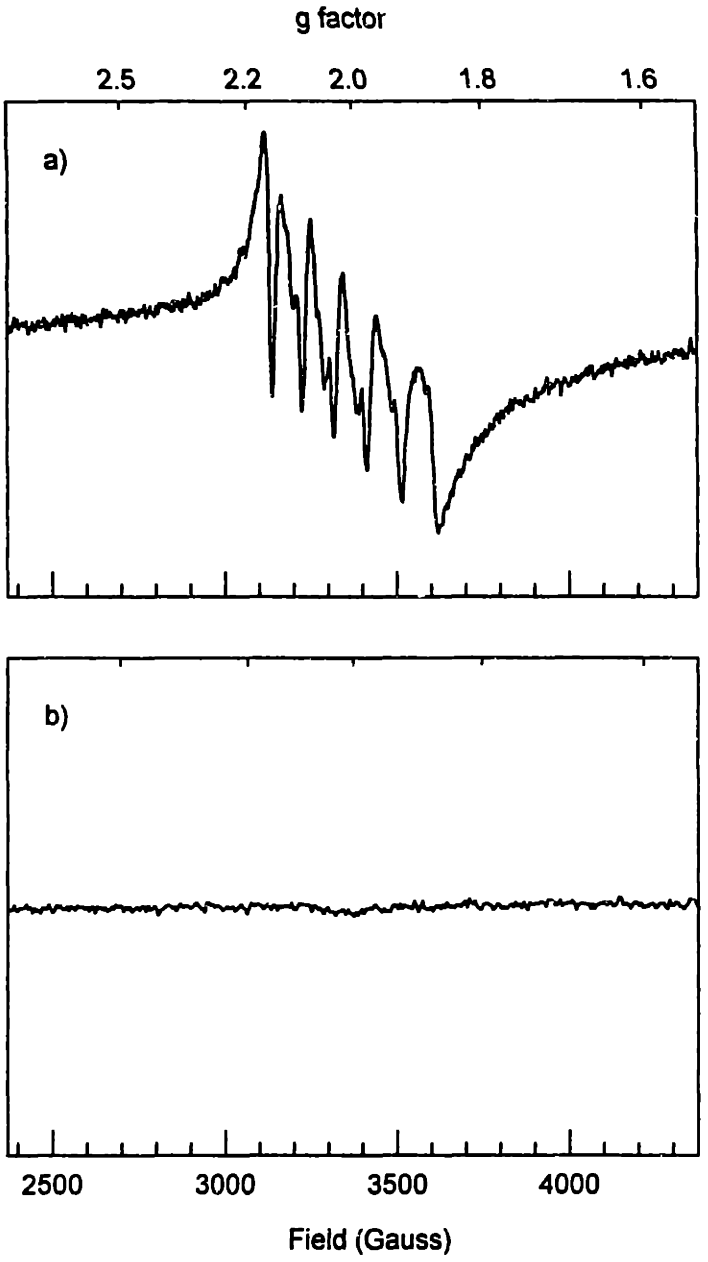

Figure 6-2: EPR spectrum of doped samples prior to, (a), and after, (b), ligand exchange. Initially a Mn six line pattern is seen. However, after repeated ligand exchange the EPR spectrum shows no manganese signal. This indicates that the EPR signal originates from Mn containing species not incorporated into the nanocrystallite core.

To overcome the apparent unreactivity of manganese towards TOPSe, we synthesized an organometallic complex containing manganese-selenium bonds, which serves as a single source MnSe precursor. Many such compounds are described in the literature, and the decomposition processes (products) of some have been well studied.[204] This scheme is promising because several investigations have described using a single source MnSe precursor (a manganese polychalcogenide anion) to produce $\sim$ 125 Å radius $Cd_{1-x}Mn_xSe$ particles, with $0 < x < 1$.[188][5]

$[MnTe(CO)_3(PEt_3)_2]_2$ and $Mn_2(\mu-SeMe)_2(CO)_8$ are synthesized in high yield and their decomposition products examined through powder x-ray diffraction (XRD) both with and without the presence of TOPO. The XRD pattern for the $[MnTe(CO)_3(PEt_3)_2]_2$ decomposition products are shown in Figures 6-3 and 6-4. Decomposition of $[MnTe(CO)_3(PEt_3)_2]_2$ is achieved by heating it in an evacuated Pyrex tube at 360°C for 30 minutes. Figure 6-3 displays the XRD pattern of the resulting black powder, which is mainly hexagonal MnTe with a small amount of cubic $MnTe_2$. Known x-ray lines of MnTe and $MnTe_2$ are plotted at the bottom of the graph and are shown as the solid and dashed lines respectively.

When the decomposition is performed by adding $[MnTe(CO)_3(PEt_3)_2]_2$ to a flask of TOPO at 300°C, the precursor immediately turns into a black solid. This material is isolated, washed twice with hexane, twice with methanol, and dried under vacuum. The XRD pattern of this product (Figure 6-4) shows a mixture of MnTe and $MnTe_2$ in approximately a 1:2 ratio. Again the known x-ray lines of MnTe and $MnTe_2$ are

[5]One difference between these quantum dots and the ones described in this section is their size. Our nanocrystallites lie in the strong confinement regime whereas 125 Å QDs are in the intermediate to weak confinement regime.

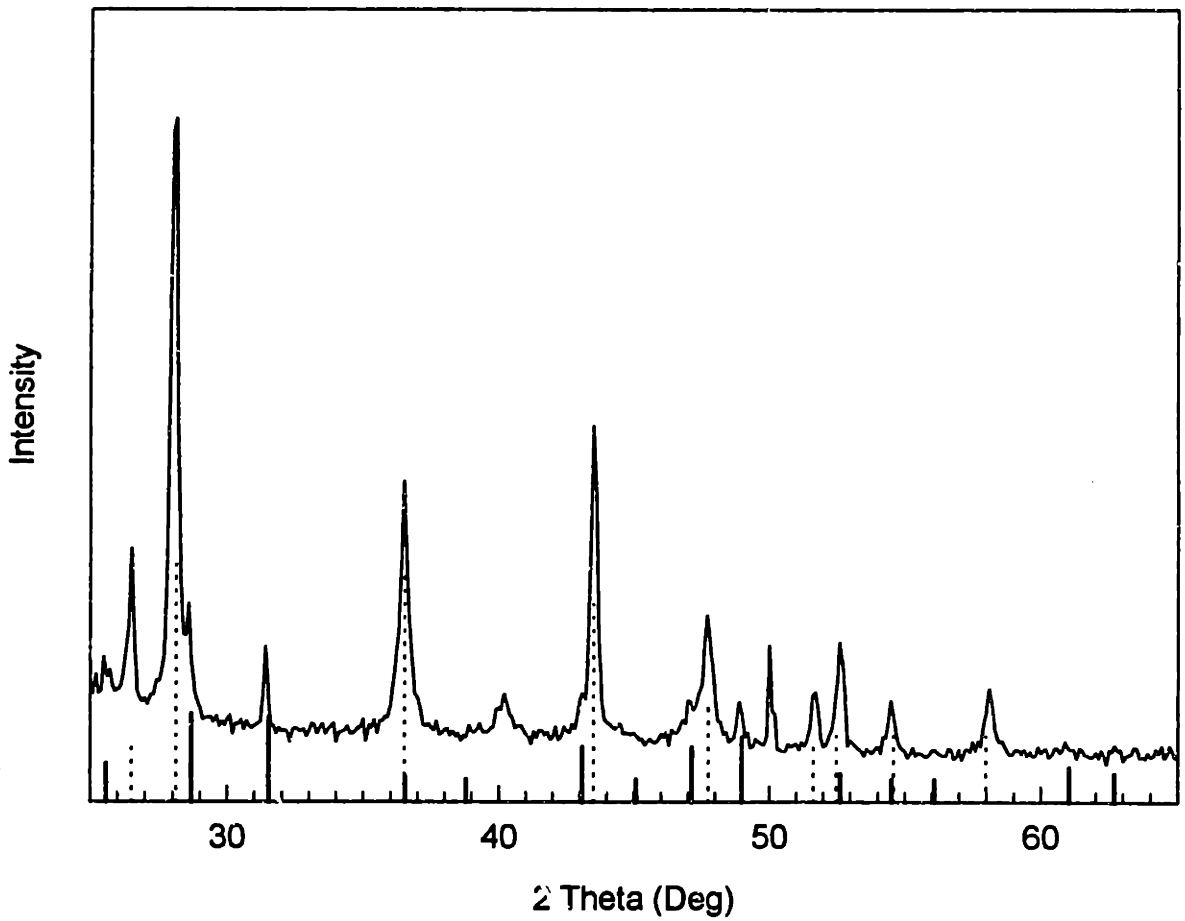

Figure 6-3: Wide angle x-ray spectrum of the precursor decomposition products in the absence of TOPO. The experimental data shows a mixture of MnTe and $MnTe_2$ based on a comparison to known x-ray lines. The solid lines at the bottom of the graph indicate known $MnTe_2$ reflections. Similarly, the dashed lines are x- ray positions for MnTe.

shown at the bottom of the graph for comparison purposes.

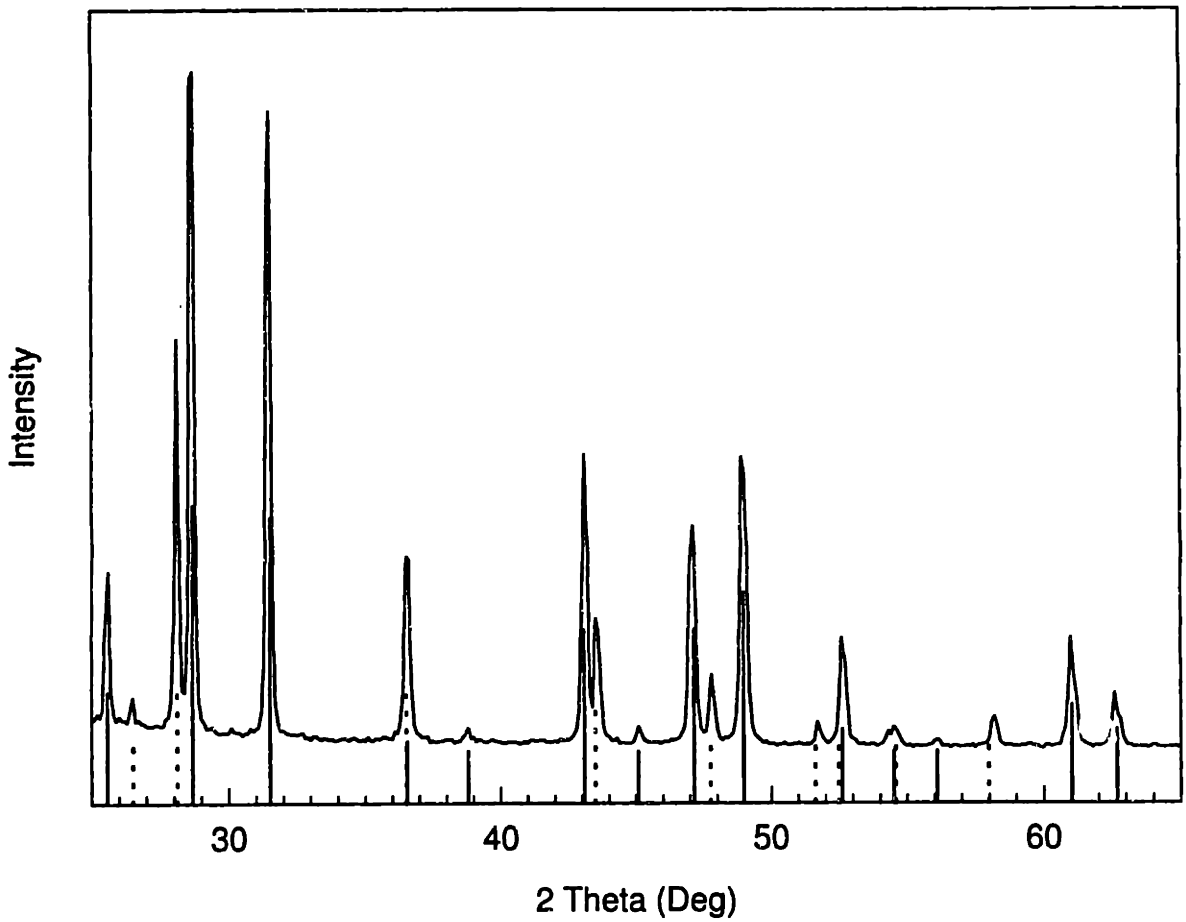

Figure 6-4: Wide angle x-ray spectrum of the precursor decomposition products in the presence of TOPO. Known x-ray lines for $MnTe_2$ (solid) and MnTe (dashed) are provided for comparison purposes.

Less Mn is present when the decomposition is performed in the presence of TOPO (more $MnTe_2$). This occurs because phosphine oxides are known to be good coordinating compounds for transition metals. In fact, TOPO is used in industry as a metal extractant. Our experiments show that it is possible to make bulk manganese chalcogenide products using these precursors with TOPO present. We expect, though, that the yield of dopant incorporated into the QD will only be a fraction of the total amount used, because of losses associated with coordination of the metal (Mn in this

case) to the phosphine oxide, TOPO. Our experiments with the decomposition of $Mn_2(\mu-SeMe)_2(CO)_8$ yield similar results. In the absence of TOPO, most of the decomposition product is MnSe. However, in the presence of TOPO, the decomposition product is Mn poor and is primarily $MnSe_2$.

6.3.1 EPR Results on Undoped CdSe QDs: A Brief Aside

During the course of investigating undoped CdSe QDs, not expected to be EPR active, an interesting observation was made. Spectra of TOPO/TOPSe capped CdSe QDs show a large asymmetric signal centered about $g \sim 2$. Another smaller signal is seen centered about $g \sim 4.5$. Comparison of the integrated absorption with an external standard gives a sizable concentration of these impurities on the order of one per QD (assuming spin 1/2).

However, we find that the signal intensities are dependent upon the extent of sample purification. This phenomenon is shown in Figures 6-5 and 6-6, which show the 9.44 GHz EPR spectra of (a) TOPO capped CdSe nanocrystallites isolated from the growth solution and (b) the same sample after multiple size selective precipitations (3 times). In the first sample (Figure 6-5), washing the surface reduces the impurity concentration by half. In the second sample (Figure 6-6), the effects of washing are more dramatic, showing a tenfold decrease in the impurity concentration. This suggests that the impurities are surface related and are not located within the crystal lattice. The identity/origin of the signal is unknown as attempts to isolate the responsible impurity species were unsuccessful.[6]

[6]The EPR spectrum of the growth solution was also taken to see if the signals were related to impurities in the technical grade TOPO, 90%. No correlation was found.

Integration of the $g \sim 2$ signal reveals a lineshape that may arise from g-anisotropy. In this case, the values of the g-tensor principal axis correspond to the resonance position of the peak and its accompanying shoulders. Values of: $g_1 \simeq 2.25$, $g_2 \simeq 2.065$, and $g_3 \simeq 2.015$ are extracted from the fits. However, the asymmetric signal might also arise from the superposition of more than one spectral feature. For instance, the signal might contain contributions from dangling bonds or surface impurities such as adsorbed oxygen (in the form of the O_2^- radical anion[211, 212]).

Examination of CdSe nanocrystallite powders at higher magnetic fields (i.e. larger spectral window) reveals a relatively large anisotropic signal at $g \sim 0.6$. The experimentally measured g factor for the conduction band electron in bulk CdSe matches this value, and similar agreement is found in their linewidths [$\sim$ 400 Gauss (bulk) and $\sim$200 Gauss (nanocrystal)].[111] This signal is seen only in powdered samples passivated with pyridine. Samples passivated with TOPO/TOPSe dispersed in hexane show no $g \sim 0.6$ signal.

Something very interesting is observed with the residual $g = 2$ signal. We find that part of this signal is light enhanced. By illuminating the sample with the output of a 300 W Xe arc lamp, a portion of the $g = 2$ signal increases by approximately a factor of 3 (Figure 6-7). The same experiment was repeated with a TFR laser (Spectra Physics) by exciting the sample on resonance at 527 nm. Again, a similar enhancement of the EPR signal is seen. The light enhanced signal has a narrow linewidth and appears to be very symmetric. The effects of illuminating the sample are long lived and EPR enhancements can easily be seen long after the excitation source is turned off ($>$ 10 min). In addition, a control experiment was performed by

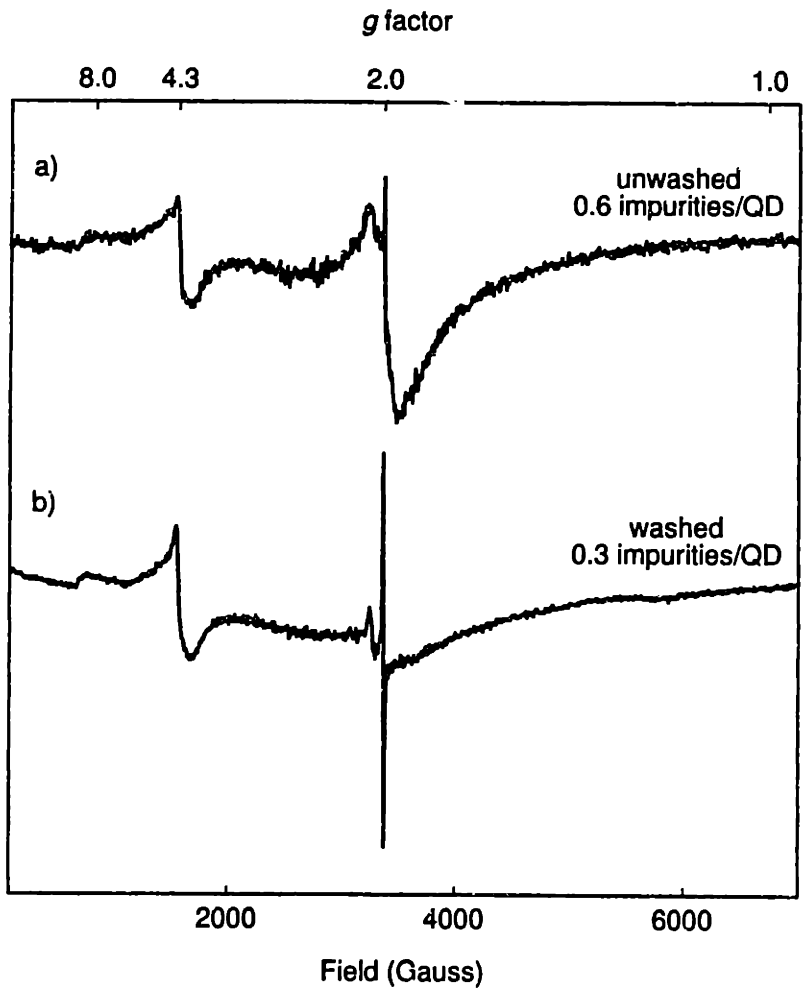

Figure 6-5: (a) EPR spectrum of unpurified CdSe QDs. Two signals are seen: a transition centered at $g \sim 4.5$ and another feature at $g \sim 2.0$. (b) EPR spectrum of the same sample after purification. The intensity of all signals has diminished. A quantitative comparison was made with an external manganese standard to determine the number of impurities per QD. These values are listed next to each spectrum and indicate that washing the sample has an effect on the impurity concentration. Prior to washing there are approximately 0.6 impurities per QD. After washing the value has fallen by half. Experimental parameters: microwave power 10 μW, microwave frequency 9.43 GHz.

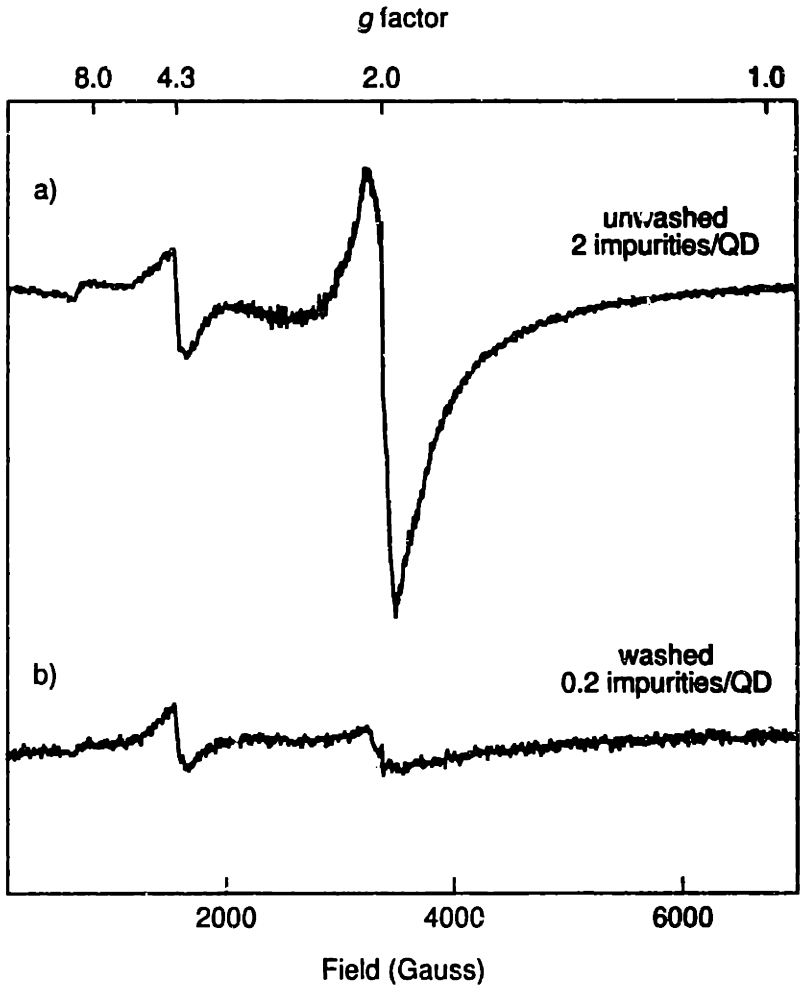

Figure 6-6: (a) EPR spectrum of unpurified CdSe QDs. Two signals are seen: a transition centered at $g \sim 4.5$ and another feature at $g \sim 2.0$. (b) EPR spectrum of the same sample after purification. The intensity of all signals has diminished. A quantitative comparison was made with an external manganese standard to determine the number of impurities per QD. These values are listed next to each spectrum and indicate that washing the sample has an effect on the impurity concentration. Prior to washing there are approximately 2 impurities per QD. After washing the value has fallen tenfold. Experimental parameters: microwave power 10 μW, microwave frequency 9.43 GHz.

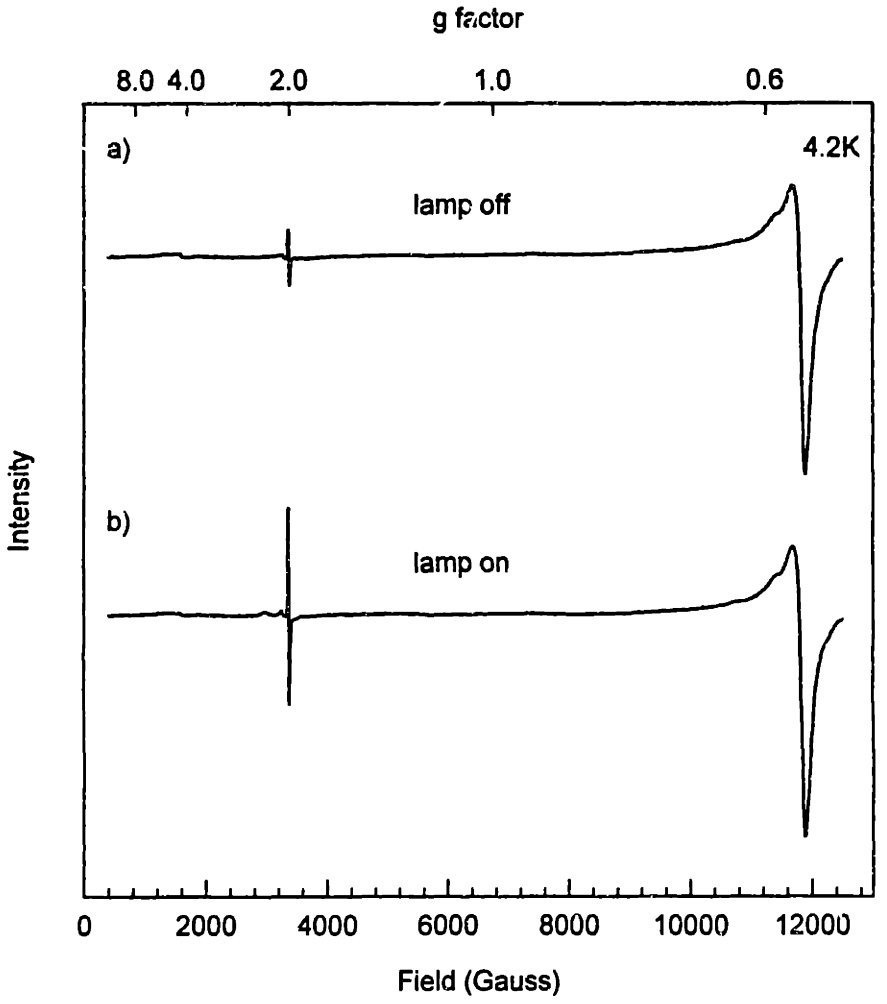

Figure 6-7: (a) EPR spectrum of CdSe powders (pyridine passivated) in the absence of light. A large signal at $g \sim 0.6$ may indicate charged QDs as the g factor is similar to that measured for the conduction band electron of CdSe. A small signal is also observed at $g \approx 2$. (b) EPR spectrum of the same sample after illuminating with white light. A 300 W Xe arc lamp is used as the excitation source. A doubled diode laser (Spectra Physics, TFR) is also used in the experiment to illuminate the sample on resonance. The large feature near $g = 0.6$ is relatively unaffected by the light. The smaller signal at $g \sim 2$, surprisingly, shows a large enhancement in its intensity. This enhancement was found to be relatively long lived, and lasts for more than 10 minutes in the absence of light.

illuminating the sample, monitoring the enhancement and warming the sample back up to room temperature. The sample was then cooled back to 4.2 K and the EPR spectrum re-taken. The $g = 2$ signal showed no enhancement. Shining light on the sample re-introduces the enhancement showing that the light initiated effect is both reproducible and reversible.

We speculate that this signal originates from the trapping of photogenerated electrons on the surface of the nanocrystallite.[213, 214] This is supported by the long enhancement lifetimes and the reversibility of the signal at higher temperatures. However, if the signal is related to the presence of trapped electrons, there ought to be a complementary hole signal. During the course of our experiments we were unable to see any hole resonances, expected to appear in the vicinity of $|g| = 1.09$. This may be due to the broadness of the signal and/or the poor signal to noise in the experiment. It may also stem from a shift in the hole resonance upon surface localization although no new signal was observed in the spectral range from $g = 8$ to $g = 0.5$.

Light enhanced spectra are most prominent when using samples passivated with pyridine, a notably bad cap for the nanocrystallites. This is evident by the dramatic drop in quantum yield between QDs passivated with TOPO/TOPSe and pyridine (10-20% to <1% at room temperature). Also, EPR enhancements are best seen in powders. Because of this, the light enhanced signal reflects the behavior of only those nanocrystallites illuminated by the pump light (i.e. the first few layers near the wall of the EPR tube). The bulk of the sample is not illuminated, making quantitative comparisons difficult.

6.3.2 Quantitatively Determining [Mn] Concentrations

In light of the above findings, special care was taken in preparing samples for all analytical measurements. $Cd_{1-x}Mn_xSe$ QDs were size selected three times, cap exchanged three times with pyridine, and brought back to TOPO/TOPSe passivation. In quantitative EPR experiments, Mn standard solutions were purposely mixed with undoped QDs. By normalizing the CdSe concentration between sample and standard we minimize matrix effects and ensure that the microwave power absorbed by the dielectric background (solvent and CdSe host) is constant between the two solutions. We also find that the presence of the nanocrystallites prevents aggregation of the Mn standard. Such clustering causes an enormous dipolar broadening of the signal. This effect is described in the literature and is also seen in the EPR spectrum of 10 μmol Mn (II) cyclohexanebutyrate solutions at temperatures down to 77 K.[215, 216]

The importance of ligand exchange in purifying doped QDs is emphasized in the Figure 6-8 which plots the normalized manganese concentration determined by EPR at selected points along the purification process. The break in the x-axis indicates a switch from size selective precipitation to pyridine cap exchange. The more than four fold decrease in the Mn concentration indicates the presence of surface bound species. After sufficient exposure to pyridine, the dopant concentration stays unchanged indicating that the remaining manganese atoms lie within the QD.

Results from both EPR and WDS experiments performed on the same $Cd_{1-x}Mn_xSe$ sample are shown in Table 6-1. There is especially good agreement between the two sets of data given that each technique calculates the CdSe host concentration differ-

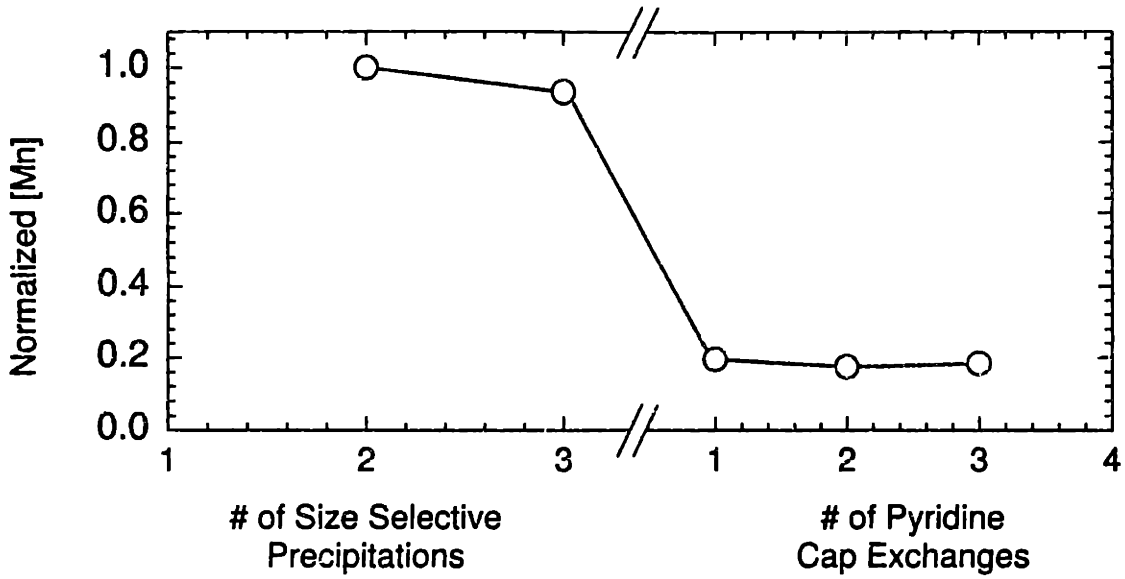

Figure 6-8: The effects of washing and ligand exchange on the detected EPR manganese concentration in doped $Cd_{1-x}Mn_xSe$ samples. The break in the x-axis indicates a switch from washings (size selective precipitations/purification) to ligand exchange.

ently: EPR relies on UV/Visible absorption spectra[7], whereas WDS directly measures a percentage for all elements present. Nanocrystallites with higher doping levels were used in these experiments to obtain reliable comparisons between the two analytical techniques. Higher doping levels were achieved at the expense of the sample size distribution.

The $Cd_{1-x}Mn_xSe$ sample was prepared by dropwise adding more manganese precursor into the reaction mixture containing doped nanocrystallites. Sample #1 shows EPR/WDS results prior to any purification. Sample #2 shows results from the same sample after one stage of purification. Sample #3 gives final results from the sample after ligand exchange to and from pyridine. These values reflect signals from

[7]The concentration of nanocrystallites is determined by assuming that all the Cd precursor decomposes to form a particular sized QD. Since the volume and absorbance of the growth solution are known an *effective* extinction coefficient is determined. Extracted values represent an upper bound.

incorporated manganese atoms, not surface impurities.

6.3.3 ^{113}Cd NMR

Results from solid state MAS NMR experiments are summarized in Figure 6-9. The bulk spectrum of CdSe, (a), is shown at the bottom of the figure. $Cd(NO_3)_2$ was chosen as a reference compound (0 ppm). The bulk spectrum was acquired by spinning the sample (7.5 kHz) at the magic angle and using a 120 s delay. The large delay was necessary due to the long T_1 relaxation time of Cd (124 ± 31 s).

The ^{113}Cd MAS NMR of undoped CdSe QDs, (b), is shown above the bulk spectrum. It is very broad ($\sim$ 100 ppm FWHM) and suggests the presence of a large chemical shift dispersion. This is the most likely source of the broadening because up to 40% of atoms in small nanocrystallites reside on the surface. The multiple chemical environments experienced by the Cd nuclei at the QD/matrix interface presents a natural source for the dispersion. Chemical shift dispersion due to large surface to volume ratios have been reported in the ^{77}Se NMR of CdSe QDs.[217] The broadening is not due to chemical shift anisotropies as they are spun out in the experiment. In the spectrum, the signal to noise is poor because of the long delay times required to prevent saturation of the transition.[8] We encountered this problem in all nanocrystalline samples, especially with the smallest QDs ($a \sim$ 10-12 Å radius). The acquisition time for the spectrum was 24 h.

The bulk $Cd_{1-x}Mn_xSe$ spectrum is shown next, (c). We observe a narrow asymmetric signal that is shifted downfield relative to the bulk undoped Cd resonance.

[8]Relaxation times for ^{113}Cd are estimated to be longer than 2 minutes

Sample #	Mn atoms per QD (EPR)	Error	Mn atoms per dot (WDS)	Error
1	9.2	± 0.6	4.2	± 0.6
2	8.6	± 0.7	2.8	± 0.4
3	1.8	± 0.5	1.0	± 0.1

Table 6.1: EPR-WDS Table comparing results of both techniques.

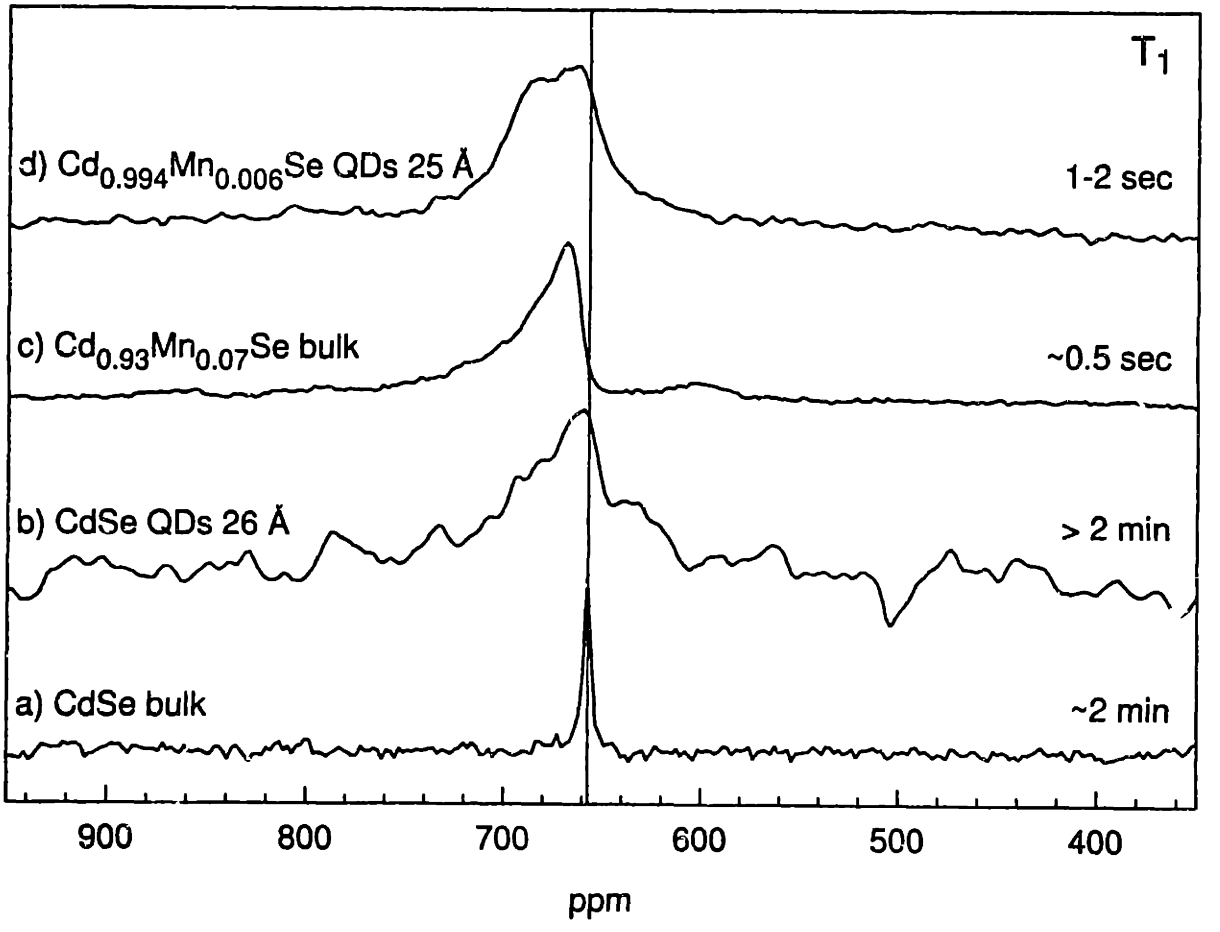

Figure 6-9: ^{113}Cd NMR results. (a) Bulk Cd NMR spectrum. (b) Spectrum of undoped 26 Å radius QDs. The T_1 is very long (> 2 min) yielding poor signal to noise. (c) Spectrum of bulk $Cd_{1-x}Mn_xSe$. The T_1 is much shorter than its undoped counterpart. A shift is also seen in the Cd resonance. (d) Spectrum of doped $Cd_{1-x}Mn_xSe$ QDs, 25 Å radius. The T_1 is considerably shorter and shifts are seen in the Cd resonance. Both strongly suggest Mn incorporation into the nanocrystallite.

The T_1 lifetime is also much shorter than its undoped counterpart (0.5 s vs > 2 min). These effects are due to the presence of the manganese impurity. Recent work by Vega on bulk DMS compounds suggests that the data can be interpreted by assuming that Cd atoms occupy concentric shells surrounding Mn^{+2} atoms distributed evenly throughout the nanocrystallite. Cadmium atoms closest to the manganese impurity experience large shifts in their resonance position. Those in the next shell are further away and, on average, experience less of a shift. Finally, those in the third shell and beyond experience little or no difference in their chemical environments. Their resonance position is unchanged from the bulk undoped resonance. The contribution from each shell is convoluted with the spatial distribution of Cd atoms to give the net chemical shift seen in the bulk doped spectrum. The experimental T_1 value of 500 ms is in reasonable agreement with that measured for other DMS compounds, $Cd_{1-x}Co_xSe$ (< 600 ms) [218] and $Cd_{1-x}Fe_xTe$ (793 ms).[219]

The NMR spectrum of $Cd_{1-x}Mn_xSe$ QDs is the topmost graph (d). Two features immediately stand out. The first is that T_1 has fallen by two orders of magnitude (from $T_1 > 2$ min to $T_1 \sim$ 1-2 s). The faster relaxation time is reflected in the better signal to noise of the spectrum. The second interesting feature is the prominent shift of the Cd resonance with respect to the undoped spectrum. Both the shift and the faster T_1 relaxation time suggest incorporation of the manganese impurity into the QD lattice. This is in qualitative agreement with EPR and WDS measurements. At this time, however, we cannot tell from the NMR data where exactly the Mn impurities lie. These measurements should be combined with results from other techniques such as EXAFS to obtain a better sense of the impurity distribution within the

nanocrystallite.

6.3.4 Optical Results

FLN, PLE and PL data from the undoped and doped samples are shown in Figures 6-10 and 6-11. Five temperatures ranging from 15 K to 1.75 K are studied. In each graph, the spectra on the left is the FLN and the complementary set of spectra on the right is the PLE. The full luminescence or PL is shown at the bottom of each graph. At each temperature five absorption/emission positions are chosen along the full luminescence profile in order to study the optical response of five "effective" QD sizes.

There are differences in the FLN/PLE spectra of doped and undoped samples seen as different phonon ratios in the luminescence and absorption. A priori, however, it is difficult to say whether these changes are due to probing "different" sizes in each sample or from sample to sample variations in the residual size distribution.[9] To obtain a more quantitative description of temperature dependent changes in the two samples, we employ a fitting routine to extract effective single QD absorption/emission lineshapes.

The FLN, PLE and PL data taken at different temperatures is fit simultaneously using a non-linear least squares fitting program. The reason for doing this is that the PLE data is contaminated with FLN information. Likewise, the FLN data is contaminated with PLE information. This is due to the residual size distribution of the sample. The convolution expressing this contamination in both absorption and

[9]Compare the large changes in the FLN/PLE lineshape between two separate excitation/emission positions in one sample.

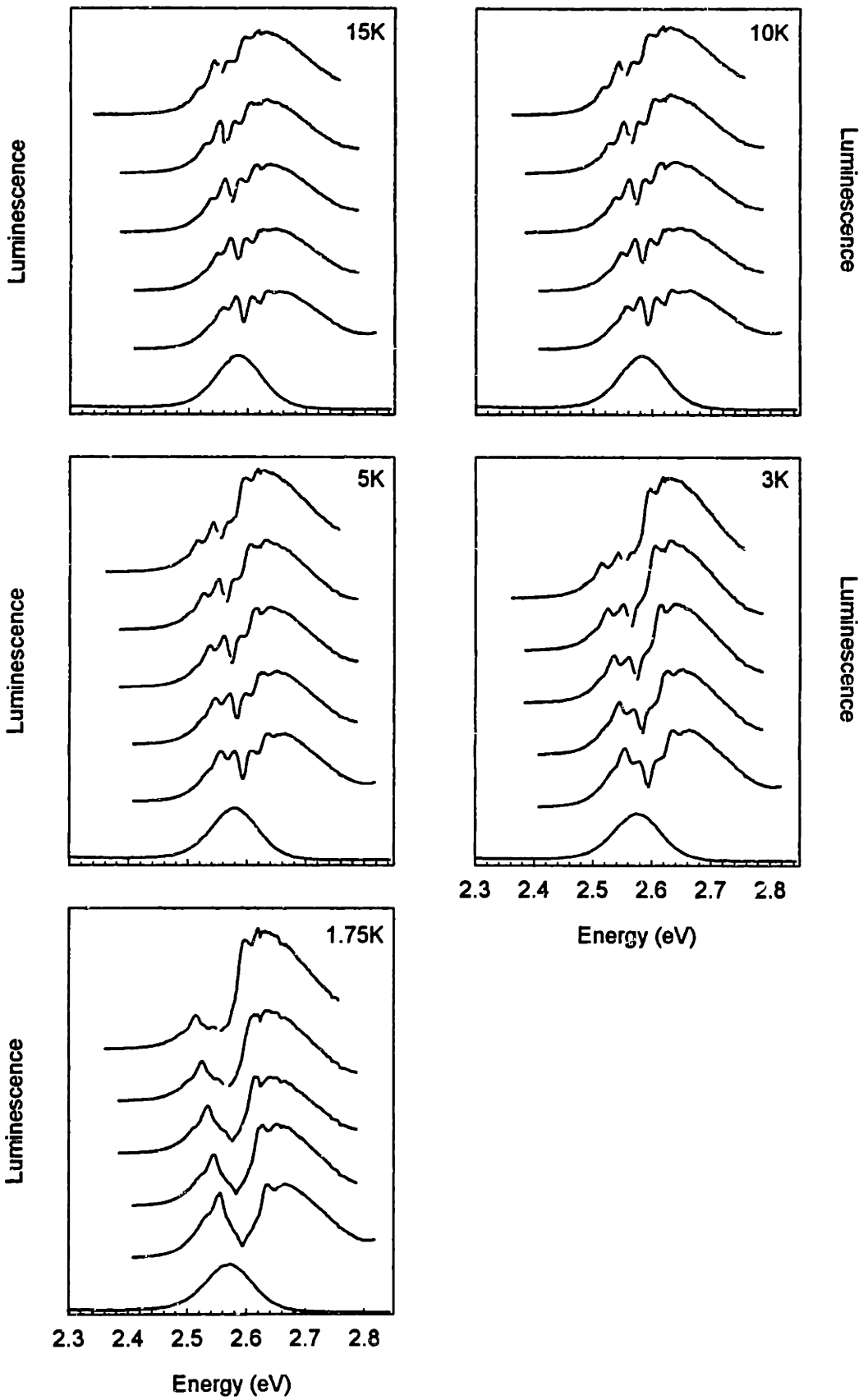

Figure 6-10: Raw FLN/PLE data for the undoped sample. Five temperatures ranging from 15 K to 1.75 K are studied. FLN spectra are on the left moving to lower energies and PLE spectra are on the right moving to higher energies. .

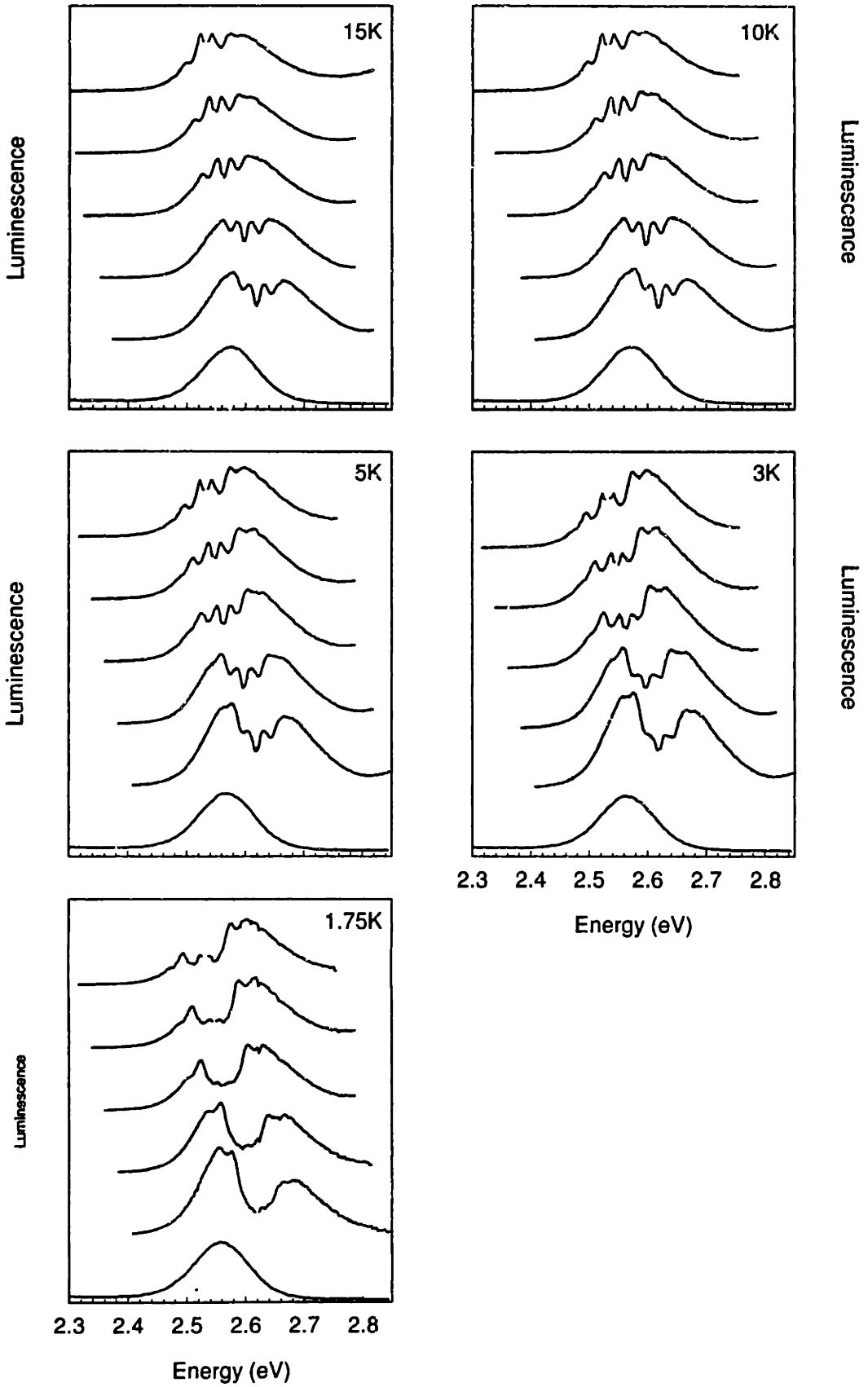

Figure 6-11: Raw FLN/PLE data for the doped sample. Five temperatures ranging from 15 K to 1.75 K are studied. FLN spectra are on the left moving to lower energies and PLE spectra are on the right moving to higher energies.

emission is given by the expression.

$$\begin{matrix} E_{FLN}(\nu_{em})|_{\nu_{exc}} \\ E_{PLE}(\nu_{exc})|_{\nu_{em}} \end{matrix} = C \int A(\nu_{exc}, \nu') E(\nu_{em}, \nu') D(\nu', \nu_0) d\nu' \tag{6.1}$$

where $D(\nu', \nu)$ is a normalized Gaussian that represent the sample's residual size distribution, E_{FLN} is the line narrowed emission, and E_{PLE} is the photoluminescence excitation spectrum. In the FLN experiment the excitation frequency, ν_{exc} is fixed and the emission position varied. Similarly, in the PLE experiment the emission position, ν_{em} is fixed and the excitation frequency is varied.

We use the fitting routine to deconvolute an effective single QD absorption/emission lineshape $A(\nu_{exc}, \nu')$ and $E(\nu_{em}, \nu')$ which best accounts for the experimental data. The absorption is modeled by the sum of three optically active states and their phonon replicas. Likewise, the emission is modeled by the corresponding zero phonon line (ZPL) and accompanying phonon replicas.

$$A(\nu_{exc}, \nu') = \sum_{l=1}^{3} \sum_{m=0}^{2} \frac{C_l}{\sqrt{2\pi\gamma_{l,m}^2}} \frac{(S_a)^m}{m!} \exp\left(-\frac{[\nu_{exc} - (\nu' + \Delta_l + m\omega_{LO})]^2}{2\gamma_{l,m}^2} \right) \tag{6.2}$$

$$E(\nu_{em}, \nu') = \sum_{n=0}^{4} \frac{1}{\sqrt{2\pi\gamma_n^2}} \frac{(S_e)^n}{n!} \exp\left(-\frac{[\nu_{em} - (\nu' - n\omega_{LO})]^2}{2\gamma_n^2} \right) \tag{6.3}$$

In the absorption, the sum is taken over all optically active states, l, and all phonon replicas, m. In the emission, the sum is over all phonon replicas, n separated by the LO phonon frequency, $\omega_{LO} = 21 - 26$ meV.[34] C_l is the oscillator strength of absorbing states, $\nu_{exc(em)}$ is the excitation (emission) position, ν' is the position of the zero phonon line in emission, Δ_l is the size dependent Stokes shift between absorbing

and emitting states and $S_{a(e)}$ is the absorption (emission) coupling constant with values 0 41 and 0.1 respectively. These numbers are consistent with recent PLE experiments on the band edge fine structure of the nanocrystallites.[118]

A phenomenological suppression coefficient is included to account for observed changes in the FLN spectra as the temperature decreases. In particular, it is observed that as the sample temperature is lowered, the Huang-Rhys parameter or integrated ratio of the one to zero phonon lines increases.[13] Similarly, an enhancement coefficient is included in the PLE fit to account for possible changes in the phonon ratio of the first optically active state.

Figure 6-12 shows results of the fitting procedure for the undoped sample. Figure 6-13 shows fitting results for the doped sample. In all cases, there is very good agreement between the fit and the data considering that the fitting routine evaluates the FLN, PLE and PL results simultaneously.

Our approximation is based on a recent fine structure model which describes the electronic structure of CdSe nanocrystallites.[63, 64] This "dark exciton" model predicts that the lowest excited state of CdSe QDs is an optically passive exciton with angular momentum projection ± 2. The model considers three perturbations which break the spherical symmetry of electronic states. When crystal field splitting, QD geometry and the electron-hole exchange interaction are considered jointly, the initially eight-fold degenerate $1S_{3/2}1S_e$ exciton is split into five fine structure states. These states are labeled by their angular momentum projection along the c axis of the nanocrystallites. There are two states with projection $N = 0$, two doubly degenerate states with projection $N = 1$ and one double degenerate state with projection $N = 2$.

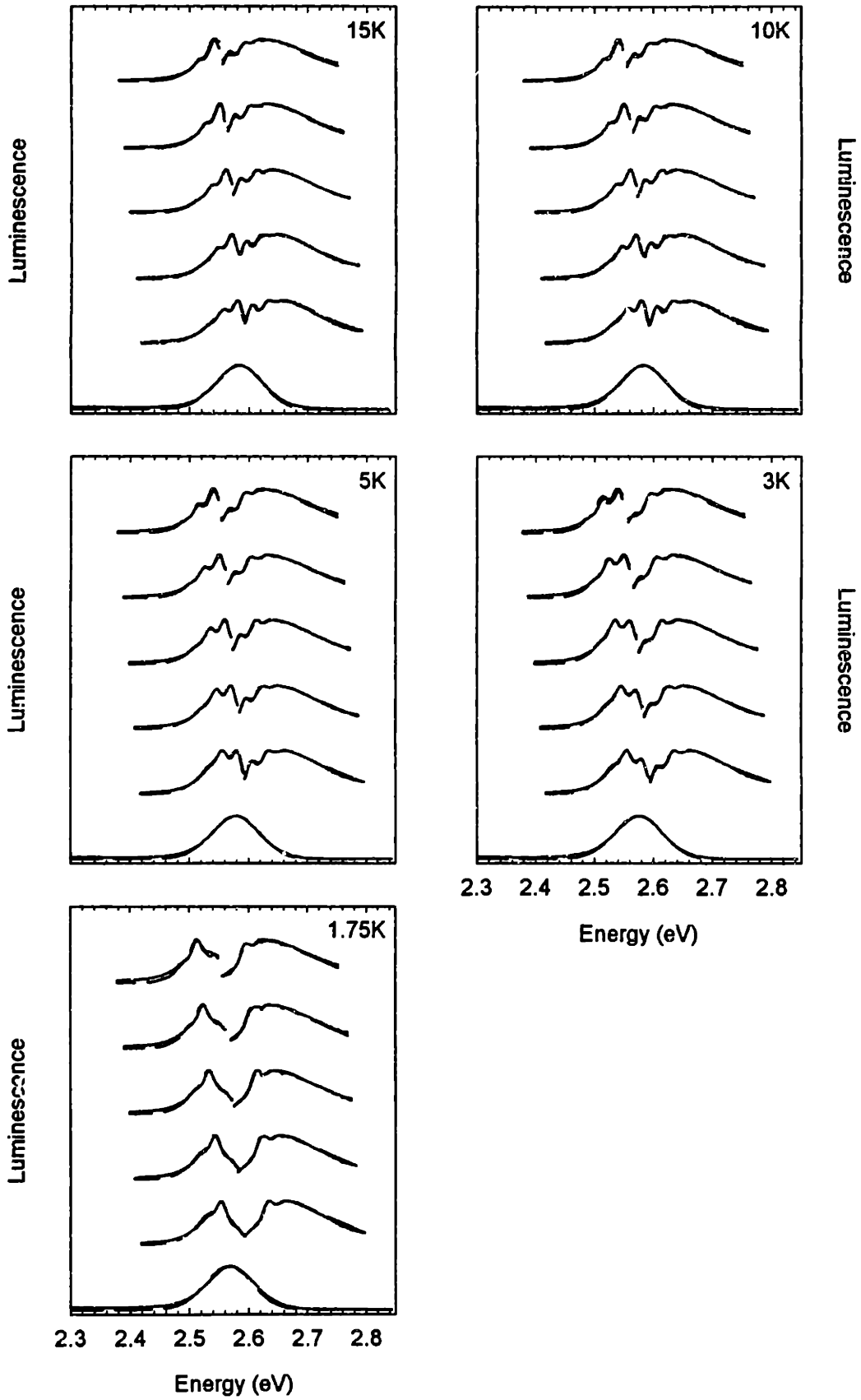

Figure 6-12: Fitting results for the undoped sample. The fit considers the effective absorption and emission lineshape which best accounts for the experimental FLN/PLE/PL data taken over five excitation/emission positions.

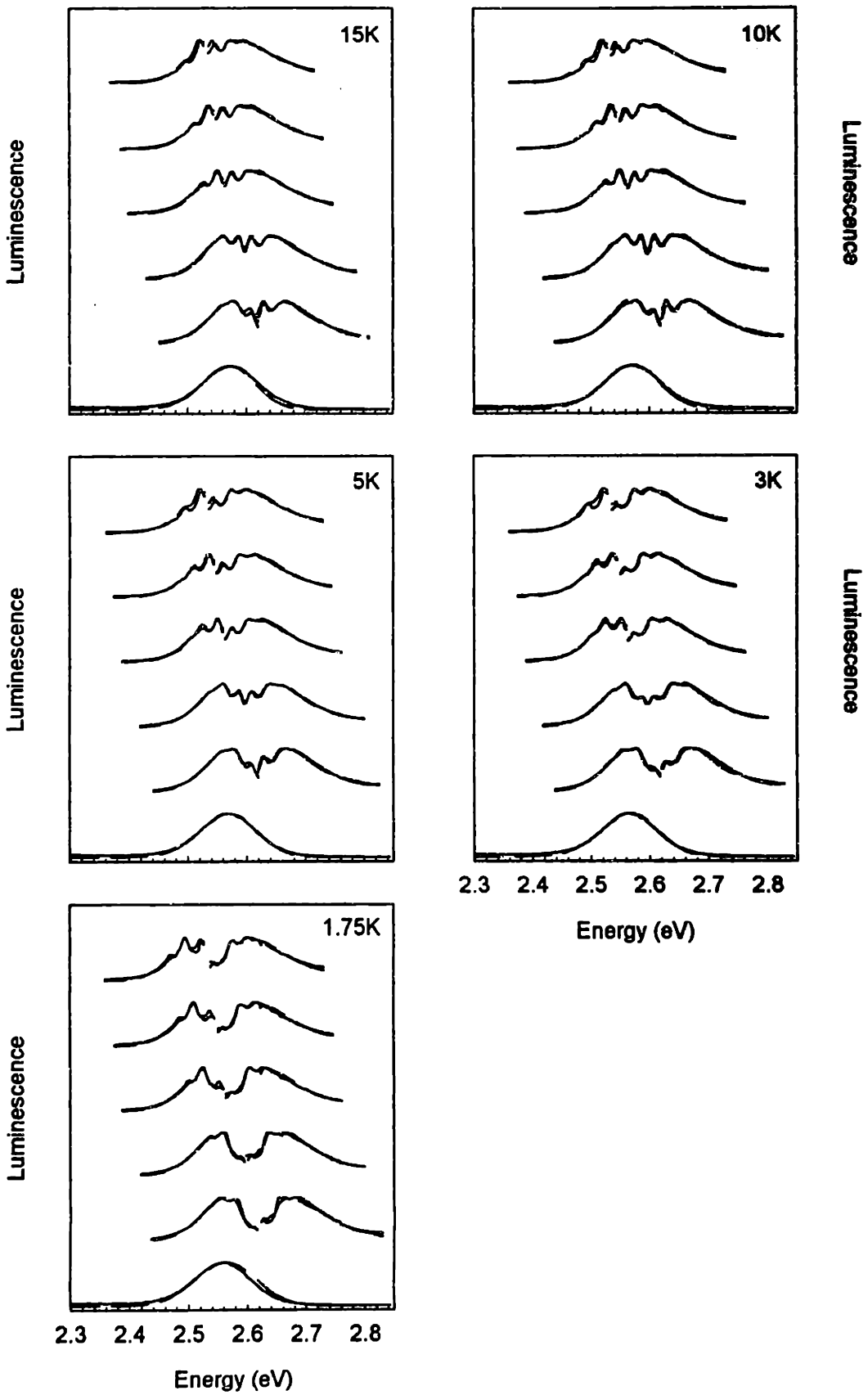

Figure 6-13: Fitting results for the doped sample. The fit considers the effective absorption and emission lineshape which best accounts for the experimental FLN/PLE/PL data taken over five excitation/emission positions.

Figure 6-14 (a) is a depiction of the five fine structure states. Optically active states are shown by solid lines and optically passive states by dashed lines. An interesting consequence of the theory is that it predicts that the exciton ground state is an optically passive dark exciton. Transitions to and from this state are formally spin forbidden in the electric dipole approximation.

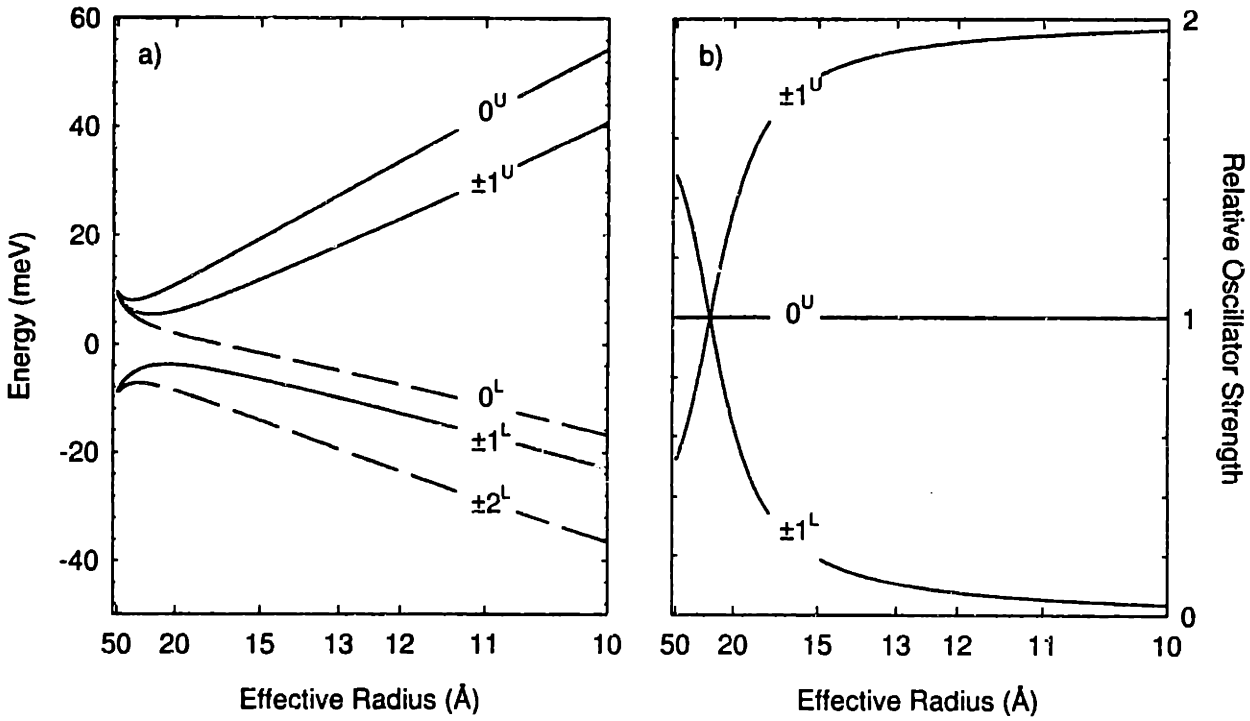

Figure 6-14: (a) Predicted band edge fine structure of the $1S_{3/2}1S_e$ exciton. Each state is labeled by its angular momentum projection along the c axis of the nanocrystallite. The superscripts "U" and "L" refer to upper and lower to distinguish states with the same angular momentum projection. Optically active (bright) states are shown by solid lines and optically passive (dark) states by dashed lines. (b) Transition oscillator strengths of the three optically active fine structure states. The transition probability of the 0^U state is size independent.

The oscillator strengths of the three optically active fine structure states are shown in Figure 6-14 (b). All oscillator strengths are plotted relative to the 0^U state which has a size independent transition probability. The oscillator strength of the $\pm1^U$

transition is largest at small sizes and decreases with increasing size. The opposite is true for the $\pm 1^L$ state. This behavior is primarily a consequence of the electron-hole exchange interaction which becomes increasingly important as the size of the QD decreases. The effects of the exchange interaction are more prominent in small nanocrystallites due to the increased spatial localization of the electron and hole. In the absence of the crystal field splitting and shape asymmetry, the electron-hole exchange interaction creates a five-fold degenerate dark exciton with angular momentum $N = 2$. Crystal field and shape perturbations lift the degeneracy of the state, splitting it into its respective angular momentum projections, $|N_m| = 2$, $|N_m| = 1$, and $|N_m| = 0$. The state with projection $N_m = 1$ is optically active ($\pm 1^L$). Since the extent of the crystal field/shape splitting varies inversely with size (i.e. the crystal field/shape contribution is more prominent relative to exchange effects at larger sizes), the $\pm 1^L$ state has more optical character at large sizes. The transition probability of the $\pm 1^U$ state behaves in the opposite manner to conserve oscillator strength.

The fine structure model has been successful in explaining many of the unusual and controversial results surrounding the band edge emission of CdSe nanocrystallites, in particular, the size dependent Stokes shift and the unusually long radiative lifetime at low temperatures.[61, 63, 13] Recent experiments focused on intentionally modifying the surface to see whether this affects the band edge emission support the fine structure model. No surface dependence is seen in the energetics of the "resonant" and "non-resonant" emission.[66, 34] Nanocrystallites passivated with different organic and inorganic ligands all show the same resonant and non-resonant Stokes shift, strongly suggesting that the emitting state is not surface related. This addresses

one of the long standing questions in the field as to whether the band edge emission of CdSe QDs originates from shallow surface states.

The fine structure model explains the band edge luminescence in terms of emission from an exciton ground state with angular momentum projection $|N_m| = 2$. This accounts for the long radiative lifetimes as transitions into and out of this state are formally spin forbidden in the electric dipole approximation. Transitions involving the dark exciton require the assistance of phonons (or another mechanism) to account for the excess angular momentum. The Stokes shift and the discrepancy between the magnitudes of the resonant and non-resonant shifts are also resolved by the theory. The resonant Stokes shift is highly size dependent and ranges from 2 meV at large sizes (appx. 30 Å radius) to 20 meV at small sizes (appx. 10 Å radius).[34] The non-resonant Stokes shift is also size dependent and ranges from 20 meV at large sizes to over 100 meV at small sizes.[34] The magnitude of the non-resonant Stokes shift is unusually large based on values of the resonant Shift because it should be possible to reproduce the non-resonant shift by convoluting the line narrowed emission (i.e. the resonant shift) with the intrinsic size distribution of the sample ($\sigma \sim 5\%$). Attempts to do so fail consistently, giving non-resonant shifts much smaller than that actually measured.[10]

The model explains the resonant Stokes shift in terms of the energy difference between the first optically active fine structure state, $\pm 1^L$, and the final emitting state, ± 2 (see Figure 6-13). The non-resonant Stokes shift, determined by comparing the peak of the first absorption feature and the peak of the full luminescence,

[10]See Chapter 3 for a more thorough discussion of this effect.

is also explained by the band edge fine structure. Since there are three optically active fine structure states, comparing the peak of the (inhomogeneously broadened) first absorption feature to the peak of the emission is analogous to comparing the mean energy of three optically active fine structure states ($\pm 1^U$, $\pm 0^U$, and $\pm 1^L$) with the position of the exciton ground state (± 2). The magnitude of the resonant and non-resonant Stokes shifts predicted by theory are in excellent agreement with experimental results. See Chapter 3 for more details.

Another key achievement of the fine structure model is that it explains the behavior of the band edge luminescence in the presence of an external magnetic field. This has long been a puzzling result because it is observed is that as the field strength increases, both the radiative lifetime and Huang-Rhys parameter decreases.[117, 13] The dark exciton model explains the field dependent results in the following fashion. There are five fine structure states, of which three are optically active and two are optically passive. Since the nanocrystallites show no preferred orientation in the sample (i.e they are randomly oriented) the external magnetic field acts to mix different fine structure states. The mixing occurs mainly when the nanocrystallite is oriented with its c axis perpendicular to the direction of the external field, and to a lesser extent when the alignment is less than perfect ($\theta \neq 90^\circ$).[11] Mixing of the dark exciton with other nearby bright states gives it optical character and lessens the strictness of the transition probabilities. Radiative recombination to the ground state becomes more probable and is observed as a decrease in both the Huang-Rhys parameter and the luminescence lifetimes.

[11] θ is the angle between the polarization vector of the light and the c axis of the nanocrystallite. No mixing occurs when $\theta = 0$ and the QD is oriented // to the external field.

Experiments on doped nanocrystallites should show essentially the same behavior as QDs in the presence of an external magnetic field. We expect that the exchange field between the manganese d electrons and the photogenerated electron and hole will behave in a similar fashion to a large magnetic field with effective intensities on the order of several kilogauss or even several Tesla. Results from temperature dependent FLN/PLE measurements are in qualitative agreement with this picture. However, rather than vary the magnetic field strength, we change the temperature. This is because thermal fluctuations of both the manganese and electron-hole spin orientation are dictated by kT. Fluctuations in the spin orientation mitigate the effects of the exchange interaction lessening the effective exchange field. At high temperatures ($\sim$ 10-15 K) we simulate low field conditions. There is little mixing of states and transitions from the Dark exciton to the ground state are less probable. We experience long lifetimes and a large Huang-Rhys parameter. At low temperatures ($\sim$ 1.75 K) kT is small and the mixing is strongest. We expect and see shorter lifetimes and smaller Huang-Rhys values.

Figure 6-15 shows results from the fitting procedure for undoped nanocrystallites. We study small QDs because exchange or dark exciton effects are expected to be largest in the smallest nanocrystallites.[63, 64] The fitting results show that there is little or no change in the absorption of the QDs. The luminescence, however, shows that with decreasing temperature the Huang-Rhys parameter increases. This is a dramatic change that occurs over the course of a few Kelvin or approximately 0.6 meV in kT.

Figure 6-16 shows fitting results from the doped sample. As the temperature

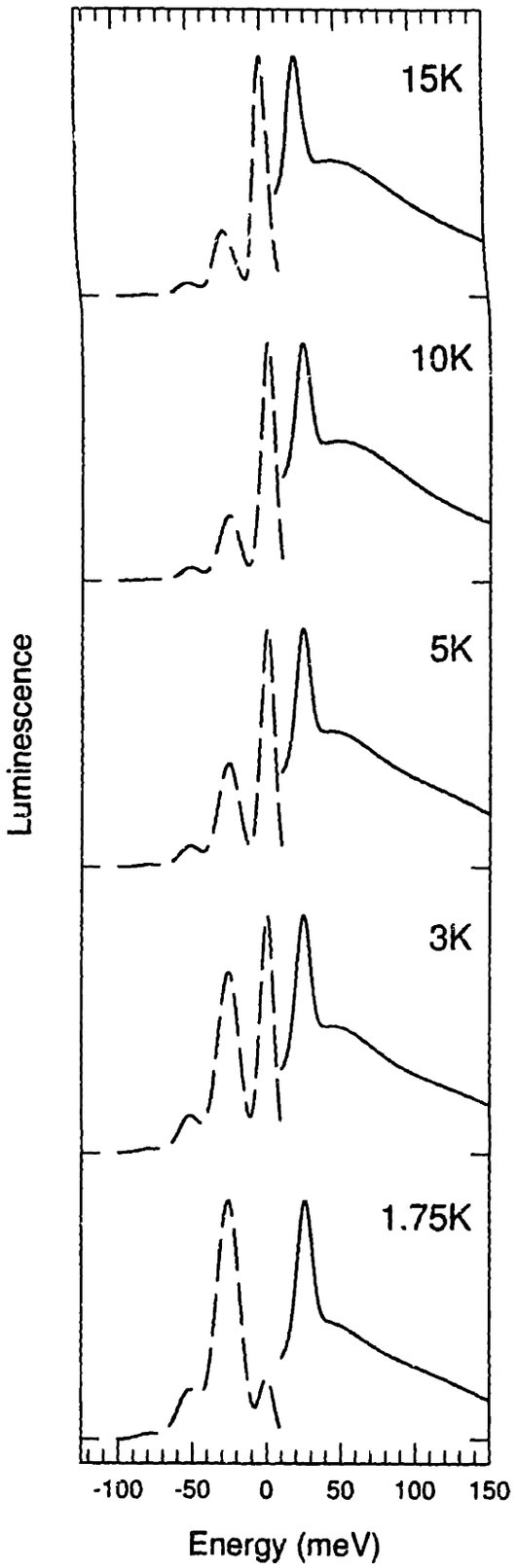

Figure 6-15: Fitting results for the undoped sample. Solid lines are the extracted absorption lineshape and dashed lines are the emission.

decreases, something very interesting happens. The emission shows no increase in the Huang-Rhys parameter. It is fairly constant over the full range of temperatures. We also see something remarkable in the absorption. A new state appears at low temperatures. This new transition has never been observed and we speculate that it is one of the five fine structure states predicted by theory.[64] Based on its position relative to the $\pm 1^L$ state, this new feature may be the 0^L exciton which is formally optically passive. The fits also indicate that a very broad feature appears in the absorption near the ZPL position. At this point it is difficult to say whether the feature is real or just an artifact of the fit but its proximity to the position of the "Dark" exciton or emitting state is startling.

Figure 6-17 shows the extracted temperature dependence of the Huang-Rhys parameter for doped and undoped samples. The undoped sample shows a dramatic upturn in the integrated phonon ration at temperatures near 3 K. The doped sample, however, shows a relatively constant Huang-Rhys parameter over the full range of temperatures. This behavior is consistent with the mixing of fine structure states through the *unaligned* exchange field of the paramagnetic impurity.

Figure 6-19 shows the behavior of the Stokes shift for the doped and undoped samples as a function of temperature. The Stokes shift of the undoped sample increases with decreasing temperature. The Stokes shift of the doped sample, however, decreases with decreasing temperature. This behavior can be understood in terms of the mixing of fine structure states. Mixing of the $\pm 1^L$ state with the neighboring 0^L state as well as with higher fine structure states ($\pm 1^U$, 0^U) causes the states to repel from each other forcing the $\pm 1^L$ and $\pm 2^L$ energy separation to decrease. This

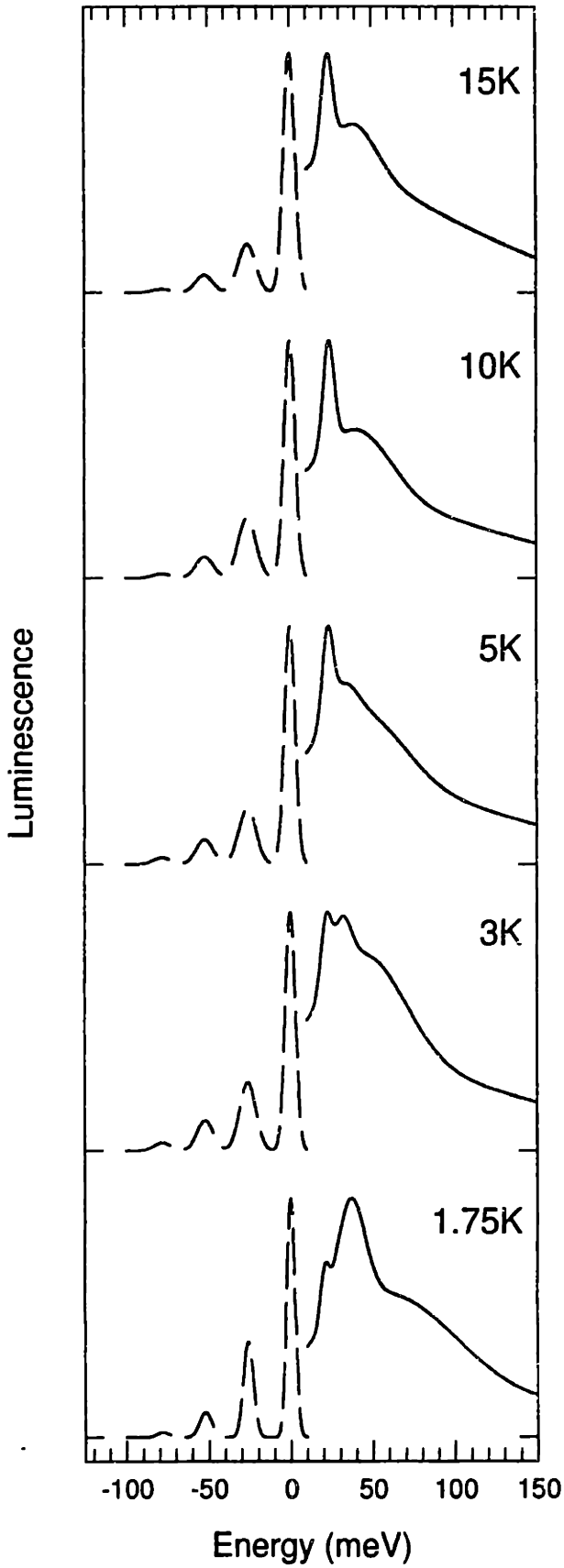

Figure 6-16: Fitting results for the doped sample. Solid lines are the extracted absorption lineshape and dashed lines are the emission.

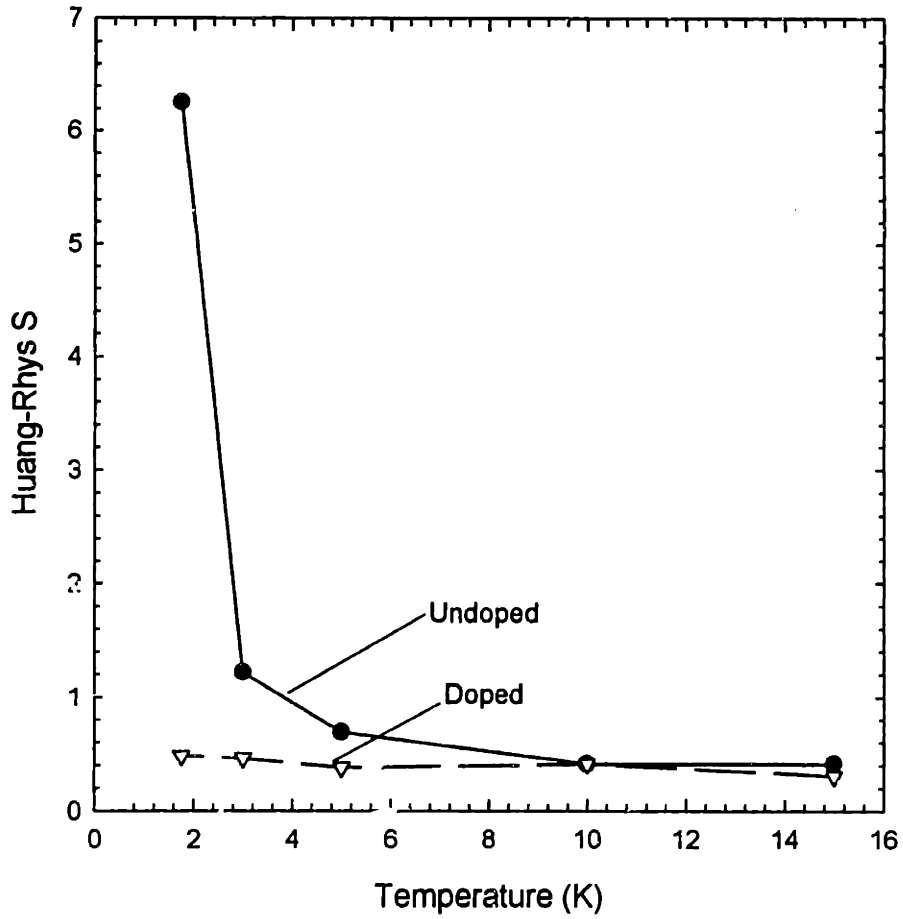

Figure 6-17: Huang-Rhys parameter for doped and undoped CdSe QDs. Results for the undoped sample are shown by the closed circles. Results for the doped sample are shown by the inverted open triangles. Solid lines are a guide to the eye. The Huang Rhys parameter for the doped sample is relatively constant over the full range of temperatures. This is consistent with the mixing of dark and bright states through the unaligned exchange field of the manganese impurity. The undoped sample, however, shows a characteristic upturn of the ratio in the region between 3 K and 1.75 K.

explains the smaller values of the resonant Stokes shift for the doped sample at low temperatures.

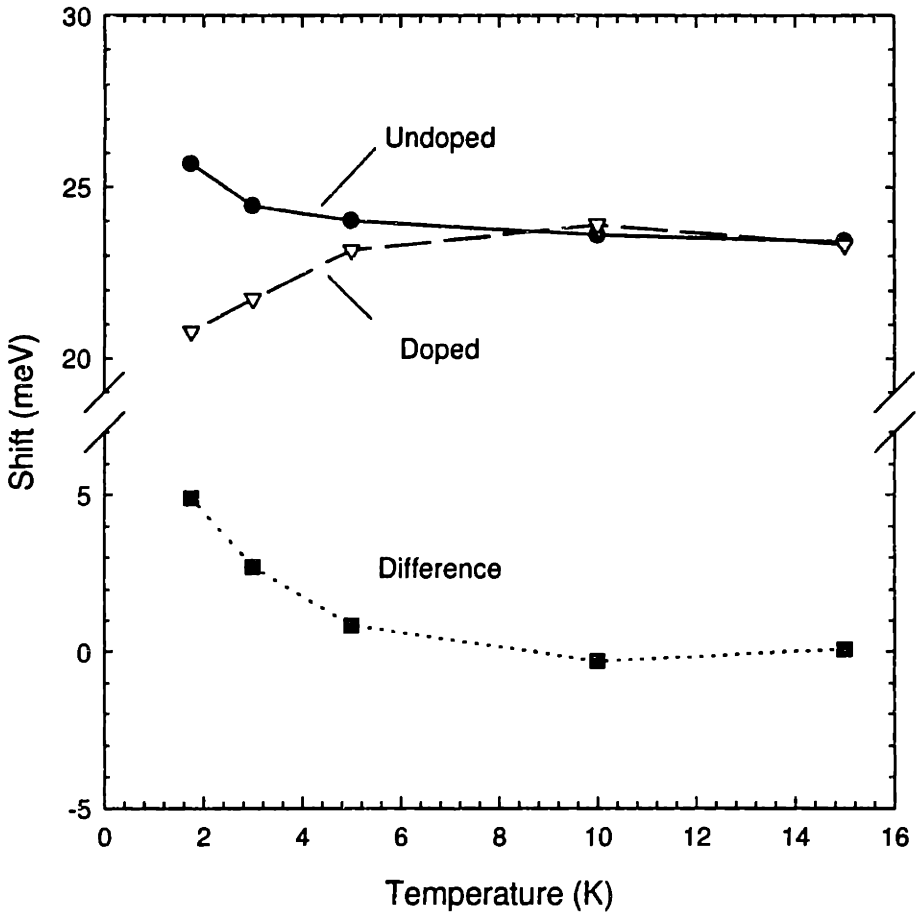

Figure 6-18: Temperature dependent Stokes shift for doped and undoped CdSe QDs. Shifts for the undoped sample are shown by closed circles. Shifts for the doped sample are given by inverted open triangles. Solid lines are a guide to the eye. The difference between the magnitude of the doped and undoped shifts is shown by closed squares. The undoped Stokes shift shows a characteristic increase between 3 K and 1.75 K. The doped sample, however, decreases between 5 K and 1.75 K.

Figure 6-18 shows the behavior of the $\pm 1^L$ oscillator strength of doped and undoped samples as a function of temperature. The graph plots the results of the fitting procedure. In the undoped sample, the $\pm 1^L$ oscillator strength increases with decreasing temperature. The doped sample, however, has a $\pm 1^L$ oscillator strength

which decreases with temperature. This can be understood in terms of the mixing of the various optically active and passive fine structure states. The $\pm 1^L$ state loses oscillator strength due to mixing with nearby dark states. The net offset between doped and undoped samples is an artifact of the fitting routine.[12]

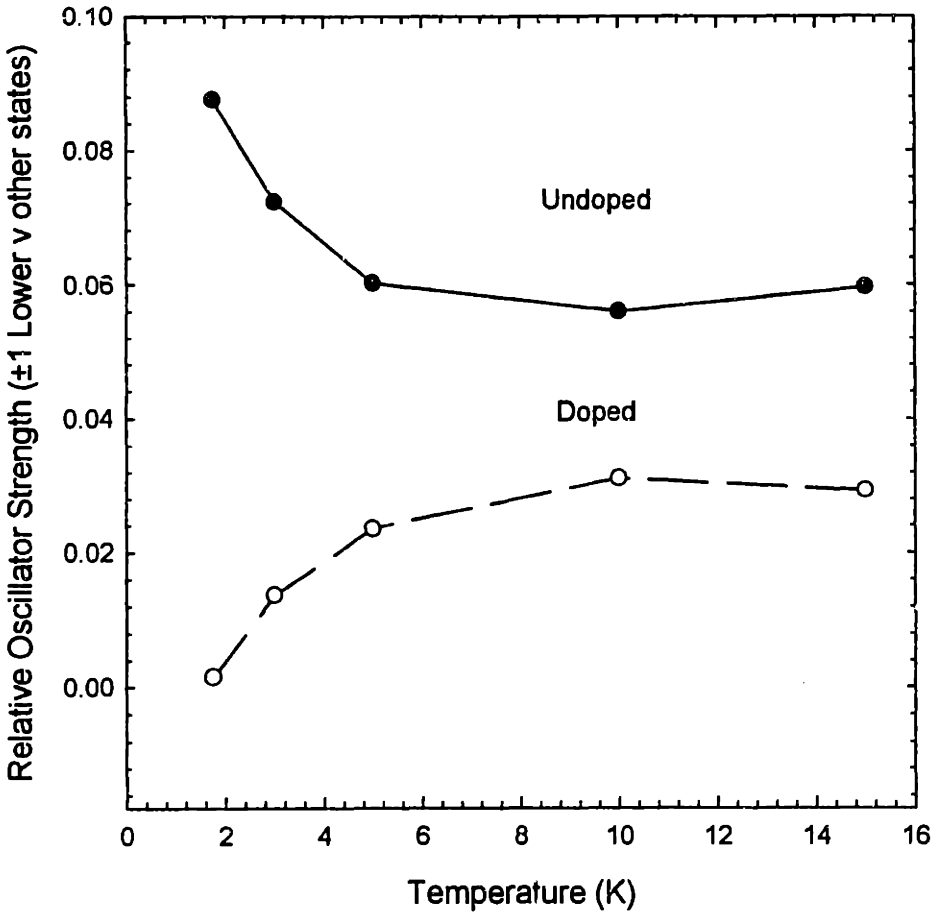

Figure 6-19: Relative oscillator strength of the $\pm 1^L$ state to all other optically active fine structure states. Results for the undoped sample are shown by closed circles. Results for the doped sample are shown by open circles. The undoped sample shows an increase in the oscillator strength based on the fits whereas the doped sample exhibits a decrease in oscillator strength with decreasing temperature.

[12]This offset arises because in the fit for the undoped sample only three states are considered. In the doped fits, however, four states were required to obtain good fitting results.

6.4 Conclusion

We have succesfully made $Cd_{1-x}Mn_xSe$ nanocrystallites which are highly crystalline and have narrow size distributions. EPR, WDS and ^{113}Cd NMR are all in qualitative/quantitative agreement and indicate incorporation of Mn^{+2} into the core lattice at doping levels of roughly one Mn atom per QD. Preliminary EPR measurements indicate that there are many paramagnetic impurities in unpurified (undoped) QDs. Careful ligand exchange experiments and sample purification show that these impurities are sensitive to the treatment of the nanocrystallites. A light enhanced EPR signal is also observed which may or may not have significant implications for the interpretation of optical experiments on undoped CdSe QDs.

Our FLN, PLE and PL experiments on doped and undoped QDs show interesting behavior from both types of samples. Doped QDs behave in a manner consistent with the presence of unaligned exchange fields due to the interaction of the electron/hole spin with the spins of the paramagnetic impurity. We observe a constant Huang-Rhys parameter and the emergence of a new state at very low temperatures. This transition may be the 0^L exciton predicted by a recent fine structure model that has succesfully accounted for many of the unusual properties of the band edge luminescence in CdSe QDs.

Chapter 7

Effects of Paramagnetic Impurities on the Band Edge Exciton Fine Structure

Temperature dependent fluorescence line narrowing (FLN) and photoluminescence excitation (PLE) experiments are conducted on Mn^{+2} doped CdSe nanocrystallites to see the effects of paramagnetic impurities on the optical properties of semiconductor QDs. A comparison with undoped samples shows that doped nanocrystallites behave in a manner consistent with the exchange induced mixing of fine structure states predicted by recent theoretical and experimental studies. These fine structure states are thought to arise from symmetry breaking perturbations to the QD electronic structure such as those arising from crystal field, shape and electron-hole exchange effects. We observe changes in the energy and oscillator strengths of the optical fine structure resulting in the activation of "dark" excitons. Apart from reinforcing

theoretical predictions, doped nanocrystallites are a means of studying the effects of magnetic fields on QD optical properties without resorting to large external fields. These materials are also potentially new systems where the competition between quantum size effects and spin-spin interactions can be investigated.

7.1 Introduction

Semiconductor nanocrystallites or quantum dots (QDs) are novel materials that have received considerable attention over the last few years.[1, 2, 3, 4] This interest stems from their potential use in light emitting diodes [5, 6, 7], optical switches, lasing materials [8] and single electron transistors [9, 10]. As materials, QDs are mesoscopic systems that span the physical size region between molecules and bulk compounds. They have sizes ranging from 10 to 100 Å in radius and exhibit interesting optical/electrical properties due to quantum confinement effects. These effects arise from the spatial confinement of excitations when the physical size of the QD is comparable to or smaller than the bulk exciton Bohr radius. To date a number of efforts have studied the optical properties of these materials.[15, 12, 11, 13, 14]

One longstanding question in the field of semiconductor QDs is the origin of the band edge luminescence. Attempts to study this have been hindered by the poor quality of samples which show predominately "deep trap" emission. Recently, high quality CdSe QDs have been synthesized allowing unprecedented studies of both the linear absorption and the band edge luminescence of the nanocrystallites. Up to ten excited states have been assigned and preliminary work has been conducted on identifying the origin of the band edge emission.[12, 63, 34] Issues of interest in the

emission are understanding the long radiative lifetimes ($\tau_r \sim 1\mu s$, 10 K) and the characteristic size dependent Stokes shift observed in both photoluminescence (PL) and FLN experiments.

Many unusual properties of the band edge luminescence have been explained by a current fine structure model which describes the band edge luminescence of CdSe QDs in terms of emission from an optically forbidden "dark" exciton.[63, 64] This accounts for both the long lifetimes and the size dependent redshift of the emission as transitions to and from this state are formally forbidden. The optical fine structure is thought to arise from symmetry breaking effects such as crystal field splitting, shape asymmetries and the electron-hole exchange interaction. This is described in more detail in Ref.[64].

While more is known about the band edge emission, some unusual observations remain unaddressed. One problem that has not been satisfactorily answered is why emission from the Dark exciton is observed from small sizes ($a \sim 10$ Å radius), at low temperatures (10 K) and in the absence of an external magnetic field. Based on experimental and theoretical considerations, the nearest optically active state is too far removed (~ 20 meV) for there to be any significant repopulation of nearby bright states. Phonon assistance (acoustic) to the recombination is also expected to be small at low temperatures. It is also inconsistent with the ultra-narrow linewidths seen in recent single QD luminescence experiments (FWHM on the order of 100 μeV).[164]

Adding to this, we find that the "resonant" Stokes shift is temperature dependent. At 1.7 K the resonant Stokes shift is larger than it is at 10 K by almost 2 meV. We also find that the Huang-Rhys S parameter or integrated ratio of one to zero phonon

lines in the FLN is temperature dependent. At low temperatures the zero phonon line of the emission is strongly suppressed relative to the one phonon line. At higher temperatures (10-15 K) the ratio reverses itself with the zero phonon line stronger than its first phonon replica. A tenfold decrease in the ratio is observed. Oddly, this behavior is similar to the effects of an external magnetic field on the Huang-Rhys S parameter.[117, 13] Under conditions of large external fields (10 T) and low temperatures (1.75 K), the zero phonon line is enhanced relative to the one phonon line. With decreasing magnetic field, the one phonon line grows in intensity and comes to dominate as in the zero field low temperature case. In effect, the magnetic field acts in the same manner as raising the temperature of the sample.

Efros has considered these results and has postulated that the low temperature, zero field, recombination occurs through a nuclear/paramagnetic spin flip assisted transition.[63][1] In this model, impurity spins interact with the spins of the photogenerated electron and hole acting as an effective magnetic field. Field strengths as large as 100 T are predicted depending on the identity of the impurity species (whether nuclear or electronic). This induced mixing of fine structure states gives oscillator strength to dark states and vice versa allowing radiative recombination from the dark exciton.

Nanocrystallites intentionally doped with manganese give us the opportunity to study the effects of paramagnetic impurities on the optical fine structure. In this sense, doped nanocrystallites are a means of testing the validity of the postulate. They may also provide a way of studying the effects of magnetic fields on the exciton

[1] Cd and Se both have nuclei that are spin active. ^{111}Cd and ^{113}Cd have spin 1/2 with natural abundances of 12.75% and 12.26% respectively. ^{77}Se also has spin 1/2 and is 7.58% abundant.

fine structure without having to resort to large external fields (> 10 T).

We perform temperature dependent FLN and PLE experiments on doped and undoped nanocrystallites to see the effects of the impurity interaction with photogenerated electrons and holes. Our results show that in the case of doped samples, the paramagnetic impurity acts to mix different fine structures states, causing shifts in the fine structure energies and a redistribution of oscillator strengths. These effects cause the appearance of a new state at slightly higher energies to the $\pm 1^L$ state and we speculate that this state is the 0^L exciton predicted by our fine structure model.[64]

7.2 Experiment

CdSe QDs are prepared according to the method described in Ref.[32] This synthesis produces high quality nanocrystallites with sizes ranging from 10 to 50 Å in radius. The QDs are passivated with the organic ligands trioctylphosphine oxide (TOPO) and trioctylphosphine selenide (TOPSe). The samples used in this study are size selected twice and subsequently passivated with pyridine. Following this, the samples are brought back to TOPO/TOPSe passivation. This surface treatment ensures that the undoped nanocrystallites are treated in the same fashion as doped ones (described below).

Doped nanocrystallites are prepared according to the method described in Ref.[220] This preparation is a variation of the original synthesis [32] where a single source manganese precursor is added to the Cd, Se injection solution. Thermal decomposition of the precursor occurs at elevated temperatures creating MnSe which is introduced into the growing nanocrystallite in concentrations of roughly 0.5 to 1 per QD. Following

the synthesis, the doped nanocrystallites are subjected to a number of purification (size selective precipitation) steps as well as ligand exchange to and from pyridine to remove excess manganese species not incorporated into the QD. Characterization of the impurity concentration is accomplished using a combination of ligand exchange and wavelength dispersive x-ray (WDS) spectroscopy. More details can be found in Ref.[220] and in Chapter 6.

Variable temperature fluorescence line narrowing (FLN) and photoluminescence excitation (PLE) experiments are conducted on both doped and undoped QDs using a SPEX Fluorolog-2 spectrofluorimeter. The entrance and exit slits of both double monochromators are set to 125 μm to give the system an optical resolution of approximately 1-2 meV. Samples are prepared by loading hexane solutions of the nanocrystallites between two sapphire flats separated by a 0.5 mm Teflon spacer. The absorbance of the samples is kept close to one to provide enough light for our experiments. The high optical density is necessary because the surface treatment of the nanocrystallites substantially decreases the quantum yield (QY) of both doped and undoped samples.

The FLN experiment is conducted by choosing five energies over the full luminescence spectrum of the nanocrystallites. The sample is then excited sequentially at each of these positions and the emission detected with the emission spectrometer/PMT. The PLE experiment follows in a similar fashion. In this experiment, however, the detector position is fixed and the excitation monochromator scanned to the blue of the emission position to reproduce the absorption profile of the nanocrystallites. The detector energy is determined by choosing the peak of the zero phonon

line (ZPL) in the line narrowed spectra. In this way, the absorption and emission of five different QD sizes is determined using one sample.

Temperatures as low as 3 K are achieved by applying vacuum to a helium vapor flow cryostat. Superluid helium is obtained by immersing the sample in liquid helium and applying vacuum.

7.3 Results

Results from temperature dependent FLN/PLE experiments on doped and undoped samples are shown in Figures 7-1 and 7-2. Five temperatures between 15 K to 1.75 K are studied (15, 10, 5, 3, 1.75 K). At each temperature, FLN and PLE scans are taken at different points along the full luminescence profile of the nanocrystallites in order to study the response of five "effective" QD sizes. The FLN (leftmost spectra) and PLE (rightmost spectra) pairs are offset for clarity. The full luminescence is shown at the bottom of each graph.

There are several qualitative differences in the doped and undoped spectra such as slight changes in the phonon ratio of the absorption and emission. However, it is difficult to distinguish differences arising from probing QDs of slightly different sizes or differences in the effective size distribution of each sample. Another complication arises from the fact that the FLN data is contaminated with PLE information and vice versa. This is due to the residual size distribution of the sample. Different sizes absorb and emit in different spectral positions and therefore scans conducted at higher energies increasingly contain contributions from *both* small and large sizes.

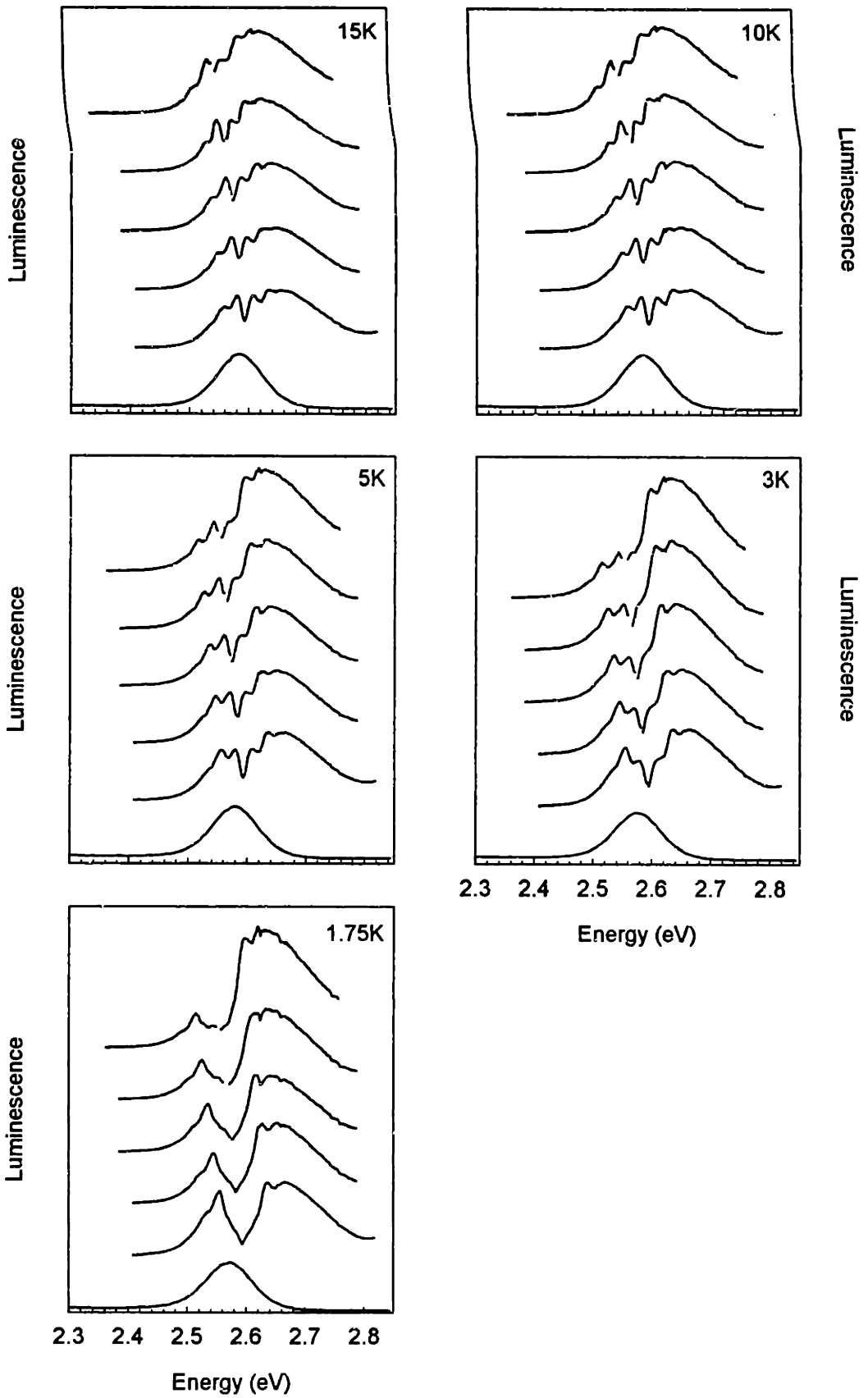

Figure 7-1: Raw FLN/PLE data for the undoped sample. Five temperatures ranging from 15 K to 1.75 K are studied. FLN spectra are on the left moving to lower energies and PLE spectra are on the right moving to higher energies.

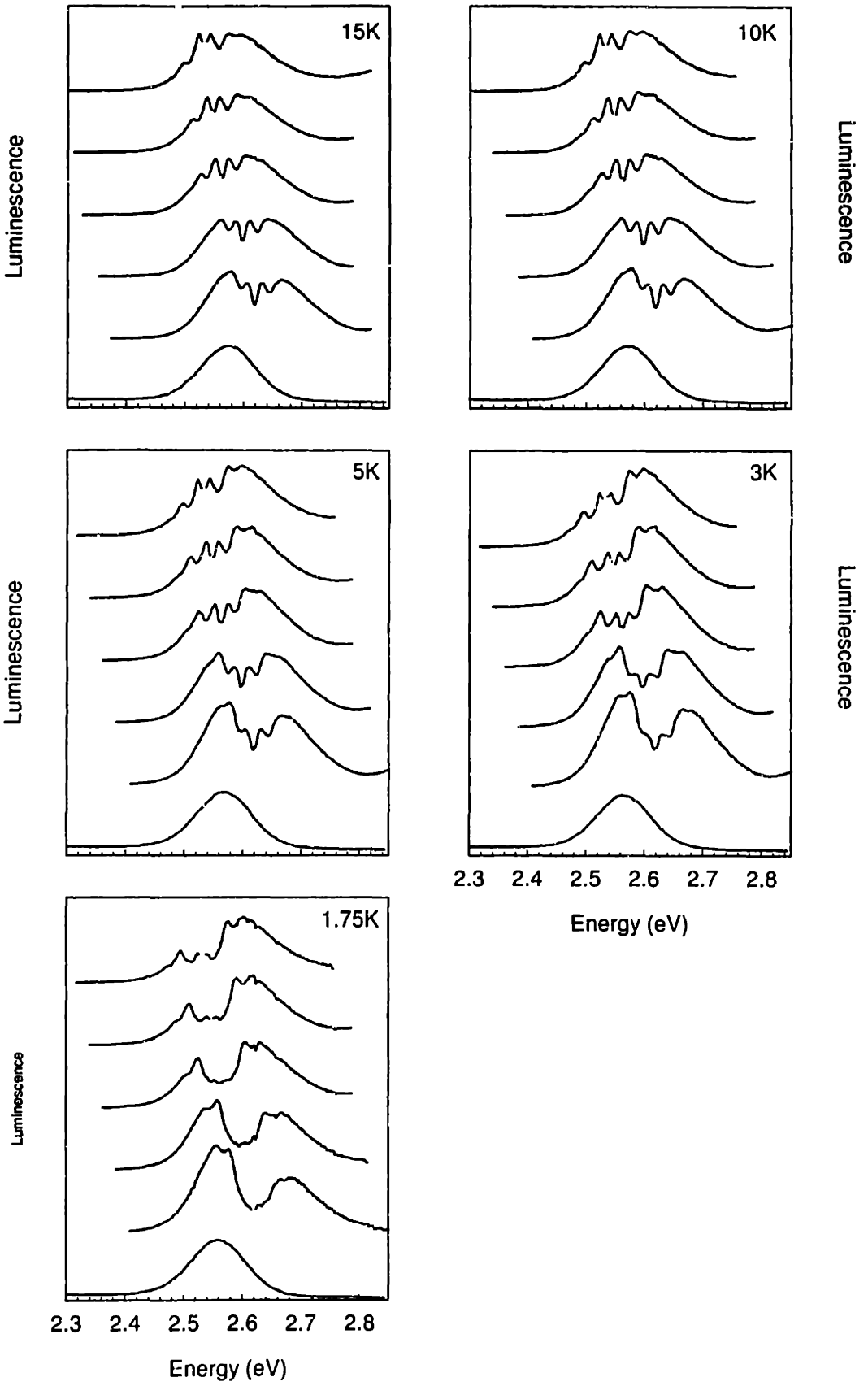

Figure 7-2: Raw FLN/PLE data for the doped sample. Five temperatures ranging from 15 K to 1.75 K are studied. FLN spectra are on the left moving to lower energies and PLE spectra are on the right moving to higher energies.

The contamination in the absorption and emission is given by the convolution integral

$$\begin{matrix} E_{FLN}(\nu_{em})|_{\nu_{exc}} \\ E_{PLE}(\nu_{exc})|_{\nu_{em}} \end{matrix} = C \int A(\nu_{exc}, \nu') E(\nu_{em}, \nu') D(\nu', \nu_0) d\nu' \tag{7.1}$$

where $D(\nu', \nu)$ is a normalized Gaussian that represents the sample's residual size distribution. E_{FLN} is the effective lineshape of the line narrowed emission and E_{PLE} is the absorption lineshape. To reproduce the FLN experiment we fix the excitation position, ν_{exc}, and vary the emission frequency, ν_{emm}. The PLE experiment follows in a similar fashion but now the emission position, ν_{emm}, is kept fixed and the excitation frequency, ν_{exc}, is varied to map out the effective absorption lineshape.

To avoid problems associated with the distribution, we employ a non-linear least squares fitting procedure to extract an effective "single" QD absorption/emission lineshape which best accounts for experimental data at each temperature. The absorption is modeled by the sum of three optically active states and their phonon replicas. Likewise, the emission is modeled by a corresponding zero phonon line and accompanying phonon replicas.

$$A(\nu_{exc}, \nu') = \sum_{l=1}^{3} \sum_{m=0}^{2} \frac{C_l}{\sqrt{2\pi\gamma_{l,m}^2}} \frac{(S_a)^m}{m!} \exp\left(-\frac{[\nu_e xc - (\nu' + \Delta_l + m\omega_{LO})]^2}{2\gamma_{l,m}^2} \right) \tag{7.2}$$

$$E(\nu_{em}, \nu') = \sum_{n=0}^{4} \frac{1}{\sqrt{2\pi\gamma_n^2}} \frac{(S_e)^n}{n!} \exp\left(-\frac{[\nu_{em} - (\nu' - n\omega_{LO})]^2}{2\gamma_n^2} \right) \tag{7.3}$$

In the absorption, the sum is taken over all optically active states, l, and all phonon replicas, m. In the emission, the sum is over all phonon replicas, n, separated by the LO phonon frequency, ω_{LO}=26 meV. C_l is the oscillator strength of the absorbing

states, ν_{exc} (ν_{emm}) is the excitation (emission) position, ν' is the position of the zero phonon line in the emission, Δ_l is the size dependent Stokes shift between absorbing and emitting states, $S_{a(e)}$ is the absorption (emission) coupling constant with values 0.41 and 0.1 respectively. These numbers are consistent with recent PLE experiments on the band edge fine structure of the nanocrystallites.[118] Fitting results are shown in Figures 7-3 and 7-4.

Our approximation is based on a recent fine structure model which considers several symmetry breaking perturbations that lift the degeneracy of the lowest excited state in CdSe QDs. The fine structure model considers contributions from crystal field splitting, shape asymmetries and the electron hole exchange interaction. In the bulk, the crystal field is responsible for a small (0.13 meV) singlet-triplet splitting of the lowest excited state. The shape asymmetry is also important because the nanocrystallites are not perfectly spherical but are rather slightly prolate.[2] Finally, the electron-hole exchange interaction is important because of the increased overlap of the electron and hole wavefunctions in low dimensional materials.[86, 162, 120, 163]

Theory predicts that rather than an eightfold degenerate exciton ground state we have five fine structure states. These states are labeled by their angular momentum projection along the "c" or unique axis of the nanocrystallites. The exciton ground state is predicted to be a two-fold degenerate fine structure state with angular momentum projection $|N_m| = 2$. This state is optically passive and behaves essentially like a triplet state as transitions to and from it are forbidden in the electric dipole approximation. There are also two two-fold degenerate states with angular momen-

[2]This is based on extensive TEM and SAXS measurements. See Appendix B

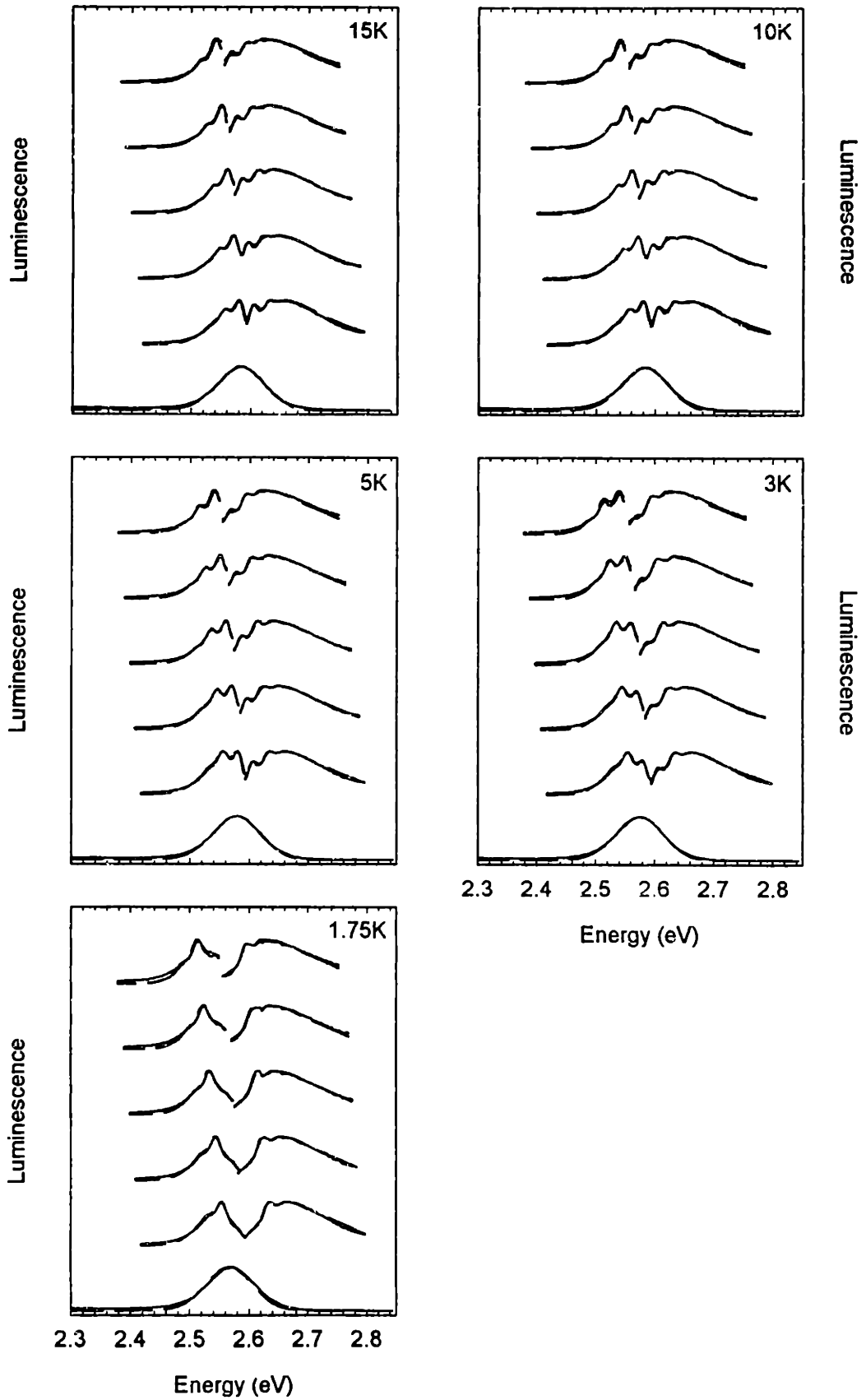

Figure 7-3: Fitting results for the undoped sample. The fit considers the effective absorption and emission lineshape which best accounts for the experimental FLN/PLE/PL data taken over five excitation/emission positions.

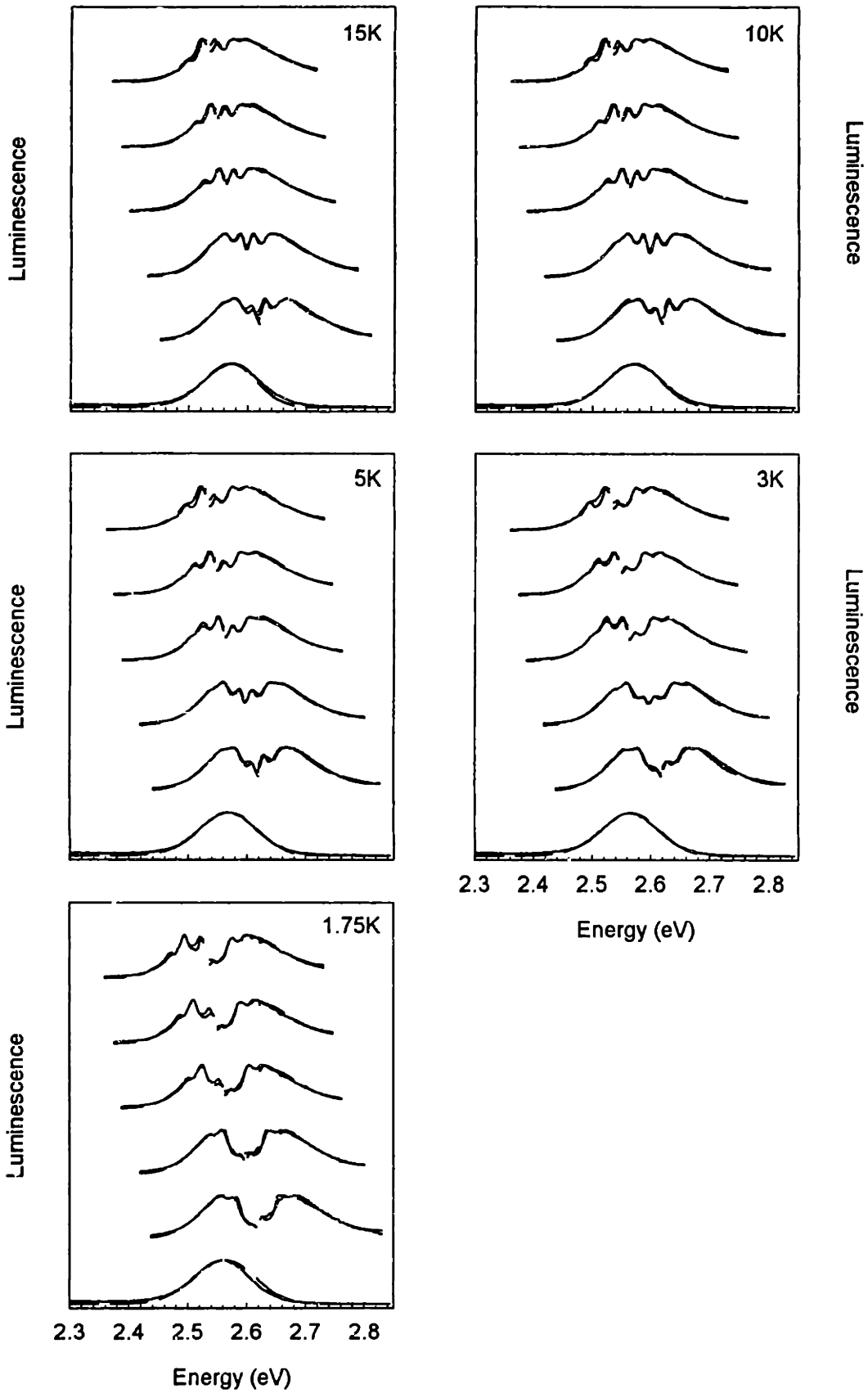

Figure 7-4: Fitting results for the doped sample. The fit considers the effective absorption and emission lineshape which best accounts for the experimental FLN/PLE/PL data taken over five excitation/emission positions.

tum projection $|N_m| = 1$ and two states with projection $|N_m| = 0$. Three of the five states are optically active and two are optically passive. This is shown in Figure 7-5 as solid and dashed lines respectively.

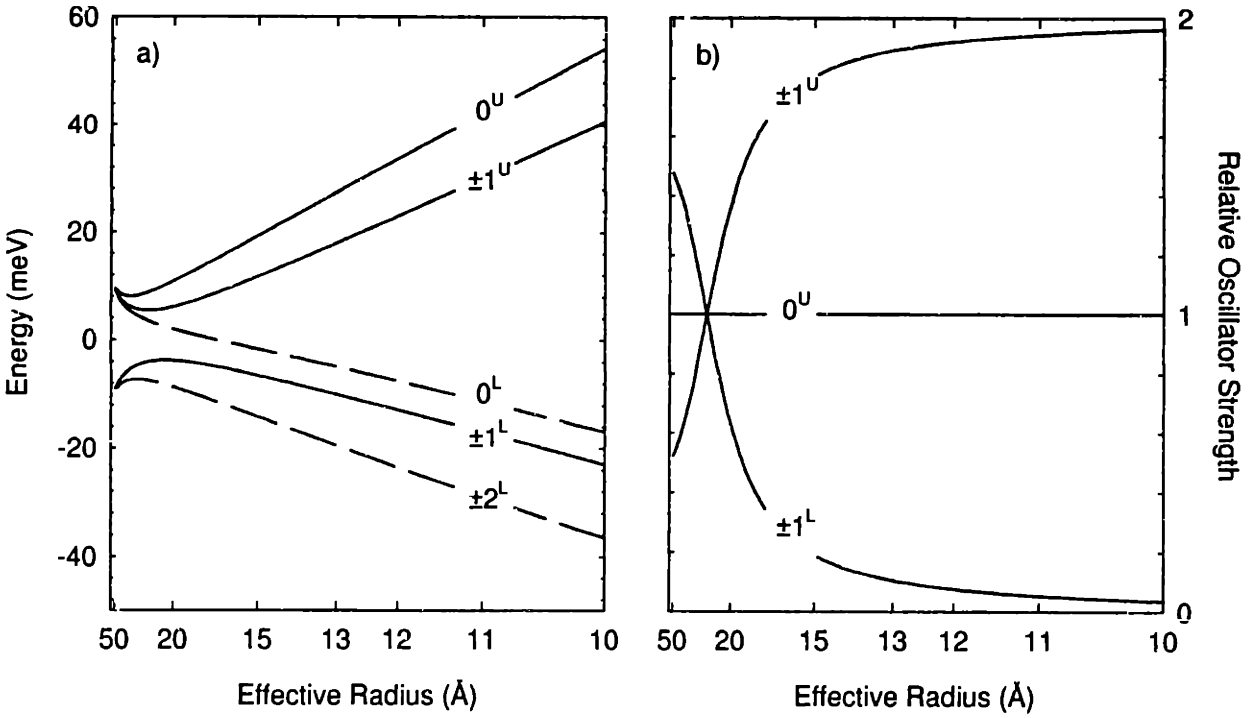

Figure 7-5: (a) Predicted band edge fine structure of the $1S_{3/2}1S_e$ exciton. Each state is labeled by its angular momentum projection along the c axis of the nanocrystallite. The superscripts "U" and "L" refer to upper and lower to distinguish states with the same angular momentum projection. Optically active (bright) states are shown by solid lines and optically passive (dark) states by dashed lines. (b) Transition oscillator strengths of the three optically active fine structure states. The transition probability of the 0^U state is size independent.

A phenomenological suppression/enhancement coefficient is included in both the emission and absorption fits to account for possible changes in the lineshape with temperature. For instance, in the FLN of undoped QDs we observe that the Huang-Rhys parameter increases with decreasing temperature.[117, 13] Similarly, to account for possible changes in the oscillator strength of the first absorbing state ($\pm1^L$) we

include another floating parameter in the absorption fit.

Figures 7-6 and 7-7 summarize the results of the fitting procedure. An effective single QD absorption/emission lineshape is extracted from the fit and is plotted as a function of temperature. The fitting results for the undoped sample show that there is little change in the absorption of the sample with decreasing temperature. In the luminescence, there are dramatic changes in the Huang-Rhys parameter or integrated ratio of the one to zero phonon lines. This effect is highly reproducible and has been seen previously.[117] Interestingly, these changes occur rather suddenly between 3 K and 1.75 K. This is less than 1 cm^{-1} or 0.125 meV in energy making it unlikely that any of these effects arise from the repopulation of nearby bright excitons.

The doped sample shows much different behavior based on the fits. In the luminescence there do not appear to be large changes in the Huang-Rhys parameter. In fact, the ratio appears constant. In the absorption, something startling happens at low temperatures. A new state appears close to the position of the first optically active ($\pm 1^L$) state. This fine structure state has not been observed before and based on its position relative to the $\pm 1^L$ state we speculate that it is the 0^L dark exciton predicted by the fine structure model.[64]

We summarize the fitting results in the following three figures which show the temperature dependence of the Huang-Rhys S parameter, the resonant Stokes shift and the relative oscillator strength of the first optically active state.

Figure 7-8 describes the temperature dependence of the Huang-Rhys S parameter. The doped sample (inverted triangles) shows a relatively constant ratio over the full range of temperatures. This is consistent with the exchange induced mixing of

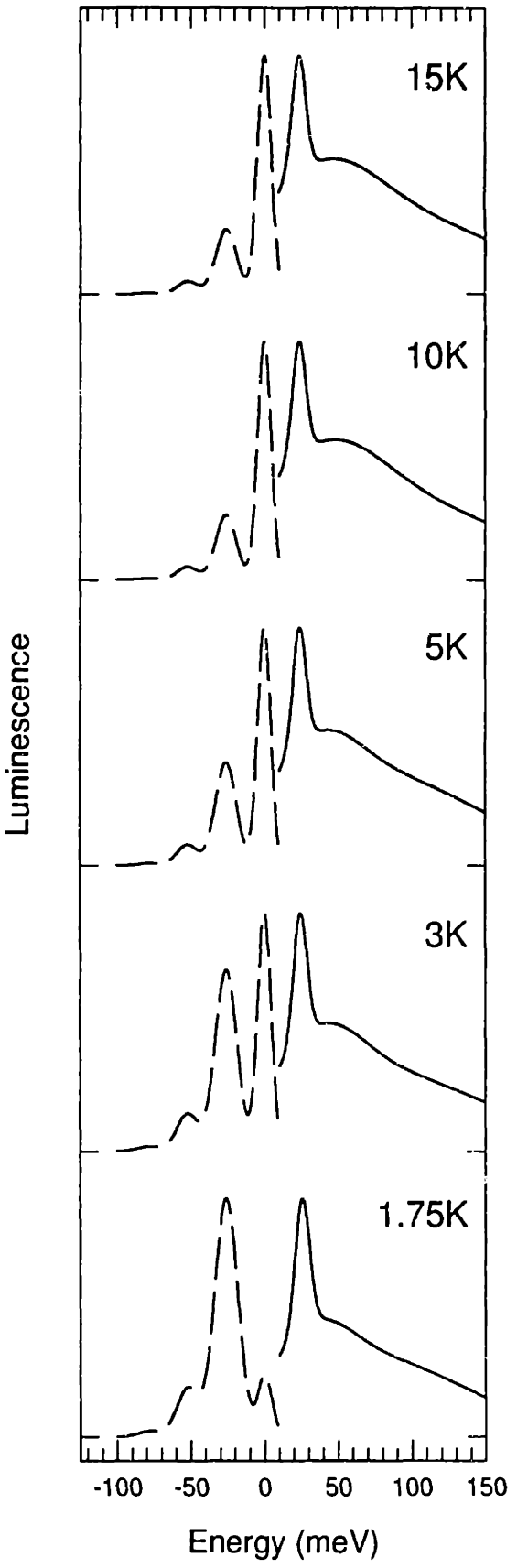

Figure 7-6: Fitting results for the undoped sample. Solid lines are the extracted absorption lineshape and dashed lines are the emission.

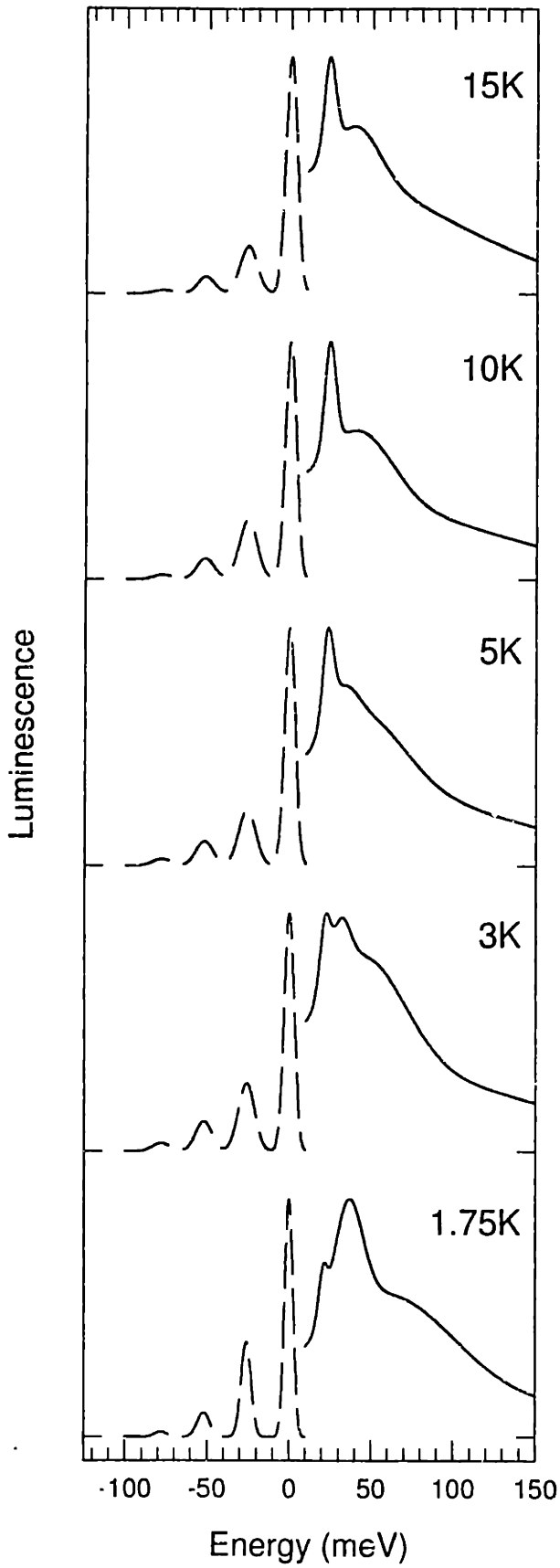

Figure 7-7: Fitting results for the doped sample. Solid lines are the extracted absorption lineshape and dashed lines are the emission.

dark and bright fine structure states where the ±2 emitting state gains oscillator strength from interactions with its three neighboring optically active states ($\pm 1^L$, $\pm 1^U$, 0^U). The undoped sample (solid circles), however, shows distinctly different behavior, especially in the region between 3 K and 1.75 K. There is a dramatic increase in the integrated phonon ratio.

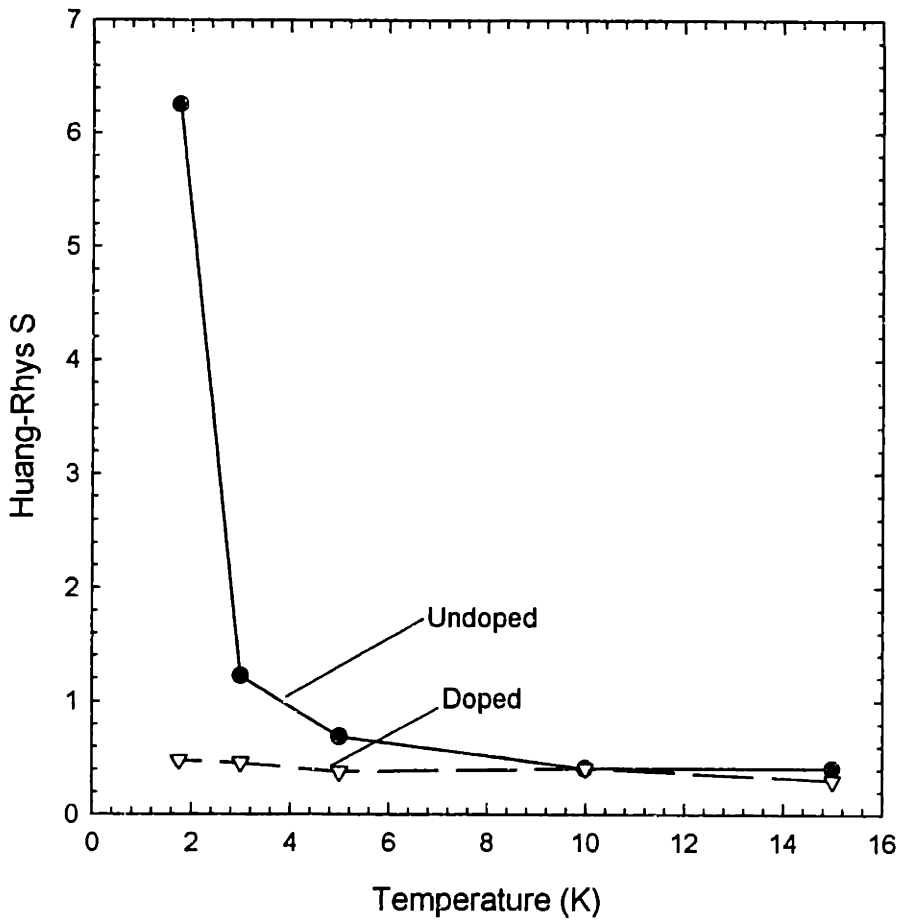

Figure 7-8: Huang-Rhys parameter for doped and undoped CdSe QDs. Results for the undoped sample are shown by the closed circles. Results for the doped sample are shown by the inverted open triangles. Solid lines are a guide to the eye. The Huang Rhys parameter for the doped sample is relatively constant over the full range of temperatures. This is consistent with the mixing of dark and bright states through the unaligned exchange field of the manganese impurity. The undoped sample, however, shows a characteristic upturn of the ratio in the region between 3 K and 1.75 K.

Assuming a mixing of fine structure states, we expect concomitant changes in

the energies of the different excitons. These are potentially second order corrections although first order effects and the role of spin flips should not be discounted. Figure 7-9 shows the results for the resonant Stokes shift in both doped and undoped samples. The doped sample (inverted triangles) shows a characteristic decrease of the resonant shift at low temperatures. The undoped sample (solid circles), however, shows an increase in the resonant shift with decreasing temperature. Again we find that the behavior of the doped sample is consistent with the exchange induced mixing of fine structure states. Interactions of both the dark exciton (± 2) and the first optically active exciton ($\pm 1^L$) with higher lying levels causes the states to repel from each other. Since the $\pm 1^L$ state interacts with a greater number of fine structure states ($\pm 1^U$, 0^L, 0^U), the net energy separation between it and the ± 2 state decreases. This is responsible for the downturn of the resonant Stokes shift at low temperatures. At higher temperatures there is more thermal energy causing spin fluctuations which mitigates the exchange interaction between the impurity and the photogenerated electron or hole. This accounts for the increase in the resonant Stokes shift at higher temperatures as state to state mixing is minimized. For comparison purposes, the difference between the resonant Stokes shift of doped and undoped samples is given by the closed squares.

Another consequence of the fine structure mixing is a change in the relative oscillator strength of both dark and bright states. Figure 7-10 shows extracted changes in the relative oscillator strength of the first optically active exciton ($\pm 1^L$) in doped and undoped nanocrystallites. The doped sample (open circles) shows a decrease of the $\pm 1^L$ oscillator strength with decreasing temperature. The undoped sample (closed

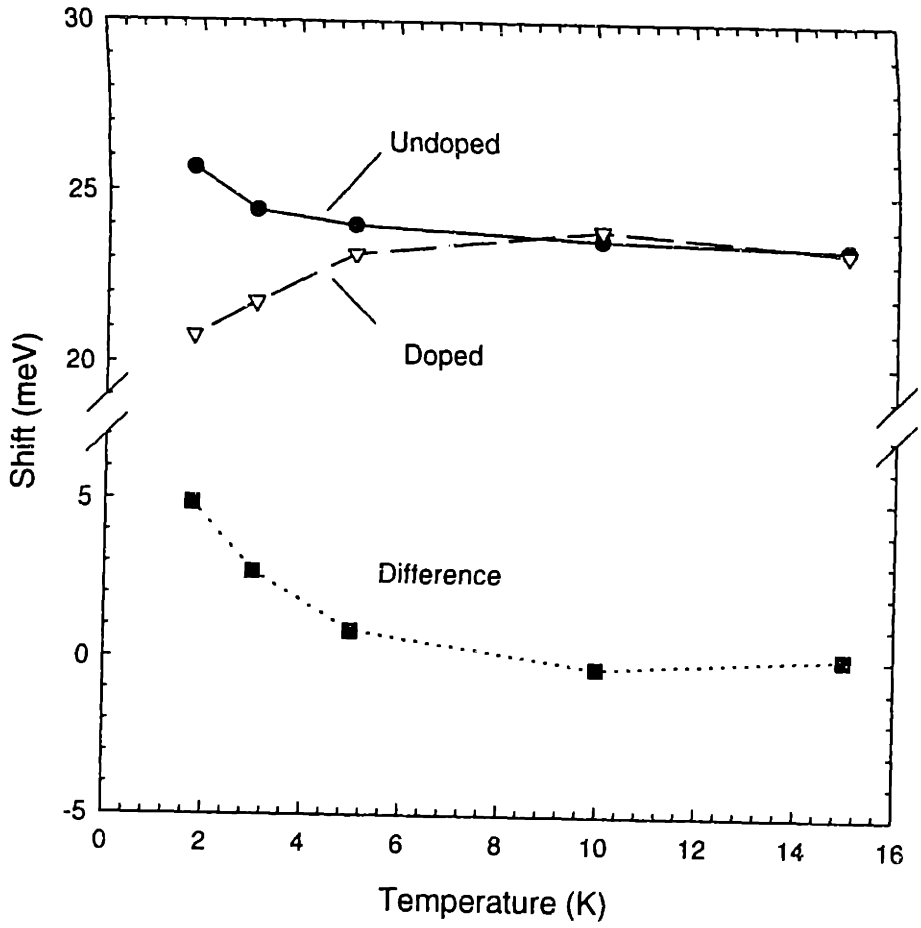

Figure 7-9: Temperature dependent Stokes shift for doped and undoped CdSe QDs. Shifts for the undoped sample are shown by closed circles. Shifts for the doped sample are given by inverted open triangles. Solid lines are a guide to the eye. The difference between the magnitude of the doped and undoped shifts is shown by closed squares. The undoped Stokes shift shows a characteristic increase between 3 K and 1.75 K. The doped sample, however, decreases between 5 K and 1.75 K.

Table 7.1: Table summarizing fitting parameters of Mn^{+2} doped sample

Temperature (K)	$\pm 1^L$ linewidth (meV)	Resonant Shift (meV)	Huang-Rhys Parameter	$\pm 1^L$ Osc. Strenght (%)
15	3.53	23.3	0.305	2.92
10	3.38	23.9	0.408	3.11
5	3.27	23.2	0.377	2.35
3	3.12	21.8	0.458	1.37
1.75	2.56	20.8	0.478	0.15

Table 7.2: Table summarizing fitting parameters of undoped sample

Temperature (K)	$\pm 1^L$ linewidth (meV)	Resonant Shift (meV)	Huang-Rhys Parameter	$\pm 1^L$ Osc. Strenght (%)
15	4.73	23.4	0.410	5.96
10	4.60	23.6	0.410	5.61
5	4.46	24.0	0.69[illegible]	6.03
3	4.60	24.5	1.220	7.22
1.75	4.88	25.7	6.256	8.76

circles) exhibits a characteristic upturn of the oscillator strength with decreasing temperature. This loss of oscillator strength in the doped sample is consistent with the appearance of a new state at slightly higher energies. Based on its position, this new state appears to be the optically passive 0^L exciton predicted by the fine structure model. It is difficult to say whether there is a concomitant increase in the oscillator strength of the ± 2 dark exciton but the fits do seem to indicate the appearance of a new state at low energies near the position of the ZPL in the emission. This is very speculative though. Growth of both new states come at the expense of the $\pm 1^L$ exciton which explains why its oscillator strength decreases with decreasing temperature.

Fitting results are summarized in Tables 7-1 and 7-2 for both doped and undoped samples.

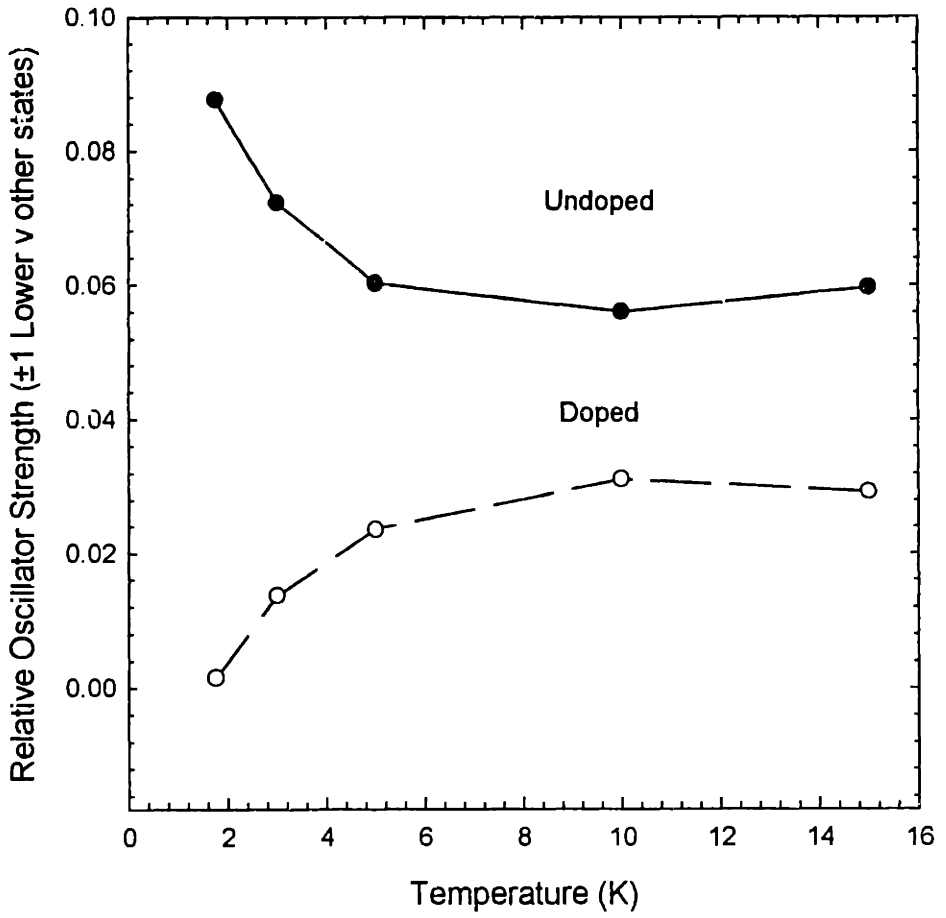

Figure 7-10: Relative oscillator strength of the $\pm 1^L$ state to all other optically active fine structure states. Results for the undoped sample are shown by closed circles. Results for the doped sample are shown by open circles. The undoped sample shows an increase in the oscillator strength based on the fits whereas the doped sample exhibits a decrease in oscillator strength with decreasing temperature.

7.4 Discussion

7.4.1 Doped Nanocrystallites

In a manner analogous to the effects of an external magnetic field, the spins of the manganese d electrons interact with the spins of the photogenerated electron and hole in the QD. This interaction behaves as an effective magnetic field which can subsequently act to mix different fine structure states in the linear absorption of the nanocrystallites.

The constant Huang-Rhys parameter, decrease of the Stokes shift and decrease of the oscillator strength with decreasing temperature can be explained in this manner. The dark exciton and the nearest bright exciton mix with each other and with higher lying states causing the observed changes in the energies and relative oscillator strengths.

Expressions describing the optical fine structure of CdSe nanocrystallites have been given in Ref.[64]. We use these wavefunctions and energies to describe the effects of the paramagnetic impurity in terms of second order perturbation theory. Without knowing the exact interaction between the electron and hole and the paramagnetic impurity we treat the interaction as an effective magnetic field. In this respect, the Hamiltonian describing the splitting and mixing of states is given by

$$\hat{H} = \frac{1}{2} g_e \mu_B \sigma H - g_h \mu_B K H \tag{7.4}$$

where g_e and g_h are the electron and hole g factors respectively, μ_B is the Bohr magneton, and K is the hole angular momentum operator. Values for the electron

and hole g factors have been determined before and are $g_e = 0.68$ and $g_h = -1.09$.[111, 112]

Using this Hamiltonian and the wavefunctions described in Ref. [64] we obtain all diagonal and off diagonal elements of an 8×8 perturbation matrix.[3] Expressions for the second order corrections to the fine structure energies are given below.

For the dark exciton with total angular momentum projection $N_m = 2$ we obtain:

$$\epsilon^{(2)}_{2,\pm 2} = \frac{\mu_B^2 B_\perp^2}{4}\left[\frac{(C^{+^2} g_e^2 + 3C^{-^2} g_h^2)}{\epsilon_2 - \epsilon_{1L}} + \frac{(C^{-^2} g_e^2 + 3C^{+^2} g_h^2)}{\epsilon_2 - \epsilon_{1U}}\right] \tag{7.5}$$

where the expression arises from the mixing of the dark exciton with the $\pm 1^U$ and $\pm 1^L$ fine structure states. In the expression μ_B is the Bohr magneton, $B_\perp = \sqrt{B_x^2 + B_y^2}$, g_e, g_h are the electron and hole g factors respectively and $C^\pm$ are size dependent coefficients described in Ref. [64]. ϵ_2 and $\epsilon_{1U,L}$ are the unperturbed energies of the interacting states.[64]

Corrections to the two states with angular momentum projection $|N_m| = 0$ are given below. Both states interact with the $\pm 1^U$ and $\pm 1^L$ fine structure states giving the energies:

$$\begin{aligned}\epsilon^{(2)}_{0^{U,L}} &= \frac{\mu_B^2 B_z^2}{4}\left[\frac{(g_e + g_h)^2}{\epsilon_{0U,L} - \epsilon_{0L,U}}\right] \\ &+ \frac{\mu_B^2 B_\perp^2}{4}\left[\frac{C^{\pm^2} g_e^2 + (2C^\pm + \sqrt{3}C^\mp)^2 g_h^2}{\epsilon_{0U,L} - \epsilon_{1U,L}} + \frac{C^{\mp^2} g_e^2 + (2C^\mp - \sqrt{3}C^\pm)^2 g_h^2}{\epsilon_{0U,L} - \epsilon_{1L,U}}\right]\end{aligned} \tag{7.6}$$

In the equation, B_z is the component of the field parallel to the c axis of the QD and

[3] See Appendix F

$\epsilon_{0U,L}$, $\epsilon_{1U,L}$ are the unperturbed energies of the interacting states.[64]

Expressions for states with total momentum projection $|N_m| = 1$ are more complicated because both projections are degenerate and couple through states with momentum projection $|N_m| = 0$. For the lower $N = 1$ state, we obtain the expression:

$$\epsilon^{(2)}_{2,\pm 1} = \lambda^{(2)}_L + \frac{\mu_B^2 B_\perp^2}{4}\left(\frac{C^{+^2} g_e^2 + 3C^{-^2} g_h^2}{\epsilon_{1L} - \epsilon_2}\right) + \mu_B^2 B_Z^2 \left(\frac{C^{+^2} C^{-^2} (g_e + g_h)^2}{\epsilon_{1L} - \epsilon_{1U}}\right) \tag{7.7}$$

where

$$\begin{aligned}
\lambda^{(2)}_L &= \frac{\mu_B^2 B_\perp^2}{8}\left[\frac{C^{-^2} g_e^2 + (\sqrt{3}C^+ + 2C^-)^2 g_h^2}{\epsilon_{1L} - \epsilon_{0L}} + \frac{C^{-^2} g_e^2 + (\sqrt{3}C^+ - 2C^-)^2 g_h^2}{\epsilon_{1L} - \epsilon_{0U}}\right] \\
&\mp \frac{\mu_B^2 B_\perp^2}{8}\sqrt{\frac{\left(C^{-^2} g_e^2 + (\sqrt{3}C^+ + 2C^-)^2 g_h^2\right)^2}{(\epsilon_{1L} - \epsilon_{0L})^2} + \frac{(C^{-^2} g_e^2 + (\sqrt{3}C^+ - 2C^-)^2 g_h^2)^2}{(\epsilon_{1L} - \epsilon_{0U})^2}} \\
&+ \frac{2\left[-\left(C^{-^2} g_e^2 + g_h^2(3C^{+^2} - 4C^{-^2})\right)^2 + 16C^{-^4} g_e^2 g_h^2\right]}{(\epsilon_{1L} - \epsilon_{0L})(\epsilon_{1L} - \epsilon_{0U})}
\end{aligned} \tag{7.8}$$

For the upper $N = 1$ state we obtain:

$$\epsilon^{(2)}_{1,\pm 1} = \lambda^{(2)}_U + \frac{\mu_B B_\perp^2}{4}\left(\frac{C^{-^2} g_e^2 + 3C^{+^2} g_h^2}{\epsilon_{1U} - \epsilon_2}\right) + \mu_B^2 B_z^2 \left(\frac{C^{+^2} C^{-^2} (g_e + g_h)^2}{\epsilon_{1U} - \epsilon_{1L}}\right) \tag{7.9}$$

where

$$\begin{aligned}
\lambda^{(2)}_U &= \frac{\mu_B^2 B_\perp^2}{8}\left[\frac{C^{+^2} g_e^2 + (2C^+ + \sqrt{3}C^-)^2 g_h^2}{\epsilon_{1U} - \epsilon_{0U}} + \frac{C^{+^2} g_e^2 + (2C^+ - \sqrt{3}C^-)^2 g_h^2}{\epsilon_{1U} - \epsilon_{0L}}\right] \\
&\mp \frac{\mu_B B_\perp^2}{8}\sqrt{\frac{\left[C^{+^2} g_e^2 + (\sqrt{3}C^- + 2C^+)^2 g_h^2\right]^2}{(\epsilon_{1U} - \epsilon_{0U})^2} + \frac{[C^{+^2} g_e^2 + (\sqrt{3}C^- - 2C^+)^2 g_h^2]^2}{(\epsilon_{1U} - \epsilon_{0L})^2}} \\
&+ \frac{2\left[-(C^{+^2} g_e^2 + g_h^2(3C^{-^2} - 4C^{+^2}))^2 + 16C^{+^4} g_e^2 g_h^2\right]}{(\epsilon_{1U} - \epsilon_{0U})(\epsilon_{1U} - \epsilon_{0L})}
\end{aligned} \tag{7.10}$$

7.4.2 Transition Probabilities

Changes in the transition probabilities due to the mixing of fine structure states have been determined. In the grossest sense, the expressions show that the 0^L dark exciton gains oscillator strength from its interaction with nearby bright states. This explains the appearance of a new state in the effective absorption of doped nanocrystallites. All equations are provided in Appendix G.[4]

7.4.3 Critical Comments

Several points ought to be mentioned at this point. Our evidence for manganese incorporation into the QD is based on repeated ligand exchange and wavelength dispersive x-ray (WDS) measurements. The surface washing is critical as we find that most of the manganese in the preparation appears to be unincorporated. We observe large drops in the effective manganese concentration with increasing number of size selective precipitations (i.e. surface treatment).[220]

From a spectroscopy viewpoint, if the manganese impurity lies within the crystal lattice there ought to be large (dramatic) changes in the optical properties of the nanocrystallites. For example in bulk CdSe, manganese doping causes the band edge absorption to shift by values over 1 eV.[221] This is not seen in our nanocrystallites as there are no substantial shifts in the peak of the $1S_{3/2}1S_e$ transition. In addition, manganese incorporation into bulk CdS and ZnS shows a characteristic manganese emission centered at approximately 580 nm or 2.14 eV.[222, 223] This has also been seen, more recently, in CdS and ZnS nanocrystallites.[197, 200, 191, 190, 224, 225,

[4]Please take the expressions with a grain of salt. Things were a bit hectic at this point.

192, 226, 227] The QDs we study are relatively small and have bandgaps over 2.6 eV. As the bandgaps are comparable to those of CdS and ZnS this should be sufficiently large to make manganese emission less prohibitive. However, no characteristic Mn^{+2} emission is observed at low temperatures.

Finally, if the manganese is incorporated into the QD and behaves in the manner outlined above, there ought to be a concomitant decrease in the radiative lifetime. We have no direct lifetime measurements on doped nanocrystallites. These measurements are rendered difficult by the sensitivity of the quantum yield to the treatment of the nanocrystal surface.[220, 34] Our doped QDs which are size selected twice, exchanged with pyridine and brought back to TOPO/TOPSe passivation to remove surface bound manganese impurities exhibit very low quantum yields at low temperatures. Preliminary work suggests a decrease in the lifetime, although it should be kept in mind that non-radiative contributions are more substantial in these samples making lifetime changes suspect without accurate QY measurements.

As a control experiment, magnetic circular dichroism (MCD) experiments were conducted on doped nanocrystallites. Assuming manganese incorporation, a sizable difference in the Zeeman splitting between doped and undoped QDs is expected. The doped QDs should exhibit substantially larger splittings as the effective field of both the impurity and the external field may be up to an order of magnitude larger than an external field acting alone. Results from the MCD measurement show little or no difference in values of the effective splitting compared to undoped nanocrystallites.

Another problem encountered during the MCD experiment is that there does not appear to be any zero field Zeeman splitting of the states (at least at 10 K where

the MCD experiment is conducted). The MCD experiment probes the absorption of left and right circularly polarized light which in turn reflects the lifted degeneracy of $|N_m| = 1$ states. At zero field, no difference in the absorption of circularly polarized light is seen. We conclude from this and other experiments that the manganese impurity most likely occupies positions near or at the surface of the nanocrystallite. This explains the lack of change in the linear absorption, the slight changes in the FLN/PLE spectra and the lack of any manganese emission.

7.4.4 Undoped Nanocrystallites

The behavior of the undoped nanocrystallites is unusual. Why it shows increases in the resonant Stokes shift, increases in the oscillator strength and increases in the Huang-Rhys parameter with decreasing temperature is still an open question. However the presence of intrinsic paramagnetic impurities in undoped CdSe quantum dots may provide an answer. The presence of such intrinsic impurities is supported by recent EPR experiments on undoped QDs which show substantial concentrations of paramagnetic species on the order of one impurity per nanocrystallite.[220][5]

Although preliminary EPR experiments indicate significant amounts of paramagnetic impurities in undoped CdSe QDs, the discovery that the spin abundance is reduced by ligand exchange and sample purification casts a shadow of doubt on the impurity argument. One possibility, though, is that paramagnetic surface species are the source of the exchange interaction with photo-generated electrons and holes. Samples used in optical experiments are typically not subjected to such rigorous sur-

[5]See also Chapter 6

face treatments because often enough, with sufficient washing, the quantum yield of the nanocrystallite plummets. However, the exchange interaction between external and internal carriers is predicted to be much smaller in magnitude. Another possibility arises from the observation that a light enhanced signal at $g = 2$ exists in the low temperature EPR spectra of CdSe QDs.[6] Trapped (photo-generated) electrons on the surface of the nanocrystallite might be responsible for the effective exchange field. Dangling bonds due to irregular surface termination and incomplete passivation may also play a role in this respect.

A possible explanation for the changes in the optical spectra follows: At low temperatures, the spins of the photogenerated electron/hole interact with the spins of the paramagnetic impurity/nucleus creating an exchange field which resembles a large magnetic field. If the impurity spin alignment occurs on a much *faster* timescale than the exciton lifetime, the field orients parallel to the QD c axis. No significant mixing of states occurs under these circumstances and the dark exciton retains much of its intrinsic triplet character. At higher temperatures (10 K), kT is large enough to cause spin fluctuations. The effective magnetic field is averaged out by the spin disorder but an instantaneous projection of the field causes partial alignment along directions not necessarily parallel to the QD c axis. This effective field mixes dark and bright fine structure states allowing radiative recombination from the Dark exciton. This argument is in qualitative agreement with experimental results showing that, in FLN experiments, when the sample temperature is lowered, the Huang-Rhys parameter increases (i.e. less light is emitted at the ZPL).

[6]See Chapter 6

Two other experimental observables are in qualitative agreement with the model. The first is that the radiative lifetime increases with temperature. The temperature dependence of the lifetime shows a striking resemblance to lifetime measurements in the presence of an external magnetic field.[63] (Stronger fields result in shorter lifetimes, presumably due to the mixing of fine structure states) In analogy to the magnetic field experiments, there is an admixture of dark and bright states at higher temperatures, shortening the lifetime of the emitting state. At lower temperatures, the preferred orientation of the effective field along the c axis prevents a mixing of states making the lifetimes longer. We also observe that as the temperature decreases, there is a concomitant increase in the resonant Stokes shift.

Another possible explanation for the behavior of undoped samples is the temperature dependent pairing and unpairing of impurity spins. In this scenario, there are unpaired spins at higher temperatures which cause the above mentioned mixing of fine structure states. In effect, we have paramagnetic impurities at 10 K and also at 5 K where low temperature EPR measurements have been conducted.[7] At lower temperatures (1.75 K), the impurity spins pair up and we no longer have paramagnetic centers. This reduces/eliminates all mixing effects between fine structure states. We therefore see an increase in the oscillator strength of the first optically active exciton, an increase in the resonant Stokes shift and a dramatic increase in the Huang-Rhys S parameter with decreasing temperature.

Comparison with results from doped samples show several large discrepancies in

[7]Our temperature dependent EPR measurements are currently inconclusive as several scans show no temperature dependence of the spin abundance whereas others show a maximum abundance between 3 K and 5 K.

our explanation for undoped QDs. This arises from the fact that we do not see spin alignment in doped samples. At all temperatures doped nanocrystallites behave in a manner consistent with the mixing of fine structure states through *unaligned* manganese spins. These differences are poignantly summarized in Figures 7-8, 7-9, and 7-10 where opposite trends in the resonant shift, oscillator strength and Huang-Rhys parameter are observed with decreasing temperature. The first description of a spin alignment mechanism in undoped nanocrystallites is therefore suspect. The second explanation based on the pairing and unpairing of impurity spins is also questionable because these dramatic changes in the optical spectra occur with only slight changes in thermal energy (~ 0.125 meV).

At this point the low temperature behavior of undoped nanocrystallites is still an unresolved mystery, although optically detected nuclear magnetic resonance (ODNMR) experiments may provide a direct correlation between spin effects and changes in the optical properties of CdSe QDs.

7.5 Conclusion

We have studied the temperature dependent absorption and emission of doped and undoped CdSe nanocrystallites. Our results show that manganese doped nanocrystallites behave in a manner consistent with the exchange induced mixing of fine structure states. Changes in the resonant Stokes shift, Huang-Rhys parameter and relative oscillator strength of optically active states are observed leading to dark exciton activation. In undoped nanocrystallites, we see unusual behavior that may potentially be explained by the presence of intrinsic paramagnetic impurities.

Appendix A

Characterization

A.1 Various Characterization Techniques

A.1.1 Transmission Electron Microscopy, TEM

In the TEM experiment, a thin or dilute sample is bombarded under high vacuum with a focused beam of electrons. Electrons that are transmitted through the material form contrast patterns that reproduce the image of the sample. This pattern arises from the scattering of electrons off of atoms composing the sample. In addition, diffracted electrons give information about the lattice structure of the material. In the case of nanocrystallites, analysis of TEM images is partially responsible for the sizing curves currently available for CdSe QDs (See Appendix B).[32] The shape of the QD (prolate, oblate, faceted, etc...) can also be determined from the image.

A.1.2 Scanning Transmission Electron Microscopy, STEM

Like TEM, a sample is bombarded with electrons under high vacuum. However, in this case the electron beam is rastered across the sample and transmitted or scattered electrons are detected. One advantage of STEM over TEM is that many signals can be collected in parallel such as dark field images, bright field images and electron diffraction patterns. Energy dispersive x-ray (EDS) and electron energy loss (EELS) spectroscopies can also be employed to determine the elemental composition of the sample. The EDS capabilities of the STEM were used in Chapter 3 to determine the relative abundance of phosphorous groups on the surface of ligand exchanged nanocrystallites.

A.1.3 Scanning Electron Microscopy, SEM

In the SEM experiment an electron beam is focused into a probe and rastered over a small area encompassing the sample. When the electrons interact with the sample a number of effects take place such as the emission of secondary electrons. These effects are highly localized to the region directly under the electron beam and can be used to modulate the brightness of a cathode ray tube rastered in sync. with the e-beam. This creates the "image" of the sample. Other detectors can be used to obtain elemental analysis of the sample. SEM was used by Kagan to characterize glassy solids of CdSe QDs.[228]

A.1.4 Energy-Dispersive X-Ray Spectroscopy, EDS

EDS is an x-ray technique based on the collection and dispersion of characteristic x-rays. In the experiment a sample is bombarded with high energy electrons. When constituent atoms of a material are ionized they emit x-rays. The energy of the emitted x-ray can then be associated with

the presence of a particular element. The intensity of the signal gives information about the relative abundance of each element in the sample. If internal standards are used, absolute quantities are obtained. As mentioned earlier, EDS was used in Chapter 3 to determine the presence of phosphorous groups on the surface of ligand exchanged nanocrystallites.

A.1.5 X-Ray Photoelectron Spectroscopy, XPS

In the XPS experiment, soft x-rays bombard a sample causing electrons to be ejected. The kinetic energy of the ejected electron is characteristic of a particular element and can be used to perform elemental analysis on a sample. Slight changes in the energy of emitted electrons can be correlated with the oxidation state of an element. XPS is also referred to as ESCA, electron spectroscopy for chemical analysis. This technique was used by Dabbousi to search for the presence of selenium oxide on the surface of ZnS overcoated CdSe QDs (a control experiment to see the quality of the ZnS passivation).[141]

A.1.6 X-Ray Diffraction, XRD

X-ray diffraction involves irradiating a sample with x-rays. These x-rays, in turn, are diffracted by the crystalline regions of the material according to Bragg's Law ($\lambda = 2\sin\theta$). The intensity of the diffracted x-rays is evaluated as a function of diffraction angle, 2θ. This information is then used to determine the crystalline arrangement of atoms in the material. Work by Murray has shown the wurtzite arrangement of atoms in CdSe QDs.[32, 141] More recently, Dinega has discovered a new crystal structure for cobalt using this method.[91]

A.1.7 X-Ray Fluorescence, XRF

As with XRD, x-ray fluorescence involves irradiating a sample with x-rays. Emitted fluorescent x-rays are analyzed with a crystal spectrometer and scintillation counter. The energies of the emitted x-rays are characteristic of individual elements allowing for elemental analysis of the sample. In addition, relative concentrations are determined from the peak intensities. Danek has used this technique to characterize ZnSe overcoated CdSe QDs.[139, 152, 229]

A.1.8 Extended X-Ray Absorption Fine Structure, EXAFS

EXAFS is not a typical experiment for studying QDs because it requires access to synchrotron x-rays. It has, however, been used to characterize the surface of CdSe QDs by Carter.[37, 230] In the experiment, the synchrotron x-ray energy is scanned from just below to just above the binding energy of a core-shell electron in a particular element. Absorption of x-rays is monitored with a detector. When the x-ray energy matches the core-shell binding energy, a steep absorption edge is seen. Above the binding energy, oscillations in the absorption are seen. EXAFS gives information about the distribution of atoms in the near vicinity of the probed element. The frequency of EXAFS is related to the interatomic distance between absorbing and neighboring atoms. The amplitude is also related to the number, type and order of neighboring atoms.

A.1.9 Ultraviolet Photoelectron Spectroscopy, UPS

This experiment involves striking a sample with highly energetic photons in the 10 to 100 eV range. Photoelectrons from valence levels and low lying core states are ejected and analyzed. In particular, the energy distribution of the emitted electrons is measured. This technique is very similar to XPS the main difference being the excitation source used, high energy photons versus x-rays. The emphasis of each technique also differs slightly. UPS is primarily used to study valence electron states. XPS with its high energies is better suited for studying deep core levels.

A.1.10 Electrons Paramagnetic Resonance, EPR

This method is used to detect unpaired electrons. In the EPR experiment, a sample is placed in an external magnetic field (typically on the order of 1 Tesla for resistive magnets) splitting the energy levels of the unpaired electron. The sample is then irradiated with microwaves. Absorption of the radiation is monitored and occurs when the microwave energy matches the energy difference of the two spin split states. A g factor is associated with the transition and gives a measure of the splitting. EPR was used in Chapter 6 to characterize manganese doped CdSe QDs.[220]

A.1.11 Solid State Nuclear Magnetic Resonance, NMR

In this experiment, a solid sample is placed in a strong external magnetic field (On the order of 10-15 Tesla with superconducting magnets). The magnetic field splits the nuclear spin states of NMR active nuclei. The transition between split spin states is probed by irradiating the sample with intense radio frequency pulses. When the nuclei relaxes to the ground spin state it emits a radio frequency signal which is detected by electromagnetic induction coils. The spectrum is plotted as intensity versus frequency or more commonly as intensity versus chemical shift. Solid state ^{31}P NMR was used by Murray to identify phosphorous species on the surface of CdSe QDs.[33] ^{113}Cd NMR was also used in Chapter 6 to characterize the manganese impurity in doped CdSe QDs.[220]

Appendix B

Sizing Curves

This section list some size dependent properties of CdSe nanocrystallites extracted from TEM/SAXS measurements. Size dependent optical properties are also presented.
We include:

1. Normal CdSe sizing curve (450 nm to 650 nm)
2. Small CdSe sizing curve (410 nm to 560 nm)
3. Low temperature sizing from band edge absorption
4. Table of size versus absorption maximum
5. Sizing determined from the peak of the band edge luminescence at RT (300K)
6. Sizing determined from the peak of the band edge luminescence at LT (10K)
7. Size dependent ellipticity of the nanocrystallites
8. Sizing summary at 300 K and 10 K (plotted as $1/a^2$)

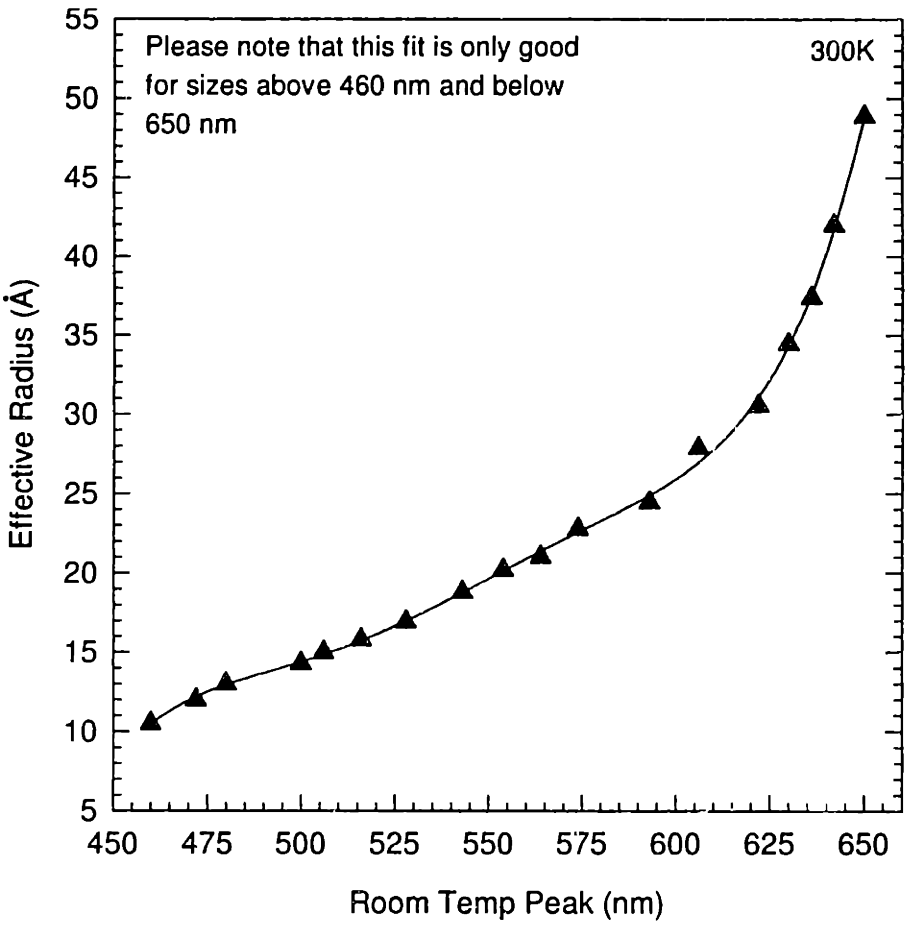

Coefficients for 5th order polynomial fit

b0=-69875.2742938567
b1=654.339157953
b2=-2.4454369856
b3=4.55948234e-3
b4=-4.2409555862e-6
b5=1.5745201754e-9

Figure B-1: This is the sizing curve used in much of our work. It is based on extensive TEM/SAXS measurements on the nanocrystallites. Note that, on average, SAXS overestimates the radius of the QD by 2.5 Å because it is sensitive to the surface passivation. TEM, on the other hand, is sensitive only to the crystalline regions of the QD and is therefore insensitive to the surface since it does not produce significant contrast. The fit is a fifth order polynomial and "includes" the surface.

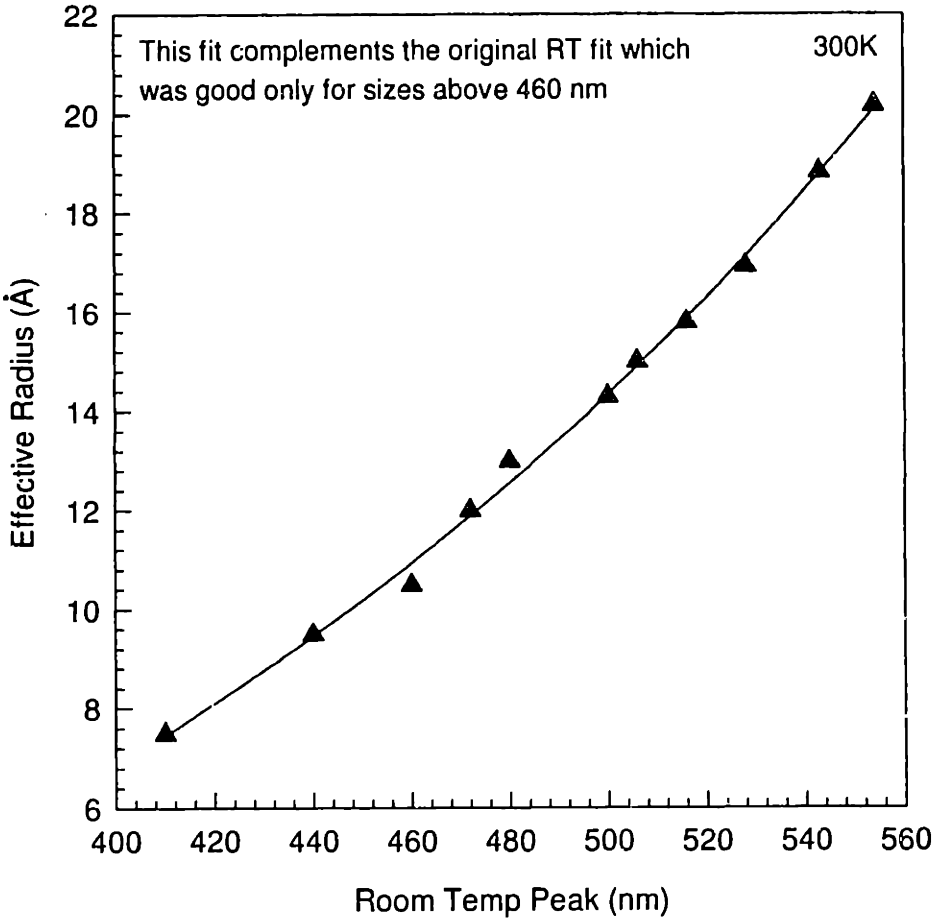

Coefficients for 3rd order polynomial fit

b0 = -30.9083047984
b1 = 0.1980854379
b2 = -4.3566268925e-4
b3 = 4.4098967408e-7
r^2 = 0.9969789108

Figure B-2: This is an extension of the earlier sizing curve. Fits including both the smallest and largest sizes were difficult. As a result, we consider the smallest sizes separately. The fit is a third order polynomial with coefficients listed above. Again, the surface is included in the fit.

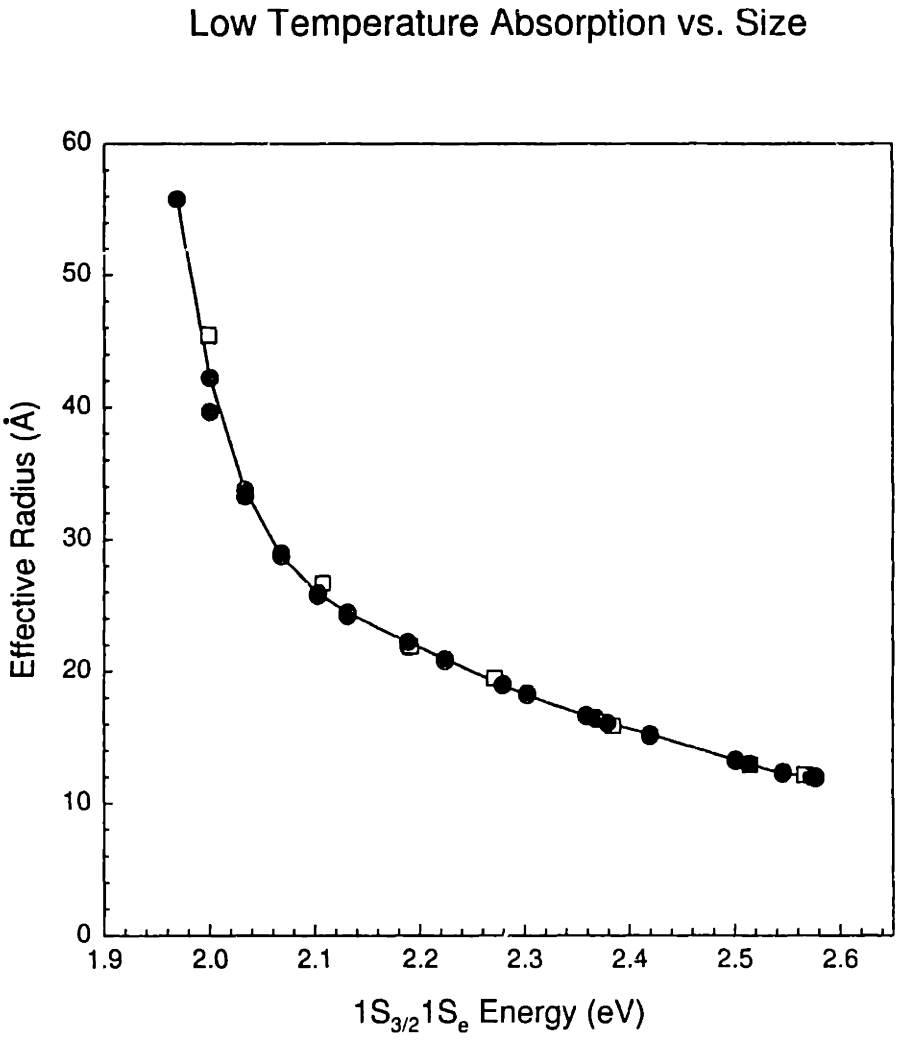

Figure B-3: This sizing curve allows one to extract sizing information from the band edge absorption maxima at 10 K. The sizing information is contained in a sixth order polynomial and does not include the surface.

Table B.1: Absorption versus size for CdSe QDs. Sizes are in effective radii.

Absorption (nm)	Size (Å)	Absorption (nm)	Size (Å)	Absorption (nm)	Size (Å)	Absorption (nm)	Size (Å)
460.00	10.41	522.00	16.33	584.00	23.76	646.00	45.07
462.00	10.79	524.00	16.54	586.00	24.01	648.00	46.92
464.00	11.13	526.00	16.76	588.00	24.26	650.00	48.91
466.00	11.43	528.00	16.98	590.00	24.51		
468.00	11.71	530.00	17.21	592.00	24.78		
470.00	11.96	532.00	17.44	594.00	25.05		
472.00	12.19	534.00	17.68	596.00	25.33		
474.00	12.40	536.00	17.92	598.00	25.63		
476.00	12.60	538.00	18.16	600.00	25.94		
478.00	12.78	540.00	18.40	602.00	26.26		
480.00	12.94	542.00	18.65	604.00	26.61		
482.00	13.10	544.00	18.90	606.00	26.98		
484.00	13.25	546.00	19.15	608.00	27.37		
486.00	13.40	548.00	19.40	610.00	27.79		
488.00	13.54	550.00	19.65	612.00	28.25		
490.00	13.68	552.00	19.90	614.00	28.74		
492.00	13.82	554.00	20.15	616.00	29.26		
494.00	13.95	556.00	20.39	618.00	29.83		
496.00	14.09	558.00	20.64	620.00	30.45		
498.00	14.24	560.00	20.89	622.00	31.12		
500.00	14.38	562.00	21.13	624.00	31.84		
502.00	14.53	564.00	21.38	626.00	32.62		
504.00	14.69	566.00	21.62	628.00	33.47		
506.00	14.84	568.00	21.86	630.00	34.39		
508.00	15.01	570.00	22.10	632.00	35.39		
510.00	15.18	572.00	22.33	634.00	36.47		
512.00	15.36	574.00	22.57	636.00	37.64		
514.00	15.54	576.00	22.81	638.00	38.91		
516.00	15.73	578.00	23.04	640.00	40.27		
518.00	15.92	580.00	23.28	642.00	41.75		
520.00	16.12	582.00	23.52	644.00	43.35		

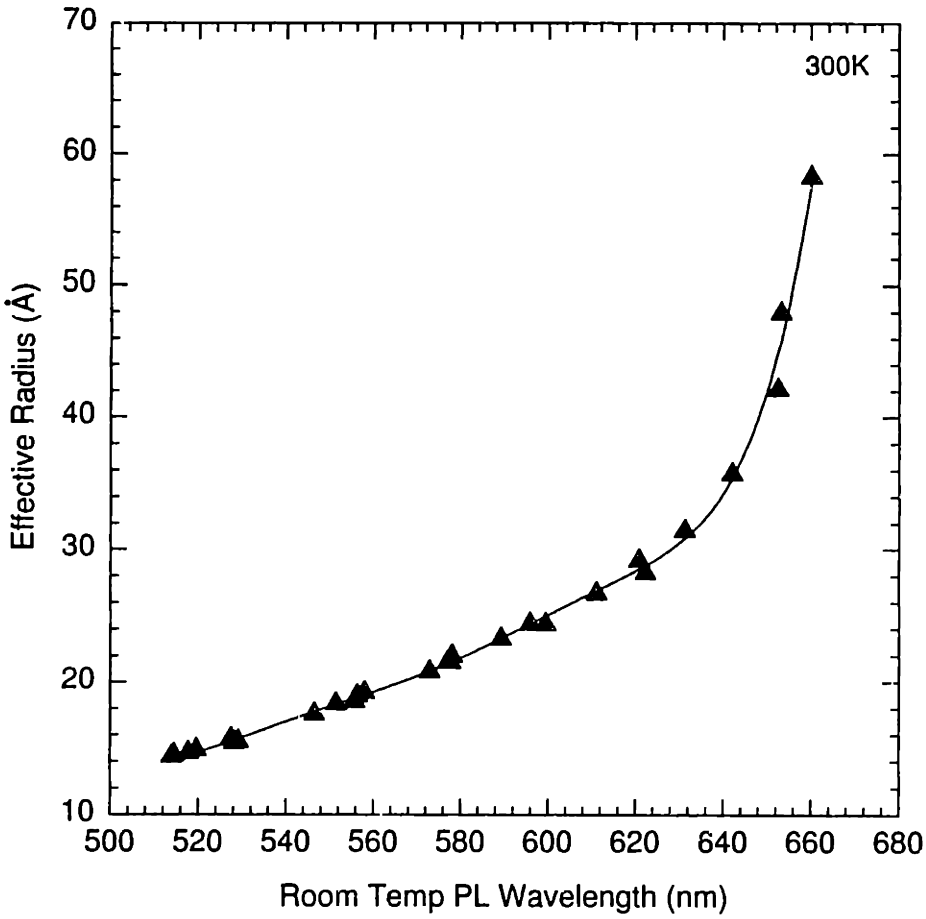

Coefficients for 7th order polynomial fit

b0 = -703469.4467567649
b1 = 15066.4163897341
b2 = -112.7903483781
b3 = 0.4264622793
b4 = -9.1505136721e-4
b5 = 1.135508734e-6
b6 = -7.6255718651e-10
b7 = 2.1518075072e-13
r^2 = 0.9954179956

Figure B-4: This curve predicts the size of a QD sample based on its band edge luminescence maximum. It is a seventh order polynomial with coefficients listed above. The surface is implicitly included in the sizes.

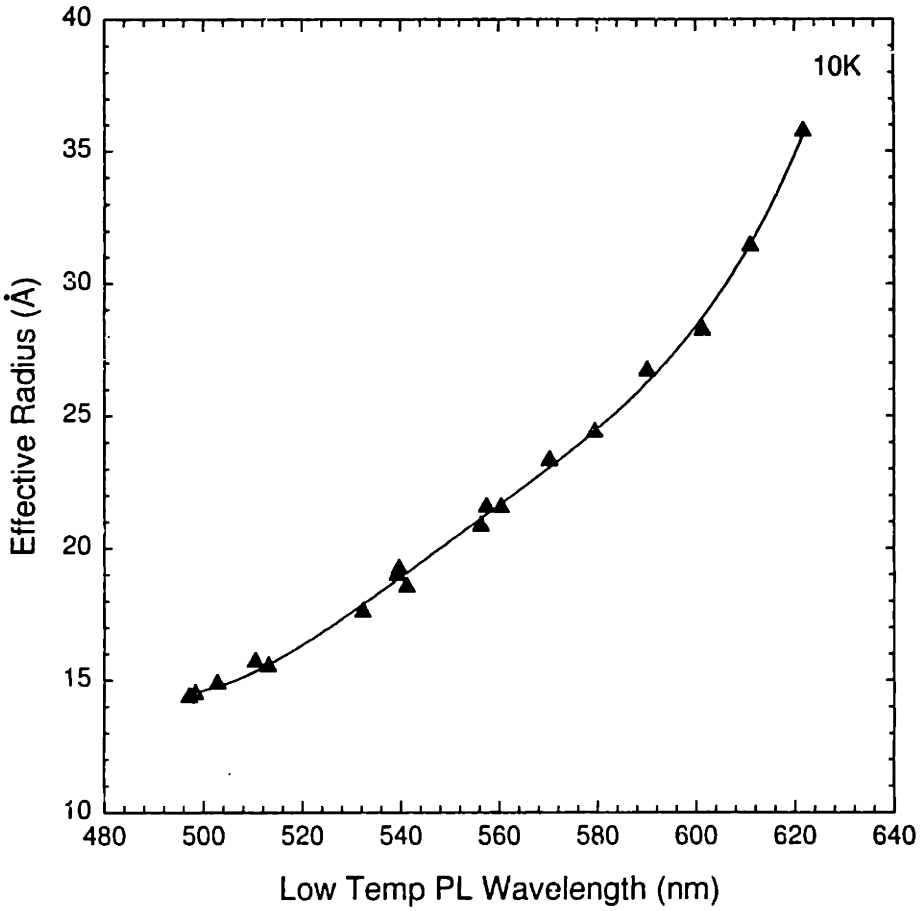

Coefficients for 4th order polynomial fit

b0=18374.4392187806
b1=-134.1901288401
b2=0.3671450135
b3=-4.4598162577e-4
b4=2.0314702866e-7
r^2=0.997877246

Figure B-5: This curve predicts the size of a QD based on the position of its low temperature (10K) band edge emission maximum. It is a fourth order polynomial with coefficients written above. The surface is implicitly included in the sizing.

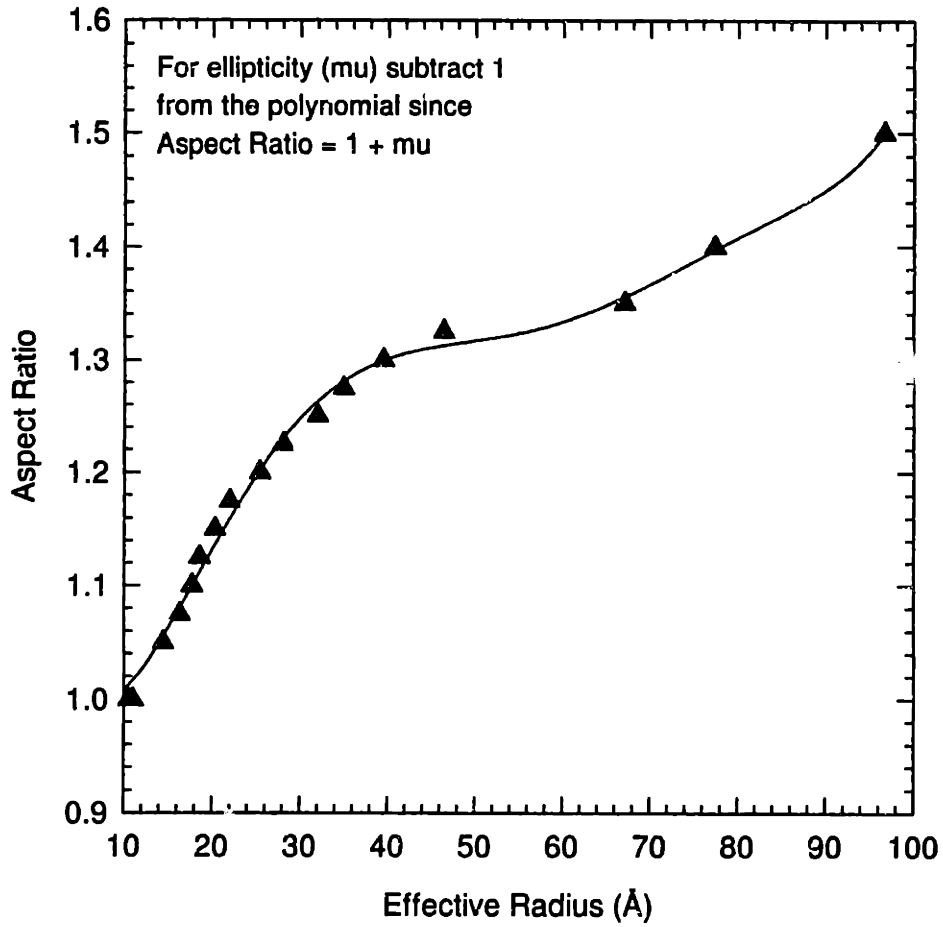

Coefficients for 6th order polynomial

b0 = 1.1013058503
b1 = -0.0342714634
b2 = 3.5071864504e-3
b3 = -1.1765924488e-4
b4 = 1.8632343193e-6
b5 = -1.418243175e-8
b6 = 4.1958481263e-11
r^2 = 0.9978111754

Figure B-6: Fit to the size dependent ellipticity of the QDs. This is based on extensive TEM/SAXS measurements. Larger QDs are seen to be prolate, elongated along the "c" or unique axis of the nanocrystallites. The fit is a sixth order polynomial and extracted coefficients are listed above. The sizing includes the surface.

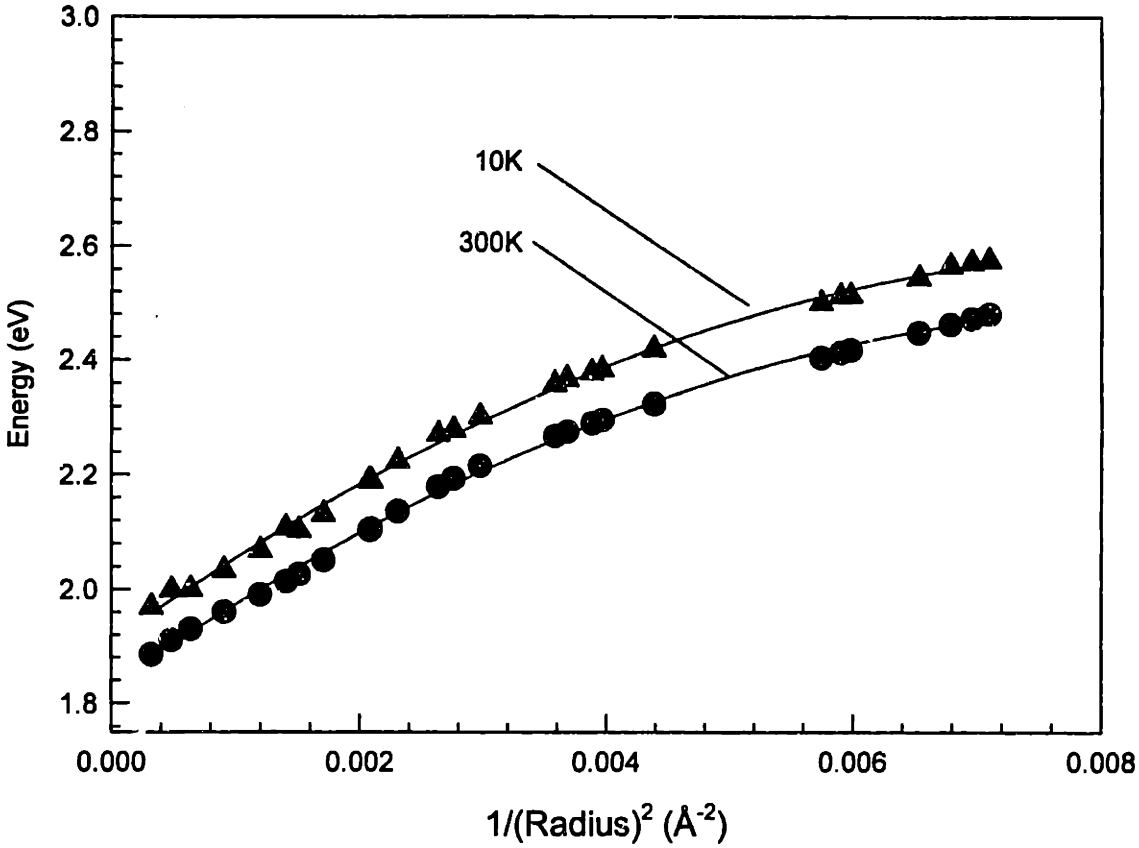

RT Coefficients for 3rd order polynomial

b0=1.8311728017
b1=151.3050734913
b2=-8615.5090657079
r ²=0.9980979041

LT Coefficients for 3rd order polynomial

b0=1.9086311762
b1=155.053319212
b2=-8687.9947039306
r ²=0.9975654414

Figure B-7: This is essentially a sizing summary of CdSe QDs both at room temperature and at low temperature. The fits are third order polynomials and are more trustworthy than the first ones presented. The data is plotted as $1/a^2$ to emphasize the effects of quantum confinement. Note, however, that there is a problem with our sizing at large sizes. Both curves should have an intercept equal to the bulk band gap at 300 K (1.74 eV) and 10 K (1.84 eV). Our predictions are 0.1 eV too large. We predict 1.83 eV at 300 K and 1.91 eV at 10 K.

Appendix C

Spherical Approximation

C.1 Description

Roughly speaking this is the problem of a particle in a three dimensional box or sphere. We need to solve Schrodinger's equation $H\Psi = E\Psi$ under spherical boundary conditions to get the energies and wavefunctions of the particle (electron, hole). This approximation leads to answers that qualitatively match observed experimental results. In the problem, the Hamiltonian is

$$H = -\frac{\hbar^2}{2m}\nabla^2 \tag{C.1}$$

where

$$\nabla^2 = \frac{1}{r^2}\frac{\partial}{\partial r}\left(r^2\frac{\partial}{\partial r}\right) + \frac{1}{r^2\sin\theta}\frac{\partial}{\partial\theta}\left(\sin\theta\frac{\partial}{\partial\theta}\right) + \frac{1}{r^2\sin^2\theta}\frac{\partial^2}{\partial\phi^2} \tag{C.2}$$

The potential is

$$U(r) = \begin{cases} 0 & \text{if } r < R \\ \infty & \text{if } r > R \end{cases} \tag{C.3}$$

so

$$\nabla^2\Psi = \frac{1}{r^2}\frac{\partial}{\partial r}(r^2\frac{\partial\Psi}{\partial r}) + \frac{1}{r^2\sin\theta}\frac{\partial}{\partial\theta}(\sin\theta\frac{\partial\Psi}{\partial\theta}) + \frac{1}{r^2\sin^2\theta}\frac{\partial^2\Psi}{\partial\phi^2}$$

and since

$$-\frac{\hbar^2}{2m}\nabla^2\Psi = E\Psi$$

$$-\frac{\hbar^2}{2m}\left[\frac{1}{r^2}\frac{\partial}{\partial r}(r^2\frac{\partial\Psi}{\partial r}) + \frac{1}{r^2\sin\theta}\frac{\partial}{\partial\theta}(\sin\theta\frac{\partial\Psi}{\partial\theta}) + \frac{1}{r^2\sin^2\theta}\frac{\partial^2\Psi}{\partial\phi^2}\right] = E\Psi$$

To simplify this multiply through by $2mr^2$.

$$-\hbar^2\left[\frac{\partial}{\partial r}(r^2\frac{\partial\Psi}{\partial r}) + \frac{1}{\sin\theta}\frac{\partial}{\partial\theta}(\sin\theta\frac{\partial\Psi}{\partial\theta}) + \frac{1}{\sin^2\theta}\frac{\partial^2\Psi}{\partial\phi^2}\right] = 2mr^2E\Psi$$

Lump all angle terms together and bring them over to the right.

$$\left[-\hbar^2\frac{\partial}{\partial r}(r^2\frac{\partial\Psi}{\partial r}) - 2mr^2E\Psi\right] - \hbar^2\left[\frac{1}{\sin\theta}\frac{\partial}{\partial\theta}(\sin\theta\frac{\partial\Psi}{\partial\theta}) + \frac{1}{\sin^2\theta}\frac{\partial^2\Psi}{\partial\phi^2}\right] = 0$$

We have two terms, one radial dependent the other angular dependent. Assume solution of the form:

$$\Psi = u(r,\theta,\phi) = \frac{1}{r}\chi(r)Y_{l,m}(\theta,\phi)$$

therefore

$$\frac{\partial\Psi}{\partial r} = Y_{l,m}(\theta,\phi)\left[\frac{1}{r}\chi'(r) - \frac{\chi(r)}{r^2}\right]$$

and

$$r^2\frac{\partial\Psi}{\partial r} = Y_{l,m}(\theta,\phi)\left[r\chi'(r) - \chi(r)\right]$$

and

$$\frac{\partial}{\partial r}(r^2\frac{\partial}{\partial r}) = Y_{l,m}(\theta,\phi)r\chi''(r)$$

Replace these terms into the main equation

$$-\hbar^2 Y_{l,m}(\theta,\phi)r\chi''(r) - 2mr^2E\Psi - \hbar^2\left[\frac{1}{\sin\theta}\frac{\partial}{\partial\theta}(\sin\theta\frac{\partial\Psi}{\partial\theta}) + \frac{1}{\sin^2\theta}\frac{\partial^2\Psi}{\partial\phi^2}\right] = 0$$

The term in square brackets is angular momentum operator $\hat{L}^2$. This has solutions of the form $\hat{L}^2Y_{l,m}(\theta,\phi) = \hbar^2 l(l+1)Y_{l,m}(\theta,\phi)$ and that $\Psi = 1/rY_{l,m}(\theta,\phi)\chi(r)$

$$-\hbar^2 Y_{l,m}(\theta,\phi)r\chi''(r) - 2mr^2E\Psi + [\hbar^2 l(l+1)]\frac{1}{r}Y_{l,m}(\theta,\phi)\chi(r) = 0$$

$$-\hbar^2 Y_{l,m}(\theta,\phi)r\chi''(r) + \frac{\hbar^2 l(l+1)}{r}Y_{l,m}(\theta,\phi)\chi(r) - 2mr^2E\frac{Y_{l,m}(\theta,\phi)\chi(r)}{r} = 0$$

Toss the angular terms.

$$\begin{aligned}
-\hbar^2 r\chi''(r) + \frac{\hbar^2 l(l+1)}{r}\chi(r) - 2mrE\chi(r) &= 0 \\
r\chi''(r) - \frac{l(l+1)\chi(r)}{r} + \frac{2mr}{\hbar^2}E\chi(r) &= 0 \\
\chi''(r) - \frac{l(l+1)\chi(r)}{r^2} + \frac{2m}{\hbar^2}E\chi(r) &= 0 \\
\chi''(r) + \left[\frac{2mE}{\hbar^2} - \frac{l(l+1)}{r^2}\right]\chi(r) &= 0
\end{aligned}$$

Let $k^2 = \frac{2mE}{\hbar^2}$

$$\chi''(r) + \left[k^2 - \frac{l(l+1)}{r^2}\right]\chi(r) = 0 \qquad \text{(C.4)}$$

If $z = kr$ then

$$\frac{\partial\phi}{\partial r} = \frac{\partial\phi}{\partial z}\frac{\partial z}{\partial r} = k\phi'$$

then

$$\chi''(r) + k^2\left[1 - \frac{l(l+1)}{z^2}\right]\chi(r) = 0$$

and

$$\chi = z^{\frac{1}{2}}\phi(z)$$

so

$$\begin{aligned}
\chi' &= z^{\frac{1}{2}}\phi'(z)k + \phi(z)\frac{1}{2}z^{-\frac{1}{2}}k \\
\chi'' &= kz^{\frac{1}{2}}\phi''(z)k + k\phi'(z)\frac{1}{2}z^{-\frac{1}{2}}k + \frac{k}{2}\left[\phi(z)(-\frac{1}{2})z^{-\frac{3}{2}}k + z^{-\frac{1}{2}}\phi'(z)k\right] \\
\chi'' &= k^2 z^{\frac{1}{2}}\phi'' + \frac{k^2}{2}\phi' z^{-\frac{1}{2}} - \frac{k^2}{4}z^{-\frac{3}{2}}\phi + \frac{k^2}{2}\phi' z^{-\frac{1}{2}} \\
\chi'' &= k^2 z^{\frac{1}{2}}\phi'' + k^2\phi' z^{-\frac{1}{2}} - \frac{k^2}{4}z^{-\frac{3}{2}}\phi
\end{aligned}$$

Replace this expression into the main equation.

$$\begin{aligned}
\chi''(r) + k^2\left[1 - \frac{l(l+1)}{z^2}\right]\chi(r) &= 0 \\
k^2 z^{\frac{1}{2}}\phi'' + k^2\phi' z^{-\frac{1}{2}} - \frac{k^2}{4}z^{-\frac{3}{2}}\phi + k^2\left[1 - \frac{l(l+1)}{z^2}\right]z^{\frac{1}{2}}\phi &= 0 \\
z^{\frac{1}{2}}\phi'' + \phi' z^{-\frac{1}{2}} - \frac{1}{4}z^{-\frac{3}{2}}\phi + \left[1 - \frac{l(l+1)}{z^2}\right]z^{\frac{1}{2}}\phi &= 0 \\
\phi'' + \phi' z^{-1} - \frac{1}{4}z^{-2}\phi + \left[1 - \frac{l(l+1)}{z^2}\right]\phi &= 0 \\
\phi'' + \frac{\phi'}{2} + \phi\left[1 - \frac{l(l+1) - 1/4}{z^2}\right] &= 0
\end{aligned}$$

We obtain:

$$\phi'' + \frac{\phi'}{2} + \phi\left[1 - \frac{(l+1/2)^2}{z^2}\right] = 0 \qquad \text{(C.5)}$$

This is the general form of Bessel equation. Solutions for the radial component follow from this. Angular solutions are as usual.

The energies and wavefunctions obtained from the solution to this problem are of the form

$$E = \frac{\hbar^2 k^2}{2m_{e,h}} \qquad \text{(C.6)}$$

and

$$\Psi_{l,m,n}(r) = \phi_{l,m,n}(r)Y_{l,m}(\theta,\phi) \qquad \text{(C.7)}$$

Here we have implicitly made the assumption of a parabolic conduction band and a parabolic valence band (2 bands). In real life, this is only a crude approximation. To get better solutions recall that the valence band of CdSe is more complicated. It is composed of three bands, the heavy hole (A), light hole (B) and split off (C) bands. In the bulk, the wavefunction for a carrier is given by the product of an envelope component (plane waves) and a Bloch term, reflecting the periodic potential in which the electron or hole resides. If we make the assumption that the QD is still large relative to the lattice constant of the material, then to a good approximation we can keep the Bloch terms intact. Only the envelope functions are affected by the new spherical boundary conditions. As a consequence, rather than plane waves, the QD envelope function is the solution to the problem of a particle in a sphere.

C.2 Preliminaries

C.2.1 Spherical Harmonics

We define the spherical harmonics here

$$Y_{0,\ 0}(\theta,\phi) = \frac{1}{\sqrt{4\pi}}$$

$$Y_{1,\ 0}(\theta,\phi) = \sqrt{\frac{3}{4\pi}}\cos\theta$$
$$Y_{1,+1}(\theta,\phi) = -\sqrt{\frac{3}{8\pi}}\sin\theta\, e^{i\phi}$$
$$Y_{1,-1}(\theta,\phi) = \sqrt{\frac{3}{8\pi}}\sin\theta\, e^{-i\phi}$$

$$Y_{2,+2}(\theta,\phi) = \sqrt{\frac{15}{32\pi}}\sin^2\theta\, e^{2i\phi}$$
$$Y_{2,+1}(\theta,\phi) = -\sqrt{\frac{15}{8\pi}}\sin\theta\cos\theta\, e^{i\phi}$$
$$Y_{2,\ 0}(\theta,\phi) = \sqrt{\frac{5}{16\pi}}(3\cos^2\theta - 1)$$
$$Y_{2,-1}(\theta,\phi) = \sqrt{\frac{15}{8\pi}}\sin\theta\cos\theta\, e^{-i\phi}$$
$$Y_{2,-2}(\theta,\phi) = \sqrt{\frac{15}{32\pi}}\sin^2\theta\, e^{-2i\phi}$$

$$Y_{3,+2}(\theta,\phi) = \sqrt{\frac{35}{5}}\cos\theta\, Y_{2,2}(\theta,\phi)$$
$$Y_{3,+1}(\theta,\phi) = \sqrt{\frac{35}{8}}\left(\cos\theta\, Y_{2,1}(\theta,\phi) - \sqrt{\frac{3}{15}}Y_{1,1}(\theta,\phi)\right)$$
$$Y_{3,\ 0}(\theta,\phi) = \sqrt{\frac{35}{9}}\left(\cos\theta\, Y_{2,0}(\theta,\phi) - \sqrt{\frac{4}{15}}Y_{1,0}(\theta,\phi)\right)$$
$$Y_{3,-1}(\theta,\phi) = \sqrt{\frac{35}{8}}\left(\cos\theta\, Y_{2,-1}(\theta,\phi) - \sqrt{\frac{3}{15}}Y_{1,-1}(\theta,\phi)\right)$$
$$Y_{3,-2}(\theta,\phi) = \sqrt{\frac{35}{5}}\cos\theta\, Y_{2,-2}(\theta,\phi)$$
$$Y_{3,+3}(\theta,\phi) = \frac{1}{\sqrt{6}}e^{i\phi}\left[\sqrt{\frac{35}{5}}\left(-\sin\theta\, Y_{2,2}(\theta,\phi) + \frac{2\cos^2\theta}{\sin\theta}Y_{2,2}(\theta,\phi)\right) - 2\cot\theta\, Y_{3,2}(\theta,\phi)\right]$$
$$Y_{3,-3}(\theta,\phi) = \frac{1}{\sqrt{6}}e^{-i\phi}\left[\sqrt{\frac{35}{5}}\left(-\sin\theta\, Y_{2,-2}(\theta,\phi) + \frac{2\cos^2\theta}{\sin\theta}Y_{2,-2}(\theta,\phi)\right) + 2\cot\theta\, Y_{3,-2}(\theta,\phi)\right]$$

C.2.2 Spherical Bessel functions

Define spherical Bessel functions here

$$
\begin{aligned}
j_0(z) &= \frac{\sin z}{z} \\
j_1(z) &= \frac{\sin z}{z^2} - \frac{\cos z}{z} \\
j_2(z) &= \left(\frac{3}{z^3} - \frac{1}{z}\right)\sin z - \frac{3}{z^2}\cos z \\
j_3(z) &= \left[\frac{5}{z^2}\left(\frac{3}{z^2} - 1\right) - \frac{1}{z^2}\right]\sin z + \left(-\frac{15}{z^3} + \frac{1}{z}\right)\cos z
\end{aligned}
$$

C.3 Hole wavefunctions with no radial part included (Summary)

The origin for these expressions will be discussed in more detail in the next section. Very briefly, however, the way to see that the equations are qualitatively correct is to add the angular momentum projections of the Bloch terms and the spherical harmonics. For example $Y_{0,0}$ and $|\frac{3}{2},\frac{3}{2}>$ adds to a total momentum projection of $\frac{3}{2}$. Also $Y_{2,2}$ and $|\frac{3}{2},-\frac{1}{2}>$ adds to a total projection of $\frac{3}{2}$.

$$
\begin{aligned}
\left|\frac{3}{2},+\frac{3}{2}\right\rangle^+ &= (Y_{00} + \frac{1}{\sqrt{5}}Y_{2,0})|\frac{3}{2},\frac{3}{2}> + \frac{2}{\sqrt{10}}Y_{2,2}|\frac{3}{2},-\frac{1}{2}> - \frac{2}{\sqrt{10}}Y_{2,1}|\frac{3}{2},\frac{1}{2}> - \frac{1}{\sqrt{5}}Y_{2,1}|\frac{1}{2},\frac{1}{2}> \\
&\quad + \frac{2}{\sqrt{5}}Y_{2,2}|\frac{1}{2},-\frac{1}{2}> \qquad \text{(C.8)}
\end{aligned}
$$

$$
\begin{aligned}
\left|\frac{3}{2},-\frac{3}{2}\right\rangle^+ &= (Y_{0,0} + \frac{1}{\sqrt{5}}Y_{2,0})|\frac{3}{2},-\frac{3}{2}> + \frac{2}{\sqrt{10}}Y_{2,-2}|\frac{3}{2},\frac{1}{2}> - \frac{2}{\sqrt{10}}Y_{2,-1}|\frac{3}{2},-\frac{1}{2}> - \frac{2}{\sqrt{5}}Y_{2,-2}|\frac{1}{2},\frac{1}{2}> \\
&\quad + \frac{1}{\sqrt{5}}Y_{2,-1}|\frac{1}{2},-\frac{1}{2}> \qquad \text{(C.9)}
\end{aligned}
$$

$$
\begin{aligned}
\left|\frac{3}{2},+\frac{1}{2}\right\rangle^+ &= \sqrt{\frac{2}{5}}Y_{2,-1}|\frac{3}{2},\frac{3}{2}> + \sqrt{\frac{2}{5}}Y_{2,2}|\frac{3}{2},-\frac{3}{2}> + Y_{0,0}|\frac{3}{2},\frac{1}{2}> - \sqrt{\frac{1}{5}}Y_{2,0}|\frac{3}{2},\frac{1}{2}> - \sqrt{\frac{2}{5}}Y_{2,0}|\frac{1}{2},\frac{1}{2}> \\
&\quad + \sqrt{\frac{3}{5}}Y_{2,1}|\frac{1}{2},-\frac{1}{2}> \qquad \text{(C.10)}
\end{aligned}
$$

$$
\begin{aligned}
\left|\frac{3}{2},-\frac{1}{2}\right\rangle^+ &= \sqrt{\frac{2}{5}}Y_{2,-2}|\frac{3}{2},\frac{3}{2}> + \sqrt{\frac{2}{5}}Y_{2,1}|\frac{3}{2},-\frac{3}{2}> + (Y_{0,0} - \sqrt{\frac{1}{5}}Y_{2,0})|\frac{3}{2},-\frac{1}{2}> + \sqrt{\frac{2}{5}}Y_{2,0}|\frac{1}{2},-\frac{1}{2}> \\
&\quad - \sqrt{\frac{3}{5}}Y_{2,-1}|\frac{1}{2},\frac{1}{2}> \qquad \text{(C.11)}
\end{aligned}
$$

$$
\begin{aligned}
\left|\frac{1}{2},+\frac{1}{2}\right\rangle^+ &= \sqrt{\frac{2}{5}}Y_{2,2}|\frac{3}{2},-\frac{3}{2}> - \frac{1}{\sqrt{10}}Y_{2,-1}|\frac{3}{2},\frac{3}{2}> - \sqrt{\frac{3}{10}}Y_{2,1}|\frac{3}{2},-\frac{1}{2}> + \frac{1}{\sqrt{5}}Y_{2,0}|\frac{3}{2},\frac{1}{2}> \\
&\quad + Y_{00}|\frac{1}{2},\frac{1}{2}> \qquad \text{(C.12)}
\end{aligned}
$$

$$\left|\frac{1}{2},-\frac{1}{2}\right\rangle^{+} = \frac{1}{\sqrt{10}}Y_{2,1}|\frac{3}{2},-\frac{3}{2}> -\sqrt{\frac{2}{5}}Y_{2,-2}|\frac{3}{2},\frac{3}{2}> +\sqrt{\frac{3}{10}}Y_{2,-1}|\frac{3}{2},\frac{1}{2}> -\frac{1}{\sqrt{5}}Y_{2,0}|\frac{3}{2},-\frac{1}{2}> + Y_{0,0}|\frac{1}{2},-\frac{1}{2}> \quad \text{(C.13)}$$

In the above expressions, the contributions from the heavy hole, light hole and split off hole are given by the following:

$|\frac{3}{2},\pm\frac{3}{2}>$ heavy hole

$|\frac{3}{2},\pm\frac{1}{2}>$ light hole

$|\frac{1}{2},\pm\frac{1}{2}>$ split off hole

C.4 Explicit calculation of the coefficients

We use tables in Zare to determine these values

C.4.1 Coefficients for $|\frac{3}{2},\frac{3}{2}>$

Based on addition of angular momentum, in order to achieve this state we require the following linear combination of angular momentum states. Here the kets on the right hand side of the equation describe the total momentum and projection for both the spherical harmonics and Bloch functions $|\text{Sphereical}_{\text{tot}}, \text{Spherical}_{\text{proj}}, \text{Bloch}_{\text{tot}}, \text{Bloch}_{\text{proj}}>$. To evaluate the coefficients in front of each term in the linear combination, we turn to the tables in Zare. Results are shown below. The origin of j and m are as follows: j is the total angular momentum of the spherical harmonic. m is the projection of the state in the coupled basis. For instance, in A ($j=0, m=\frac{3}{2}$) and in B ($j=2, m=\frac{3}{2}$).

$$|\frac{3}{2},\frac{3}{2}> = A|0,0,\frac{3}{2},\frac{3}{2}> +B|2,2,\frac{3}{2},-\frac{1}{2}> +C|2,1,\frac{3}{2},\frac{1}{2}> +D|2,0,\frac{3}{2},\frac{3}{2}> +E|2,1,\frac{1}{2},\frac{1}{2}> + F|2,2,\frac{1}{2},-\frac{1}{2}> \quad \text{(C.14)}$$

where

$$A = \left\langle 0,0,\frac{3}{2},+\frac{3}{2}|\frac{3}{2},\frac{3}{2}\right\rangle = \sqrt{\frac{(j+m-\frac{1}{2})(j+m+\frac{1}{2})(j+m+\frac{3}{2})}{(2j+1)(2j+2)(2j+3)}} = 1$$

$$B = \left\langle 2,2,\frac{3}{2},-\frac{1}{2}|\frac{3}{2},\frac{3}{2}\right\rangle = -(j-3m-1/2)\sqrt{\frac{(j+m+\frac{1}{2})}{(2j-1)(2j+1)(2j+2)}} = \frac{2}{\sqrt{10}}$$

$$C = \left\langle 2,1,\frac{3}{2},+\frac{1}{2}|\frac{3}{2},\frac{3}{2}\right\rangle = -(j+3m-1/2)\sqrt{\frac{(j-m+\frac{1}{2})}{(2j-1)(2j+1)(2j+2)}} = -\frac{2}{\sqrt{10}}$$

$$D = \left\langle 2,0,\frac{3}{2},+\frac{3}{2}|\frac{3}{2},\frac{3}{2}\right\rangle = \sqrt{\frac{3(j+m-\frac{1}{2})(j-m+\frac{1}{2})(j-m+\frac{3}{2})}{(2j-1)(2j+1)(2j+2)}}$$

$$
\begin{aligned}
&= \frac{1}{\sqrt{5}} \\
E = \left\langle 2,1,\frac{1}{2},+\frac{1}{2}|\frac{3}{2},\frac{3}{2}\right\rangle &= -\sqrt{\frac{(j+m+\frac{1}{2})}{(2j+1)}} \\
&= -\frac{2}{\sqrt{5}} \\
F = \left\langle 2,2,\frac{1}{2},-\frac{1}{2}|\frac{3}{2},\frac{3}{2}\right\rangle &= \sqrt{\frac{(j+m+\frac{1}{2})}{(2j+1)}} \\
&= \frac{2}{\sqrt{5}}
\end{aligned}
$$

C.4.2 Coefficients for $|\frac{3}{2},-\frac{3}{2}>$

We require the following linear combination of angular momentum states

$$
\begin{aligned}
|\tfrac{3}{2},-\tfrac{3}{2}> \;=\; & A|0,0,\tfrac{3}{2},-\tfrac{3}{2}>+B|2,-2,\tfrac{3}{2},\tfrac{1}{2}>+C|2,-1,\tfrac{3}{2},-\tfrac{1}{2}>+D|2,0,\tfrac{3}{2},-\tfrac{3}{2}>+E|2,-2,\tfrac{1}{2},\tfrac{1}{2}> \\
& +F|2,-1,\tfrac{1}{2},-\tfrac{1}{2}>
\end{aligned} \tag{C.15}
$$

where

$$
\begin{aligned}
A = \left\langle 0,\ \ 0,\frac{3}{2},-\frac{3}{2}|\frac{3}{2},-\frac{3}{2}\right\rangle &= \sqrt{\frac{(j-m-\frac{1}{2})(j-m+\frac{1}{2})(j-m+\frac{3}{2})}{(2j+1)(2j+2)(2j+3)}} \\
&= 1 \\
B = \left\langle 2,-2,\frac{3}{2},+\frac{1}{2}|\frac{3}{2},-\frac{3}{2}\right\rangle &= -(j+3m-1/2)\sqrt{\frac{(j-m+\frac{1}{2})}{(2j-1)(2j+1)(2j+2)}} \\
&= \frac{2}{\sqrt{10}} \\
C = \left\langle 2,-1,\frac{3}{2},-\frac{1}{2}|\frac{3}{2},-\frac{3}{2}\right\rangle &= -(j-3m-1/2)\sqrt{\frac{(j+m+\frac{1}{2})}{(2j-1)(2j+1)(2j+2)}} \\
&= -\frac{2}{\sqrt{10}} \\
D = \left\langle 2,\ \ 0,\frac{3}{2},-\frac{3}{2}|\frac{3}{2},-\frac{3}{2}\right\rangle &= \sqrt{\frac{3(j+m+\frac{1}{2})(j+m+\frac{3}{2})(j-m-\frac{1}{2})}{(2j-1)(2j+1)(2j+2)}} \\
&= \frac{1}{\sqrt{5}} \\
E = \left\langle 2,-2,\frac{1}{2},+\frac{1}{2}|\frac{3}{2},-\frac{3}{2}\right\rangle &= -\sqrt{\frac{(j-m+\frac{1}{2})}{(2j+1)}} \\
&= -\frac{2}{\sqrt{5}} \\
F = \left\langle 2,-1,\frac{1}{2},-\frac{1}{2}|\frac{3}{2},-\frac{3}{2}\right\rangle &= \sqrt{\frac{(j+m+\frac{1}{2})}{(2j+1)}} \\
&= \frac{1}{\sqrt{5}}
\end{aligned}
$$

C.4.3 Coefficients for $|\frac{3}{2},\frac{1}{2}>$

We require the following linear combination of angular momentum states

$$|\tfrac{3}{2},\tfrac{1}{2}> = A|0,0,\tfrac{3}{2},\tfrac{1}{2}> +B|2,2,\tfrac{3}{2},-\tfrac{3}{2}> +C|2,1,\tfrac{3}{2},-\tfrac{1}{2}> +D|2,0,\tfrac{3}{2},\tfrac{1}{2}> +E|2,-1,\tfrac{3}{2},\tfrac{3}{2}> +F|2,0,\tfrac{1}{2},\tfrac{1}{2}> +G|2,1,\tfrac{1}{2},-\tfrac{1}{2}> \quad \text{(C.16)}$$

where

$$\begin{aligned}
A = \left\langle 0,\ 0,\tfrac{3}{2},+\tfrac{1}{2}|\tfrac{3}{2},\tfrac{1}{2}\right\rangle &= \sqrt{\frac{3(j+m+\frac{1}{2})(j+m+\frac{3}{2})(j-m+\frac{3}{2})}{(2j+1)(2j+2)(2j+3)}} \\
&= 1 \\
B = \left\langle 2,+2,\tfrac{3}{2},-\tfrac{3}{2}|\tfrac{3}{2},\tfrac{1}{2}\right\rangle &= \sqrt{\frac{3(j+m+\frac{1}{2})(j+m+\frac{3}{2})(j-m-\frac{1}{2})}{(2j-1)(2j+1)(2j+2)}} \\
&= \sqrt{\frac{2}{5}} \\
C = \left\langle 2,+1,\tfrac{3}{2},-\tfrac{1}{2}|\tfrac{3}{2},\tfrac{1}{2}\right\rangle &= -(j-3m-1/2)\sqrt{\frac{(j+m+\frac{1}{2})}{(2j-1)(2j+1)(2j+2)}} \\
&= 0 \\
D = \left\langle 2,\ 0,\tfrac{3}{2},+\tfrac{1}{2}|\tfrac{3}{2},\tfrac{1}{2}\right\rangle &= -(j+3m-1/2)\sqrt{\frac{(j-m+\frac{1}{2})}{(2j-1)(2j+1)(2j+2)}} \\
&= -\sqrt{\frac{1}{5}} \\
E = \left\langle 2,-1,\tfrac{3}{2},+\tfrac{3}{2}|\tfrac{3}{2},\tfrac{1}{2}\right\rangle &= \sqrt{\frac{3(j+m-\frac{1}{2})(j-m+\frac{1}{2})(j-m+\frac{3}{2})}{(2j-1)(2j+1)(2j+2)}} \\
&= \sqrt{\frac{2}{5}} \\
F = \left\langle 2,\ 0,\tfrac{1}{2},+\tfrac{1}{2}|\tfrac{3}{2},\tfrac{1}{2}\right\rangle &= -\sqrt{\frac{(j-m+\frac{1}{2})}{(2j+1)}} \\
&= -\sqrt{\frac{2}{5}} \\
G = \left\langle 2,+1,\tfrac{1}{2},-\tfrac{1}{2}|\tfrac{3}{2},\tfrac{1}{2}\right\rangle &= \sqrt{\frac{(j+m+\frac{1}{2})}{(2j+1)}} \\
&= \sqrt{\frac{3}{5}}
\end{aligned}$$

C.4.4 Coefficients for $|\frac{3}{2},-\frac{1}{2}>$

We require the following linear combination of angular momentum states

$$|\tfrac{3}{2},-\tfrac{1}{2}>^{+} = A|0,0,\tfrac{3}{2},-\tfrac{1}{2}> +B|2,1,\tfrac{3}{2},-\tfrac{3}{2}> +C|2,0,\tfrac{3}{2},-\tfrac{1}{2}> +D|2,-1,\tfrac{3}{2},\tfrac{1}{2}> +E|2,-2,\tfrac{3}{2},\tfrac{3}{2}> +F|2,0,\tfrac{1}{2},-\tfrac{1}{2}> +G|2,-1,\tfrac{1}{2},\tfrac{1}{2}> \quad \text{(C.17)}$$

where

$$
\begin{aligned}
A = \left\langle 0,\ \ 0, \frac{3}{2}, -\frac{1}{2} \middle| \frac{3}{2}, -\frac{1}{2} \right\rangle &= \sqrt{\frac{3(j+m+\frac{3}{2})(j-m+\frac{1}{2})(j-m+\frac{3}{2})}{(2j+1)(2j+2)(2j+3)}} \\
&= 1 \\
B = \left\langle 2, +1, \frac{3}{2}, -\frac{3}{2} \middle| \frac{3}{2}, -\frac{1}{2} \right\rangle &= \sqrt{\frac{3(j+m+\frac{1}{2})(j+m+\frac{3}{2})(j-m-\frac{1}{2})}{(2j-1)(2j+1)(2j+2)}} \\
&= \sqrt{\frac{2}{5}} \\
C = \left\langle 2,\ \ 0, \frac{3}{2}, -\frac{1}{2} \middle| \frac{3}{2}, -\frac{1}{2} \right\rangle &= -(j-3m-1/2)\sqrt{\frac{(j+m+\frac{1}{2})}{(2j-1)(2j+1)(2j+2)}} \\
&= -\sqrt{\frac{1}{5}} \\
D = \left\langle 2, -1, \frac{3}{2}, +\frac{1}{2} \middle| \frac{3}{2}, -\frac{1}{2} \right\rangle &= -(j+3m-1/2)\sqrt{\frac{(j-m+\frac{1}{2})}{(2j-1)(2j+1)(2j+2)}} \\
&= 0 \\
E = \left\langle 2, -2, \frac{3}{2}, +\frac{3}{2} \middle| \frac{3}{2}, -\frac{1}{2} \right\rangle &= \sqrt{\frac{3(j+m-\frac{1}{2})(j-m+\frac{1}{2})(j-m+\frac{3}{2})}{(2j-1)(2j+1)(2j+2)}} \\
&= \sqrt{\frac{2}{5}} \\
F = \left\langle 2,\ \ 0, \frac{1}{2}, -\frac{1}{2} \middle| \frac{3}{2}, -\frac{1}{2} \right\rangle &= \sqrt{\frac{(j+m+\frac{1}{2})}{(2j+1)}} \\
&= \sqrt{\frac{2}{5}} \\
G = \left\langle 2, -1, \frac{1}{2}, +\frac{1}{2} \middle| \frac{3}{2}, -\frac{1}{2} \right\rangle &= -\sqrt{\frac{(j-m+\frac{1}{2})}{(2j+1)}} \\
&= -\sqrt{\frac{3}{5}}
\end{aligned}
$$

C.4.5 Coefficients for $|\frac{1}{2}, \frac{1}{2}>$

We require the following linear combination of angular momentum states

$$
|\tfrac{1}{2}, \tfrac{1}{2}>^{+} = A|0, 0, \tfrac{1}{2}, \tfrac{1}{2}> + B|2, 2, \tfrac{3}{2}, -\tfrac{3}{2}> + C|2, 1, \tfrac{3}{2}, -\tfrac{1}{2}> + D|2, 0, \tfrac{3}{2}, \tfrac{1}{2}> + E|2, -1, \tfrac{3}{2}, \tfrac{3}{2}> \tag{C.18}
$$

where

$$
\begin{aligned}
A = \left\langle 0,\ \ 0, \frac{1}{2}, +\frac{1}{2} \middle| \frac{1}{2}, \frac{1}{2} \right\rangle &= \sqrt{\frac{(j+m+\frac{1}{2})}{(2j+1)}} \\
&= 1 \\
B = \left\langle 2, +2, \frac{3}{2}, -\frac{3}{2} \middle| \frac{1}{2}, \frac{1}{2} \right\rangle &= \sqrt{\frac{(j+m-\frac{1}{2})(j+m+\frac{1}{2})(j+m+\frac{3}{2})}{(2j-1)(2j)(2j+1)}}
\end{aligned}
$$

$$= \sqrt{\frac{2}{5}}$$

$$C = \left\langle 2,+1,\frac{3}{2},-\frac{1}{2}|\frac{1}{2},\frac{1}{2}\right\rangle = -\sqrt{\frac{3(j+m-\frac{1}{2})(j+m+\frac{1}{2})(j-m-\frac{1}{2})}{(2j-1)(2j)(2j+1)}}$$

$$= -\sqrt{\frac{3}{10}}$$

$$D = \left\langle 2,\ 0,\frac{3}{2},+\frac{1}{2}|\frac{1}{2},\frac{1}{2}\right\rangle = \sqrt{\frac{3(j+m-\frac{1}{2})(j-m-\frac{1}{2})(j-m+\frac{1}{2})}{(2j-1)(2j)(2j+1)}}$$

$$= \sqrt{\frac{1}{5}}$$

$$E = \left\langle 2,-1,\frac{3}{2},+\frac{3}{2}|\frac{1}{2},\frac{1}{2}\right\rangle = -\sqrt{\frac{(j-m-\frac{1}{2})(j-m+\frac{1}{2})(j-m+\frac{3}{2})}{(2j-1)(2j)(2j+1)}}$$

$$= -\frac{1}{\sqrt{10}}$$

C.4.6 Coefficients for $|\frac{1}{2},-\frac{1}{2}>$

We require the following linear combination of angular momentum states

$$|\frac{1}{2},-\frac{1}{2}>^{+} = A|0,0,\frac{1}{2},-\frac{1}{2}> + B|2,-2,\frac{3}{2},\frac{3}{2}> + C|2,1,\frac{3}{2},\frac{1}{2}> + D|2,0,\frac{3}{2},-\frac{1}{2}> + E|2,1,\frac{3}{2},-\frac{3}{2}> \tag{C.19}$$

where

$$A = \left\langle 0,\ 0,\frac{1}{2},-\frac{1}{2}|\frac{1}{2},-\frac{1}{2}\right\rangle = \sqrt{\frac{(j-m+\frac{1}{2})}{(2j+1)}}$$

$$= 1$$

$$B = \left\langle 2,-2,\frac{3}{2},+\frac{3}{2}|\frac{1}{2},-\frac{1}{2}\right\rangle = -\sqrt{\frac{(j-m-\frac{1}{2})(j-m+\frac{1}{2})(j-m+\frac{3}{2})}{(2j-1)(2j)(2j+1)}}$$

$$= -\sqrt{\frac{2}{5}}$$

$$C = \left\langle 2,-1,\frac{3}{2},+\frac{1}{2}|\frac{1}{2},-\frac{1}{2}\right\rangle = \sqrt{\frac{3(j+m-\frac{1}{2})(j-m-\frac{1}{2})(j-m+\frac{1}{2})}{(2j-1)(2j)(2j+1)}}$$

$$= \sqrt{\frac{3}{10}}$$

$$D = \left\langle 2,\ 0,\frac{3}{2},-\frac{1}{2}|\frac{1}{2},-\frac{1}{2}\right\rangle = -\sqrt{\frac{3(j+m-\frac{1}{2})(j+m+\frac{1}{2})(j-m-\frac{1}{2})}{(2j-1)(2j)(2j+1)}}$$

$$= -\sqrt{\frac{1}{5}}$$

$$E = \left\langle 2,+1,\frac{3}{2},-\frac{3}{2}|\frac{1}{2},-\frac{1}{2}\right\rangle = \sqrt{\frac{(j+m-\frac{1}{2})(j+m+\frac{1}{2})(j+m+\frac{3}{2})}{(2j-1)(2j)(2j+1)}}$$

$$= \frac{1}{\sqrt{10}}$$

C.5 Hole wavefunction with radial contribution (Summary)

We list the total hole wavefunctions here (even). This includes the radial part of the wavefunction. Exact evaluation of the radial components is discussed in the next section. However, a quick qualitative way in which one can check the correctness of the function goes as follows: Grigoryan has determined the wavefunctions for spherical quantum dots and has showed it to be of the form (this is just a column vector explicitly split into an upper half and a lower half)

$$\Psi_j^+ = \begin{pmatrix} R_{h2}^+\phi_{j-3/2}^{(4)} + R_{h1}^+\phi_{j+1/2}^{(4)} \\ R_s^+\phi_{j+1/2}^{(2)} \end{pmatrix} \tag{C.20}$$

In the equation, $\phi_{j-3/2}^{(4)}$ and $\phi_{j+1/2}^{(4)}$ are 4 by 1 vectors describing the particular contribution of spherical harmonics to the hole wavefunction when we deal with heavy hole and light hole Bloch terms (we did this in the previous section using Zare tables). $\phi_{j+1/2}^+$ is a 2 by 1 vector describing the spherical harmonic contribution to the wavefunction when we deal with split off Bloch terms. Terms with the subscript $j-3/2$ essentially deal with states having "s" envelope functions and terms with the subscript $j+1/2$ deal with those having "d" envelope functions. So practically speaking, we associate R_{h2}^+ with $Y_{0,0}$ and R_{h1}^+ with $Y_{2,\pm2}$, $Y_{2,\pm1}$, and $Y_{2,0}$ when the Bloch terms are either heavy hole or light hole. In the case of split off hole Bloch terms we use R_s^+.

$$\begin{aligned} |\tfrac{3}{2},+\tfrac{3}{2}>^+ &= \left(R_{h2en}(r)Y_{0,0} + \frac{1}{\sqrt{5}}R_{h1en}(r)Y_{2,0}\right)|\tfrac{3}{2},\tfrac{3}{2}> + \left(\frac{2}{\sqrt{10}}R_{h1en}(r)Y_{2,2}\right)|\tfrac{3}{2},-\tfrac{1}{2}> \\ &+ \left(-\frac{2}{\sqrt{10}}R_{h1en}(r)Y_{2,1}\right)|\tfrac{3}{2},\tfrac{1}{2}> + \left(-\frac{1}{\sqrt{5}}R_{sen}(r)Y_{2,1}\right)|\tfrac{1}{2},\tfrac{1}{2}> \\ &+ \left(\frac{2}{\sqrt{5}}R_{sen}(r)Y_{2,2}\right)|\tfrac{1}{2},-\tfrac{1}{2}> \end{aligned} \tag{C.21}$$

$$\begin{aligned} |\tfrac{3}{2},-\tfrac{3}{2}>^+ &= \left(R_{2en}(r)Y_{0,0} + \frac{1}{\sqrt{5}}R_{h1en}(r)Y_{2,0}\right)|\tfrac{3}{2},-\tfrac{3}{2}> + \left(\frac{2}{\sqrt{10}}R_{h1en}(r)Y_{2,-2}\right)|\tfrac{3}{2},\tfrac{1}{2}> \\ &+ \left(-\frac{2}{\sqrt{10}}R_{h1en}(r)Y_{2,-1}\right)|\tfrac{3}{2},-\tfrac{1}{2}> + \left(-\frac{2}{\sqrt{5}}R_{sen}(r)Y_{2,-2}\right)|\tfrac{1}{2},\tfrac{1}{2}> \\ &+ \left(\frac{1}{\sqrt{5}}R_{sen}(r)Y_{2,-1}\right)|\tfrac{1}{2},-\tfrac{1}{2}> \end{aligned} \tag{C.22}$$

$$\begin{aligned} |\tfrac{3}{2},+\tfrac{1}{2}>^+ &= \left(\sqrt{\frac{2}{5}}R_{h1en}(r)Y_{2,-1}\right)|\tfrac{3}{2},\tfrac{3}{2}> + \left(\sqrt{\frac{2}{5}}R_{h1en}(r)Y_{2,2}\right)|\tfrac{3}{2},-\tfrac{3}{2}> + (R_{h2en}(r)Y_{0,0})|\tfrac{3}{2},\tfrac{1}{2}> \\ &+ \left(-\sqrt{\frac{1}{5}}R_{h1en}(r)Y_{2,0}\right)|\tfrac{3}{2},\tfrac{1}{2}> + \left(-\sqrt{\frac{2}{5}}R_{sen}(r)Y_{2,0}\right)|\tfrac{1}{2},\tfrac{1}{2}> \\ &+ \left(\sqrt{\frac{3}{5}}R_{sen}(r)Y_{2,1}\right)|\tfrac{1}{2},-\tfrac{1}{2}> \end{aligned} \tag{C.23}$$

$$|\tfrac{3}{2},-\tfrac{1}{2}>^+ = \left(\sqrt{\frac{2}{5}}R_{h1en}(r)Y_{2,-2}\right)|\tfrac{3}{2},\tfrac{3}{2}> + \left(\sqrt{\frac{2}{5}}R_{h1en}(r)Y_{2,1}\right)|\tfrac{3}{2},-\tfrac{3}{2}>$$

$$+\left(R_{h2en}(r)Y_{0,0}-\sqrt{\frac{1}{5}}R_{h1en}(r)Y_{2,0}\right)|\frac{3}{2},-\frac{1}{2}>+\left(\sqrt{\frac{2}{5}}R_{sen}(r)Y_{2,0}\right)|\frac{1}{2},-\frac{1}{2}>$$
$$+\left(-\sqrt{\frac{3}{5}}R_{sen}(r)Y_{2,-1}\right)|\frac{1}{2},\frac{1}{2}> \quad \text{(C.24)}$$

$$|\frac{1}{2},+\frac{1}{2}>^{+} = \sqrt{\frac{2}{5}}R_{h1en}(r)Y_{2,2}|\frac{3}{2},-\frac{3}{2}>-\frac{1}{\sqrt{10}}R_{h1en}(r)Y_{2,-1}|\frac{3}{2},\frac{3}{2}>-\sqrt{\frac{3}{10}}R_{h1en}(r)Y_{2,1}|\frac{3}{2},-\frac{1}{2}>$$
$$+\frac{1}{\sqrt{5}}R_{h1en}(r)Y_{2,0}|\frac{3}{2},\frac{1}{2}>+R_{sen}(r)Y_{0,0}|\frac{1}{2},\frac{1}{2}> \quad \text{(C.25)}$$

$$|\frac{1}{2},-\frac{1}{2}>^{+} = \frac{1}{\sqrt{10}}R_{h1en}(r)Y_{2,1}|\frac{3}{2},-\frac{3}{2}>-\sqrt{\frac{2}{5}}R_{h1en}(r)Y_{2,-2}|\frac{3}{2},\frac{3}{2}>+\sqrt{\frac{3}{10}}R_{h1en}(r)Y_{2,-1}|\frac{3}{2},\frac{1}{2}>$$
$$-\frac{1}{\sqrt{5}}R_{h1en}(r)Y_{2,0}|\frac{3}{2},-\frac{1}{2}>+R_{sen}(r)Y_{0,0}|\frac{1}{2},-\frac{1}{2}> \quad \text{(C.26)}$$

C.6 Determining the radial functions

In general, the radial functions can be written as linear combinations of spherical Bessel functions of the same order. (The linear combination is composed of three elements reflecting the three possible wavevectors of the valence band, k_l, k_h, k_s. The subscripts indicate light, heavy and split off) There are three radial functions that we wish to determine, of orders l (for hh and lh), l+2 (for hh and lh) and l+2 (exclusively for soh). These functions are denoted as $R_{h2}(r), R_{h1}(r)$ and $R_s(R)$. What is unknown is the relative contributions of the three Bessel functions composing each radial function.

$$R_{h1}(r) = c_1 J_{F+1/2}(k_l r) + c_2 J_{F+1/2}(k_h r) + c_3 J_{F+1/2}(k_s r)$$

$$R_{h2}(r) = -c_1\sqrt{\frac{3(2F-1)}{2F+3}}J_{F-3/2}(k_l r) + c_2\sqrt{\frac{2F+3}{3(2F-1)}}J_{F-3/2}(k_h r) - c_3\sqrt{\frac{2(2F-1)}{2F+3}}J_{F-3/2}(k_s r)$$

$$R_s(r) = c_1\sqrt{\frac{F}{2F+3}}\left(\frac{2\epsilon-(\gamma 1+2\gamma)k_l^2}{\gamma k_l^2}\right)J_{F+1/2}(k_l r) + c_3\sqrt{\frac{F}{2F+3}}\left(\frac{2\epsilon-(\gamma_1+2\gamma)k_s^2}{\gamma k_s^2}\right)J_{F+1/2}(k_s r)$$

where the required wavevectors are

$$k_l = \sqrt{\frac{C}{(\gamma 1-2\gamma)(\gamma 1+4\gamma)}\left[C_2+\sqrt{C_2^2-4\epsilon(\epsilon-\Delta)(\gamma_1-2\gamma)(\gamma_1+4\gamma)}\right]} \quad \text{(C.27)}$$

$$k_s = \sqrt{\frac{C}{(\gamma 1-2\gamma)(\gamma 1+4\gamma)}\left[C_2-\sqrt{C_2^2-4\epsilon(\epsilon-\Delta)(\gamma_1-2\gamma)(\gamma_1+4\gamma)}\right]} \quad \text{(C.28)}$$

$$k_h = \sqrt{\frac{2C\epsilon}{\gamma_1-2\gamma}} \quad \text{(C.29)}$$

In the above equations, $\Delta = 0.42$ eV is the spin orbit coupling, $\gamma_1 = 2.04$, $\gamma = 0.58$, C is $m_e/\hbar^2$ in units of $1/(\text{eV}\cdot\text{Angstrom}^2)$, and $C_2 = 2\epsilon(\gamma_1+\gamma)-\Delta(\gamma_1+2\gamma)$.

By applying the QD boundary condition at the surface of the particle, we obtain as set of linear equations. Solving for the coefficients c_1, c_2, and c_3 means solving for an overdetermined set of linear equations and leads to an infinite number of solutions. By arbitrarily guessing the value of one of the elements, say c_1, the other two c_2 and c_3 are determined. Practically speaking, this is done by

finding the conditions under which the matrix of prefactors has a determinant of zero. To do this we must already know the energy of the state in question,ϵ , as well as the Luttinger parameters γ and $\gamma 1$

$$\begin{pmatrix} G_1 & G_2 & G_3 \\ G_4 & G_5 & G_6 \\ G_7 & G_8 & G_9 \end{pmatrix} \begin{pmatrix} c_1 \\ c_2 \\ c_3 \end{pmatrix} = \begin{pmatrix} 0 \\ 0 \\ 0 \end{pmatrix} \tag{C.30}$$

in effect equivalent to finding the conditions where

$$\begin{vmatrix} G_1 & G_2 & G_3 \\ G_4 & G_5 & G_6 \\ G_7 & G_8 & G_9 \end{vmatrix} = 0 \tag{C.31}$$

Here

Order of spherical Bessel function is F+1/2

$$\begin{aligned} G_1(d) &= j_2(k_l d) \\ G_2(d) &= j_2(k_h d) \\ G_3(d) &= j_2(k - sd) \end{aligned}$$

Order of spherical Bessel function is F-3/2

$$\begin{aligned} G_4(d) &= -\sqrt{\frac{3(2F-1)}{2F+3}} j_0(k_l d) \\ G_5(d) &= \sqrt{\frac{2F+3}{3(2F-1)}} j_0(k_h d) \\ G_6(d) &= -1\sqrt{\frac{3(2F-1)}{2F+3}} j_0(k_s d) \end{aligned}$$

Order of spherical Bessel function is F+1/2

$$\begin{aligned} G_7(d) &= \sqrt{\frac{F}{2F+3}} \left[\frac{2\epsilon - (\gamma_1 + 2\gamma)k_l^2}{\gamma k_l^2}\right] j_2(k_l d) \\ G_8(d) &= 0 \\ G_9(d) &= \sqrt{\frac{F}{2F+3}} [\frac{2\epsilon - (\gamma_1 + 2\gamma)k_s^2}{\gamma k_s^2}] j_2(k_s d) \end{aligned}$$

The same idea applies for odd wavefunctions as discussed in Grigoryan.

Appendix D

Polarized Light

D.1 Interactions with Polarized Light

D.1.1 Linearly Polarized Light

$$\vec{e} = (e_x, e_y, e_z) \tag{D.1}$$

$$\vec{p} = (p_x, p_y, p_z) \tag{D.2}$$

$$\vec{e} \cdot \vec{p} = e_x p_x + e_y p_y + e_z p_z \tag{D.3}$$

$$\vec{e} \cdot \vec{p} = e_z p_z + e_+ p_- + e_- p_+ \tag{D.4}$$

where

$$e_+ = \frac{1}{\sqrt{2}}(e_x + ie_y)$$

$$e_- = \frac{1}{\sqrt{2}}(e_x - ie_y)$$

$$p_+ = \frac{1}{\sqrt{2}}(p_x + ip_y)$$

$$p_- = \frac{1}{\sqrt{2}}(p_x - ip_y)$$

Evaluating operators for finding selection rules, linear polarization

When evaluating the selection rules for linearly polarized light, there are three operators that we need to determine.

1. e_z^2
2. $e_+ e_-$
3. $e_- e_+$

First term

$$e_z^2 = \cos^2\theta \tag{D.5}$$

Second term

$$\begin{aligned} e_+e_- &= \frac{1}{2}(e_x + ie_y)(e_x - ie_y) \\ &= \frac{1}{2}(e_x^2 - ie_xe_y + ie_ye_x + e_y^2) \\ &= \frac{1}{2}(e_x^2 + e_y^2) \\ &= \frac{1}{2}(\sin^2\theta) \\ e_+e_- &= \frac{1}{2}(\sin^2\theta) \end{aligned} \tag{D.6}$$

We used the relations

$$e_z = \cos\theta \tag{D.7}$$

$$e_x = \sin\theta\cos\phi \tag{D.8}$$

$$e_y = \sin\theta\sin\phi \tag{D.9}$$

Third and final term. This is actually the same as the second term so we don't work out the details and just present the result.

$$e_-e_+ = \frac{1}{2}(\sin^2\theta) \tag{D.10}$$

D.1.2 Circularly Polarized Light

This section describes the operators required for describing circularly polarized light. The notation becomes a bit convoluted but should be reasonably understandable.

$$\hat{e}^{\pm} = (\hat{e}_x^{\pm}, \hat{e}_y^{\pm}, \hat{e}_z^{\pm}) \tag{D.11}$$

where

$$\hat{e}_x^{\pm} = e_x \pm i\acute{e}_x$$

$$\hat{e}_y^{\pm} = e_y \pm i\acute{e}_y$$

$$\hat{e}_z^{\pm} = e_z \pm i\acute{e}_z$$

Here the superscripts and the $\pm$ reflect the circular polarization of the light. Basically e and e' are two polarization vectors that are mutually orthogonal to each other and to the direction of the light propagation.

$$\hat{e}^{\pm} \cdot p = \hat{e}_z^{\pm}p_z + \hat{e}_+^{\pm}p_- + \hat{e}_-^{\pm}p_+ \tag{D.12}$$

where

$$\hat{e}_+^{\pm} = \frac{1}{\sqrt{2}}(\hat{e}_x^{\pm} + i\hat{e}_y^{\pm})$$

$$\hat{e}_-^{\pm} = \frac{1}{\sqrt{2}}(\hat{e}_x^{\pm} - i\hat{e}_y^{\pm})$$

$$p_+ = \frac{1}{\sqrt{2}}(p_x + ip_y)$$

$$p_- = \frac{1}{\sqrt{2}}(p_x - ip_y)$$

Evaluating operators for finding selection rules, circular polarization

When using this operator to find selection rules the following three terms will be encountered:

1. $\hat{e}_z^{\pm 2}$
2. $\hat{e}_+^{\pm}\hat{e}_-^{\mp}$
3. $\hat{e}_-^{\pm}\hat{e}_+^{\mp}$

We determine these terms explicitly in the following section.
First term:

$$\begin{aligned} \hat{e}_z^{\pm 2} &= (e_z \pm i\acute{e}_z)^2 \\ &= (e_z \pm i\acute{e}_z)(e_z \mp i\acute{e}_z) \\ &= e_z^2 + \acute{e}_z^2 \\ |\hat{e}_z^{\pm}|^2 &= e_z^2 + \acute{e}_z^2 \end{aligned} \tag{D.13}$$

where $e_z = \cos\theta_e$ and $\acute{e}_z = \cos\acute{\theta}_e$

$$|\hat{e}_z^{\pm}|^2 = \cos^2\theta_e + \cos^2\acute{\theta}_e \tag{D.14}$$

Since

$$e_x^2 + e_y^2 + e_z^2 = 1$$

and

$$\acute{e}_x^2 + \acute{e}_y^2 + \acute{e}_z^2 = 1$$

we also determine that:

$$1 - \cos^2\theta_e = e_x^2 + e_y^2$$

$$1 - \cos^2\acute{\theta}_e = \acute{e}_x^2 + \acute{e}_y^2$$

Second term:

$$\hat{e}_+^{\pm}\hat{e}_-^{\mp} = \frac{1}{2}[(\hat{e}_x^{\pm} + i\hat{e}_y^{\pm})(\hat{e}_x^{\mp} - i\hat{e}_y^{\mp})]$$

Here break up the $\hat{e}^{\pm}$ terms into their two mutually orthogonal components e and e'

$$\begin{aligned} &= \frac{1}{2}[(e_x \pm i\acute{e}_z) + i(e_y \pm i\acute{e}_y)][(e_x \mp i\acute{e}_z) - i(e_y \mp i\acute{e}_y)] \\ &= \frac{1}{2}[(e_x \pm i\acute{e}_z)(e_x \mp i\acute{e}_x) + (e_y \pm i\acute{e}_y)(e_y \mp i\acute{e}_y) - i(e_x \pm i\acute{e}_x)(e_y \mp i\acute{e}_y) + i(e_y \pm i\acute{e}_y)(e_x \mp i\acute{e}_x)] \\ &= \frac{1}{2}[e_x^2 + \acute{e}_x^2 + e_y^2 + \acute{e}_y^2 - i(e_x \pm i\acute{e}_x)(e_y \mp i\acute{e}_y) + i(e_y \pm i\acute{e}_y)(e_x \mp i\acute{e}_x)] \\ &= \frac{1}{2}[e_x^2 + \acute{e}_x^2 + e_y^2 + \acute{e}_y^2 - i(e_x e_y + \acute{e}_x\acute{e}_y \mp ie_x\acute{e}_y \pm i\acute{e}_x e_y) + i(e_x e_y + \acute{e}_x\acute{e}_y \mp i\acute{e}_x e_y \pm ie_x\acute{e}_y)] \\ &= \frac{1}{2}[e_x^2 + \acute{e}_x^2 + e_y^2 + \acute{e}_y^2 \mp e_x\acute{e}_y \pm \acute{e}_x e_y \pm \acute{e}_x e_y \mp e_x\acute{e}_y] \\ &= \frac{1}{2}[e_x^2 + \acute{e}_x^2 + e_y^2 + \acute{e}_y^2 \mp 2e_x\acute{e}_y \pm 2\acute{e}_x e_y] \end{aligned}$$

Now we introduce the angle relations as in previous section

$$\begin{aligned} &= \frac{1}{2}[(1 - e_z^2) + (1 - \acute{e}_z^2) \mp 2(e_x\acute{e}_y - \acute{e}_x e_y)] \\ &= \frac{1}{2}[1 - \cos^2\theta_e + 1 - \cos^2\acute{\theta}_e \mp 2(e_x\acute{e}_y - \acute{e}_x e_y)] \end{aligned}$$

$$= \frac{1}{2}[(2 - \cos^2\theta_e - \cos^2\acute{\theta}_e) \mp 2(e_x\acute{e}_y - \acute{e}_x e_y)]$$

Recall that $\cos^2\theta + \cos^2\theta_e + \cos^2\acute{\theta}_e = 1$ which is a property of three mutually orthogonal vectors. The equation becomes:

$$= \frac{1}{2}[2 - (1 - \cos^2\theta) \mp 2(e_x\acute{e}_y - \acute{e}_x e_y)]$$

Everything is now expressed in terms of θ. We can now simplify the expression (getting rid of all primed values) if we recall the vector relationships

$$\acute{e}_y = [e\ c]_y$$

and

$$\acute{e}_x = [e\ c]_x$$

The expression then becomes

$$= \frac{1}{2}[1 + \cos^2\theta \mp 2(e_x[e\ c]_y - e_y[e\ c]_x)]$$

and we know that

$$[e\ c]_y = e_z c_x - c_z e_x$$
$$[e\ c]_x = e_y c_z - c_y e_z$$

$$= \frac{1}{2}[1 + \cos^2\theta \mp 2(e_x(e_z c_x - c_z e_x) - e_y(e_y c_z - c_y e_z))]$$
$$= \frac{1}{2}[1 + \cos^2\theta \mp 2(-c_z(e_x^2 + e_y^2) + e_z(e_x c_x + e_y c_y))]$$

Now add and subtract $e_z^2 c_z$ to the last term in parenthesis within the brackets

$$= \frac{1}{2}[1 + \cos^2\theta \mp 2(-c_z(e_x^2 + e_y^2) + e_z(e_x c_x + e_y c_y + e_z c_z) - e_z^2 c_z)]$$

Recall that $e_x c_x + e_y c_y + e_z c_z = 0$ because $e \cdot c = 0$. The expression simplifies to

$$= \frac{1}{2}[1 + \cos^2\theta \mp 2(-c_z(e_x^2 + e_y^2 + e_z^2))]$$

Recall that $e_x^2 + e_y^2 + e_z^2 = 1$

$$= \frac{1}{2}[1 + \cos^2\theta \pm 2c_z]$$

where $c_z = \cos\theta$ The expression now becomes

$$= \frac{1}{2}[1 + \cos^2\theta \pm 2\cos\theta]$$
$$= \frac{1}{2}(1 \pm \cos\theta)^2$$

$$|\hat{e}_+^{\pm}|^2 = \hat{e}_+^{\pm}\hat{e}_-^{\mp} = \frac{1}{2}(1 \pm \cos\theta)^2 \tag{D.15}$$

Likewise the same procedure can be conducted for the third term. We obtain:

$$|\hat{e}_-^{\pm}|^2 = \hat{e}_-^{\pm}\hat{e}_+^{\mp} = \frac{1}{2}(1 \mp \cos\theta)^2 \tag{D.16}$$

Appendix E

Selection Rules

E.1 Preliminaries

E.1.1 Linearly Polarized Light

Explicit calculations of the selection rules are given in the next section. In this section, however, we give examples of the types of expressions that are involved. Three terms of interest are:

1. $< s|e \cdot p|z >$
2. $< s|e \cdot p|x + iy >$
3. $< s|e \cdot p|x - iy >$

First term:

$$< s|e_z p_z + e_+ p_- + e_- p_+|z >$$

where from Appendix D, $e \cdot p = e_z p_z + e_+ p_- + e_- p_+$. The raising and lowering operators (p_+ and p_-) do not do anything here. Eliminate these terms immediately. We are left with

$$\begin{aligned} < s|e_z p_z|z > &= e_z < s|p_z|z > \\ &= e_z P \end{aligned}$$

where P is the Kane interband matrix element.

$$= P\cos\theta \tag{E.1}$$

Second term:

$$< s|e_z p_z + e_+ p_- + e_- p_+|x + iy >$$

We drop the z term because it does not act on the ket. Also drop the p_+ term because it will cancel itself when it operates on the ket. We are left with

$$\begin{aligned} &= < s|e_+ p_-|x + iy > \\ &= \frac{1}{\sqrt{2}} < s|e_+(p_x - ip_y)|x + iy > \\ &= \frac{1}{\sqrt{2}} e_+ < s|p_x - ip_y|x + iy > \\ &= \frac{1}{\sqrt{2}} e_+ < s|p_x x + p_y y > \end{aligned}$$

$$= \frac{1}{\sqrt{2}} e_+ (< s|p_x|x > + < s|p_y|y >)$$
$$= \frac{2}{\sqrt{2}} e_+ P = \frac{2}{\sqrt{2}} P e_+$$

This gives

$$= \frac{2}{\sqrt{2}} P e_+$$

The second term is

$$< s|e \cdot p|x + iy >= \frac{2}{\sqrt{2}} P e_+ \tag{E.2}$$

Third term:
The third term can be evaluated in a similar manner. We skip the details and present the result

$$< s|e \cdot p|x - iy >= \frac{2}{\sqrt{2}} P e_- \tag{E.3}$$

E.1.2 Fine Structure Transition Probabilities, Linear Polarization

In this section we derive the transition probabilities as described in the Efros 1996 PRB. This is for linearly polarized light. I include all details for completeness. Once the first state has been determined, later evaluations will skip many details.

First State $|2,1>$

In the electron-hole representation, this state is written as

$$|2,1>_{e,h} = iC^- |\frac{1}{2}, \frac{1}{2}> + C^+ |\frac{3}{2}, -\frac{1}{2}> \tag{E.4}$$

where the hole Bloch terms are

$$\mu_{1/2} = \frac{i}{\sqrt{6}}(x + iy) \downarrow - i\sqrt{\frac{2}{3}} z \uparrow$$

$$\mu_{3/2} = \frac{1}{\sqrt{2}}(x + iy) \uparrow$$

The above notation can be understood as follows. $|2,1>$ represents the total angular momentum and projection of *both* the electron and hole. The kets on the right hand side of the equation are the individual angular momentum projections of the electron and hole written as,|hole, electron >. An easy way to check if the linear combination is qualitatively correct is to sum individual electron and hole contributions to see if it adds up to the total projection on the left ket. For example, 1/2+1/2=1 and 3/2-1/2=1.

To evaluate transition probabilities we convert the wavefunction to the electron-electron notation. This is done by taking the complex conjugate of the hole Bloch term and flipping all spin projections ($\uparrow$ to $\downarrow$ and vice versa).

$$|2,1>_{e,e} = -C^- |\frac{1}{\sqrt{6}}(x - iy) \uparrow - \sqrt{\frac{2}{3}} z \downarrow > |s \uparrow > + \frac{C^+}{\sqrt{2}} |(x - iy) \downarrow > |s \downarrow > \tag{E.5}$$

In each of the terms above, the first ket is the hole Bloch term and the second ket is the electron contribution (spin up is given by $|s\uparrow>$, likewise, spin down by $|s\downarrow>$). We write everything in the uncoupled representation to make things easier. Accessing the $|2,1>$ state involves the following transitions based on the above coupled expression.

$$-C^- < s\uparrow \ |e\cdot p|\frac{1}{\sqrt{6}}(x-iy)\uparrow -\sqrt{\frac{2}{3}}z\downarrow > +\frac{C^+}{\sqrt{2}} < s\downarrow \ |e\cdot p|(x-iy)\downarrow >$$

Eliminate all spin flip transitions. Practically speaking, throw away any terms if the arrows on the bra and ket are pointed in opposite directions. After doing this, we are left with

$$-C^- < s\uparrow \ |e\cdot p|\frac{1}{\sqrt{6}}(x-iy)\uparrow > +\frac{C^+}{\sqrt{2}} < s\downarrow \ |e\cdot p|(x-iy)\downarrow >$$

Expand all inner terms (dropping all z terms)

$$-\frac{C^-}{\sqrt{6}} < s\uparrow \ |e_+p_- + e_-p_+|(x-iy)\uparrow > +\frac{C^+}{\sqrt{2}} < s\downarrow \ |e_+p_+ + e_-p_+|(x-iy)\downarrow >$$

Several of these terms will cancel out with itself. Eliminate any momentum operator with the same subscript sign as the sum or difference sign in the ket it will operate on. We are left with

$$-\frac{C^-}{\sqrt{6}} < s\uparrow \ |e_-p_+|(x-iy)\uparrow > +\frac{C^+}{\sqrt{2}} < s\downarrow \ |e_-p_+|(x-iy)\downarrow >$$

Move the polarization term outside

$$-\frac{C^-}{\sqrt{6}}e_- < s\uparrow \ |p_+|(x-iy)\uparrow > +\frac{C^+}{\sqrt{2}}e_- < s\downarrow \ |p_+|(x-iy)\downarrow >$$

Expand the momentum operator

$$-\frac{C^-}{\sqrt{6}\sqrt{2}}e_- < s\uparrow \ |p_x+ip_y|(x-iy)\uparrow > +\frac{C^+}{\sqrt{2}\sqrt{2}}e_- < s\downarrow \ |p_x+ip_y|(x-iy)\downarrow >$$

$$-\frac{C^-}{2\sqrt{3}}e_-[< s|p_x|x> + < s|p_y|y>] + \frac{C^+}{2}e_-[< s|p_x|x> + < s|p_y|y>]$$

Recall the Kane interband matrix element

$$-\frac{C^-}{2\sqrt{3}}e_-(2P) + \frac{C^+}{2}e_-(2P)$$

We obtain the relation

$$< 0|e\cdot p|2,1> = \left(-\frac{C^-e_-P}{\sqrt{3}} + C^+e_-P\right) \tag{E.6}$$

The transition probability is expressed as

$$P_1^L = K|< 0|e\cdot p|2,1>|^2 \tag{E.7}$$

where K is the square of the overlap integral $K = \frac{2}{a}\left|\int dr r \sin\frac{\pi r}{a}R_o(r)\right|^2$

$$= K\left(-\frac{C^-e_-P}{\sqrt{3}} + C^+e_-P\right)\left(-\frac{C^-e_+P}{\sqrt{3}} + C^+e_+P\right)$$

(note that $C^{\pm}$ is real valued when working out this expression)

$$= K\left(\frac{C^{-^2}e_-e_+P^2}{3} + C^{+^2}e_-e_+P^2 - \frac{2C^+C^-e_-e_+P^2}{\sqrt{3}}\right)$$

$$= KP^2|e_-|^2\left(\frac{C^{-^2}}{3} + C^{+^2} - \frac{2C^+C^-}{\sqrt{3}}\right)$$

$$= \frac{KP^2|e_-|^2}{3}(C^{-^2} + 3C^{+^2} - 2\sqrt{3}C^+C^-)$$

recall from Appendix D that

$$|\hat{e}_-|^2 = \frac{1}{2}\sin^2\theta$$

and

$$C^{-^2} = \frac{\sqrt{f^2+d}-f}{2\sqrt{f^2+d}}$$

$$C^{+^2} = \frac{\sqrt{f^2+d}+f}{2\sqrt{f^2+d}}$$

$$C^+C^- = \frac{\sqrt{d}}{2\sqrt{f^2+d}}$$

Substituting everything into the equation we get

$$= \frac{KP^2|e_-|^2}{3}\left[\frac{\sqrt{f^2+d}-f}{2\sqrt{f^2+d}} + 3\frac{\sqrt{f^2+d}+f}{2\sqrt{f^2+d}} - \frac{2\sqrt{3}\sqrt{d}}{2\sqrt{f^2+d}}\right]$$

$$= \frac{KP^2|e_-|^2}{3}\left(\frac{2\sqrt{f^2+d}+f-\sqrt{3d}}{\sqrt{f^2+d}}\right)$$

$$= \frac{KP^2\sin^2\theta}{3}\left(\frac{2\sqrt{f^2+d}+f-\sqrt{3d}}{2\sqrt{f^2+d}}\right)$$

The transition probability to $|2,1>$ is therefore

$$P_{2,1} = \frac{KP^2\sin^2\theta}{3}\left(\frac{2\sqrt{f^2+d}+f-\sqrt{3d}}{2\sqrt{f^2+d}}\right) \tag{E.8}$$

Similar work can be done to determine the transition probabilities to the other fine structure states. I will include all calculations for completeness but will forgo detailed explanations (This is very similar to the calculation for circularly polarized selection rules and more information can be found in the next section if needed).

Transition probability for $|2,-1>$

In the electron-hole notation the wavefunction is

$$|2,-1>_{e,h} = iC^+|-\frac{3}{2},\frac{1}{2}> + C^-|-\frac{1}{2},-\frac{1}{2}>$$

where

$$\mu_{-3/2} = \frac{i}{\sqrt{2}}(x-iy)\downarrow$$

$$\mu_{-1/2} = 1\sqrt{6}(x-iy)\uparrow + \sqrt{\frac{2}{3}}z\downarrow$$

Electron-electron notation

$$|2,-1>_{e,e}= iC^{+}|\frac{i}{\sqrt{2}}(x-iy)\downarrow>|s\uparrow>+C^{-}|\frac{1}{\sqrt{6}}(x-iy)\uparrow+\sqrt{\frac{2}{3}}z\downarrow>|s\downarrow>$$

Transition to $|2,-1>$ in uncoupled representation

$$-\frac{C^{+}}{\sqrt{2}}<s\uparrow|e\cdot p|(x+iy)\uparrow>+C^{-}<s\downarrow|e\cdot p|\frac{1}{\sqrt{6}}(x+iy)\downarrow+\sqrt{\frac{2}{3}}z\uparrow>$$

Eliminate spin flip terms

$$-\frac{C^{+}}{\sqrt{2}}<s\uparrow|e\cdot p|(x+iy)\uparrow>+C^{-}<s\downarrow|e\cdot p|\frac{1}{\sqrt{6}}(x+iy)\downarrow>$$

Eliminate z terms and self canceling momentum operator

$$-\frac{C^{+}}{\sqrt{2}}<s\uparrow|e_{+}p_{-}|(x+iy)\uparrow>+\frac{C^{-}}{\sqrt{6}}<s\downarrow|e_{+}p_{-}|(x+iy)\downarrow>$$

$$-\frac{C^{+}}{\sqrt{2}}e_{+}<s\uparrow|p_{-}|(x+iy)\uparrow>+\frac{C^{-}}{\sqrt{6}}e_{+}<s\downarrow|p_{-}|(x+iy)\downarrow>$$

$$-\frac{C^{+}}{2}e_{+}<s\uparrow|p_{x}-ip_{y}|(x+iy)\uparrow>+\frac{C^{-}}{2\sqrt{3}}e_{+}<s\downarrow|p_{x}-ip_{y}|(x+iy)\downarrow>$$

$$-\frac{C^{+}e_{+}(2P)}{2}+\frac{C^{-}e_{+}(2P)}{2\sqrt{3}}$$

$$<0|e\cdot p|2,-1>=\left(\frac{C^{-}e_{+}P}{\sqrt{3}}-C^{+}e_{+}P\right) \tag{E.9}$$

The transition probability is

$$P_{2,-1}=K|<0|e\cdot p|2,-1>|^{2} \tag{E.10}$$

$$\begin{aligned}
&= K\left(\frac{C^{-}e_{+}P}{\sqrt{3}}-C^{+}e_{+}P\right)\left(\frac{C^{-}e_{-}P}{\sqrt{3}}-C^{+}e_{-}P\right)\\
&= K\left(\frac{C^{-^{2}}e_{+}e_{-}P^{2}}{3}+C^{+^{2}}e_{+}e_{-}P^{2}-\frac{2}{\sqrt{3}}C^{+}C^{-}e_{+}e_{-}P^{2}\right)\\
&= \frac{KP^{2}|e_{+}|^{2}}{3}(C^{-^{2}}+3C^{+^{2}}-2\sqrt{3}C^{+}C^{-})
\end{aligned}$$

Use relations for $C^{\pm}$

$$\begin{aligned}
&= \frac{KP^{2}|e_{+}|^{2}}{3}\left(\frac{\sqrt{f^{2}+d}-f}{2\sqrt{f^{2}+d}}+\frac{3\sqrt{f^{2}+d}+3f}{2\sqrt{f^{2}+d}}-\frac{2\sqrt{3d}}{2\sqrt{f^{2}+d}}\right)\\
&= \frac{KP^{2}|e_{+}|^{2}}{3}\left(\frac{2\sqrt{f^{2}+d}+f-\sqrt{3d}}{\sqrt{f^{2}+d}}\right)\\
&= \frac{KP^{2}\sin^{2}\theta}{3}\left(\frac{2\sqrt{f^{2}+d}+f-\sqrt{3d}}{2\sqrt{f^{2}+d}}\right)
\end{aligned}$$

The final transition probability is

$$P_{2,-1} = \frac{KP^2 \sin^2\theta}{3}\left(\frac{2\sqrt{f^2+d}+f-\sqrt{3d}}{2\sqrt{f^2+d}}\right) \tag{E.11}$$

Transition probability for $|2,0>$

In the electron-hole representation the wavefunction is

$$|2,0>_{e,h} = \frac{1}{\sqrt{2}}\left[i|-\frac{1}{2},\frac{1}{2}> + |\frac{1}{2},-\frac{1}{2}>\right] \tag{E.12}$$

where

$$\mu_{-1/2} = \frac{1}{\sqrt{6}}(x-iy)\uparrow + \sqrt{\frac{2}{3}}z\downarrow$$

$$\mu_{1/2} = \frac{i}{\sqrt{6}}(x+iy)\downarrow - i\sqrt{\frac{2}{3}}z\uparrow$$

Convert to electron-electron representation (skipping many steps)

$$|2,0>_{e,e} = -\frac{i}{2\sqrt{3}}|(x+iy)\downarrow + 2z\uparrow> |s\uparrow> - \frac{i}{2\sqrt{3}}|(x-iy)\uparrow - 2z\downarrow> |s\downarrow> \tag{E.13}$$

Transition in uncoupled representation

$$-\frac{i}{2\sqrt{3}} < s\uparrow |e\cdot p|(x+iy)\downarrow + 2z\uparrow > - \frac{i}{2\sqrt{3}} < s\downarrow |e\cdot p|(x-iy)\uparrow - 2z\downarrow >$$

Eliminate spin flip transitions

$$-\frac{i}{2\sqrt{3}} < s\uparrow |e\cdot p|2z\uparrow > + \frac{i}{2\sqrt{3}} < s\downarrow |e\cdot p|2z\downarrow >$$

Expand momentum operator

$$-\frac{ie_z}{\sqrt{3}} < s|p_z|z > + \frac{ie_z}{\sqrt{3}} < s|p_z|z >$$

$$\frac{ie_z}{\sqrt{3}}(- < s|p_z|z > + < s|p_z|z >) = 0$$

We obtain

$$< 0|e\cdot p|2,0 >= 0 \tag{E.14}$$

Transition probability for $|2,0>$ is

$$P_{2,0} = 0 \tag{E.15}$$

Transition probability for $|1,0>$

In the electron-hole representation the wavefunction is expressed as

$$|1,0>_{e,h} = \frac{1}{\sqrt{2}}\left[-i|-\frac{1}{2},\frac{1}{2}> + |\frac{1}{2},-\frac{1}{2}>\right] \tag{E.16}$$

where

$$\mu_{-1/2} = \frac{1}{\sqrt{6}}(x-iy)\uparrow + \sqrt{\frac{2}{3}}z\downarrow$$

$$\mu_{1/2} = \frac{i}{\sqrt{3}}(x+iy)\downarrow - i\sqrt{\frac{2}{3}}z\uparrow$$

Express in the electron-electron representation (skipping many steps)

$$|1,0>_{e,e} = \frac{i}{2\sqrt{3}}|(x+iy)\downarrow +2z\uparrow> |s\uparrow> - \frac{i}{2\sqrt{3}}|(x-iy)\uparrow -2z\downarrow> |s\downarrow> \tag{E.17}$$

Express transition in uncoupled representation

$$\frac{i}{2\sqrt{3}} < s\uparrow |e\cdot p|(x+iy)\downarrow +2z\uparrow > - \frac{i}{2\sqrt{3}} < s\downarrow |e\cdot p|(x-iy)\uparrow -2z\downarrow >$$

Eliminate spin flip terms

$$\frac{i}{2\sqrt{3}} < s\uparrow |e\cdot p|2z\uparrow > + \frac{i}{2\sqrt{3}} < s\downarrow |e\cdot p|2z\downarrow >$$

Expand momentum operator

$$\begin{aligned} &= \frac{ie_z}{\sqrt{3}} < s|p_z|z > + \frac{ie_z}{\sqrt{3}} < s|p_z|z > \\ &= \frac{2ie_zP}{\sqrt{3}} \end{aligned}$$

We obtain

$$< 0|e\cdot p|1,0 > = \frac{2ie_zP}{\sqrt{3}} \tag{E.18}$$

The transition probability is expressed as

$$\begin{aligned} P_{1,0} &= K|<0|e\cdot p|1,0>|^2 \\ &= KP^2\frac{4}{3}|e_z|^2 \\ &= KP^2\frac{4}{3}(\cos^2\theta) \end{aligned} \tag{E.19}$$

The final expression is

$$P_{1,0} = \frac{4}{3}KP^2\cos^2\theta \tag{E.20}$$

Transition probability for $|2,2>$

In the electron-hole representation, the wavefunction is written as

$$|2,2>_{e,h} = |\frac{3}{2},\frac{1}{2}> \tag{E.21}$$

where

$$\mu_{3/2} = \frac{1}{\sqrt{2}}(x+iy)\uparrow$$

Express in the electron-electron representation

$$|2,2>_{e,e} = \frac{1}{\sqrt{2}}|(x-iy)\downarrow > |s\uparrow > \tag{E.22}$$

Express transition to this state in uncoupled representation

$$< s \uparrow |\hat{e}^{\pm} p| \frac{1}{\sqrt{2}}(x - iy) \downarrow >$$

This is a spin flip transition and is not allowed formally. We obtain

$$< 0|e \cdot p|2, 2 >= 0 \tag{E.23}$$

therefore

$$P_{2,2} = 0 \tag{E.24}$$

Transition probability for $|2, -2>$

In the electron-hole representation, the wavefunction is written as

$$|2, -2 >_{e,h} = |-\frac{3}{2}, -\frac{1}{2}> \tag{E.25}$$

where

$$\mu_{3/2} = \frac{i}{\sqrt{2}}(x - iy) \downarrow$$

Express in the electron-electron representation

$$|2, -2 >_{e,e} = -\frac{i}{\sqrt{2}}|(x + iy) \uparrow > |s \downarrow > \tag{E.26}$$

Express transition to this state in uncoupled representation

$$< s \downarrow |e \cdot p| - \frac{i}{\sqrt{2}}(x + iy) \uparrow >$$

This is a spin flip transition and is not allowed formally. We obtain

$$< 0|e \cdot p|2, -2 >= 0 \tag{E.27}$$

therefore

$$P_{2,-2} = 0 \tag{E.28}$$

E.1.3 Circularly Polarized Light

Before we go into any further details we need to determine expressions for the following terms. These terms will arise during the course of our calculations. (Note that this is very similar to the situation for linearly polarized light)

1. $< s|\hat{e}^{\pm} \cdot p|z >$
2. $< s|\hat{e}^{\pm} \cdot p|x + iy >$
3. $< s|\hat{e}^{\pm} \cdot p|x - iy >$

where recall

$$\hat{e}^{\pm} \cdot p = \hat{e}^{\pm}_{z} p_z + \hat{e}^{\pm}_{+} p_{-} + \hat{e}^{\pm}_{-} p_{+}$$

Also recall that the superscript $\pm$ reflects the polarization of the light. The circularly polarized light is composed of two mutually orthogonal polarization vectors, e and e'. First term:

$$< s|\hat{e}_z^{\pm} p_z + \hat{e}_+^{\pm} p_- + \hat{e}_-^{\pm} p_+|z >$$

Here the raising and lowering operators in brackets have no effect (recall definitions of p_+ and p_-) on the ket. Drop these terms. We are left with

$$\begin{aligned} < s|\hat{e}_z^{\pm} p_z|z > &= \hat{e}_z^{\pm} < s|p_z|z > \\ &= \hat{e}_z^{\pm} P \end{aligned}$$

where P is the Kane interband matrix element. We obtain the relation

$$< s|\hat{e}_z^{\pm} p_z|z >= \hat{e}_z^{\pm} P \tag{E.29}$$

Second term:

$$< s|\hat{e}_z^{\pm} p_z + \hat{e}_+^{\pm} p_- + \hat{e}_-^{\pm} p_+|x + iy >$$

Drop z terms because they have no effect on the ket. Also drop the raising operator, p_+, because it cancels with itself once it operates on the ket.

$$\begin{aligned} &= < s|\hat{e}_+^{\pm} p_-|x + iy > \\ &= \frac{1}{\sqrt{2}} < s|\hat{e}_+^{\pm}(p_x - ip_y)|x + iy > \\ &= \frac{1}{\sqrt{2}} \hat{e}_+^{\pm} < s|p_x - ip_y|x + iy > \\ &= \frac{1}{\sqrt{2}} \hat{e}_+^{\pm} < s|p_x x + p_y y > \\ &= \frac{1}{\sqrt{2}} \hat{e}_+^{\pm}(< s|p_x|x > + < s|p_y|y >) \\ &= \frac{2}{\sqrt{2}} \hat{e}_+^{\pm} P = \frac{2}{\sqrt{2}} P \hat{e}_+^{\pm} \end{aligned}$$

The second term becomes

$$< s|\hat{e}^{\pm} p|x + iy >= \frac{2}{\sqrt{2}} P \hat{e}_+^{\pm} \tag{E.30}$$

Evaluate the third term in the same manner. We do it again for completeness. The third term is:

$$< s|\hat{e}_z^{\pm} p_z + \hat{e}_+^{\pm} p_- + \hat{e}_-^{\pm} p_+|x - iy >$$

Drop the z term and also the term with the lowering momentum operator, p_-.

$$\begin{aligned} &= < s|\hat{e}_-^{\pm} p_+|x - iy > \\ &= \frac{1}{\sqrt{2}} < s|\hat{e}_-^{\pm}(p_x + ip_y)|x - iy > \\ &= \frac{1}{\sqrt{2}} \hat{e}_-^{\pm} < s|p_x + ip_y|x - iy > \\ &= \frac{1}{\sqrt{2}} \hat{e}_-^{\pm} < s|p_x x + p_y y > \\ &= \frac{1}{\sqrt{2}} \hat{e}_-^{\pm}(< s|p_x|x > + < s|p_y|y >) \end{aligned}$$

$$= \frac{2}{\sqrt{2}}\hat{e}_-^{\pm}P = \frac{2}{\sqrt{2}}P\hat{e}_-^{\pm}$$

The third term becomes:

$$< s|\hat{e}^{\pm}p|x - iy >= \frac{2}{\sqrt{2}}P\hat{e}_-^{\pm} \tag{E.31}$$

E.1.4 Fine Structure Transition Probabilities, Circular Polarization

In this section we will derive the selection rules for the absorption of right and left circularly polarized light. I include all details for completeness.

First State $|2,1>$

In the electron-hole representation, this state is written as

$$|2,1>_{e,h}= iC^-|\frac{1}{2},\frac{1}{2}> + C^+|\frac{3}{2},-\frac{1}{2}> \tag{E.32}$$

where the hole Bloch terms are

$$\mu_{1/2} = \frac{i}{\sqrt{6}}(x+iy)\downarrow - i\sqrt{\frac{2}{3}}z\uparrow$$

$$\mu_{3/2} = \frac{1}{\sqrt{2}}(x+iy)\uparrow$$

We convert the wavefunction to the electron-electron notation. This is done by taking the complex conjugate of the hole Bloch term and flipping all spin projections($\uparrow$ to $\downarrow$ and vice versa).

$$|2,1>_{e,e}= -C^-|\frac{1}{\sqrt{6}}(x-iy)\uparrow - \sqrt{\frac{2}{3}}z\downarrow > |s\uparrow > + \frac{C^+}{\sqrt{2}}|(x-iy)\downarrow > |s\downarrow > \tag{E.33}$$

In each of the terms above, the first ket is the hole Bloch term and the second ket is the electron contribution. We write everything in the uncoupled representation to make things easier. Accessing the $|2,1>$ state involves the following transitions based on the above coupled expression (look familiar?).

$$-C^- < s\uparrow\ |\hat{e}^{\pm}p|\frac{1}{\sqrt{6}}(x-iy)\uparrow - \sqrt{\frac{2}{3}}z\downarrow > + \frac{C^+}{\sqrt{2}} < s\downarrow\ |\hat{e}^{\pm}p|(x-iy)\downarrow >$$

Any term that involves a spin flip transition can be eliminated. (i.e. if arrows on bra and ket are in opposite directions, that term can be thrown away) When this is done we are left with.

$$-C^- < s\uparrow\ |\hat{e}^{\pm}p|\frac{1}{\sqrt{6}}(x-iy)\uparrow > + \frac{C^+}{\sqrt{2}} < s\downarrow\ |\hat{e}^{\pm}p|(x-iy)\downarrow >$$

Expand all inner terms (also dropping all z terms because they do not operate on the ket)

$$-\frac{C^-}{\sqrt{6}} < s\uparrow\ |\hat{e}_+^{\pm}p_- + \hat{e}_-^{\pm}p_+|(x-iy)\uparrow > + \frac{C^+}{\sqrt{2}} < s\downarrow\ |\hat{e}_+^{\pm}p_+ + \hat{e}_-^{\pm}p_+|(x-iy)\downarrow >$$

Several of these terms will cancel out with itself. Eliminate any momentum operator with the same subscript sign as the sum or difference sign in the ket it will operate on. We are left with

$$-\frac{C^-}{\sqrt{6}} < s\uparrow \ |\hat{e}_-^{\pm} p_+|(x-iy)\uparrow > + \frac{C^+}{\sqrt{2}} < s\downarrow \ |\hat{e}_-^{\pm} p_+|(x-iy)\downarrow >$$

Move the polarization term outside

$$-\frac{C^-}{\sqrt{6}}\hat{e}_-^{\pm} < s\uparrow \ |p_+|(x-iy)\uparrow > + \frac{C^+}{\sqrt{2}}\hat{e}_-^{\pm} < s\downarrow \ |p_+|(x-iy)\downarrow >$$

Expand the momentum operator

$$-\frac{C^-}{\sqrt{6}\sqrt{2}}\hat{e}_-^{\pm} < s\uparrow \ |p_x + ip_y|(x-iy)\uparrow > + \frac{C^+}{\sqrt{2}\sqrt{2}}\hat{e}_-^{\pm} < s\downarrow \ |p_x + ip_y|(x-iy)\downarrow >$$

$$-\frac{C^-}{2\sqrt{3}}\hat{e}_-^{\pm}[< s|p_x|x > + < s|p_y|y >] + \frac{C^+}{2}\hat{e}_-^{\pm}[< s|p_x|x > + < s|p_y|y >]$$

Recall Kane interband matrix element

$$-\frac{C^-}{2\sqrt{3}}\hat{e}_-^{\pm}(2P) + \frac{C^+}{2}\hat{e}_-^{\pm}(2P)$$

We obtain the relation

$$< 0|\hat{e}^{\pm} p|2,1 >= (-\frac{C^-\hat{e}_-^{\pm} P}{\sqrt{3}} + C^+\hat{e}_-^{\pm} P) \tag{E.34}$$

The transition probability is

$$P_1^L = K|< 0|\hat{e}^{\pm} p|2,1 >|^2 \tag{E.35}$$

$$= K\left(-\frac{C^-\hat{e}_-^{\pm} P}{\sqrt{3}} + C^+\hat{e}_-^{\pm} P\right)\left(-\frac{C^-\hat{e}_+^{\mp} P}{\sqrt{3}} + C^+\hat{e}_+^{\mp} P\right)$$

(note that $C^{\pm}$ is real valued)

$$= K\left(\frac{C^{-^2}\hat{e}_-^{\pm}\hat{e}_+^{\mp} P^2}{3} + C^{+^2}\hat{e}_-^{\pm}\hat{e}_+^{\mp} P^2 - \frac{2C^+C^-\hat{e}_-^{\pm}\hat{e}_+^{\mp} P^2}{\sqrt{3}}\right)$$

$$= KP^2|\hat{e}_-^{\pm}|^2\left(\frac{C^{-^2}}{3} + C^{+^2} - \frac{2C^+C^-}{\sqrt{3}}\right)$$

$$= \frac{KP^2|\hat{e}_-^{\pm}|^2}{3}(C^{-^2} + 3C^{+^2} - 2\sqrt{3}C^+C^-)$$

where recall

$$|\hat{e}_-^{\pm}|^2 = \frac{1}{2}(1 \mp \cos\theta)^2$$

$$C^{-^2} = \frac{\sqrt{f^2+d} - f}{2\sqrt{f^2+d}}$$

$$C^{+^2} = \frac{\sqrt{f^2+d} + f}{2\sqrt{f^2+d}}$$

and

$$C^+C^- = \frac{\sqrt{d}}{2\sqrt{f^2+d}}$$

Substituting everything into the equation we get

$$\begin{aligned} &= \frac{KP^2|\hat{e}_-^{\pm}|^2}{3}\left[\frac{\sqrt{f^2+d}-f}{2\sqrt{f^2+d}} + 3\frac{\sqrt{f^2+d}+f}{2\sqrt{f^2+d}} - \frac{2\sqrt{3}\sqrt{d}}{2\sqrt{f^2+d}}\right] \\ &= \frac{KP^2|\hat{e}_-^{\pm}|^2}{3}\left(\frac{2\sqrt{f^2+d}+f-\sqrt{3d}}{2\sqrt{f^2+d}}\right) \\ &= \frac{KP^2(1\mp\cos\theta)^2}{3}\left(\frac{2\sqrt{f^2+d}+f-\sqrt{3d}}{2\sqrt{f^2+d}}\right) \end{aligned}$$

The transition probability to $|2,1>$ is therefore

$$P_{2,1} = \frac{KP^2(1\mp\cos\theta)^2}{3}\left(\frac{2\sqrt{f^2+d}+f-\sqrt{3d}}{2\sqrt{f^2+d}}\right) \tag{E.36}$$

Similar work can be done to determine the transition probabilities to the other fine structure states. I will include all calculations for completeness but will forgo detailed explanation.

Transition probability for $|2,-1>$

In the electron-hole notation the wavefunction is

$$|2,-1>_{e,h} = iC^+|-\frac{3}{2},\frac{1}{2}> + C^-|-\frac{1}{2},-\frac{1}{2}>$$

where

$$\mu_{-3/2} = \frac{i}{\sqrt{2}}(x-iy)\downarrow$$

$$\mu_{-1/2} = 1\sqrt{6}(x-iy)\uparrow + \sqrt{\frac{2}{3}}z\downarrow$$

Electron-electron notation

$$|2,-1>_{e,e} = iC^+|\frac{i}{\sqrt{2}}(x-iy)\downarrow>|s\uparrow> + C^-|\frac{1}{\sqrt{6}}(x-iy)\uparrow + \sqrt{\frac{2}{3}}z\downarrow>|s\downarrow>$$

Transition to $|2,-1>$ in uncoupled representation

$$-\frac{C^+}{\sqrt{2}} < s\uparrow|\hat{e}^{\pm}p|(x+iy)\uparrow> + C^- < s\downarrow|\hat{e}^{\pm}p|\frac{1}{\sqrt{6}}(x+iy)\downarrow + \sqrt{\frac{2}{3}}z\uparrow>$$

Eliminate spin flip terms

$$-\frac{C^+}{\sqrt{2}} < s\uparrow|\hat{e}^{\pm}p|(x+iy)\uparrow> + C^- < s\downarrow|\hat{e}^{\pm}p_|\frac{1}{\sqrt{6}}(x+iy)\downarrow>$$

Eliminate z terms and self canceling momentum operator

$$-\frac{C^+}{\sqrt{2}} < s\uparrow|\hat{e}_+^{\pm}p_-|(x+iy)\uparrow> + \frac{C^-}{\sqrt{6}} < s\downarrow|\hat{e}_+^{\pm}p_-|(x+iy)\downarrow>$$

$$-\frac{C^+}{\sqrt{2}}\hat{e}_+^{\pm} < s\uparrow|p_-|(x+iy)\uparrow> + \frac{C^-}{\sqrt{6}}\hat{e}_+^{\pm} < s\downarrow|p_-|(x+iy)\downarrow>$$

$$-\frac{C^+}{2}\hat{e}_+^{\pm} < s\uparrow|p_x - ip_y|(x+iy)\uparrow> + \frac{C^-}{2\sqrt{3}}\hat{e}_+^{\pm} < s\downarrow|p_x - ip_y|(x+iy)\downarrow>$$

$$-\frac{C^+\hat{e}_+^{\pm}(2P)}{2} + \frac{C^-\hat{e}_+^{\pm}(2P)}{2\sqrt{3}}$$

$$< 0|\hat{e}^{\pm}p|2,-1> = \left(\frac{C^-\hat{e}_+^{\pm}P}{\sqrt{3}} - C^+\hat{e}_+^{\pm}P\right) \tag{E.37}$$

The transition probability is

$$P_{2,-1} = K|<0|\hat{e}^{\pm}p|2,-1>|^2 \tag{E.38}$$

$$\begin{aligned}
&= K\left(\frac{C^-\hat{e}_+^{\pm}P}{\sqrt{3}} - C^+\hat{e}_+^{\pm}P\right)\left(\frac{C^-\hat{e}_-^{\mp}P}{\sqrt{3}} - C^+\hat{e}_-^{\mp}P\right)\\
&= K\left(\frac{C^{-^2}\hat{e}_+^{\pm}\hat{e}_-^{\mp}P^2}{3} + C^{+^2}\hat{e}_+^{\pm}\hat{e}_-^{\mp}P^2 - \frac{2}{\sqrt{3}}C^+C^-\hat{e}_+^{\pm}\hat{e}_-^{\mp}P^2\right)\\
&= \frac{KP^2|\hat{e}_+^{\pm}|^2}{3}(C^{-^2} + 3C^{+^2} - 2\sqrt{3}C^+C^-)
\end{aligned}$$

Use relations for $C^{\pm}$

$$\begin{aligned}
&= \frac{KP^2|\hat{e}_+^{\pm}|^2}{3}\left(\frac{\sqrt{f^2+d}-f}{2\sqrt{f^2+d}} + \frac{3\sqrt{f^2+d}+3f}{2\sqrt{f^2+d}} - \frac{2\sqrt{3d}}{2\sqrt{f^2+d}}\right)\\
&= \frac{KP^2|\hat{e}_+^{\pm}|^2}{3}\left(\frac{2\sqrt{f^2+d}+f-\sqrt{3d}}{\sqrt{f^2+d}}\right)\\
&= \frac{KP^2(1\pm\cos\theta)^2}{3}\left(\frac{2\sqrt{f^2+d}+f-\sqrt{3d}}{2\sqrt{f^2+d}}\right)
\end{aligned}$$

The final transition probability is

$$P_{2,-1} = \frac{KP^2(1\pm\cos\theta)^2}{3}\left(\frac{2\sqrt{f^2+d}+f-\sqrt{3d}}{2\sqrt{f^2+d}}\right) \tag{E.39}$$

Transition probability for $|2,0>$

In the electron-hole representation the wavefunction is

$$|2,0>_{e,h} = \frac{1}{\sqrt{2}}\left[i|-\frac{1}{2},\frac{1}{2}> + |\frac{1}{2},-\frac{1}{2}>\right] \tag{E.40}$$

where

$$\mu_{-1/2} = \frac{1}{\sqrt{6}}(x-iy)\uparrow + \sqrt{\frac{2}{3}}z\downarrow$$

$$\mu_{1/2} = \frac{i}{\sqrt{6}}(x+iy)\downarrow - i\sqrt{\frac{2}{3}}z\uparrow$$

Convert to electron-electron representation (skipping many steps)

$$|2,0>_{e,e}= -\frac{i}{2\sqrt{3}}|(x+iy)\downarrow +2z\uparrow> |s\uparrow> -\frac{i}{2\sqrt{3}}|(x-iy)\uparrow -2z\downarrow> |s\downarrow> \tag{E.41}$$

Transition in uncoupled representation

$$-\frac{i}{2\sqrt{3}} < s\uparrow |\hat{e}^{\pm}p|(x+iy)\downarrow +2z\uparrow > -\frac{i}{2\sqrt{3}} < s\downarrow |\hat{e}^{\pm}p|(x-iy)\uparrow -2z\downarrow >$$

Eliminate spin flip transitions

$$-\frac{i}{2\sqrt{3}} < s\uparrow |\hat{e}^{\pm}p|2z\uparrow > +\frac{i}{2\sqrt{3}} < s\downarrow |\hat{e}^{\pm}p|2z\downarrow >$$

Expand momentum operator

$$-\frac{i\hat{e}_z^{\pm}}{\sqrt{3}} < s|p_z|z > +\frac{i\hat{e}_z^{\pm}}{\sqrt{3}} < s|p_z|z >$$

$$\frac{i\hat{e}_z^{\pm}}{\sqrt{3}}(- < s|p_z|z > + < s|p_z|z >) = 0$$

We obtain

$$< 0|\hat{e}^{\pm}p|2,0 >= 0 \tag{E.42}$$

Transition probability for $|2,0>$ is

$$P_{2,0} = 0 \tag{E.43}$$

Transition probability for $|1,0>$

In the electron-hole representation the wavefunction is expressed as

$$|1,0>_{e,h}= \frac{1}{\sqrt{2}}\left[-i|-\frac{1}{2},\frac{1}{2}> +|\frac{1}{2},-\frac{1}{2}>\right] \tag{E.44}$$

where

$$\mu_{-1/2} = \frac{1}{\sqrt{6}}(x-iy)\uparrow +\sqrt{\frac{2}{3}}z\downarrow$$

$$\mu_{1/2} = \frac{i}{\sqrt{6}}(x+iy)\downarrow -i\sqrt{\frac{2}{3}}z\uparrow$$

Express in the electron-electron representation (skipping many steps)

$$|1,0>_{e,e}= \frac{i}{2\sqrt{3}}|(x+iy)\downarrow +2z\uparrow> |s\uparrow> -\frac{i}{2\sqrt{3}}|(x-iy)\uparrow -2z\downarrow> |s\downarrow> \tag{E.45}$$

Express transition in uncoupled representation

$$\frac{i}{2\sqrt{3}} < s\uparrow |\hat{e}^{\pm}p|(x+iy)\downarrow +2z\uparrow > -\frac{i}{2\sqrt{3}} < s\downarrow |\hat{e}^{\pm}p|(x-iy)\uparrow -2z\downarrow >$$

Eliminate spin flip terms

$$\frac{i}{2\sqrt{3}} < s\uparrow |\hat{e}^{\pm}p|2z\uparrow > +\frac{i}{2\sqrt{3}} < s\downarrow |\hat{e}^{\pm}p|2z\downarrow >$$

Expand momentum operator

$$= \frac{i\hat{e}_z^{\pm}}{\sqrt{3}} < s|p_z|z > + \frac{i\hat{e}_z^{\pm}}{\sqrt{3}} < s|p_z|z >$$
$$= \frac{2i\hat{e}_z^{\pm} P}{\sqrt{3}}$$

We obtain

$$< 0|\hat{e}^{\pm} p|1,0 > = \frac{2i\hat{e}_z^{\pm} P}{\sqrt{3}} \tag{E.46}$$

The transition probability is expressed as

$$P_{1,0} = |< 0|\hat{e}^{\pm} p|1,0 >|^2 \tag{E.47}$$
$$= KP^2 \frac{4}{3} |\hat{e}_z^{\pm}|^2$$
$$= KP^2 \frac{4}{3} (\sin^2 \theta)$$

The final expression is

$$P_{1,0} = \frac{4}{3} KP^2 \sin^2 \theta \tag{E.48}$$

Transition probability for $|1,1>$

In the electron-hole representation the wavefunction is

$$|1,1 >= -iC^+ |\frac{1}{2}, \frac{1}{2} > + C^- |\frac{3}{2}, -\frac{1}{2} > \tag{E.49}$$

where

$$\mu_{1/2} = \frac{i}{\sqrt{6}}(x + iy) \downarrow - i\sqrt{\frac{2}{3}} z \uparrow$$

$$\mu_{3/2} = \frac{1}{\sqrt{2}}(x + iy) \uparrow$$

Convert to the electron-electron representation

$$|1,1 >_{e,c} = C^+ |\frac{1}{\sqrt{6}}(x - iy) \uparrow - \sqrt{\frac{2}{3}} z \downarrow > |s \uparrow > + \frac{C^-}{\sqrt{2}} |(x - iy) \downarrow > |s \downarrow > \tag{E.50}$$

Express transition in the uncoupled representation

$$C^+ < s \uparrow |\hat{e}^{\pm} p| \frac{1}{\sqrt{6}}(x - iy) \uparrow - \sqrt{\frac{2}{3}} z \downarrow > + \frac{C^-}{\sqrt{2}} < s \downarrow |\hat{e}^{\pm} p|(x - iy) \downarrow >$$

Eliminate z terms and self canceling momentum operator terms

$$\frac{C^+}{\sqrt{6}} < s \uparrow |\hat{e}_-^{\pm} p_+|(x - iy) \uparrow > + \frac{C^-}{\sqrt{2}} < s \downarrow |\hat{e}_-^{\pm} p_+|(x - iy) \downarrow >$$

Expand momentum operator

$$\frac{C^+ \hat{e}_-^{\pm}(2P)}{2\sqrt{3}} + \frac{C^- \hat{e}_-^{\pm}(2P)}{2}$$

$$\hat{e}^{\pm}_{-}P\left(\frac{C^{+}}{\sqrt{3}}+C^{-}\right)$$

We obtain the expression

$$< 0|\hat{e}^{\pm}p|1,1 >= \hat{e}^{\pm}_{-}P\left(\frac{C^{+}}{\sqrt{3}}+C^{-}\right) \tag{E.51}$$

The transition probability is of the form

$$\begin{aligned}
P_{1,1} &= K| < 0|\hat{e}^{\pm}p|1,1 > |^2 \qquad \text{(E.52)}\\
&= KP^2|\hat{e}^{\pm}_{-}|^2(\frac{C^{+}}{\sqrt{3}}+C^{-})^2\\
&= \frac{KP^2(1\mp\cos\theta)^2}{2}\left(\frac{C^{+^2}}{3}+\frac{3C^{-^2}}{3}+\frac{2\sqrt{3}C^{+}C^{-}}{3}\right)\\
&= \frac{KP^2(1\mp\cos\theta)^2}{2(3)}\left(\frac{\sqrt{f^2+d}+f}{2\sqrt{f^2+d}}+\frac{3\sqrt{f^2+d}-3f}{2\sqrt{f^2+d}}+\frac{2\sqrt{3d}}{2\sqrt{f^2+d}}\right)\\
&= \frac{KP^2(1\mp\cos\theta)^2}{2(3)}\left(\frac{2\sqrt{f^2+d}-f+\sqrt{3d}}{\sqrt{f^2+d}}\right)\\
&= \frac{KP^2(1\mp\cos\theta)^2}{3}\left(\frac{2\sqrt{f^2+d}-f+\sqrt{3d}}{2\sqrt{f^2+d}}\right)
\end{aligned}$$

The transition probability is

$$P_{1,1} = \frac{KP^2(1\mp\cos\theta)^2}{3}\left(\frac{2\sqrt{f^2+d}-f+\sqrt{3d}}{2\sqrt{f^2+d}}\right) \tag{E.53}$$

Transition probability for $|1,-1>$

In the electron-hole representation, the wavefunction is written as

$$|1,-1>= -iC^{-}|-\frac{3}{2},\frac{1}{2}>+C^{+}|-\frac{1}{2},-\frac{1}{2}> \tag{E.54}$$

where

$$\mu_{-3/2}=\frac{i}{\sqrt{2}}(x-iy)\downarrow$$

$$\mu_{-1/2}=\frac{1}{\sqrt{6}}(x-iy)\uparrow+\sqrt{\frac{2}{3}}z\downarrow$$

Express everything in the electron-electron representation

$$\frac{C^{-}}{\sqrt{2}}|(x+iy)\uparrow>+C^{+}|\frac{1}{\sqrt{6}}(x+iy)\downarrow+\sqrt{\frac{2}{3}}z\uparrow> \tag{E.55}$$

Express transition to this state in uncoupled representation

$$\frac{C^{-}}{\sqrt{2}}< s\uparrow|\hat{e}^{\pm}p|(x+iy)\uparrow>+C^{+}< s\downarrow|\hat{e}^{\pm}p|\frac{1}{\sqrt{6}}(x+iy)\downarrow+\sqrt{\frac{2}{3}}z\uparrow>$$

Remove terms involving spin flip

$$\frac{C^{--}}{\sqrt{2}} < s\uparrow|\hat{e}^{\pm}p|(x+iy)\uparrow > + C^{+} < s\downarrow|\hat{e}^{\pm}p|\frac{1}{\sqrt{6}}(x+iy)\downarrow >$$

Remove z momentum terms and all self canceling momentum terms

$$\frac{C^{-}}{\sqrt{2}} < s\uparrow|\hat{e}^{\pm}_{+}p_{-}|(x+iy)\uparrow > + C^{+} < s\downarrow|\hat{e}^{\pm}_{+}p_{-}|\frac{1}{\sqrt{6}}(x+iy)\downarrow + \sqrt{\frac{2}{3}}z\uparrow >$$

$$= \frac{C^{-}\hat{e}^{\pm}_{+}(2P)}{2} + \frac{C^{+}\hat{e}^{\pm}_{+}(2P)}{2\sqrt{3}}$$

We obtain

$$< 0|\hat{e}^{\pm}p|1,-1 >= \hat{e}^{\pm}_{+}P\left(\frac{C^{+}}{\sqrt{3}} + C^{-}\right) \tag{E.56}$$

The transition probability is of the form

$$\begin{aligned}
P_{1,-1} &= KP^2|\hat{e}^{\pm}_{+}|^2\left(\frac{C^{+}}{\sqrt{3}} + C^{-}\right)^2 \qquad \text{(E.57)}\\
&= KP^2\frac{(1\pm\cos\theta)^2}{2}\left(\frac{C^{+^2}}{3} + C^{-^2} + \frac{2}{\sqrt{3}}C^{+}C^{-}\right)\\
&= \frac{KP^2}{3}\frac{(1\pm\cos\theta)^2}{2}(C^{+^2} + 3C^{-^2} + 2\sqrt{3}C^{+}C^{-})\\
&= \frac{KP^2}{3}\frac{(1\pm\cos\theta)^2}{2}\left(\frac{\sqrt{f^2+d}+f}{2\sqrt{f^2+d}} + \frac{3\sqrt{f^2+d}-3f}{2\sqrt{f^2+d}} + \frac{2\sqrt{3d}}{2\sqrt{f^2+d}}\right)\\
&= \frac{KP^2}{3}\frac{(1\pm\cos\theta)^2}{2}\left(\frac{4\sqrt{f^2+d}-2f+2\sqrt{3d}}{2\sqrt{f^2+d}}\right)\\
&= \frac{KP^2}{3}(1\pm\cos\theta)^2\left(\frac{2\sqrt{f^2+d}-f+\sqrt{3d}}{2\sqrt{f^2+d}}\right)
\end{aligned}$$

The transition probability is

$$P_{1,-1} = \frac{KP^2(1\pm\cos\theta)^2}{3}\left(\frac{2\sqrt{f^2+d}-f+\sqrt{3d}}{2\sqrt{f^2+d}}\right) \tag{E.58}$$

Transition probability for $|2,2>$

In the electron-hole representation, the wavefunction is written as

$$|2,2>_{e,h} = |\frac{3}{2},\frac{1}{2}> \tag{E.59}$$

where

$$\mu_{3/2} = \frac{1}{\sqrt{2}}(x+iy)\uparrow$$

Express in the electron-electron representation

$$|2,2>_{e,e} = \frac{1}{\sqrt{2}}|(x-iy)\downarrow > |s\uparrow > \tag{E.60}$$

Express transition to this state in uncoupled representation

$$< s \uparrow |\hat{e}^{\pm} p| \frac{1}{\sqrt{2}}(x - iy) \downarrow >$$

This is a spin flip transition and is not allowed formally. We obtain

$$< 0|\hat{e}^{\pm} p|2, 2 >= 0 \tag{E.61}$$

therefore

$$P_{2,2} = 0 \tag{E.62}$$

Transition probability for $|2, -2>$

In the electron-hole representation, the wavefunction is written as

$$|2, -2 >_{e,h} = |-\frac{3}{2}, -\frac{1}{2}> \tag{E.63}$$

where

$$\mu_{3/2} = \frac{i}{\sqrt{2}}(x - iy) \downarrow$$

Express in the electron-electron representation

$$|2, -2 >_{e,e} = -\frac{i}{\sqrt{2}}|(x + iy) \uparrow > |s \downarrow > \tag{E.64}$$

Express transition to this state in uncoupled representation

$$< s \downarrow |\hat{e}^{\pm} p| - \frac{i}{\sqrt{2}}(x + iy) \uparrow >$$

This is a spin flip transition and is not allowed formally. We obtain

$$< 0|\hat{e}^{\pm} p|2, -2 >= 0 \tag{E.65}$$

therefore

$$P_{2,-2} = 0 \tag{E.66}$$

E.1.5 Angle averaging transition probabilities

The following two results will be used

$$\frac{1}{4\pi} \iint \sin^2 \theta \, dv = \frac{2}{3} \tag{E.67}$$

$$\frac{1}{4\pi} \iint \cos^2 \theta \, dv = \frac{1}{3} \tag{E.68}$$

We angle average $P_{2,1}$ as an example

$$\overline{P_{2,1}} = \frac{1}{4\pi} \iint \frac{K P^2 N^{U,L}}{3} (1 \mp \cos\theta)^2 \sin\theta \, d\theta \, d\phi \tag{E.69}$$

where

$$N^{U,L} = \left(\frac{2\sqrt{f^2+d} \mp f \pm \sqrt{3d}}{2\sqrt{f^2+d}} \right)$$

$$= \frac{KP^2N^{U,L}}{3(4\pi)} \iint (1 + \cos^2\theta \mp 2\cos\theta) \sin\theta \; d\theta \; d\phi$$

$$= \frac{KP^2N^{U,L}}{3(2)} \int (1 + \cos^2\theta \mp 2\cos\theta) \sin\theta \; d\theta$$

$$= \frac{KP^2N^{U,L}}{3(2)} \int_0^\pi \sin\theta + \cos^2\theta \sin\theta \mp 2\cos\theta \sin\theta \; d\theta$$

$$= \frac{KP^2N^{U,L}}{3(2)} \left[-cos\theta|_0^\pi + \int_0^\pi \cos^\theta \sin\theta \mp \int_0^\pi 2\cos\theta \sin\theta \; d\theta \right]$$

In the first integral let $x = \cos\theta$ and $dx = -\sin\theta$ evaluated from 1 to -1. In the second integral recall that $\sin 2\theta = 2\cos\theta \sin\theta$

$$= \frac{KP^2N^{U,L}}{3(2)} \left[2 - \int_1^{-1} x^2 dx \mp \int_0^\pi \sin 2\theta \; d\theta \right]$$

$$= \frac{KP^2N^{U,L}}{3(2)} \left[2 - \frac{1}{3}(-2) \pm \frac{1}{2} \cos 2\theta \Big|_0^\pi \right]$$

We obtain the angle averaged probability

$$\overline{P_{2,1}} = \frac{4}{9} KP^2N^{U,L} \tag{E.70}$$

Appendix F

Matrices

This section lists all the important matrices used to determine the energies and splittings of fine structure states in Chapters 2, 4, and 5.

F.1 Crystal Field and Shape Asymmetry

	$\|2,+2\rangle$	$\|2,+1\rangle$	$\|2,\ 0\rangle$	$\|2,-1\rangle$	$\|2,-2\rangle$	$\|1,+1\rangle$	$\|1,\ 0\rangle$	$\|1,-1\rangle$
$\langle 2,+2\|$	$-\frac{4}{7}$	0	0	0	0	0	0	0
$\langle 2,+1\|$	0	$-\frac{4}{7}(C^{-2}-C^{+2})$	0	0	0	$-\Delta C^{+}C^{-}$	0	0
$\langle 2,\ 0\|$	0	0	$\frac{4}{7}$	0	0	0	0	0
$\langle 2,-1\|$	0	0	0	$-\frac{4}{7}(C^{-2}-C^{+2})$	0	0	0	$\Delta C^{+}C^{-}$
$\langle 2,-2\|$	0	0	0	0	$-\frac{4}{7}$	0	0	0
$\langle 1,+1\|$	0	$-\Delta C^{+}C^{-}$	0	0	0	$\frac{4}{7}(C^{+2}-C^{-2})$	0	0
$\langle 1,\ 0\|$	0	0	0	0	0	0	$\frac{4}{7}$	0
$\langle 1,-1\|$	0	0	0	$\Delta C^{+}C^{-}$	0	0	0	$\frac{4}{7}(C^{+2}-C^{-2})$

Table F.1: This matrix shows elements from CFSE and shape asymmetries. All values are determined in the coupled basis. Δ as well as the size dependent coefficients, C^{+} and C^{-} are defined in Chapter 2.

F.2 Exchange Interaction

	$\|2,+2\rangle$	$\|2,+1\rangle$	$\|2,\ 0\rangle$	$\|2,-1\rangle$	$\|2,-2\rangle$	$\|1,+1\rangle$	$\|1,\ 0\rangle$	$\|1,-1\rangle$
$\langle 2,+2\|$	$-\frac{3\eta}{2}$	0	0	0	0	0	0	0
$\langle 2,+1\|$	0	$\frac{\eta}{2}(3C^{+2}-C^{-2})$	0	0	0	$\eta(2C^{+}C-+i\sqrt{3})$	0	0
$\langle 2,\ 0\|$	0	0	$\frac{\eta}{2}$	0	0	0	$i2\eta$	0
$\langle 2,-1\|$	0	0	0	$\frac{\eta}{2}(3C^{+2}-C^{-2})$	0	0	0	$\eta(-2C^{+}C^{-}+i\sqrt{3})$
$\langle 2,-2\|$	0	0	0	0	$-\frac{3\eta}{2}$	0	0	0
$\langle 1,+1\|$	0	$\eta(2C^{+}C^{-}-i\sqrt{3})$	0	0	0	$\frac{\eta}{2}(3C^{-2}-C^{+2})$	0	0
$\langle 1,\ 0\|$	0	0	$-i2\eta$	0	0	0	$\frac{\eta}{2}$	0
$\langle 1,-1\|$	0	0	0	$\eta(-2C^{+}C^{-}-i\sqrt{3})$	0	0	0	$\frac{\eta}{2}(3C^{-2}-C^{+2})$

Table F.2: This matrix contains elements resulting from the electron-hole exchange interaction. Values are expressed in the coupled basis where the exchange parameter, η is defined in Chapter 2. Fine structure energies are determined by diagonalizing this matrix together with the crystal field/shape matrix shown above.

F.3 Zeeman Hamiltonian

	$\|2,+2\rangle$	$\|2,+1\rangle$	$\|2,0\rangle$	$\|2,-1\rangle$	$\|2,-2\rangle$	$\|1,+1\rangle$	$\|1,0\rangle$	$\|1,-1\rangle$
$\langle 2,+2\|$	$A(g_e-3g_h)$	$\frac{\mu_B H_-}{2}F_1$	0	0	0	$\frac{\mu_B H_-}{2}F_7$	0	0
$\langle 2,+1\|$	$\frac{\mu_B H_+}{2}F_1^*$	AB	$\frac{\mu_B H_-}{2\sqrt{2}}F_2$	0	0	$-\mu_B H_z C^{\pm} g_t$	$\frac{\mu_B H_-}{2\sqrt{2}}F_8$	0
$\langle 2,0\|$	0	$\frac{\mu_B H^+}{2\sqrt{2}}F_2^*$	0	$\frac{\mu_B H_-}{2\sqrt{2}}F_3$	0	$\frac{\mu_B H_+}{2\sqrt{2}}F_9$	$-Ag_t$	$\frac{\mu_B H_-}{2\sqrt{2}}F_{10}$
$\langle 2,-1\|$	0	0	$\frac{\mu_B H_+}{2\sqrt{2}}F_3^*$	AC	$\frac{\mu_B H_-}{2}F_4$	0	$\frac{\mu_B H_+}{2\sqrt{2}}F_{11}$	$-\mu_B H_z C^{\pm} g_t$
$\langle 2,-2\|$	0	0	0	$\frac{\mu_B H_+}{2}F_4^*$	$A(3g_h-g_e)$	0	0	$\frac{\mu_B H_+}{2}F_{12}$
$\langle 1,+1\|$	$\frac{\mu_B H_+}{2}F_7^*$	$-\mu_B H_z C^{\pm} g_t$	$\frac{\mu_B H_-}{2\sqrt{2}}F_9^*$	0	0	AD	$\frac{\mu_B H_-}{2\sqrt{2}}F_5$	0
$\langle 1,0\|$	0	$\frac{\mu_B H_+}{2\sqrt{2}}F_8^*$	$-Ag_t$	$\frac{\mu_B H_-}{2\sqrt{2}}F_{11}^*$	0	$\frac{\mu_B H_+}{2\sqrt{2}}F_5^*$	0	$\frac{\mu_B H_-}{2\sqrt{2}}F_6$
$\langle 1,-1\|$	0	0	$\frac{\mu_B H_+}{2\sqrt{2}}F_{10}^*$	$-\mu_B H_z C^{\pm} g_t$	$\frac{\mu_B H_-}{2}F_{12}^*$	0	$\frac{\mu_B H_+}{2\sqrt{2}}F_6^*$	AE

Table F.3: Zeeman Hamiltonian written in the coupled basis. This describes the effects of the magnetic field on the various fine structure states determined in Chapter 2. Considering the effects in first order perturbation theory yield the splittings and effective g-factors described in Chapters 4 and 5. This is the general case where crystal field, shape and Zeeman splittings are all perturbations.

where

$$\begin{aligned} g_+ &= g_e + g_h \\ C^{\pm} &= C^+ C^- \end{aligned}$$

On Diagonals

$$\begin{aligned} A &= \frac{\mu_B H_z}{2} \\ B &= [(C^{-^2} - C^{+^2})g_e - (C^{-^2} + 3C^{+^2})g_h] \\ C &= [(C^{+^2} - C^{-^2})g_e + (3C^{+^2} + C^{-^2})g_h] \\ D &= [(C^{+^2} - C^{-^2})g_e - (C^{+^2} + 3C^{-^2})g_h] \\ E &= [(C^{-^2} - C^{+^2})g_e + (3C^{-^2} + C^{+^2})g_h] \end{aligned}$$

Off Diagonals

$$\begin{aligned} F_1 &= -iC^-\sqrt{3}g_h + C^+ g_e \\ F_2 &= -iC^- g_e - (\sqrt{3}C^+ + 2C^-)g_h \\ F_3 &= -iC^- g_e - (\sqrt{3}C^+ + 2C^-)g_h \\ F_4 &= -iC^+ g_e - \sqrt{3}C^- g_h \\ F_5 &= iC^+ g_e - (2C^+ + \sqrt{3}C^-)g_h \\ F_6 &= iC^+ g_e - (\sqrt{3}C^- + 2C^+)g_h \\ F_7 &= C^- g_e + i\sqrt{3}C^+ g_h \\ F_8 &= -iC^- g_e + (2C^- - \sqrt{3}C^+)g_h \\ F_9 &= -iC^+ g_e + (2C^+ - \sqrt{3}C^-)g_h \\ F_{10} &= -iC^+ g_e + (\sqrt{3}C^- - 2C^+)g_h \\ F_{11} &= -iC^- g_e + (\sqrt{3}C^+ - 2C^-)g_h \\ F_{12} &= -iC^- g_e + \sqrt{3}C^+ g_h \end{aligned}$$

F.4 Zeeman Hamiltonian (large sizes)

F.4.1 Uncoupled Basis

	$\|3/2,\uparrow\rangle$	$\|1/2,\uparrow\rangle$	$\|-1/2,\uparrow\rangle$	$\|-3/2,\uparrow\rangle$	$\|3/2,\downarrow\rangle$	$\|1/2,\downarrow\rangle$	$\|1/2,\downarrow\rangle$	$\|-3/2,\downarrow\rangle$
$\langle 3/2,\uparrow\|$	$-\frac{3\eta}{2}$	0	0	0	0	0	0	0
$\langle 1/2,\uparrow\|$	0	$-\frac{\eta}{2}$	0	0	0	0	0	0
$\langle -1/2,\uparrow\|$	0	0	$\frac{\eta}{2}$	0	0	0	0	0
$\langle -3/2,\uparrow\|$	0	0	0	$\frac{3\eta}{2}$	0	0	0	0
$\langle 3/2,\downarrow\|$	0	0	0	0	$\frac{3\eta}{2}$	0	0	0
$\langle 1/2,\downarrow\|$	0	0	0	0	0	$\frac{\eta}{2}$	0	0
$\langle -1/2,\downarrow\|$	0	0	0	0	0	0	$-\frac{\eta}{2}$	0
$\langle -3/2,\downarrow\|$	0	0	0	0	0	0	0	$-\frac{3\eta}{2}$

	$\|3/2,\uparrow\rangle$	$\|1/2,\uparrow\rangle$	$\|-1/2,\uparrow\rangle$	$\|-3/2,\uparrow\rangle$	$\|3/2,\downarrow\rangle$	$\|1/2,\downarrow\rangle$	$\|1/2,\downarrow\rangle$	$\|-3/2,\downarrow\rangle$
$\langle 3/2,\uparrow\|$	$A(g_e-3g_h)$	0	0	0	$\frac{g_e\mu_B H_-}{2}$	0	0	0
$\langle 1/2,\uparrow\|$	0	$A(g_e-g_h)$	0	0	0	$\frac{g_e\mu_B H_-}{2}$	0	0
$\langle -1/2,\uparrow\|$	0	0	$A(g_e+g_h)$	0	0	0	$\frac{g_e\mu_B H_-}{2}$	0
$\langle -3/2,\uparrow\|$	0	0	0	$A(g_e+3g_h)$	0	0	0	$\frac{g_e\mu_B H_-}{2}$
$\langle 3/2,\downarrow\|$	$\frac{g_e\mu_B H_+}{2}$	0	0	0	$A(g_e+3g_h)$	0	0	0
$\langle 1/2,\downarrow\|$	0	$\frac{g_e\mu_B H_+}{2}$	0	0	0	$A(g_e+g_h)$	0	0
$\langle -1/2,\downarrow\|$	0	0	$\frac{g_e\mu_B H_+}{2}$	0	0	0	$A(g_e-g_h)$	0
$\langle -3/2,\downarrow\|$	0	0	0	$\frac{g_e\mu_B H_+}{2}$	0	0	0	$A(g_e-3g_h)$

Table F.4: Zeeman Hamiltonian (uncoupled basis) for very large QDs where the magnetic field splitting, $g_e\mu_B H_z$ is on the same order as the exchange parameter, η. Both energies are small compared to the values of the crystal field and shape splitting, Δ. Add the two matrices on this page to obtain the full Hamiltonian.

where $A = \frac{\mu_B H_z}{2}$

The two matrices can be obtained as follows. First use Δ as base energies. Everything else is a perturbation to this. Now in Eq. 14 (Chapter 2) we are left with η terms. Drop all off diagonal η terms to get the first matrix on this page (these off diagonal values are small and can be neglected. Look at denominator in first order perturbation theory.). To consider magnetic field terms look at Eq. 30 of Chapter 2. Here drop all g_h terms closest to the diagonal. This gives the second matrix on this page. The reason for dropping g_h terms is that they will enter as first order terms. However since their contribution depends on the energy separation between states (i.e denominator) they are small and can be neglected. Exact energies obtained from diagonalizing the total Zeeman/exchange matrix. Note that this is better done in the uncoupled basis. The coupled basis is described on the next page but it is clear that much more work is needed to diagonalize this matrix.

$$\varepsilon^L_{\pm 2} = -\frac{\Delta}{2} \mp \frac{3}{2}\mu_B g_h H_z - \frac{1}{2}\sqrt{(3\eta \mp \mu_B g_e H_z)^2 + (\mu_B g_e)^2 H_\perp^2} \quad \text{(F.1)}$$

$$\varepsilon^L_{\pm 1} = -\frac{\Delta}{2} \mp \frac{3}{2}\mu_B g_h H_z + \frac{1}{2}\sqrt{(3\eta \mp \mu_B g_e H_z)^2 + (\mu_B g_e)^2 H_\perp^2} \quad \text{(F.2)}$$

$$\varepsilon^U_{\pm 1} = \frac{\Delta}{2} \mp \frac{1}{2}\mu_B g_h H_z - \frac{1}{2}\sqrt{(\eta \mp \mu_B g_e H_z)^2 + (\mu_B g_e)^2 H_\perp^2} \quad \text{(F.3)}$$

$$\varepsilon^{U,L}_0 = \frac{\Delta}{2} \mp \frac{1}{2}\mu_B g_h H_z + \frac{1}{2}\sqrt{(\eta \mp \mu_B g_e H_z)^2 + (\mu_B g_e)^2 H_\perp^2} \quad \text{(F.4)}$$

F.4.2 Coupled Basis

	$\|2,+2\rangle$	$\|2,+1\rangle$	$\|2,0\rangle$	$\|2,-1\rangle$	$\|2,-2\rangle$	$\|1,+1\rangle$	$\|1,0\rangle$	$\|1,-1\rangle$
$\langle 2,+2\|$	$-\frac{3\eta}{2}$	0	0	0	0	0	0	0
$\langle 2,+1\|$	0	$\frac{\eta}{2}(3C^{+2}-C^{-2})$	0	0	0	$2\eta C^{\pm}$	0	0
$\langle 2,0\|$	0	0	$\frac{\eta}{2}$	0	0	0	0	0
$\langle 2,-1\|$	0	0	0	$\frac{\eta}{2}(3C^{+2}-C^{-2})$	0	0	0	$-2\eta C^{\pm}$
$\langle 2,-2\|$	0	0	0	0	$-\frac{3\eta}{2}$	0	0	0
$\langle 1,+1\|$	0	$2\eta C^{\pm}$	0	0	0	$\frac{\eta}{2}(3C^{-2}-C^{+2})$	0	0
$\langle 1,0\|$	0	0	0	0	0	0	$\frac{\eta}{2}$	0
$\langle 1,-1\|$	0	0	0	$-2\eta C^{\pm}$	0	0	0	$\frac{\eta}{2}(3C^{-2}-C^{+2})$

	$\|2,+2\rangle$	$\|2,+1\rangle$	$\|2,0\rangle$	$\|2,-1\rangle$	$\|2,-2\rangle$	$\|1,+1\rangle$	$\|1,0\rangle$	$\|1,-1\rangle$
$\langle 2,+2\|$	$A(g_e-3g_h)$	$\frac{C^+B_-}{2}$	0	0	0	$\frac{C^-B_-}{2}$	0	0
$\langle 2,+1\|$	$\frac{C^+B_+}{2}$	AB	$-\frac{iC^-}{2\sqrt{2}}B_-$	0	0	$-H_z\mu_B C^{\pm}g_t$	$-\frac{iC^-}{2\sqrt{2}}B_-$	0
$\langle 2,0\|$	0	$\frac{iC^-}{2\sqrt{2}}B_+$	$\frac{\eta}{2}$	$-\frac{iC^-}{2\sqrt{2}}(B_-)$	0	$-\frac{iC^+}{\sqrt{2}}B_+$	0	$-\frac{iC^+}{2\sqrt{2}}B_-$
$\langle 2,-1\|$	0	0	$\frac{iC^-}{2\sqrt{2}}B_+$	AB	$\frac{iC^+}{2}B_-$	0	$-\frac{iC^-}{2\sqrt{2}}B_+$	$-H_z\mu_B C^{\pm}g_t$
$\langle 2,-2\|$	0	0	0	$-\frac{iC^+}{2}B_+$	$A(g_e-3g_h)$	0	0	$-\frac{iC^-}{2}B_+$
$\langle 1,+1\|$	$\frac{C^-B_+}{2}$	$-H_z\mu_B C^{\pm}g_t$	$\frac{iC^+}{2\sqrt{2}}B_-$	0	0	AC	$\frac{iC^+}{2\sqrt{2}}B_-$	0
$\langle 1,0\|$	0	$\frac{iC^-}{2\sqrt{2}}B_+$	0	$\frac{iC^-}{2\sqrt{2}}B_-$	0	$\frac{-iC^+}{2\sqrt{2}}B_+$	0	$\frac{iC^+}{2\sqrt{2}}B_-$
$\langle 1,-1\|$	0	0	$\frac{iC^+}{2\sqrt{2}}B_+$	$-H_z\mu_B C^{\pm}g_t$	$\frac{iC^-}{2}B_-$	0	$-\frac{iC^+}{2\sqrt{2}}B_+$	AC

Table F.5: Zeeman Hamiltonian (coupled basis) for very large QDs where the magnetic field splitting, $g_e\mu_B H_z$ is on the same order as the exchange parameter, η. Both energies are small compared to the values of the crystal field and shape splitting, Δ. Add the two matrices on this page to obtain the full Hamiltonian.

where
On Diagonals

$$\begin{aligned} A &= \frac{\mu_B H_z}{2} \\ B &= [C^{-2}(g_e-g_h)-C^{+2}(g_e+3g_h)] \\ C &= [C^{+2}(g_e-g_h)-C^{-2}(g_e+3g_h)] \end{aligned}$$

Off Diagonals

$$\begin{aligned} B_- &= g_e\mu_B H_- \\ B_+ &= g_e\mu_B H_+ \\ g_t &= g_e+g_h \\ C^{\pm} &= C^+C^- \end{aligned}$$

Appendix G

Second Order Corrections

This section lists work to determine second order corrections to the various fine structure states. The second order term mainly serves to mix the fine structure states together, giving oscillator strength to dark states and vice versa. It also perturbs the energies causing states to repel from each other.

G.1 Angle Average Magnetic Field

Before going of we will need values for the magnitude of the field parallel to the c axis and for the field perpendicular to c axis. The parallel component acts to Zeeman split states and the perpendicular component mixes the fine structure states.

$$\begin{aligned} H_x &= H\sin(\theta)\cos(\phi) \\ H_y &= H\sin(\theta)\cos(\phi) \\ H_z &= H\cos(\theta) \end{aligned} \tag{G.1}$$

where

$$H_x^2 + H_y^2 + H_z^2 = H^2$$

Define

$$H_\perp = \sqrt{H_x^2 + H_y^2}$$

therefore

$$H_\perp = H\sin(\theta)$$

G.1.1 Angle Average H_z^2

$$\begin{aligned} &\frac{1}{4\pi}\int_0^{\pi}\int_0^{2\pi} H^2\cos^2(\theta)\sin(\theta)d\theta d\phi \\ &= \frac{H^2}{2}\int_0^{\pi}\cos^2(\theta)\sin(\theta)d\theta \end{aligned} \tag{G.2}$$

let $x = \cos(\theta)$; $dx = -\sin(\theta)d\theta$

$$\begin{aligned} &= \frac{-H^2}{2}\int_1^{-1} x^2 dx \\ &= \frac{-H^2}{2}\frac{x^3}{3}\Big|_1^{-1} \end{aligned}$$

$$H_z^2 = \frac{H^2}{3} \tag{G.3}$$

G.1.2 Angle Average $H_\perp^2$

$$H_\perp^2 = H^2 \sin^2(\theta) \tag{G.4}$$

$$\frac{1}{4\pi}\int_0^{\pi}\int_0^{2\pi} H^2 \sin^2(\theta)\sin(\theta)d\theta d\phi \tag{G.5}$$

$$= \frac{H^2}{2}\int_0^{\pi} sin^3(\theta)d\theta$$

where $\sin^3(\theta) = \sin^2(\theta)\sin(\theta) = [1-\cos^2(\theta)]\sin(\theta)$

$$= \frac{H^2}{2}\int_0^{\pi}[\sin(\theta) - \cos^2(\theta)\sin(\theta)]d\theta$$
$$= \frac{H^2}{2}\left[-\cos(\theta)|_0^{\pi} - \int_0^{\pi}\cos^2(\theta)\sin(\theta)d\theta\right]$$

where $x = \cos(\theta)$ and $dx = -\sin(\theta)d\theta$

$$= -\frac{H^2}{2}(-2) + \frac{H^2}{2}\int_1^{-1} x^2 dx$$
$$= H^2 - \frac{H^2}{3}$$
$$= \frac{2}{3}H^2$$

$$H_\perp^2 = \frac{2}{3}H^2 \tag{G.6}$$

G.2 Second Order Non-Degenerate Correction to $|2,2>$

This work is based on the Zeeman Hamiltonian presented in Appendix F. The Dark exciton couples to 1 Upper and 1 Lower states only.

$$\epsilon_2^{(2)} = \frac{|<2,2|H'|2,1>|^2}{\epsilon_2 - \epsilon_{1^L}} + \frac{|<2,2|H'|1,1>|^2}{\epsilon_2 - \epsilon_{1^U}}$$
$$= \frac{|\frac{\mu_B B_-}{2}(-iC^-\sqrt{3}g_h + C^+g_e)|^2}{\epsilon_2 - \epsilon_{1^L}} + \frac{|\frac{\mu_B B_-}{2}(C^-g_e + i\sqrt{3}C^+g_h)|^2}{\epsilon_2 - \epsilon_{1^U}}$$
$$= \frac{\mu_B^2 B_\perp^2}{4}\left[\frac{(-iC^-\sqrt{3}g_h + C^+g_e)(iC^-\sqrt{3}g_h) + C^+g_e)}{\epsilon_2 - \epsilon_{1^L}} + \frac{(C^-g_e + i\sqrt{3}C^+g_h)(C^-g_e - i\sqrt{3}C^+g_h)}{\epsilon_2 - \epsilon_{1^U}}\right]$$
$$= \frac{\mu_B^2 B_\perp^2}{4}\left[\frac{3C^{-^2}g_h^2 + C^{+^2}g_e^2}{\epsilon_2 - \epsilon_{1^L}} + \frac{C^{-^2}g_e^2 + 3C^{+^2}g_h^2}{\epsilon_2 - \epsilon_{1^U}}\right] \tag{G.7}$$

G.3 Second Order Non-Degenerate Correction to $|2,-2>$

As before, this work is based on Zeeman Hamiltonian in Appendix F.

$$\begin{aligned}
\epsilon_2^{(2)} &= \frac{|<2,-2|H'|2,-1>|^2}{\epsilon_2-\epsilon_{1L}} + \frac{|<2,-2|H'|1,-1>|^2}{\epsilon_2-\epsilon_{1U}} \\
&= \frac{\left|\frac{\mu_B B_+}{2}(iC^+g_e-\sqrt{3}C^-g_h)\right|^2}{\epsilon_2-\epsilon_{1L}} + \frac{\left|\frac{\mu_B B_+}{2}(-iC^-g_e+\sqrt{3}C^+g_h)\right|^2}{\epsilon_2-\epsilon_{1U}} \\
&= \frac{\mu_B^2 B_\perp^2}{4}\left[\frac{(iC^+g_e-\sqrt{3}C^-g_h)(-iC^+g_e-\sqrt{3}C^-g_h)}{\epsilon_2-\epsilon_{1L}} + \frac{(-iC^-g_e+\sqrt{3}C^+g_h)(iC^-g_e+\sqrt{3}C^+g_h)}{\epsilon_2-\epsilon_{1U}}\right] \\
&= \frac{\mu_B^2 B_\perp^2}{4}\left[\frac{(C^{+^2}g_e^2+3C^{-^2}g_h^2)}{\epsilon_2-\epsilon_{1L}} + \frac{(C^{-^2}g_e^2+3C^{+^2}g_h^2)}{\epsilon_2-\epsilon_{1U}}\right] \qquad \text{(G.8)}
\end{aligned}$$

G.4 Second Order Non-Degenerate Correction to $|2,0>$

Based on the Zeeman matrix in Appendix F.

$$\begin{aligned}
\epsilon_{0^L}^{(2)} &= \frac{|<2,0|H'|2,1>|^2}{\epsilon_{0L}-\epsilon_{1L}} + \frac{|<2,0|H'|2,-1>|^2}{\epsilon_{0L}-\epsilon_{1L}} + \frac{|<2,0|H'|1,1>|^2}{\epsilon_{0L}-\epsilon_{1U}} + \frac{|<2,0|H'|1,-1>|^2}{\epsilon_{0L}-\epsilon_{1U}} \\
&+ \frac{|<2,0|H'|1,0>|^2}{\epsilon_{0L}-\epsilon_{0U}} \\
&= \frac{\left|\frac{\mu_B B_+}{2\sqrt{2}}(iC^-g_e-(\sqrt{3}C^++2C^-)g_h)\right|^2}{\epsilon_{0L}-\epsilon_{1L}} + \frac{\left|\frac{\mu_B B_-}{2\sqrt{2}}(-iC^-g_e-(\sqrt{3}C^++2C^-)g_h)\right|^2}{\epsilon_{0L}-\epsilon_{1L}} \\
&+ \frac{\left|\frac{\mu_B B_+}{2\sqrt{2}}(-iC^+g_e+(2C^+-\sqrt{3}C^-)g_h)\right|^2}{\epsilon_{0L}-\epsilon_{1U}} + \frac{|\frac{\mu_B B_-}{2\sqrt{2}}(-iC^+g_e+(\sqrt{3}C^--2C^+)g_h)|^2}{\epsilon_{0L}-\epsilon_{1U}} \\
&+ \frac{\mu_B^2 B_z^2}{4}\frac{(g_e+g_h)^2}{\epsilon_{0L}-\epsilon_{0U}} \\
&= \frac{\mu_B^2 B_\perp^2}{8}\left[\frac{C^{-^2}g_e^2+(\sqrt{3}C^++2C^-)^2g_h^2}{\epsilon_{0L}-\epsilon_{1L}} + \frac{C^{-^2}g_e^2+(\sqrt{3}C^++2C^-)^2g_h^2}{\epsilon_{0L}-\epsilon_{1L}}\right. \\
&+ \left.\frac{C^{+^2}g_e^2+(2C^+-\sqrt{3}C^-)^2g_h^2}{\epsilon_{0L}-\epsilon_{1U}} + \frac{C^{+^2}g_e^2+(\sqrt{3}C^--2C^+)^2g_h^2}{\epsilon_{0L}-\epsilon_{1U}}\right] \\
&+ \frac{\mu_B^2 B_z^2}{4}\frac{(g_e+g_h)^2}{\epsilon_{0L}-\epsilon_{0U}} \\
&= \frac{\mu_B^2 B_\perp^2}{8}\left[2\frac{C^{-^2}g_e^2+(\sqrt{3}C^++2C^-)^2g_h^2}{\epsilon_{0L}-\epsilon_{1L}} + 2\frac{C^{+^2}g_e^2+(2C^+-\sqrt{3}C^-)^2g_h^2}{\epsilon_{0L}-\epsilon_{1U}}\right]
\end{aligned}$$

$$+ \quad \frac{\mu_B^2 B_z^2}{4} \frac{(g_e + g_h)^2}{\epsilon_{0L} - \epsilon_{0U}}$$

$$= \frac{\mu_B^2 B_\perp^2}{4} \left[\frac{C^{-^2} g_e^2 + (\sqrt{3}C^+ + 2C^-)^2 g_h^2}{\epsilon_{0L} - \epsilon_{1L}} + \frac{C^{+^2} g_e^2 + (2C^+ - \sqrt{3}C^-)^2 g_h^2}{\epsilon_{0L} - \epsilon_{1U}} \right]$$

$$+ \quad \frac{\mu_B^2 B_z^2}{4} \frac{(g_e + g_h)^2}{\epsilon_{0L} - \epsilon_{0U}} \tag{G.9}$$

G.5 Second Order Non-Degenerate Correction to $|1,0>$

Based on the Zeeman matrix in Appendix F.

$$\epsilon_{0U}^{(2)} = \frac{|<1,0|H'|1,1>|^2}{\epsilon_{0U} - \epsilon_{1U}} + \frac{|<1,0|H'|1,-1>|^2}{\epsilon_{0U} - \epsilon_{1U}} + \frac{|<1,0|H'|2,1>|^2}{\epsilon_{0U} - \epsilon_{1L}} + \frac{|<1,0|H'|2,-1>|^2}{\epsilon_{0U} - \epsilon_{1L}}$$

$$+ \quad \frac{|<1,0|H'|2,0>|^2}{\epsilon_{0U} - \epsilon_{0L}}$$

$$= \frac{\left|\frac{\mu_B B_+}{2\sqrt{2}}(-iC^+ g_e - (2C^+ + \sqrt{3}C^-) g_h)\right|^2}{\epsilon_{0U} - \epsilon_{1U}} + \frac{\left|\frac{\mu_B B_-}{2\sqrt{2}}(iC^+ g_e - (\sqrt{3}C^- + 2C^+) g_h)\right|^2}{\epsilon_{0U} - \epsilon_{1U}}$$

$$+ \quad \frac{\left|\frac{\mu_B B_+}{2\sqrt{2}}(iC^- g_e + (2C^- - \sqrt{3}C^+) g_h)\right|^2}{\epsilon_{0U} - \epsilon_{1L}} + \frac{\left|\frac{\mu_B B_-}{2\sqrt{2}}(iC^- g_e + (\sqrt{(3)}C^+ - 2C^-) g_h)\right|^2}{\epsilon_{0U} - \epsilon_{1L}}$$

$$+ \quad \frac{\left|-\frac{\mu_B B_z}{2}(g_e + g_h)\right|^2}{\epsilon_{0U} - \epsilon_{0L}}$$

$$= \frac{\mu_B^2 B_\perp^2}{8} \left[\frac{C^{+^2} g_e^2 + (2C^+ + \sqrt{3}C^-)^2 g_h^2}{\epsilon_{0U} - \epsilon_{1U}} + \frac{C^{+^2} g_e^2 + (\sqrt{3}C^- + 2C^+)^2 g_h^2}{\epsilon_{0U} - \epsilon_{1U}} \right.$$

$$\left. + \quad \frac{C^{-^2} g_e^2 + (2C^- - \sqrt{3}C^+)^2 g_h^2}{\epsilon_{0U} - \epsilon_{1L}} + \frac{C^{-^2} g_e^2 + (\sqrt{3}C^+ - 2C^-)^2 g_h^2}{\epsilon_{0U} - \epsilon_{1L}} \right]$$

$$+ \quad \frac{\mu_B^2 B_z^2}{4} \frac{(g_e + g_h)^2}{\epsilon_{0U} - \epsilon_{0L}}$$

$$= \frac{\mu_B^2 B_\perp^2}{8} \left[2\frac{C^{+^2} g_e^2 + (2C^+ + \sqrt{3}C^{--})^2 g_h^2}{\epsilon_{0U} - \epsilon_{1U}} + 2\frac{C^{-^2} g_e^2 + (2C^- - \sqrt{3}C^+)^2 g_h^2}{\epsilon_{0U} - \epsilon_{1L}} \right]$$

$$+ \quad \frac{\mu_B^2 B_z^2}{4} \frac{(g_e + g_h)^2}{\epsilon_{0U} - \epsilon_{0L}}$$

$$= \frac{\mu_B^2 B_\perp^2}{4} \left[\frac{C^{+^2} g_e^2 + (2C^+ + \sqrt{3}C^-)^2 g_h^2}{\epsilon_{0U} - \epsilon_{1U}} + \frac{C^{-^2} g_e^2 + (2C^- - \sqrt{3}C^+)^2 g_h^2}{\epsilon_{0U} - \epsilon_{1L}} \right]$$

$$+ \quad \frac{\mu_B^2 B_z^2}{4} \frac{(g_e + g_h)^2}{\epsilon_{0U} - \epsilon_{0L}} \tag{G.10}$$

G.6 Second Order Degenerate and Non-Degenerate Correction to $|2,1>$ and $|2,-1>$

This is slightly different because the 1 Lower and 1 Upper states each couple to their + and − projections through 0 Lower and 0 Upper states. This degeneracy is removed in second order non-degenerate perturbation theory.

G.6.1 Degenerate Correction

Consider:

$$\sum_k \left(\sum_n H_{j,n} H_{n,k} - \lambda \delta_{j,k} \right) \tag{G.11}$$

$$\begin{vmatrix} \frac{|<2,1|H'|2,0>|^2}{\epsilon_{1L}-\epsilon_{0L}} + \frac{|<2,1|H'|1,0>|^2}{\epsilon_{1L}-\epsilon_{0U}} - \lambda^{(2)} & \frac{<2,1|H'|2,0><2,0|H'|2,-1>}{\epsilon_{1L}-\epsilon_{0L}} + \frac{<2,1|H'|1,0><1,0|H'|2,-1>}{\epsilon_{1L}-\epsilon_{0U}} \\ \frac{<2,-1|H'|2,0><2,0|H'|2,1>}{\epsilon_{1L}-\epsilon_{0L}} + \frac{<2,-1|H'|1,0><1,0|H'|2,1>}{\epsilon_{1L}-\epsilon_{0U}} & \frac{|<2,-1|H'|2,0>|^2}{\epsilon_{1L}-\epsilon_{0L}} + \frac{|<2,-1|H'|1,0>|^2}{\epsilon_{1L}-\epsilon_{0U}} - \lambda^{(2)} \end{vmatrix}$$

$$= \begin{vmatrix} A-\lambda^{(2)} & B \\ B^* & A-\lambda^{(2)} \end{vmatrix}$$

$$(A-\lambda^{(2)})^2 = B^*B$$

$$\lambda^{(2)} = A \mp \sqrt{B^*B}$$

where

$$\begin{aligned} A &= \frac{|<2,1|H'|2,0>|^2}{\epsilon_{1L}-\epsilon_{0L}} + \frac{|<2,1|H'|1,0>|^2}{\epsilon_{1L}-\epsilon_{0U}} \\ &= \frac{\mu_B^2 B_\perp^2}{8} \frac{\left|-iC^- g_e - (\sqrt{3}C^+ + 2C^-) g_h\right|^2}{\epsilon_{1L}-\epsilon_{0L}} + \frac{\mu_B^2 B_\perp^2}{8} \frac{|-iC^- g_e - (\sqrt{3}C^+ - 2C^-) g_h|^2}{\epsilon_{1L}-\epsilon_{0U}} \\ &= \frac{\mu_B^2 B_\perp^2}{8} \left[\frac{C^{-2} g_e^2 + (\sqrt{3}C^+ + 2C^-)^2 g_h^2}{\epsilon_{1L}-\epsilon_{0L}} + \frac{C^{-2} g_e^2 + (\sqrt{3}C^+ - 2C^-)^2 g_h^2}{\epsilon_{1L}-\epsilon_{0U}} \right] \end{aligned}$$

$$\begin{aligned} B^*B &= \left| \frac{\frac{\mu_B B_-}{2\sqrt{2}}[-iC^- g_e - (\sqrt{3}C^+ + 2C^-) g_h] \frac{\mu_B B_-}{2\sqrt{2}}[-iC^- g_e - (\sqrt{3}C^+ + 2C^-) g_h]}{\epsilon_{1L}-\epsilon_{0L}} \right. \\ &+ \left. \frac{\frac{\mu_B B_-}{2\sqrt{2}}[-iC^- g_e + (2C^- - \sqrt{3}C^+) g_h] \frac{\mu_B B_-}{2\sqrt{2}}[iC^- g_e + (\sqrt{3}C^+ - 2C^-) g_h]}{\epsilon_{1L}-\epsilon_{0U}} \right|^2 \\ &= \frac{\mu_B^4 B_\perp^4}{64} \left| \frac{(-iC^- g_e - (\sqrt{3}C^+ + 2C^-) g_h)^2}{\epsilon_{1L}-\epsilon_{0L}} \right. \\ &+ \left. \frac{(-iC^- g_e + (2C^- - \sqrt{3}C^+) g_h)(iC^- g_e + (\sqrt{(3)}C^+ - 2C^-) g_h)}{\epsilon_{1L}-\epsilon_{0U}} \right|^2 \end{aligned}$$

$$= \frac{\mu_B^4 B_\perp^4}{64}\left|\frac{(-iC^- g_e - (\sqrt{3}C^+ + 2C^-)g_h)^2}{\epsilon_{1L} - \epsilon_{0L}} + \frac{(C^- g_e - i(\sqrt{3}C^+ - 2C^-)g_h)^2}{\epsilon_{1L} - \epsilon_{0U}}\right|^2$$

$$= \frac{\mu_B^4 B_\perp^4}{64}\left[\frac{(C^{-2} g_e^2 + (\sqrt{3}C^+ + 2C^-)^2 g_h^2)^2}{(\epsilon_{1L} - \epsilon_{0L})^2} + \frac{(C^{-2} g_e^2 + (\sqrt{3}C^+ - 2C^-)^2 g_h^2)^2}{(\epsilon_{1L} - \epsilon_{0U})^2}\right.$$

$$\left. + 2\frac{-(C^{-2} g_e^2 + g_h^2(3C^{+2} - 4C^{-2}))^2 + 16C^{-4} g_e^2 g_h^2}{(\epsilon_{1L} - \epsilon_{0L})(\epsilon_{1L} - \epsilon_{0U})}\right]$$

$$\sqrt{B^* B} = \sqrt{\left[\frac{(C^{-2} g_e^2 + (\sqrt{3}C^+ + 2C^-)^2 g_h^2)^2}{(\epsilon_{1L} - \epsilon_{0L})^2} + \frac{(C^{-2} g_e^2 + (\sqrt{3}C^+ - 2C^-)^2 g_h^2)^2}{(\epsilon_{1L} - \epsilon_{0U})^2}\right.}$$

$$\left. + 2\frac{-(C^{-2} g_e^2 + g_h^2(3C^{+2} - 4C^{-2}))^2 + 16C^{-4} g_e^2 g_h^2}{(\epsilon_{1L} - \epsilon_{0L})(\epsilon_{1L} - \epsilon_{0U})}\right]$$

Summary:

$$\sqrt{B^* B} = \sqrt{\left[\frac{(C^{-2} g_e^2 + (\sqrt{3}C^+ + 2C^-)^2 g_h^2)^2}{(\epsilon_{1L} - \epsilon_{0L})^2} + \frac{(C^{-2} g_e^2 + (\sqrt{3}C^+ - 2C^-)^2 g_h^2)^2}{(\epsilon_{1L} - \epsilon_{0U})^2}\right.}$$

$$\left. + 2\frac{-(C^{-2} g_e^2 + g_h^2(3C^{+2} - 4C^{-2}))^2 + 16C^{-4} g_e^2 g_h^2}{(\epsilon_{1L} - \epsilon_{0L})(\epsilon_{1L} - \epsilon_{0U})}\right] \tag{G.12}$$

$$\lambda^{(2)} = \frac{\mu_B^2 B_\perp^2}{8}\left[\frac{C^{-2} g_e^2 + (\sqrt{3}C^+ + 2C^-)^2 g_h^2}{\epsilon_{1L} - \epsilon_{0L}} + \frac{C^{-2} g_e^2 + (\sqrt{3}C^+ - 2C^-)^2 g_h^2}{\epsilon_{1L} - \epsilon_{0U}}\right]$$

$$\mp \sqrt{\left[\frac{(C^{-2} g_e^2 + (\sqrt{3}C^+ + 2C^-)^2 g_h^2)^2}{(\epsilon_{1L} - \epsilon_{0L})^2} + \frac{(C^{-2} g_e^2 + (\sqrt{3}C^+ - 2C^-)^2 g_h^2)^2}{(\epsilon_{1L} - \epsilon_{0U})^2}\right.}$$

$$\left. + 2\frac{-(C^{-2} g_e^2 + g_h^2(3C^{+2} - 4C^{-2}))^2 + 16C^{-4} g_e^2 g_h^2}{(\epsilon_{1L} - \epsilon_{0L})(\epsilon_{1L} - \epsilon_{0U})}\right] \tag{G.13}$$

G.6.2 Non-Degenerate Correction to $|2,1>$

$$\frac{|<2,1|H'|2,2>|^2}{\epsilon_{1L} - \epsilon_2} + \frac{|<2,1|H'|1,1>|^2}{\epsilon_{1L} - \epsilon_{1U}}$$

$$= \frac{|\frac{\mu_B B_+}{2}(iC^-\sqrt{3}g_h + C^+ g_e)|^2}{\epsilon_{1L} - \epsilon_2} + \frac{|-\mu_B B_z C^+ C^- (g_e + g_h)|^2}{\epsilon_{1L} - \epsilon_{1U}}$$

$$= \frac{\mu_B^2 B_\perp^2}{4}\left[\frac{(iC^-\sqrt{3}g_h + C^+ g_e)(-iC^-\sqrt{3}g_h + C^+ g_e)}{\epsilon_{1L} - \epsilon_2}\right] + \frac{\mu_B^2 B_z^2 C^{+2} C^{-2}(g_e + g_h)^2}{\epsilon_{1L} - \epsilon_{1U}}$$

$$= \frac{\mu_B^2 B_\perp^2}{4}\left[\frac{3C^{-2} g_h^2 + C^{+2} g_e^2}{\epsilon_{1L} - \epsilon_2}\right] + \frac{\mu_B^2 B_z^2 C^{+2} C^{-2}(g_e + g_h)^2}{\epsilon_{1L} - \epsilon_{1U}} \tag{G.14}$$

G.6.3 Non-Degenerate Correction to $|2,-1>$

$$\frac{|<2,-1|H'|2,-2>|^2}{\epsilon_{1L}-\epsilon_2}+\frac{|<2,-1|H'|1,-1>|^2}{\epsilon_{1L}-\epsilon_{1U}}$$

$$\begin{aligned}
&= \frac{|\frac{\mu_B B_-}{2}(-iC^+g_e-\sqrt{3}C^-g_h)|^2}{\epsilon_{1L}-\epsilon_2}+\frac{|-\mu_B B_z C^+C^-(g_e+g_h)|^2}{\epsilon_{1L}-\epsilon_{1U}}\\
&= \frac{\mu_B^2B_\perp^2}{4}\left[\frac{(-iC^+g_e-\sqrt{3}C^-g_h)(iC^+g_e-\sqrt{3}C^-g_h)}{\epsilon_{1L}-\epsilon_2}\right]+\frac{\mu_B^2B_Z^2C^{+^2}C^{-^2}(g_e+g_h)^2}{\epsilon_{1L}-\epsilon_{1U}}\\
&= \frac{\mu_B^2B_\perp^2}{4}\left[\frac{C^{+^2}g_e^2+3C^{-^2}g_h^2}{\epsilon_{1L}-\epsilon_2}\right]+\frac{\mu_B^2B_Z^2C^{+^2}C^{-^2}(g_e+g_h)^2}{\epsilon_{1L}-\epsilon_{1U}}
\end{aligned} \tag{G.15}$$

G.7 Second Order Degenerate and Non-Degenerate Correction to $|1,1>$ and $|1,-1>$

Again this is a little bit complicated because degeneracy encountered in second order with coupling occuring through 0 state.

G.7.1 Degenerate Correction

Consider:

$$\sum_k\left(\sum_n H_{j,n}H_{n,k}-\lambda\delta_{j,k}\right) \tag{G.16}$$

$$\begin{vmatrix}
\frac{|<1,1|H'|1,0>|^2}{\epsilon_{1U}-\epsilon_{0U}}+\frac{|<1,1|H'|2,0>|^2}{\epsilon_{1U}-\epsilon_{0L}}-\lambda^{(2)} & \frac{<1,1|H'|1,0><1,0|H'|1,-1>}{\epsilon_{1U}-\epsilon_{0U}}+\frac{<1,1|H'|2,0><2,0|H'|1,-1>}{\epsilon_{1U}-\epsilon_{0L}}\\
\frac{<1,-1|H'|1,0><1,0|H'|1,1>}{\epsilon_{1U}-\epsilon_{0U}}+\frac{<1,-1|H'|2,0><2,0|H'|1,1>}{\epsilon_{1U}-\epsilon_{0L}} & \frac{|<1,-1|H'|1,0>|^2}{\epsilon_{1U}-\epsilon_{0U}}+\frac{|<1,-1|H'|2,0>|^2}{\epsilon_{1U}-\epsilon_{0L}}-\lambda^{(2)}
\end{vmatrix}$$

$$=\begin{vmatrix} A-\lambda^{(2)} & B \\ B^* & A-\lambda^{(2)} \end{vmatrix}$$

$$(A-\lambda^{(2)})^2=B^*B$$

$$\lambda^{(2)}=A\mp\sqrt{B^*B}$$

where

$$\begin{aligned}
A &= \frac{|<1,1|H'|1,0>|^2}{\epsilon_{1U}-\epsilon_{0U}}+\frac{|<1,1|H'|2,0>|^2}{\epsilon_{1U}-\epsilon_{0L}}\\
&= \frac{|\frac{\mu_B B_-}{2\sqrt{2}}(iC^+g_e-(2C^++\sqrt{3}C^-)g_h)|^2}{\epsilon_{1U}-\epsilon_{0U}}+\frac{|\frac{\mu_B B_-}{2\sqrt{2}}(iC^+g_e+(2C^+-\sqrt{3}C^-)g_h)|^2}{\epsilon_{1U}-\epsilon_{0L}}\\
&= \frac{\mu_B B_\perp^2}{8}\left[\frac{(iC^+g_e-(2C^++\sqrt{3}C^-)g_h)(-iC^+g_e-(2C^++\sqrt{3}C^-)g_h)}{\epsilon_{1U}-\epsilon_{0U}}\right.
\end{aligned}$$

$$+ \frac{(iC^+g_e + (2C^+ - \sqrt{3}C^-)g_h)(-iC^+g_e + (2C^+ - \sqrt{3}C^-)g_h)}{\epsilon_{1U} - \epsilon_{0L}}\Bigg]$$

$$= \frac{\mu_B^2 B_\perp^2}{8}\left[\frac{C^{+2}g_e^2 + (2C^+ + \sqrt{3}C^-)^2 g_h^2}{\epsilon_{1U} - \epsilon_{0U}} + \frac{C^{+2}g_e^2 + (2C^+ - \sqrt{3}C^-)^2 g_h^2}{\epsilon_{1U} - \epsilon_{0L}}\right]$$

$$B^*B = \left|\frac{\frac{\mu_B B_-}{2\sqrt{2}}[iC^+g_e - (2C^+ + \sqrt{3}C^-)g_h]\frac{\mu_B B_-}{2\sqrt{2}}[iC^+g_e - (\sqrt{3}C^- + 2C^+)g_h]}{\epsilon_{1U} - \epsilon_{0U}}\right.$$

$$+ \left.\frac{\frac{\mu_B B_-}{2\sqrt{2}}[iC^+g_e + (2C^+ - \sqrt{3}C^-)g_h]\frac{\mu_B B_-}{2\sqrt{2}}[-iC^+g_e + (\sqrt{3}C^- - 2C^+)g_h]}{\epsilon_{1U} - \epsilon_{0L}}\right|^2$$

$$= \frac{\mu_B^4 B_\perp^4}{64}\left|\frac{(iC^+g_e - (\sqrt{3}C^- + 2C^+)g_h)^2}{\epsilon_{1U} - \epsilon_{0U}} + \frac{(C^+g_e + i(\sqrt{3}C^- - 2C^+)g_h)^2}{\epsilon_{1U} - \epsilon_{0L}}\right|^2$$

$$= \frac{\mu_B^4 B_\perp^4}{64}\left[\frac{(C^{+2}g_e^2 + (\sqrt{3}C^- + 2C^+)^2 g_h^2)^2}{(\epsilon_{1U} - \epsilon_{0U})^2} + \frac{(C^{+2}g_e^2 + (\sqrt{3}C^- - 2C^+)^2 g_h^2)^2}{(\epsilon_{1U} - \epsilon_{0L})^2}\right.$$

$$+ \left. 2\frac{-(C^{+2}g_e^2 + g_h^2(3C^{-2} - 4C^{+2}))^2 + 16C^{+4}g_e^2 g_h^2}{(\epsilon_{1U} - \epsilon_{0U})(\epsilon_{1U} - \epsilon_{0L})}\right]$$

$$\sqrt{B*B} = \frac{\mu_B^2 B_\perp^2}{8}\sqrt{\left[\frac{(C^{+2}g_e^2 + (\sqrt{3}C^- + 2C^+)^2 g_h^2)^2}{(\epsilon_{1U} - \epsilon_{0U})^2} + \frac{(C^{+2}g_e^2 + (\sqrt{3}C^- - 2C^+)^2 g_h^2)^2}{(\epsilon_{1U} - \epsilon_{0L})^2}\right.}$$

$$+ \left.\sqrt{2\frac{-(C^{+2}g_e^2 + g_h^2(3C^{-2} - 4C^{+2}))^2 + 16C^{+4}g_e^2 g_h^2}{(\epsilon_{1U} - \epsilon_{0U})(\epsilon_{1U} - \epsilon_{0L})}}\right]$$

Summary:

$$\sqrt{B*B} = \frac{\mu_B^2 B_\perp^2}{8}\sqrt{\left[\frac{(C^{+2}g_e^2 + (\sqrt{3}C^- + 2C^+)^2 g_h^2)^2}{(\epsilon_{1U} - \epsilon_{0U})^2} + \frac{(C^{+2}g_e^2 + (\sqrt{3}C^- - 2C^+)^2 g_h^2)^2}{(\epsilon_{1U} - \epsilon_{0L})^2}\right.}$$

$$+ \left.\sqrt{2\frac{-(C^{+2}g_e^2 + g_h^2(3C^{-2} - 4C^{+2}))^2 + 16C^{+4}g_e^2 g_h^2}{(\epsilon_{1U} - \epsilon_{0U})(\epsilon_{1U} - \epsilon_{0L})}}\right] \tag{G.17}$$

$$\lambda^{(2)} = \frac{\mu_B^2 B_\perp^2}{8}\left[\frac{C^{+2}g_e^2 + (2C^+ + \sqrt{3}C^-)^2 g_h^2}{\epsilon_{1U} - \epsilon_{0U}} + \frac{C^{+2}g_e^2 + (2C^+ - \sqrt{3}C^-)^2 g_h^2}{\epsilon 1^U - \epsilon_{0L}}\right]$$

$$\mp \frac{\mu_B^2 B_\perp^2}{8}\sqrt{\left[\frac{(C^{+2}g_e^2 + (\sqrt{3}C^- + 2C^+)^2 g_h^2)^2}{(\epsilon_{1U} - \epsilon_{0U})^2} + \frac{(C^{+2}g_e^2 + (\sqrt{3}C^- - 2C^+)^2 g_h^2)^2}{(\epsilon_{1U} - \epsilon_{0L})^2}\right.}$$

$$+ \left.\sqrt{2\frac{-(C^{+2}g_e^2 + g_h^2(3C^{-2} - 4C^{+2}))^2 + 16C^{+4}g_e^2 g_h^2}{(\epsilon_{1U} - \epsilon_{0U})(\epsilon_{1U} - \epsilon_{0L})}}\right] \tag{G.18}$$

G.7.2 Non-Degenerate Correction to $|1,1>$

$$\frac{|<1,1|H'|2,2>|^2}{\epsilon_{1U} - \epsilon_2} + \frac{|<1,1||2,1>|^2}{\epsilon_{1U} - \epsilon_{1L}}$$

$$= \frac{|\frac{\mu_B B_+}{2}(C^- g_e - i\sqrt{3}C^+ g_h)|^2}{\epsilon_{1U} - \epsilon_2} + \frac{|-\mu_B B_z C^+ C^- (g_e + g_h)|^2}{\epsilon_{1U} - \epsilon_{1L}}$$
$$= \frac{\mu_B^2 B_\perp^2}{4}\left[\frac{C^{-^2} g_e^2 + 3C^{+^2} g_h^2}{\epsilon_{1U} - \epsilon_2}\right] + \frac{\mu_B^2 B_z^2 C^{+^2} C^{-^2}(g_e + g_h)^2}{\epsilon_{1U} - \epsilon_{1L}} \quad \text{(G.19)}$$

G.7.3 Non-Degenerate Correction to $|1,-1>$

$$\frac{|<1,-1|H'|2,2>|^2}{\epsilon_{1U} - \epsilon_2} + \frac{|<1,-1|H'|2,1>|^2}{\epsilon_{1U} - \epsilon_{1L}}$$

$$= \frac{|\frac{\mu_B B_-}{2}(iC^- g_e + \sqrt{3}C^+ g_h)|^2}{\epsilon_{1U} - \epsilon_2} + \frac{|-\mu_B B_z C^+ C^- (g_e + g_h)|^2}{\epsilon_{1U} - \epsilon_{1L}}$$
$$= \frac{\mu_B^2 B_\perp^2}{4}\left[\frac{C^{-^2} g_e^2 + 3C^{+^2} g_h^2}{\epsilon_{1U} - \epsilon_2}\right] + \frac{\mu_B^2 B_z^2 C^{+^2} C^{-^2}(g_e + g_h)^2}{\epsilon_{1U} - \epsilon_{1L}} \quad \text{(G.20)}$$

G.7.4 Total Summary for 1 Upper and 1 Lower States

Above we presented degenerate and non-degenerate second order contributions to the $|2,1>$, $|2,-1>$, $|1,1>$ and $|1,-1>$ states. The full correction to the fine structure energy is a sum of degenerate and non-degenerate contributions for each state. On a quick aside, a check on whether the corrections are correct is to take the trace of the diagonalized matrix. All degenerate and non-degenerate corrections for all fine structure states should cancel out (i.e. energy conserved).

G.8 Corrections to Transition Probabilities

Second order corrections in energy also lead to corrections in wavefunctions.

G.8.1 Dark Exciton $|2,2>$

$$|2,2>' = |2,2> + A|2,1> + B|1,1>$$

where

$$A = \frac{\mu_B B_-}{2}\left(\frac{-iC^-\sqrt{3}g_h + C^+ g_e}{\epsilon_2 - \epsilon_{1L}}\right)$$
$$B = \frac{\mu_B B_-}{2}\left(\frac{C^- g_e + i\sqrt{3}C^+ g_h}{\epsilon_2 - \epsilon_{1U}}\right)$$

$$<0|e\cdot p|2,2>' = <0|e\cdot p|2,2> + A<0|e\cdot p|2,1> + B<0|e\cdot p|1,1> \quad \text{(G.21)}$$

where $<0|e\cdot p|2,2> = 0$

$$<0|e\cdot p|2,2>' = A<0|e\cdot p|2,1> + B<0|e\cdot p|1,1>$$
$$= \left[A\left(\frac{-C^- e\_P}{\sqrt{3}} + C^+ e\_P\right) + B\left(\frac{C^+ e\_P}{\sqrt{3}} + C^- e\_P\right)\right]$$

$$|<0|e\cdot p|2,2>|^2 = \left|A\left(\frac{-C^- e\_P}{\sqrt{3}} + C^+ e\_P\right) + B\left(\frac{C^+ e\_P}{\sqrt{3}} + C^- e\_P\right)\right|^2$$

$$
\begin{aligned}
&= \left[A^*\left(\frac{-C^-e_+P}{\sqrt{3}}+C^+e_+P\right)+B^*\left(\frac{C^+e_+P}{\sqrt{3}}+C^-e_+P\right)\right]\\
&\times \left[A\left(\frac{-C^-e_-P}{\sqrt{3}}+C^+e_-P\right)+B\left(\frac{C^+e_-P}{\sqrt{3}}+C^-e_-P\right)\right]
\end{aligned}
$$

$$
\begin{aligned}
&= A^*A\left(\frac{-C^-e_+P}{\sqrt{3}}+C^+e_+P\right)\left(\frac{-C^-e_-P}{\sqrt{3}}+C^+e_-P\right)\\
&+ B^*B\left(\frac{C^+e_+P}{\sqrt{3}}+C^-e_+P\right)\left(\frac{C^+e_-P}{\sqrt{3}}+C^-e_-P\right)\\
&+ A^*B\left(\frac{-C^-e_+P}{\sqrt{3}}+C^+e_+P\right)\left(\frac{C^+e_-P}{\sqrt{3}}+C^-e_-P\right)\\
&+ B^*A\left(\frac{C^+e_+P}{\sqrt{3}}+C^-e_+P\right)\left(\frac{-C^-e_-P}{\sqrt{3}}+C^+e_-P\right)
\end{aligned}
$$

$$
\begin{aligned}
&= A^*AP_{2,1}+B^*BP_{1,1}\\
&+ A^*B\left(\frac{-C^-e_+P}{\sqrt{3}}+C^+e_+P\right)\left(\frac{C^+e_-P}{\sqrt{3}}+C^-e_-P\right)\\
&+ B^*A\left(\frac{C^+e_+P}{\sqrt{3}}+C^-e_+P\right)\left(\frac{-C^-e_-P}{\sqrt{3}}+C^+e_-P\right)
\end{aligned}
$$

Simplify expressions using $e_+e_- = \frac{\sin^2(\theta)}{2}$

$$
\begin{aligned}
&= A^*AP_{2,1}+B^*BP_{1,1}\\
&+ A^*B\left(-\frac{C^+C^-e_+e_-P^2}{3}-\frac{C^{-^2}e_+e_-P^2}{\sqrt{3}}+\frac{C^{+^2}e_+e_-P^2}{\sqrt{3}}+C^+C^-e_+e_-P^2\right)\\
&+ B^*A\left(-\frac{C^+C^-e_+e_-P^2}{3}+\frac{C^{+^2}e_+e_-P^2}{\sqrt{3}}-\frac{C^{-^2}e_+e_-P^2}{\sqrt{3}}+C^+C^-e_+e_-P^2\right)
\end{aligned}
$$

$$
\begin{aligned}
&= A^*AP_{2,1}+B^*BP_{1,1}\\
&+ A^*BP^2\ \frac{\sin^2(\theta)}{2}\left(-\frac{C^+C^-}{3}-\frac{C^{-^2}}{\sqrt{3}}+\frac{C^{+^2}}{\sqrt{3}}+C^+C^-\right)\\
&+ B^*AP^2\ \frac{\sin^2(\theta)}{2}\left(-\frac{C^+C^-}{3}+\frac{C^{+^2}}{\sqrt{3}}-\frac{C^{-^2}}{\sqrt{3}}+C^+C^-\right)
\end{aligned}
$$

$$
\begin{aligned}
&= A^*AP_{2,1}+B^*BP_{1,1}\\
&+ \frac{P^2\sin^2(\theta)}{2}\left(\frac{2}{3}C^+C^--\frac{C^{-^2}}{\sqrt{3}}+\frac{C^{+^2}}{\sqrt{3}}\right)(A^*B+B^*A)
\end{aligned}
$$

where

$$C^+ = \sqrt{\frac{\sqrt{f^2+d}+f}{2\sqrt{f^2+d}}}$$

$$C^- = \sqrt{\frac{\sqrt{f^2+d}-f}{2\sqrt{f^2+d}}}$$

$$C^+C^- = \frac{\sqrt{d}}{2\sqrt{f^2+d}}$$

$$\begin{aligned} &= A^*AP_{2,1} + B^*BP_{1,1} \\ &+ \frac{P^2\sin^2(\theta)}{6}\left(\frac{\sqrt{d}+\sqrt{3}f}{\sqrt{f^2+d}}\right)(A^*B + B^*A) \end{aligned}$$

where

$$A^*B = \frac{\mu_B^2 B_\perp^2}{4}\frac{(iC^-\sqrt{3}g_h + C^+g_e)}{\epsilon_2 - \epsilon_{1L}}\frac{(C^-g_e + i\sqrt{3}C^+g_h)}{\epsilon_2 - \epsilon_{1U}}$$

and

$$B^*A = \frac{\mu_B^2 B_\perp^2}{4}\frac{(C^-g_e - i\sqrt{3}C^+g_h)}{\epsilon_2 - \epsilon_{1U}}\frac{(-iC^-\sqrt{3}g_h + C^+g_e)}{\epsilon_2 - \epsilon_{1L}}$$

$$\begin{aligned} &= A^*AP_{2,1} + B^*BP_{1,1} \\ &+ \frac{\mu_B B_\perp^2}{2}C^+C^-(g_e^2 - 3g_h^2)\frac{1}{(\epsilon_2 - \epsilon_{1U})(\epsilon_2 - \epsilon_{1L})} \end{aligned}$$

Summary:

$$P'_{2,2} = |A|^2P_{2,1} + |B|^2P_{1,1} + \frac{KP^2\sin^2(\theta)}{6}\left(\frac{\sqrt{d}+\sqrt{3}f}{\sqrt{f^2+d}}\right)C \qquad \text{(G.22)}$$

where

$$\begin{aligned} A &= \frac{\mu_B B_-}{2}\left(\frac{-iC^-\sqrt{3}g_h + C^+g_e}{\epsilon_2 - \epsilon_{1L}}\right) \\ B &= \frac{\mu_B B_-}{2}\left(\frac{C^-g_e + i\sqrt{3}C^+g_h}{\epsilon_2 - \epsilon_{1U}}\right) \\ C &= \frac{\mu_B B_\perp^2}{2}C^+C^-(g_e^2 - 3g_h^2)\frac{1}{(\epsilon_2 - \epsilon_{1U})(\epsilon_2 - \epsilon_{1L})} \end{aligned}$$

G.8.2 Dark Exciton $|2,-2>$

This is very similar to the previous case. I will forgo detailed work.

$$\begin{aligned} |2,-2>' &= |2,-2> + A|2,-1> + B|1,-1> \\ <0|e\cdot p|2,-2>' &= <0|e\cdot p|2,-2> + A<0|e\cdot p|2,-1> + B<0|e\cdot p|1,-1> \end{aligned}$$

where one term drops out immediately

$$\begin{aligned} <0|e\cdot p|2,-2>' &= A<0|e\cdot p|2,-1> + B<0|e\cdot p|1,-1> \\ &= A\left(\frac{C^-e_+P}{\sqrt{3}} - C^+e_+P\right) + B\left(\frac{C^+e_+P}{\sqrt{3}} + C^-e_+P\right) \\ |<0|e\cdot p|2,-2>'|^2 &= \left|A\left(\frac{C^-e_+P}{\sqrt{3}} - C^+e_+P\right) + B\left(\frac{C^+e_+P}{\sqrt{3}} + C^-e_+P\right)\right|^2 \end{aligned}$$

$$
\begin{aligned}
&= \left[A^*(\frac{C^-e_-P}{\sqrt{3}} - C^+e_-P) + B^*(\frac{C^+e_-P}{\sqrt{3}} + C^-e_-P)\right] \\
&\times \left[A(\frac{C^-e_+P}{\sqrt{3}} - C^+e_+P) + B(\frac{C^+e_+P}{\sqrt{3}} + C^-e_+P)\right]
\end{aligned}
$$

$$
\begin{aligned}
&= |A|^2P_{2,-1} + |B|^2P_{1,-1} + \frac{KP^2\sin^2(\theta)}{6}(-2C^+C^- + \sqrt{3}C^{-^2} - \sqrt{3}C^{+^2})(A^*B + B^*A) \\
&= |A|^2P_{2,-1} + |B|^2P_{1,-1} - \frac{KP^2\sin^2(\theta)}{6}\left(\frac{\sqrt{d}+\sqrt{3}f}{2\sqrt{f^2+d}}\right)(A^*B + B^*A) \\
&= |A|^2P_{2,-1} + |B|^2P_{1,-1} - \frac{KP^2\sin^2(\theta)}{6}\left(\frac{\sqrt{d}+\sqrt{3}f}{2\sqrt{f^2+d}}\right)C
\end{aligned}
$$

Summary:

$$
P_{2,-2} = |A|^2P_{2,-1} + |B|^2P_{1,-1} - \frac{KP^2\sin^2(\theta)}{6}\left(\frac{\sqrt{d}+\sqrt{3}f}{2\sqrt{f^2+d}}\right)C \tag{G.23}
$$

where

$$
\begin{aligned}
A &= \frac{\mu_B B_+}{2}\frac{(iC^+g_e - \sqrt{3}C^-g_h)}{\epsilon_2 - \epsilon_{1L}} \\
B &= \frac{\mu_B B_+}{2}\frac{(-iC^-g_e + \sqrt{3}C^+g_h)}{\epsilon_2 - \epsilon_{1U}} \\
C &= -\frac{\mu_B B_\perp^2}{2}\frac{C^+C^-(g_e^2 + 3g_h^2)}{(\epsilon_2 - \epsilon_{1L})(\epsilon_2 - \epsilon_{1U})}
\end{aligned}
$$

G.8.3 Dark Exciton $|2,0>$

I will forgo many of the details.

$$
|2,0>' = A|2,1> + B|2,-1> + C|1,1> + D|1,-1> + E|1,0> \tag{G.24}
$$

where

$$
<0|e\cdot p|2,0> = 0
$$

$$
\begin{aligned}
<0|e\cdot p|2,0>' &= A<0|e\dot{p}|2,1> + B<0|e\cdot p|2,-1> + C<0|e\cdot p|1,1> \\
&+ D<0|e\cdot p|1,-1> + E<0|e\cdot p|1,0>
\end{aligned}
$$

Find hidden relations:

$$
\begin{aligned}
a &= <0|e\cdot p|2,1> \\
a &= e_-p\left(-\frac{C^-}{\sqrt{3}} + C^+\right) \\
b &= <0|e\cdot p|2,-1> \\
b &= -e_+p\left(-\frac{C^-}{\sqrt{3}} + C^+\right)
\end{aligned}
$$

therefore $b = -a^*$

$$
\begin{aligned}
c &= <0|e\cdot p|1,1> \\
c &= e_{-}p\left(\frac{C^{+}}{\sqrt{3}}+C^{-}\right)
\end{aligned}
$$

$$
\begin{aligned}
d &= <0|e\cdot p|1,-1> \\
d &= e_{+}p(\frac{C^{+}}{\sqrt{3}}+C^{-})
\end{aligned}
$$

therefore $d = c^{*}$

$$
\begin{aligned}
e &= <0|e\cdot p|1,0> \\
e &= \frac{2ie_{z}P}{\sqrt{3}}
\end{aligned}
$$

$$<0|e\cdot p|2,0>'= Aa - Bb^{*} + Cc + Dc^{*} + Ee$$

Now find hidden symmetries in the coefficients:

$$
\begin{aligned}
A &= <2,0|H'|2,1>/\Delta\epsilon \\
A &= \frac{\mu_{B}B_{+}}{2\sqrt{2}}\left(\frac{iC^{-}g_{e}-(\sqrt{3}C^{+}+2C^{-})g_{h}}{\epsilon_{0L}-\epsilon_{1L}}\right)
\end{aligned}
$$

$$
\begin{aligned}
B &= <2,0|H'|2,-1>/\Delta\epsilon \\
B &= \frac{\mu_{B}B_{-}}{2\sqrt{2}}\left(\frac{-iC^{-}g_{e}-(\sqrt{3}C^{+}+2C^{-})g_{h}}{\epsilon_{0L}-\epsilon_{1L}}\right)
\end{aligned}
$$

therefore $B = A^{*}$

$$
\begin{aligned}
C &= <2,0|H'|1,1>/\Delta\epsilon \\
C &= \frac{\mu_{B}B_{+}}{2\sqrt{2}}\left(\frac{-iC^{+}g_{e}+(2C^{+}-\sqrt{3}C^{-})g_{h}}{\epsilon_{0L}-\epsilon_{1U}}\right)
\end{aligned}
$$

$$
\begin{aligned}
D &= <2,0|H'|1,-1>/\Delta\epsilon \\
D &= -\frac{\mu_{B}B_{-}}{2\sqrt{2}}\left(\frac{iC^{+}g_{e}+(2C^{+}-\sqrt{3}C^{-})g_{h}}{\epsilon_{0L}-\epsilon_{1U}}\right)
\end{aligned}
$$

therefore $D = -C^{*}$

$$|<0|e\cdot p|2,0>'|^{2} = |Aa - A^{*}a^{*}|^{2} + |Cc - C^{*}c^{*}|^{2} + |E|^{2}|e|^{2} + \text{Interference} \qquad \text{(G.25)}$$

Interference Terms

1. $(Aa - A^{*}a^{*})^{*}(Cc - C^{*}c^{*})$
2. $(Cc - C^{*}c^{*})^{*}(Aa - A^{*}a^{*})$
3. $(Aa - A^{*}a^{*})^{*}(Ee)$.
4. $(Ee)^{*}(Aa - A^{*}a^{*})$
5. $(Cc - C^{*}c^{*})^{*}(Ee)$
6. $(Ee)^{*}(Cc - C^{*}c^{*})$

After much work we obtain:

$$\begin{aligned}
|<0|e\cdot p|2,0>'|^2 &= \frac{4}{3}|E|^2 e_z^2 K P^2 \\
&+ \frac{\frac{KP^2}{2}(-\frac{C^-}{\sqrt{3}}+C^+)^2}{(\epsilon_{0L}-\epsilon_{1L})^2} C^{-^2} g_e^2\mu_B^2 B^2\sin^4(\theta) \\
&+ \frac{\frac{KP^2}{2}(\frac{C^+}{\sqrt{3}}+C^-)^2}{(\epsilon_{0L}-\epsilon_{1U})^2} C^{+^2} g_e^2\mu_B^2 B^2\sin^4(\theta) \\
&- \frac{KP^2(\frac{2}{3}C^+C^- + \frac{1}{\sqrt{3}}(C^{+^2}-C^{-^2}))}{(\epsilon_{0L}-\epsilon_{1L})(\epsilon_{0L}-\epsilon_{1U})} \\
&+ \frac{\frac{4Ee_z\mu_B KP^2}{\sqrt{6}}(-\frac{C^-}{\sqrt{3}}+C^+)}{(\epsilon_{0L}-\epsilon_{1L})} C^- g_e B\sin^2(\theta) \\
&- \frac{\frac{4Ee_z\mu_B KP^2}{\sqrt{6}}(\frac{C^+}{\sqrt{3}}+C^-)}{(\epsilon_{0L}-\epsilon_{1U})} C^+ g_e B\sin^2(\theta)
\end{aligned}$$

This simplifies to:

$$\begin{aligned}
P_{2,0} &= \frac{4}{3}|E|^2 e_z^2 K P^2 \\
&+ \frac{KP^2}{2} g_e^2\mu_B^2 B^2\sin^4(\theta)\left[\frac{(-\frac{C^-}{\sqrt{3}}+C^+)C^-}{\epsilon_{0L}-\epsilon_{1L}} - \frac{(\frac{C^+}{\sqrt{3}}+C^-)C^+}{\epsilon_{0L}-\epsilon_{1U}}\right]^2 \\
&+ \frac{4Ee_z\mu_B KP^2}{\sqrt{6}}(g_e B\sin^2(\theta))\left[\frac{(-\frac{C^-}{\sqrt{3}}+C^+)C^-}{\epsilon_{0L}-\epsilon_{1L}} - \frac{(\frac{C^+}{\sqrt{3}}+C^-)C^+}{\epsilon_{0L}-\epsilon_{1U}}\right] \qquad \text{(G.26)}
\end{aligned}$$

where $E = <2,0|H'|1,0>/\Delta\epsilon = -\frac{\mu_B B_z(g_e+g_h)}{\epsilon_{0L}-\epsilon_{0U}}$

G.8.4 Bright Exciton $|1,0>$

This is similar to the 0 lower state.

$$|1,0>' = |1,0> + A|2,1> + B|2,-1> + C|1,1> + D|1,-1> \qquad \text{(G.27)}$$

where $<0|e\cdot p|2,0> = 0$ and let $E = 1$

$$\begin{aligned}
<0|e\cdot p|1,0>' &= A<0|e\cdot p|2,1> + B<0|e\cdot p|2,-1> + C<0|e\cdot p|1,1> \\
&+ D<0|e\cdot p|1,-1> + E<0|e\cdot p|1,0>
\end{aligned}$$

Look for hidden relations:

$$\begin{aligned}
a &= <0|e\cdot p|2,1> \\
a &= e_P\left(-\frac{C^-}{\sqrt{3}}+C^+\right) \\
b &= <0|e\cdot p|2,-1>
\end{aligned}$$

$$b = -e_+ P\left(-\frac{C^-}{\sqrt{3}} + C^+\right)$$

therefore $b = -a^*$

$$\begin{aligned} c &= < 0|e \cdot p|1,1 > \\ c &= e_- P(\frac{C^+}{\sqrt{3}} + C^-) \end{aligned}$$

$$\begin{aligned} d &= < 0|e \cdot p|1,-1 > \\ d &= e_+ P(\frac{C^+}{\sqrt{3}} + C^-) \end{aligned}$$

therefore $d = c^*$

$$\begin{aligned} e &= < 0|e \cdot p|1,0 > \\ e &= \frac{2ie_z P}{\sqrt{3}} \end{aligned}$$

$$< 0|e \cdot p|1,0 >' = Aa - Ba^* + Cc + Dc^* + Ee$$

Now find hidden relations in coefficients:

$$\begin{aligned} A &= < 1,0|H'|2,1 > /\Delta\epsilon \\ A &= \frac{\mu_B B_+}{2\sqrt{2}}(\frac{iC^- g_e + (2C^- - \sqrt{3}C^+)g_h}{\epsilon_{1''} - \epsilon_{1'}}) \end{aligned}$$

$$\begin{aligned} B &= < 1,0|H'|2,-1 > /\Delta\epsilon \\ B &= -\frac{\mu_B B_-}{2\sqrt{2}}\left(\frac{-iC^- g_e + (2C^- - \sqrt{3}C^+)g_h}{\epsilon_{1''} - \epsilon_{1'}}\right) \end{aligned}$$

therefore $B = -A^*$

$$\begin{aligned} C &= < 1,0|H'|1,1 > /\Delta\epsilon \\ C &= \frac{\mu_B B_+}{2\sqrt{2}}(\frac{-iC^+ g_e - (2C^+ + \sqrt{3}C^-)g_h}{\epsilon_{0''} - \epsilon_{1''}}) \end{aligned}$$

$$\begin{aligned} D &= < 1,0|H'|1,-1 > /\Delta\epsilon \\ D &= \frac{\mu_B B_-}{2\sqrt{2}}(\frac{iC^+ g_e - (2C^+ + \sqrt{3}C^-)g_h}{\epsilon_{0''} - \epsilon_{1''}}) \end{aligned}$$

therefore $D = C^*$

$$| < 0|e \cdot p|1,0 >' |^2 = |Aa + A^* a^*|^2 + |Cc + C^* c^*|^2 + |e|^2 + \text{Interference} \qquad \text{(G.28)}$$

Interference Terms

1. $(Aa + A^* a^*)^*(Cc + C^* c^*)$
2. $(Cc + C^* c^*)^*(Aa + A^* a^*)$
3. $(Aa + A^* a^*)^*(e)$
4. $(e)^*(Aa + A * a^*)$

5. $(Cc + C^*c^*)^*e$

6. $(e)^*(Cc + C^*c^*)$

After a lot of work we obtain:

$$\begin{aligned}
|<0|e\cdot p|1,0>|^2 &= \frac{4}{3}e_=^2 KP^2 \\
&+ \frac{KP^2}{2}g_h^2\mu_B^2B^2\sin^4(\theta)\left(\frac{(-\frac{C^-}{\sqrt{3}}+C^+)(2C^- - \sqrt{3}C^+)}{(\epsilon_{1^U}-\epsilon_{1^L})}\right)^2 \\
&+ \frac{KP^2}{2}g_h^2\mu_B^2B^2\sin^4(\theta)\left(\frac{(\frac{C^+}{\sqrt{3}}+C^-)(2C^+ + \sqrt{3}C^-)}{(\epsilon_{0^U}-\epsilon_{1^U})}\right)^2 \\
&- \frac{KP^2(\frac{2}{3}C^+C^- + \frac{1}{\sqrt{3}}(C^{+^2}-C^{-^2}))(C^+C^- - 2\sqrt{3}(C^{+^2}-C^{-^2}))}{(\epsilon_{1^U}-\epsilon_{1^L})(\epsilon_{0^U}-\epsilon_{1^U})}g_h^2\mu_B^2B^2\sin^4(\theta)
\end{aligned}$$

This simplifies to:

$$\begin{aligned}
P_{1,0} &= \frac{4}{3}e_=^2 KP^2 \\
&+ \frac{KP^2}{2}g_h^2\mu_B^2B^2\sin^4(\theta)\left[\frac{(-\frac{C^-}{\sqrt{3}}+C^+)(2C^- - \sqrt{3}C^+)}{\epsilon_{0^U}-\epsilon_{1^L}} - \frac{(\frac{C^+}{\sqrt{3}}+C^-)(2C^+ + \sqrt{3}C^-)}{\epsilon_{0^U}-\epsilon_{1^U}}\right]^2
\end{aligned} \quad (G.29)$$

G.8.5 Bright Exciton $|1,1>$

This is a bit more complicated because this state is degenerate with its other projection. The diagonalization we did to get the second order corrections to the energies also provides the eigenvectors of the correct zeroth order wavefunction (i.e. the true wavefunction of this state is a linear combination of $|1,1>$ and $|1,-1>$).

$$|1,1>' = |1,1> + a|1,-1>$$

after normalizing

$$|1,1>' = \frac{1}{\sqrt{1+|a|^2}}|1,1> + \frac{a}{\sqrt{1+|a|^2}}|1,-1> \quad (G.30)$$

Now rather than recalculate all the matrix elements of the 8×8 perturbation matrix, we take a shortcut and introduce into $|1,1>$ and $|1,-1>$ in the expression above, their corresponding form using non-degenerate perturbation theory.

$$\begin{aligned}
|1,\ 1> &= |1,\ 1> + A\,|2,\ 2> + B\,|2,\ 1> + C\,|2,0> + D\,|1,0> \\
|1,-1> &= |1,-1> + A'|2,-2> + B'|2,-1> + C'|2,0> + D'|1,0>
\end{aligned}$$

drop all dark states and rename things

$$\begin{aligned}
|1,\ 1> &= |1,\ 1> + B\,|2,\ 1> + D\,|1,0> \\
|1,-1> &= |1,-1> + B'|2,-1> + D'|1,0>
\end{aligned}$$

reintroduce into above numbered expression

$$
\begin{aligned}
|1,1>' &= x_1\,[|1,\ \ 1> + B\,|2,\ \ 1> + D\,|1,0>] \\
&+ x_2\,[|1,-1> + B'|2,-1> + D'|1,0>]
\end{aligned}
\tag{G.31}
$$

where x_1 and x_2 are shorthand expression for coefficients in front of $|1,1>$ and $|1,-1>$ above. We subsequently obtain the expression:

$$
\begin{aligned}
<0|e\cdot p|1,1>' &= [x_1 <0|e\cdot p|1,1> + x_2 <0|e\cdot p|1,-1>] \\
&+ [x_1 B <0|e\cdot p|2,1> + x_2 B' <0|e\cdot p|2,-1>] \\
&+ [x_1 D <0|e\cdot p|1,0> + x_2 D' <0|e\cdot p|1,0>]
\end{aligned}
$$

Look for hidden relations:

$$
\begin{aligned}
a &= <0|e\cdot p|1,1> \\
a &= e_- P\left(\frac{C^+}{\sqrt{3}} + C^-\right)
\end{aligned}
$$

$$
\begin{aligned}
a^* &= <0|e\cdot p|1,-1> \\
a^* &= e_+ P\left(\frac{C^+}{\sqrt{3}} + C^-\right)
\end{aligned}
$$

$$
\begin{aligned}
b &= <0|e\cdot p|2,1> \\
b &= e_- P\left(-\frac{C^-}{\sqrt{3}} + C^+\right)
\end{aligned}
$$

$$
\begin{aligned}
-b^* &= <0|e\cdot p|2,-1> \\
-b^* &= -e_+ P\left(-\frac{C^-}{\sqrt{3}} + C^+\right)
\end{aligned}
$$

$$
\begin{aligned}
d &= <0|e\cdot p|1,0> \\
d &= \frac{2ie_z P}{\sqrt{3}}
\end{aligned}
$$

$$
\begin{aligned}
<0|e\cdot p|1,1> &= [x_1 a + x_2 a^*] \\
&+ [x_1 B b - x_2 B' b^*] \\
&+ [x_1 D d + x_2 D' d]
\end{aligned}
$$

Look for relations in the coefficients:

$$
\begin{aligned}
B &= <1,1|H'|2,1>/\Delta\epsilon \\
B &= -\frac{\mu_B B_z C^+ C^- (g_e + g_h)}{\epsilon_{1u} - \epsilon_{1L}}
\end{aligned}
$$

$$
\begin{aligned}
B' &= <1,-1|H'|2,-1>/\Delta\epsilon \\
B' &= -\frac{\mu_B B_z C^+ C^- (g_e + g_h)}{\epsilon_{1u} - \epsilon_{1L}}
\end{aligned}
$$

therefore $B = B'$

$$
\begin{aligned}
D &= <1,1|H'|1,0>/\Delta\epsilon \\
D &= \frac{\frac{\mu_B B_-}{2\sqrt{2}}\left[iC^+ g_e - (2C^+ + \sqrt{3}C^-)g_h\right]}{\epsilon_{1U} - \epsilon_{0U}} \\
D' &= <1,-1|H'|1,0>/\Delta\epsilon \\
D' &= \frac{\frac{\mu_B B_+}{2\sqrt{2}}\left[-iC^+ g_e - (\sqrt{3}C^- + 2C^+)g_h\right]}{\epsilon_{1U} - \epsilon_{0U}}
\end{aligned}
$$

therefore $D' = D^*$

$$
\begin{aligned}
<0|e\cdot p|1,1>' &= [x_1 a + x_2 a^*] \\
&+ [x_1 Bb - x_2 b^* B] \\
&+ [x_1 Dd + x_2 D^* d]
\end{aligned}
$$

We obtain the expression:

$$|<0|e\cdot p|1,1>'|^2 = |x_1 a + x_2 a^*|^2 + |B|^2|x_1 b - x_2 b^*|^2 + |d|^2|x_1 D + x_2 D^*|^2 + \text{Interference} \quad \text{(G.32)}$$

Interference Terms

1. $(x_1 a + x_2 a^*)^* B(x_1 b - x_2 b^*)$
2. $B(x_1 b - x_2 b^*)^*(x_1 a + x_2 a^*)$
3. $(x_1 a + x_2 a^*)^* d(x_1 D + x_2 D^*)$
4. $d^*(x_1 D + x_2 D^*)^*(x_1 a + x_2 a^*)$
5. $B(x_1 b - x_2 b^*)^* d(x_1 D + x_2 D^*)$
6. $d^*(x_1 D + x_2 D^*)^* B(x_1 b - x_2 b^*)$

After a lot of work and angle averaging over ϕ we obtain:

$$
\begin{aligned}
|<0|e\cdot p|1,1>'|^2 &= KP^2\left(\frac{C^+}{\sqrt{3}} + C^-\right)\frac{\sin^2(\theta)}{2} \\
&+ KP^2|C|^2\left(-\frac{C^-}{\sqrt{3}} + C^-\right)\frac{\sin^2(\theta)}{2} \\
&+ KP^2 C\left(\frac{2}{3}C^+C^- + \frac{1}{\sqrt{3}}(C^{+^2} - C^{-^2})\right)\sin^2(\theta)(x_1^2 - |x_2|^2) \\
&+ \frac{\frac{B^2\sin^2(\theta)}{2}(C^{+^2} g_e^2 + (2C^+ + \sqrt{3}C^-)^2 g_h^2)\left(\frac{e_x^2\mu_B^2 KP^2}{6}\right)}{(\epsilon_{1U} - \epsilon_{0U})^2} \\
&+ \frac{\left(\frac{2e_x\mu_B KP^2}{\sqrt{6}}\right)\left(\frac{C^+}{\sqrt{3}} + C^-\right)}{\epsilon_{1U} - \epsilon_{0U}} B\sin^2(\theta)(C^+ g_e)(|x_2|^2 - x_1^2) \\
&+ \frac{C\left(\frac{2e_x\mu_B KP^2}{\sqrt{6}}\right)\left(-\frac{C^-}{\sqrt{3}} + C^+\right)}{\epsilon_{1U} - \epsilon_{0U}}(-C^+ g_e B\sin^2(\theta))
\end{aligned}
\quad \text{(G.33)}
$$

where $C = <1,1|H'|2,1>/\Delta\epsilon = -\frac{\mu_B B_x C^+ C^-(g_e + g_h)}{\epsilon_{1U} - \epsilon_{1L}}$

G.8.6 Bright Exciton $|1,-1>$

This is very similar to the above case. Should be reasonably symmetric expression.

$$|1,-1>' = -a|1,1>+|1,-1>$$

After normalizing

$$|1,-1>' = -\frac{a}{\sqrt{1+|a|^2}}|1,1>+\frac{1}{\sqrt{1+|a|^2}}|1,-1> \tag{G.34}$$

Now we introduce non-degenerate correction to wavefunctions as a shortcut, rather than recalculate all matrix elements of the 8×8 perturbation matrix.

$$\begin{aligned} |1,\ 1> &= |1,\ 1>+A\,|2,\ 2>+B\,|2,\ 1>+C\,|2,0>+D\,|1,0> \\ |1,-1> &= |1,-1>+A'|2,-2>+B'|2,-1>+C'|2,0>+D'|1,0> \end{aligned}$$

drop all dark terms and rename things

$$\begin{aligned} |1,\ 1> &= |1,\ 1>+B\,|2,\ 1>+D\,|1,0> \\ |1,-1> &= |1,-1>+B'|2,-1>+D'|1,0> \end{aligned}$$

reintroduce into the above expression:

$$\begin{aligned} |1,-1>' &= x_1[|1,\ 1>+B\,|2,\ 1>+D\,|1,0>] \\ &+ x_2[|1,-1>+B'|2,-1>+D'|1,0>] \end{aligned} \tag{G.35}$$

where x_1 and x_2 are shorter names for the coefficients in front of $|1,1>$ and $|1,-1>$ above. We obtain the expression:

$$\begin{aligned} <0|e\cdot p|1,-1>' &= [x_1<0|e\cdot p|1,1>+x_2<0|e\cdot p|1,-1>] \\ &+ [x_1B<0|e\cdot p|2,1>+x_2B'<0|e\cdot p|2,-1>] \\ &+ [x_1D<0|e\cdot p|1,0>+x_2D'<0|e\cdot p|1,0>] \end{aligned}$$

Look for hidden relations in the expression

$$\begin{aligned} a &= <0|e\cdot p|1,1> \\ a &= e\_P\left(\frac{C^+}{\sqrt{3}}+C^-\right) \\ a^* &= <0|e\cdot p|1,-1> \\ a^* &= e_+P\left(\frac{C^+}{\sqrt{3}}+C^-\right) \\ b &= <0|e\cdot p|2,1> \\ b &= e\_P\left(-\frac{C^-}{\sqrt{3}}+C^+\right) \\ -b^* &= <0|e\cdot p|2,-1> \\ -b^* &= -e_+P\left(-\frac{C^-}{\sqrt{3}}+C^+\right) \\ d &= <0|e\cdot p|1,0> \end{aligned}$$

$$d = \frac{2ie_zP}{\sqrt{3}}$$

$$\begin{aligned} <0|e\cdot p|1,-1> &= [x_1a + x_2a^*] \\ &+ [x_1Bb - x_2B'b^*] \\ &+ [x_1Dd + x_2D'd] \end{aligned}$$

Look now for hidden relations in the coefficients

$$\begin{aligned} B &= <1,1|H'|2,1>/\Delta\epsilon \\ B &= -\frac{\mu_B B_z C^+C^-(g_e+g_h)}{\epsilon_1{}^U - \epsilon_1{}^L} \\ B' &= <1,-1|H'|2,-1>/\Delta\epsilon \\ B' &= -\frac{\mu_B B_z C^+C^-(g_e+g_h)}{\epsilon_1{}^U - \epsilon_1{}^L} \end{aligned}$$

therefore $B = B'$

$$\begin{aligned} D &= <1,1|H'|1,0>/\Delta\epsilon \\ D &= \frac{\frac{\mu_B B_-}{2\sqrt{2}}(iC^+g_e - (2C^+ + \sqrt{3}C^-)g_h)}{\epsilon_1{}^U - \epsilon_0{}^U} \\ D' &= <1,-1|H'|1,0>/\Delta\epsilon \\ D' &= \frac{\frac{\mu_B B_+}{2\sqrt{2}}(-iC^+g_e - (2C^+ + \sqrt{3}C^-)g_h)}{\epsilon_1{}^U - \epsilon_0{}^U} \end{aligned}$$

therefore $D' = D^*$

$$\begin{aligned} <0|e\cdot p|1,-1>' &= [x_1a + x_2a^*] \\ &+ B[x_1b - x_2b^*] \\ &+ d[x_1D + x_2D^*] \end{aligned}$$

We have the expression:

$$|<0|e\cdot p|1,-1>'|^2 = |x_1a + x_2a^*|^2 + |B|^2|x_1b - x_2b^*|^2 + |d|^2|x_1D + x_2D^*|^2 + \text{Interference} \quad \text{(G.36)}$$

Interference Terms

1. $(x_1a + x_2a^*)^*B(x_1b - x_2b^*)$
2. $(Bx_1b - x_2b^*)^*(x_1a + x_2a^*)$
3. $(x_1a + x_2a^*)^*d(x_1D + x_2D^*)$
4. $d^*(x_1D + x_2D^*)^*(x_1a + x_2a^*)$
5. $B(x_1b - x_2b^*)^*d(x_1D + x_2D^*)$
6. $d^*(x_1D + x_2D^*)^*B(x_1b - x_2b^*)$

After a lot of work and angle averaging over ϕ we obtain the expression:

$$\begin{aligned}
|<0|e\cdot p|1,-1>|^2 &= KP^2\left(\frac{C^+}{\sqrt{3}}+C^-\right)^2\frac{\sin^2(\theta)}{2} \\
&+ |C|^2KP^2\left(-\frac{C^-}{\sqrt{3}}+C^+\right)^2\frac{\sin^2(\theta)}{2} \\
&+ CKP^2\left(\frac{2}{3}C^+C^- + \frac{1}{\sqrt{3}}(C^{+^2}-C^{-^2})\right)\sin^2(\theta)(|x_1|^2-x_2^2) \\
&+ \frac{\frac{B^2\sin^2(\theta)}{2}(C^{+^2}g_e^2+(2C^++\sqrt{3}C^-)^2g_h^2)\left(\frac{e_z^2\mu_B^2KP^2}{6}\right)}{(\epsilon_{1U}-\epsilon_{0U})^2} \\
&+ \frac{\left(\frac{e_z\mu_BKP^2}{\sqrt{6}}\right)\left(\frac{C^+}{\sqrt{3}}+C^-\right)}{\epsilon_{1U}-\epsilon_{0U}}(2B\sin^2(\theta))(C^+g_e(x_2^2-|x_1|^2)) \\
&+ \frac{C\left(\frac{2e_z\mu_BKP^2}{\sqrt{6}}\right)\left(-\frac{C^-}{\sqrt{3}}+C^+\right)}{\epsilon_{1U}-\epsilon_{0U}}(C^+g_e)(-B\sin^2(\theta))
\end{aligned} \tag{G.37}$$

where $C = <1,1|H'|2,1>/\Delta\epsilon = -\frac{\mu_B B_z C^+C^-(g_e+g_h)}{\epsilon_{1U}-\epsilon_{1L}}$

G.8.7 Bright Exciton $|2,1>$

This is analogous work to the 1 upper state described previously. Work provided for completeness.

$$|2,1>' = |2,1>+a|2,-1>$$

after normalizing

$$|2,1>' = \frac{1}{\sqrt{1+|a|^2}}|2,1>+\frac{a}{\sqrt{1+|a|^2}}|2,-1>$$

Rather than recalculate all the matrix elements of the perturbation matrix,we take shortcut and introduce nondegenerate perturbation expansion into the above expression to get the correct perturbed wavefunction.

$$\begin{aligned}
|2,\ 1> &= |2,\ 1>+A\,|2,\ 2>+B\,|2,0>+C\,|1,\ 1>+D\,|1,0> \\
|2,-1> &= |2,-1>+A'|2,-2>+B'|2,0>+C'|1,-1>+D'|1,0>
\end{aligned}$$

drop all dark terms and rename things

$$\begin{aligned}
|2,\ 1> &= |2,\ 1>+C\,|1,\ 1>+D\,|1,0> \\
|2,-1> &= |2,-1>+C'|1,-1>+D'|1,0>
\end{aligned}$$

reintroduce into the above expression

$$\begin{aligned}
|2,1>' &= x_1[|2,\ 1>+C\,|1,\ 1>+D\,|1,0>] \\
&+ x_2[|2,-1>+C'|1,-1>+D'|1,0>]
\end{aligned} \tag{G.38}$$

where x_1 and x_2 are shorter names for the coefficients in front of $|2,1>$ and $|2,-1>$ above. We obtain the expression:

$$\begin{aligned}
<0|e\cdot p|2,1>' &= [x_1<0|e\cdot p|2,1>+x_2<0|e\cdot p|2,-1>] \\
&+ [x_1C<0|e\cdot p|1,1>+x_2C'<0|e\cdot p|1,-1>]
\end{aligned}$$

$$+ \quad [x_1 D < 0|e\cdot p|1,0> + x_2 D' < 0|e\cdot p|1,0>]$$

Look for hidden relations:

$$\begin{aligned} a &= < 0|e\cdot p|2,1> \\ a &= e_- P\left(-\frac{C^-}{\sqrt{3}} + C^+\right) \end{aligned}$$

$$\begin{aligned} -a^* &= < 0|e\cdot p|2,-1> \\ -a^* &= -e_+ P\left(-\frac{C^-}{\sqrt{3}} + C^+\right) \end{aligned}$$

$$\begin{aligned} c &= < 0|e\cdot p|1,1> \\ c &= e_- P\left(\frac{C^+}{\sqrt{3}} + C^-\right) \end{aligned}$$

$$\begin{aligned} c^* &= < 0|e\cdot p|1,-1> \\ c^* &= e_+ P\left(\frac{C^+}{\sqrt{3}} + C^-\right) \end{aligned}$$

$$\begin{aligned} d &= < 0|e\cdot p|1,0> \\ d &= \frac{2ie_z P}{\sqrt{3}} \end{aligned}$$

$$\begin{aligned} < 0|e\cdot p|2,1> &= [x_1 a - x_2 a^*] \\ &+ [x_1 Cc + x_2 C'c^*] \\ &+ [x_1 Dd + x_2 D'd] \end{aligned}$$

Look for additional relations in the coefficients:

$$\begin{aligned} C &= < 2,1|H'|1,1 > /\Delta\epsilon \\ C &= -\frac{\mu_B B_z C^+ C^- (g_e + g_h)}{\epsilon_{1L} - \epsilon_{1U}} \end{aligned}$$

$$\begin{aligned} C' &= < 2,-1|H'|1,-1 > /\Delta\epsilon \\ C' &= -\frac{\mu_B B_z C^+ C^- (g_e + g_h)}{\epsilon_{1L} - \epsilon_{1U}} \end{aligned}$$

therefore $C' = C$

$$\begin{aligned} D &= < 2,1|H'|1,0 > /\Delta\epsilon \\ D &= \frac{\frac{\mu_B B_-}{2\sqrt{2}}(-iC^- g_e + (2C^- - \sqrt{3}C^+) g_h)}{\epsilon_{1L} - \epsilon_{0U}} \end{aligned}$$

$$\begin{aligned} D' &= < 2,-1|H'|1,0 > /\Delta\epsilon \\ D' &= \frac{-\frac{\mu_B B_+}{2\sqrt{2}}(iC^- g_e + (2C^- - \sqrt{3}C^+) g_h)}{\epsilon_{1L} - \epsilon_{0U}} \end{aligned}$$

therefore $D' = -D^*$

$$\begin{aligned} < 0|e\cdot p|2,1>' &= [x_1a - x_2a^*] \\ &+ C[x_1c + x_2c^*] \\ &+ d[Dx_1 - D^*x_2] \end{aligned}$$

We obtain the expression:

$$|< 0|e\cdot p|2,1>|^2 = |x_1a - x_2a^*|^2 + |C|^2|x_1c + x_2c^*|^2 + |d|^2|Dx_1 - D^*x_2|^2 + \text{Interference} \quad \text{(G.39)}$$

Interference Terms

1. $(x_1a - x_2a^*)^*C(x_1c + x_2c^*)$
2. $C^*(x_1c + x_2c^*)^*(x_1a - x_2a^*)$
3. $(x_1a - x_2a^*)^*d(Dx_1 - D^*x_2)$
4. $d^*(Dx_1 - D^*x_2)^*(x_1a - x_2a^*)$
5. $C^*(x_1c + x_2c^*)^*d(Dx_1 - D^*x_2)$
6. $d^*(Dx_1 - D^*x_2)^*C(x_1c + x_2c^*)$

After much work and angle averaging over ϕ we obtain the expression:

$$\begin{aligned} |< 0|e\cdot p|2,1>|^2 &= KP^2\left(-\frac{C^-}{\sqrt{3}} + C^+\right)^2\frac{\sin^2(\theta)}{2} \\ &+ |C|^2KP^2\left(\frac{C^+}{\sqrt{3}} + C^-\right)^2\frac{\sin^2(\theta)}{2} \\ &+ CKP^2\left(\frac{2}{3}C^+C^- + \frac{1}{\sqrt{3}}(C^{+^2} - C^{-^2})\right)\sin^2(\theta)(x_1^2 - |x_2|^2) \\ &+ \frac{\frac{B^2\sin^2(\theta)}{2}(C^{-^2}g_e^2 + (2C^- - \sqrt{3}C^+)^2g_h^2)\left(\frac{\epsilon_x^2\mu_B^2KP^2}{6}\right)}{(\epsilon_{1L} - \epsilon_{0U})^2} \\ &+ \frac{\left(\frac{2\epsilon_x\mu_BKP^2}{\sqrt{6}}\right)\left(-\frac{C^-}{\sqrt{3}} + C^+\right)}{\epsilon_{1L} - \epsilon_{0U}}B\sin^2(\theta)(C^-g_e)(x_1^2 - |x_2|^2) \\ &+ \frac{C\left(\frac{2\epsilon_x\mu_BKP^2}{\sqrt{6}}\right)\left(\frac{C^+}{\sqrt{3}} + C^-\right)}{\epsilon_{1L} - \epsilon_{0U}}(C^-g_eB\sin^2(\theta)) \end{aligned} \quad \text{(G.40)}$$

where $C =< 2,1|H'|1,1 > /\Delta\epsilon = -\frac{\mu_BB_xC^+C^-(g_e+g_h)}{\epsilon_{1L}-\epsilon_{1U}}$

G.8.8 Bright Exciton $|2,-1>$

Again this is similar to the cases presented above. We present the work for completeness.

$$|2,-1>' = -a|2,1> + |2,-1>$$

after normalizing

$$|2,-1:' = -\frac{a}{\sqrt{1+|a|^2}}|2,1> + \frac{1}{\sqrt{1+|a|^2}}|2,-1> \quad \text{(G.41)}$$

Rather than recalculate matrix elements of the 8×8 perturbation matrix we insert the nondegencrate expansion into the above expression.

$$\begin{aligned} |2,\ 1> &= |2,\ 1> + A\,|2,\ 2> + B\,|2,0> + C\,|1,\ 1> + D\,|1,0> \\ |2,-1> &= |2,-1> + A'|2,-2> + B'|2,0> + C'|1,-1> + D'|1,0> \end{aligned}$$

drop all dark terms and rename

$$\begin{aligned} |2,\ 1> &= |2,\ 1> + C\,|1,\ 1> + D\,|1,0> \\ |2,-1> &= |2,-1> + C'|1,-1> + D'|1,0> \end{aligned}$$

reintroduce into the above equation

$$\begin{aligned} |2,-1>' &= x_1[|2,\ 1> + C\,|1,\ 1> + D\,|1,0>] \\ &+ x_2[|2,-1> + C'|1,-1> + D'|1,0>] \end{aligned} \tag{G.42}$$

where x_1 and x_2 are shorthand for the normalization coefficients in the above expression. We subsequently obtain the expression:

$$\begin{aligned} <0|e\cdot p|2,-1>' &= [x_1 <0|e\cdot p|2,1> + x_2 <0|e\cdot p|2,-1>] \\ &+ [x_1 C <0|e\cdot p|1,1> + x_2 C <0|e\cdot p|1,-1>] \\ &+ [x_1 dD + x_2 dD'] \end{aligned}$$

Look for hidden relations in the expression

$$\begin{aligned} a &= <0|e\cdot p|2,1> \\ a &= e_- P\left(-\frac{C^-}{\sqrt{3}} + C^+\right) \end{aligned}$$

$$\begin{aligned} -a^* &= <0|e\cdot p|2,-1> \\ -a^* &= -e_+ P\left(-\frac{C^-}{\sqrt{3}} + C^+\right) \end{aligned}$$

$$\begin{aligned} c &= <0|e\cdot p|1,1> \\ c &= e_- P\left(\frac{C^+}{\sqrt{3}} + C^-\right) \end{aligned}$$

$$\begin{aligned} c^* &= <0|e\cdot p|1,-1> \\ c^* &= e_+ P\left(\frac{C^+}{\sqrt{3}} + C^-\right) \end{aligned}$$

$$\begin{aligned} d &= <0|e\cdot p|1,0> \\ d &= \frac{2ie_z P}{\sqrt{3}} \end{aligned}$$

$$\begin{aligned} <0|e\cdot p|2,-1> &= [x_1 a - x_2 a^*] \\ &+ [x_1 Cc + x_2 C'c^*] \\ &+ [x_1 Dd + x_2 D'd] \end{aligned}$$

Look for hidden relations in the coefficients

$$\begin{aligned} C &= <2,1|H'|1,1>/\Delta\epsilon \\ C &= -\frac{\mu_B B_z C^+ C^- (g_e + g_h)}{\epsilon_{1L} - \epsilon_{1U}} \end{aligned}$$

$$\begin{aligned} C' &+ <2,-1|H'|1,-1>/\Delta\epsilon \\ C' &= -\frac{\mu_B B_z C^+ C^- (g_e + g_h)}{\epsilon_{1L} - \epsilon_{1U}} \end{aligned}$$

therefore $C = C'$

$$\begin{aligned} D &= <2,1|H'|1,0>/\Delta\epsilon \\ D &= \frac{\frac{\mu_B B_-}{2\sqrt{2}}(-iC^- g_e + (2C^- - \sqrt{3}C^+)g_h)}{\epsilon_{1L} - \epsilon_{0U}} \end{aligned}$$

$$\begin{aligned} D' &= <2,-1|H'|1,0>/\Delta\epsilon \\ D' &= \frac{-\frac{\mu_B B_+}{2\sqrt{2}}(iC^- g_e + (2C^- - \sqrt{3}C^+)g_h)}{\epsilon_{1L} - \epsilon_{0U}} \end{aligned}$$

therefore $D' = -D^*$

$$\begin{aligned} <0|e\cdot p|2,-1>' &= [x_1 a - x_2 a^*] \\ &+ [x_1 C c + x_2 C c^*] \\ &+ [x_1 D d - x_2 D^* d] \end{aligned}$$

We obtain the expression:

$$|<0|e\cdot p|2,1>|^2 = |x_1 a - x_2 a^*|^2 + |C|^2|x_1 c + x_2 c^*|^2 + |d|^2|Dx_1 - D^* x_2|^2 + \text{Interference} \quad \text{(G.43)}$$

Interference Terms

1. $(x_1 a - x_2 a^*)^* C(x_1 c + x_2 c^*)$
2. $C^*(x_1 c + x_2 c^*)^*(x_1 a - x_2 a^*)$
3. $(x_1 a - x_2 a^*)^* d(Dx_1 - D^* x_2)$
4. $d^*(Dx_1 - D^* x_2)^*(x_1 a - x_2 a^*)$
5. $C^*(x_1 c + x_2 c^*)^* d(Dx_1 - D^* x_2)$
6. $d^*(Dx_1 - D^* x_2)^* C(x_1 c + x_2 c^*)$

After a lot of work and angle averaging over ϕ we obtain:

$$\begin{aligned} |<0|e\cdot p|2,-1>|^2 &= KP^2\left(-\frac{C^-}{\sqrt{3}} + C^+\right)^2 \frac{\sin^2(\theta)}{2} \\ &+ |C|^2 KP^2\left(\frac{C^+}{\sqrt{3}} + C^-\right)^2 \frac{\sin^2(\theta)}{2} \\ &+ CKP^2\left(\frac{2}{3}C^+C^- + \frac{1}{\sqrt{3}}(C^{+2} - C^{-2})\right)\sin^2(\theta)(|x_1|^2 - x_2^2) \end{aligned}$$

$$+ \frac{\frac{B^2\sin^2(\theta)}{2}(C^{-2}g_e^2 + (2C^- - \sqrt{3}C^+)^2 g_h^2)\left(\frac{e_s^2\mu_H^2KP^2}{6}\right)}{(\epsilon_{1L} - \epsilon_{0U})^2}$$

$$+ \frac{\left(\frac{2e_s\mu_BKP^2}{\sqrt{6}}\right)\left(-\frac{C^-}{\sqrt{3}} + C^+\right)}{\epsilon_{1L} - \epsilon_{0U}} B\sin^2(\theta)(C^- g_e)(|x_1|^2 - x_2^2)$$

$$+ \frac{C\left(\frac{2e_s\mu_BKP^2}{\sqrt{6}}\right)\left(\frac{C^+}{\sqrt{3}} + C^-\right)}{\epsilon_{1L} - \epsilon_{0U}}(C^- g_e B\sin^2(\theta)) \qquad \text{(G.44)}$$

where $C = < 2,1|H'|1,1 > /\Delta\epsilon = -\frac{\mu_B B_s C^+ C^- (g_e + g_h)}{\epsilon_{1L} - \epsilon_{1U}}$

Appendix H

MCD Signal

H.1 Phenomenological modeling of the MCD signal

Assume that one Gaussian splits symmetrically under the influence of an external magnetic field. Take difference of the two functions to model the difference spectrum.

$$f(x) = \frac{1}{\sqrt{2\pi}\sigma} e^{-\frac{(x-x_0)^2}{2\sigma^2}} \tag{H.1}$$

becomes

$$\begin{aligned} MCD(x) &= \frac{1}{\sqrt{2\pi}\sigma} e^{-\frac{[x-(x_0+\Delta x)]^2}{2\sigma^2}} - \frac{1}{\sqrt{2\pi}\sigma} e^{-\frac{[x-(x_0-\Delta x)]^2}{2\sigma^2}} \\ &= \frac{1}{\sqrt{2\pi}\sigma} \left[e^{-\frac{[x-(x_0+\Delta x)]^2}{2\sigma^2}} - e^{-\frac{[x-(x_0-\Delta x)]^2}{2\sigma^2}} \right] \end{aligned} \tag{H.2}$$

Expand each of the exponents. For the first exponential:

$$\begin{aligned} \frac{1}{2\sigma^2}[x-(x_0+\Delta x)]^2 &= \frac{1}{2\sigma^2}[(x-x_0)-\Delta x]^2 \\ &= \frac{1}{2\sigma^2}[(x-x_0)^2 + \Delta x^2 - 2(x-x_0)\Delta x] \\ &= \frac{1}{2\sigma^2}[(x-x_0)^2 + \Delta x^2] - \frac{(x-x_0)\Delta x}{\sigma^2} \end{aligned}$$

Same procedure for the second exponent, yielding:

$$\begin{aligned} MCD(x) &= \frac{1}{\sqrt{2\pi}\sigma} \left[e^{-\frac{[(x-x_0)^2+\Delta x^2]}{2\sigma^2}} e^{\frac{(x-x_0)\Delta x}{\sigma^2}} - e^{-\frac{[(x-x_0)^2+\Delta x^2]}{2\sigma^2}} e^{-\frac{(x-x_0)\Delta x}{\sigma^2}} \right] \\ &= \frac{1}{\sqrt{2\pi}\sigma} e^{-\frac{[(x-x_0)^2+\Delta x^2]}{2\sigma^2}} \left[e^{\frac{(x-x_0)\Delta x}{\sigma^2}} - e^{-\frac{(x-x_0)\Delta x}{\sigma^2}} \right] \end{aligned}$$

where

$$e^x = 1 + x + \frac{x^2}{2} + \ldots \tag{H.3}$$

As an approximation, keep only the first two terms. First exponential in brackets becomes:

$$1+\frac{(x-x_0)\Delta x}{\sigma^2}+\ldots$$

Second exponential in brackets becomes:

$$1-\frac{(x-x_0)\Delta x}{\sigma^2}+\ldots$$

Equation becomes:

$$MCD(x)=\frac{1}{\sqrt{2\pi}\sigma}e^{-\frac{[(x-x_0)^2+\Delta x^2]}{2\sigma^2}}\left[\frac{2(x-x_0)\Delta x}{\sigma^2}\right]=e^{-\frac{\Delta x^2}{2\sigma^2}}\left[\frac{1}{\sqrt{2\pi}\sigma}e^{-\frac{(x-x_0)^2}{2\sigma^2}}\frac{2(x-x_0)\Delta x}{\sigma^2}\right] \quad \text{(H.4)}$$

If we make the approximation that $\sigma \gg \Delta x$ then we can drop the first exponential. The resulting function approximates the unnormalized MCD signal observed in the experiment.

$$MCD(x)\approx\left(\frac{1}{\sqrt{2\pi}\sigma}e^{-\frac{[(x-x_0)^2+\Delta x^2]}{2\sigma^2}}\right)\left(\frac{2(x-x_0)\Delta x}{\sigma^2}\right) \quad \text{(H.5)}$$

The procedure can be readily applied for finding the MCD signal from two or more gaussians.

H.2 Fine structure net splitting

We now extend the analysis to consider the predicted fine structure. We also extract from this analysis the net splitting of the state when inhomogeneously broadened. Pretend that we have three optically active states. We model the absorption of right circularly polarized light.

$$\begin{aligned}A_+(\epsilon) &= A\int \frac{C_1^U}{\sqrt{2\pi}\sigma}e^{\frac{-[\epsilon-(\epsilon_1^U+\delta_1^U)]^2}{2\sigma^2}}+\frac{C_1^L}{\sqrt{2\pi}\sigma}e^{\frac{-[\epsilon-(\epsilon_1^L+\delta_1^L)]^2}{2\sigma^2}}+\frac{C_0^U}{\sqrt{2\pi}\sigma}e^{\frac{-(\epsilon-\epsilon_0^U)^2}{2\sigma^2}}+\frac{C_{-1}^U}{\sqrt{2\pi}\sigma}e^{\frac{-[\epsilon-(\epsilon_1^U-\delta_1^U)]^2}{2\sigma^2}}\\ &\quad+\frac{C_{-1}^L}{\sqrt{2\pi}\sigma}e^{\frac{-[\epsilon-(\epsilon_1^L-\delta_1^L)]^2}{2\sigma^2}}d\cos\theta\end{aligned}$$

Let

$$\begin{aligned}\epsilon_{+1}^U&=\epsilon_1^U+\delta_1^U\\ \epsilon_{-1}^U&=\epsilon_1^U-\delta_1^U\\ \epsilon_{+1}^L&=\epsilon_1^L+\delta_1^L\\ \epsilon_{-1}^L&=\epsilon_1^L-\delta_1^L\end{aligned}$$

$$\begin{aligned}A_+(\epsilon) &= A\int \frac{C_1^U}{\sqrt{2\pi}\sigma}e^{\frac{-(\epsilon-\epsilon_{+1}^U)^2}{2\sigma^2}}+\frac{C_1^L}{\sqrt{2\pi}\sigma}e^{\frac{-(\epsilon-\epsilon_{+1}^L)^2}{2\sigma^2}}+\frac{C_0^U}{\sqrt{2\pi}\sigma}e^{\frac{-(\epsilon-\epsilon_0^U)^2}{2\sigma^2}}+\frac{C_{-1}^U}{\sqrt{2\pi}\sigma}e^{\frac{-(\epsilon-\epsilon_{-1}^U)^2}{2\sigma^2}}\\ &\quad+\frac{C_{-1}^L}{\sqrt{2\pi}\sigma}e^{\frac{-(\epsilon-\epsilon_{-1}^L)^2}{2\sigma^2}}d\cos\theta\end{aligned} \quad \text{(H.6)}$$

In general, desire Δ that is angle independent

$$=\frac{A}{\sqrt{2\pi}\sigma}\int C_1^U e^{\frac{-[(\epsilon-\Delta)-(\epsilon_{+1}^U-\Delta)]^2}{2\sigma^2}}+C_1^L e^{\frac{-[(\epsilon-\Delta)-(\epsilon_{+1}^L-\Delta)]^2}{2\sigma^2}}+C_0^U e^{\frac{-[(\epsilon-\Delta)-(\epsilon_0^U-\Delta)]^2}{2\sigma^2}}$$

$$+C_{-1}^{U}e^{\frac{-[(\epsilon-\Delta)-(\epsilon_{-1}^{U}-\Delta)]^2}{2\sigma^2}}+C_{-1}^{L}e^{\frac{-[(\epsilon-\Delta)-(\epsilon_{-1}^{L}-\Delta)]^2}{2\sigma^2}}d\cos\theta$$

$$\begin{aligned}=\ & \frac{A}{\sqrt{2\pi}\sigma}\int C_1^U e^{-\frac{(\epsilon-\Delta)^2}{2\sigma^2}+\frac{(\epsilon-\Delta)(\epsilon_{+1}^{U}-\Delta)}{\sigma^2}-\frac{(\epsilon_{+1}^{U}-\Delta)^2}{2\sigma^2}}+C_1^L e^{-\frac{(\epsilon-\Delta)^2}{2\sigma^2}+\frac{(\epsilon-\Delta)(\epsilon_{+1}^{L}-\Delta)}{\sigma^2}-\frac{(\epsilon_{+1}^{L}-\Delta)^2}{2\sigma^2}}\\ &+C_0^U e^{-\frac{(\epsilon-\Delta)^2}{2\sigma^2}+\frac{(\epsilon-\Delta)(\epsilon_{0}^{U}-\Delta)}{\sigma^2}-\frac{(\epsilon_{0}^{U}-\Delta)^2}{2\sigma^2}}+C_{-1}^U e^{-\frac{(\epsilon-\Delta)^2}{2\sigma^2}+\frac{(\epsilon-\Delta)(\epsilon_{-1}^{U}-\Delta)}{\sigma^2}-\frac{(\epsilon_{-1}^{U}-\Delta)^2}{2\sigma^2}}\\ &+C_{-1}^L e^{-\frac{(\epsilon-\Delta)^2}{2\sigma^2}+\frac{(\epsilon-\Delta)(\epsilon_{-1}^{L}-\Delta)}{\sigma^2}-\frac{(\epsilon_{-1}^{L}-\Delta)^2}{2\sigma^2}}d\cos\theta\end{aligned}$$

Pull out common terms and recall that integral of normalized Gaussian = 1

$$\begin{aligned}=\ & \frac{A}{\sqrt{2\pi}\sigma}e^{\frac{-(\epsilon-\Delta)^2}{2\sigma^2}}\int C_1^U e^{\frac{(\epsilon-\Delta)(\epsilon_{+1}^{U}-\Delta)}{\sigma^2}}+C_1^L e^{\frac{(\epsilon-\Delta)(\epsilon_{+1}^{L}-\Delta)}{\sigma^2}}+C_0^U e^{\frac{(\epsilon-\Delta)(\epsilon_{0}^{U}-\Delta)}{\sigma^2}}+C_{-1}^U e^{\frac{(\epsilon-\Delta)(\epsilon_{-1}^{U}-\Delta)}{\sigma^2}}\\ &+C_{-1}^L e^{\frac{(\epsilon-\Delta)(\epsilon_{-1}^{L}-\Delta)}{\sigma^2}}d\cos\theta\end{aligned}$$

Assume that Δ has no θ dependence and that $\sigma \gg \epsilon_{\pm 1} - \Delta$ (fine structure splitting) Also apply approximation of exponential.

$$\begin{aligned}=\ & \frac{A}{\sqrt{2\pi}\sigma}e^{\frac{-(\epsilon-\Delta)^2}{2\sigma^2}}\int C_1^U\left(1+\frac{(\epsilon-\Delta)(\epsilon_{+1}^{U}-\Delta)}{\sigma^2}\right)+C_1^L\left(1+\frac{(\epsilon-\Delta)(\epsilon_{+1}^{L}-\Delta)}{\sigma^2}\right)\\ &+C_0^U\left(1+\frac{(\epsilon-\Delta)(\epsilon_{0}^{U}-\Delta)}{\sigma^2}\right)+C_{-1}^U\left(1+\frac{(\epsilon-\Delta)(\epsilon_{-1}^{U}-\Delta)}{\sigma^2}\right)+C_{-1}^L\left(1+\frac{(\epsilon-\Delta)(\epsilon_{-1}^{L}-\Delta)}{\sigma^2}\right)d\cos\theta\end{aligned}$$

$$\begin{aligned}=\ & \frac{A}{\sqrt{2\pi}\sigma}e^{\frac{-(\epsilon-\Delta)^2}{2\sigma^2}}\int(C_1^U+C_1^L+C_0^U+C_{-1}^U+C_{-1}^L)+\left[C_1^U\frac{(\epsilon-\Delta)(\epsilon_{+1}^{U}-\Delta)}{\sigma^2}+C_1^L\frac{(\epsilon-\Delta)(\epsilon_{+1}^{L}-\Delta)}{\sigma^2}\right.\\ &\left.+C_0^U\frac{(\epsilon-\Delta)(\epsilon_{0}^{U}-\Delta)}{\sigma^2}+C_{-1}^U\frac{(\epsilon-\Delta)(\epsilon_{-1}^{U}-\Delta)}{\sigma^2}+C_{-1}^L\frac{(\epsilon-\Delta)(\epsilon_{-1}^{L}-\Delta)}{\sigma^2}\right]d\cos\theta\end{aligned}$$

$$\begin{aligned}=\ & \frac{A}{\sqrt{2\pi}\sigma}e^{\frac{-(\epsilon-\Delta)^2}{2\sigma^2}}\int(C_1^U+C_1^L+C_0^U+C_{-1}^U+C_{-1}^L)+\frac{(\epsilon-\Delta)}{\sigma^2}\left[C_1^U(\epsilon_{+1}^{U}-\Delta)+C_1^L(\epsilon_{+1}^{L}-\Delta)\right.\\ &\left.+C_0^U(\epsilon_{0}^{U}-\Delta)+C_{-1}^U(\epsilon_{-1}^{U}-\Delta)+C_{-1}^L(\epsilon_{-1}^{L}-\Delta)\right]d\cos\theta\end{aligned}$$

The second term in brackets simplifies to

$$\frac{(\epsilon-\Delta)}{\sigma^2}\left[C_1^U(\epsilon_{+1}^{U}-\Delta)+C_1^L(\epsilon_{+1}^{L}-\Delta)+C_0^U(\epsilon_{0}^{U}-\Delta)+C_{-1}^U(\epsilon_{-1}^{U}-\Delta)+C_{-1}^L(\epsilon_{-1}^{L}-\Delta)\right]$$

where

$$\Delta=\frac{\int C_1^U\epsilon_{+1}^{U}+C_1^L\epsilon_{+1}^{L}+C_0^U\epsilon_{0}^{U}+C_{-1}^U\epsilon_{-1}^{U}+C_{-1}^L\epsilon_{-1}^{L}d\cos\theta}{\int(C_1^U+C_1^L+C_0^U+C_{-1}^U+C_{-1}^L)d\cos\theta}$$

Note that

$$C_1^U \neq C_{-1}^U$$

$$C_1^L \neq C_{-1}^L$$

and that

$$\begin{aligned} C^U{}_1 &= N^U(1-\cos\theta)^2 \\ C^U_{-1} &= N^U(1+\cos\theta)^2 \\ C^L{}_1 &= N^L(1-\cos\theta)^2 \\ C^L_{-1} &= N^L(1+\cos\theta)^2 \\ C^U{}_0 &= N_0\sin^2\theta \end{aligned}$$

where

$$N_0 = \frac{4}{3}KP^2$$

Angle average the numerator

$$= \int_{-1}^{1} N^U(1-\cos\theta)^2\epsilon^U_{+1}+N^L(1-\cos\theta)^2\epsilon^L_{+1}+N_0\sin^2\theta\epsilon^U_0+N^U(1+\cos\theta)^2\epsilon^U_{-1}+N^L(1+\cos\theta)^2\epsilon^L_{-1}d\cos\theta$$

where

$$\begin{aligned} \epsilon^U_{+1} &= \epsilon^U_1+\delta^U_1 \\ \epsilon^U_{-1} &= \epsilon^U_1-\delta^U_1 \\ \epsilon^L_{+1} &= \epsilon^L_1+\delta^L_1 \\ \epsilon^L_{-1} &= \epsilon^L_1-\delta^L_1 \end{aligned}$$

$$\begin{aligned} = \int_{-1}^{1} & N^U(1-\cos\theta)^2(\epsilon^U_1+\delta^U_1)+N^L(1-\cos\theta)^2(\epsilon^L_1+\delta^L_1)+N_0\sin^2\theta\epsilon^U_0+N^U(1+\cos\theta)^2(\epsilon^U_1-\delta^U_1) \\ & +N^L(1+\cos\theta)^2(\epsilon^L_1-\delta^L_1)d\cos\theta \end{aligned}$$

Split this expression into two terms; one is magnetic field dependent and the other is not

$$\begin{aligned} = & \int_{-1}^{1}(N^U\epsilon^U_1+N^L\epsilon^L_1)(1-\cos\theta)^2+N_0\sin^2\theta\epsilon^U_0+(N^U\epsilon^U_{-1}+N^L\epsilon^L_{-1})(1+\cos\theta)^2d\cos\theta \\ & +\int_{-1}^{1}N^U\delta^U_1[(1-\cos\theta)^2-(1+\cos\theta)^2]+N^L\delta^L_1[(1-\cos\theta)^2-(1+\cos\theta)^2]d\cos\theta \end{aligned}$$

The first integral contains the field independent terms. The second integral contains the field dependent terms. Right now we are only concerned with the field dependent terms and will evaluate this term more closely

$$\int_{-1}^{1}N^U\delta^U_1[(1-\cos\theta)^2-(1+\cos\theta)^2]+N^L\delta^L_1[(1-\cos\theta)^2-(1+\cos\theta)^2]d\cos\theta$$

$$= \int_{-1}^{1}N^U\delta^U_1(-4\cos\theta)+N^L\delta^L_1(-4\cos\theta)d\cos\theta$$

where recall that all δ terms have $\cos\theta$ dependence. Explicitly consider this dependence for a moment as we integrate.

$$= \int_{-1}^{1}N^U\delta^U_1(-4\cos^2\theta)+N^L\delta^L_1(-4\cos^2\theta)d\cos\theta$$

$$
\begin{aligned}
&= -4N^U\delta_1^U\frac{x^3}{3}\Big|_{-1}^{1} - 4N^L\delta_1^L\frac{x^3}{3}\Big|_{-1}^{1} \\
&= -\frac{4N^U\delta_1^U}{3}(2) - \frac{4N^L\delta_1^L}{3}(2) \\
&= -\frac{8}{3}(N^U\delta_1^U + N^L\delta_1^L)
\end{aligned}
$$

The numerator can be expressed as $A-\frac{8}{3}(N^U\delta_1^U+N^L\delta_1^L)$ where A contains all the field independent terms lumped together for convenience. Evaluate the denominator now

$$
\begin{aligned}
&= \int_{-1}^{1} C_1^U + C_1^L + C_0^U + C_{-1}^U + C_{-1}^L d\cos\theta \\
&= \int_{-1}^{1} N^U[(1-\cos\theta)^2 + (1+\cos\theta)^2] + N^L[(1-\cos\theta)^2 + (1+\cos\theta)^2] + N_0\sin^2\theta \\
&= \int_{-1}^{1} 2N^U(1+\cos^2\theta) + 2N^L(1+\cos^2\theta) + N_0\sin^2\theta d\cos\theta \\
&= \int_{-1}^{1} 2(N^U+N^L)(1+\cos^2\theta) + N_0(1-\cos^2\theta)d\cos\theta \\
&= 2(N^U+N^L)\int_{-1}^{1}(1+x^2)dx + N_0\int_{-1}^{1}(1-x^2)dx \\
&= 2(N^U+N^L)\left(2+\frac{x^3}{3}\Big|_{-1}^{1}\right) + N_0\left(2-\frac{x^3}{3}\Big|_{-1}^{1}\right) \\
&= \frac{16}{3}(N^U+N^L) + \frac{4}{3}N_0
\end{aligned}
$$

combining numerator and denominator

$$\Delta = \frac{A-\frac{8}{3}(N^U\delta_1^U+N^L\delta_1^L)}{\frac{16}{3}(N^U+N^L)+\frac{4}{3}N_0} \tag{H.7}$$

$$\Delta = \Delta_0 + \Delta_+ \tag{H.8}$$

where

$$\Delta_0 = \frac{A}{\frac{16}{3}(N^U+N^L)+\frac{4}{3}N_0} \tag{H.9}$$

$$\Delta_+ = \frac{-\frac{8}{3}(N^U\delta_1^U+N^L\delta_1^L)}{\frac{16}{3}(N^U+N^L)+\frac{4}{3}N_0} \tag{H.10}$$

Putting everything together

$$A_+(\epsilon) = \frac{A}{\sqrt{2\pi}\sigma}e^{-\frac{[\epsilon-(\Delta_0+\Delta_+)]^2}{2\sigma^2}}\int_{-1}^{1} C_1^U + C_1^L + C_0^U + C_{-1}^U + C_{-1}^L d\cos\theta$$

Call integral term "C"

$$A_+(\epsilon) = \frac{AC}{\sqrt{2\pi}\sigma}e^{-\frac{[\epsilon-(\Delta_0+\Delta_+)]^2}{2\sigma^2}}$$

Do the same for $A_-(\epsilon)$. I will skip all of the steps and move on to the determination of Δ_-.

$$\Delta = \frac{\int C_1^U \epsilon_{+1}^U + C_1^L \epsilon_{+1}^L + C_0^U \epsilon_0^U + C_{-1}^U \epsilon_{-1}^U + C_{-1}^L \epsilon_{-1}^L d\cos\theta}{\int (C_1^U + C_1^L + C_0^U + C_{-1}^U + C_{-1}^L) d\cos\theta}$$

where

$$\begin{aligned} C^U{}_1 &= N^U(1+\cos\theta)^2 \\ C_{-1}^U &+ N^U(1-\cos\theta)^2 \\ C^L{}_1 &= N^L(1+\cos\theta)^2 \\ C_{-1}^L &= N^L(1-\cos\theta)^2 \\ C^U{}_0 &= N_0 \sin^2\theta \end{aligned}$$

and

$$N_0 = \frac{4}{3} K P^2$$

Numerator

$$\begin{aligned} &= \int_{-1}^{1} C_1^U \epsilon_{+1}^U + C_1^L \epsilon_{+1}^L + C_0^U \epsilon_0^U + C_{-1}^U \epsilon_{-1}^U + C_{-1}^L \epsilon_{-1}^L d\cos\theta \\ &= \int_{-1}^{1} C_1^U(\epsilon_1^U + \delta_1^U) + C_1^L(\epsilon_1^L + \delta_1^L) + C_0^U \epsilon_0^U + C_{-1}^U(\epsilon_1^U - \delta_1^U) + C_{-1}^L(\epsilon_1^L - \delta_1^L) \end{aligned}$$

Just look at field dependent terms

$$\begin{aligned} &= \int_{-1}^{1} C_1^U \delta_1^U + C_1^L \delta_1^L - C_{-1}^U \delta_1^U - C_{-1}^L \delta_1^L d\cos\theta \\ &= \int_{-1}^{1} N^U(1+\cos\theta)^2\delta_1^U + N^L(1+\cos\theta)^2\delta_1^L - N^U(1-\cos\theta)^2\delta_1^U - N^L(1-\cos\theta)^2\delta_1^L d\cos\theta \\ &= \int_{-1}^{1} N^U\delta_1^U[(1+\cos\theta)^2 - (1-\cos\theta)^2] + N^L\delta_1^L[(1+\cos\theta)^2 - (1-\cos\theta)^2] d\cos\theta \\ &= \int_{-1}^{1} N^U\delta_1^U(4\cos\theta) + N^L\delta_1^L(4\cos\theta) d\cos\theta \end{aligned}$$

Consider δ explicit $\cos\theta$ dependence

$$\begin{aligned} &= \int_{-1}^{1} N^U\delta_1^U(4\cos^2\theta) + N^L\delta_1^L(4\cos^2\theta) d\cos\theta \\ &= 4(N^U\delta_1^U + N^L\delta_1^L)\int_{-1}^{1} \cos^2\theta d\cos\theta \\ &= 4(N^U\delta_1^U + N^L\delta_1^L)\left.\frac{x^3}{3}\right|_{-1}^{1} \\ &= \frac{8}{3}(N^U\delta_1^U + N^L\delta_1^L) \end{aligned}$$

The numerator is

$$A + \frac{8}{3}(N^U\delta_1^U + N^L\delta_1^L)$$

Our expression for Δ is

$$\Delta = \Delta_0 + \Delta_-$$

where

$$\begin{aligned} \Delta_0 &= \frac{A}{\frac{16}{3}(N^U + N^L) + \frac{4}{3}N_0} \\ \Delta_- &= \frac{\frac{8}{3}(N^U\delta_1^U + N^L\delta_1^L}{\frac{16}{3}(N^U + N^L) + \frac{4}{3}N_0} \end{aligned} \tag{H.11}$$

We obtain the expression for $A_-(\epsilon)$

$$A_-(\epsilon) = \frac{AC}{\sqrt{2\pi}\sigma} e^{\frac{-|\epsilon-(\Delta_0+\Delta_-)|^2}{2\sigma^2}}$$

Combine both $A_-(\epsilon)$ and $A_+(\epsilon)$ to obtain the MCD signal

$$\begin{aligned} MCD(\epsilon) &= A_-(\epsilon) - A_+(\epsilon) \\ &= \frac{AC}{\sqrt{2\pi}\sigma}\left(e^{-\frac{|\epsilon-(\Delta_0+\Delta_-)|^2}{2\sigma^2}} - e^{-\frac{|\epsilon-(\Delta_0+\Delta_+)|^2}{2\sigma^2}}\right) \end{aligned} \tag{H.12}$$

Expand both exponents and recall that $\sigma \gg \Delta_\pm$

$$-\frac{(\epsilon-\Delta_0)^2}{2\sigma^2} + \frac{(\epsilon-\Delta_0)\Delta_+}{\sigma^2} - \frac{\Delta_+^2}{2\sigma^2}$$

$$-\frac{(\epsilon-\Delta_0)^2}{2\sigma^2} + \frac{(\epsilon-\Delta_0)\Delta_-}{\sigma^2} - \frac{\Delta_-^2}{2\sigma^2}$$

$$\begin{aligned} &= \frac{AC}{\sqrt{2\pi}\sigma}\left(e^{-\frac{(\epsilon-\Delta_0)^2}{2\sigma^2}+\frac{(\epsilon-\Delta_0)\Delta_-}{\sigma^2}} - e^{-\frac{(\epsilon-\Delta_0)^2}{2\sigma^2}+\frac{(\epsilon-\Delta_0)\Delta_+}{\sigma^2}}\right) \\ &= \frac{AC}{\sqrt{2\pi}\sigma} e^{-\frac{(\epsilon-\Delta_0)^2}{2\sigma^2}}\left(e^{\frac{(\epsilon-\Delta_0)\Delta_-}{\sigma^2}} - e^{\frac{(\epsilon-\Delta_0)\Delta_+}{\sigma^2}}\right) \end{aligned}$$

Make approximation for exponential

$$\begin{aligned} &= \frac{AC}{\sqrt{2\pi}\sigma} e^{-\frac{(\epsilon-\Delta_0)^2}{2\sigma^2}}\left(1 + \frac{(\epsilon-\Delta_0)\Delta_-}{\sigma^2} - (1 + \frac{(\epsilon-\Delta_0)\Delta_+}{\sigma^2})\right) \\ &= \frac{AC}{\sqrt{2\pi}\sigma} e^{-\frac{(\epsilon-\Delta_0)^2}{2\sigma^2}} \frac{(\epsilon-\Delta_0)}{\sigma^2}(\Delta_- - \Delta_+) \\ MCD(\epsilon) &= \frac{AC}{\sqrt{2\pi}\sigma} e^{-\frac{(\epsilon-\Delta_0)^2}{2\sigma^2}} \frac{(\epsilon-\Delta_0)}{\sigma^2}(\Delta_- - \Delta_+) \end{aligned} \tag{H.13}$$

where

$$(\Delta_- - \Delta_+) = \frac{(N^U\delta_1^U + N^L\delta_1^L)}{(N^U + N^L + \frac{1}{4}N_0)} \tag{H.14}$$

Bibliography

[1] L. E. Brus, J. Chem. Phys. **80**, 4403 (1984).

[2] L. E. Brus, Appl. Phys. A **53**, 465 (1991).

[3] A. P. Alivisatos, Science **16**, 933 (1996), review.

[4] A. P. Alivisatos, J. Phys. Chem. **100**, 13226 (1996), review.

[5] V. Colvin, M. Schlamp, and A. P. Alivisatos, Nature **370**, 354 (1994).

[6] B. O. Dabbousi, M. G. Bawendi, O. Onitsuka, and M. F. Rubner, Appl. Phys. Lett. **66**, 1316 (1995).

[7] H. Mattoussi et al., J. Appl. Phys. , in press.

[8] J. D. Berger et al., Phys. Rev. B **55**, 4910 (1997).

[9] D. L. Klein, R. Roth, A. K. L. Lim, A. P. Alivisatos, and P. L. McEuen, Nature **389**, 699 (1997).

[10] D. L. Klein, P. L. McEuen, J. E. B. Katari, R. Roth, and A. P. Alivisatos, Appl. Phys. Lett. **68**, 2575 (1996).

[11] W. Hoheisel, V. L. Colvin, C. S. Johnson, and A. P. Alivisatos, J. Chem. Phys. **101**, 8455 (1994).

[12] D. J. Norris, A. Sacra, C. B. Murray, and M. G. Bawendi, Phys. Rev. Lett. **72**, 2612 (1994).

[13] M. Nirmal, C. B. Murray, and M. G. Bawendi, Phys. Rev. B **50**, 2293 (1994).

[14] A. Sacra, D. J. Norris, C. B. Murray, and M. G. Bawendi, J. Chem. Phys. **103**, 5236 (1995).

[15] A. I. Ekimov et al., J. Opt. Soc. Am. B **10**, 100 (1993).

[16] R. Dingle, Advances in Solid State Physics , 21 P.W. (1975).

[17] A. Harstein and A. Fowler, Proceedings of the Thirteenth International Conference on the Physics of Semiconductors , 741 (1976).

[18] J. Tersoff and R. M. Tromp, Phys. Rev. Lett. **70**, 2782 (1993).

[19] S. Tsukamoto, Y. Nagamune, M. Nishioka, and Y. Arakawa, Appl. Phys. Lett. **62**, 49 (1993).

[20] P. L. McEuen, Science **278**, 1729 (1997).

[21] A. I. Ekimov, A. A. Onushchenko, and V. A. Tsekhomskii, Fiz. Khim. Stekla **6**, 511 (1980).

[22] A. Ekimov, J. Luminescence **70**, 1 (1996), review.

[23] A. I. Ekimov and A. A. Onushchenko, Sov. Phys. Semicond. **16**, 775 (1982).

[24] A. I. Ekimov and A. A. Onushchenko, JETP Lett. **34**, 345 (1981).

[25] C. T. Dameron et al., Nature **338**, 596 (1989).

[26] M. L. Steigerwald et al., J. Am. Chem. Soc. **110**, 3046 (1988).

[27] L. Levy, N. Feltin, D. Ingert, and M. Pileni, J. Phys. Chem. B **101**, 9153 (1997).

[28] A. Zrenner et al., Phys. Rev. Lett. **72**, 3382 (1994).

[29] C. W. Snyder, B. G. Orr, and H. Munekata, Appl. Phys. Lett. **62**, 46 (1993).

[30] S. Fafard, D. Leonard, J. L. Merz, and P. M. Petroff, Appl. Phys. Lett. **65**, 1388 (1994).

[31] D. Leonard, M. Krishnamurthy, C. M. Reaves, S. P. Denbaars, and P. M. Petroff, Appl. Phys. Lett. **63**, 3203 (1993).

[32] C. B. Murray, D. J. Norris, and M. G. Bawendi, J. Am. Chem. Soc. **115**, 8706 (1993).

[33] L. R. Becerra, C. B. Murray, R. G. Griffin, and M. G. Bawendi, J. Chem. Phys. **100**, 3297 (1994).

[34] M. Kuno, J. K. Lee, B. O. Dabbousi, F. V. Mikulec, and M. G. Bawendi, J. Chem. Phys. **106**, 9869 (1997).

[35] A. N. Goldstein, C. M. Echer, and A. P. Alivisatos, Science **256**, 1425 (1992).

[36] S. H. Tolbert and A. P. Alivisatos, Science **265**, 373 (1994).

[37] A. C. Carter et al., Phys. Rev. B **55**, 13822 (1997).

[38] Y. Wang, N. Herron, K. Moller, and T. Bein, Solid State Commun. **77**, 33 (1991).

[39] N. F. Borrelli, D. W. Hall, H. J. Holland, and D. W. Smith, J. Appl. Phys. **61**, 5399 (1987).

[40] A. Fojtik, H. Weller, U. Koch, and A. Henglein, Ber. Bunsenges. Phys. Chem. **88**, 969 (1984).

[41] A. Eychmuller, A. Hasselbarth, L. Katsikas, and H. Weller, Ber. Bunsenges. Phys. Chem. **95**, 79 (1991).

[42] H. Weller, A. Fojtik, and A. Henglein, Chemical Physics Letters **117**, 485 (1985).

[43] L. Spanhel, M. Haase, H. Weller, and A. Henglein, J. Am. Chem. Soc. **109**, 5649 (1987).

[44] M. O'Neil, J. Marohn, and G. McLendon, J. Phys. Chem. **94**, 4356 (1990).

[45] T. Dannhauser, M. O'Neil, K. Johansson, D. Whitten, and G. McLendon, J. Phys. Chem. **90**, 6074 (1986).

[46] Y. Wang and N. Herron, J. Phys. Chem. **91**, 257 (1987).

[47] N. Chestnoy, T. D. Harris, R. Hull, and L. E. Brus, J. Phys. Chem. **90**, 3393 (1986).

[48] S. Flugge, Practical Quantum Mechanics, page 155, Berlin, 1971, Springer.

[49] A. L. Efros and A. L. Efros, Sov. Phys. Semicond. **16**, 772 (1982).

[50] L. Banyai and S. W. Koch, *Semiconductor Quantum Dots*, chapter 1, World Scientific, 1993.

[51] G. B. Grigoryan, E. M. Kazaryan, A. L. Efros, and T. V. Yazeva, Sov. Phys. Solid State **32**, 1031 (1990).

[52] A. L. Efros, Phys. Rev. B **46**, 7448 (1992).

[53] M. I. Dyakonov and V. I. Perel, Theory of Optical Spin Orientation of Electrons and Nuclei in Semiconductors, in *Optical Orientation*, edited by F. Meier and B. P. Zakharchenya, number 8, page 11, Amsterdam, 1984, Elsevier.

[54] E. O. Kane, J. Chem. Phys. Solids **1**, 249 (1957).

[55] P. D. J. Calcott, K. J. Nash, L. T. Canham, M. J. Kane, and D. Brumhead, J. Phys. Condens. Matter **5**, L91 (1993).

[56] F. Koch, V. Petrova-Koch, and T. Muschik, J. Luminescence **57**, 271 (1993).

[57] V. Petrova-Koch et al., Appl. Phys. Lett. **61**, 943 (1992).

[58] F. Koch et al., in *Proc. 21st Int. Conf. Phys. Semicond.*, page 1483, Singapore, 1993, World Scientific.

[59] F. Koch et al., Mater. Res. Soc. Symp. Proc. **283**, 197 (1993).

[60] M. G. Bawendi et al., Phys. Rev. Lett. **65**, 1623 (1990).

[61] M. G. Bawendi, P. J. Carroll, W. L. Wilson, and L. E. Brus, J. Chem. Phys. **96**, 946 (1992).

[62] D. J. Norris and M. G. Bawendi, J. Chem. Phys. **103**, 5260 (1995).

[63] M. Nirmal et al., Phys. Rev. Lett. **75**, 3728 (1995).

[64] A. L. Efros et al., Phys. Rev. B **54**, 4843 (1996).

[65] A. Hasselbarth, A. Eychmuller, and H. Weller, Chem. Phys. Lett. **203**, 271 (1993).

[66] O. I. Micic, J. Sprague, Z. Lu, and A. J. Nozik, Appl. Phys. Lett. **68**, 3150 (1996).

[67] O. I. Micic et al., J. Phys. Chem. B **101**, 4904 (1997).

[68] O. I. Micic, C. J. Curtis, K. M. Jones, J. R. Sprague, and A. J. Nozik, J. Phys. Chem. **98**, 4966 (1994).

[69] O. I. Micic and A. J. Nozik, J. Luminescence **70**, 95 (1996), review.

[70] M. Grundmann et al., Phys. Rev. Lett. **74**, 4043 (1995).

[71] B. K. Meyer et al., Appl. Phys. Lett. **63**, 1930 (1993).

[72] B. K. Meyer et al., Appl. Phys. Lett. **63**, 2120 (1993).

[73] J. R. Sachleben et al., Chem. Phys. Lett. **198**, 431 (1992).

[74] J. E. B. Katari, V. L. Colvin, and A. P. Alivisatos, J. Phys. Chem. **98**, 4109 (1994).

[75] H. Lu and A. Zunger, Phys. Rev. B , submitted.

[76] Y. R. Wang and C. B. Duke, Phys. Rev. B **37**, 6417 (1988).

[77] T. Richard, P. Lefebvre, H. Mathieu, and J. Allegre, Phys. Rev. B **53**, 7287 (1996).

[78] K. Leung, S. Pokrant, and K. B. Whaley, Phys. Rev. B **57**, 12291 (1998).

[79] K. J. Nash, P. D. J. Calcott, L. T. Canham, and R. J. Needs, Phys. Rev. B **51**, 17698 (1995).

[80] U. Woggon, O. Wind, F. Gindele, E. Tsitsishvili, and M. Muller, J. Luminescence **70**, 269 (1996), review.

[81] U. Woggon, F. Gindele, O. Wind, and C. Klingshirn, Phys. Rev. B **54**, 1506 (1996).

[82] M. Chamarro, C. Gourdon, P. Lavallard, O. Lublinskaya, and A. I. Ekimov, Phys. Rev. B **53**, 1336 (1996).

[83] M. Chamarro, C. Gourdon, and P. Lavallard, J. Luminescence **70**, 223 (1996), review.

[84] M. Chamarro, C. Gourdon, P. Lavallard, and A. I. Ekimov, Jpn. J. Appl. Phys. **34** (1995).

[85] M. Chamarro, C. Gourdon, P. Lavallard, O. Lublinskaya, and A. I. Ekimov, Il Nuovo Cimento **17** (1995).

[86] P. D. J. Calcott, K. J. Nash, L. T. Canham, M. J. Kane, and D. Brumhead, J. Luminescence **57**, 257 (1993).

[87] S. Nomura, Y. Segawa, and T. Kobayashi, Phys. Rev. B **49**, 13571 (1994).

[88] T. Vossmeyer et al., J. Phys. Chem. **98**, 7665 (1994).

[89] J. R. Heath, C. M. Knobler, and D. V. Leff, J. Phys. Chem. B **101**, 189 (1997).

[90] R. L. Whetten et al., Advanced materials **8**, 428 (1996).

[91] D. P. Dinega and M. G. Bawendi, unpublished.

[92] S. Sun and C. B. Murray, unpublished.

[93] C. B. Murray, C. R. Kagan, and M. G. Bawendi, Science **270**, 1335 (1995).

[94] C. R. Pidgeon and R. N. Brown, Phys. Rev. **146**, 575 (1966).

[95] R. L. Aggarwal, Modulation Techniques, Number 9 in Semiconductors and Semimetals, page 151, New York, 1974, Academic Press.

[96] D. J. Norris and M. G. Bawendi, Phys. Rev. B **53**, 16338 (1996).

[97] A. I. Ekimov, Physica Scripta **39**, 217 (1991).

[98] P. A. M. Rodrigues, G. Tamulaitis, P. Y. Yu, and S. H. Risbud, Solid State Commun. **94**, 583 (1995).

[99] J. B. Stark, W. H. Knox, and D. S. Chemla, Phys. Rev. B **46**, 7919 (1992).

[100] J. M. Luttinger and W. Kohn, Phys. Rev. **97**, 869 (1955).

[101] A. I. Ekimov, A. A. Onushchenko, A. G. Plukhin, and A. L. Efros, Sov. Phys. JETP **61**, 891 (1985).

[102] J. B. Xia, Phys. Rev. B **40**, 8500 (1989).

[103] K. J. Vahala and P. C. Sercel, Phys. Rev. Lett. **65**, 239 (1990).

[104] P. C. Sercel and K. J. Vahala, Phys. Rev. B **42**, 3690 (1990).

[105] A. L. Efros and A. V. Rodina, Solid State Commun. **72**, 645 (1989).

[106] G. L. Bir and G. E. Pikus, in *Symmetry and Strain-Induced Effects in Semiconductors*, New York, 1975, Wiley.

[107] A. L. Efros and A. V. Rodina, Phys. Rev. B **47**, 10005 (1993).

[108] L. E. Brus, unpublished.

[109] E. I. Rashba, Sov. Phys. JETP **9**, 1213 (1959).

[110] V. P. Kochereshko, G. V. Mikhailov, and I. N. Ural'tsev, Sov. Phys. Solid State **25**, 439 (1983).

[111] W. W. Piper, Proc. 7th Int. Conf. II-VI Semicond. Comp. , 839 (1967), Providence, R. I.

[112] B. L. Gel'mont and M. I. D'yakonov, Sov. Phys. Semicond. **7**, 1345 (1974).

[113] L. D. Landau and E. M. Lifshitz, *Relativistic Quantum Theory*, Pergamon Press, 1965.

[114] T. Itoh, M. Nishijima, A. I. Ekimov, A. L. Efros, and M. Rosen, Phys. Rev. Lett **74**, 1645 (1995).

[115] S. Nomura et al., J. Luminescence **70**, 144 (1996), review.

[116] M. C. Klein, F. Hache, D. Ricard, and C. Flytzanis, Phys. Rev. B **42**, 11123 (1990).

[117] M. Nirmal, C. B. Murray, D. J. Norris, and M. G. Bawendi, Z. Phys. D **26**, 361 (1993).

[118] D. J. Norris, A. L. Efros, M. Rosen, and M. G. Bawendi, Phys. Rev. B **53**, 16347 (1996).

[119] S. Schmitt-Rink, D. A. B. Miller, and D. S. Chemla, Phys. Rev. B **35**, 8113 (1987).

[120] T. Takagahara, Phys. Rev. B **47**, 4569 (1993).

[121] J. J. Shiang, S. H. Risbud, and A. P. Alivisatos, J. Chem. Phys. **98**, 8432 (1993).

[122] J. J. Shiang, R. K. Grubbs, and A. P. Alivisatos, submitted.

[123] J. J. Shiang, A. P. Alivisatos, and K. B. Whaley, submitted.

[124] A. L. Efros, Phonons in Semiconductor Nanostructures, page 299, Boston-London, 1993, Kluwer Academic Publishers.

[125] D. J. Norris, M. Nirmal, A. Sacra, C. B. Murray, and M. G. Bawendi, Z. Phys. D **26**, 355 (1993).

[126] J. M. Luttinger, Phys. Rev. **102**, 1030 (1956).

[127] G. Dresselhaus, A. F. Kip, and C. Kittel, Phys. Rev. **98**, 368 (1955).

[128] A. P. Alivisatos, A. L. Harris, N. J. Levinos, M. L. Steigerwald, and L. E. Brus, J. Chem. Phys. **89**, 4001 (1988).

[129] E. F. Hilinski, P. A. Lucas, and Y. Wang, J. Chem. Phys. **89**, 3435 (1988).

[130] N. Peyghambarian et al., IEEE J. Quantum Electronics , 2516 (1989).

[131] P. Roussignol, D. Ricard, C. Flytzanis, and N. Neuroth, Phys. Rev. Lett. **62**, 312 (1989).

[132] U. Woggon, S. Gaponenko, W. Langbein, A. Uhrig, and C. Klingshirn, Phys. Rev. B **47**, 3684 (1993).

[133] D. M. Mittleman et al., Phys. Rev. B **49**, 14435 (1994).

[134] M. E. Schmidt, S. A. Blanton, M. A. Hines, and P. Guyot-Sionnest, Phys. Rev. B **53**, 12629 (1996).

[135] S. A. Majetich, A. C. Carter, J. Belot, and R. D. McCullough, J. Phys. Chem. **98**, 13705 (1994).

[136] S. A. Majetich and A. C. Carter, J. Phys. Chem. **97**, 8727 (1993).

[137] H. Mattoussi, A. W. Cumming, C. B. Murray, M. G. Bawendi, and R. Ober, J. Chem. Phys. **105**, 9890 (1996).

[138] H. Mattoussi, A. W. Cumming, C. B. Murray, M. G. Bawendi, and R. Ober, submitted.

[139] M. Danek, K. F. Jensen, C. B. Murray, and M. G. Bawendi, J. Cryst. Growth **145**, 714 (1994).

[140] M. Hines and P. Guyot-Sionnest, J. Phys. Chem. **100**, 468 (1996).

[141] B. O. Dabbousi et al., J. Phys. Chem. B **101**, 9463 (1997).

[142] M. G. B. Drew, D. A. Rice, and D. M. Williams, Inorganica Chimica Acta **118**, 165 (1986).

[143] M. Kolosky, J. Vialle, and T. Cotel, J. Chromatography **299**, 436 (1984).

[144] P. A. W. Dean, Can. J. Chem. **59**, 3221 (1981).

[145] P. A. W. Dean and M. K. Hughes, Can. J. Chem. **58**, 180 (1980).

[146] M. A. Marcus et al., Nanostruc. Mater. **1**, 323 (1992).

[147] G. E. Maciel and R. V. James, Inorg. Chem. **3**, 1650 (1964).

[148] A. R. Kortan et al., J. Am. Chem. Soc. **112**, 1327 (1990).

[149] C. F. Hoener et al., J. Phys. Chem. **96**, 3812 (1992).

[150] A. Eychmuller, A. Mews, and H. Weller, Chem. Phys. Lett. **208** (1993).

[151] A. Hasselbarth et al., J. Phys. Chem. **97**, 5333 (1993).

[152] M. Danek, K. F. Jensen, C. B. Murray, and M. G. Bawendi, Appl. Phys. Lett. **65**, 2795 (1994).

[153] Y. Tian, T. Newton, N. A. Kotov, D. M. Guldi, and J. H. Fendler, J. Phys. Chem. **100**, 8927 (1996).

[154] L. Saviot, B. Champagnon, E. Duval, I. A. Kudriavtsec, and A. I. Ekimov, J. Non-Cryst. Solids **238**, 1996 (197).

[155] E. Roca, C. Trallero-Giner, and M. Cardona, Phys. Rev. B **49**, 13704 (1994).

[156] W. S. O. Rodden, C. M. S. Torres, and C. N. Ironside, Semicond. Sci. Technol. **10**, 807 (1995).

[157] D. Bersani and P. P. Lottici, Phys. Status. Solidi B **174**, 575 (1992).

[158] I. H. Campbell and P. M. Fauchet, Solid State Commun. **58**, 739 (1986).

[159] H. Richter, Z. P. Wang, and L. Ley, Solid State Commun. **39**, 625 (1981).

[160] S. W. Koch, Y. Z. Hu, B. Fluegel, and N. Peyghambarian, J. Cryst. Growth **117**, 592 (1992).

[161] Y. Z. Hu, M. Lindberg, and S. W. Koch, Phys. Rev. B **42**, 1713 (1990).

[162] R. Romestain and G. Fishman, Phys. Rev. B **49**, 1774 (1994).

[163] Y. Chen et al., Excitons in Confined Systems, page 200, New York, 1987, Springer Verlag.

[164] S. A. Empedocles, D. J. Norris, and M. G. Bawendi, Phys. Rev. Lett. **77**, 3873 (1996).

[165] S. Nomura et al., Jpn. J. Appl. Phys. **34** (1995).

[166] S. Nomura, Y. Segawa, and T. Kobayashi, Solid State Commun. **87**, 313 (1993).

[167] K. Ando, Y. Yamada, and V. A. Shakin, Phys. Rev. B **47**, 13462 (1993).

[168] S. Nomura, K. Misawa, Y. Segawa, and T. Kobayashi, Phys. Rev. B **47**, 16024 (1993).

[169] P. J. Stephens, Ann. Rev. Phys. Chem. **25**, 201 (1974).

[170] A. D. Buckingham and P. J. Stephens, Ann. Rev. Phys. Chem. **17**, 399 (1966).

[171] P. N. Schatz and A. J. McCaffery, Quart. Rev. **23**, 352 (1969).

[172] R. G. Wheeler and J. O. Dimmock, Phys. Rev. Lett. **3**, 372 (1959).

[173] R. G. Wheeler and J. O. Dimmock, Phys. Rev. **125**, 1805 (1962).

[174] D. C. Reynolds, C. W. Litton, and T. C. Collins, Phys. Rev. **156**, 881 (1967).

[175] C. H. Henry, K. Nassau, and J. W. Shiever, Phys. Rev. B **4**, 2453 (1971).

[176] H. Venghaus, S. Suga, and K. Cho, Phys. Rev. B **16**, 4419 (1977).

[177] J. Donecker and J. Kluge, Phys. Stat. Sol. B **81**, 199 (1977).

[178] M. A. Chamarro, C. Gourdon, and P. Lavallard, Semicond. Sci. Technol. **8**, 1868 (1993).

[179] W. Heller and U. Bockelmann, Phys. Rev. B **55**, 4871 (1997).

[180] N. J. Traynor, R. T. Harley, and R. J. Warburton, Phys. Rev. B **51**, 7361 (1995).

[181] D. M. Hofmann, K. Oettinger, A. L. Efros, and B. K. Meyer, Phys. Rev. B **55**, 9924 (1997).

[182] T. Wimbauer, K. Oettinger, A. L. Efros, B. K. Meyer, and H. Brugger, Phys. Rev. B **50**, 8889 (1994).

[183] M. J. Snelling et al., Phys. Rev. B **44**, 11345 (1991).

[184] K. Zhu and T. Kobayashi, Solid State Commun. **92**, 353 (1994).

[185] M. Kuno, M. Nirmal, M. G. Bawendi, A. L. Efros, and M. Rosen, J. Chem. Phys. **108**, 4242 (1998).

[186] T. Trindade, P. O'Brien, and X. Zhang, Chem. Mater. **9**, 523 (1997).

[187] S. Dhingra, K.-W. Kim, and M. G. Kanatzidis, Mat. Res. Soc. Symp. Proc. **204**, 163 (1991).

[188] K.-W. Kim, J. A. Cowen, S. Dhingra, and M. Kanatzidis, Mat. Res. Soc. Symp. Proc. **272**, 27 (1992).

[189] K. Yanata, K. Su i, and Y. Oka, J. Appl. Phys. **73**, 4595 (1993).

[190] R. N. Bhargava, D. Gallagher, X. Hong, and A. Nurmikko, Phys. Rev. Lett. **72**, 416 (1994).

[191] R. N. Bhargava, D. Gallagher, and T. Welker, J. Luminescence **60** (1994).

[192] D. Gallagher, W. E. Heady, J. M. Racz, and R. N. Bhargava, J. Cryst. Growth **138**, 970 (1994).

[193] K. Yanata and Y. Oka, Jpn. J. Appl. Phys. **34** (1995).

[194] R. J. Bandaranayake, M. Smith, J. Y. Lin, H. X. Jiang, and C. M. Sorensen, IEEE Trans. on Magnetics **30**, 4930 (1994).

[195] K. Sooklal, B. S. Cullum, S. M. Angel, and C. J. Murphy, J. Phys. Chem. **100**, 4551 (1996).

[196] L. Levy, J. F. Hochepied, and M. P. Pileni, J. Phys. Chem. **100**, 18322 (1996).

[197] G. Counio, S. Esnouf, T. Gacoin, and J.-P. Boilot, J. Phys. Chem. **100**, 20021 (1996).

[198] J. K. Furdyna, J. Appl. Phys. **64** (1988).

[199] D. D. Awschalom, J. M. Hong, L. L. Chang, and G. Grinstein, Phys. Rev. Lett. **59**, 1733 (1987).

[200] R. N. Bhargava, J. Luminescence **70**, 85 (1996), review.

[201] A. K. Bhattacharjee, Phys. Rev. B **51**, 9912 (1995).

[202] R. D. Closson, J. Kozikowski, and T. H. Coffield, J. Org. Chem. **22**, 598 (1957).

[203] M. I. Bruce, M. J. Liddell, and G. N. Pain, in *Inorganic Synthesis*, page 171, New York, 1989, Wiley.

[204] M. L. Steigerwald and C. E. Rice, J Am. Chem. Soc. **110**, 4228 (1988).

[205] S. M. Stuczynski, Y. U. Kwon, and M. L. Steigerwald, J. Organomet. Chem. **449**, 167 (1993).

[206] A. P. Coleman et al., Polyhedron **13**, 1277 (1994).

[207] N. Welcman and I. Rot, J. Chem. Soc. , 7515 (1965).

[208] A. Chemseddine, Mat. Res. Soc. Symp. Proc. **346**, 881 (1994).

[209] G. N. Pain et al., J. Cryst. Growth **107**, 632 (1991).

[210] P. J. Wright, B. Cockayne, A. F. Cattell, P. J. Dean, and A. D. Pitt, J. Cryst. Growth **59**, 155 (1982).

[211] R. F. Howe and W. C. Timmer, J. Chem. Phys. **85**, 6129 (1986).

[212] R. F. Howe and M. Gratzel, J. Phys. Chem. **89**, 4495 (1985).

[213] S. Omi et al., J. Non-Cryst. Solids **178**, 129 (1994).

[214] J. Lambe, J. Baker, and C. Kikuchi, Phys. Rev. Lett. **3**, 270 (1959).

[215] R. T. Ross, J. Chem. Phys. **42**, 3919 (1965).

[216] B. T. Allen and D. W. Nebert, J. Chem. Phys. **41**, 1983 (1964).

[217] A. M. Thayer, M. L. Steigerwald, T. M. Duncan, and D. C. Douglass, Phys. Rev. Lett. **60**, 2673 (1988).

[218] V. Ladizhansky, A. Faraggi, V. Lyahovitskaya, and S. Vega, Phys. Rev. B **56**, 6712 (1997).

[219] M. Gavish, S. Vega, and D. Zamir, Phys. Rev. B **48**, 2191 (1993).

[220] F. V. Mikulec et al., unpublished.

[221] J. Antoszewski and E. K. Pecold, Solid State Commun. **34**, 733 (1980).

[222] M. M. Moriwaki, R. Y. Tao, R. R. Galazka, W. M. Becker, and J. W. Richardson.

[223] W. Giriat and J. Stankiewicz, Phys. Stat. Sol. A **59**, K79 (1980).

[224] D. Gallagher, W. E. Heady, J. M. Racz, and R. N. Bhargava, J. Mater. Res. **10**, 870 (1995).

[225] Y. L. Soo et al., Phys. Rev. B **50**, 7602 (1994).

[226] T. A. Kennedy, E. R. Glaser, P. B. Klein, and R. N. Bhargava, submitted , submitted.

[227] T. A. Kennedy, E. R. Glaser, P. B. Klein, and R. N. Bhargava, submitted , submitted.

[228] C. R. Kagan, C. B. Murray, and M. G. Bawendi, Phys. Rev. B **54**, 8633 (1996).

[229] M. Danek, K. F. Jensen, C. B. Murray, and M. G. Bawendi, Chem. of Materials **8**, 173 (1996).

[230] J. Rockenberger et al., J. Phys. Chem. B **101**, 2691 (1997).

Index